Research Topics

Preparation and application of intelligent bioactive nanocolloids

Edited by
Yu Luo, Xin Li, Andrij Pich and Bo Yin

Published in
Frontiers in Bioengineering and Biotechnology

FRONTIERS EBOOK COPYRIGHT STATEMENT

The copyright in the text of individual articles in this ebook is the property of their respective authors or their respective institutions or funders. The copyright in graphics and images within each article may be subject to copyright of other parties. In both cases this is subject to a license granted to Frontiers.

The compilation of articles constituting this ebook is the property of Frontiers.

Each article within this ebook, and the ebook itself, are published under the most recent version of the Creative Commons CC-BY licence. The version current at the date of publication of this ebook is CC-BY 4.0. If the CC-BY licence is updated, the licence granted by Frontiers is automatically updated to the new version.

When exercising any right under the CC-BY licence, Frontiers must be attributed as the original publisher of the article or ebook, as applicable.

Authors have the responsibility of ensuring that any graphics or other materials which are the property of others may be included in the CC-BY licence, but this should be checked before relying on the CC-BY licence to reproduce those materials. Any copyright notices relating to those materials must be complied with.

Copyright and source acknowledgement notices may not be removed and must be displayed in any copy, derivative work or partial copy which includes the elements in question.

All copyright, and all rights therein, are protected by national and international copyright laws. The above represents a summary only. For further information please read Frontiers' Conditions for Website Use and Copyright Statement, and the applicable CC-BY licence.

ISSN 1664-8714
ISBN 978-2-8325-4190-6
DOI 10.3389/978-2-8325-4190-6

About Frontiers

Frontiers is more than just an open access publisher of scholarly articles: it is a pioneering approach to the world of academia, radically improving the way scholarly research is managed. The grand vision of Frontiers is a world where all people have an equal opportunity to seek, share and generate knowledge. Frontiers provides immediate and permanent online open access to all its publications, but this alone is not enough to realize our grand goals.

Frontiers journal series

The Frontiers journal series is a multi-tier and interdisciplinary set of open-access, online journals, promising a paradigm shift from the current review, selection and dissemination processes in academic publishing. All Frontiers journals are driven by researchers for researchers; therefore, they constitute a service to the scholarly community. At the same time, the *Frontiers journal series* operates on a revolutionary invention, the tiered publishing system, initially addressing specific communities of scholars, and gradually climbing up to broader public understanding, thus serving the interests of the lay society, too.

Dedication to quality

Each Frontiers article is a landmark of the highest quality, thanks to genuinely collaborative interactions between authors and review editors, who include some of the world's best academicians. Research must be certified by peers before entering a stream of knowledge that may eventually reach the public - and shape society; therefore, Frontiers only applies the most rigorous and unbiased reviews. Frontiers revolutionizes research publishing by freely delivering the most outstanding research, evaluated with no bias from both the academic and social point of view. By applying the most advanced information technologies, Frontiers is catapulting scholarly publishing into a new generation.

What are Frontiers Research Topics?

Frontiers Research Topics are very popular trademarks of the *Frontiers journals series*: they are collections of at least ten articles, all centered on a particular subject. With their unique mix of varied contributions from Original Research to Review Articles, Frontiers Research Topics unify the most influential researchers, the latest key findings and historical advances in a hot research area.

Find out more on how to host your own Frontiers Research Topic or contribute to one as an author by contacting the Frontiers editorial office: frontiersin.org/about/contact

Preparation and application of intelligent bioactive nanocolloids

Topic editors
Yu Luo — Shanghai University of Engineering Sciences, China
Xin Li — Leibniz Institute for Interactive Materials (DWI), Germany
Andrij Pich — RWTH Aachen University, Germany
Bo Yin — Fudan University, China

Citation
Luo, Y., Li, X., Pich, A., Yin, B., eds. (2024). *Preparation and application of intelligent bioactive nanocolloids*. Lausanne: Frontiers Media SA.
doi: 10.3389/978-2-8325-4190-6

Table of contents

frontiers | Frontiers in Bioengineering and Biotechnology

ORIGINAL RESEARCH
published: 31 May 2022
doi: 10.3389/fbioe.2022.922159

Influence of Colonies' Morphological Cues on Cellular Uptake Capacity of Nanoparticles

Siyuan Huang[1,2†], Qi Su[3†], Xiaoqiang Hou[1,2], Kuankuan Han[1,2], Shufang Ma[1], Bingshe Xu[1]* and Yingjun Yang[1]*

[1]Materials Institute of Atomic and Molecular Science, Shaanxi University of Science and Technology, Xi'an, China, [2]School of Materials Science and Engineering, Shaanxi University of Science and Technology, Xi'an, China, [3]Department of Critical Care Medicine, Shanghai General Hospital, Shanghai Jiao Tong University School of Medicine, Shanghai, China

OPEN ACCESS

Edited by:
Yu Luo,
Shanghai University of Engineering Sciences, China

Reviewed by:
Jingchao Li,
Donghua University, China
Puyang Gong,
Southwest Minzu University, China

Correspondence:
Bingshe Xu
xubingshe@sust.edu.cn
Yingjun Yang
yang.yingjun@sust.edu.cn

†These authors have contributed equally to this work

Specialty section:
This article was submitted to Nanobiotechnology, a section of the journal Frontiers in Bioengineering and Biotechnology

Received: *17 April 2022*
Accepted: *26 April 2022*
Published: *31 May 2022*

Citation:
Huang S, Su Q, Hou X, Han K, Ma S, Xu B and Yang Y (2022) Influence of Colonies' Morphological Cues on Cellular Uptake Capacity of Nanoparticles. Front. Bioeng. Biotechnol. 10:922159. doi: 10.3389/fbioe.2022.922159

High transmembrane delivery efficiency of nanoparticles has attracted substantial interest for biomedical applications. It has been proved that the desired physicochemical properties of nanoparticles were efficient for obtaining a high cellular uptake capacity. On the other hand, biophysical stimuli from *in situ* microenvironment were also indicated as another essential factor in the regulation of cellular uptake capacity. Unfortunately, the influence of colony morphology on cellular uptake capacity was rarely analyzed. In this study, micropatterned PDMS stencils containing circular holes of 800/1,200 μm in diameter were applied to control colonies' size. The amino-modified nanoparticles were cocultured with micropatterned colonies to analyze the influence of colonies' morphology on the cellular uptake capacity of nanoparticles. Consequently, more endocytosed nanoparticles in larger colonies were related with a bigger dose of nanoparticles within a larger area. Additionally, the high cell density decreased the membrane–nanoparticles' contacting probability but enhanced clathrin-mediated endocytosis. With these contrary effects, the cells with medium cell density or located in the peripheral region of the micropatterned colonies showed a higher cellular uptake capacity of nanoparticles.

Keywords: morphological cues, micropattern, cellular uptake, nanoparticles, colony

INTRODUCTION

Recently, various nanoparticles were designed and prepared for biomedical applications (Li et al., 2019; Li et al., 2021; Yang et al., 2021). Efficient cellular uptake of nanoparticles (NPs) is recognized as the prime condition for the achievement of high-yield therapeutic efficacy (Iversen et al., 2011; Liang et al., 2020). Tuning the physicochemical properties of NPs is an approachable route to improving the cellular uptake capacity (Oh and Park, 2014; Li et al., 2021). However, the optimization of NPs' surface properties may lead to the cytotoxicity of NPs (Lewinski et al., 2008). On the other hand, cell–NP interaction and cellular uptake processes were also efficient for the regulation of cellular uptake capacity (Adjei et al., 2014). Therefore, novel techniques depending on the modulation of cell behaviors were required to avoid side effects of NP properties' optimization. Previous evidence demonstrated that the biophysical stimuli from *in situ* microenvironment can be applied to manipulate the cellular uptake process (Huang et al., 2017). It is worth noting that physical boundary conditions were critical in regulating cell behaviors (Yang et al., 2018; Wang et al., 2021a). For instance, the effects of a single cell's morphological cues on cell functions were revealed by

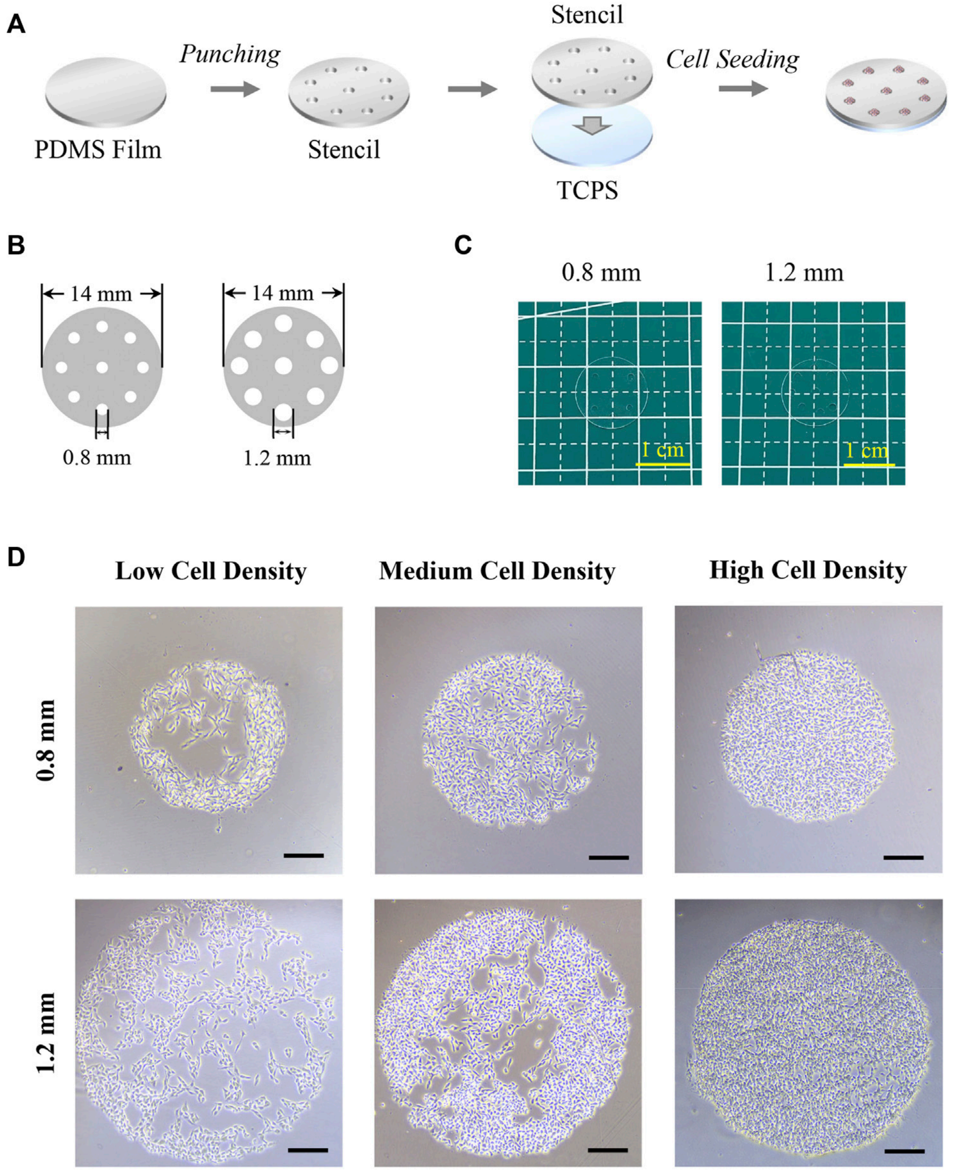

FIGURE 1 | Preparation of PDMS stencils and morphology of micropatterned colonies. **(A)** Scheme of PDMS stencil's preparation and application in cell culture. **(B)** Illustration of PDMS stencils' structure. **(C)** Photography of PDMS stencils. **(D)** Microscopic images of micropatterned melanoma colonies. Scale bar: 200 μm.

micropatterning techniques (Yang et al., 2019b; Wang et al., 2021b). Additionally, the significant influence of spatial factors on colonies' tumorigenesis (Lee et al., 2016; Lee et al., 2020) and gastrulation (Deglincerti et al., 2016; Morgani et al., 2018) has been explored by many studies. All of these results indicated the importance of morphological cues in regulating the functions of a cell or colony. Recently, the relationship between cellular uptake capacity and single cell morphology has been illustrated (Wang et al., 2016; Yang et al., 2019a; Wang et al., 2022). Whereas, in scientific research and clinical practice, a multicellular colony was more common than single-cell status. Unfortunately, even the influence of morphological cues on colonies' behaviors was explained, and their effects on colonies' uptake capacity were still unclear. In this case, elucidating the relationship between colonies' morphological cues and the cellular uptake capacity of NPs will provide some essential information for the improvement of NPs' uptake efficacy through regulating physical boundary conditions.

In this study, the effects of colonies' morphology on the cellular uptake capacity of NPs were investigated by using micropatterned PDMS stencils. The PDMS stencils containing circular micro-holes of 0.8 and 1.2 mm in diameter were prepared to control colonies' size. The melanoma cells with different seeding densities were cultured on the stencils to form micropatterned colonies with different sizes and cell densities. Then, the amino-modified fluorescence polystyrene NPs were incubated with micropatterned colonies to investigate the influence of colonies' morphology on the cellular uptake capacity. Firstly, the distribution of cells and endocytosed NPs in micropatterned colonies was observed and analyzed. To explore the reason for morphological cues affecting cellular uptake capacity, the cell morphology and cytoskeleton structure were also characterized.

MATERIALS AND METHODS

Preparation of PDMS Stencils

The stencils were prepared by a simple punching process. In detail, the PDMS film with 100 μm in thickness was commercially purchased from Hangzhou Bald Advanced Materials Technology Co., Ltd. The PDMS films were firstly cut into a circular shape of 14 mm in diameter. Then, the holes of 0.8 mm or 1.2 mm in diameter were manufactured on the circular PDMS film by using a specific puncher. Before cell seeding, the prepared stencils were firstly sterilized by immersing in 70% ethanol for 20 min and rinsing in PBS solution twice. Finally, the stencils were placed in a 24-well plate for cell culture.

Cell Culture

Melanoma cells (B16) were purchased from Procell Lifer Science & Technology Co., Ltd. and subcultured in DMEM medium (Mishu (Xi'an) Biotechnology Co., Ltd.) supplied with 10% FBS (Biological Industries Israel Beit Haemek Ltd.) and 1% penicillin–streptomycin (Mishu (Xi'an) Biotechnology Co., Ltd.). A 1 ml cell suspension with 4×10^4, 6×10^4, and 8×10^4 cells/ml in cell density was seeded in each well. After being cultured in a humidified CO_2 incubator for 6 h, the medium with suspending cells was refreshed. Then, the samples were further incubated for 18 h for the following experiments.

Nuclei Staining and Cell Density Analysis

After cell seeding for 24 h, the samples were rinsed with prewarmed PBS and fixed with 4% cold paraformaldehyde (Shanghai Aladdin Biochemical Technology Co., Ltd.) for 10 min. Then, the samples were permeabilized by 1% Triton X-100 (Shanghai Aladdin Biochemical Technology Co., Ltd.) for 2 min and stained by 1‰ DAPI (Shandong Sparkjade Scientific Instruments Co., Ltd.) in PBS for 10 min. The fluorescence of DAPI was observed and recorded by a fluorescence microscope (MF52-N, Guangzhou Micro-shot Technology Co., Ltd.). The fluorescence images were applied to analyze cell distribution. To count cells in different regions, the colony was firstly separated into the peripheral region and central region. To get the same area of the peripheral region and central region, the radius of the central region was set as 0.28 mm for micropatterned colonies with 0.8 mm in diameter and 0.42 mm for colonies with 1.2 mm in diameter. The cell numbers at the peripheral or central regions were counted from DAPI staining fluorescence images by analyzing the particles processed in ImageJ. More than 50 fluorescent images were applied to get heat maps, and five representative fluorescence images were analyzed to get quantitative data.

Cellular Uptake Capacity Analysis

After the cell seeding process for 24 h, the medium was replaced by a fresh medium with 1% amino-modified fluorescent PS NPs (100 nm, Xi'an ruixi Biological Technology Co., Ltd.) and further incubated for another 24 h in a humidified CO_2 incubator. Then, the samples were harvested and incubated with 0.4% trypan blue (Shanghai Aladdin Biochemical Technology Co., Ltd.) for 5 min to quench the fluorescence of extracellular NPs. Finally, the samples were fixed with 4% paraformaldehyde and stained with 1‰ DAPI. The fluorescence of NPs and DAPI was observed and recorded by fluorescence microscopy. The percentage and fluorescence intensity of NP-positive cells were calculated to evaluate the cellular uptake capacity. To define NP-positive cells, the integrated gray value (IGV) and area (A) of each cell were calculated by ImageJ. To get the corrected IGV, the region without cell attachment was selected as the background to calculate $IGV_{background}$ and $A_{background}$. Then, the corrected IGV was calculated by $(IGV/A\text{-}IGV_{background}/A_{background}) \times A$. The NP-positive cells were defined as the cells with corrected IGV two times higher than the $IGV_{background}$. The percentage of NP-positive cells was calculated by the number of NP-positive cells divided by the total cell number. The corrected IGV of nanoparticle-positive cells was also recorded to evaluate the cellular uptake capacity. More than 30 fluorescent images of each group were analyzed.

Actin and Nuclei Staining

After cells were cultured within stencils for 24 h, the samples were fixed by 4% paraformaldehyde for 10 min and permeabilized by 1% Triton X-100 for 2 min at room temperature. Then, the samples were blocked with 2% bovine serum albumin (BSA, Shanghai Aladdin Biochemical Technology Co., Ltd.) in PBS for 30 min at room temperature. Then, actin was stained by incubating the samples with Alexa Fluor-594 phalloidin (Beijing Solarbio Science & Technology Co., Ltd.) at a dilution ratio of 1:40 in PBS for 20 min at room temperature. Nuclei were stained with 1‰ DAPI at room temperature in the dark for 10 min. After being washed with PBS three times, the fluorescence images of each sample were observed and recorded by a fluorescence microscope. Fifty fluorescent images were applied to obtain heat maps.

Blebbistatin and Dynasore Treatment

Blebbistatin (Shanghai Aladdin Biochemical Technology Co., Ltd.) and dynasore (Shanghai Aladdin Biochemical Technology Co., Ltd.) were applied to disturb the cytoskeleton organization and inhibit the dynamin activity. In detail, after the cell was cultured on stencils for 16 h, the medium was refreshed by a cell-cultured medium with 1 ng/ml blebbistatin or 40 μM dynasore. After further culturing for 8 h, the medium was replaced by a fresh medium with 1% amino-modified fluorescent NPs and 1 ng/ml blebbistatin or 40 μM dynasore. After further culturing in a humidified CO_2 incubator for another 24 h, the samples were harvested and treated with 0.4% trypan blue for 5 min. Before fluorescence observation, the samples were stained with DAPI. The percentage and fluorescence intensity of

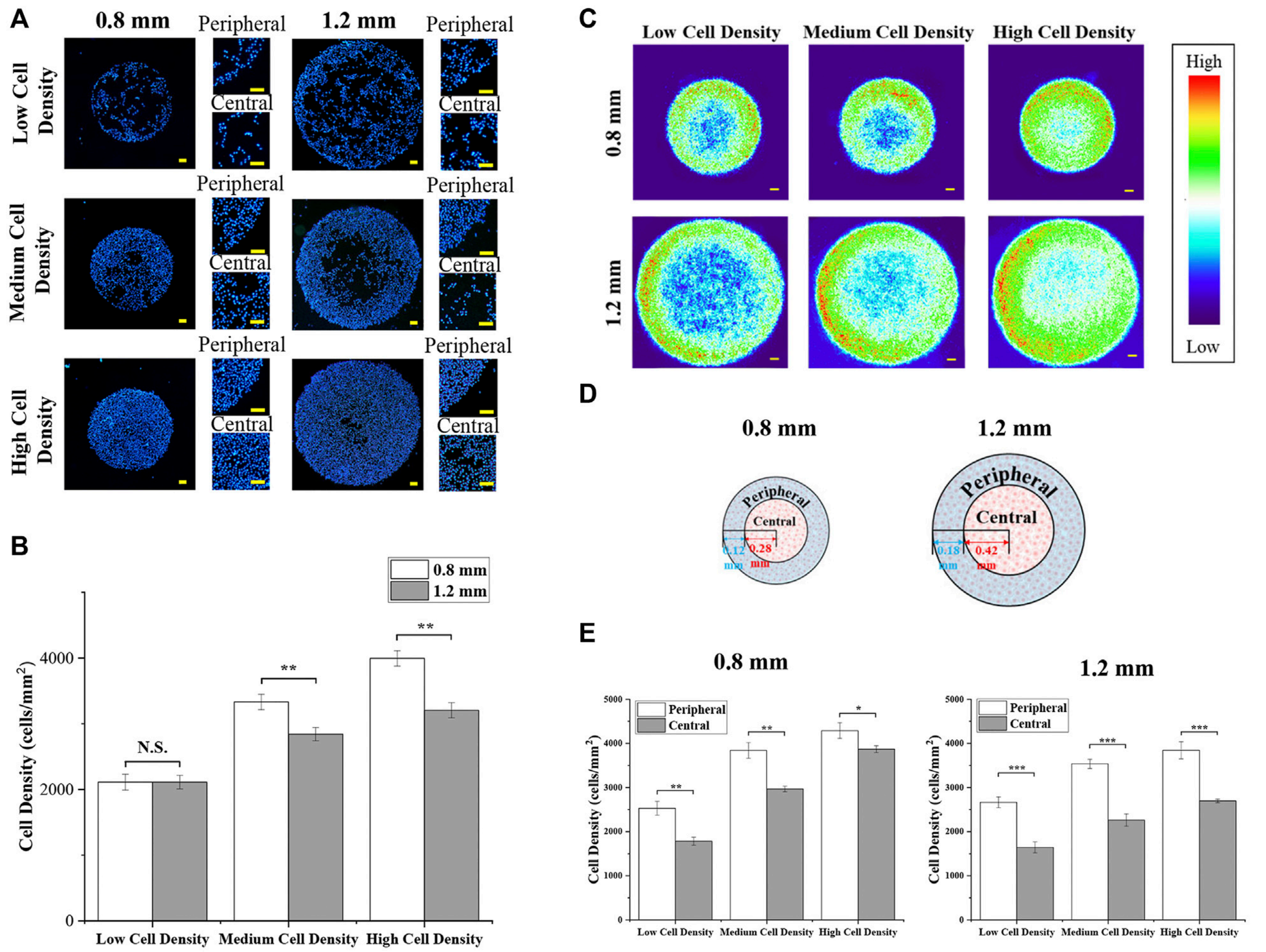

FIGURE 2 | Cell distribution of micropatterned colonies. **(A)** Distribution of DAPI-stained nuclei in colonies with different diameters and cell densities. Scale bar: 50 μm. **(B)** Cell density of micropatterned colonies. **(C)** Heat maps of DAPI-stained nuclei. Scale bar: 50 μm. **(D)** Illustration of the peripheral region and central region in micropatterned colonies. **(E)** Cell density of the defined peripheral and central regions in micropatterned colonies with different diameters and cell densities. Data are presented as means ± SDs ($n = 5$). *$p < 0.05$, **$p < 0.01$, ***$p < 0.001$.

NP-positive cells were also analyzed as previously described. More than 30 fluorescent images were analyzed.

Statistical Analysis

The significant difference among samples was performed using a one-way analysis of variance (ANOVA) with Tukey's *post hoc* test for multiple comparisons. The data are presented as means ± standard deviations (SDs). It is considered to be a statistically significant difference when $p < 0.05$.

RESULTS

Preparation and Characterization of Stencils

As shown in **Figure 1A**, PDMS stencils were prepared by the punching process and applied for cell culture. The micro-holes with 0.8 mm or 1.2 mm in diameter were fabricated on a circular PDMS film with 14 mm in diameter by using a specific puncher (**Figures 1B, C**). The diameter of the holes was 849.5 ± 33.9 μm and 1,273.7± 62.6 μm. After sterilization, the PDMS stencils tightly adhered to TCPS (tissue culture polystyrene) surfaces in 24-well plates for the following cell experiments. Since the PDMS film's hydrophobic properties do not encourage cell adhesion (Subramaniam and Sethuraman, 2014), cells tended to adhere to the TCPS surface that bore micro-holes from the PDMS stencils (Choi et al., 2012). After the cell was cultured with PDMS stencils, colonies were formed within micro-holes of the stencil and the morphology of the colonies was controlled by PDMS stencils (**Figure 1D**). After cell adhesion, the unadhered cells were easily removed by the medium refreshing process. Additionally, the stencil-associated micropatterning method had no significant influence on cell viability (**Supplementary Figure S1**).

Cell Distribution

After the formation of micropatterned colonies, the diameter of the micropatterned melanoma colonies was 835.9 ± 14.1 μm and

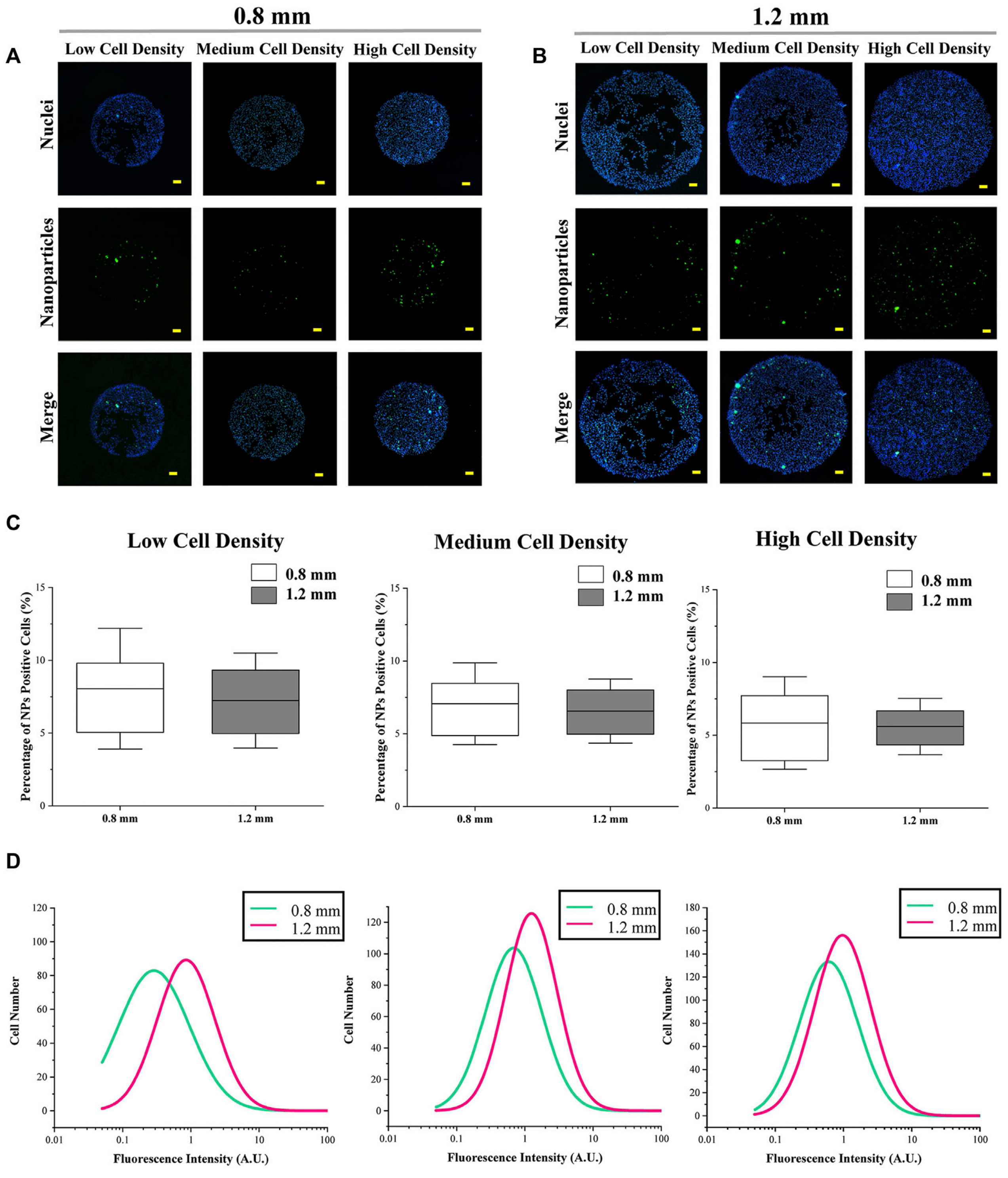

FIGURE 3 | Cellular uptake capacity of micropatterned colonies with different sizes. **(A,B)** Representative images of fluorescent NPs and nuclei. Scale bar: 50 μm. **(C)** Percentage of NP-positive cells. Data are presented as means ± SDs (*n* > 30). **(D)** Fluorescence intensity of NP-positive cells (*n* > 3,000).

1,262.2 ± 18.4 μm. Then, the nuclei were stained to characterize the cell distribution. As shown in **Figure 2A**, the density of melanoma cells was controlled by seeding density. With few cells seeding, there was no significant difference in cell density between different sizes of colonies (**Figure 2B**). With increased seeding density, the cell density of colonies with 0.8 mm in

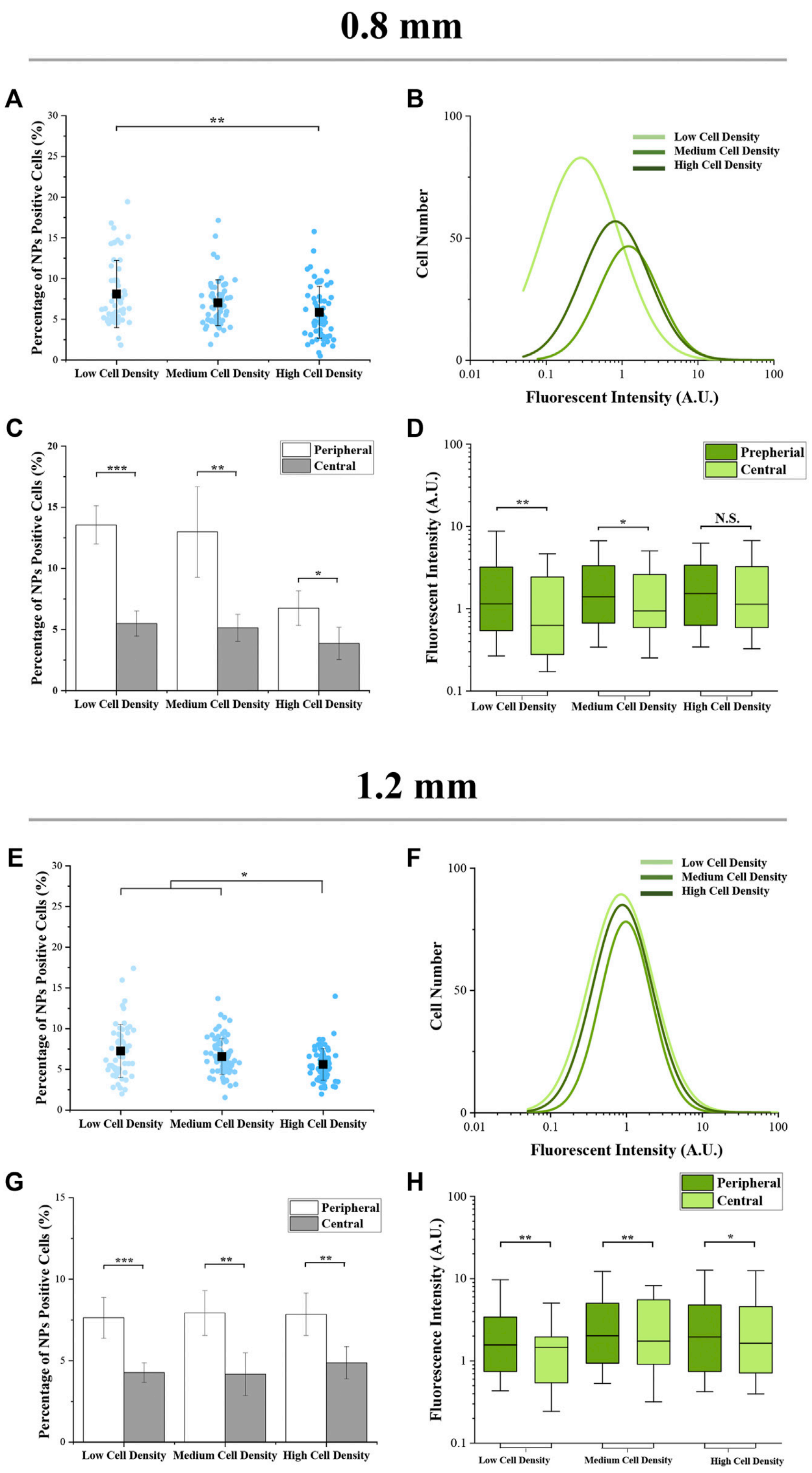

FIGURE 4 | Cellular uptake capacity of micropatterned colonies with different regions. **(A,E)** Percentage of NP-positive cells within whole colonies. Data are presented as means ± SDs (n > 30). **(B,F)** Distribution curves of NP-positive cells' intensity (n > 3,000). **(C,G)** Percentage of NP-positive cells at the peripheral and central regions. Data are presented as means ± SDs (*n* = 5). **(D,H)** Fluorescence intensity of NP-positive cells at the peripheral and central regions. Data are presented as means ± SDs (n > 100). **p* < 0.05, ***p* < 0.01, ****p* < 0.001.

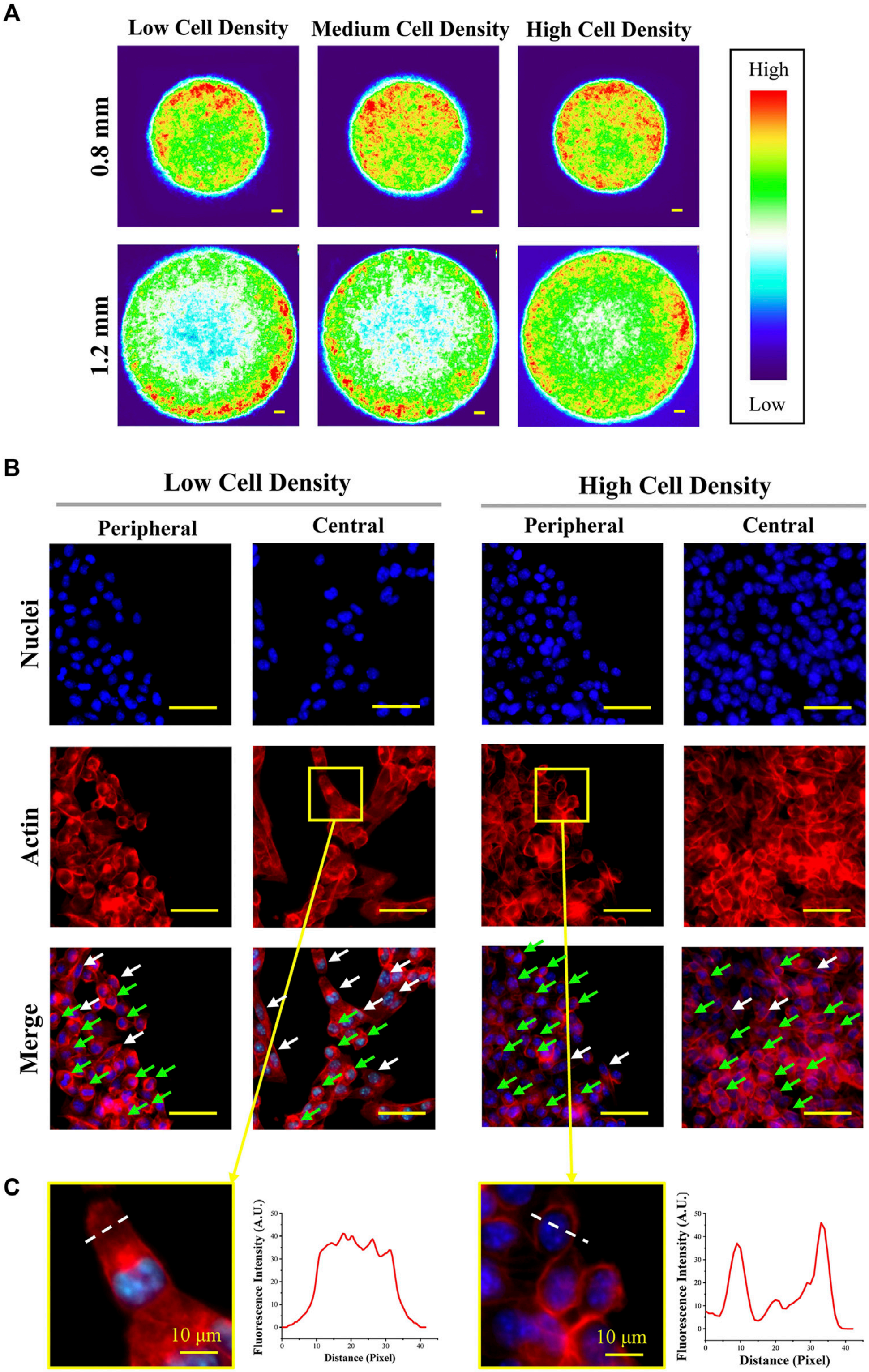

FIGURE 5 | Structure of actin at the peripheral and central regions of colonies. **(A)** Heat maps of actin-stained fluorescent images. Scale bar: 50 μm. **(B)** Representative magnified fluorescent images of stained nuclei and actin (*d* = 1.2 mm). Scale bar: 50 μm. **(C)** Representative images and fluorescence intensity curves of spindle-shaped and circular-shaped melanoma cells (*d* = 1.2 mm). Scale bar: 10 μm.

diameter was higher than the colonies with 1.2 mm in diameter (**Figure 2B**).

Furthermore, cells predominantly adhered at the peripheral region of micropatterned colonies. To observe more clearly, more than 50 fluorescent images were applied to create heat maps (**Figure 2B**). The heat maps showed the same phenomenon that melanoma cells concentrated in the peripheral region of micropatterned colonies, especially at low cell density. To quantitatively analyze the cell density at a different region of colonies, the central and peripheral regions with the same area were set, as shown in **Figure 2C**. As **Figure 2D**shows thequantitative results, the cell density in the peripheral region was significantly higher than in the central region. In addition, with cell density increased, cells were more homogeneously distributed within smaller colonies.

Cellular Uptake Capacity

The cellular uptake of amino group-modified fluorescent PS NPs is shown in **Figures 3A,B**. The cellular uptake capacity was indicated by the percentage and fluorescence intensity of NP-positive cells. The percentage of NP-positive cells was related to the ratio of cells, which could uptake NPs, and the fluorescence intensity of NP-positive cells was applied to indicate the amount of endocytosed NPs in each cell. In the results, colony size did not have a significant effect on the percentage of NP-positive cells (**Figure 3C**). On the other hand, the fluorescence intensity of cells in micropatterned colonies with 1.2 mm in diameter was higher than in the smaller colonies (d = 0.8 mm) (**Figure 3D**).

Furthermore, within the colonies having the same size, as the cell seeding density increased, the percentage of NP-positive cells was decreased (**Figures 4A,E**. It was interesting that the fluorescence intensity of cells with a medium density was higher than the cells with low or high density (**Figures 4B,F**). On the other hand, for the results of spatial factor that regulated the cellular uptake capacity, the percentage and fluorescence intensity of NP-positive cells (**Figures 4C,G** and **Figures 4D,H**) in the peripheral region were significantly higher than the cells located in the central region. To explore the reason for these phenomena, the cytoskeleton of melanoma cells was analyzed.

Structure of Cytoskeleton

Since previous studies have demonstrated that the cellular uptake capacity is tightly related to the structure of the cytoskeleton (Wang et al., 2021a; Wang et al., 2021b; Wang et al., 2021c), the actin structure was characterized in this study. The structure of the cytoskeleton was analyzed by actin-stained fluorescence images (**Supplementary Figure S2**). The heat maps of actin (**Figure 5A**) revealed that actin was concentrated in the peripheral region of micropatterned colonies. This result had a good agreement with cell uneven distribution. As shown in the magnified fluorescent images (**Figure 5B**), more spindle-shaped cells (white arrow) were observed in the central region of the micropatterned colony with low cell seeding density. In contrast, more circular-shaped cells (green arrow) were found in peripheral regions with high cell density. In addition, actin was concentrated in the cortical region in circular-shaped cells and homogeneously distributed in spindle-shaped cells (**Figure 5C**).

Influence of Cytoskeleton on Cellular Uptake Capacity

To explore the function of cytoskeleton in the cellular uptake process, the cytoskeleton was disrupted. As shown in **Figure 6A**, actin was disturbed by blebbistatin before and during cellular uptake experiments. After blebbistatin treatment, there was no significant influence on the actin organization of spindle-shaped cells. In contrast, actin in the cortical region of cells with high density disappeared and was randomly distributed within the cytoplasm. In addition, the percentage (**Figure 6C**; **Supplementary Figure S3A**) and fluorescence intensity (**Figure 6D**; **Supplementary Figure S3B**) of NP-positive cells were slightly decreased after blebbistatin treatment.

Influence of Dynamin on Cellular Uptake Capacity

In addition, at the final step of clathrin-mediated endocytosis (CME), cortical actin is collaborated with dynamin to separate clathrin-coated pits from the plasma membrane (Merrifield et al., 2002; Grassart et al., 2014). It means that cortical actin is functionalized not only at the process of endocytic membrane' invagination but also at the endocytic vesicles' separation. Therefore, the function of cortical actin and dynamin in the regulation of cellular uptake capacity was also investigated by the inhibition of dynamin activity. In this case, dynasore was applied to inhibit dynamin activity (Macia et al., 2006). As shown in **Figure 7A**, dynasore was incubated with colonies before and during cellular uptake experiments. Quantitative data revealed that the percentage (**Figure 7C**; **Supplementary Figure S4A**) and fluorescence intensity (**Figure 7D**; **Supplementary Figure S4B**) of NP-positive cells were significantly decreased after dynasore treatment. In addition, the fluorescence intensity has no significant difference with different cell seeding densities after dynasore treatment (**Figure 7D**).

DISCUSSION

In this study, micropatterned PDMS stencils were applied to control the morphology of melanoma colonies. After micropatterned colonies formed, the size and morphology of colonies were easily controlled by PDMS stencils and the cell density was regulated by the cell seeding process. For each colony, the cells were predominately located in the peripheral region. This phenomenon was similar to the cells cultured in microwell plates. This uneven distribution of cells has been explained by the effect of the meniscus (Freshney, 2010).

Then, the results of cellular uptake capacity and morphological cues of colonies were comprehensively analyzed. Firstly, the fluorescence intensity of NP-positive cells in a larger colony was higher than the cells in a smaller colony (**Figure 3D**). In common sense, with homogeneously distributed

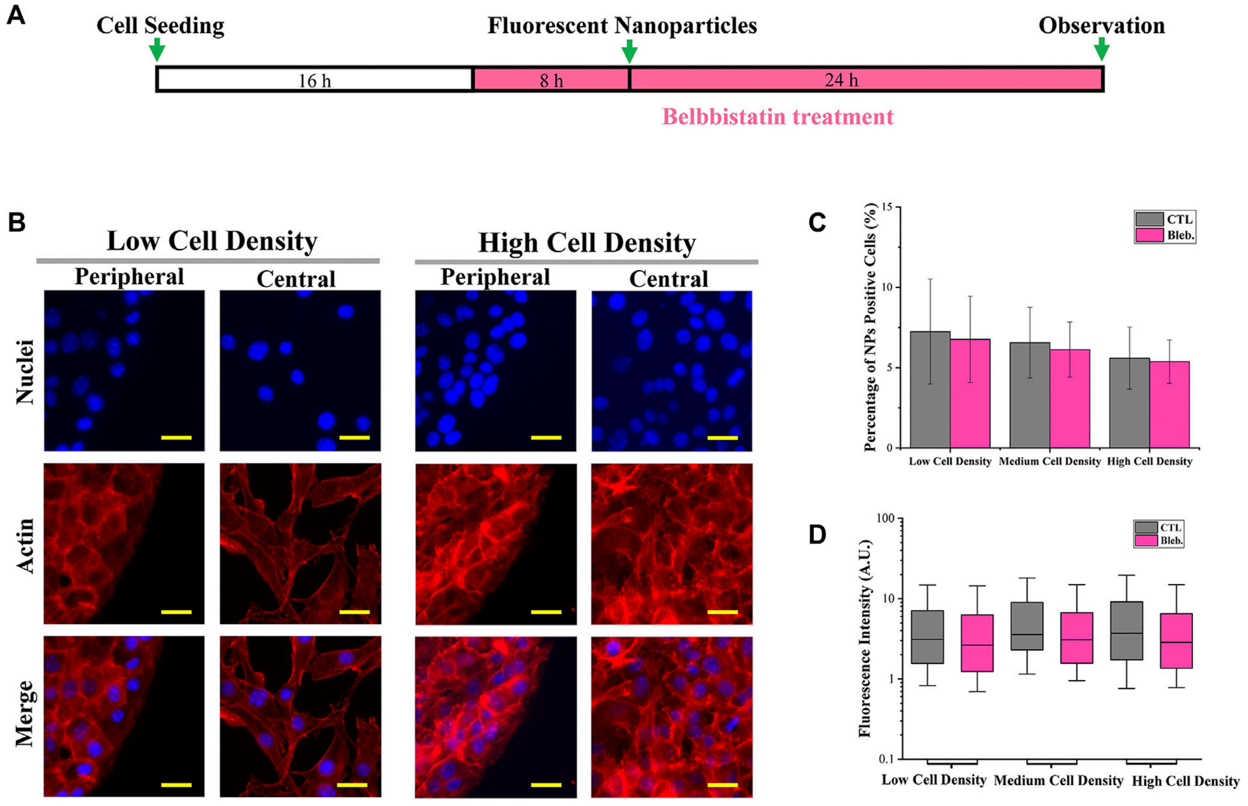

FIGURE 6 | Influence of the cytoskeleton structure on cellular uptake capacity. **(A)** Scheme of blebbistatin treatment. **(B)** Structure of actin after blebbistatin treatment (*d* = 1.2 mm). Scale bar: 50 μm. **(C)** Percentage of NP-positive cells after blebbistatin treatment (*d* = 1.2 mm). Data are presented as means ± SDs (*n* > 30). **(D)** Fluorescence intensity of NP-positive cells after blebbistatin treatment (1.2 mm). Data are presented as means ± SDs (*n* > 300).

NPs, the colonies with a larger spreading area have a higher contact probability with NPs. Thus, this phenomenon was considered to be the result of a bigger dose of NPs. In addition, the role of cell density and spatial factors in the regulation of cellular uptake capacity was also analyzed. With cell density increased, more concentrated cells showed circular morphology and a smaller spreading area (**Figure 5B**). This smaller spreading area induced a lower contact probability between the plasma membrane and NPs and finally decreased the percentage of NP-positive cells (**Figures 4A,E**) (Wang et al., 2016; Khetan et al., 2019). In contrast, the fluorescence intensity of positive cells with medium density was higher than the cells with low density (**Figures 4B,F**). It means that even if the percentage of NP-positive cells decreased, the cellular uptake capacity of each individual cell was enhanced by higher cell density. These controversial results indicated that the increased cell density could enhance the cellular uptake capacity of an individual cell but decrease the contacting probability between the cytoplasm membrane and NPs. Moreover, this inference was also supported by the decreased fluorescence intensity of NP-positive cells with the highest cell density.

Furthermore, with the result of uneven cell distribution in micropatterned colonies (**Figure 2**), the concentrated cells in the peripheral region have the highest percentage and fluorescence intensity of NP-positive cells (**Figure 4**). It also indicated that the higher cellular uptake capacity was related to higher cell density. In this case, the structure and functions of the cytoskeleton were characterized. The cells with higher density showed more circular-shaped cells with the typical cortical actin. As previously reported, the cortical actin was critical for invagination of the endocytic membrane in CME (Galletta et al., 2010; Chaudhuri et al., 2011). Additionally, some research already revealed that CME is a primary approach for the cellular uptake of amino-modified NPs (Jiang et al., 2010). Thus, cortical actin was considered a critical factor in the regulation of the cellular capacity of NPs. Therefore, the higher cell density-enhanced cellular uptake capacity benefited from cortical actin-accelerated CME in circular-shaped cells with high cell density. To verify the functions of cortical actin in the regulation of cellular uptake capacity, the actin organization was disrupted by blebbistatin (a specific myosin II inhibitor that can reduce cortical actin-mediated cortex tension) (Lu et al., 2008; Tinevez et al., 2009). For the results, with the disappearance of cortical actin, cellular uptake capacity was decreased (**Figure 6**). This could be further evidence to support the fact that the higher cellular uptake capacity of concentrated cells benefited from the cortical actin-enhanced CME. Additionally, since the cortical actin also takes effect on dynamin during the endocytic membrane's separation (Loebrich, 2014), the dynamin was suppressed by dynasore treatment. After dynasore treatment,

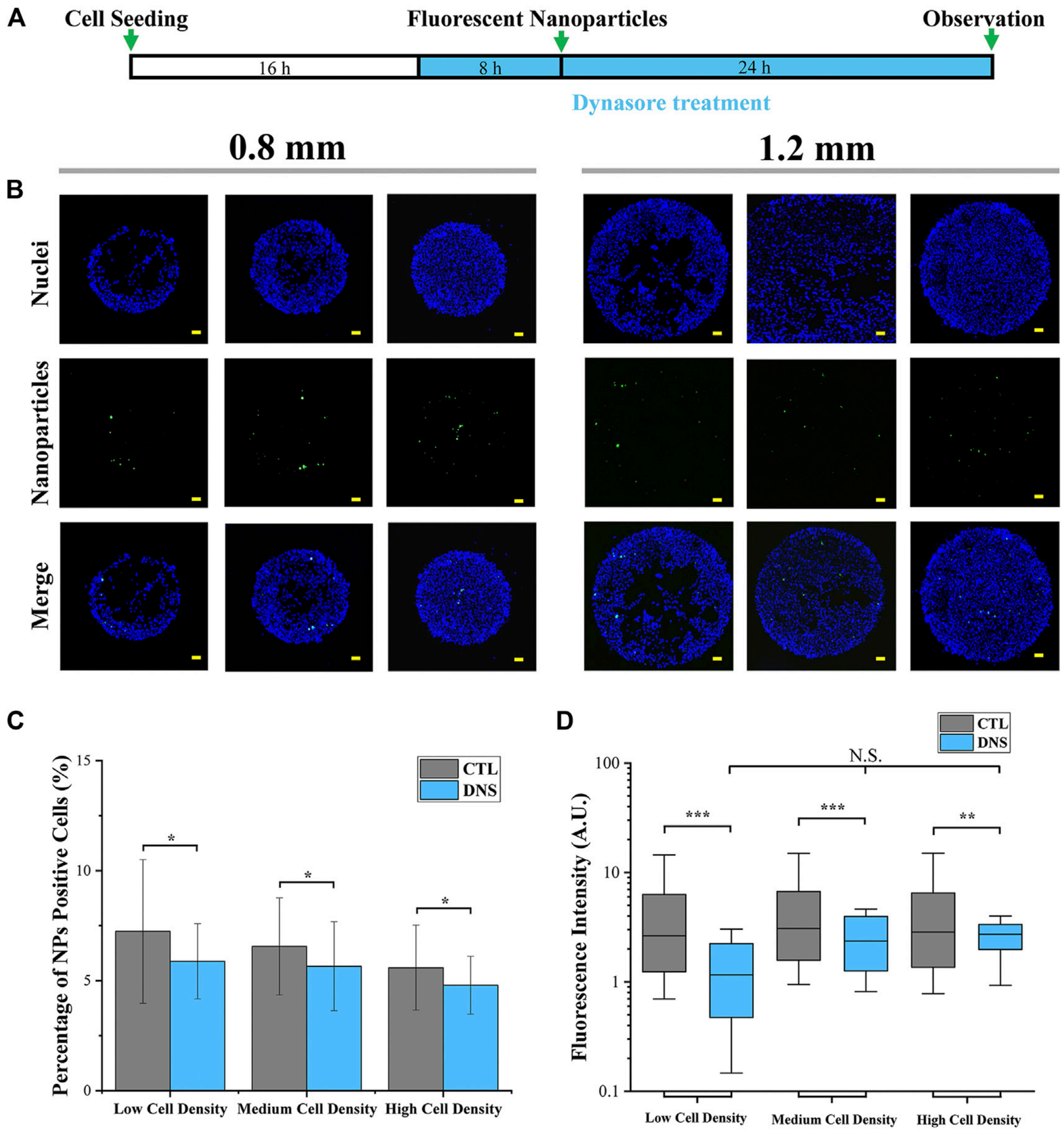

FIGURE 7 | Influence of dynamin on cellular uptake capacity. **(A)** Scheme of dynasore treatment. **(B)** Representative fluorescent images of cellular uptake after dynasore treatment. Scale bar: 50 μm. **(C)** Percentage of NP-positive cells after dynasore treatment (1.2 mm). Data are presented as means ± SDs (*n* > 30). **(D)** Fluorescence intensity of NP-positive cells after dynasore treatment (1.2 mm). Data are presented as means ± SDs (*n* > 300). **p* < 0.05, ****p* < 0.001.

the significantly decreased cellular uptake capacity was independent of cell density (**Figure 7D**). The effects of dynamin demonstrated the improved cellular uptake in higher cell density was mainly contributed by cortical actin assisted membrane separation.

In summary, with a bigger dose of NPs, larger colonies endocytosed more NPs. In addition, the contrary effects of high cell density on the cellular uptake of NPs were revealed. Firstly, the concentrated cells with a circular shape showed typical cortical actin that can accelerate CME. On the other hand, the negative effect of high cell density on the cellular uptake capacity was associated with a decreased contacting probability between NPs and cytoplasm membrane. For these reasons, cells with higher density (intermediate seeding density or located at the peripheral region of micropatterned colonies) showed a higher cellular uptake capacity of NPs.

CONCLUSION

In this research, PDMS stencils were prepared and applied to control the morphologies of melanoma colonies. Subsequently, the influence of morphological cues on cellular uptake capacity has been revealed. The results indicated that more endocytosed NPs in larger colonies were related to a bigger dose of NPs within larger areas. In addition, with cell density increased, the cellular uptake capacity was simultaneously enhanced by the cortical actin-accelerated CME and was inhibited by the decreased contacting probability of NPs and cytoplasm membrane. As a result, cells with intermediate seeding density or located in the peripheral region of micropatterned colonies showed the highest cellular uptake capacity of NPs.

DATA AVAILABILITY STATEMENT

The raw data supporting the conclusions of this article will be made available by the authors without undue reservation.

AUTHOR CONTRIBUTIONS

Experimental design: YY and BX; experiments: SH, QS, XH, and KH; data analysis: SH, QS, and SM; and manuscript writing: YY, QS, and BX. The final version has been approved by all of the authors.

FUNDING

This research was supported by the Foundation of Shaanxi University of Science and Technology (Grant No. 126021993) and the Natural Science Foundation of Shaanxi Province in China (Grant No. 2021JQ-545).

SUPPLEMENTARY MATERIAL

The Supplementary Material for this article can be found online at: https://www.frontiersin.org/articles/10.3389/fbioe.2022.922159/full#supplementary-material

REFERENCES

Adjei, I. M., Sharma, B., and Labhasetwar, V. (2014). "Nanoparticles: Cellular Uptake and Cytotoxicity," in *Nanomaterial: Impacts on Cell Biology and Medicine*. Editors D. G. Capco and Y. Chen (Dordrecht, Netherlands: Springer), 73–91. doi:10.1007/978-94-017-8739-0_5

Chaudhuri, A., Battaglia, G., and Golestanian, R. (2011). The Effect of Interactions on the Cellular Uptake of Nanoparticles. *Phys. Biol.* 8 (4), 046002. doi:10.1088/1478-3975/8/4/046002

Choi, J. H., Lee, H., Jin, H. K., Bae, J.-s., and Kim, G. M. (2012). Micropatterning of Neural Stem Cells and Purkinje Neurons Using a Polydimethylsiloxane (PDMS) Stencil. *Lab. Chip* 12 (23), 5045–5050. doi:10.1039/C2LC40764G

Deglincerti, A., Etoc, F., Guerra, M. C., Martyn, I., Metzger, J., Ruzo, A., et al. (2016). Self-organization of Human Embryonic Stem Cells on Micropatterns. *Nat. Protoc.* 11 (11), 2223–2232. doi:10.1038/nprot.2016.131

Freshney, R. I. (2010). "Problem Solving," in *Culture of Animal Cells* (Hoboken, New Jersey: John Wiley & Sons), 569–591.

Galletta, B. J., Mooren, O. L., and Cooper, J. A. (2010). Actin Dynamics and Endocytosis in Yeast and Mammals. *Curr. Opin. Biotechnol.* 21 (5), 604–610. doi:10.1016/j.copbio.2010.06.006

Grassart, A., Cheng, A. T., Hong, S. H., Zhang, F., Zenzer, N., Feng, Y., et al. (2014). Actin and Dynamin2 Dynamics and Interplay during Clathrin-Mediated Endocytosis. *J. Cell Biol.* 205 (5), 721–735. doi:10.1083/jcb.201403041

Huang, G., Li, F., Zhao, X., Ma, Y., Li, Y., Lin, M., et al. (2017). Functional and Biomimetic Materials for Engineering of the Three-Dimensional Cell Microenvironment. *Chem. Rev.* 117 (20), 12764–12850. doi:10.1021/acs.chemrev.7b00094

Iversen, T.-G., Skotland, T., and Sandvig, K. (2011). Endocytosis and Intracellular Transport of Nanoparticles: Present Knowledge and Need for Future Studies. *Nano Today* 6 (2), 176–185. doi:10.1016/j.nantod.2011.02.003

Jiang, X., Dausend, J., Hafner, M., Musyanovych, A., Röcker, C., Landfester, K., et al. (2010). Specific Effects of Surface Amines on Polystyrene Nanoparticles in Their Interactions with Mesenchymal Stem Cells. *Biomacromolecules* 11 (3), 748–753. doi:10.1021/bm901348z

Khetan, J., Shahinuzzaman, M., Barua, S., and Barua, D. (2019). Quantitative Analysis of the Correlation between Cell Size and Cellular Uptake of Particles. *Biophysical J.* 116 (2), 347–359. doi:10.1016/j.bpj.2018.11.3134

Lee, J., Abdeen, A. A., Wycislo, K. L., Fan, T. M., and Kilian, K. A. (2016). Interfacial Geometry Dictates Cancer Cell Tumorigenicity. *Nat. Mater* 15 (8), 856–862. doi:10.1038/nmat4610

Lee, J., Molley, T. G., Seward, C. H., Abdeen, A. A., Zhang, H., Wang, X., et al. (2020). Geometric Regulation of Histone State Directs Melanoma Reprogramming. *Commun. Biol.* 3 (1), 341. doi:10.1038/s42003-020-1067-1

Lewinski, N., Colvin, V., and Drezek, R. (2008). Cytotoxicity of Nanoparticles. *Small* 4 (1), 26–49. doi:10.1002/smll.200700595

Li, J., Cui, D., Huang, J., He, S., Yang, Z., Zhang, Y., et al. (2019). Organic Semiconducting Pro-nanostimulants for Near-Infrared Photoactivatable Cancer Immunotherapy. *Angew. Chem. Int. Ed.* 58 (36), 12680–12687. doi:10.1002/anie.201906288

Li, X., Sun, H., Li, H., Hu, C., Luo, Y., Shi, X., et al. (2021). Multi-Responsive Biodegradable Cationic Nanogels for Highly Efficient Treatment of Tumors. *Adv. Funct. Mater.* 31 (26), 2100227. doi:10.1002/adfm.202100227

Liang, K., Li, Z., Luo, Y., Zhang, Q., Yin, F., Xu, L., et al. (2020). Intelligent Nanocomposites with Intrinsic Blood-Brain-Barrier Crossing Ability Designed for Highly Specific MR Imaging and Sonodynamic Therapy of Glioblastoma. *Small* 16 (8), 1906985. doi:10.1002/smll.201906985

Loebrich, S. (2014). The Role of F-Actin in Modulating Clathrin-Mediated Endocytosis: Lessons from Neurons in Health and Neuropsychiatric Disorder. *Commun. Integr. Biol.* 7, e28740. doi:10.4161/cib.28740

Lu, L., Oswald, S. J., Ngu, H., and Yin, F. C.-P. (2008). Mechanical Properties of Actin Stress Fibers in Living Cells. *Biophysical J.* 95 (12), 6060–6071. doi:10.1529/biophysj.108.133462

Macia, E., Ehrlich, M., Massol, R., Boucrot, E., Brunner, C., and Kirchhausen, T. (2006). Dynasore, a Cell-Permeable Inhibitor of Dynamin. *Dev. Cell* 10 (6), 839–850. doi:10.1016/j.devcel.2006.04.002

Merrifield, C. J., Feldman, M. E., Wan, L., and Almers, W. (2002). Imaging Actin and Dynamin Recruitment during Invagination of Single Clathrin-Coated Pits. *Nat. Cell Biol.* 4 (9), 691–698. doi:10.1038/ncb837

Morgani, S. M., Metzger, J. J., Nichols, J., Siggia, E. D., and Hadjantonakis, A.-K. (2018). Micropattern Differentiation of Mouse Pluripotent Stem Cells Recapitulates Embryo Regionalized Cell Fate Patterning. *eLife* 7, e32839. doi:10.7554/eLife.32839

Park, J. H., and Oh, N. (2014). Endocytosis and Exocytosis of Nanoparticles in Mammalian Cells. *Ijn* 9 (Suppl. 1), 51–63. doi:10.2147/IJN.S26592

Subramaniam, A., and Sethuraman, S. (2014). "Biomedical Applications of Nondegradable Polymers," in *Natural and Synthetic Biomedical Polymers*. Editors S. G. Kumbar, C. T. Laurencin, and M. Deng (Oxford: Elsevier), 301–308. doi:10.1016/b978-0-12-396983-5.00019-3

Tinevez, J.-Y., Schulze, U., Salbreux, G., Roensch, J., Joanny, J.-F., and Paluch, E. (2009). Role of Cortical Tension in Bleb Growth. *Proc. Natl. Acad. Sci. U.S.A.* 106 (44), 18581–18586. doi:10.1073/pnas.0903353106

Wang, X., Hu, X., Li, J., Russe, A. C. M., Kawazoe, N., Yang, Y., et al. (2016). Influence of Cell Size on Cellular Uptake of Gold Nanoparticles. *Biomater. Sci.* 4 (6), 970–978. doi:10.1039/c6bm00171h

Wang, Y., Yang, Y., Wang, X., Kawazoe, N., Yang, Y., and Chen, G. (2021a). The Varied Influences of Cell Adhesion and Spreading on Gene Transfection of Mesenchymal Stem Cells on a Micropatterned Substrate. *Acta Biomater.* 125, 100–111. doi:10.1016/j.actbio.2021.01.042

Wang, Y., Yang, Y., Wang, X., Yoshitomi, T., Kawazoe, N., Yang, Y., et al. (2021b). Micropattern-controlled Chirality of Focal Adhesions Regulates the

Cytoskeletal Arrangement and Gene Transfection of Mesenchymal Stem Cells. *Biomaterials* 271, 120751. doi:10.1016/j.biomaterials.2021.120751

Wang, Y., Yang, Y., Yoshitomi, T., Kawazoe, N., Yang, Y., and Chen, G. (2021c). Regulation of Gene Transfection by Cell Size, Shape and Elongation on Micropatterned Surfaces. *J. Mater. Chem. B* 9 (21), 4329–4339. doi:10.1039/D1TB00815C

Wang, Y., Yoshitomi, T., Kawazoe, N., Yang, Y., and Chen, G. (2022). Micropattern-Controlled Cell Density and its Effect on Gene Transfection of Mesenchymal Stem Cells. *Adv. Mater. Inter* 271, 2101978. doi:10.1002/admi.202101978

Yang, Y., Wang, X., Huang, T.-C., Hu, X., Kawazoe, N., Tsai, W.-B., et al. (2018). Regulation of Mesenchymal Stem Cell Functions by Micro-nano Hybrid Patterned Surfaces. *J. Mater. Chem. B* 6 (34), 5424–5434. doi:10.1039/c8tb01621f

Yang, Y., Wang, X., Hu, X., Kawazoe, N., Yang, Y., and Chen, G. (2019a). Influence of Cell Morphology on Mesenchymal Stem Cell Transfection. *ACS Appl. Mater. Interfaces* 11 (2), 1932–1941. doi:10.1021/acsami.8b20490

Yang, Y., Wang, X., Wang, Y., Hu, X., Kawazoe, N., Yang, Y., et al. (2019b). Influence of Cell Spreading Area on the Osteogenic Commitment and Phenotype Maintenance of Mesenchymal Stem Cells. *Sci. Rep.* 9 (1), 6891. doi:10.1038/s41598-019-43362-9

Yang, Z., Luo, Y., Hu, Y., Liang, K., He, G., Chen, Q., et al. (2021). Photothermo-Promoted Nanocatalysis Combined with H 2 S-Mediated Respiration Inhibition for Efficient Cancer Therapy. *Adv. Funct. Mater.* 31 (8), 2007991. doi:10.1002/adfm.202007991

Conflict of Interest: The authors declare that the research was conducted in the absence of any commercial or financial relationships that could be construed as a potential conflict of interest.

Publisher's Note: All claims expressed in this article are solely those of the authors and do not necessarily represent those of their affiliated organizations, or those of the publisher, the editors, and the reviewers. Any product that may be evaluated in this article, or claim that may be made by its manufacturer, is not guaranteed or endorsed by the publisher.

Copyright © 2022 Huang, Su, Hou, Han, Ma, Xu and Yang. This is an open-access article distributed under the terms of the Creative Commons Attribution License (CC BY). The use, distribution or reproduction in other forums is permitted, provided the original author(s) and the copyright owner(s) are credited and that the original publication in this journal is cited, in accordance with accepted academic practice. No use, distribution or reproduction is permitted which does not comply with these terms.

frontiers | Frontiers in Bioengineering and Biotechnology

ORIGINAL RESEARCH
published: 06 June 2022
doi: 10.3389/fbioe.2022.919235

Albumin-Stabilized Manganese Oxide/ Semiconducting Polymer Nanocomposites for Photothermal-Chemodynamic Therapy of Hepatic Carcinoma

Qi Su[1]†, Changcun Liu[2]†, Jingyi Zhu[3], Mengbin Ding[4], Zhen Zhang[4], Jingchao Li[4]* and Qin Zhang[5]**

[1]Department of Critical Care Medicine, Shanghai General Hospital, Shanghai Jiao Tong University School of Medicine, Shanghai, China, [2]Department of Nuclear Medicine, Shanghai General Hospital, Shanghai Jiao Tong University School of Medicine, Shanghai, China, [3]School of Pharmaceutical Sciences, Nanjing Tech University, Nanjing, China, [4]Shanghai Engineering Research Center of Nano-Biomaterials and Regenerative Medicine, College of Chemistry, Chemical Engineering and Biotechnology, Donghua University, Shanghai, China, [5]Institute of Translational Medicine, Shanghai University, Shanghai, China

Hepatic carcinoma is one of the most common cancers worldwide, while its treatment remains a great challenge. Traditional therapeutic methods often have disadvantages such as limited therapeutic efficacy and potential side effects. In this study, we report the construction of bovine serum albumin (BSA)–stabilized manganese oxide (MnO_2)/ semiconducting polymer (SP) nanocomposites to combine photothermal therapy (PTT) and chemodynamic therapy (CDT) for treatment of hepatic carcinoma in living mouse models. Such nanocomposites are composed of BSA, SP, and MnO_2 as the stabilizer, PTT, and CDT agent, respectively. SP produced local heat under near-infrared (NIR) laser irradiation for PTT, and MnO_2 nanoparticles mediated CDT in the tumor microenvironment, leading to apoptosis of cancer cells. Such nanocomposite-mediated combinational therapy showed a much higher efficacy in inhibiting growth of subcutaneous HepG2 tumors in nude mice than sole treatment. This study thus provides a multifunctional nanoplatform for safe and effective treatment of hepatic carcinoma.

Keywords: hepatic carcinoma, photothermal therapy, chemodynamic therapy, combinational therapy, nanocomposites

OPEN ACCESS

Edited by:
Xin Li,
DWI—Leibniz-Institut für Interaktive Materialien, Germany

Reviewed by:
Xijian Liu,
Shanghai University of Engineering Sciences, China
Huan Peng,
University of California, Los Angeles, United States
Weijing Yang,
Zhengzhou University, China

****Correspondence:***
Jingyi Zhu
zhujy1210@njtech.edu.cn
Jingchao Li
jcli@dhu.edu.cn
Qin Zhang
sabrina_1985@shu.edu.cn

†These authors have contributed equally to this work

Specialty section:
This article was submitted to Nanobiotechnology, a section of the journal Frontiers in Bioengineering and Biotechnology

Received: *13 April 2022*
Accepted: *25 April 2022*
Published: *06 June 2022*

Citation:
Su Q, Liu C, Zhu J, Ding M, Zhang Z, Li J and Zhang Q (2022) Albumin-Stabilized Manganese Oxide/ Semiconducting Polymer Nanocomposites for Photothermal-Chemodynamic Therapy of Hepatic Carcinoma. Front. Bioeng. Biotechnol. 10:919235. doi: 10.3389/fbioe.2022.919235

INTRODUCTION

Hepatic carcinoma has been the fifth common type of cancer and third common cause of cancer-related deaths over the world (Zhou et al., 2018; Liu et al., 2020; Qi et al., 2021). Traditional approaches for treatment of hepatic carcinoma include surgery, chemotherapy, and radiotherapy (Golubnitschaja et al., 2016; Wang et al., 2019; Zhu et al., 2019). Surgery is still one of the first-choice treatments for hepatic carcinoma, but tumor recurrence rates after surgery are higher than 40%, which restricts the long-term survival of patients (Depalo et al., 2017). Although chemotherapy has exhibited a remarkable curative effect with great success in clinical practice, it often has disadvantages such as poor tumor specificity, high systemic toxicity, and adverse effects (Tian et al., 2010). Radiotherapy usually faces the common dilemmas of poor efficacy, severe side effects,

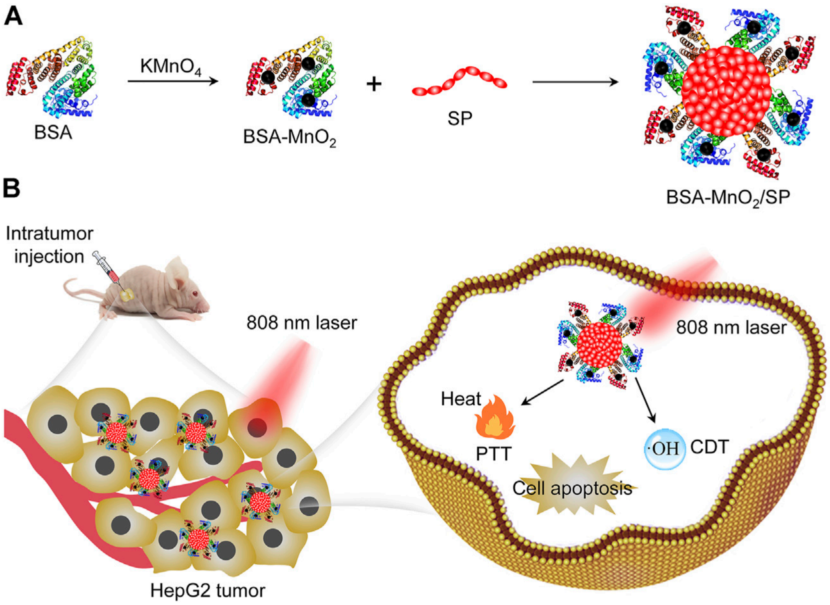

FIGURE 1 | Construction of $BSA\text{-}MnO_2/SP$ nanocomposites for combinational PTT and CDT of hepatic carcinoma. **(A)** Schematic illustration of synthesis of $BSA\text{-}MnO_2/SP$ nanocomposites. **(B)** Schematic illustration of $BSA\text{-}MnO_2/SP$ nanocomposite–mediated combinational PTT and CDT.

and radioresistance (De Ruysscher et al., 2019). Therefore, exploration of efficient and safe strategies for treatment of hepatic carcinoma is in high demand.

Unlike traditional treatment, photothermal therapy (PTT) utilizes photothermal conversion agents to convert light energy into heat energy, thereby increasing the temperature of the surrounding environment and causing the death of cancer cells (Hu et al., 2018; Jung et al., 2018; Liu et al., 2019). As external laser irradiation can precisely target tumor tissues, PTT can minimize the damage to the surrounding normal tissues and thus shows high specificity (Li et al., 2019; Li et al., 2020; Yuan et al., 2020). Chemodynamic therapy (CDT) is an emerging tumor treatment method that utilizes Fenton and Fenton-like reactions in the tumor microenvironment to generate highly toxic hydroxyl radicals (OH) for inducing cell apoptosis (Wang et al., 2020; Hao et al., 2021; Tian et al., 2021). CDT has high tumor specificity and selectivity and low toxicity in normal tissues, but the limited content of endogenous hydrogen peroxide (H_2O_2) and high concentrations of antioxidants in the tumor microenvironment can lead to unsatisfactory therapeutic effects (Cao et al., 2019; Ming et al., 2020; Yu et al., 2021). Since it is difficult for a single treatment method to achieve the desired therapeutic effect, a combination of different treatment modalities is expected to improve the antitumor efficacy (Li et al., 2018b; Hu et al., 2019; Chen et al., 2021). Therefore, the combination of PTT with CDT has not only shown high selectivity for cancer treatment but also improved therapeutic efficacy.

With the development of nanotechnology, a large number of nanoparticles with different functions and properties have been used as therapeutic agents for cancer treatment (Gai et al., 2018; Sahu et al., 2020; Siddique and Chow, 2020). Nanoparticles can improve the stability, water solubility, and pharmacokinetics of small-molecular anticancer drugs and allow the delivery of drugs into tumor sites for improved chemotherapy (Begines et al., 2020; Manzano and Vallet-Regí, 2020; Yu et al., 2020). Some nanoparticles can generate heat or highly toxic reactive oxygen species (ROS) upon external stimuli or reactions with endogenous chemical stimuli in the tumor microenvironment to show therapeutic actions (Chen et al., 2016; Son et al., 2020; Tang et al., 2020). In addition, nanoparticles can mediate combinational therapy through integrating different therapeutic components into a single nanosystem (Zhang et al., 2017; Zhang et al., 2018; Shrestha et al., 2019). Therefore, nanoparticle-mediated combinational therapy should provide an alternative strategy for treatment of hepatic carcinoma.

Herein, we report the construction of bovine serum albumin (BSA)–stabilized manganese oxide (MnO_2)/semiconducting polymer (SP) nanocomposites for combinational PTT and CDT of hepatic carcinoma in living mouse models. BSA was utilized as both a reductant and a template to synthesize $BSA\text{-}MnO_2$ nanoparticles, which served as a stabilizer to construct $BSA\text{-}MnO_2/SP$ nanocomposites (**Figure 1A**). MnO_2 nanoparticles have been utilized for cancer therapy as they can mediate Fenton-like reactions in the tumor microenvironment to generate OH (Ou et al., 2021). Due to its good biocompatibility and excellent optical property, SP can be used for PTT (Li et al., 2018a). Under 808 nm laser irradiation, MnO_2 and SP mediated the generation of OH and local heat in tumors for CDT and PTT, respectively. Such a combinational therapy showed an improved efficacy in completely inhibiting the growth of subcutaneous HepG2 tumors in nude mice (**Figure 1B**).

MATERIALS AND METHODS

Materials

BSA and SP were purchased from Sigma-Aldrich (St. Louis, United States). Singlet oxygen sensor green (SOSG) and the cell counting kit-8 (CCK-8) agent was purchased from Thermo Fisher Scientific (Invitrogen, United States) and Dojindo Laboratories (Kumamoto, Japan), respectively. RPMI 1640 medium, penicillin-streptomycin, and fetal bovine serum (FBS) were obtained from Gibco (Grand Island, NY, United States). Ultrapure water used in all experiments was prepared using a water purification system (PALL Cascada, MI, United States). All other chemicals were purchased from Sinopharm Chemical Reagent Co. Ltd. (Shanghai, China).

Synthesis of BSA-MnO$_2$/SP Nanocomposites

BSA-MnO$_2$ nanoparticles were synthesized according to the procedures reported previously (Liu et al., 2021; Chen et al., 2022). In brief, aqueous solution of KMnO$_4$ (3 ml, 10.5 mg/ml) was dropwise added to BSA solution (7 ml, 35.7 mg/ml) under sonication, and the resulting solution was vigorously stirred at 37°C for 2 h. After purification *via* dialysis (molecular weight cut-off = 8–14 kDa), BSA-MnO$_2$ nanoparticles were obtained. To synthesize BSA-MnO$_2$/SP nanocomposites, SP dissolved in tetrahydrofuran (1 ml, 0.5 mg/ml) was rapidly injected into the solution of BSA-MnO$_2$ nanoparticles, and the resulting solution was treated by sonication for 5 min. After removal of tetrahydrofuran *via* a nitrogen flow and filtration of the remaining solution *via* a 220 nm PVDF filter, BSA-MnO$_2$/SP nanocomposites were obtained. To synthesize BSA/SP nanoparticles as control, SP dissolved in tetrahydrofuran (1 ml, 0.5 mg/ml) was rapidly injected into BSA solution under sonication for 5 min.

Characterization Techniques

Transmission electron microscope (TEM) images were obtained using a Tecnai G2 TEM (United States). Dynamic light scattering (DLS) and zeta potential measurement were conducted on a Zetasizer Nano-series (Nano-ZS90, Malvern, United Kindom). UV-vis spectra were obtained using a Persee spectrophotometer (TU-1810, Beijing, China). Fluorescence spectra were recorded on a fluorescence spectrophotometer (RF-6000, SHIMADZU, Japan).

Evaluation of Photothermal Property

To evaluate the photothermal property of BSA/SP and BSA-MnO$_2$/SP, the solutions containing BSA/SP or BSA-MnO$_2$/SP at an SP concentration of 100 μg/ml were irradiated by 808 nm laser at different power densities (0.5, 1.0, and 1.5 W/cm^2) for 5 min. Thermal images were obtained using a thermal infrared camera, and the temperatures during laser irradiation were recorded. In addition, the solutions of BSA/SP or BSA-MnO$_2$/SP at different SP concentrations (12.5, 25, 50, and 100 μg/ml) were irradiated by 808 nm laser at a power density of 1.0 W/cm^2 for 5 min to evaluate the influence of nanoparticle concentrations on temperature. Moreover, the solutions were treated by laser on/off at least five times to evaluate the photothermal stability of BSA/SP and BSA-MnO$_2$/SP nanoparticles.

Evaluation of OH Generation Efficacy

The solutions containing BSA-MnO$_2$ or BSA-MnO$_2$/SP at a Mn concentration of 10 μg/ml were mixed with the solution of methylene blue (MB) with or without the addition of glutathione (GSH, 0.5 mM) and H$_2$O$_2$ (100 μM). After incubation for 10 min, the absorbance of the solutions was measured using a Persee spectrophotometer (TU-1810, Beijing, China). To evaluate PTT-amplified OH generation, the mixed solutions were irradiated by 808 nm laser at a power density of 1.0 W/cm^2 for 5 min, and then the absorbance of solutions was measured using a spectrophotometer.

In Vitro Cytotoxicity Assay

HepG2 cancer cells were cultured in RPMI 1640 cell culture medium containing penicillin and streptomycin and 10% FBS at 37°C. The cells were seeded in 96-well plates (1 × 10^4 cells/well) and cultured for 24 h, and then the cells were incubated with BSA/SP or BSA-MnO$_2$/SP nanoparticles at different SP concentrations (6.25, 12.5, 25, 50, and 100 μg/ml) for 24 h. The cell culture medium was discarded, the cells were carefully washed with phosphate buffer solution (PBS), and a fresh medium containing a 10% CCK-8 agent was added into each well; then the cells were incubated for another 4 h. The absorbance of each well was measured using a microplate reader to calculate the cell viability. The cells treated with PBS were used as control.

In Vitro Therapeutic Efficacy Evaluation

HepG2 cells seeded in 96-well plates (1 × 10^4 cells/well) were incubated with BSA/SP or BSA-MnO$_2$/SP nanoparticles at SP concentration of 100 μg/ml with or without the addition of H$_2$O$_2$ (100 μM) for 24 h. Then laser irradiation (808 nm, 1.0 W/cm^2) of cells was conducted for 5 min, and the cells were incubated for another 12 h. After that, a CCK-8 assay was used to evaluate the cell viability.

Establishment of HepG2 Tumor Models

Nude mice (female, 4–6 weeks) were purchased from JieSiJie Laboratory Animal Co. Ltd. (Shanghai, China). All animal experiments were conducted according to the procedures permitted by the Institutional Anima Care and Treatment Committee of Donghua University. The suspension of HepG2 cells in PBS was subcutaneously injected into the right flank of each mouse (2 × 10^6 cells/mouse). HepG2 tumor–bearing nude mice were used for *in vivo* experiments after 10 days of tumor implantation.

In Vivo PTT of Tumors

HepG2 tumor–bearing mice were randomly divided into two groups (n = 3), and PBS solutions of BSA/SP or BSA-MnO$_2$/SP nanoparticles (20 μL, SP concentration = 250 μg/ml) were intratumorally administrated into tumor tissues. At 30 min after injection, the tumors were irradiated by 808 nm laser (1.0 W/cm^2) for 10 min. During laser irradiation, a thermal camera was used to obtain thermal images of the mice, and the temperatures in the tumor sites were measured by analyzing

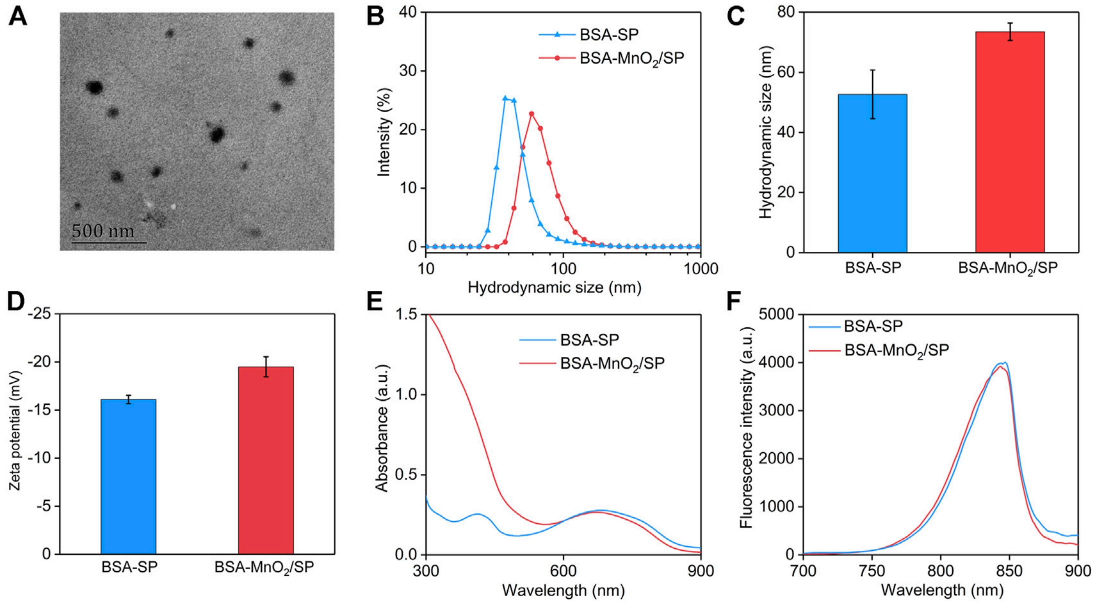

FIGURE 2 | Preparation and characterization of BSA-MnO_2/SP nanocomposites. **(A)** Representative TEM image of BSA-MnO_2/SP nanocomposites. **(B)** DLS profiles of BSA-SP nanoparticles and BSA-MnO_2/SP nanocomposites. **(C)** Hydrodynamic sizes of BSA-SP nanoparticles and BSA-MnO_2/SP nanocomposites measured using DLS. **(D)** Zeta potentials of BSA-SP nanoparticles and BSA-MnO_2/SP nanocomposites. **(E)** Absorbance spectra of BSA-SP nanoparticles and BSA-MnO_2/SP nanocomposites. **(F)** Fluorescence spectra of BSA-SP nanoparticles and BSA-MnO_2/SP nanocomposites.

the thermal images. Temperature curves as a function of laser irradiating time were obtained.

In Vivo Antitumor Efficacy Evaluation

The HepG2 tumor–bearing mice were randomly divided into four groups: PBS, BSA-MnO_2/SP, BSA/SP + laser, and BSA-MnO_2/SP + laser ($n = 4$). The mice were intratumorally administrated with 20 µl PBS and PBS solutions of BSA/SP or BSA-MnO_2/SP nanoparticles (SP concentration = 250 µg/ml). For laser irradiation groups, the tumors were irradiated by 808 nm laser (1.0 W/cm^2) for 10 min at 30 min after injection. After treatment, the sizes of the tumors and the body weights of mice were recorded every 2 days for 18 days. The volumes of the tumors were calculated as follows: $V = (\text{length}) \times (\text{width})^2/2$. The relative tumor volumes were calculated as V/V_0 (V_0 is the tumor volume at day 0). At day 18, the mice were sacrificed to extract tumors, and the tumor weights were measured.

Statistical Analysis

The data were expressed as mean ± standard deviation. The statistically significant differences were analyzed *via* unpaired student's *t*-test. $^*p < 0.05$, $^{**}p < 0.01$, and $^{***}p < 0.001$ denoted statistical significance.

RESULTS AND DISCUSSION

Preparation and Characterization of BSA-MnO_2/SP Nanocomposites

BSA-MnO_2 nanoparticles were first synthesized with BSA acting as both a reductant and a template. TEM imaging showed that the formed BSA-MnO_2 nanoparticles had a spherical morphology (**Supplementary Figure S1**). The hydrodynamic size and zeta potential of BSA-MnO_2 nanoparticles were measured to be 7.2 nm and −15.6 mV, respectively (**Supplementary Figure S2**). BSA-MnO_2 nanoparticles were then used as a stabilizer to prepare BSA-MnO_2/SP nanocomposites through sonication. Poly(cyclopentadithiophene-alt-benzothiadiazole) with excellent optical property and photothermal conversion efficacy was used as the SP (Li et al., 2018b). The formed BSA-MnO_2/SP nanocomposites showed a spherical morphology, as observed from the TEM image (**Figure 2A**). The hydrodynamic size of BSA-MnO_2/SP nanocomposites measured by DLS was 73.5 nm, which was larger than that of BSA-SP nanoparticles (52.7 nm) (**Figures 2B,C**). The zeta potential of BSA-MnO_2/SP nanocomposites was measured to be −19.5 mV, which was similar to that of BSA-SP nanoparticles (−16.1 mV) (**Figure 2D**).

The optical properties of nanoparticles are important for their different applications (Peng and Chen, 2018; Peng et al., 2020a; Peng et al., 2020b), which were then investigated. The characteristic absorbance of SP at 680 nm was observed in the absorbance spectra of both BSA-SP and BSA-MnO_2/SP (**Figure 2E**). In addition, BSA-SP nanoparticles and BSA-MnO_2/SP nanocomposites had similar fluorescence property, with the fluorescence emission at around 845 nm (**Figure 2F**). These results indicating that the existence of MnO_2 nanoparticles did not obviously affect the optical properties of nanoparticles.

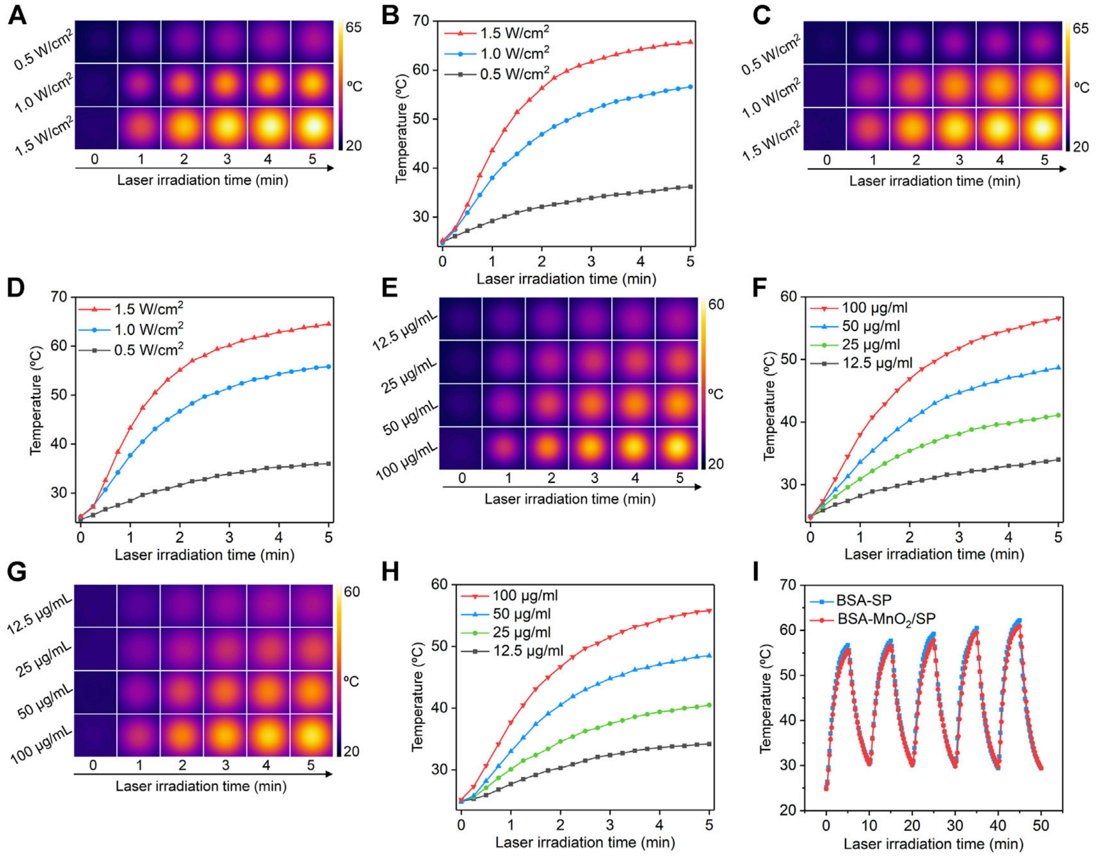

FIGURE 3 | Evaluation of photothermal conversion efficacy. **(A)** Thermal imaging of solutions containing BSA-MnO$_2$/SP nanocomposites under 808 nm laser irradiation at power densities of 0.5, 1.0, and 1.5 W/cm^2. **(B)** Temperature curves of BSA-MnO$_2$/SP nanocomposite solution under 808 nm laser irradiation at different power densities. **(C)** Thermal imaging of solutions containing BSA/SP nanoparticles under 808 nm laser irradiation at power densities of 0.5, 1.0, and 1.5 W/cm^2. **(D)** Temperature curves of BSA/SP nanoparticle solution under 808 nm laser irradiation at different power densities. **(E)** Thermal imaging of solutions containing BSA-MnO$_2$/SP nanocomposites at concentrations of 12.5, 25, 50, and 100 μg/ml under 808 nm laser irradiation at a power density of 1.0 W/cm^2. **(F)** Temperature curves of BSA-MnO$_2$/SP nanocomposite solutions at different concentrations under 808 nm laser irradiation (1.0 W/cm^2). **(G)** Thermal imaging of solutions containing BSA/SP nanoparticles at concentrations of 12.5, 25, 50, and 100 μg/ml under 808 nm laser irradiation at a power density of 1.0 W/cm^2. **(H)** Temperature curves of BSA/SP nanoparticle solutions at different concentrations under 808 nm laser irradiation (1.0 W/cm^2). **(I)** Photothermal stability evaluation of BSA/SP nanoparticles and BSA-MnO$_2$/SP nanocomposites after five cycles of laser on/off.

Evaluation of Photothermal Conversion Efficacy

To evaluate the photothermal conversion efficacy, the solutions containing nanoparticles were treated with 808 nm laser, and the temperatures of the solutions were recorded. At the same concentration, the temperatures of the solutions containing BSA-MnO$_2$/SP nanocomposites gradually increased under laser irradiation (**Figure 3A**). To confirm power density–dependent temperature increase, the commonly used laser densities (0.5, 1.0, and 1.5 W/cm^2) were used. The temperature increased much more obviously at a higher power density of laser, which reached 36.2, 56.6, and 65.7°C after 5 min of laser irradiation at power densities of 0.5, 1.0, and 1.5 W/cm^2, respectively (**Figure 3B**). After 5 min of laser irradiation, the temperatures of the solutions reached the maximum. These results suggested that higher power density could lead to a higher temperature increase for BSA-MnO$_2$/SP nanocomposites. The power density–dependent temperature increase was also observed for BSA/SP nanoparticles (**Figures 3C,D**). At a power density of 1.0 W/cm^2, the temperature of the solutions containing BSA-MnO$_2$/SP nanocomposites increased diversely at different concentrations (**Figure 3E**). At concentrations of 12.5, 25, 50, and 100 μg/ml, the solution temperature increased to 34.0, 41.1, 48.7, and 56.6°C after 5 min of laser irradiation, respectively (**Figure 3F**). Similar tendencies were also observed for BSA/SP nanoparticles, and the temperature increase was much more obvious at a higher concentration (**Figures 3G,H**).

The photothermal stability of nanoparticles was then evaluated. After five cycles of laser on/off, the temperature increases of solutions containing BSA/SP nanoparticles and BSA-MnO$_2$/SP nanocomposites did not have any decreases (**Figure 3I**), suggesting their excellent photothermal stability. The slight increases in maximal temperatures for solutions after more cycles of laser irradiation might be due to high

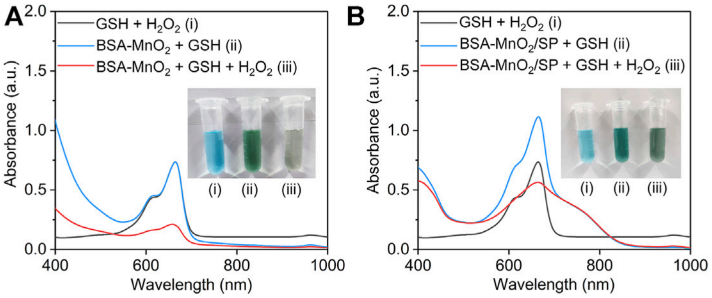

FIGURE 4 | Evaluation of OH generation efficacy. **(A)** Evaluation of OH generation *via* BSA-MnO_2 nanoparticle–mediated Fenton-like reaction using MB as an indicator. **(B)** Evaluation of OH generation *via* BSA-MnO_2/SP nanocomposite–mediated Fenton-like reaction using MB as an indicator. **(C)** Evaluation of OH generation for BSA-MnO_2/SP nanocomposites without or with 808 nm laser irradiation (1.0 W/cm^2) for 5 min.

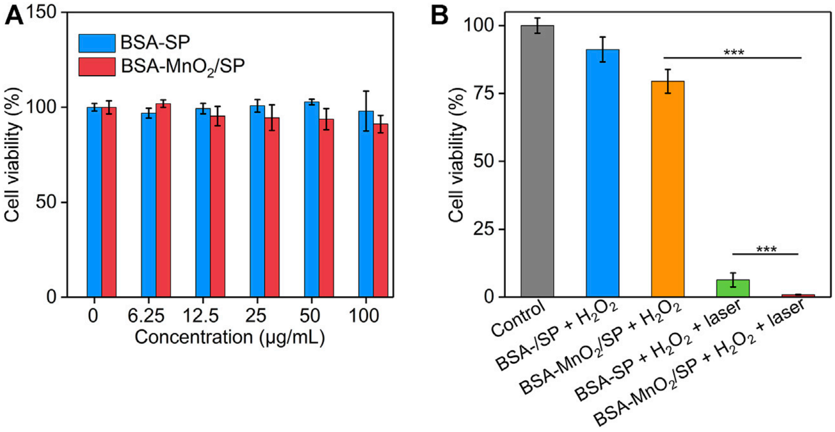

FIGURE 5 | Evaluation of *in vitro* therapeutic efficacy. **(A)** Cell viability of HepG2 cells after incubation with BSA/SP nanoparticles or BSA-MnO_2/SP nanocomposites at different SP concentrations for 24 h. **(B)** Cell viability of HepG2 cells after incubation with BSA/SP nanoparticles or BSA-MnO_2/SP nanocomposites in the presence of H_2O_2 (100 μM) without or with 808 nm laser irradiation (1.0 W/cm^2) for 5 min.

temperature–mediated evaporation of water to increase the concentrations of nanoparticles. In addition, the temperatures were similar for BSA/SP nanoparticles and BSA-MnO_2/SP nanocomposites at the same concentration and laser irradiation time. This indicated that BSA/SP nanoparticles and BSA-MnO_2/SP nanocomposites had similar photothermal conversion efficacy.

Evaluation of OH Generation Efficacy

The generation of OH *via* MnO_2-mediated Fenton-like reaction was evaluated using MB as the indicator. The characteristic absorption peak of MB at 665 nm did not have obvious changes for GSH + MB + H_2O_2 and BSA-MnO_2 + GSH + MB groups, while that was obviously reduced for the BSA-MnO_2 + GSH + MB + H_2O_2 group (**Figure 4A**), which suggested the generation of OH *via* Fenton-like reaction for BSA-MnO_2 nanoparticles. The characteristic absorption peak of MB was still high in the BSA-MnO_2/SP + GSH + MB group, which was obviously reduced in the BSA-MnO_2/SP + GSH + MB + H_2O_2 group (**Figure 4B**), indicating the OH generation for BSA-MnO_2/SP nanocomposites. In addition, the decrease in the characteristic absorption peak of MB in the BSA-MnO_2/SP + GSH + MB + H_2O_2 group was much more obvious after 808 nm laser irradiation (**Figure 4C**), which suggested the enhanced generation of OH after 808 nm laser irradiation. These results suggested that the Fenton-like reaction effect of BSA-MnO_2/SP nanocomposites could be accelerated by the PTT-mediated temperature rise, and thus, PTT and CDT showed a synergistic effect.

Evaluation of *In Vitro* Therapeutic Efficacy

The *in vitro* cytotoxicity of BSA/SP nanoparticles and BSA-MnO_2/SP nanocomposites was evaluated using the CCK-8 assay. After treatment with BSA/SP nanoparticles for 24 h, the cell viability of HepG2 cells did not have obvious changes even at a high concentration of 100 μg/ml when compared to the control group (**Figure 5A**), which indicated the good cytocompatibility of BSA/SP nanoparticles. After incubation with BSA-MnO_2/SP nanocomposites, the cell viability reduced with the increase in concentration, which should be due to the slight cytotoxicity induced by MnO_2 nanoparticles.

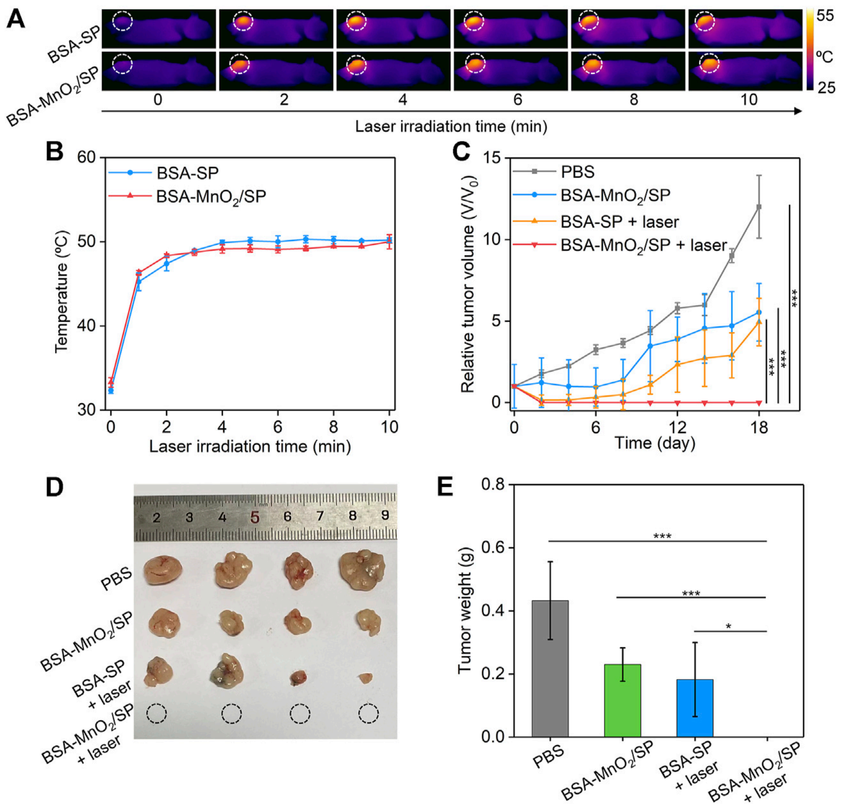

FIGURE 6 | Evaluation of *in vivo* antitumor efficacy. **(A)** Thermal imaging of HepG2 tumor–bearing nude mice after treatment with BSA/SP nanoparticles or BSA-MnO_2/SP nanocomposites under 808 nm laser irradiation (1.0 W/cm^2) for different times. **(B)** Temperature changes in tumor sites for BSA/SP nanoparticle– or BSA-MnO_2/SP nanocomposite–injected mice at different laser irradiating times. **(C)** Relative tumor volumes of HepG2 tumor–bearing mice after different treatments. **(D)** Photographs of tumors from HepG2 tumor–bearing mice after different treatments for 18 days. **(E)** Tumor weight of HepG2 tumor–bearing mice after different treatments for 18 days.

The *in vitro* therapeutic efficacy of nanoparticles was then investigated (**Figure 5B**). Without 808 nm laser irradiation, the cell viability of HepG2 cells did not have obvious changes after treatment with BSA/SP nanoparticles and H_2O_2, while that significantly reduced to 79.5% after treatment with BSA-MnO_2/SP nanocomposites and H_2O_2, suggesting the generation of highly toxic OH for BSA-MnO_2/SP nanocomposite–mediated CDT. With 808 nm laser irradiation, the cell viability of HepG2 cells after treatment with BSA/SP nanoparticles and H_2O_2 was only 6.3% due to BSA/SP nanoparticle–mediated PTT. In addition, the cell viability of HepG2 cells after treatment of BSA-MnO_2/SP nanocomposites and H_2O_2 with 808 nm laser irradiation was 0.87%, which was 91.3- and 7.2-fold lower than that in the BSA-MnO_2/SP + H_2O_2 and BSA/SP + H_2O_2 + laser group, respectively. These results indicated the amplified *in vitro* therapeutic efficacy of BSA-MnO_2/SP nanocomposite–mediated combinational PTT and CDT compared to sole CDT and PTT.

Evaluation of *In Vivo* Antitumor Efficacy

To evaluate the *in vivo* therapeutic efficacy, HepG2 tumor–bearing mice were randomly divided into four groups, and PBS, BSA/SP nanoparticles, or BSA-MnO_2/SP nanocomposites were locally injected into tumor sites, followed by irradiation of tumors with 808 nm laser (1.0 W/cm^2). Although the temperatures of nanoparticle solutions reached the maximum after 5 min of laser irradiation, a longer period of laser irradiation (10 min) was conducted to achieve ideal therapeutic efficacy. Under laser irradiation, the temperatures of tumor sites gradually increased with the laser irradiating time for both BSA/SP– and BSA-MnO_2/SP–injected mice (**Figure 6A**). The temperatures at different irradiating times for these two groups were similar, which reached the maximum (around 50.2°C) after 10 min of laser irradiation (**Figure 6B**). Note that the temperature of tumor sites for PBS-injected mice did not have obvious changes under laser irradiation (**Supplementary Figure S3**). These results suggested that BSA/SP and BSA-MnO_2/SP showed a similar *in vivo* PTT effect.

The *in vivo* therapeutic efficacy was evaluated by monitoring tumor growth. The tumor growth of BSA-MnO_2/SP–injected mice without laser irradiation was inhibited by 2.2-fold compared to that in control mice (**Figure 6C**), which should be due to the CDT effect. The tumor growth was inhibited by 2.4-fold after BSA/SP nanoparticle injection with 808 nm laser irradiation because of the PTT effect. It should be noteworthy that the growth of tumors was completely inhibited after BSA-

MnO_2/SP nanocomposite injection and laser irradiation, which was due to the combinational action of PTT and CDT. After treatment for 18 days, no tumors were observed for the BSA-MnO_2/SP + laser group, and the tumors in the BSA-MnO_2/SP and BSA/SP + laser groups were smaller than those in the control group (**Figure 6D**). The tumor weight in the BSA-MnO_2/SP + laser group was 0 g, while that was 0.43, 0.23, and 0.18 g for the control, BSA-MnO_2/SP, and BSA/SP + laser group, respectively (**Figure 6E**). These results suggested that BSA-MnO_2/SP after laser irradiation showed the highest antitumor efficacy due to the combinational action of CDT and PDT. In addition, the body weight of mice after different treatments remained nearly unchanged (**Supplementary Figure S4**), indicating that BSA-MnO_2/SP–mediated therapy did not cause significant toxicity.

CONCLUSION

We have reported the construction of BSA-MnO_2/SP nanocomposites for combinational PTT and CDT of hepatic carcinoma in living mouse models. Such BSA-MnO_2/SP nanocomposites could be synthesized *via* a facile two-step procedure. The formed BSA-MnO_2/SP nanocomposites showed a high photothermal conversion efficacy under 808 nm laser irradiation and efficient OH generation efficacy *via* a Fenton-like reaction. By mediating the combinational action of PTT and CDT, BSA-MnO_2/SP nanocomposites led to much higher efficacy in killing HepG2 cancer cells *in vitro* than to their counterparts. Such a treatment strategy could afford an obviously enhanced antitumor efficacy in inhibiting the growth of subcutaneous HepG2 tumors in living mice. In view of the flexible and facile construction of nanocomposites, this nanoplatform can be integrated with other therapeutic components (such as chemodrugs and immunotherapeutic drugs) to achieve multimodal therapy of different types of tumors. By modifying the targeting ligands on the surface to increase their accumulation into tumor sites after systematic administration, these nanocomposites can be used for targeted treatment of tumors.

DATA AVAILABILITY STATEMENT

The raw data supporting the conclusion of this article will be made available by the authors, without undue reservation.

ETHICS STATEMENT

The animal study was reviewed and approved by the Institutional Anima Care and Treatment Committee of Donghua University.

AUTHOR CONTRIBUTIONS

JZ, JL, and QZ, the corresponding authors, contributed toward conception, design of the study, and revision of the manuscript; JZ, QS, and CL contributed toward acquisition, analysis, and interpretation of the data and drafting of the article. MD and ZZ contributed toward acquisition of the data and analysis. All authors read and approved the final manuscript.

FUNDING

This study was supported by the Science and Technology Commission of Shanghai Municipality (22ZR1424900, 22ZR1401100, 20DZ2254900) and the Fundamental Research Funds for the Central Universities (2232021A-05).

SUPPLEMENTARY MATERIAL

The Supplementary Material for this article can be found online at https://www.frontiersin.org/articles/10.3389/fbioe.2022.919235/full#supplementary-material

REFERENCES

Begines, B., Ortiz, T., Pérez-Aranda, M., Martínez, G., Merinero, M., Argüelles-Arias, F., et al. (2020). Polymeric Nanoparticles for Drug Delivery: Recent Developments and Future Prospects. *Nanomaterials* 10, 1403. doi:10.3390/nano10071403

Cao, S., Fan, J., Sun, W., Li, F., Li, K., Tai, X., et al. (2019). A Novel Mn-Cu Bimetallic Complex for Enhanced Chemodynamic Therapy with Simultaneous Glutathione Depletion. *Chem. Commun.* 55, 12956–12959. doi:10.1039/c9cc06040e

Chen, T., Chu, Q., Li, M., Han, G., and Li, X. (2021). Fe_3O_4@Pt Nanoparticles to Enable Combinational Electrodynamic/chemodynamic Therapy. *J. Nanobiotechnol.* 19, 206. doi:10.1186/s12951-021-00957-7

Chen, W., Zhang, C., Chen, D., Li, Y., Wu, S., Xu, C., et al. (2022). Tumor Redox Microenvironment Modulating Composite Hydrogels for Enhanced Sonodynamic Therapy of Colorectal Cancer. *J. Mat. Chem. B* 10, 1960–1968. doi:10.1039/d2tb00170e

Chen, Y.-W., Su, Y.-L., Hu, S.-H., and Chen, S.-Y. (2016). Functionalized Graphene Nanocomposites for Enhancing Photothermal Therapy in Tumor Treatment. *Adv. Drug Deliv. Rev.* 105, 190–204. doi:10.1016/j.addr.2016.05.022

De Ruysscher, D., Niedermann, G., Burnet, N. G., Siva, S., Lee, A. W. M., and Hegi-Johnson, F. (2019). Radiotherapy Toxicity. *Nat. Rev. Dis. Prim.* 5, 13. doi:10.1038/s41572-019-0064-5

Depalo, N., Iacobazzi, R. M., Valente, G., Arduino, I., Villa, S., Canepa, F., et al. (2017). Sorafenib Delivery Nanoplatform Based on Superparamagnetic Iron Oxide Nanoparticles Magnetically Targets Hepatocellular Carcinoma. *Nano Res.* 10, 2431–2448. doi:10.1007/s12274-017-1444-3

Gai, S., Yang, G., Yang, P., He, F., Lin, J., Jin, D., et al. (2018). Recent Advances in Functional Nanomaterials for Light-Triggered Cancer Therapy. *Nano today* 19, 146–187. doi:10.1016/j.nantod.2018.02.010

Golubnitschaja, O., Yeghiazaryan, K., Stricker, H., Trog, D., Schild, H. H., and Berliner, L. (2016). Patients with Hepatic Breast Cancer Metastases Demonstrate Highly Specific Profiles of Matrix Metalloproteinases MMP-2 and MMP-9 after SIRT Treatment as Compared to Other Primary and Secondary Liver Tumours. *BMC Cancer* 16, 357. doi:10.1186/s12885-016-2382-2

Hao, Y.-N., Zhang, W.-X., Gao, Y.-R., Wei, Y.-N., Shu, Y., and Wang, J.-H. (2021). State-of-the-art Advances of Copper-Based Nanostructures in the Enhancement of Chemodynamic Therapy. *J. Mat. Chem. B* 9, 250–266. doi:10.1039/d0tb02360d

Hu, J.-J., Cheng, Y.-J., and Zhang, X.-Z. (2018). Recent Advances in Nanomaterials for Enhanced Photothermal Therapy of Tumors. *Nanoscale* 10, 22657–22672. doi:10.1039/c8nr07627h

Hu, J.-J., Liu, M.-D., Chen, Y., Gao, F., Peng, S.-Y., Xie, B.-R., et al. (2019). Immobilized Liquid Metal Nanoparticles with Improved Stability and Photothermal Performance for Combinational Therapy of Tumor. *Biomaterials* 207, 76–88. doi:10.1016/j.biomaterials.2019.03.043

Jung, H. S., Verwilst, P., Sharma, A., Shin, J., Sessler, J. L., and Kim, J. S. (2018). Organic Molecule-Based Photothermal Agents: an Expanding Photothermal Therapy Universe. *Chem. Soc. Rev.* 47, 2280–2297. doi:10.1039/c7cs00522a

Li, B., Gong, T., Xu, N., Cui, F., Yuan, B., Yuan, Q., et al. (2020). Improved Stability and Photothermal Performance of Polydopamine-Modified Fe_3O_4 Nanocomposites for Highly Efficient Magnetic Resonance Imaging-Guided Photothermal Therapy. *Small* 16, 2003969. doi:10.1002/smll.202003969

Li, J., Jiang, R., Wang, Q., Li, X., Hu, X., Yuan, Y., et al. (2019). Semiconducting Polymer Nanotheranostics for NIR-II/Photoacoustic Imaging-Guided Photothermal Initiated Nitric Oxide/Photothermal Therapy. *Biomaterials* 217, 119304. doi:10.1016/j.biomaterials.2019.119304

Li, J., Xie, C., Huang, J., Jiang, Y., Miao, Q., and Pu, K. (2018a). Semiconducting Polymer Nanoenzymes with Photothermic Activity for Enhanced Cancer Therapy. *Angew. Chem. Int. Ed.* 57, 3995–3998. doi:10.1002/anie.201800511

Li, J., Zhen, X., Lyu, Y., Jiang, Y., Huang, J., and Pu, K. (2018b). Cell Membrane Coated Semiconducting Polymer Nanoparticles for Enhanced Multimodal Cancer Phototheranostics. *ACS Nano* 12, 8520–8530. doi:10.1021/acsnano.8b04066

Liu, J., Qing, X., Zhang, Q., Yu, N., Ding, M., Li, Z., et al. (2021). Oxygen-Producing Proenzyme Hydrogels for Photodynamic-Mediated Metastasis-Inhibiting Combinational Therapy. *J. Mat. Chem. B* 9, 5255–5263. doi:10.1039/d1tb01009c

Liu, M., Tu, J., Feng, Y., Zhang, J., and Wu, J. (2020). Synergistic Co-delivery of Diacid Metabolite of Norcantharidin and ABT-737 Based on Folate-Modified Lipid Bilayer-Coated Mesoporous Silica Nanoparticle against Hepatic Carcinoma. *J. Nanobiotechnol.* 18, 114. doi:10.1186/s12951-020-00677-4

Liu, Y., Bhattarai, P., Dai, Z., and Chen, X. (2019). Photothermal Therapy and Photoacoustic Imaging via Nanotheranostics in Fighting Cancer. *Chem. Soc. Rev.* 48, 2053–2108. doi:10.1039/c8cs00618k

Manzano, M., and Vallet-Regí, M. (2020). Mesoporous Silica Nanoparticles for Drug Delivery. *Adv. Funct. Mat.* 30, 1902634. doi:10.1002/adfm.201902634

Ming, J., Zhu, T., Yang, W., Shi, Y., Huang, D., Li, J., et al. (2020). Pd@Pt-GOx/HA as a Novel Enzymatic Cascade Nanoreactor for High-Efficiency Starving-Enhanced Chemodynamic Cancer Therapy. *ACS Appl. Mat. Interfaces* 12, 51249–51262. doi:10.1021/acsami.0c15211

Ou, J., Tian, H., Wu, J., Gao, J., Jiang, J., Liu, K., et al. (2021). MnO_2-Based Nanomotors with Active Fenton-like Mn^{2+} Delivery for Enhanced Chemodynamic Therapyrapy. *ACS Appl. Mat. Interfaces* 13, 38050–38060. doi:10.1021/acsami.1c08926

Peng, H., Borg, R. E., Dow, L. P., Pruitt, B. L., and Chen, I. A. (2020a). Controlled Phage Therapy by Photothermal Ablation of Specific Bacterial Species Using Gold Nanorods Targeted by Chimeric Phages. *Proc. Natl. Acad. Sci. U.S.A.* 117, 1951–1961. doi:10.1073/pnas.1913234117

Peng, H., Borg, R. E., Nguyen, A. B. N., and Chen, I. A. (2020b). Chimeric Phage Nanoparticles for Rapid Characterization of Bacterial Pathogens: Detection in Complex Biological Samples and Determination of Antibiotic Sensitivity. *ACS Sens.* 5, 1491–1499. doi:10.1021/acssensors.0c00654

Peng, H., and Chen, I. A. (2018). Rapid Colorimetric Detection of Bacterial Species through the Capture of Gold Nanoparticles by Chimeric Phages. *ACS Nano* 13, 1244–1252. doi:10.1021/acsnano.8b06395

Qi, Y., Pan, Y., Gu, F., Wei, S., Fei, C., and Han, J. (2021). Construction and Characterization of Folate-Functionalized Curdlan-Trilysine siRNA Delivery Platform for *In Vivo* Hepatic Carcinoma Treatment. *Colloids Surf. B.* 198, 111491. doi:10.1016/j.colsurfb.2020.111491

Sahu, A., Kwon, I., and Tae, G. (2020). Improving Cancer Therapy through the Nanomaterials-Assisted Alleviation of Hypoxia. *Biomaterials* 228, 119578. doi:10.1016/j.biomaterials.2019.119578

Shrestha, B., Tang, L., and Romero, G. (2019). Nanoparticles-Mediated Combination Therapies for Cancer Treatment. *Adv. Ther.* 2, 1900076. doi:10.1002/adtp.201900076

Siddique, S., and Chow, J. C. L. (2020). Application of Nanomaterials in Biomedical Imaging and Cancer Therapy. *Nanomaterials* 10, 1700. doi:10.3390/nano10091700

Son, S., Kim, J. H., Wang, X., Zhang, C., Yoon, S. A., Shin, J., et al. (2020). Multifunctional Sonosensitizers in Sonodynamic Cancer Therapy. *Chem. Soc. Rev.* 49, 3244–3261. doi:10.1039/c9cs00648f

Tang, Z. m., Liu, Y. y., Ni, D. l., Zhou, J. j., Zhang, M., Zhao, P. r., et al. (2020). Biodegradable Nanoprodrugs:“delivering” ROS to Cancer Cells for Molecular Dynamic Therapy. *Adv. Mat.* 32, 1904011. doi:10.1002/adma.201904011

Tian, Q., Xue, F., Wang, Y., Cheng, Y., An, L., Yang, S., et al. (2021). Recent Advances in Enhanced Chemodynamic Therapy Strategies. *Nano Today* 39, 101162. doi:10.1016/j.nantod.2021.101162

Tian, Q., Zhang, C.-N., Wang, X.-H., Wang, W., Huang, W., Cha, R.-T., et al. (2010). Glycyrrhetinic Acid-Modified Chitosan/poly (Ethylene Glycol) Nanoparticles for Liver-Targeted Delivery. *Biomaterials* 31, 4748–4756. doi:10.1016/j.biomaterials.2010.02.042

Wang, H., Liu, Y., Shen, K., Dong, Y., Sun, J., Shu, Y., et al. (2019). A Comparison between Radiofrequency Ablation Combined with Transarterial Chemoembolization and Surgical Resection in Hepatic Carcinoma: A Meta-Analysis. *J. Cancer Res. Ther.* 15, 1617–1623. doi:10.4103/jcrt.JCRT_503_19

Wang, X., Zhong, X., Liu, Z., and Cheng, L. (2020). Recent Progress of Chemodynamic Therapy-Induced Combination Cancer Therapy. *Nano Today* 35, 100946. doi:10.1016/j.nantod.2020.100946

Yu, L., Xu, M., Xu, W., Xiao, W., Jiang, X.-H., Wang, L., et al. (2020). Enhanced Cancer-Targeted Drug Delivery Using Precoated Nanoparticles. *Nano Lett.* 20, 8903–8911. doi:10.1021/acs.nanolett.0c03982

Yu, P., Li, X., Cheng, G., Zhang, X., Wu, D., Chang, J., et al. (2021). Hydrogen Peroxide-Generating Nanomedicine for Enhanced Chemodynamic Therapy. *Chin. Chem. Lett.* 32, 2127–2138. doi:10.1016/j.cclet.2021.02.015

Yuan, Z., Lin, C., He, Y., Tao, B., Chen, M., Zhang, J., et al. (2020). Near-infrared Light-Triggered Nitric-Oxide-Enhanced Photodynamic Therapy and Low-Temperature Photothermal Therapy for Biofilm Elimination. *ACS Nano* 14, 3546–3562. doi:10.1021/acsnano.9b09871

Zhang, C., Shi, G., Zhang, J., Niu, J., Huang, P., Wang, Z., et al. (2017). Redox- and Light-Responsive Alginate Nanoparticles as Effective Drug Carriers for Combinational Anticancer Therapy. *Nanoscale* 9, 3304–3314. doi:10.1039/c7nr00005g

Zhang, Y., Yang, D., Chen, H., Lim, W. Q., Phua, F. S. Z., An, G., et al. (2018). Reduction-sensitive Fluorescence Enhanced Polymeric Prodrug Nanoparticles for Combinational Photothermal-Chemotherapy. *Biomaterials* 163, 14–24. doi:10.1016/j.biomaterials.2018.02.023

Zhou, B., Wang, R., Chen, F., Zhao, L., Wang, P., Li, X., et al. (2018). ^{99m}Tc-labeled RGD-Polyethylenimine Conjugates with Entrapped Gold Nanoparticles in the Cavities for Dual-Mode SPECT/CT Imaging of Hepatic Carcinoma. *ACS Appl. Mat. Interfaces* 10, 6146–6154. doi:10.1021/acsami.7b17107

Zhu, H., Han, W., Gan, Y., Li, Q., Li, X., Shao, L., et al. (2019). Combined Modality Therapy Based on Hybrid Gold Nanostars Coated with Temperature Sensitive Liposomes to Overcome Paclitaxel-Resistance in Hepatic Carcinoma. *Pharmaceutics* 11, 683. doi:10.3390/pharmaceutics11120683

Conflict of Interest: The authors declare that the research was conducted in the absence of any commercial or financial relationships that could be construed as a potential conflict of interest.

Publisher’s Note: All claims expressed in this article are solely those of the authors and do not necessarily represent those of their affiliated organizations, or those of the publisher, the editors, and the reviewers. Any product that may be evaluated in this article, or claim that may be made by its manufacturer, is not guaranteed or endorsed by the publisher.

Copyright © 2022 Su, Liu, Zhu, Ding, Zhang, Li and Zhang. This is an open-access article distributed under the terms of the Creative Commons Attribution License (CC BY). The use, distribution or reproduction in other forums is permitted, provided the original author(s) and the copyright owner(s) are credited and that the original publication in this journal is cited, in accordance with accepted academic practice. No use, distribution or reproduction is permitted which does not comply with these terms.

ORIGINAL RESEARCH
published: 22 June 2022
doi: 10.3389/fbioe.2022.939158

Manganese-Based Prussian Blue Nanocatalysts Suppress Non-Small Cell Lung Cancer Growth and Metastasis *via* Photothermal and Chemodynamic Therapy

Danruo Fang*[1†], *Zeyu Liu*[2†], *Hansong Jin*[3], *Xiulin Huang*[1], *Yongxin Shi*[1] and *Suqin Ben*[1]

[1]Department of Respiratory and Critical Care Medicine, Shanghai General Hospital, Shanghai Jiao Tong University School of Medicine, Shanghai, China, [2]Department of Respiratory and Critical Care Medicine, Shanghai Jiao Tong University Affiliated Sixth People's Hospital, Shanghai, China, [3]Department of Thoracic Surgery, Shanghai General Hospital, Shanghai Jiao Tong University School of Medicine, Shanghai, China

OPEN ACCESS

Edited by:
Yu Luo,
Shanghai University of Engineering Sciences, China

Reviewed by:
Zhouqi Meng,
Yale University, United States
Benqing Zhou,
Shantou University, China

****Correspondence:***
Suqin Ben
bensuqin012@163.com

†These authors have contributed equally to this work

Specialty section:
This article was submitted to Nanobiotechnology, a section of the journal Frontiers in Bioengineering and Biotechnology

Received: *08 May 2022*
Accepted: *27 May 2022*
Published: *22 June 2022*

Citation:
Fang D, Liu Z, Jin H, Huang X, Shi Y and Ben S (2022) Manganese-Based Prussian Blue Nanocatalysts Suppress Non-Small Cell Lung Cancer Growth and Metastasis via Photothermal and Chemodynamic Therapy.
Front. Bioeng. Biotechnol. 10:939158.
doi: 10.3389/fbioe.2022.939158

Based on the safety of prussian blue (PB) in biomedical application, we prepared manganese-based prussian blue (MnPB) nanocatalysts to achieve enhanced photothermal therapy and chemodynamic therapy. And we conducted a series of experiments to explore the therapeutic effects of MnPB nanoparticles (NPs) on non-small cell lung cancer (NSCLC) *in vivo* and *in vitro*. For *in vitro* experiments, the MnPB NPs suppressed growth of A549 cells by reactive oxygen species upregulation and near-infrared irradiation. Moreover, the MnPB NPs could inhibit lung cancer metastasis through downregulating the matrix metalloproteinase (MMP)-2 and MMP-9 expression in A549 cells. And for *in vivo* experiments, the MnPB NPs inhibited the growth of xenografted tumor effectively and were biologically safe. Meanwhile, Mn^{2+} as a T1-weighted agent could realize magnetic resonance imaging-guided diagnosis and treatment. To sum up, the results in this study clearly demonstrated that the MnPB NPs had remarkable effects for inhibiting the growth and metastasis of NSCLC and might serve as a promising multifunctional nanoplatform for NSCLC treatment.

Keywords: MnPB nanoparticles, non-small cell lung cancer, chemodynamic therapy, photothermal therapy, metastatic lung cancer

INTRODUCTION

Lung cancer is a common and severe global health problem, as it has become the first and third major cause of cancer related mortality among males and females respectively (Altorki et al., 2019; Zheng et al., 2021). And non-small cell lung cancer (NSCLC) is the main histological subtype, accounting for about 85% (Oser et al., 2015). Although recent therapeutic advances in surgery, chemoradiotherapy and targeted therapy, a substantial proportion of patients (75%) diagnosed

---

Abbreviations: CCK-8, cell counting kit-8; CDT, chemodynamic therapy; DCFH-DA, dichlorodihydrofluorescein diacetate; DLS, dynamic light scattering; ECM, extracellular matrix; EMT, epithelial-to-mesenchymal transition; FDA, Food and Drug Administration; HRP, horseradish peroxidase; H_2O_2, hydrogen peroxide; MB, methylene blue; MMP, matrix metalloproteinase; MRI, magnetic resonance imaging; NIR, near-infrared; NPs, nanoparticles; NSCLC, non-small cell lung cancer; PB, prussian blue; PBS, phosphate buffered saline; PI, propidium iodide; PS, phosphatidylserine; PTT, photothermal therapy; ROS, reactive oxygen species; TEM, transmission electron microscopy; XRD, X-ray powder diffraction.

with metastatic lung cancer has poor 5-year relative survival rate (6%) (Siegel et al., 2021). Additionally, drug resistance, toxicity and limited efficacy of many therapeutic compounds are pivotal impediments to the successful treatment of NSCLC. Consequently, it is critical to develop other safe and effective treatments to combat this deadly disease.

Recently, with the rapid progress of nanomedicine, nanoparticle systems have attracted considerable attention for various applications of tumor diagnosis and treatment (Lim et al., 2015; Li J. et al., 2021). And some new therapeutic modalities, including photothermal therapy (PTT) and chemodynamic therapy (CDT), exhibit good effect on tumor treatment (Guan et al., 2021; Sun et al., 2021). PTT, as a promising non-invasive cancer treatment strategy, can convert photon energy into heat to eradicate tumor cells (Li et al., 2020; Zhao H. et al., 2021). And PTT exhibits several advantages, including limited side-effects, high spatial selectivity and minimal injury to normal tissues (Wang et al., 2020a; Zheng et al., 2020; He et al., 2021). Meanwhile, CDT is an emerging nanocatalyst-based cancer treatment, which decomposes hydrogen peroxide (H_2O_2) to generate toxic reactive oxygen species (ROS) by Fenton or Fenton-like reactions (Wang et al., 2020b; Yang et al., 2021). It is well known that ROS can induce protein, DNA, and lipid damage to cause tumor cell death (Goldstein et al., 1993; Lin et al., 2020). The combination of PTT and CDT has been drawing more and more research attention because of their high-efficacy (Manivasagan et al., 2022).

Prussian blue (PB), a mixed-valence iron (III) hexacyanoferrate (II), has been widely explored as a powerful tool in biomedical research due to some superior properties, including excellent biocompatibility, good biodegradability, easy synthesis and favorable thermal stability (Busquets and Estelrich, 2020; Gao et al., 2020). Besides, PB has been authorized by USA Food and Drug Administration (FDA) as a safe material for clinical applications (Odda et al., 2019). But PB nanoparticles (NPs) with low catalase-like activity and low photothermal conversion efficiency are not promising agents for PTT and CDT (Dacarro et al., 2018; Gao et al., 2020). Moreover, although PB NPs have been reported as T1-weighted contrast agents for magnetic resonance imaging (MRI) (Shokouhimehr et al., 2010), they have a weak effect on longitudinal relaxation (r1), resulting in the low diagnostic ability of tumor (Li et al., 2014). Since Mn^{2+}, Zn^{2+} and Gd^{3+} have good performance on enhancing T1 weighted MRI, it is an effective strategy to add metal ions into PB NPs for improving r1 value (Cai et al., 2015; Shou et al., 2020; Zhao W. et al., 2021). The manganese-based prussian blue (MnPB) nanocatalysts fabricated in this study not only possess excellent CDT/PTT effect, but also show high longitudinal relaxivity. Mn^{2+} in MnPB NPs enhances catalase-like activity of PB and improves PTT function resulting from strengthening optical absorption or shifting absorption to the near-infrared (NIR) region. Therefore, MnPB NPs in this study have strong synergistic effects and may shed light on potential therapies for growth and metastatic of NSCLC.

Tumor metastasis is a complicated mechanism involving tumor cell adhesion, migration and the degradation of the extracellular matrix (ECM) (Paolillo and Schinelli, 2019). Matrix metalloproteinases (MMPs) are zinc-dependent endopeptidases, playing a critical role in degrading the ECM (Gonzalez-Avila et al., 2019). Among MMPs, MMP2 and MMP9 are important members of MMP family, involving in the invasion and metastasis of NSCLC by degrading basement membrane and matrix collagen (Dong et al., 2013; Wang et al., 2018). A large number of scientific studies have shown that MMP2 and MMP9 are highly expressed in lung cancer tissues (Li et al., 2019; Han et al., 2020). Furthermore, the downregulation of MMP2/MMP9 can significantly inhibit tumor cell proliferation, invasion and metastasis (Itoh et al., 1999; Poudel et al., 2016). We found that MnPB NPs synthesized in our study could significantly inhibit MMP-2/MMP-9 expression and might be promising therapeutic agents to suppress growth and metastasis of NSCLC.

In the current study, we fully explored the anti-NSCLC effect of novel MnPB nanocatalysts *in vitro* and *in vivo*. The experimental results showed that MnPB nanocatalysts could serve as effective MRI-guided agents for synergistic chemodynamic/photothermal therapy and inhibit the growth and metastasis of NSCLC effectively.

MATERIALS AND METHODS

Materials

$MnCl_2·4H_2O$ (AR, 99.0%) and $K_4[Fe(CN)_6]·3H_2O$ (≥99.99%, metals basis) were acquired from Macklin Biochemical Technology Co., Ltd. (Shanghai, China) and Aladdin Chemistry Co., Ltd. (Shanghai, China) respectively. Citric acid was acquired from Sinopharm Chemical Reagent Co., Ltd. (Shanghai, China). Absolute ethyl alcohol (C_2H_5OH; AR) was purchased from Sinopharm Chemical Reagent Co., Ltd. (Shanghai, China). The deionized water (H_2O) was purified with a Milli-Q system (Millipore, Bedford, MA, United States). All chemicals and solvents were not further purified to use.

Synthesis of Manganese-Based Prussian Blue Nanoparticles

MnPB NPs were creatively synthesized by a facile ion-exchange method on the grounds of the co-precipitation strategy. First, $MnCl_2·4H_2O$ (0.3 mM) and citric acid (0.5 mM) dissolved in the deionized water (20 ml) were heated to 60°C for 5 min. The obtained mixture was served as solution A. Then, $K_4[Fe(CN)_6]$ (0.4 mM) and citric acid (0.4 mM) were added together in the deionized water (20 ml) to become solution B. The solution B was also heated to 60°C for 5 min under magnetically stirring. Next, the solution B was added dropwise to the solution A. Then the mixed solution was magnetically stirred and kept at 60°C for 2 min. And the collected product was subsequently washed by deionized water and ethonal after the reaction was cooled down to room temperature. Finally, washed solution was then dried at 60 °C in a vacuum oven for 24 h.

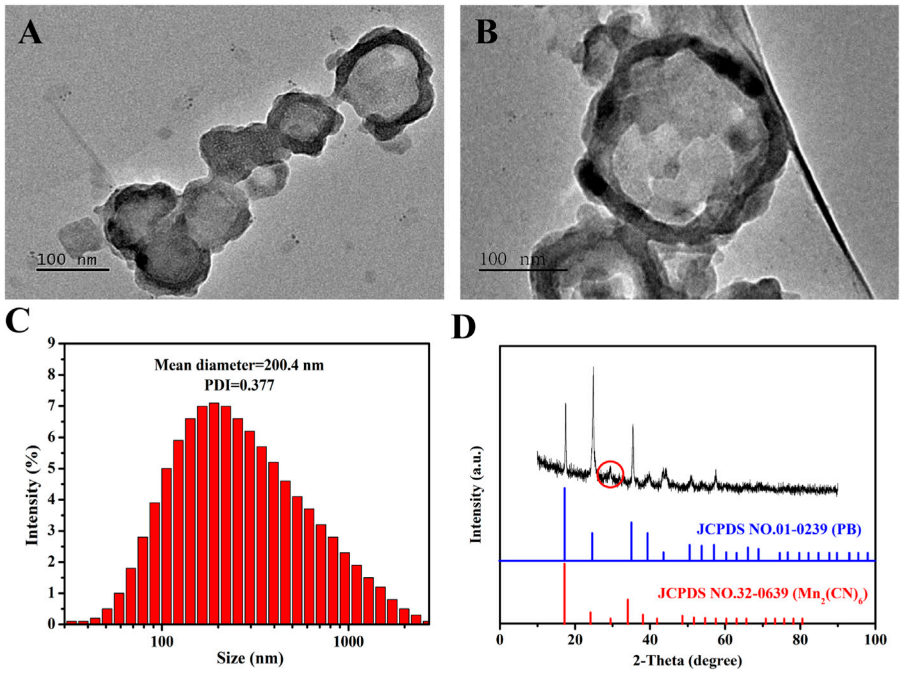

FIGURE 1 | The characterization of MnPB NPs. **(A,B)** TEM micrographs of MnPB NPs. **(C)** The hydrodynamic size of MnPB NPs. And the zeta potential of MnPB NPs is −30.53 mV. **(D)** XRD patterns of as-synthesized MnPB NPs.

Characterization of Manganese-Based Prussian Blue Nanoparticles

The particle size and morphology of MnPB NPs were measured by a JEM-JEOL-200 transmission electron microscopy (TEM, Tokyo, Japan) operating at 200 kV. The hydrodynamic size of MnPB NPs was analyzed by dynamic light scattering (DLS, Brookhaven Instrument Corporation, United States). And we used X-ray powder diffraction (XRD, Rigaku, Japan) to reveal the crystal structure and functional group of MnPB NPs.

Photothermal Properties of Manganese-Based Prussian Blue Nanoparticles

To evaluate the light absorption ability of MnPB NPs, the absorbance of MnPB NPs at various concentrations (100, 200 and 400 μg/ml) was measured *via* ultraviolet-visible-NIR (UV-vis-NIR) spectrophotometer (Agilent, CA, United States). Next, aqueous dispersion of MnPB NPs with different concentrations was exposed to irradiation with a NIR laser (808 nm, 1.0 W/cm^2). During laser irradiation period, we used an infrared thermal imaging camera (Fotric, China) to record the temperature change. Next, 200 μg/ml solution of MnPB NPs was irradiated with the 808 nm NIR laser light (1.0 W/cm^2) for another 10 min and cooled down to the room temperature to get temperature curves and photothermal conversion efficiency (η) of MnPB NPs. The formula of η is as follows:

$$\eta = \frac{hS(T_{max} - T_{surr}) - Q_{Dis}}{I(1 - 10^{-A_{808}})}$$

where h is the heat transfer coefficient, S is the surface area of the container, T_{max} is the maximum steady-state temperature of the sample solution, T_{surr} is the ambient surrounding temperature, Q_{Dis} is the heat input due to light absorption by the solvent and container, I is the laser power, and A_{808} is the absorbance of the sample solution at 808 nm (Liu X. et al., 2014).

Determination of Reactive Oxygen Species Generation

The ROS generation tests were divided into three groups: (1) H_2O_2 (200 μM) solution; (2) MnPB (1 mg/ml) solution; (3) MnPB (1 mg/ml) + H_2O_2 (200 μM) solution. Then we added methylene blue (MB) (5 μg/ml) in two groups to detect the ROS generation. And the UV-vis-NIR absorption spectra of these solutions were scanned in time-scan mode.

Cytotoxicity

BEAS-2B cells (normal human bronchial epithelial cells) and A549 cells (human lung adenocarcinoma cells) were inoculated into 96-well plates respectively and cultured for 24 h. Then the culture mediums were replaced by the fresh mediums with various concentrations of MnPB NPs. After 24 h of treatment, the mediums were detected by cell counting kit-8 (CCK-8) assay (Beyotime Biotechnology, China).

In Vitro Reactive Oxygen Species Detection

A549 cells were cultured in the 6-well plates and categorized into four groups: the control group, the H_2O_2 (100 μM) group,

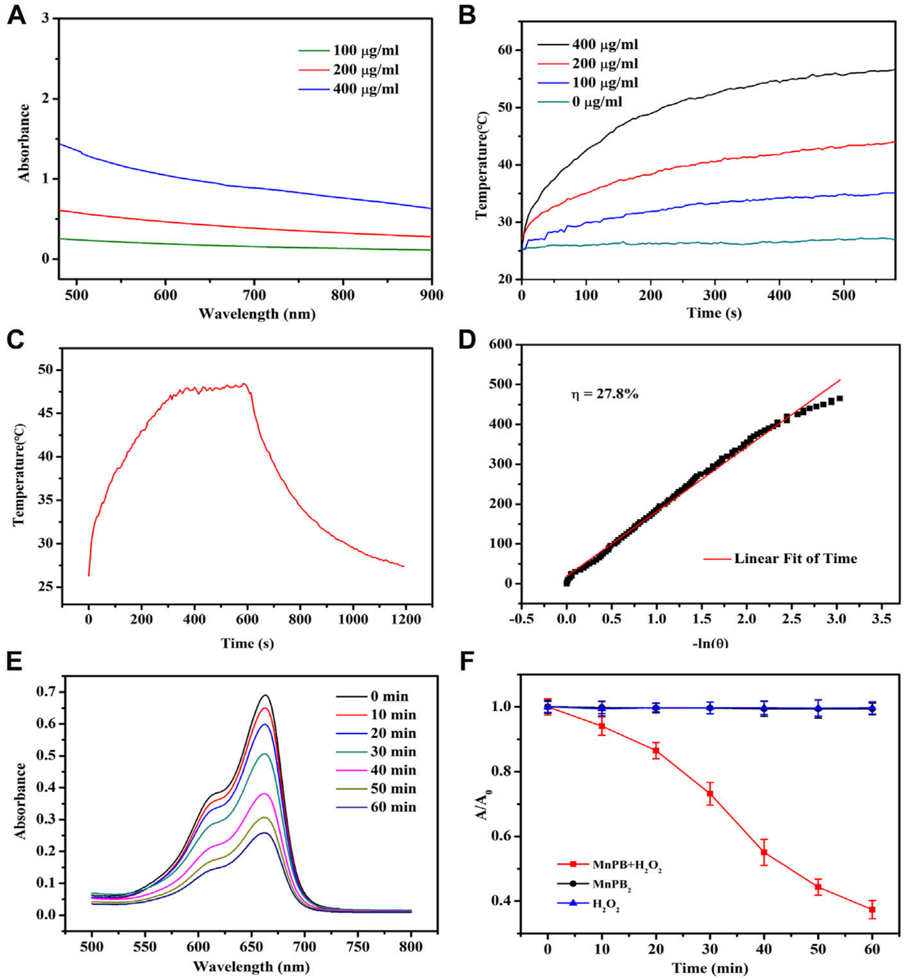

FIGURE 2 | The photothermal properties of MnPB NPs. **(A)** UV–vis–NIR absorption spectra of MnPB NPs at varying concentrations. **(B)** Temperature profiles of MnPB NPs at various concentrations under NIR laser irradiation (808 nm, 1.0 W/cm^2). **(C)** The heating-cooling curve of MnPB NPs at 200 μg/ml under NIR laser irradiation (808 nm, 1.0 W/cm^2). **(D)** Red linear regression curve for natural cooling process. **(E)** Degradation of MB treated with MnPB NPs and H_2O_2 versus time. **(F)** Absorbance of MB at 664 nm in different groups.

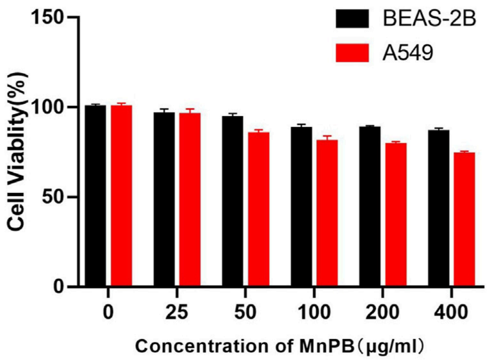

FIGURE 3 | Cytotoxicity of MnPB NPs in A549 cells and BEAS-2B cells.

the MnPB (400 μg/ml) group and the MnPB (400 μg/ml) + H_2O_2 (100 μM) group. After 24 h of treatment, intracellular ROS levels were assessed using the probe solution 2, 7-dichlorodihydrofluorescein diacetate (DCFH-DA, Beyotime Biotechnology, China). After incubated with DCFH-DA for 20 min, the cells were washed three times with PBS and replaced with serum-free mediums. Last, images were obtained under a fluorescence microscope (Leica DMi8, Leica, Germany).

Calcine-AM/Propidium Iodide Test and Annexin V-FITC Apoptosis Assay

The percentage of living and dead cells of A549 cells was examined by Calcine-AM/propidium iodide (PI) test and the apoptosis of A549 cells was detected the Annexin V-FITC apoptosis kit. For the Calcine-AM/PI test (Beyotime Biotechnology, China), A549 cells were cultured in the complete medium at pH 6.5 and divided into six groups: 1) control; 2) NIR; 3) H_2O_2 (100 μM); 4) MnPB (400 μg/ml) + NIR; 5) MnPB (400 μg/ml) + H_2O_2 (100 μM); 6) MnPB

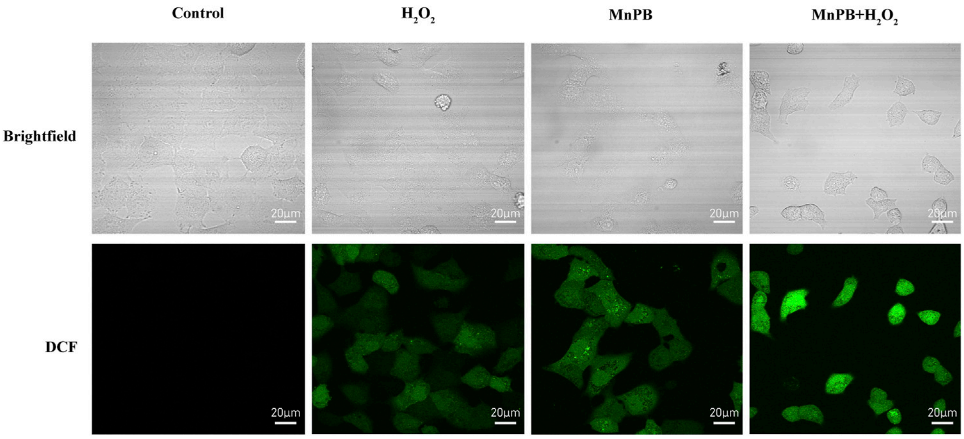

FIGURE 4 | The MnPB NPs increase the intracellular ROS production in non-small lung cancer cells. Confocal images of intracellular ROS generation and corresponding brightfield images in A549 cells in different groups. Scale bar, 20 μm.

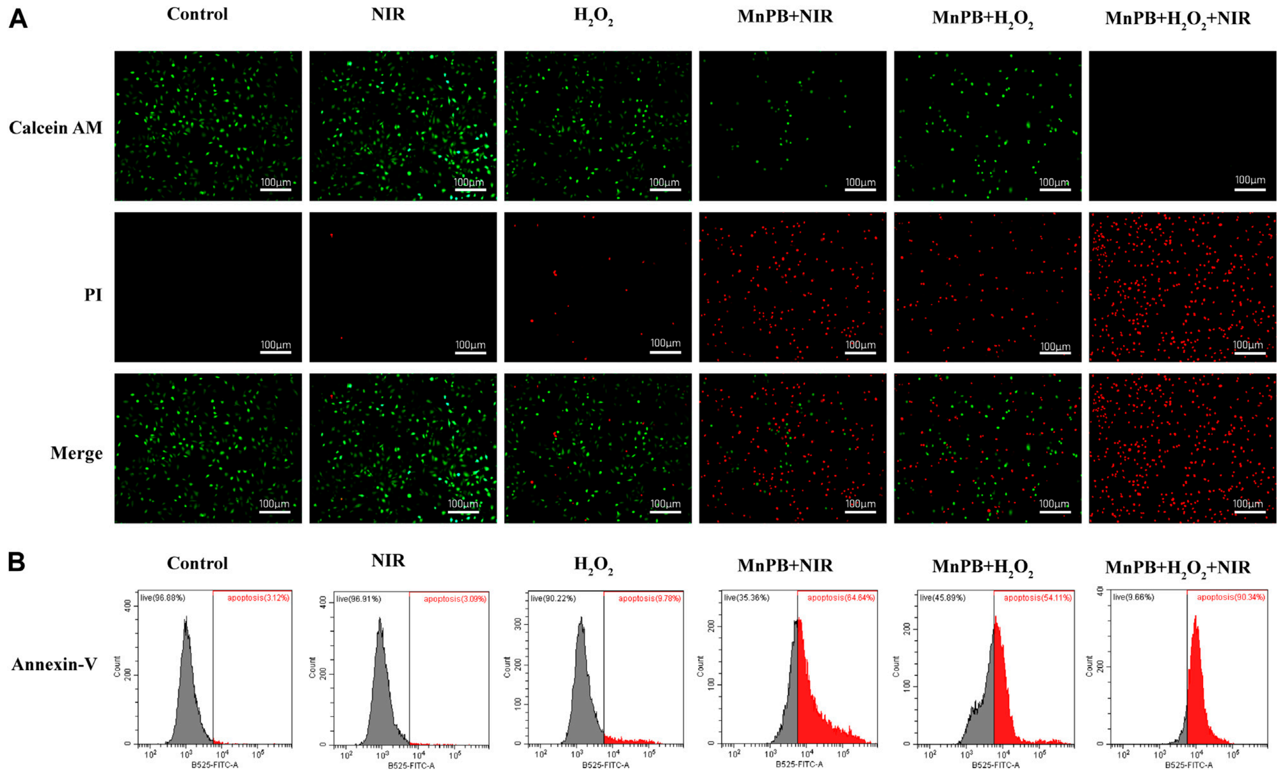

FIGURE 5 | The MnPB NPs can induce cell apoptosis by ROS upregulation and NIR irradiation. **(A)** Confocal images of A549 cells stained with Calcein-AM and PI after different treatments. Scale bar, 100 μm. **(B)** Flow cytometry analysis of cell apoptosis with Annexin V-FITC staining.

(400 μg/ml) + H_2O_2 (100 μM) + NIR. After 12 h of corresponding treatments, the group 2, 4, and 6 were irradiated with 808 nm NIR (1.0 W/cm^2) for 10 min. Then, cells were dyed with Calcein-AM and PI for 15 min. Finally, we acquired images using a fluorescence microscope (Leica DMi8, Leica, Germany).

In Annexin V-FITC apoptosis assay (Multi Sciences, China), the cell grouping and treatments were consistent with the Calcine-AM/PI experiment. A549 cells were collected and washed with cold PBS. Next, the cells were resuspended in 1 × binding buffer (500 μl) containing Annexin V-FITC (5 μl) and incubated for 5 min in the dark.

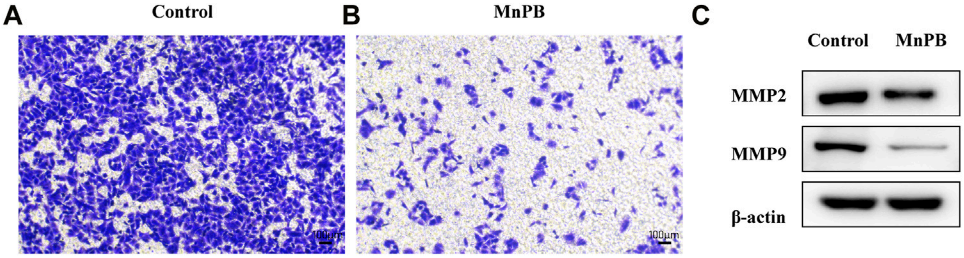

FIGURE 6 | The MnPB NPs inhibit the metastasis of non-small lung cancer cells. **(A)** and **(B)** Migration capacity of A549 cells exposed to MnPB NPs. **(C)** MMP2 and MMP9 expression of A549 cells in different groups.

And we utilized flow cytometry (cytoflex LX, Beckman Coulter) to assess the ratio of apoptotic cells.

Transwell Migration Assay

We used 24-well Transwell chambers (Corning, United States) with a polycarbonate filter membrane of 8 μm pore size for migration assays. A549 cells were divided into two groups: the control group and the MnPB group. At 24 h after starvation, A549 cells of control group were resuspended in the serum-free RPMI 1640 medium and cells of MnPB group were resuspended in serum-free RPMI 1640 medium with MnPB NPs (400 μg/ml). Subsequently, the A549 cells were added to the upper chamber and the lower plate was filled with RPMI 1640 medium containing 10% FBS. After 24 h, A549 cells migrated to the membranes of the upper chamber were fixed with 4% paraformaldehyde and stained with crystal violet. Ultimately, images were obtained using a fluorescence microscope (Leica DMi8, Leica, Germany).

Western Blot Analysis

A549 cells were grown in the 6-well plates and divided into the control group and the MnPB group. Protein harvesting and immunoblotting were performed as previously described (Fang et al., 2021). The primary antibodies included anti-MMP2 (Abcam, United States), anti-MMP9 (Abclonal, China) and anti-β-actin (Proteintech, China). And corresponding secondary antibodies were goat anti-rabbit IgG horseradish peroxidase (HRP) and goat anti-mouse IgG-HRP (Jackson Immunoresearch, United States).

In Vivo Xenograft Assay

When the tumor volume reached the size of 7–9 mm, mice were randomly divided into four groups ($n = 6$ per group). The mice were treated as follows: 1) control; 2) PBS + NIR; 3) MnPB (2 mg/ml); 4) MnPB (2 mg/ml) + NIR. After 8 h of intravenous injection, the mice of group 2 and 4 were exposed to the irradiation (808 nm, 1 W/cm^2) for 10 min and the change of temperature on tumor was recorded by a thermal imaging camera (FLIR A300). Meanwhile, tumor size and body weight of mice were measured ever 2 days. And the major organs were collected for histological analysis and the tumor samples were fixed and embedded for immunohistochemistry and immunofluorescence after 14 days.

Ki67 Staining and TUNEL Assay

The tumor tissue specimens of each group were fixed with 4% paraformaldehyde, embedded in paraffin and sectioned. For Ki67 staining, the section slides were incubated by anti-Ki67 antibody (Abcam, United States) at 4°C overnight and then incubated for 1 h with secondary antibody at room temperature. Next, the sections were stained with diaminobenzidine (DAB) and hematoxylin respectively, dehydrated and mounted. And for TUNEL staining, the tissue blocks were incubated with TUNEL reaction mixture of TUNEL apoptosis detection kit (Servicebio, Wuhan, China) according to the manufacturer's illustrations. And we used a microscope (Leica DMi8, Leica, Germany) to acquire images.

In Vivo Magnetic Resonance Imaging

Tumor-bearing mice were received intratumoral injection of 200 μl MnPB NPs at the concentration of 2 mg/ml. Then the mice were scanned by a 3.0T MRI system before and 1 h after injection. In this way, the high-resolution T1-weighted MRI scan images were successfully acquired. The T1-weighted MRI parameters were as follows: pulse waiting time (TR) = 500 ms, echo time (TE) = 15 ms, slice thickness (ST) = 2.0 mm, field of view (FOV) = 60 mm × 60 mm.

Statistical Analysis

All measurements were expressed as mean ± standard deviation (SD). And the data was analyzed by GraphPad Prism 7. Differences between groups were tested using the paired or unpaired two-tailed Student's t-test. Besides, $^{*}p < 0.05$, $^{**}p < 0.01$, $^{***}p < 0.001$, $^{****}p < 0.0001$ were regarded to be significantly different.

RESULTS AND DISCUSSION

Characterization and Properties of Manganese-Based Prussian Blue Nanoparticles

We synthesized the MnPB NPs using a conventional method, which substituted $FeCl_3$ with $MnCl_2$ to produce Mn-based PB. And the average size, shape and morphology of MnPB NPs were observed by TEM. The solid MnPB NPs were displayed in **Figures 1A,B**. And as we can see, the hydrodynamic size of

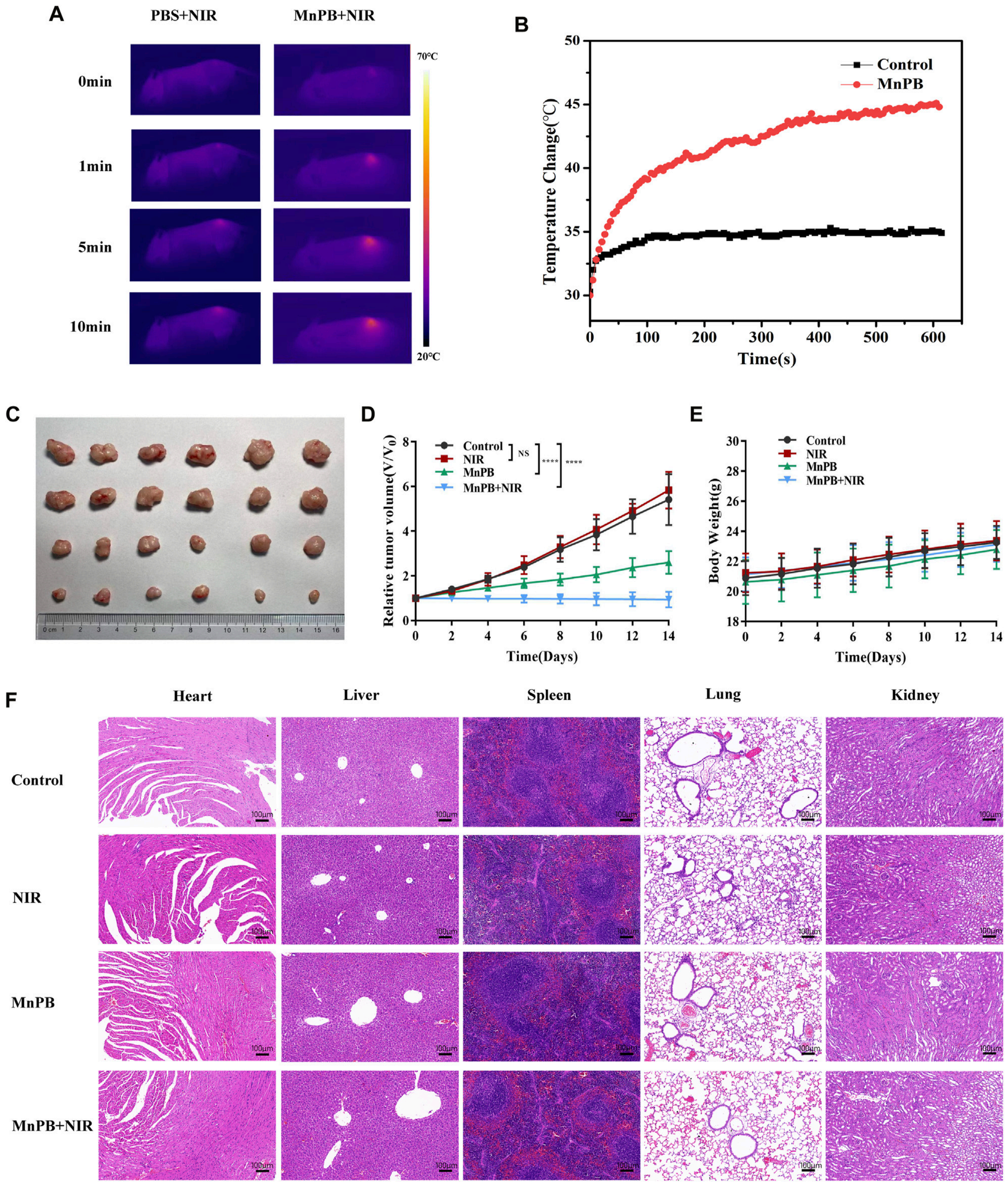

FIGURE 7 | The MnPB NPs inhibit the growth of tumor xenografts in nude mice. **(A)** Pictures recorded by a thermal imaging camera during NIR irradiation. **(B)** Temperature curve of tumor areas in mice. **(C)** The tumor picture taken at day 14. **(D)** Relative tumor volume curve and **(E)** body weight curve of mice with various treatments. **(F)** H&E staining of main organs from mice in different groups. Scale bar, 100 μm.

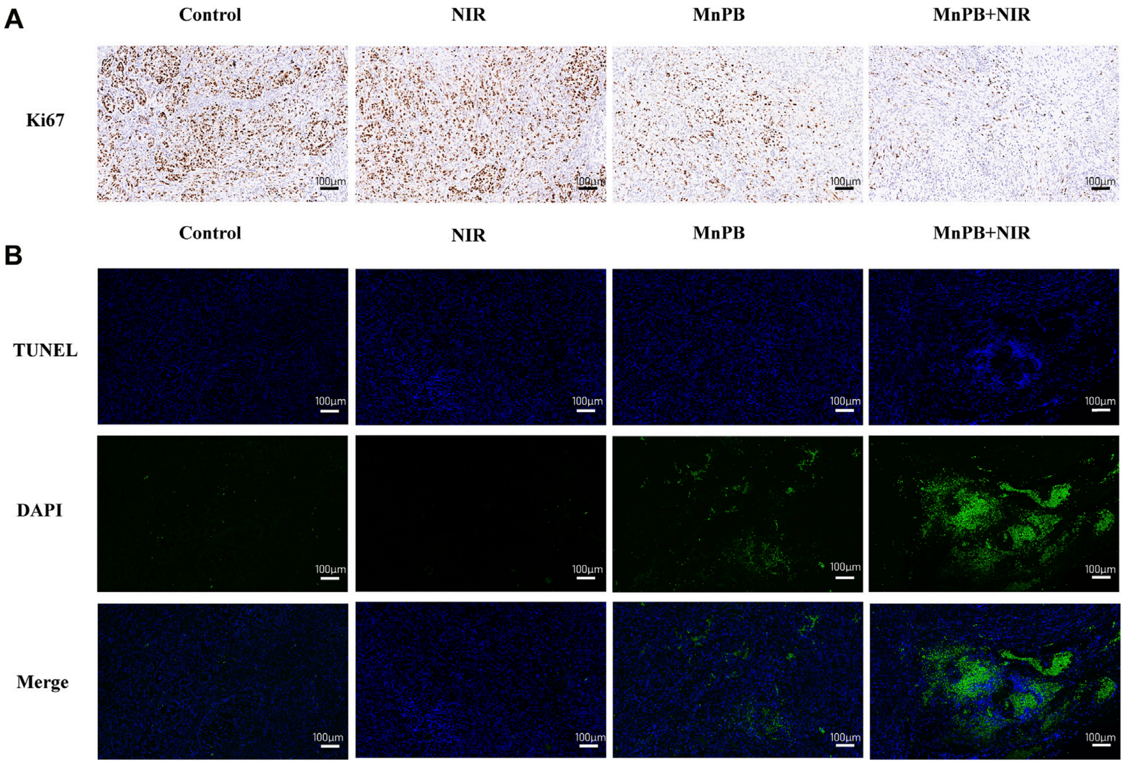

FIGURE 8 | The MnPB NPs inhibit the growth of non-small lung cancer *in vivo*. **(A)** Ki67 staining and **(B)** TUNEL staining images of tumors. Scale bar, 100 μm.

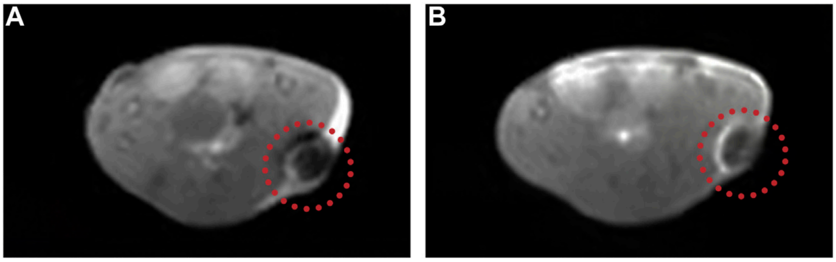

FIGURE 9 | The MnPB NPs can be used as excellent T1 contrast agents. **(A)** Representative T1-weighted MRI images of A549 tumor-bearing mice before and **(B)** after intratumoral injection of MnPB NPs.

MnPB NPs was measured to be 200.4 nm (**Figures 1C**), which was consistent to the size of TEM image. Then **Figure 1D** showed the XRD patterns of as-synthesized MnPB NPs, which revealed the characteristic peaks of PB and Mn^{2+}, in accordance with the standard PB (JCPDS. 01-0239) and $Mn_2(CN)_6$ (JCPDS. 32-0639). The above results indicated the successful construction of MnPB NPs.

To confirm the photothermal properties of MnPB NPs, UV−vis−NIR spectra of MnPB NPs with various concentrations were measured. As can be seen from **Figure 2A**, MnPB NPs exhibited strong and wide absorbance from visible wavelength to NIR wavelength ranges, illustrating the excellent light absorption ability of MnPB NPs. Then we further tested the photothermal performance of MnPB NPs at different concentrations under exposure of NIR light irradiation. At any given concentration of MnPB NPs, temperature rose steadily when the irradiation time increased (**Figure 2B**). With concentrations up until 400 μg/ml, the temperature rose above 50°C after 5 min of NIR light irradiation. It has been found that cells will die rapidly due to microvascular thrombosis and ischemia, as the temperature reaches above 45°C (Knavel and Brace, 2013). Thus, the photothermal ablation of MnPB NPs is highly sufficient to irreversibly ablate tumor cells. The photothermal conversion efficiency (η) indicates the capability of converting light energy into thermal energy. The ŋ value of MnPB NPs was figured out to be 27.8%, which was higher than ŋ of PB NPs (only 16.02%) (**Figures 2C,D**) (Guan et al., 2021). These results suggested that MnPB NPs possessed excellent photothermal properties and were promising PTT agents for tumor treatment.

MB dye test is a simple procedure to evaluate hydroxyl radicals (•OH) formed in the Fenton's reaction. And MB will turn from blue in color to colorless in the presence of •OH, which can be detected by a spectrophotometer (Satoh et al., 2007). As shown in the **Figure 2E**, MB displayed an absorbance peak at a wavelength of 664 nm, and the intensity decreased over time in MnPB NPs + H_2O_2 group, revealing the degradation of MB. And compared to the MnPB NPs group and H_2O_2 group, the absorbance measured at 664 nm in MnPB NPs + H_2O_2 group declined sharply, confirming that MnPB NPs could generate ROS effectively under the catalysis of H_2O_2 (**Figure 2F**). These observations demonstrated that the CDT of MnPB NPs had high efficiency and MnPB NPs might have powerful ability to inhibit the growth and metastasis of tumor.

The Manganese-Based Prussian Blue Nanoparticles Inhibit the Growth of A549 Cells by Reactive Oxygen Species Upregulation and Near-Infrared Irradiation

Biocompatibility of therapeutic agents is a critical feature for biomedical application. So the biocompatibility of MnPB NPs in normal bronchial epithelial cells and lung adenocarcinoma cells were firstly measured by CCK8 method. As **Figure 3** shown, MnPB NPs exhibited no obvious cytotoxicity in both BEAS-2B and A549 cells at the maximum concentration of 400 μg/ml, which suggested excellent biocompatibility of MnPB NPs. Then we further evaluated the treatment effect of MnPB NPs with PTT and CDT in A549 cells.

CDT is a new therapeutic approach for the treatment of tumor depending on Fenton and Fenton-like reactions. The Fenton reaction is defined as the production of highly oxidized •OH or O_2 from H_2O_2 by catalyzing the transition metal ions or their compounds (Tang et al., 2019). To confirm the CDT effect of MnPB NPs *in vitro*, we used DCFH-DA probe to detect the ROS production (**Figure 4**; **Supplementary Figure S1**). The images displayed that, compared to the control group, DCF fluorescence intensity increased slightly when A549 cells were treated with H_2O_2 or MnPB NPs. And when treated with both H_2O_2 and MnPB NPs, most cells revealed intense green fluorescence signal. The findings suggested that MnPB NPs had a high efficiency of ROS generation through reacting with H_2O_2 in tumor microenvironment (TME) *via* Fenton and Fenton-like reactions. These reactions can be explained as follows:

$$Fe^{2+} + H_2O_2 \rightarrow Fe^{3+} + \cdot OH + OH^- \tag{1}$$

$$Mn^{2+} + H_2O_2 \rightarrow Mn^{2+} + \cdot OH + OH^- \tag{2}$$

Then based on the outstanding photothermal conversion performance of MnPB NPs, we applied two other methods to estimate the cell viability of A549 cells by combing PTT and CDT. First, we used Calcine-AM/PI test to detect the percentage of living and dead cells. Live cells were dyed with Calcein AM exhibiting green fluorescence, and dead cells were stained with PI showing red fluorescence. As shown in **Figure 5A**; **Supplementary Figure S2**, the green/red fluorescence intensity of A549 cells exposed under NIR irradiation had no significant difference, compared to the control group, indicating that cell viability was not affected by NIR irradiation. And H_2O_2 treatment increased the percentage of dead cells slightly. Besides, when A549 cells were treated with MnPB NPs with NIR light exposure or MnPB NPs with H_2O_2, the percentage of dead cells increased substantially, suggesting that the PTT and CDT of MnPB NPs had excellent performance respectively in A549 cells. And when A549 cells were treated with both PTT and CDT, we could only observe strong red fluorescence, revealing that the combination of PTT and CDT exerted potent efficacy to kill NSCLC cells.

Next, we used the Annexin V-FITC apoptosis assay to determine the apoptosis rate of A549 cells by flow cytometry. Apoptotic cells express phosphatidylserine (PS) on the outer layer of the cell membrane and can be recognized by Annexin-V specifically (Chen et al., 2008). As we can see in **Figure 5B** and **Supplementary Figure S3**, there was no obvious difference between the control group and the NIR group. But the rate of apoptosis increased to 9.78% in the H_2O_2 group. After treatment of MnPB NPs with NIR light exposure and MnPB NPs with H_2O_2, the rate of apoptosis obviously increased to 64.64% and 54.11%. Importantly, when cells were treated with MnPB NPs and exposed to both H_2O_2 and NIR irradiation, the percentage of apoptotic cells dramatically increased to 90.34%. The results were in good agreement with the observation of Calcine-AM/PI test, further demonstrating that PTT and CDT of MnPB NPs could act a strong synergy to inhibit growth of NSCLC cells.

The Manganese-Based Prussian Blue Nanoparticles Inhibit the Migration of A549 Cells by Decreasing the Matrix Metalloproteinases Expression

It is known that metastasis is a key feature of malignant tumors and major cause of death in cancer. Therefore, inhibition of tumor metastasis is extremely important in lung cancer treatment. Tumor metastasis is a complex multistep process related to cell migration, invasion, epithelial-to-mesenchymal transition (EMT), ECM degradation and intravascular circulation (Xu et al., 2014; Liu et al., 2021). Among these processes, the degradation of ECM is a critical step during the development of tumor metastasis (Eble and Niland, 2019). Here we utilized transwell assay to assess the inhibitory effect of MnPB NPs in A549 cells. It was obvious that the MnPB NPs significantly slowed down the migration of A549 cells (**Figures 6A,B**; **Supplementary Figure S4**).

It is proved that activity of matrix-degrading protease is important in the degradation of ECM, which plays an important role in invasion and migration of tumor. MMP2 and MMP9 reportedly degrade type IV collagen in the basement membrane, which is related to tumor metastasis (Wang et al., 2018). To further elucidate the inhibitory effects of MnPB NPs, we detected the activity of MMP2 and MMP9 in A549 cells. The MMP2 and MMP9 expressions were significantly attenuated by MnPB NPs, compared to the control group (**Figure 6C**; **Supplementary Figure S5**). To sum up, MnPB NPs can effectively inhibit the metastasis of A549 cells.

The Manganese-Based Prussian Blue Nanoparticles Inhibit Xenografted Tumor Growth

According to the excellent therapeutic efficacy of *in vitro* studies presented above, we further assessed the *in vivo* performance of MnPB NPs. The tumor-bearing mice were randomly divided into four groups as follows ($n = 6$ per group): 1) control; 2) PBS + NIR; 3) MnPB NPs; 4) MnPB NPs + NIR. The mice of group 2, 3 and 4 were received 200 μl PBS or MnPB NPs intravenously. And the mice of group 2 and 4 were exposed under irradiation with an 808 nm NIR laser (1 W/cm^2) for 10 min after 8 h of intravenous injection. During laser irradiation, we captured the change of tumor temperature by a thermal camera (**Figures 7A,B**). The temperature of tumor in group 2 only increased to ~35°C, while the tumor temperature of group 4 rose rapidly above 45°C, which was high enough to induce tumor cell death. And the typical tumor pictures and the change in relative tumor volume (**Figures 7C,D**) demonstrated that only NIR had no influence to tumor growth, while only MnPB NPs could effectively inhibit the growth of tumor due to CDT effect. Surprisingly, treatment of MnPB NPs and NIR irradiation greatly contributed to the inhibition of tumor growth, which revealed that PTT and CDT of MnPB NPs have superior synergistic effect. Moreover, the body weight of mice in each group did not loss significantly during the treatment (**Figure 7E**). And we further examined the histology of main organs by H&E staining (**Figure 7F**). There were no appreciable abnormalities and pathological injury among the groups, indicating that MnPB NPs were biologically safe *in vivo*.

We also used immunocytochemistry and immunofluorescence to assess cell proliferation and apoptosis of tumor tissue sections (**Figures 8A,B**; **Supplementary Figures S6, S7**). Compared to the control group, the expression of the proliferative marker Ki67 declined and cell apoptosis increased in the group 3 and 4. And resulting from synergistic therapeutic effect of CDT and PTT, most of the cells were apoptotic in group 4. These results clearly indicated that MnPB NPs with NIR irradiation led to severe cell damage and inhibited tumor growth efficiently *in vivo*.

The Manganese-Based Prussian Blue Nanoparticles Serve as Great T1 Contrast Agents

MRI is a widely used tool to diagnose clinical diseases with good soft tissue contrast and high spatial resolution (Yang et al., 2011; Liang et al., 2020). Nowadays, it is requisite to develop a multifunctional nanoplatform which includes noninvasive therapy methods and imaging technology (Zeng et al., 2019; Li X. et al., 2021). In our study, since MnPB NPs contained Mn^{2+}, they could serve as T1 contrast agents. So we explored the T1-weighted imaging property of MnPB NPs *in vivo* (**Figures 9A,B**). The results showed that the MRI signal became brighter obviously after intratumoral injection of MnPB NPs, demonstrating that the MnPB NPs could act as effective T1 contrast agents.

CONCLUSION

PB is well known as a safe photothermal agent in the treatment of tumor (Fu et al., 2012; Lu et al., 2020). In our study, we fabricated Mn-based PB nanocatalysts to acquire enhanced synergetic effect of PTT and CDT under the guidance of MRI. By the combination of PTT and CDT, the MnPB NPs induced cell death effectively of NSCLC *in vivo* and *in vitro*. And they had inhibitory effect on the metastasis of NSCLC cells *via* decreasing the expression of MMP2 and MMP9. Moreover, the MnPB NPs exhibited excellent T1-weighted imaging performance *in vivo*. Therefore, the results above confirmed that the MnPB NPs had the potential in treating NSCLC, and also could be used as excellent T1 contrast agents to diagnose NSCLC.

DATA AVAILABILITY STATEMENT

The raw data supporting the conclusions of this article will be made available by the authors, without undue reservation.

ETHICS STATEMENT

The animal study was reviewed and approved by the Laboratory Animal Ethics Committee of Shanghai General Hospital.

AUTHOR CONTRIBUTIONS

DF and ZL have contributed equally to this work. DF designed and conducted a series of experiments. ZL wrote the original draft. HJ analyzed the experimental data. XH established the animal model. YS proofread the manuscript. SB supervised the experiments and provided funding. All the authors read and approved the final manuscript.

FUNDING

This work was financially supported by the National Natural Science Foundation of China (Grant 81570018).

SUPPLEMENTARY MATERIAL

The Supplementary Material for this article can be found online at: https://www.frontiersin.org/articles/10.3389/fbioe.2022.939158/full#supplementary-material

REFERENCES

Altorki, N. K., Markowitz, G. J., Gao, D., Port, J. L., Saxena, A., Stiles, B., et al. (2019). The Lung Microenvironment: an Important Regulator of Tumour Growth and Metastasis. *Nat. Rev. Cancer* 19, 9–31. doi:10.1038/s41568-018-0081-9

Busquets, M. A., and Estelrich, J. (2020). Prussian Blue Nanoparticles: Synthesis, Surface Modification, and Biomedical Applications. *Drug Discov. Today* 25, 1431–1443. doi:10.1016/j.drudis.2020.05.014

Cai, X., Gao, W., Ma, M., Wu, M., Zhang, L., Zheng, Y., et al. (2015). A Prussian Blue-Based Core-Shell Hollow-Structured Mesoporous Nanoparticle as a Smart Theranostic Agent with Ultrahigh pH-Responsive Longitudinal Relaxivity. *Adv. Mat.* 27, 6382–6389. doi:10.1002/adma.201503381

Chen, S., Cheng, A.-C., Wang, M.-S., and Peng, X. (2008). Detection of Apoptosis Induced by New Type Gosling Viral Enteritis Virus *In Vitro* through Fluorescein Annexin V-FITC/PI Double Labeling. *World J. Gastroenterol.* 14, 2174–2178. doi:10.3748/wjg.14.2174

Dacarro, G., Taglietti, A., and Pallavicini, P. (2018). Prussian Blue Nanoparticles as a Versatile Photothermal Tool. *Molecules* 23, 1414. doi:10.3390/molecules23061414

Dong, Q.-z., Wang, Y., Tang, Z.-p., Fu, L., Li, Q.-c., Wang, E.-d., et al. (2013). Derlin-1 Is Overexpressed in Non-small Cell Lung Cancer and Promotes Cancer Cell Invasion via EGFR-ERK-Mediated Up-Regulation of MMP-2 and MMP-9. *Am. J. Pathology* 182, 954–964. doi:10.1016/j.ajpath.2012.11.019

Eble, J. A., and Niland, S. (2019). The Extracellular Matrix in Tumor Progression and Metastasis. *Clin. Exp. Metastasis* 36, 171–198. doi:10.1007/s10585-019-09966-1

Fang, D., Jin, H., Huang, X., Shi, Y., Liu, Z., and Ben, S. (2021). PPy@Fe_3O_4 Nanoparticles Inhibit Tumor Growth and Metastasis through Chemodynamic and Photothermal Therapy in Non-small Cell Lung Cancer. *Front. Chem.* 9, 789934. doi:10.3389/fchem.2021.789934

Fu, G., Liu, W., Feng, S., and Yue, X. (2012). Prussian Blue Nanoparticles Operate as a New Generation of Photothermal Ablation Agents for Cancer Therapy. *Chem. Commun.* 48, 11567–11569. doi:10.1039/c2cc36456e

Gao, X., Wang, Q., Cheng, C., Lin, S., Lin, T., Liu, C., et al. (2020). The Application of Prussian Blue Nanoparticles in Tumor Diagnosis and Treatment. *Sensors* 20, 6905. doi:10.3390/s20236905

Goldstein, S., Meyerstein, D., and Czapski, G. (1993). The Fenton Reagents. *Free Radic. Biol. Med.* 15, 435–445. doi:10.1016/0891-5849(93)90043-t

Gonzalez-Avila, G., Sommer, B., Mendoza-Posada, D. A., Ramos, C., Garcia-Hernandez, A. A., and Falfan-Valencia, R. (2019). Matrix Metalloproteinases Participation in the Metastatic Process and Their Diagnostic and Therapeutic Applications in Cancer. *Crit. Rev. Oncology/Hematology* 137, 57–83. doi:10.1016/j.critrevonc.2019.02.010

Guan, S., Liu, X., Fu, Y., Li, C., Wang, J., Mei, Q., et al. (2022). A Biodegradable "Nano-Donut" for Magnetic Resonance Imaging and Enhanced Chemo/photothermal/chemodynamic Therapy through Responsive Catalysis in Tumor Microenvironment. *J. Colloid Interface Sci.* 608, 344–354. doi:10.1016/j.jcis.2021.09.186

Han, L., Sheng, B., Zeng, Q., Yao, W., and Jiang, Q. (2020). Correlation between MMP2 Expression in Lung Cancer Tissues and Clinical Parameters: a Retrospective Clinical Analysis. *BMC Pulm. Med.* 20, 283. doi:10.1186/s12890-020-01317-1

He, T., Luo, Y., Zhang, Q., Men, Z., Su, T., Fan, L., et al. (2021). Hyalase-Mediated Cascade Degradation of a Matrix Barrier and Immune Cell Penetration by a Photothermal Microneedle for Efficient Anticancer Therapy. *ACS Appl. Mat. Interfaces* 13, 26790–26799. doi:10.1021/acsami.1c06725

Itoh, T., Tanioka, M., Matsuda, H., Nishimoto, H., Yoshioka, T., Suzuki, R., et al. (1999). Experimental Metastasis Is Suppressed in MMP-9-Deficient Mice. *Clin. Exp. Metastasis* 17, 177–181. doi:10.1023/a:1006603723759

Knavel, E. M., and Brace, C. L. (2013). Tumor Ablation: Common Modalities and General Practices. *Tech. Vasc. Interventional Radiology* 16, 192–200. doi:10.1053/j.tvir.2013.08.002

Li, J., Yu, X., Jiang, Y., He, S., Zhang, Y., Luo, Y., et al. (2021). Second Near-Infrared Photothermal Semiconducting Polymer Nanoadjuvant for Enhanced Cancer Immunotherapy. *Adv. Mat.* 33, 2003458. doi:10.1002/adma.202003458

Li, W., Jia, M., Wang, J., Lu, J., Deng, J., Tang, J., et al. (2019). Association of MMP9-1562C/T and MMP13-77A/G Polymorphisms with Non-small Cell Lung Cancer in Southern Chinese Population. *Biomolecules* 9, 107. doi:10.3390/biom9030107

Li, X., Lovell, J. F., Yoon, J., and Chen, X. (2020). Clinical Development and Potential of Photothermal and Photodynamic Therapies for Cancer. *Nat. Rev. Clin. Oncol.* 17, 657–674. doi:10.1038/s41571-020-0410-2

Li, X., Sun, H., Li, H., Hu, C., Luo, Y., Shi, X., et al. (2021). Multi-Responsive Biodegradable Cationic Nanogels for Highly Efficient Treatment of Tumors. *Adv. Funct. Mater.* 31, 2100227. doi:10.1002/adfm.202100227

Li, Z., Zeng, Y., Zhang, D., Wu, M., Wu, L., Huang, A., et al. (2014). Glypican-3 Antibody Functionalized Prussian Blue Nanoparticles for Targeted MR Imaging and Photothermal Therapy of Hepatocellular Carcinoma. *J. Mat. Chem. B* 2, 3686–3696. doi:10.1039/c4tb00516c

Liang, K., Li, Z., Luo, Y., Zhang, Q., Yin, F., Xu, L., et al. (2020). Intelligent Nanocomposites with Intrinsic Blood-Brain-Barrier Crossing Ability Designed for Highly Specific MR Imaging and Sonodynamic Therapy of Glioblastoma. *Small* 16, 1906985. doi:10.1002/smll.201906985

Lim, E.-K., Kim, T., Paik, S., Haam, S., Huh, Y.-M., and Lee, K. (2015). Nanomaterials for Theranostics: Recent Advances and Future Challenges. *Chem. Rev.* 115, 327–394. doi:10.1021/cr300213b

Lin, L., Wang, S., Deng, H., Yang, W., Rao, L., Tian, R., et al. (2020). Endogenous Labile Iron Pool-Mediated Free Radical Generation for Cancer Chemodynamic Therapy. *J. Am. Chem. Soc.* 142, 15320–15330. doi:10.1021/jacs.0c05604

Liu, Q.-L., Zhang, Z., Wei, X., and Zhou, Z.-G. (2021). Noncoding RNAs in Tumor Metastasis: Molecular and Clinical Perspectives. *Cell. Mol. Life Sci.* 78, 6823–6850. doi:10.1007/s00018-021-03929-0

Liu, X., Li, B., Fu, F., Xu, K., Zou, R., Wang, Q., et al. (2014). Facile Synthesis of Biocompatible Cysteine-Coated CuS Nanoparticles with High Photothermal Conversion Efficiency for Cancer Therapy. *Dalton Trans.* 43, 11709–11715. doi:10.1039/c4dt00424h

Lu, L., Zhang, C., Zou, B., and Wang, Y. (2020). Hollow Prussian Blue Nanospheres for Photothermal/Chemo-Synergistic Therapy. *Int. J. Nanomedicine* 15, 5165–5177. doi:10.2147/IJN.S252505

Manivasagan, P., Joe, A., Han, H.-W., Thambi, T., Selvaraj, M., Chidambaram, K., et al. (2022). Recent Advances in Multifunctional Nanomaterials for Photothermal-Enhanced Fenton-based Chemodynamic Tumor Therapy. *Mater. Today Bio* 13, 100197. doi:10.1016/j.mtbio.2021.100197

Odda, A. H., Xu, Y., Lin, J., Wang, G., Ullah, N., Zeb, A., et al. (2019). Plasmonic MoO_{3-x} Nanoparticles Incorporated in Prussian Blue Frameworks Exhibit Highly Efficient Dual Photothermal/photodynamic Therapy. *J. Mat. Chem. B* 7, 2032–2042. doi:10.1039/c8tb03148g

Oser, M. G., Niederst, M. J., Sequist, L. V., and Engelman, J. A. (2015). Transformation from Non-small-cell Lung Cancer to Small-Cell Lung Cancer: Molecular Drivers and Cells of Origin. *Lancet Oncol.* 16, e165–e172. doi:10.1016/S1470-2045(14)71180-5

Paolillo, M., and Schinelli, S. (2019). Extracellular Matrix Alterations in Metastatic Processes. *Int. J. Mol. Sci.* 20, E4947. doi:10.3390/ijms20194947

Poudel, B., Ki, H.-H., Luyen, B. T. T., Lee, Y.-M., Kim, Y.-H., and Kim, D.-K. (2016). Triticumoside Induces Apoptosis via Caspase-dependent Mitochondrial Pathway and Inhibits Migration through Downregulation of MMP2/9 in Human Lung Cancer Cells. *Acta Biochim. Biophys. Sin.* 48, 153–160. doi:10.1093/abbs/gmv124

Satoh, A. Y., Trosko, J. E., and Masten, S. J. (2007). Methylene Blue Dye Test for Rapid Qualitative Detection of Hydroxyl Radicals Formed in a Fenton's Reaction Aqueous Solution. *Environ. Sci. Technol.* 41, 2881–2887. doi:10.1021/es0617800

Shokouhimehr, M., Soehnlen, E. S., Hao, J., Griswold, M., Flask, C., Fan, X., et al. (2010). Dual Purpose Prussian Blue Nanoparticles for Cellular Imaging and Drug Delivery: a New Generation of T1-Weighted MRI Contrast and Small Molecule Delivery Agents. *J. Mat. Chem.* 20, 5251. doi:10.1039/b923184f

Shou, P., Yu, Z., Wu, Y., Feng, Q., Zhou, B., Xing, J., et al. (2020). Zn 2+ Doped Ultrasmall Prussian Blue Nanotheranostic Agent for Breast Cancer Photothermal Therapy under MR Imaging Guidance. *Adv. Healthc. Mat.* 9, 1900948. doi:10.1002/adhm.201900948

Siegel, R. L., Miller, K. D., Fuchs, H. E., and Jemal, A. (2021). Cancer Statistics, 2021. *CA A Cancer J. Clin.* 71, 7–33. doi:10.3322/caac.21654

Sun, H., Yu, T., Li, X., Lei, Y., Li, J., Wang, X., et al. (2021). Second Near-Infrared Photothermal-Amplified Immunotherapy Using Photoactivatable Composite Nanostimulators. *J. Nanobiotechnol* 19, 433. doi:10.1186/s12951-021-01197-5

Tang, Z., Liu, Y., He, M., and Bu, W. (2019). Chemodynamic Therapy: Tumour Microenvironment-Mediated Fenton and Fenton-like Reactions. *Angew. Chem. Int. Ed.* 58, 946–956. doi:10.1002/anie.201805664

Wang, X., Fan, L., Cheng, L., Sun, Y., Wang, X., Zhong, X., et al. (2020a). Biodegradable Nickel Disulfide Nanozymes with GSH-Depleting Function for High-Efficiency Photothermal-Catalytic Antibacterial Therapy. *iScience* 23, 101281. doi:10.1016/j.isci.2020.101281

Wang, X., Yang, B., She, Y., and Ye, Y. (2018). The lncRNA TP73-AS1 Promotes Ovarian Cancer Cell Proliferation and Metastasis via Modulation of MMP2 and MMP9. *J. Cell Biochem.* 119, 7790–7799. doi:10.1002/jcb.27158

Wang, X., Zhong, X., Liu, Z., and Cheng, L. (2020b). Recent Progress of Chemodynamic Therapy-Induced Combination Cancer Therapy. *Nano Today* 35, 100946. doi:10.1016/j.nantod.2020.100946

Xu, H., Hou, Z., Zhang, H., Kong, H., Li, X., Wang, H., et al. (2014). An Efficient Trojan Delivery of Tetrandrine by poly(N-Vinylpyrrolidone)-Block-Poly(ε-Caprolactone) (PVP-B-PCL) Nanoparticles Shows Enhanced Apoptotic Induction of Lung Cancer Cells and Inhibition of its Migration and Invasion. *Int. J. Nanomedicine* 9, 231–242. doi:10.2147/IJN.S55541

Yang, H., Zhuang, Y., Sun, Y., Dai, A., Shi, X., Wu, D., et al. (2011). Targeted Dual-Contrast T1- and T2-Weighted Magnetic Resonance Imaging of Tumors Using Multifunctional Gadolinium-Labeled Superparamagnetic Iron Oxide Nanoparticles. *Biomaterials* 32, 4584–4593. doi:10.1016/j.biomaterials.2011.03.018

Yang, Z., Luo, Y., Hu, Y., Liang, K., He, G., Chen, Q., et al. (2021). Photothermo-Promoted Nanocatalysis Combined with H_2S-Mediated Respiration Inhibition for Efficient Cancer Therapy. *Adv. Funct. Mat.* 31, 2007991. doi:10.1002/adfm.202007991

Zeng, K., Xu, Q., Ouyang, J., Han, Y., Sheng, J., Wen, M., et al. (2019). Coordination Nanosheets of Phthalocyanine as Multifunctional Platform for Imaging-Guided Synergistic Therapy of Cancer. *ACS Appl. Mat. Interfaces* 11, 6840–6849. doi:10.1021/acsami.8b22008

Zhao, H., Wang, J., Li, X., Li, Y., Li, C., Wang, X., et al. (2021). A Biocompatible Theranostic Agent Based on Stable Bismuth Nanoparticles for X-Ray Computed Tomography/magnetic Resonance Imaging-Guided Enhanced Chemo/photothermal/chemodynamic Therapy for Tumours. *J. Colloid Interface Sci.* 604, 80–90. doi:10.1016/j.jcis.2021.06.174

Zhao, W., Yu, X., Peng, S., Luo, Y., Li, J., and Lu, L. (2021). Construction of Nanomaterials as Contrast Agents or Probes for Glioma Imaging. *J. Nanobiotechnol* 19, 125. doi:10.1186/s12951-021-00866-9

Zheng, Q., Dong, H., Mo, J., Zhang, Y., Huang, J., Ouyang, S., et al. (2021). A Novel STAT3 Inhibitor W2014-S Regresses Human Non-small Cell Lung Cancer Xenografts and Sensitizes EGFR-TKI Acquired Resistance. *Theranostics* 11, 824–840. doi:10.7150/thno.49600

Zheng, Z., Chen, Q., Rong, S., Dai, R., Jia, Z., Peng, X., et al. (2020). Two-stage Activated Nano-Truck Enhanced Specific Aggregation and Deep Delivery for Synergistic Tumor Ablation. *Nanoscale* 12, 15845–15856. doi:10.1039/d0nr03661g

Conflict of Interest: The authors declare that the research was conducted in the absence of any commercial or financial relationships that could be construed as a potential conflict of interest.

Publisher's Note: All claims expressed in this article are solely those of the authors and do not necessarily represent those of their affiliated organizations, or those of the publisher, the editors and the reviewers. Any product that may be evaluated in this article, or claim that may be made by its manufacturer, is not guaranteed or endorsed by the publisher.

Copyright © 2022 Fang, Liu, Jin, Huang, Shi and Ben. This is an open-access article distributed under the terms of the Creative Commons Attribution License (CC BY). The use, distribution or reproduction in other forums is permitted, provided the original author(s) and the copyright owner(s) are credited and that the original publication in this journal is cited, in accordance with accepted academic practice. No use, distribution or reproduction is permitted which does not comply with these terms.

Frontiers in Bioengineering and Biotechnology

TYPE Brief Research Report
PUBLISHED 22 July 2022
DOI 10.3389/fbioe.2022.973141

Check for updates

OPEN ACCESS

EDITED BY
Xin Li,
DWI—Leibniz-Institut für Interaktive Materialien, Germany

REVIEWED BY
Zhiyuan Shi,
University Hospital of Cologne, Germany
Guoying Wang,
Macquarie University, Australia

*CORRESPONDENCE
Yi Lu,
y.lu@biotec.rwth-aachen.de
Meilin Zhu,
jay70281@163.com
Wenjie Sun,
wenjie@wmu.edu.cn

†These authors have contributed equally to this work

SPECIALTY SECTION
This article was submitted to Nanobiotechnology, a section of the journal Frontiers in Bioengineering and Biotechnology

RECEIVED 19 June 2022
ACCEPTED 01 July 2022
PUBLISHED 22 July 2022

CITATION
Kong L, Zhu J, Su H, Zhao L, Lu Y, Zhu M and Sun W (2022), Phenylboronic acid conjugated multifunctional nanogels with ^{131}I-labeling for targeted SPECT imaging and radiotherapy of breast adenocarcinoma.
Front. Bioeng. Biotechnol. 10:973141.
doi: 10.3389/fbioe.2022.973141

COPYRIGHT
© 2022 Kong, Zhu, Su, Zhao, Lu, Zhu and Sun. This is an open-access article distributed under the terms of the Creative Commons Attribution License (CC BY). The use, distribution or reproduction in other forums is permitted, provided the original author(s) and the copyright owner(s) are credited and that the original publication in this journal is cited, in accordance with accepted academic practice. No use, distribution or reproduction is permitted which does not comply with these terms.

Phenylboronic acid conjugated multifunctional nanogels with ^{131}I-labeling for targeted SPECT imaging and radiotherapy of breast adenocarcinoma

Lingdan Kong[1†], Jingyi Zhu[2†], Hongxing Su[3], Lingzhou Zhao[3], Yi Lu[4*], Meilin Zhu[5*] and Wenjie Sun[1*]

[1]School of Ophthalmology and Optometry, School of Biomedical Engineering, Wenzhou Medical University, Wenzhou, China, [2]School of Pharmaceutical Sciences, Nanjing Tech University, Nanjing, China, [3]Department of Nuclear Medicine, Shanghai General Hospital, Shanghai Jiao Tong University School of Medicine, Shanghai, China, [4]Institute of Biotechnology, RWTH Aachen University, Aachen, Germany, [5]School of Basic Medical Sciences, Ningxia Medical University, Yinchuan, China

We report a new ^{131}I-labeling functional platform for targeted single-photon emission computed tomography (SPECT) imaging and radiotherapy of breast adenocarcinoma. In this study, polyethyleneimine (PEI) based nanogels ($P.NH_2$ NGs) were prepared by water/oil polymerization, modified with targeted agent phenylboronic acid (PBA), and labeled with radionuclide ^{131}I. The NGs without ^{131}I-labeling own a spherical structure, uniform size distribution, and good cell viability. After ^{131}I-labeling, the obtained ^{131}I-PBA-PHP NGs displayed much higher cellular uptake than the non-targeted NGs due to the good softness and fluidity of NGs and the PBA targeting. The *in vivo* results demonstrated that ^{131}I-PBA-PHP NGs could specifically target breast cancer cells and efficiently aggregate into xenograft breast adenocarcinoma for tumor SPECT imaging and specific radiotherapy. The developed ^{131}I-labeling NGs may be used as a promising platform for efficient radioactive theranostic nanoplatform of tumor.

KEYWORDS
phenylboronic acid, nanogel, SPECT imaging, radiotherapy, breast adenocarcinoma

Introduction

The rapid development of nanotechnology and the in-depth understanding of tumor biology have promoted the application of nanotechnology in the field of tumor molecular medicine, especially in the fields of medical imaging (Li et al., 2017; Qi et al., 2018; Siddique and Chow, 2020), tumor molecular diagnosis (Combes et al., 2021; Wang et al., 2022) and anticancer therapy (Qin et al., 2017; Cheng et al., 2021; Li et al., 2022a). In recent years, based on the continuous development of nanomaterials, the organic combination of diagnosis and treatment can be achieved through the design of a variety of nano-drug systems, so as to realize the integrated treatment of tumor diagnosis and treatment (Zhu et al., 2021). Nuclear medicine can realize real-time imaging and specific treatment of tumor simultaneously with radionuclides and radio-labeled compounds. Single-photon emission computed tomography (SPECT) is one of the most important methods in nuclear medical imaging, which has the characteristics of high sensitivity, functional imaging and quantitative diagnosis (Fu et al., 2020). Among the radionuclides commonly used in clinical practice, iodine-131 (^{131}I) has the advantages of easy labeling, long half-life ($t_{1/2}$ = 8.01 d) and suitable radiation ability compared with other radionuclides, which can be used in SPECT imaging and radiotherapy simultaneously.

However, radionuclides have shortcomings such as short blood circulation time and poor specificity *in vivo*. Some studies indicate that the appropriate nanocarrier system of radionuclides can be an effective vehicle to achieve enhanced tumor accumulation (Li et al., 2016). Therefore, the combination of radionuclide and nanocarrier enables radionuclides efficiently to distribute in target tissues, and further achieve accurate imaging and effective treatment in target tissues, especially in the terms of tumor theranostic (Pellico et al., 2021). There is a wide variety of nanomaterials, and nanomaterials used in nuclear medicine are constantly updated, including dendritic macromolecules (Ghoreishi et al., 2017; Li et al., 2019), polymer micelles (Ramos Oda et al., 2017; Aranda-Lara et al., 2021), microspheres (Wu et al., 2022), and nanogels (NGs) (Drude et al., 2017; Li et al., 2021a; Li et al., 2022b). Among them, NGs are hydrogel particles with three-dimensional network structure formed by hydrophilic or amphiphilic polymer chains through physical or chemical crosslinking (Maddiboyina et al., 2022). It is an aqueous dispersion with good swelling properties and biocompatibility. And it is easy to synthesize and functionalize, is controllable in size, and has efficient drug loading capacity and good stability (Li et al., 2021b). According to the favorable characteristics, NG can be utilized as an ideal medical nanocarrier, which can integrate targeted molecules (Liang et al., 2016; Yang et al., 2019), therapeutic drugs (Peng et al., 2020; Li et al., 2021; Wang et al., 2021) and imaging reagents (Theune et al., 2019; Zhou et al., 2020) into one nanosystem.

Due to the excellent drug loading capacity of NGs, the SPECT imaging and radiotherapeutic property of radionuclide ^{131}I, this study intends to build a NG functional platform based on polyethyleneimine (PEI) to realize accurate tumor diagnosis and high-efficient treatment. The synthesis steps were as follows. PEI and bisacrylamide (BIS) were reacted *via* Michael-Addition reaction to produce PEI-based NGs ($P.NH_2$ NGs). Then 3-(4'-hydroxyphenyl) propionic acid N-hydroxysuccinimide (HPAO) was covalently cross-linked as a radionuclide linking molecule. Further modification of PEGylated phenylboronic acid (PBA) endowed the $P.NH_2$ NGs with specific targeting to sialylated epitopes overexpressed on the surface of diversities of tumor cells. Finally, the remaining amino groups on the surface of PEI were acetylated and labeled with radionuclide ^{131}I to obtain the final functionalized NGs. The resulting ^{131}I-PBA-PHP NGs can specifically target breast cancer cells and efficiently aggregate into xenograft breast adenocarcinoma for tumor SPECT imaging and specific radiotherapy. This study provides an alternative strategy for clinical integrated diagnosis and treatment of breast cancer.

Methods

Evaluation of cellular uptake efficiency

In order to detect the intracellular intake of different NGs by cells, fluorescein isothiocyanate (FI) was modified on the surface of the PHP NGs and PBA-PHP NGs. The endowed fluorescence characteristics of PHP NGs and PBA-PHP NGs can be detected by flow cytometry. A density of 2×10^5 cells per well were seeded into a 12-well plate and cultured for a period of time to guarantee 80% cell adherence. The culture medium was replaced by 1 ml DMEM containing 100 μL PHP NGs and PBA-PHP NGs. The final concentration of each NGs was 50 and 100 μg/ml, respectively. Incubation for another 6 h, all the NGs were sucked out and cleaned with PBS for 3 times. After trypsin suspension and mild centrifugation, the cells were dissolved in 1 ml PBS and analyzed by flow cytometry (BD Biosciences, Franklin lake, NJ, United States).

Additionally, the radiotherapy effect of radioactive ^{131}I-PHP and ^{131}I-PBA-PHP NGs was also evaluated. The subsequent operation steps were the same as described in Cytotoxicity Assay section (Supplementary Material), except that the additive materials were replaced with radioactive NGs. Similarly, the absorption value of the orifice plate at 450 nm was measured.

Single-photon emission computed tomography imaging of tumor *in vivo*

Female BALB/C nude mice (about 20 g, 3–4 weeks) were subcutaneously inoculated with 4T1 cells into the right shoulder of a mouse with a density of $2{\times}10^6$ cells/mouse. When the tumor grew to the size of 0.3–0.5 cm^3, the mice were kept for further use. Notably, all the tumor bearing mice were fed drinking water containing 1% potassium iodide for one week prior to SPECT imaging to reduce thyroid uptake of ^{131}I-labeled NGs. Before SPECT imaging, tumor bearing mice were anesthetized with sodium pentobarbital (40 mg/kg) through intraperitoneal injection. Then, the prepared ^{131}I-PHP NGs and ^{131}I-PBA-PHP NGs were injected into mice *via* a tail vein. At 30 min, 1, 2, 4, 6, 8, 12, and 16 h post-injection, SPECT imaging of tumor bearing mice *in vivo* were recorded. At 16 h post-injection, the tumor-bearing mice were randomly selected from each group and died of excessive anesthesia. The main organs and tumor tissues were collected to test their radioactive activities.

Study on tumor radiotherapy *in vivo*

Similarly, tumor models were established in accordance with the above methods. When the tumors grew to the favorable size, normal saline (NS) solutions containing ^{131}I-PHP NGs (1 mg/ml in NS, 200 μL) and ^{131}I-PBA-PHP NGs (1 mg/ml in NS, 200 μL), respectively, were injected into the mice through a tail vein every 3 days (a total of four injections). NS (200 μL), no radioactive PHP NGs (1 mg/ml in NS, 200 μL) and PBA-PHP NGs (1 mg/ml in NS, 200 μL) were set as control. After that, tumor growth volume and body weight were monitored every 3 days. The tumor sizes were measured as follows: $V = 0.5 \times x \times y^2$ (x represent the longest axis and y represent the shortest axis of the tumor). The relative tumor volume was calculated as below: $\Delta V\% = V/V_0 \times 100\%$, where V_0 is the volume before injection and V is the tumor volume at different time points. After the treatment, the survival period of the tumor bearing mice was continued to be monitored, and the death of each group was recorded for survival statistics.

Pathologic analysis

The tumor bearing mice with different treatments (NS, PHP, PBA-PHP, ^{131}I-PHP, and ^{131}I-PBA-PHP NGs) were sacrificed according to the guidelines for the euthanasia of animals at 15 days and the tumorous tissues were collected. Hematoxylin & eosin (H&E) and terminal deoxynucleotidyl transferase-mediated dUTP-biotin nick end labeling (TUNEL) staining were performed. Finally, the apoptotic cells from TUNEL staining samples were observed and photographed by a Leica DM IL LED inverted phase contrast microscope, and the apoptotic cells were counted by free selection in the picture.

Long-term biotoxicity

The long-term biotoxicity of the tumor model was evaluated after 15 days of materials injection. All mice were anesthetized. Major organs including lung, liver, spleen, kidney, and heart were harvested, fixed, embedded with paraffin, and followed by the H&E staining. Finally, the staining sections of tissues and organs were observed by a phase contrast microscope.

Statistical analysis

The significant difference of the experimental data was analyzed through one-way ANOVA method, $^*p < 0.05$, $^{**}p < 0.01$, and $^{***}p < 0.001$, respectively.

Results and discussion

Characterization of ^{131}I-PBA-PHP NGs

Through the water/oil (W/O) polymerization and Michael-Addition reactions, the initial P.NH$_2$ NGs was synthesized by cross-linking PEI with BIS. Subsequently, the generated P.NH$_2$ NGs reacted with HPAO and as-prepared COOH-PEG-PBA by means of N-hydroxysuccinimide ester group of HPAO and carboxyl group of COOH-PEG-PBA to form PBA-PHP.NH$_2$ NGs. Followed by acetylation of the remaining amino groups of PBA-PHP.NH$_2$ NGs and labeling ^{131}I onto the PBA-PHP.NH$_2$ NGs *via* HPAO, the final ^{131}I-PBA-PHP NGs were constructed (Scheme 1).

A series of characterization methods were carried out to analyze the composition, morphology, size and basic properties of ^{131}I-PBA-PHP NGs. The intermediate products COOH-PEG-PBA and PH.NH$_2$ NGs were characterized by ^{1}H NMR first (Supplementary Figure S1). The distinct peaks at 7.7–7.8 ppm and 3.3–3.7 ppm in the ^{1}H NMR spectrum of PBA-PEG-COOH were associated with the typical characteristic protons on the phenyl group of PBA and the alkoxy of PEG respectively, reflecting the successful formation of COOH-PEG-PBA (Supplementary Figure S1A). Through integration the characteristic peaks of PBA and PEG, it can be figured out every PEG conjugated with 0.4 PBA. And the district peaks at 6.8–7.1 ppm and 2.0–3.2 ppm in the ^{1}H NMR spectrum of PH.NH$_2$ NGs corresponding to the characteristic protons on the phenol group of HPAO and alkyl skeleton of PEI, revealing the successful conjugation of HPAO onto PEI (Supplementary Figure S1B). Through integration the characteristic peaks of HPAO and PEI, it can be figured out every PEI conjugated with 9.6 HPAO. As a kind of cationic polymer, P.NH$_2$ NGs tended to bind protons *via* surface amino group. Hence, P.NH$_2$ NGs demonstrated the relatively high Zeta potential (60.0 ± 1.2 mV). After modification with HPAO, COOH-PEG-PBA or *m*PEG-COOH, and acetic anhydride, the generated series of products (PH.NH$_2$ NGs, PHP.NH$_2$ NGs, PBA-PHP.NH$_2$ NGs, PHP NGs, and PBA-PHP NGs) have different Zeta potentials. Due to the gradually reducing of remaining amino group on the surface of P.NH$_2$ NGs, different NGs displayed the decreasing trend of Zeta potential (Supplementary Figure S2A). And the hydrodynamic diameters of PHP NGs and PBA-PHP NGs were determined to be 342.6 ± 11.5 nm and 389.2 ± 7.1 nm, respectively, which were within acceptable size range (Supplementary Figure S2B). The morphologies and sizes of the formed PHP NGs and PBA-PHP NGs were recorded by SEM. The mean diameters of PHP NGs and PBA-PHP NGs with the spheroidal structure could be analyzed to be 245.3 ± 64.3 nm and 262.2 ± 70.3 nm, respectively (Figure 1A). It was remarkable that the sizes of PHP NGs and PBA-PHP NGs measured by DLS were larger than that detected by SEM, which was attributed to the basic swelling property of NGs in water within the DLS

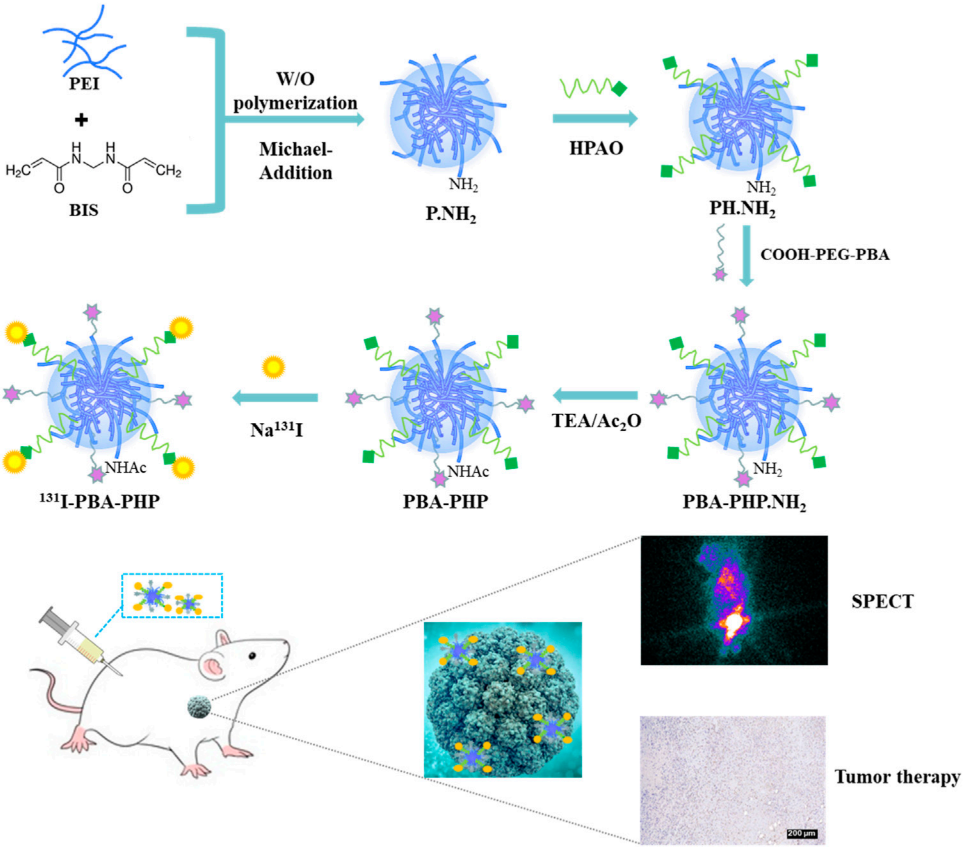

SCHEME 1
Illustration of ^{131}I-PBA-PHP NGs preparation for SPECT imaging and radiotherapy of xenograft breast adenocarcinoma.

testing process, rather than the compression of NG networks during the drying process for the SEM recording. After labeling ^{131}I onto PHP NGs and PBA-PHP NGs, the radiochemical yields of ^{131}I-PHP NGs and ^{131}I-PBA-PHP NGs were reached to 71.5% ± 2.8% and 74.4% ± 5.9%, respectively (Supplementary Figure S3A). After purification with ITLC, the radiochemical purities of ^{131}I-PHP NGs and ^{131}I-PBA-PHP NGs were approached to 99%. Followed by radiostability characterization at various time points, both of ^{131}I-PHP NGs and ^{131}I-PBA-PHP NGs displayed the satisfactory radiostability, which have the relatively high radiochemical purities (> 90%) even after labeling for 24 h (Supplementary Figure S3B).

In vitro cancer cell inhibition efficacy

After incubation with PHP NGs, PBA-PHP NGs, ^{131}I-PHP NGs, and ^{131}I-PBA-PHP NGs for 24 h, CCK-8 assay was carried out to evaluate their inhibition efficiency towards 4T1 cells. PHP NGs and PBA-PHP NGs treated cells had high cell viability (>95%) even when the concentration went up to 200 μg/ml, indicating the favorable biocompatibility of PHP NGs and PBA-PHP NGs (Supplementary Figure S4). However, ^{131}I-PHP NGs and ^{131}I-PBA-PHP NGs presented a certain degree of inhibition towards 4T1 cells, which was solely attributed to the radiotherapeutic effect of ^{131}I. And it revealed the radioactive dose-dependent cancer cell inhibition, the higher radioactive concentration, the lower cell viability the materials caused. And the radiotherapeutic efficiency of ^{131}I-PHP NGs and ^{131}I-PBA-PHP NGs towards 4T1 cells are different. ^{131}I-PBA-PHP NGs showed significantly higher inhibition efficiency than ^{131}I-PHP NGs towards 4T1 cells, especially at radioactive concentration of 400 μCi/ml and 600 μCi/ml ($p < 0.05$). The good inhibition effect of ^{131}I-PBA-PHP NGs towards 4T1 cells probably attribute to the PBA-mediate targeting ability, which could specifically bind to sialylated epitopes overexpressed on the surface of 4T1 cells (Figure 1B).

Evaluation of cellular uptake efficiency

To assess the PBA mediated targeting ability, FI was utilized as a fluorescent tracer to modify onto the PBA-PHP NGs after HPAO modification. As control, the FI modified PHP NGs were

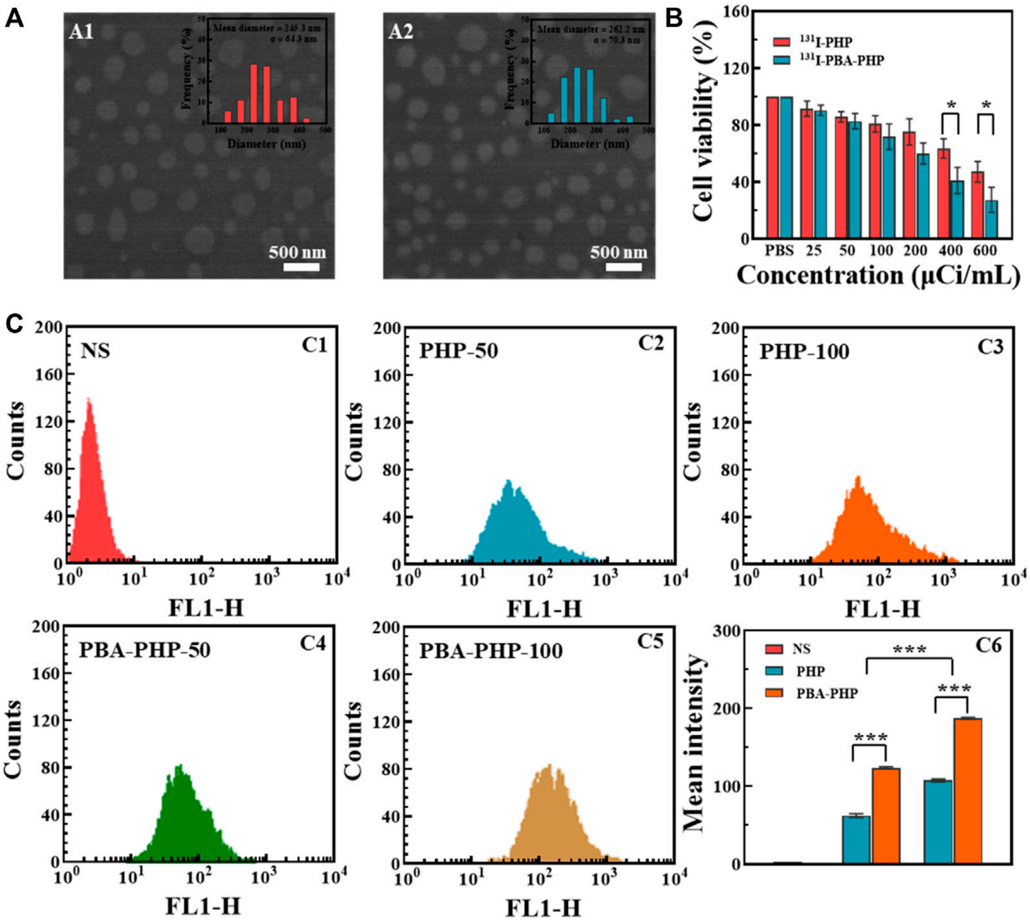

FIGURE 1
(A) SEM images of (A1) PHP NGs and (A2) PBA-PHP NGs. **(B)** CCK-8 assay of 4T1 cells incubated with ^{131}I-PHP NGs and ^{131}I-PBA-PHP NGs at different radioactive concentrations for 24 h, respectively. **(C)** Flow cytometry tests of 4T1 cells treated with C1: NS; C2: PHP NGs (50 μg/ml); C3: PHP NGs (100 μg/ml); C4: PBA-PHP NGs (50 μg/ml)and C5: PBA-PHP NGs (100 μg/ml) for 6 h, respectively. C6: The statistical analysis of the mean fluorescence of cells treated with PHP NGs and PBA-PHP NGs. *$p < 0.05$, ***$p < 0.001$.

also synthesized following the same steps, subsequently. Through the flow cytometry analysis, the mean fluorescence intensity of 4T1 cells was enhanced with the increasing concentration of PHP NGs and PBA-PHP NGs, suggesting the concentration-dependent cellular uptake manner. And the PBA-PHP NGs treated cells exhibited much higher fluorescence intensity than the PHP NGs treated cells at the same concentration ($p < 0.001$, Figure 1C). The high fluorescence intensity of 4T1 cells after treated with PBA-PHP NGs reveals the targeting efficiency of PBA.

Single-photon emission computed tomography imaging of tumor *in vivo*

Based on the inherent property of ^{131}I, the *in vivo* SPECT imaging of ^{131}I-PBA-PHP NGs treated tumor bearing mice should be further investigated. Among the SPECT images of tumor bearing mice with different administrations, the prominent tumor signals could be found in the ^{131}I-PBA-PHP NGs treated tumor bearing mice from 2 h to 16 h post-injection. In comparison, the ^{131}I-PHP NGs treated tumor bearing mice had the relatively weak tumor SPECT signals from 2 h to 16 h post-injection (Figure 2A). Due to the high imaging sensitivity of radionuclide ^{131}I, the differences of the imaging signals between ^{131}I-PBA-PHP NGs and ^{131}I-PHP NGs treated tumor bearing mice could be highlighted, suggesting that the larger amount of ^{131}I-PBA-PHP NGs could be delivered into tumor site than ^{131}I-PHP NGs based on the PBA-mediated targeting effect. Thereafter, the tumor-to-background ratio (TBR) at different time point was also recorded through collecting the SPECT signal intensities of corresponding sites. The quantitative analysis result manifested that the TBR of ^{131}I-PBA-PHP NGs treated tumor bearing mice had the sharply raised stage from

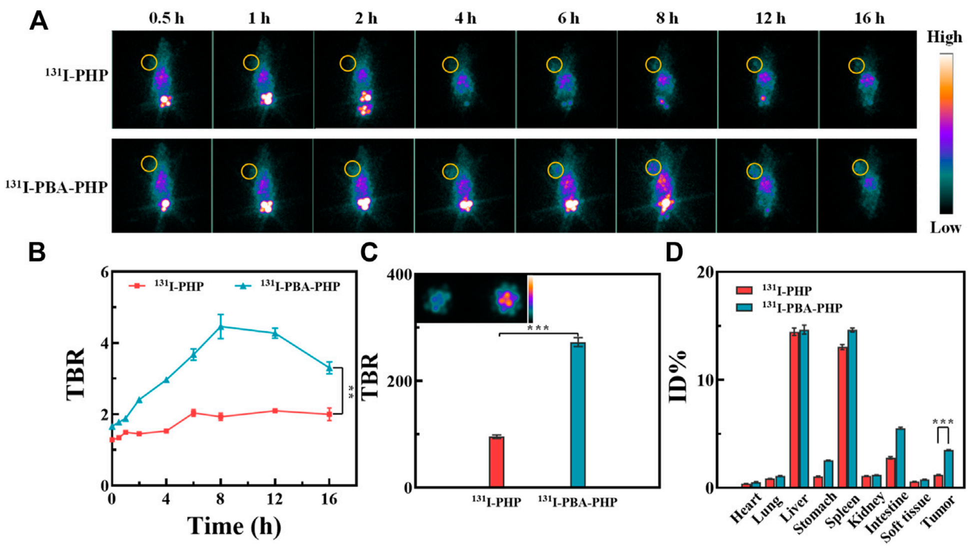

FIGURE 2
(A) SPECT images and **(B)** the corresponding TBR of 4T1 tumor bearing mice post-injection of ^{131}I-PHP NGs and ^{131}I-PBA-PHP NGs at various time points, respectively. **(C)** The SPECT images of *ex vivo* tumors at 16 h post-injection of different materials. **(D)** The relative SPECT signal intensities of major organs at 16 h post-injection of different materials. $^{\#}$The yellow circle points out the tumor site. **$p < 0.01$, ***$p < 0.001$.

0.5 h to 8 h and the gradually declined stage from 8 h to 16 h. The peak value of TBR could be found at 8 h post-injection of ^{131}I-PBA-PHP NGs. However, the ^{131}I-PHP NGs treated tumor bearing mice had the almost constant TBR within 16 h post-injection. The TBR of ^{131}I-PBA-PHP NGs treated tumor bearing mice was significantly higher than that of ^{131}I-PHP NGs treated tumor bearing mice at the same time point within 16 h ($p < 0.01$, Figure 2B). The quantitative analysis result is consistent with the SPECT images of tumor bearing mice, further suggesting the targeting effect of PBA moiety. The SPECT imaging of *ex vivo* tumors further verified the different tumor accumulation of different materials. The inserted SPECT image of *ex vivo* tumors clearly revealed the signal differences between ^{131}I-PBA-PHP NGs and ^{131}I-PHP NGs treated tumor bearing mice. And the *ex vivo* tumor signal intensity of ^{131}I-PBA-PHP NGs treated tumor bearing mice is almost 2.9 folds that of ^{131}I-PHP NGs treated tumor bearing mice (Figure 2C). Finally, the SPECT signal intensities of major organs from the treated tumor bearing mice were collected. The results displayed the biodistribution of different materials *in vivo*. Large amounts of ^{131}I-PBA-PHP NGs and ^{131}I-PHP NGs could accumulate into liver, spleen, and intestine. A small quantity of ^{131}I-PBA-PHP NGs and ^{131}I-PHP NGs could accumulate into heart, lung, stomach, kidney, soft tissue, and tumor. Moreover, ^{131}I-PBA-PHP NGs had the significantly higher tumor accumulation than that of ^{131}I-PHP NGs ($p < 0.001$), reflecting the PBA induced high tumor accumulation of ^{131}I-PBA-PHP NGs (Figure 2D).

In vivo tumor inhibition efficacy

The tumor inhibition efficacy of ^{131}I-PBA-PHP NGs was further studied from the perspectives of tumor growth, body weight change, and survival rate statistic. The tumor bearing mice treated with NS, PHP NGs, PBA-PHP NGs, and ^{131}I-PHP NGs were set as control groups. Through tumor inoculation, materials injection, and a period of therapy, the tumor inhibition efficacy was assessed (Figure 3A). In terms of tumor growth, the NS, PBA-PHP NGs, and PHP NGs treated tumor bearing mice had the similar tumor growth trend and the tumors grew fast. Due to the radiotherapeutic function of ^{131}I, ^{131}I-PHP NGs group possessed a certain anti-tumor efficacy, and its tumor growth trend was relatively slower than that of the mice with injection of NS, PBA-PHP NGs, and PHP NGs. Above all, the tumor bearing mice with injection of ^{131}I-PBA-PHP NGs displayed the slowest tumor growth trend among all the groups. Through statistical analysis, the tumor volume of ^{131}I-PBA-PHP NGs group was significantly smaller than that of NS group after 15 days' therapy ($p < 0.05$). The best anti-tumor efficacy of ^{131}I-PBA-PHP NGs among all the materials manifested the role of PBA, which could cause the high tumor accumulation of ^{131}I-PBA-PHP NGs *via* the PBA-mediated targeting effect (Figure 3B). As for body weight changes of tumor bearing mice with injection of NS, PHP NGs, PBA-PHP NGs, ^{131}I-PHP NGs, and ^{131}I-PBA-PHP NGs, all the mice had the similar body weight change trend without enormous weight fluctuation, revealing their great

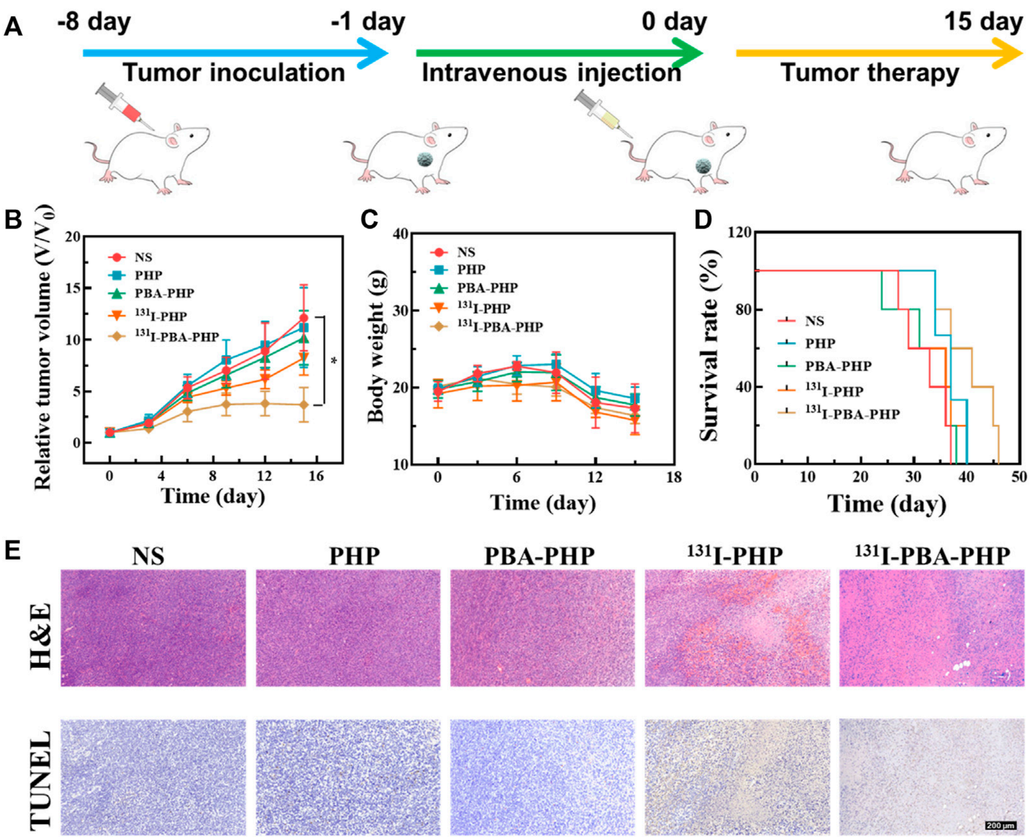

FIGURE 3
(A) Illustration of treatment process of tumor inoculation, intravenous injection, and tumor therapy of 4T1 tumor bearing mice. **(B)** The relative tumor volume, **(C)** body weight, **(D)** survival rate, and **(E)** representative tumor H&E and TUNEL images of mice with various treatments. The scale bar inserted in panel represents 200 μm. $^{*}p < 0.05$.

biocompatibility (Figure 3C). The survival rate of mice reflected the anti-tumor efficiency of ^{131}I-PBA-PHP NGs indirectly. ^{131}I-PBA-PHP NGs group obviously prolonged the lifetime of mice. Until 47th day, all the mice injected with ^{131}I-PBA-PHP NGs were dead. However, the mice with treatment of NS, PHP NGs, PBA-PHP NGs, and ^{131}I-PHP NGs respectively were dead before 40th day. The superior therapeutic efficacy suggested the PBA-mediated targeted delivery of ^{131}I-PBA-PHP NGs towards tumor (Figure 3D).

Pathologic analysis

After the whole treatment, the pathological analysis was performed to deeply assess the anti-tumor efficiency of ^{131}I-PBA-PHP NGs *via* H&E staining and TUNEL assay of tumor. The tumor necrosis and apoptosis could be stained pink and brown respectively in H&E and TUNEL images of tumor, From the H&E and TUNEL images of tumor, it was evident that the ^{131}I-PBA-PHP NGs group presented largest region of tumor necrosis and apoptosis among all the five groups (Figure 3E). Subsequently, through quantitatively analyzing the tumor apoptosis rate from the TUNEL staining images (Supplementary Figure S5), it could be ranked as following order PHP NGs (9.2%) < PBA-PHP NGs (18.8%) < ^{131}I-PHP NGs (59.6%) < ^{131}I-PBA-PHP NGs (76.6%), clearly showing that the area of tumor necrosis and apoptosis of ^{131}I-PBA-PHP NGs group was larger than that of ^{131}I-PHP NGs group ($p < 0.01$). Through the above comprehensive investigation, ^{131}I-PBA-PHP NGs possess good anti-tumor efficiency, which is attributed to the targeting effect of PBA and radiotherapeutic function of radioactive ^{131}I. In the meantime, the major organs of the treated tumor bearing mice were harvested and H&E staining was performed. Through observing the H&E images of major organs, there was no visible necrosis or abnormality area, manifesting the favorable biosafety of ^{131}I-PBA-PHP NGs *in vivo* (Supplementary Figure S6).

Conclusion

On the whole, we constructed and synthesized the multifunctional ^{131}I-PBA-PHP NGs for SPECT imaging and radiotherapy of xenograft breast adenocarcinoma. Through the W/O polymerization and Michael-Addition reactions, P.NH_2 NGs were prepared. Followed by reacting with HPAO, COOH-PEG-PBA, acetylation and ^{131}I labeling, the ^{131}I-PBA-PHP NGs were constructed. The generated ^{131}I-PBA-PHP NGs with a spherical structure and favorable radiostability own targeting property towards sialylated epitopes overexpressed on the surface of 4T1 cells. With linking of PBA, the PBA-PHP NGs manifest the improved cellular uptake in comparison with PHP NGs. Above all, the formed ^{131}I-PBA-PHP NGs enable the targeted SPECT imaging and radiotherapy of 4T1 tumor bearing mice *in vivo*. The excellent targeting moiety PBA has the great potential to be conjugated onto the other polymers to build intelligent nanosystems for tumor theranostic.

Data availability statement

The original contributions presented in the study are included in the article/Supplementary Material, further inquiries can be directed to the corresponding authors.

Ethics statement

The animal study was reviewed and approved by the ethics committee of Shanghai General Hospital and conformed to the National Institutes of Health Guidelines (2020AW087).

Author Contributions

LK: methodology, writing—original draft preparation; JZ: formal analysis and writing—original draft preparation; HS: formal analysis; LZ: methodology, resources, formal analysis; YL: writing—review and editing and supervision; MZ: writing—review and editing and supervision and funding acquisition; WS: conceptualization, writing—review and editing, supervision, project administration and funding acquisition.

Funding

The study was supported by the Zhejiang National Nature Science Foundation (LQ21H120008), the National Natural Science Foundation of China (21807059), the Ningxia Key Research and Development Program (2020BFG03005), and Ningxia Natural Science Foundation (2022AAC03136).

Conflict of interest

The authors declare that the research was conducted in the absence of any commercial or financial relationships that could be construed as a potential conflict of interest.

Publisher's note

All claims expressed in this article are solely those of the authors and do not necessarily represent those of their affiliated organizations, or those of the publisher, the editors and the reviewers. Any product that may be evaluated in this article, or claim that may be made by its manufacturer, is not guaranteed or endorsed by the publisher.

Supplementary material

The Supplementary Material for this article can be found online at: https://www.frontiersin.org/articles/10.3389/fbioe.2022.973141/full#supplementary-material.

References

Aranda-Lara, L., Ocampo Garcia, B. E., Isaac-Olive, K., Ferro-Flores, G., Melendez-Alafort, L., Morales-Avila, E., et al. (2021). Drug delivery systems-based dendrimers and polymer micelles for nuclear diagnosis and therapy. *Macromol. Biosci.* 21, 2000362. doi:10.1002/mabi.202000362

Cheng, Z., Li, M. Y., Dey, R., and Chen, Y. H. (2021). Nanomaterials for cancer therapy: current progress and perspectives. *J. Hematol. Oncol.* 14, 85. doi:10.1186/s13045-021-01096-0

Combes, G. F., Vuckovic, A. M., Bakulic, M. P., Antoine, R., Bonacic-Koutecky, V., Trajkovic, K., et al. (2021). Nanotechnology in tumor biomarker detection: the potential of liganded nanoclusters as nonlinear optical contrast agents for molecular diagnostics of cancer. *Cancers* 13, 4206. doi:10.3390/cancers13164206

Drude, N., Singh, S., Winz, O. H., Moeller, M., Mottaghy, F. M., Morgenroth, A., et al. (2017). Multistage passive and active delivery of radiolabeled nanogels for superior tumor penetration efficiency. *Biomacromolecules* 18, 2489–2498. doi:10.1021/acs.biomac.7b00629

Fu, H., Du, B. L., Chen, Z. J., and Li, Y. S. (2020). Radiolabeled peptides for SPECT and PET imaging in the detection of breast cancer: preclinical and clinical perspectives. *Curr. Med. Chem.* 27, 6987–7002. doi:10.2174/0929867327666200128110827

Ghoreishi, S. M., Khalaj, A., Bitarafan-Rajabi, A., Azar, A. D., Ardestani, M. S., Assadi, A., et al. (2017). Novel 99mTc-radiolabeled anionic linear globular PEG-based dendrimer-chlorambucil: non-invasive method for iIn-vVivo biodistribution. *Drug Res. (Stuttg).* 67, 149–155. doi:10.1055/s-0042-118448

Li, X., Hetjens, L., Wolter, N., Li, H. L., Shi, X. Y., Pich, A., et al. (2022b). Charge-reversible and biodegradable chitosan-based microgels for lysozyme-triggered release of vancomycin. *J. Adv. Res.*. doi:10.1016/j.jare.2022.02.014

Li, X., Kong, L., Hu, W., Zhang, C., Pich, A., Shi, X., et al. (2022a). Safe and efficient 2D molybdenum disulfide platform for cooperative imaging-guided photothermal-selective chemotherapy: a preclinical study. *J. Adv. Res.* 37, 255–266. doi:10.1016/j.jare.2021.08.004

Li, X., Ouyang, Z. J., Li, H. L., Hu, C. L., Saha, P., Xing, L. X., et al. (2021a). Dendrimer-decorated nanogels: Efficient nanocarriers for biodistribution *in vivo* and chemotherapy of ovarian carcinoma. *Bioact. Mat.* 6, 3244–3253. doi:10.1016/j.bioactmat.2021.02.031

Li, X., Sun, H. T., Li, H. L., Hu, C. L., Luo, Y., Shi, X. Y., et al. (2021b). Multi-responsive biodegradable cationic nanogels for highly efficient treatment of tumors. *Adv. Funct. Mat.* 31, 2100227. doi:10.1002/adfm.202100227

Li, X., Xing, L. X., Zheng, K. L., Wei, P., Du, L. F., Shen, M. W., et al. (2017). Formation of gold nanostar-coated hollow mesoporous silica for tumor multimodality imaging and photothermal Therapy. *ACS Appl. Mat. Interfaces* 9, 5817–5827. doi:10.1021/acsami.6b15185

Li, X., Xiong, Z. G., Xu, X. Y., Luo, Y., Peng, C., Shen, M. W., et al. (2016). ^{99m}Tc-Labeled multifunctional low-generation dendrimer-entrapped gold nanoparticles for targeted SPECT/CT dual-mode imaging of tumors. *ACS Appl. Mat. Interfaces* 8, 19883–19891. doi:10.1021/acsami.6b04827

Li, Y. J., Zhao, L. Z., Xu, X. Y., Sun, N., Qiao, W. L., Xing, Y., et al. (2019). Design of ^{99m}Tc-labeled low generation dendrimer-entrapped gold nanoparticles for targeted single photon emission computed tomography/computed tomography imaging of gliomas. *J. Biomed. Nanotechnol.* 15, 1201–1212. doi:10.1166/jbn.2019.2760

Li, Z., Huang, J., and Wu, J. (2021). pH-Sensitive nanogels for drug delivery in cancer therapy. *Biomater. Sci.* 9, 574–589. doi:10.1039/d0bm01729a

Liang, K., Ng, S. Y., Lee, F., Lim, J., Chung, J. E., Lee, S. S., et al. (2016). Targeted intracellular protein delivery based on hyaluronic acid-green tea catechin nanogels. *Acta Biomater.* 33, 142–152. doi:10.1016/j.actbio.2016.01.011

Maddiboyina, B., Desu, P. K., Vasam, M., Challa, V. T., Surendra, A. V., Rao, R. S., et al. (2022). An insight of nanogels as novel drug delivery system with potential hybrid nanogel applications. *J. Biomaterials Sci. Polym. Ed.* 33, 262–278. doi:10.1080/09205063.2021.1982643

Pellico, J., Gawne, P. J., and de Rosales, R. T. M. (2021). Radiolabelling of nanomaterials for medical imaging and therapy. *Chem. Soc. Rev.* 50, 3355–3423. doi:10.1039/d0cs00384k

Peng, S. J., Wang, H., Zhao, W., Xin, Y. J., Liu, Y., Yu, X. R., et al. (2020). Zwitterionic polysulfamide drug nanogels with microwave augmented tumor accumulation and on-demand drug release for enhanced cancer therapy. *Adv. Funct. Mat.* 30, 2001832. doi:10.1002/adfm.202001832

Qi, G. B., Gao, Y. J., Wang, L., and Wang, H. (2018). Self-assembled peptide-based nanomaterials for biomedical imaging and therapy. *Adv. Mat.* 30, 1703444. doi:10.1002/adma.201703444

Qin, W. W., Huang, G., Chen, Z. G., and Zhang, Y. Q. (2017). Nanomaterials in targeting cancer stem cells for cancer therapy. *Front. Pharmacol.* 8, 1. doi:10.3389/fphar.2017.00001

Ramos Oda, C. M., Fernandes, R. S., de Arajo Lopes, S. C., de Oliveira, M. C., Cardoso, V. N., Santos, D. M., et al. (2017). Synthesis, characterization and radiolabeling of polymeric nano-micelles as a platform for tumor delivering. *Biomed. Pharmacother.* 89, 268–275. doi:10.1016/j.biopha.2017.01.144

Siddique, S., and Chow, J. C. L. (2020). Application of nanomaterials in biomedical imaging and cancer Therapy. *Nanomaterials* 10, 1700. doi:10.3390/nano10091700

Theune, L. E., Buchmann, J., Wedepohl, S., Molina, M., Laufer, J., Calderon, M., et al. (2019). NIR- and thermo-responsive semi-interpenetrated polypyrrole nanogels for imaging guided combinational photothermal and chemotherapy. *J. Control. Release* 311, 147–161. doi:10.1016/j.jconrel.2019.08.035

Wang, H., Gao, L. F., Fan, T. J., Zhang, C., Zhang, B., Al-Hartomy, O. A., et al. (2021). Strategic design of intelligent-responsive nanogel carriers for cancer therapy. *ACS Appl. Mat. Interfaces* 13, 54621–54647. doi:10.1021/acsami.1c13634

Wang, J. L., Zhu, L., Wang, C., Lei, S. B., and Yang, Y. L. (2022). Nanotechnology for detection of circulating tumor cells and extracellular vesicles. *Prog. Chem.* 34, 178–197. doi:10.7536/pc210346

Wu, X., Ge, L. M., Shen, G. H., He, Y., Xu, Z. L., Li, D. F., et al. (2022). 131I-labeled silk fibroin microspheres for radioembolic therapy of rat hepatocellular carcinoma. *ACS Appl. Mat. Interfaces* 14, 21848–21859. doi:10.1021/acsami.2c00211

Yang, H. Y., Li, Y., Jang, M. S., Fu, Y., Wu, T. P., Lee, J. H., et al. (2019). Green preparation of pH-responsive and dual targeting hyaluronic acid nanogels for efficient protein delivery. *Eur. Polym. J.* 121, 109342. doi:10.1016/j.eurpolymj.2019.109342

Zhou, W., Yang, G. Z., Ni, X. Y., Diao, S. C., Xie, C., Fan, Q. L., et al. (2020). Recent advances in crosslinked nanogel for multimodal imaging and cancer therapy. *Polymers* 12, 1902. doi:10.3390/polym12091902

Zhu, W., Wei, Z. Q., Han, C., and Weng, X. S. (2021). Nanomaterials as promising theranostic tools in nanomedicine and their applications in clinical disease diagnosis and treatment. *Nanomaterials* 11, 3346. doi:10.3390/nano11123346

frontiers | Frontiers in Bioengineering and Biotechnology

ORIGINAL RESEARCH
published: 25 July 2022
doi: 10.3389/fbioe.2022.926253

Intelligent Nanomaterials for Solar Energy Harvesting: From Polar Bear Hairs to Unsmooth Nanofiber Fabrication

Qingli Wang [1], ***Ji-Huan He*** [2,3]* **and** ***Zhi Liu*** [4]*

[1]*Department of Postgraduates, Shanghai University of Engineering Science, Shanghai, China,* [2]*School of Mathematics and Information Science, Henan Polytechnic University, Jiaozuo, China,* [3]*National Engineering Laboratory for Modern Silk, College of Textile and Clothing Engineering, Soochow University, Suzhou, China,* [4]*School of Textile and Garment, Anhui Polytechnic University, Wuhu, China*

OPEN ACCESS

Edited by:
Yu Luo,
Shanghai University of Engineering Sciences, China

Reviewed by:
Jinfa Ming,
Qingdao University, China
Jamal Zare,
Shahrekord University, Iran
Mohammad Malikan,
Gdansk University of Technology, Poland

****Correspondence:***
Ji-Huan He
hejihuan@suda.edu.cn
Zhi Liu
liuzhi@ahpu.edu.cn

Specialty section:
This article was submitted to Nanobiotechnology,
a section of the journal Frontiers in Bioengineering and Biotechnology

Received: *22 April 2022*
Accepted: *16 May 2022*
Published: *25 July 2022*

Citation:
Wang Q, He J-H and Liu Z (2022) Intelligent Nanomaterials for Solar Energy Harvesting: From Polar Bear Hairs to Unsmooth Nanofiber Fabrication.
Front. Bioeng. Biotechnol. 10:926253.
doi: 10.3389/fbioe.2022.926253

Polar bears can live in an extremely cold environment due to their hairs which possess some remarkable properties. The hollow structure of the hair enables the bear to absorb energy from water, and the white and transparent hairs possess amazing optical properties. However, the surface morphology function of bear hairs has been little-studied. Herein, we demonstrate that the micro-structured scales distributed periodically along the hair can absorb maximal radiative flux from the Sun. This polar bear hair effect has the ability for the hair surface not to reflect radiation with a wavelength of about 500 nm. Mimicking the polar bears' solar performance in the fabrication of nanofibers will certainly stimulate intelligent nanomaterials for efficient solar energy absorption. Therefore, a new technology is discussed in this work for the fabrication of periodic unsmooth nanofibers toward solar energy harvesting.

Keywords: biomimetic, polar bear hair, energy absorption, selective light absorption, moth-eye effect, bubble electrospinning

INTRODUCTION

Recently, various devices have been developed for energy harvesting, such as the nanofluids (He and Elazem, 2022), the spring-pendulum systems (Wu et al., 2018; He et al., 2022a), and the low-frequency vibration systems (Zhang and Cai., 2012; He C.-H. et al., 2021; He et al., 2022b). In addition to the abovementioned methods, the nanotechnology for solar energy harvesting (Satharasinghe et al., 2020) is totally new and is quite promising. Though solar energy harvesting has attracted much attention due to the inexhaustible green energy, its efficiency is relatively low. Interestingly, some natural animals have a special ability to absorb solar energy with extremely high efficiency, benefiting from the amazing surface morphology of their hairs, for example, the wolverine (gulo-gulo) hair (Liu et al., 2018).

The polar bear (*Ursus maritimus*) is the largest predator in the Arctic region. As a kind of marine mammal, the animal is born on land but spends most of its time in the sea to absorb energy from water through its hairs (He et al., 2011; Jia et al., 2017). In order to survive in a harsh environment as low as −50°C in the Arctic, this huge animal has an extensive fat layer of up to 10 cm and bulky furs, which help protect against the cold surrounding. Polar bear fur consists of a layer of dense underfur and an outer layer of guard hairs, which are transparent and white in color (Bechshøft et al., 2012; Dietz et al., 2013). The white hairs contribute to camouflaging the bear in the snow and ice-covered environment (Ferguson et al., 1998; Stegmaier et al., 2009). As a protein fiber, the polar bear hair is not much different in appearance from other protein fibers such as the wool fiber (Fan et al., 2019) and down fiber (Yang et al., 2011). Much attention has been paid to the optical properties (Lavigne and Øritsland, 1974bib_Lavigne_and_Øritsland_1974; Grojean et al., 1980 and 1981; Koon, 1998) and chemical properties of polar bear hairs, and many biomimetic designs were proposed, including thermally insulating fabrics (Cui et al., 2018), textile solar light collectors (Bahners et al., 2008), and polar bear hair–based solar sensors (Tributsch et al., 1990). Many researchers have studied hair cortisol concentration (Mislan et al., 2016), which is considered a biomarker. Furthermore, the morphology and structure, especially the hollow structure of polar bear hairs, have also been studied extensively (Zhang et al., 2009). The fractal theory is a useful tool to reveal its biomechanism (Wang et al., 2015; Wang et al., 2018). However, energy absorption with regards to the scale distribution on polar bear hairs has not been studied yet, and this study intends to state its energy absorption based on the hair's morphology. Many research studies have revealed that the graphene distribution in a composite affected its properties greatly (Zuo and Liu, 2021; Zuo, 2021). Geometry is always the main factor affecting materials' properties (He, et al., 2021b) so that the energy absorption property of the polar bear hair.

MATERIALS AND METHODS

Nano-scale surface morphology greatly affects a surface's chemistry property (Marmur, 2004; Li X.-X. et al., 2021), friction property (Cao et al., 2021; Bains et al., 2020), and reflection property (Selkowitz 2021). According to the geometric potential theory (Peng and He, 2020; Han and He, 2021), a nano-scale surface can produce high geometric potential. It was reported that Fangzhu's nano-scale surface can collect water molecules from the air (He and El-Dib, 2021; Wu et al., 2021). Gecko adhesion and the mimicking smart adhesion can also be explained by its nano-scale spatulas (Wang et al., 2019; Li et al., 2020). Here, an experiment is designed to study the nano-scale surface morphology of polar bear hairs.

Experimental Materials

The hair was obtained from a 2-year-old male polar bear in the Laohutan Pole Aquarium in Dalian, China. Polyvinyl alcohol (PVA, 1750 ± 50) was purchased from Sinopharm Chemical Reagent Co., Ltd. (Shanghai, China).

Experimental Instruments

The JEOL JSM-5600LV scanning electron microscope (SEM) with a magnification of 18-300,000 (Japan Electronics Co. Ltd.) and the S-4800 field emission scanning electron microscope (FE-SEM) (Hitachi Ltd., Japan) with resolutions of 1.0 nm (15 kV), 2.0 nm (1 kV), and 1.4 nm (1 kV, Deceleration mode) were used in our experiment. The scale density (scale/mm) and scale thickness on the hair surface were measured through the SEM images.

Experimental Process

First, we rinsed the samples with distilled water to remove debris from their surface. Second, the samples were washed with 0.1 M phosphate buffer three times (15 min per time). Third, the samples were fixed on the sample stage and sprayed in the ion sputter instrument. Finally, the samples were evaluated under the SEM and FE-SEM. In the electrospinning process, the PVA was dissolved in an aqueous solution (8 wt%) at 98°C for 4 h. The spinning parameters were as follows: the voltage was 20 kV, and the collector distance was 25 cm. After the spinning process, the resulting membrane was stretched with a draw ratio of 1.5 times. The draw process was carried out using a universal testing machine (Instron 3,365, Instron, Norwood, MA) (gauge length: 20 mm and cross-head speed: 0.2 mm/s) at 25 ± 0.5°C and 60 ± 5% relative humidity.

Nanoscale Surface Morphology

Before studying the polar bear hair effect, we give a brief introduction to the moth-eye, which can absorb all night light (Wilson and Hutley, 1982). This property is important for the nocturnal insect to escape from predators.

Figure 1 is the schematic diagram of the moth-eye effect. The height of protuberances is about $h = 220$ nm, and the diameter of the microtrichia is about $d = 200$ nm.

It was reported that the reflectance is very low for wavelengths $2d < \lambda < 2.5h$ (Nosonovsky and Bhushan, 2013), meaning that the wavelengths between 440 and 550 nm are all absorbed by the nocturnal insect.

The surface geometry of the moth eye is periodic, and it was used for the biomimetic design of an optically transparent microwave absorber with a periodic array of properly shaped glass caps (Kwon et al., 2021). A similar phenomenon occurs in the polar bear hair, and we carried out an experiment to study the morphology of the hair surface.

RESULTS AND DISCUSSION

Figure 2 shows the morphology of the polar bear hair surface structure. **Figures 2A–C** are SEM images of the same hair at the magnifications × 1,000, × 2,000 and × 5,000, respectively. **Figure 3** shows the FE-SEM of the polar bear hair surface structure. As we can see from **Figures 2** and **3**, the surface of polar bear hair fibers is not smooth, and there is a scale structure similar to the surface of wool fibers. Meanwhile, these figures also show that the polar bear hair fibers were covered with periodic scales in regular shapes. Scale density was relatively small, 70–90 scales/mm, and the scale edges seemed to be wavy or serrated. The scales are thicker at the top, and the scale thickness is about 0.5 μm.

Similar to the moth effect (Nosonovsky and Bhushan, 2013), polar bear hair enables the animal to absorb as much energy as possible from natural light. According to **Figures 2** and **3**, polar bear hair can be geometrically illustrated, as shown in **Figure 4**.

The periodicity of the surface morphology of polar bear hair is similar to that of the moth eye and also shows a similar optical property to absorb light energy. Polar bear hairs are white and transparent to convert light energy to its body. The hair surface morphology (**Figure 4**) can increase transmission and reduce reflection. If the thickness of the scales is almost equal to the

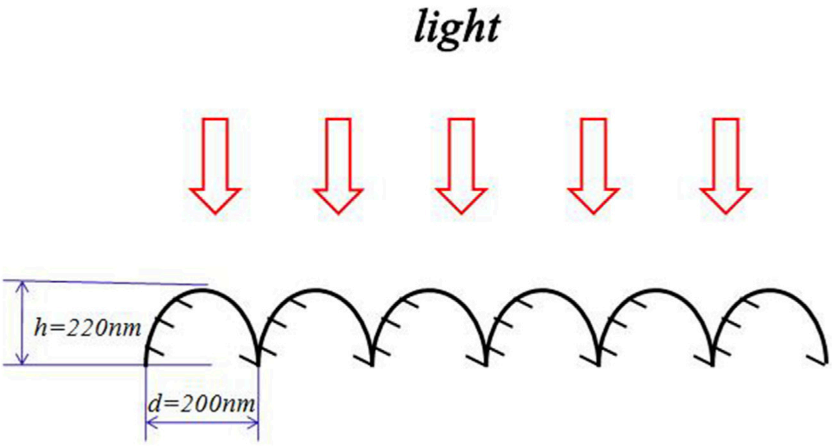

FIGURE 1 | Schematic diagram of the moth-eye effect (Nosonovsky and Bhushan,2013).

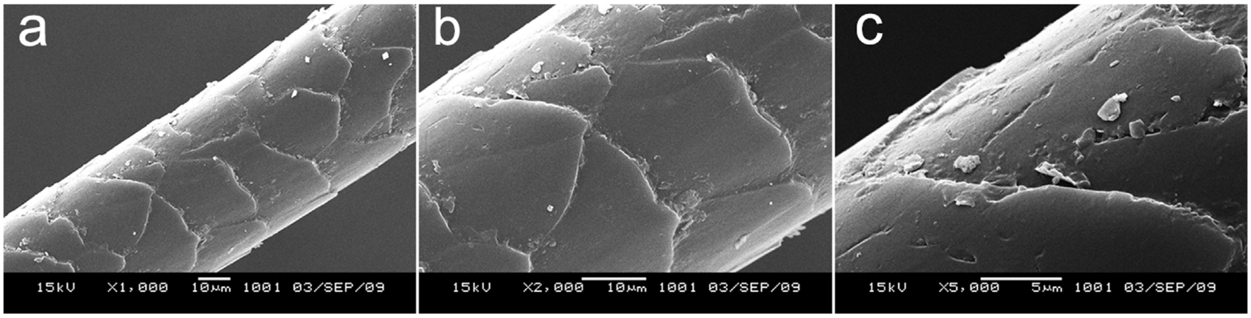

FIGURE 2 | Polar bear hair surface structure by SEM with different magnifications **(A)** ×1,000, **(B)** ×2,000, and **(C)** ×5,000.

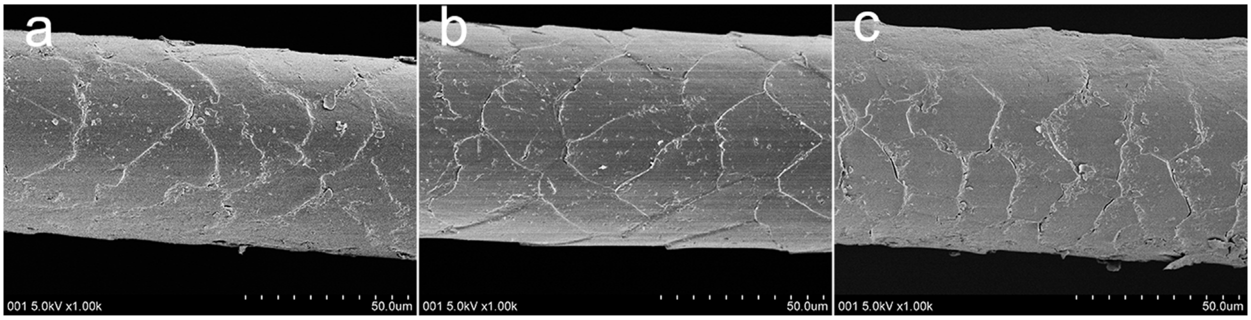

FIGURE 3 | Polar bear hair surface structure by FE-SEM **(A-C)** different locations on the hair surface.

light wavelength (Nosonovsky and Bhushan, 2013), the light will not be reflected. Our experimental data reveal that the scale thickness is about 500 nm, corresponding to the spectrum of 500 nm wavelength. According to the laws of radiative heat transfer, the radiative flux from the Sun maximizes at a wavelength of about 0.5 μm (Scamarcio et al., 1997; Thuillier et al., 2003) (**Figure 5**). The polar bear hair effect is the ability of a micro-structured optical surface not to reflect light with the highest energy.

The general approaches to fabricating smooth nanofibers are electrospinning (Gao et al., 2021; Liu et al., 2021) and bubble electrospinning (He and Qian, 2022; Qian and He, 2022). However, Lin, et al., 2021 suggested a general strategy for the fabrication of unsmooth nanofibers. Yao and He (2020) used the geometric potential theory to control the surface morphology of nanofibers. These references suggested that the unsmooth nanofibers can be fabricated by the electrospinning method.

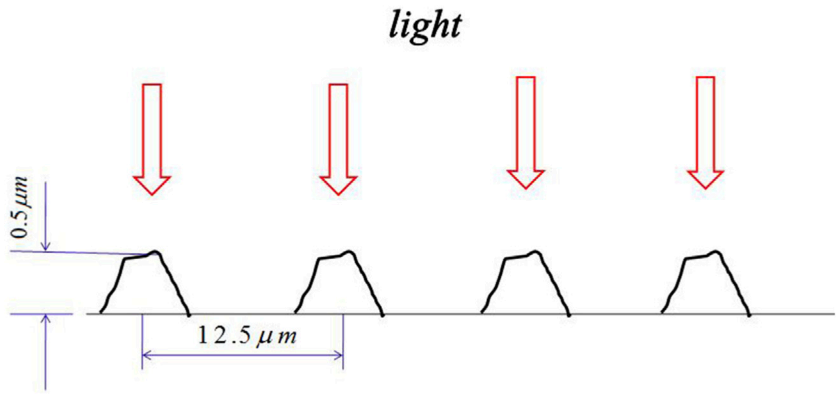

FIGURE 4 | Schematic diagram of the polar bear hair effect.

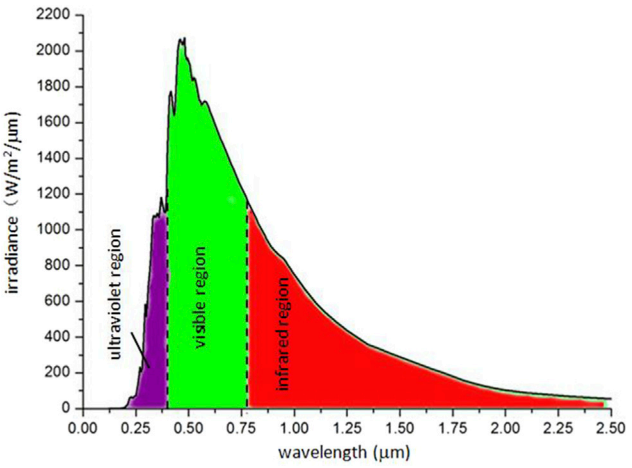

FIGURE 5 | Maximal solar spectral irradiance at 500 nm wavelength.

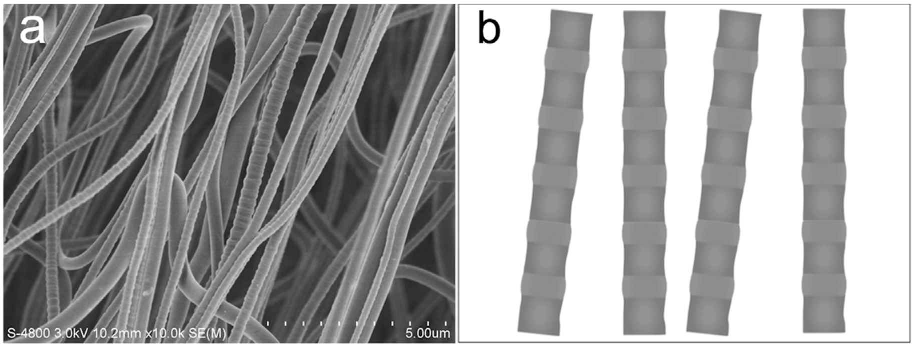

FIGURE 6 | (A) Morphology of the periodic unsmooth PVA nanofiber. **(B)** Schematic diagram of the periodic bamboo-like unsmooth PVA nanofiber.

Here, inspired by the natural polar bear, a new technology is discussed for the fabrication of periodic unsmooth nanofibers for solar energy harvesting (Liu et al., 2015). As shown in **Figure 6**, the resulting PVA nanofibers were endowed with peculiar morphology with a periodic unsmooth surface after being stretched (**Figure 6A**). The bulges with a diameter of about 80 nm were successfully constructed and periodically spread along the nanofiber axis (**Figure 6A**), exhibiting a similar appearance to natural bamboo (**Figure 6B**). The mutational surface morphology from a smooth surface to a bamboo-like unsmooth surface by the stretching method suggests a promising strategy to mimic the polar bear's solar performance in the fabrication of intelligent nanomaterials for efficient solar energy–absorption.

The nanofibers with a periodic unsmooth surface are potentially of great technological interest for the development of solar energy absorption, and their other applications include invisibility devices, electronic sensors, applied surface science, photonics, physics, microelectronics, nanomaterials, advanced textile, photothermo-promoted nanocatalysis, photothermal semiconduction, photoactivatable cancer immunotherapy, and environmental science (Li et al., 2019; Li X. et al., 2021; Li J. et al., 2021; Yang et al., 2021). We anticipate that this article will be a starting point for more sophisticated studies of intelligent nanomaterials for solar energy harvesting for solar cells (Pavlovic et al., 2021; Alshikhi and Kayfeci 2022) or solar collector systems (Al-Rabeeah et al., 2022). The periodic structure of nanomaterials *via* bioinspiration for energy gives many promises and great challenges (Gong et al., 2019).

CONCLUSION

Similar to the moth-eye effect, polar bear hair characteristics along the longitudinal direction were studied by means of SEM and FE-SEM, respectively. The result shows that the micro-structured scales distributed periodically along the hair can absorb maximal radiative flux from the Sun. Mimicking the polar bear's solar energy harvesting property, we fabricated nanofibers with a periodic unsmooth surface, which exhibits the potential of stimulating intelligent nanomaterials for efficient solar energy absorption. The bio-mimic design of solar energy materials by bubble electrospinning can be used in the infrared stealth technology. Polar bear hair–inspired biomaterials with selective light absorption will attract much attention in the future.

DATA AVAILABILITY STATEMENT

The original contributions presented in the study are included in the article/Supplementary Material; further inquiries can be directed to the corresponding authors.

AUTHOR CONTRIBUTIONS

J-HH conceptualized the study. QW performed the experiments. J-HH, QW, and ZL analyzed and processed the data. QW and ZL wrote and reviewed the manuscript.

REFERENCES

Al-Rabeeah, A. Y., Seres, I., and Farkas, I. (2022). Recent Improvements of the Optical and Thermal Performance of the Parabolic Trough Solar Collector Systems. *FU Mech. Eng.* 20 (1), 073–094. doi:10.22190/FUME201106030A

Alshikhi, O., and Kayfeci, M. (2022). Experimental Investigation of Using Graphene Nanoplatelets and Hybrid Nanofluid as Coolant in Photovoltaic Thermal Systems. *Therm. Sci.* 26 (1), 195–208. doi:10.2298/TSCI200524348A

Bahners, T., Schlosser, U., Gutmann, R., and Schollmeyer, E. (2008). Textile Solar Light Collectors Based on Models for Polar Bear Hair. *Sol. Energy Mater. Sol. Cells* 92 (12), 1661–1667. doi:10.1016/j.solmat.2008.07.023

Bains, P. S., Grewal, J. S., Sidhu, S. S., Kaur, S., and Singh, G. (2020). Surface Modification of Ring-Traveler of Textile Spinning Machine for Substantiality. *FU Mech. Eng.* 18 (1), 031–042. doi:10.22190/FUME190623005B

Bechshøft, T. Ø., Rigét, F. F., Sonne, C., Letcher, R. J., Muir, D. C. G., Novak, M. A., et al. (2012). Measuring Environmental Stress in East Greenland Polar Bears, 1892-1927 and 1988-2009: What Does Hair Cortisol Tell Us? *Environ. Int.* 45, 15–21. doi:10.1016/j.envint.2012.04.005

Cao, H., Tian, Y., and Meng, Y. (2021). A Fracture-Induced Adhesive Wear Criterion and its Application to the Simulation of Wear Process of the Point Contacts Under Mixed Lubrication Condition. *FU Mech. Eng.* 19 (1), 023–038. doi:10.22190/FUME210108021C

Cui, Y., Gong, H., Wang, Y., Li, D., and Bai, H. (2018). A Thermally Insulating Textile Inspired by Polar Bear Hair. *Adv. Mat.* 30 (14), 1706807. doi:10.1002/adma.201706807

Dietz, R., Rigét, F. F., Sonne, C., Born, E. W., Bechshøft, T., McKinney, M. A., et al. (2013). Three Decades (1983-2010) of Contaminant Trends in East Greenland Polar Bears (*Ursus maritimus*). Part 1: Legacy Organochlorine Contaminants. *Environ. Int.* 59, 485–493. doi:10.1016/j.envint.2012.09.004

Fan, J., Yang, X., and Liu, Y. (2019). Fractal Calculus for Analysis of Wool Fiber: Mathematical Insight of its Biomechanism. *J. Eng. Fibers Fabr.* 14. 1–4. doi:10.1177/1558925019872200

Ferguson, S. H., Taylor, M. K., Born, E. W., and Messier, F. (1998). Fractals, Sea-Ice Landscape and Spatial Patterns of Polar Bears. *J. Biogeogr.* 25, 1081–1092.

Gao, L., Wang, Y., and Xu, L. (2021). Mechanism Study of Highly Ordered Jets in an Improved Electrospinning Process. *Therm. Sci.* 25 (3B), 2327–2334. doi:10.2298/TSCI200124122G

Gong, C., Sun, S., Zhang, Y., Sun, L., Su, Z., Wu, A., et al. (2019). Hierarchical Nanomaterials via Biomolecular Self-Assembly and Bioinspiration for Energy and Environmental Applications. *Nanoscale* 11 (10), 4147–4182. doi:10.1039/C9NR00218A

Grojean, R. E., Sousa, J. A., and Henry, M. C. (1980). Utilization of Solar Radiation by Polar Animals: An Optical Model for Pelts. *Appl. Opt.* 19 (3), 339–346. doi:10.1364/AO.19.000339

Grojean, R. E., Sousa, J. A., and Henry, M. C. (1981). Utilization of Solar Radiation by Polar Animals: An Optical Model for Pelts; Authors' Reply to an Alternative Explanation. *Appl. Opt.* 20 (11), 1896–1897. doi:10.1364/AO.20.001896

Han, C., and He, J.-H. (2021). Effect of Fabric Surface's Cleanliness on its Moisture/Air Permeability. *Therm. Sci.* 25 (2B), 1517–1521. doi:10.2298/TSCI2102517H

He, J. H., and Elazem, N. Y. A. (2022). The Carbon Nanotube-Embedded Boundary Layer Theory for Energy Harvesting. *Facta Univ-Ser Mech.* 1. 1. doi:10.22190/FUME220221011H

He, J.-H., and El-Dib, Y. O. (2021). Homotopy Perturbation Method with Three Expansions for Helmholtz-Fangzhu Oscillator. *Int. J. Mod. Phys. B* 35 (24), 2150244. doi:10.1142/S0217979221502441

He, J.-H., Qian, M.-Y., and Li, Y. (2022). The Maximal Wrinkle Angle During the Bubble Collapse and its Application to the Bubble Electrospinning. *Front. Mat.* 8, 800567. doi:10.3389/fmats.2021.800567

He, J.-H., Wang, Q.-L., and Sun, J. (2011). Can Polar Bear Hairs Absorb Environmental Energy? *Therm. Sci.* 15 (3), 911–913. doi:10.2298/TSCI1103911H

He, C.-H., Liu, C., He, J.-H., and Gepreel, K. A. (2021a). Low Frequency Property of a Fractal Vibration Model for a Concrete Beam. *Fractals* 29 (05), 2150117. doi:10.1142/S0218348X21501176

He, C.-H., Liu, S.-H., Liu, C., and Mohammad-Sedighi, H. (2022b). A Novel Bond Stress-Slip Model for 3-D Printed Concretes. *Discret Cont Dyn-S* 15, 1669. doi:10.3934/dcdss.2021161

He, C.-H., Amer, T. S., Tian, D., Abolila, A. F., and Galal, A. A. (2022a). Controlling the Kinematics of a Spring-Pendulum System Using an Energy Harvesting Device. *J. Low Freq. Noise, Vib. Act. Control.* 1. 1. doi:10.1177/14613484221077474

He, J.-H., Moatimid, G. M., and Zekry, M. H. (2022b). Forced Nonlinear Oscillator in a Fractal Space. *FU Mech. Eng.* 20 (1), 001–020. doi:10.22190/FUME220118004H

Jia, H., Guo, J., and Zhu, J. (2017). Comparison of the Photo-Thermal Energy Conversion Behavior of Polar Bear Hair and Wool of Sheep. *J. Bionic Eng.* 14 (4), 616–621. doi:10.1016/S1672-6529(16)60427-4

Koon, D. W. (1998). Is Polar Bear Hair Fiber Optic? *Appl. Opt.* 37 (15), 3198–3200. doi:10.1364/AO.37.003198

Kwon, H., D'Aguanno, G., and Alú, A. (2021). Optically Transparent Microwave Absorber Based on Water-Based Moth-Eye Structures. *Opt. Express* 29 (6), 9190–9198. doi:10.1364/oe.418220

Lavigne, D. M., and Øritsland, N. A. (1974). Black Polar Bears. *Nature* 251 (5472), 218–219. doi:10.1038/251218b0

Li, J., Cui, D., Huang, J., He, S., Yang, Z., Zhang, Y., et al. (2019). Organic Semiconducting Pro-Nanostimulants for Near-Infrared Photoactivatable Cancer Immunotherapy. *Angew. Chem. Int. Ed.* 58, 12680–12687. doi:10.1002/ange.20190628810.1002/anie.201906288

Li, X., Li, Y., Li, Y., and He, J. (2020). Gecko-Like Adhesion in the Electrospinning Process. *Results Phys.* 16, 102899. doi:10.1016/j.rinp.2019.102899

Li, X.-X., Tian, D., and He, J.-H. (2021a). High Energy Surface as a Receptor in Electrospinning: A Good Switch for Hydrophobicity to Hydrophilicity. *Therm. Sci.* 25 (3), 2205–2212. doi:10.2298/TSCI191120107L

Li, X., Sun, H., Li, H., Hu, C., Luo, Y., Shi, X., et al. (2021b). Multi-Responsive Biodegradable Cationic Nanogels for Highly Efficient Treatment of Tumors. *Adv. Funct. Mater.* 31 (26), 2100227. doi:10.1002/adfm.202100227

Li, J., Yu, X., Jiang, Y., He, S., Zhang, Y., Luo, Y., et al. (2021c). Second Near-Infrared Photothermal Semiconducting Polymer Nanoadjuvant for Enhanced Cancer Immunotherapy. *Adv. Mat.* 33 (4), 2003458. doi:10.1002/adma.202003458

Lin, L., Liu, Y.-Q., Li, Y.-Y., Shen, Y., and He, J.-H. (2021). Fabrication of PVDF/PES Nanofibers with Unsmooth Fractal Surfaces by Electrospinning: A General Strategy and Formation Mechanism. *Therm. Sci.* 25, 1287–1294. doi:10.2298/TSCI191201024L

Liu, Z., Sun, Q.-L., and He, J.-H. (2015). Fabrication of Unsmooth Bamboo-Like Nanofibers. *Therm. Sci.* 19 (4), 1450–1451. doi:10.2298/TSCI1504450L

Liu, H., Bahi, A., and Ko, F. K. (2018). A One Dimensional Heat Transfer Model for Wolverine (Gulo-Gulo) Hair. *Ijcst* 30, 548–558. doi:10.1108/IJCST-08-2017-0108

Liu, L., Liu, Y.-Q., Li, Y.-Y., Shen, Y., and He, J.-H. (2021). Dropping in Electrospinning Process: A General Strategy for Fabrication of Microspheres. *Therm. Sci.* 25, 1295–1303. doi:10.2298/TSCI191228025L

Marmur, A. (2004). The Lotus Effect: Superhydrophobicity and Metastability. *Langmuir* 20 (9), 3517–3519. doi:10.1021/la036369u

Mislan, P., Derocher, A. E., St. Louis, V. L., Richardson, E., Lunn, N. J., and Janz, D. M. (2016). Assessing Stress in Western Hudson Bay Polar Bears Using Hair Cortisol Concentration as a Biomarker. *Ecol. Indic.* 71, 47–54. doi:10.1016/j.ecolind.2016.06.034

Nosonovsky, M., and Bhushan, B. (2013). *Multiscale Dissipative Mechanisms and Hierarchical Surfaces: Friction, Superhydrophobicity, and Biomimetics*. Beijing, China: Peking University Press.

Pavlovic, A., Fragassa, C., Bertoldi, M., and Mikhnych, V. (2021). Thermal Behavior of Monocrystalline Silicon Solar Cells: A Numerical and Experimental Investigation on the ModuleEncapsulation Materials. *J. Appl. Comput. Mech.* 7 (3), 1847–1855. doi:10.22055/JACM.2021.37852.3101

Peng, N.-b., and He, J.-h. (2020). Insight into the Wetting Property of a Nanofiber Membrane by the Geometrical Potential. *Nanotec.* 14 (1), 64–70. doi:10.2174/1872210513666191120104149

Qian, M.-Y., and He, J.-H. (2022). Collection of Polymer Bubble as a Nanoscale Membrane. *Surfaces Interfaces* 28, 101665. doi:10.1016/j.surfin.2021.101665

Satharasinghe, A., Hughes-Riley, T., and Dias, T. (2020). A Review of Solar Energy Harvesting Electronic Textiles. *Sensors* 20 (20), 5938. doi:10.3390/s20205938

Scamarcio, G., Capasso, F., Sirtori, C., Faist, J., Hutchinson, A. L., Sivco, D. L., et al. (1997). High-Power Infrared (8-Micrometer Wavelength) Superlattice Lasers. *Science* 276 (5313), 773–776. doi:10.1126/science.276.5313.773

Selkowitz, S. (2021). Reflections on Surface Morphology. *Nat. Energy* 6 (5), 456–457. doi:10.1038/s41560-021-00835-4

Stegmaier, T., Linke, M., and Planck, H. (2009). Bionics in Textiles: Flexible and Translucent Thermal Insulations for Solar Thermal Applications. *Phil. Trans. R. Soc. A* 367, 1749–1758. doi:10.1098/rsta.2009.0019

Thuillier, G., Hersé, M., Foujols, T., Peetermans, W., Gillotay, D., Simon, P. C., et al. (2003). The Solar Spectral Irradiance from 200 to 2400 Nm as Measured by the SOLSPEC Spectrometer from the ATLAS and EURECA Missions. *Sol. Phys.* 214 (1), 1–22. doi:10.1023/A:1024048429145

Tributsch, H., Goslowsky, H., Küppers, U., and Wetzel, H. (1990). Light Collection and Solar Sensing Through the Polar Bear Pelt. *Sol. Energy Mat.* 21 (2-3), 219–236. doi:10.1016/0165-1633(90)90056-7

Wang, Q.-L., Li, Z.-B., Kong, H.-Y., and He, J.-H. (2015). Fractal Analysis of Polar Bear Hairs. *Therm. Sci.* 19, 143–144. doi:10.2298/TSCI15S1S43W

Wang, Q., Shi, X., He, J.-H., and Li, Z. B. (2018). Fractal Calculus and its Application to Explanation of Biomechanism of Polar Bear Hairs. *Fractals* 26 (06), 1850086. doi:10.1142/S0218348X1850086X

Wang, C., Xu, L., Liu, G., Ren, Y., Lv, J., Gao, D., et al. (2019). Smart Adhesion by Surface Treatment Experimental and Theoretical Insights. *Therm. Sci.* 23 (4), 2355–2363. doi:10.2298/TSCI1904355W

Wilson, S. J., and Hutley, M. C. (1982). The Optical Properties of 'Moth Eye' Antireflection Surfaces. *Opt. Acta Int. J. Opt.* 29 (7), 993–1009. doi:10.1080/713820946

Wu, Y., Qiu, J., Zhou, S., Ji, H., Chen, Y., and Li, S. (2018). A Piezoelectric Spring Pendulum Oscillator Used for Multi-Directional and Ultra-Low Frequency Vibration Energy Harvesting. *Appl. Energy* 231, 600–614. doi:10.1016/j.apenergy.2018.09.082

Wu, P., Ling, W., Li, X., He, X., and Xie, L. (2021). Dynamics Research of Fangzhu's Nanoscale Surface. *J. Low Freq. Noise, Vib. Act. Control* 41, 479–487. doi:10.1177/14613484211052753

Shu Yang, S., Weidong Yu, W., and Ning Pan, N. (2011). Fractal Phenomenon in Sound Absorbing Behavior of Down Fiber Assembly. *Text. Res. J.* 81 (11), 1139–1144. doi:10.1177/0040517511398949

Yang, Z., Luo, Y., Hu, Y., Liang, K., He, G., Chen, Q., et al. (2021). Photothermo-Promoted Nanocatalysis Combined with H 2 S-Mediated Respiration Inhibition for Efficient Cancer Therapy. *Adv. Funct. Mat.* 31 (8), 2007991. doi:10.1002/adfm.202007991

Yao, X., and He, J.-H. (2020). On Fabrication of Nanoscale Non-Smooth Fibers with High Geometric Potential and Nanoparticle's Non-Linear Vibration. *Therm. Sci.* 24 (4), 2491–2497. doi:10.2298/TSCI2004491Y

Zhang, Y., and Cai, C. S. (2012). A Retrofitted Energy Harvester for Low Frequency Vibrations. *Smart Mat. Struct.* 21 (7), 075007. doi:10.1088/0964-1726/21/7/075007

Zhang, H. J., Chen, Z., Zhu, Y. L., Du, Z. Q., and Yu, W. D. (2009). Characterization for Hair Morphology and Structure of Cold-Resistant Animals. *J. Xi'an Polytech. Univ.* 23 (2), 333–339. doi:10.13338/j.issn.1674-649x.2009.02.073

Zuo, Y.-T., and Liu, H.-J. (2021). Fractal Approach to Mechanical and Electrical Properties of Graphene/Sic Composites. *FU Mech. Eng.* 19 (2), 271–284. doi:10.22190/FUME201212003Z

Zuo, Y. T. (2021). Effect of SiC Particles on Viscosity of 3-D Print Paste: A Fractal Rheological Model and Experimental Verification. *Therm. Sci.* 25 (3B), 2405–2409. doi:10.2298/tsci200710131z

Conflict of Interest: The authors declare that the research was conducted in the absence of any commercial or financial relationships that could be construed as a potential conflict of interest.

Publisher's Note: All claims expressed in this article are solely those of the authors and do not necessarily represent those of their affiliated organizations, or those of the publisher, the editors, and the reviewers. Any product that may be evaluated in this article, or claim that may be made by its manufacturer, is not guaranteed or endorsed by the publisher.

Copyright © 2022 Wang, He and Liu. This is an open-access article distributed under the terms of the Creative Commons Attribution License (CC BY). The use, distribution or reproduction in other forums is permitted, provided the original author(s) and the copyright owner(s) are credited and that the original publication in this journal is cited, in accordance with accepted academic practice. No use, distribution or reproduction is permitted which does not comply with these terms.

frontiers | Frontiers in Bioengineering and Biotechnology

TYPE Mini Review
PUBLISHED 05 August 2022
DOI 10.3389/fbioe.2022.958095

Check for updates

OPEN ACCESS

EDITED BY
Xin Li,
DWI – Leibniz-Institut für Interaktive Materialien, Germany

REVIEWED BY
Longgang Wang,
Yanshan University, China
Sushanta Sethi,
Indian Institute of Technology Bombay, India
Peter Rodič,
Institut Jožef Stefan (IJS), Slovenia

*CORRESPONDENCE
Hongbo Mu,
mhb506@nefu.edu.cn
Mingming Zhang,
zhangmingming@hrbmu.edu.cn

†These authors have contributed equally to this work

SPECIALTY SECTION
This article was submitted to Nanobiotechnology, a section of the journal Frontiers in Bioengineering and Biotechnology

RECEIVED 31 May 2022
ACCEPTED 04 July 2022
PUBLISHED 05 August 2022

CITATION
Ge-Zhang S, Yang H, Ni H, Mu H and Zhang M (2022), Biomimetic superhydrophobic metal/nonmetal surface manufactured by etching methods: A mini review.
Front. Bioeng. Biotechnol. 10:958095.
doi: 10.3389/fbioe.2022.958095

COPYRIGHT
© 2022 Ge-Zhang, Yang, Ni, Mu and Zhang. This is an open-access article distributed under the terms of the Creative Commons Attribution License (CC BY). The use, distribution or reproduction in other forums is permitted, provided the original author(s) and the copyright owner(s) are credited and that the original publication in this journal is cited, in accordance with accepted academic practice. No use, distribution or reproduction is permitted which does not comply with these terms.

Biomimetic superhydrophobic metal/nonmetal surface manufactured by etching methods: A mini review

Shangjie Ge-Zhang[1†], Hong Yang[1†], Haiming Ni[1], Hongbo Mu[1*] and Mingming Zhang[2*]

[1]College of Science, Northeast Forestry University, Harbin, China, [2]College of Bioinformatics Science and Technology, Harbin Medical University, Harbin, China

As an emerging fringe science, bionics integrates the understanding of nature, imitation of nature, and surpassing nature in one aspect, and it organically combines the synergistic complementarity of function and structure–function integrated materials which is of great scientific interest. By imitating the microstructure of a natural biological surface, the bionic superhydrophobic surface prepared by human beings has the properties of self-cleaning, anti-icing, water collection, anti-corrosion and oil–water separation, and the preparation research methods are increasing. The preparation methods of superhydrophobic surface include vapor deposition, etching modification, sol–gel, template, electrostatic spinning, and electrostatic spraying, which can be applied to fields such as medical care, military industry, ship industry, and textile. The etching modification method can directly modify the substrate, so there is no need to worry about the adhesion between the coating and the substrate. The most obvious advantage of this method is that the obtained superhydrophobic surface is integrated with the substrate and has good stability and corrosion resistance. In this article, the different preparation methods of bionic superhydrophobic materials were summarized, especially the etching modification methods, we discussed the detailed classification, advantages, and disadvantages of these methods, and the future development direction of the field was prospected.

KEYWORDS
bionic modification, superhydrophobic surface, micro/nanostructure, etching modification method, chemical etching method, laser-etching method

1 Introduction

Nature is always the source of our inspiration. By observing the structural diversity, functional specificity, and environmental responsiveness of natural organisms, human beings have discovered many different biological structures and functions, thus creating more and more new materials and structures through technological innovation and cross-fertilization across disciplines. Bionic materials are materials prepared by simulating the unique structure or characteristics of organisms (Suresh Kumar et al., 2020; Koch et al., 2008). Biomimetic superhydrophobic surfaces, which are prepared by using the superhydrophobic phenomena related to biological structures in nature (Table 1), such as lotus leaves (Sun and Guo, 2019; Lv et al., 2020), butterfly wings (Zheng et al., 2007; Shao et al., 2019) and rice leaves (Wu et al., 2011; Lee et al., 2013; Rius-Ayra et al., 2018), have attracted wide attention and research because of outstanding self-cleaning (Barthlott and Neinhuis, 1997; Fürstner et al., 2005; Ming et al., 2005), anti-icing (Liu et al., 2020; Sun et al., 2020), anti-corrosion (Liu et al., 2014; Wei et al., 2021a; Zhang et al., 2022), and oil–water separation (Wang et al., 2015a; Saleh et al., 2020; Rasouli et al., 2021; Yao et al., 2021) properties. In recent years, with the deepening of the research in the micro-field, micro-nano materials have developed rapidly, and they have been developed into intelligent responsiveness (Li et al., 2017a; Chang et al., 2018; Li et al., 2021a), environmental remediation (Kumari et al., 2019; Sajjadi et al., 2021), biodegradability (Li et al., 2021b; Li et al., 2022a; Li et al., 2022b), nano-probe imaging (Li et al., 2016; Li et al., 2017b; Li et al., 2019a; Li et al., 2022c), and other characteristics, which are widely used in many fields (Waked, 2011; Khandelwal et al., 2016; Scalisi, 2017; Li et al., 2019b; Siddiqui et al., 2019), especially medicine (Li et al., 2021c; Lu et al., 2021). Biomimetic superhydrophobic surface combines the cutting-edge technologies of bionics and micro-nano fields, and has great development prospects.

The study of superhydrophobic principle can be traced back to 1805, when T. Young (Young, 1805) established Young's equation of ideal smooth solid surface state, which set a theoretical precedent for studying the wettability of materials. Later, Wensel and Cassie summarized Wensel model (Wenzel, 1936) and Cassie–Baxter model (Cassie and Baxter, 1944) by studying the relationship between surface roughness and wettability. Recent further research shows that superhydrophobic surfaces can be divided into five types (Wang and Jiang, 2007). This classification includes steady-state and transition state, which can explain the phenomena that were difficult to explain by previous theories (Yilgor et al., 2012; Liu et al., 2017a; Chen et al., 2021).

Contact angle and rolling angle are important parameters to characterize the wettability of droplets on solid surfaces, and are also the initial evaluation indexes of biomimetic superhydrophobic surfaces (Aussillous and Quéré, 2001; Richard et al., 2002; Michael and Bhushan, 2007; Nosonovsky and Bhushan, 2008). With the development of research, researchers have made biomimetic superhydrophobic surfaces with multiple functions. Since then, the application fields of biomimetic superhydrophobic surfaces have been expanded by leaps and bounds, included

TABLE 1 The surface structure of typical organisms.

Biological surface	Properties	References
Lotus leaf	Superhydrophobic, self-cleaning	Barthlott and Neinhuis, (1997)
Rose petal	Superhydrophobic, high surface adhesion	(Feng et al., 2008; Zheng et al., 2019)
Rice leaf	Superhydrophobic, directional transport	(Feng et al., 2002; Wu et al., 2011)
Nepenthes	Directional transport, water harvesting	(Bohn and Federle, 2004; Wong et al., 2011; Chen et al., 2016)
Purple setcreasea	Double-sided superhydrophobic	Guo and Liu, (2007)
Watermelon leaf	Single-order scale hydrophobic structure	Guo and Liu, (2007)
Peanut leaf	Superhydrophobic, high surface adhesion	(Yang et al., 2014; Gou and Guo, 2018; Qu et al., 2020)
Bamboo leaf	Anti-icing, high surface adhesion	(Yuan et al., 2014; Wan et al., 2021; Wan et al., 2022)
Gecko foot	High surface adhesion, self-cleaning	(Autumn et al., 2002; Wang et al., 2012; Watson et al., 2015; Basak, 2020)
Cicada wing	Self-cleaning, anti-reflective	(Watson and Watson, 2004; Stoddart et al., 2006; Zhang et al., 2006; Xie et al., 2017; Román-Kustas et al., 2020)
Shark skin	Self-cleaning, underwater drag reduction	(Ball, 1999; Bechert et al., 2000; Bixler and Bhushan, 2013)
Penguin feather	Anti-icing, liquid guidance	(Wang et al., 2016a; Alizadeh-Birjandi et al., 2020)
Butterfly wings	Self-cleaning, liquid-directed	(Qian et al., 1900; Fang et al., 2008)
Spider silk	Collecting water	Zheng et al. (2010)
Earthworm	Drag reduction, lubrication	Zhao et al. (2018)
Mosquito compound eyes	Superhydrophobic, anti-fog	Gao et al. (2007)

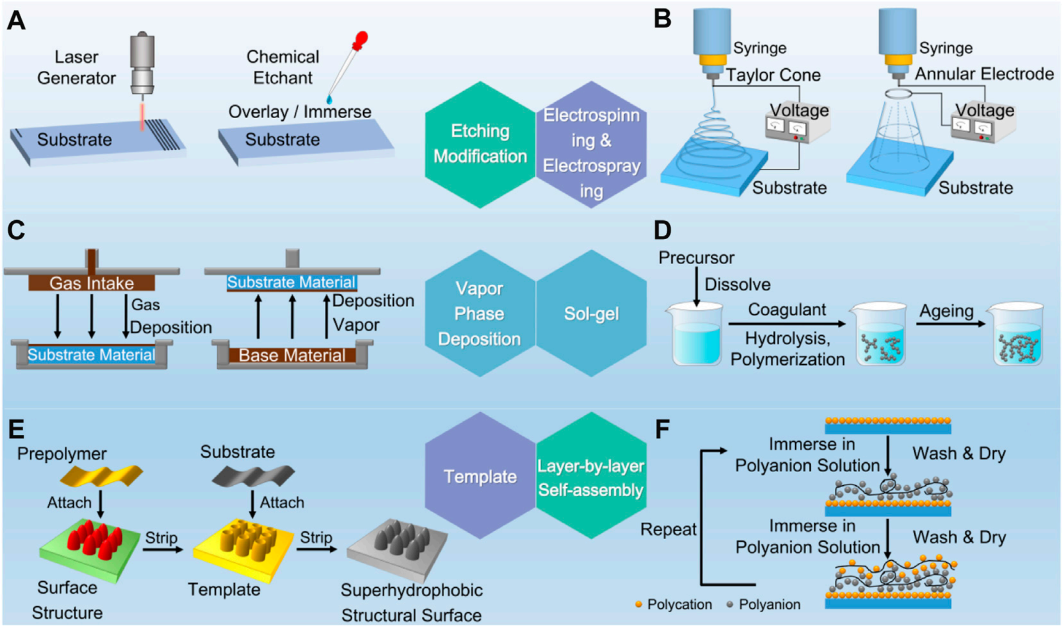

FIGURE 1
Etching modification **(A)**, electrospinning and electrospraying **(B)**, vapor phase deposition **(C)**, sol–gel **(D)**, template **(E)** and layer-by-layer self-assembly **(F)** methods developed to fabricate superhydrophobic surfaces.

adhesive-responsive superhydrophobic surfaces for sensors (Gao et al., 2019; Liu et al., 2019), industrial anticorrosive superhydrophobic surfaces which can effectively slow down the damage of metal oxide layers and resist strong acid/alkali corrosion (Li et al., 2019c; Ran et al., 2019; Ijaola et al., 2020), superhydrophilic/superhydrophobic surfaces which can realize industrial wastewater treatment and offshore oil spill treatment by using oil–water separation characteristics (Feng et al., 2004; Jayaramulu et al., 2016; Yang et al., 2018; Song et al., 2022), and superhydrophobic coatings with anti-icing and light transmission properties for outdoor glass and photovoltaic converters (Li et al., 2009; Liu et al., 2015a; Cui and Pakkanen, 2020; Zhu et al., 2021). In addition, diversified bionic superhydrophobic surfaces were widely used in modern military (Dong et al., 2013; Wang et al., 2015b; Jiaqiang et al., 2018), microfluidic control (Stratakis et al., 2011; Kong, 2021), fabric and textile industry (Hoefnagels et al., 2007; Xing et al., 2022) and other extended fields.

In this mini review, we reviewed the superhydrophobic surfaces and principles in nature. Section 2 introduced several different preparation methods, with emphasis on the preparation of biomimetic superhydrophobic surfaces by etching modification. Particularly, we discussed the unique advantages and disadvantages of etching modification. Finally, the conclusion of this review and the prospect of the research field in the future were described (Section 3).

2 Biomimetic superhydrophobic surface preparation methods

With the deepening of research, the preparation methods of bionic superhydrophobic surfaces were gradually diversified. Figure 1 shows the common preparation methods of superhydrophobic surfaces. Generally speaking, the core idea of preparing biomimetic superhydrophobic surface is to imitate the microstructure of biological surface and modify it with low surface energy substances. According to the order of construction, it can be classified into two categories. The first category is to construct micro-nano rough structures on smooth surfaces, and then decorate them with low surface energy materials. The second category is to directly sketch micro-nano rough structures on low surface energy materials.

In Table 2, we also show the characteristics of typical preparation methods of bionic superhydrophobic materials to understand their advantages and disadvantages. From the table, we can systematically understand the characteristics of various methods, including preparation principle, production cost, production speed, equipment requirement, environmental friendliness, and mechanical durability. It should be emphasized that the characteristics here are for most experiments that use this method to construct bionic superhydrophobic surfaces.

Among these methods, the etching modification method will be described in detail later. In addition, it is not difficult to find

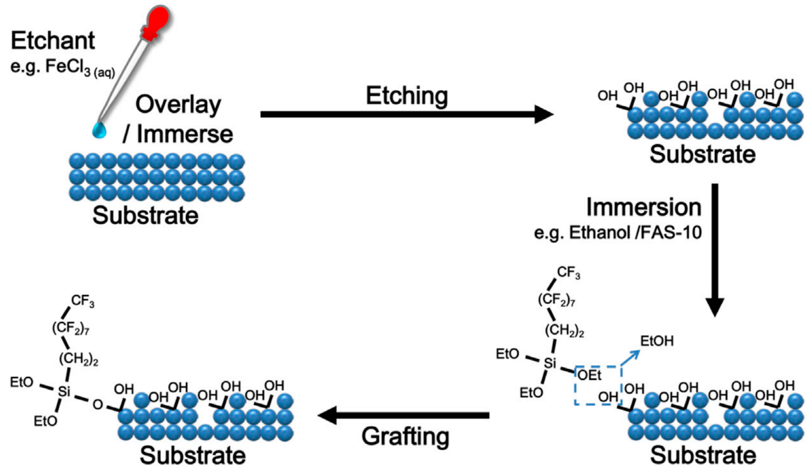

FIGURE 2
Schematic diagram of chemical etching and grafting.

TABLE 2 Comparison of preparation methods of superhydrophobic surface.

Preparation method	Principle	Cost	Efficiency	Equipment requirement	Environmental friendliness	Durability	References
Chemical etching	Etchant etching	Inexpensive	Efficient	Low-demand	Harmful	Nondurable	(Liao et al., 2014; Qu et al., 2018; Peng et al., 2019; Attar et al., 2020)
Laser etching	High-energy laser beam	Expensive	Inefficient	High-demand	Harmless	Durable	(Liu et al., 2017b; Pan et al., 2019; Yang et al., 2019; Zheng et al., 2020; Li et al., 2021d)
Chemical vapor deposition	Chemical vapor reaction	Inexpensive	Fair	Low-demand	Harmful	Durable	(Jiang et al., 2016; Sun et al., 2017; Aljumaily et al., 2018; Guo et al., 2019)
Physical vapor deposition	Vaporization followed by deposition	Inexpensive	Efficient	High-demand	Harmless	Fair	(Du et al., 2020; Böke et al., 2016; Tavana et al., 2006)
Electrospinning and electrospraying method	Droplet spraying and stretching in electric field	Inexpensive	Efficient	Low-demand	Harmless	Nondurable	(Ke et al., 2014; Du et al., 2021; Deo et al., 2022)
Sol-gel method	Hydrolytic condensation of compounds under liquid phase	Inexpensive	Inefficient	Low-demand	Harmful	Nondurable	(Tadanaga et al., 2000; Manoharan et al., 2021)
Template method	Post-compression modifications	Fair	Inefficient	Low-demand	Harmless	Durable	(Lee et al., 2010; Xu et al., 2011; Zhang et al., 2020a)
Layer-by-layer self-assembly method	Inter-particle electrostatic interaction	Inexpensive	Inefficient	Low-demand	Harmless	Nondurable	(Yang et al., 2013; Brown and Bhushan, 2015)

that the above-mentioned methods all have a common feature, namely, self-cleaning. At present, self-cleaning has basically become a common property of superhydrophobic surfaces (Parkin and Palgrave, 2005; Sethi and Manik, 2018). The most direct way to achieve self-cleaning effect is to use extremely low rolling angle. The accumulated dirt particles can be effectively cleaned by fast-sliding water droplets (Liu et al., 2015b; Sharma et al., 2021). Photocatalytic reaction can effectively decompose pollutants and achieve the purpose of more efficient self-cleaning (Afzal et al., 2014; Wang et al., 2021a). Compared with simply using droplets to roll away dirt, this more active self-cleaning method is more suitable for places with more pollutants such as oil pollution and organic matter (Mor et al., 2004; Rus et al., 2013; Moghaddasi and Mohammadizadeh, 2022).

In modern research, before the formulation and product development of self-cleaning superhydrophobic materials, molecular dynamics is more and more used for simulation to predict the target performance, which can take into account the self-cleaning performance and the durability brought by the adhesion between film and substrate (Sethi et al., 2022). Through molecular dynamics simulation optimization and experimental verification, Sethi's research team comprehensively predicted and explained the surface behavior, substrate adhesion, and overall performance of the blend, which was beneficial to determine the volume, surface, and interface characteristics of the best formula before the preparation of bionic superhydrophobic surface coating, reducing the workload in actual preparation, improving work efficiency and product performance (Sethi et al., 2019; Sethi et al., 2020a; Sethi et al., 2020b).

2.1 Etching modification methods

Etching is a simple and effective method to achieve bionic superhydrophobic effect. This method is through selective etching to realize the processing of micro-nano double-ordered structure on the substrate surface (Ellinas et al., 2021).

Wet etching and dry etching are two main ways of etching. In wet etching, the etching substrate is soaked or coated with chemical reagents (such as acid, alkali, etc.), and the etching solution reacts with the material to remove specific surface materials (Huang et al., 2011; Yeganeh and Mohammadi, 2018; Jayarama et al., 2021). Dry etching is a process that uses laser or plasma to react with the substrate surface to form volatile substances, or directly bombards the substrate surface to corrode it (Lee, 1979; Elhadj et al., 20122012; Wang et al., 2021b; Fan et al., 2021). The following section will introduce wet chemical etching and dry laser etching, as well as their application scope, advantages and disadvantages.

2.1.1 Chemical etching method

Generally, metals and alloys are the most suitable substrates for chemical etching, especially magnesium alloys or aluminum alloys (Panda, 2021; Peng et al., 2021). By controlling the concentration of etching solution and etching time, the structural characteristics of superhydrophobic surface, such as roughness, can be effectively changed (Wei et al., 2021b; Guo et al., 2021; Krishnan et al., 2021; Zheng et al., 2021) (Figure 2).

Strong acids, such as HCl and H_2SO_4 are common and effective etching solutions. Kumar et al. (Kumar and Gogoi, 2018) used HNO_3-HCl mixture to etch aluminum plate, and then treated it with high-density hexadecyl trimethoxysilane (HDTMS) toluene solution to construct a superhydrophobic surface with the static contact angle of 162.0 ± 4.2° and the rolling angle of 4 ± 0.5°. Besides good superhydrophobic self-cleaning performance, the surface also showed good thermal stability, chemical stability, and mechanical stability. Nguyen et al. (Nguyen et al., 2021) etched with HCl solution and deposited with FOTS (fluorooctatrichlorosilane) to prepare superhydrophobic aluminum plates with low ice adhesion strength and long freezing time. In addition, a model for calculating the freezing time was put forward, and the comparison between the experimental and theoretical calculation showed excellent consistency, which provided guidance for understanding the icing phenomenon and designing the ice-repellent surface. Campbell et al. (Gray-Munro and Campbell, 2017) combined the chemical etching of H_2SO_4-H_2O_2 with the deposition of silicone coating to construct a lotus leaf-like structure on the surface of magnesium alloy, which had excellent stability in aqueous solution. By this way, the surface degradation rate of biodegradable superhydrophobic magnesium alloy with biocompatibility was controlled, which was significant in medical application. Saleh et al. (Saleh and Baig, 2019) functionalized stainless steel with octadecyl trichlorosilane (ODTCS) after structural treatment with H_2SO_4, and obtained superhydrophobic and superhydrophilic properties. Experiments showed that the separation efficiency of various nonpolar organic components from water was over 99%, which was expected to be used to separate oil from water. In addition, HF in inorganic acid is also a good etching solution (Qu et al., 2007; Zhang et al., 2015; Du et al., 2018; Kim et al., 2018; Xu et al., 2019; Zhang et al., 2020b; Shaikh et al., 2021).

Compared with inorganic acids, organic acids are less used for etching, because most inorganic acids are relatively more stable and lower in cost. Ou et al. (Ou et al., 2019) sprayed cold galvanized coating on iron substrate, then etched with acetic acid, and finally modified with stearic acid. The superhydrophobic sample surface with an apparent contact angle of 168.4 ± 1.5° and a rolling angle of 3.5 ± 1.2° was obtained. This sample combined the respective characteristics of zinc coating and superhydrophobic surface in terms of metal corrosion resistance, which had rapid manufacturing process, good mechanical durability, and easy repair. Wu et al. (Wu et al., 2012) compared the etching effects of aluminum alloy samples in three different acid solutions (acetic acid, hydrochloric acid, and oxalic acid), and found that the mixed solution of oxalic acid and hydrochloric acid was the better etching combination. Similarly, they found that better surface roughness can be obtained by adjusting the concentration of Cl^- ion and oxalate ion in acid solution. This provided a new strategy for controllable preparation of superhydrophobic films on aluminum alloys, which could be used in practical industrial applications. Chen et al. (Chen et al., 2010) proposed a superhydrophobic surface preparation method without hydrophobic treatment, which was directly obtained by soaking aluminum in the mixed solution of HCl and acetic acid. In addition, they also studied the effect of acetic acid content on the surface structure.

Besides acidic solutions, other kinds of solutions have been widely used. NaOH is the most commonly used alkaline etchant, which is usually used to etch aluminum alloy (Saleema et al., 2010; Huang et al., 2015; Lomga et al., 2017; Nguyen-Tri et al., 2019a; Tudu et al., 2019; Yang et al., 2022). In Peng's work (Peng and Deng, 2015), NH_3 was selected as the etchant of aluminum, and the superamphiphobic sample obtained by hot ammonia solution etching and fluorosilane modification had excellent chemical stability. This simple, economical, environment-friendly, and efficient method could be used in the fields of oil-proof and water-proof. Wan et al. (Wan et al., 2018) combined ammonia etching and hydrothermal treatment to construct superhydrophobic surface on copper substrate modified by 1H,1H,2H,2H-perfluorodecyl triethoxysilane (PFDTES), which showed good waterproof, anti-corrosion and anti-adhesion properties in simulated seawater and humid air. Parin et al. (Parin et al., 2018) used three different salt solution etchants, namely $AlCl_3$, $FeCl_3$ and $CuCl_2$, to obtain superhydrophobic aluminum surfaces by chemical etching and fluorosilane deposition, respectively, which confirmed that different etchants would produce different surface micro-nanostructures. Rodič et al. (Rodič et al., 2020) etched aluminum in $FeCl_3$ solution, and then grafted at ambient temperature directly in an ethanol solution of 1H,1H,2H,2H-perfluorodecyltriethoxysilane. The prepared superhydrophobic surface has the characteristics of self-cleaning and anti-icing. Moreover, the promotion of dropwise condensation significantly improved the heat transfer coefficient, so that the sample could be widely used in heat transfer industry. Wang et al. (Wang et al., 2016b) chemically etched magnesium in $CuCl_2$ solution, and then modified it with oleic acid to prepare superhydrophobic surface with contact angle of 155°. Song et al. (Song et al., 2012) developed a rapid preparation method of superhydrophobic materials, in which aluminum was immersed in $CuCl_2$ solution and then modified with ethanol solution of fluoroalkyl silane, and the whole process only took a few seconds. This convenient and efficient method may have the potential of large-scale preparation.

Chemical etching can be divided into two-step method (Milosev et al., 2017; Milošev et al., 2019; Rodič et al., 2022) and one-step method (Chen et al., 2010) in addition to the classification of etching solution. This is classified according to the operation steps. The two-step method is chemical etching and then coating, while the one-step method is chemical etching and coating in the same step (Varshney et al., 2016).

Chemical etching is a simple, quick and low-cost method, which can be used in a large scale. However, the etching solution used in the operation process is toxic to human health and the environment. In addition, the specific shape and thickness of the micro-nano double-ordered structure are difficult to control, and the mechanical durability of the surface is not high. Under the condition of over-etching, the microsurface roughness of the substrate decreases, and even the basic mechanical properties of the substrate are destroyed, which is also an important problem. Therefore, the preparation of green etchant, the optimization of etching process, the precise control of substrate surface morphology and thickness, and the reduction of environmental pollution risk are the key development paths that chemical etching needs to explore in the future.

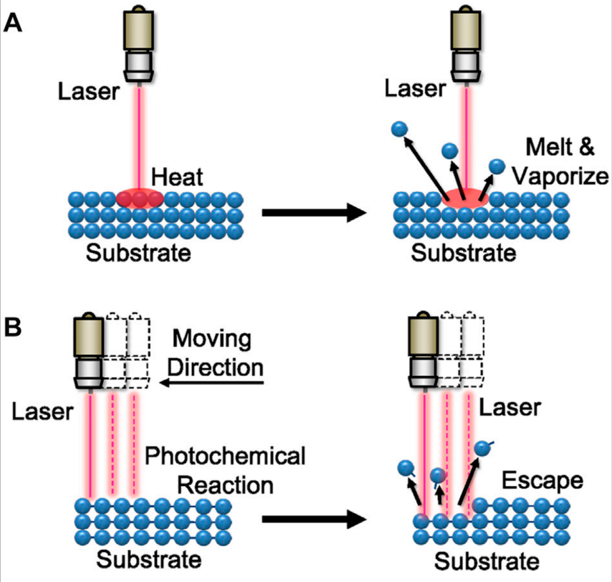

FIGURE 3
Schematic diagram of **(A)** laser heat treatment and **(B)** cold treatment.

2.1.2 Laser-etching method

As shown in Figure 3, laser etching can be divided into heat treatment and cold treatment according to its reaction principle (He et al., 2019; Ehrhardt et al., 2021). Irradiating the substrate surface with high-energy laser beam, the generated high temperature melts and vaporizes the material in a short time. After cooling, the superhydrophobic surface is constructed, which is called laser heat treatment. Cold treatment is a method of breaking chemical bonds in materials through photochemical reaction and constructing superhydrophobic surfaces after cooling. This technology has been widely used in various materials, including metal, glass, and polymer (Fadeeva et al., 2011; Lu et al., 2017; Dinh et al., 2018; Kostal et al., 2018; Li et al., 2019d; Ma et al., 2019; Stratakis et al., 2020).

Boinovich et al. (Boinovich et al., 2017) used Al–Mg alloy as the substrate, and proved that laser treatment can endow the surface with multi-peak roughness and change the composition

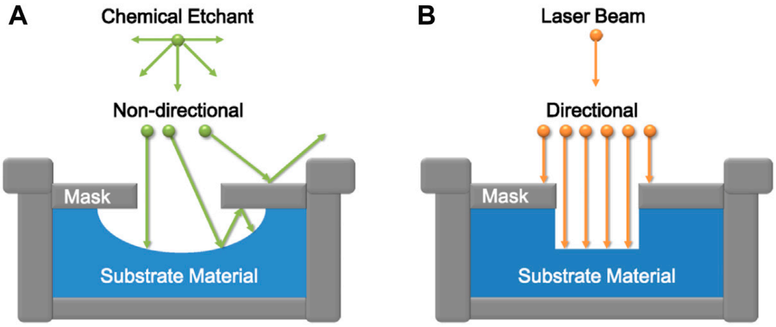

FIGURE 4
Directional comparison between **(A)** chemical etching and **(B)** laser etching.

of the surface layer. This research had overcome the obstacles of metal materials in industrial application, such as easy corrosion, poor cold resistance or weak thermal shock stress resistance. Li et al. (Li et al., 2018) prepared periodic microscale papillary pit microstructure on magnesium alloy surface by laser ablation. After chemical etching with $AgNO_3$ and surface modification with stearic acid, the prepared surface has superhydrophobic property, and the maximum contact angle reaches 158.2°. By adjusting the microstructure, such as the center distance of pits, the surface can change from low adhesion to high adhesion. In addition, due to the high degree of independent selection and accuracy of laser etching, the surface structure that meets the requirements of experimenters can be perfectly reproduced. Using this characteristic of laser etching, superhydrophobic surfaces with excellent anisotropy can be easily prepared (Yong et al., 2014; Fang et al., 2018; Lasagni et al., 2018; Cai et al., 2019; Tuo et al., 2019; Bai et al., 2020; Rong et al., 2021; Yang et al., 2021). In another study, femtosecond laser and picosecond laser were used to construct nanostructures of aluminum, copper, and galvanized steel, respectively, and then aging in vacuum was used to replace low surface energy modification. This method of combining ultrafast laser surface nanostructures with vacuum aging was suitable for a wide range of self-cleaning applications (Khan et al., 2021). In addition to the metal matrix, Chen et al. (Chen et al., 2018) showed a method of manufacturing bionic reed leaves by laser treating the surface of structured polydimethylsiloxane (PDMS). Du et al. (Du et al., 2022) proposed a one-step laser-etching method for manufacturing superhydrophobic silicone rubber with bionic layered micro/nano structure, whose contact angle and sliding angle can be adjusted according to the number of laser-etching cycles, which is beneficial to different application requirements. It was a potential candidate to protect flexible electronics equipment in rainy days and acid/alkali environments. Inspired by the hexagonal microstructure array of mosquito's compound eye, He et al. (He et al., 2021) made multifunctional superhydrophobic self-cleaning glass with anti-fog and anti-icing by laser texturing. Jing et al. (Jing et al., 2022) used picosecond laser to etch glass substrate and chemically modified it by silanization to prepare superhydrophobic surface with high adhesion. They also pointed out that laser-induced micro/nano structure depends on laser energy to a great extent and significantly affects adhesion, while scanning times have a slight effect on surface morphology and adhesion.

Laser-etching method has high precision and controllability. By controlling the laser type, irradiation time and light intensity, the surface microstructure with controllable direction can be obtained on different substrates (Figure 4), which is suitable for most materials. In addition, no harmful substances are produced during the experiment, which is undoubtedly environment-friendly. In recent years, with the rapid development of 3D laser printing technology and femtosecond laser technology, researchers have been able to complete custom etching of various complex microstructures. However, because the laser synthesis equipment is very complex, expensive, energy-intensive, and the action area of a single laser beam is relatively small, it is not suitable for industrial large-scale preparation of superhydrophobic materials, and it is currently in the laboratory stage.

2.1.3 Mixed-etching method

The etching methods mentioned in the above two chapters usually use different substrates (Table 3), but they can actually be used in combination. For example, Xia et al. (Xia et al., 2022) compared three methods: chemical etching, laser etching, and chemical-laser mixed etching, and pointed out that specific chemical-laser mixed etching parameters can effectively prepare uniform hierarchical structure on aluminum alloy surface, achieving excellent hydrophobicity, and low ice adhesion. When this method was applied to the wing manufacturing, the obtained wing may prevent the aircraft from freezing and protect the aerospace safety. Dong et al. (Dong et al., 2011) also prepared a hydrophobic copper surface with tunable regular microstructure and

TABLE 3 Simple summary of common etching methods of different substrates.

Substrate	Common methods	References
Aluminum (Al)	Chemical Etching (Cl^- Ion)	(Ran et al., 2019; Zhang et al., 2019; Ellinas et al., 2021)
Magnesium (Mg)	Chemical Etching (SO_4^- Ion)	(Ran et al., 2019; Ellinas et al., 2021; Peng et al., 2021)
Stainless Steel	Chemical Etching (Cl^- Ion)	(Nanda et al., 2019; Saleh and Baig, 2019; Ellinas et al., 2021)
Glass	Laser Etching (Plasma)	(Li et al., 2018; Wu et al., 2021; Gao et al., 2022)
Polymer	Laser Etching (Plasma)	(Dimitrakellis and Gogolides, 2018; Lee et al., 2018; Nguyen-Tri et al., 2019b; Nageswaran et al., 2019)

random nanostructure whose water contact angle is about 153°. The regular microstructure was obtained by nanosecond pulse laser etching, while the random nanostructure was determined by chemical etching. The regular microstructure was obtained by nanosecond pulse laser etching, while the random nanostructure was determined by chemical etching. Liu et al. (Liu et al., 2013) dipped the aluminum alloy in HNO_3 and $Cu(NO_3)_2$ after laser processing, and finally modified it with DTS ($CH_3(CH_2)_{11}Si(OCH_3)_3$) to prepare the bionic superhydrophobic surface with high adhesion. It is easy to find that these two methods can also be used together with other etching methods to achieve better bionic superhydrophobic effect (Li et al., 2014; Gu et al., 2017; Tian et al., 2017; Feng et al., 2022a; Feng et al., 2022b). Rodič et al. (Rodič and Milošev, 2019) made highly hydrophobic aluminum surface in NaOH solution containing various alkoxysilanes by one-step ultrasonic process, which had corrosion resistance, self-cleaning, and anti-icing characteristics. These mixed preparation processes provided a new way for the preparation of various materials.

3 Summary

This article summarized the basic principle and model of superhydrophobic, epitomized the structure and wetting characteristics of biological superhydrophobic surfaces in nature, reviewed various preparation methods of bionic superhydrophobic materials, emphasized the etching method, and discussed the research status and challenges of superhydrophobic applications. As described in detail above, the chemical etching method is simple, fast, low-cost and has the potential for large-scale application. Its disadvantage is that it is harmful to the environment and human body, and excessive etching will cause the mechanical properties of samples to be destroyed. Laser etching has controllable and customizable surface morphology, but it is expensive and inefficient. The mixed use of the two methods has indeed achieved the effect of complementing each other's strengths to a certain extent, but it is undeniable that the equipment price and pollution have not been improved.

4 Outlook

Science and technology originates from nature and is superior to nature. The research of bionic superhydrophobic surface started from the early imitation of natural animal and plant surface structures, and now it has expanded to the creative behavior of designing structures and modifying materials independently, especially the birth of laser etching, which greatly improved the structural accuracy. The related properties of superhydrophobic surfaces have also developed from simple hydrophobicity to many directions, including anti-icing, water collection, directional transportation and wetting behavior transformation, which has brought about significant changes in the fields of industrial life and national defense science and technology development. The single bionic superhydrophobic surface can no longer meet the actual needs, and the research of multifunctional bionic superhydrophobic surface has become a hot topic discussed by scholars. However, with the continuous expansion and deepening of the research in the field of etching, the existing problems in the process of preparing bionic superhydrophobic surfaces by etching are also exposed. For example, the environmental friendliness and mechanical properties of chemical etching need to be improved, and laser etching needs to consider how to improve efficiency, reduce equipment costs and achieve mass production. In view of the research hotspots and existing problems, we put forward the following prospects:

(1) Superhydrophobic surface should be further developed toward multifunction. Based on the superhydrophobic function, the surface has many functions, such as antibacterial (Zhan et al., 2022), anti-ultraviolet, anti-radiation, underwater drag reduction, and performance change. It improves the applicability of superhydrophobic materials in many fields and environments, and has far-reaching significance for industrial application. Additionally, if the micro-nano structure is directly built on stealth coating materials (wave absorbing materials, light transmitting materials, light guiding materials, etc.), it will have the characteristics of anti-reflection, anti-radiation, and drag reduction, further increasing its concealment and maneuverability. The stealth surface made by this method

is likely to make a major breakthrough in modern national defense and military fields.

(2) To improve the chemical and mechanical stability, the appearance of self-healing superhydrophobic coating provides a new development direction for related research (Sam et al., 2019; Chang et al., 2020). The mechanism of intrinsic self-healing superhydrophobic coating is to introduce dynamic chemical bonds into the internal structure of the material. When the material is damaged, the damaged chemical bonds will be restored to the initial state due to dynamic equilibrium, so that the structure and state of the material can be restored. The external self-repairing super-hydrophobic coating can be stimulated by changing the conditions, such as light and temperature, so that the repairing agent inside the material can be released and migrated to the damaged part, and thus the damaged surface can be healed. However, considering the complex environment in practical engineering application, besides self-healing, the wear resistance, acid and alkali resistance and long-term weather resistance of superhydrophobic coating itself need to be further improved.

(3) For the materials with weak hydrophobicity and easy to be polluted by oily substances, it is necessary to further study the super-double hydrophobic materials that are both hydrophobic and oleophobic, and make them into responsive materials, that is, to switch or switch the surface free energy by external stimulation. In addition, perfluoro silanes, which has both hydrophobic and oleophobic properties, is a target worthy of consideration.

(4) Aiming at the problems of strong pollution and high-energy consumption, the development of new biomaterials and new energy sources provides some guiding ideas for the preparation of green, environmentally friendly, low-cost, and reliable superhydrophobic surfaces.

(5) The effects of surface geometry size, wettability, and surface composition on superhydrophobic properties, especially the quantitative research directly related to hysteresis angle, need to be deepened, which is not only to be studied by etching method, but also to be explored by all methods.

(6) It is still necessary to study the preparation of superhydrophobic materials at low cost to enhance the practicability and expand the application fields.

To sum up, the future development direction of preparing bionic superhydrophobic surface by etching method is to combine the advantages of the two methods and develop a set of durable, energy-saving, low-cost, and mass-production preparation methods that meet the multifunctional application requirements of superhydrophobic surface. Only by realizing the industrial production of superhydrophobic surfaces can we really get out of the laboratory and into life.

Author contributions

SG-Z: writing—original draft preparation, reviewing and editing, and drawing the graphs and schematic. HY: methodology, investigation, reviewing and editing, and drawing the graphs and schematic. HN: reviewing and editing. HM: supervision and reviewing and editing. MZ: supervision and reviewing and editing.

Funding

This work was supported by the Fundamental Research Funds for the Central Universities (No. 2572020BC07) and the National Natural Science Foundation of China.

Conflict of interest

The authors declare that the research was conducted in the absence of any commercial or financial relationships that could be construed as a potential conflict of interest.

Publisher's note

All claims expressed in this article are solely those of the authors and do not necessarily represent those of their affiliated organizations, or those of the publisher, the editors, and the reviewers. Any product that may be evaluated in this article, or claim that may be made by its manufacturer, is not guaranteed or endorsed by the publisher.

References

Afzal, S., Daoud, W. A., and Langford, S. J. (2014). Superhydrophobic and photocatalytic self-cleaning cotton. *J. Mat. Chem. A* 2 (42), 18005–18011. doi:10.1039/c4ta02764g

Alizadeh-Birjandi, E., Tavakoli-Dastjerdi, F., Leger, J. S., Faull, K. F., Davis, S. H., Rothstein, J. P., et al. (2020). Delay of ice formation on penguin feathers. *Eur. Phys. J. Spec. Top.* 229 (10), 1881–1896. doi:10.1140/epjst/e2020-900273-x

Aljumaily, M. M., Alsaadi, M. A., Das, R., Hashim, N. A., AlOmar, M. K., Alayan, H. M., et al. (2018). Optimization of the synthesis of superhydrophobic carbon nanomaterials by chemical vapor deposition. *Sci. Rep.* 8 (1), 2278. doi:10.1038/s41598-018-21051-3

Attar, M. R., Khajavian, E., Hosseinpour, S., and Davoodi, A. (2020). Fabrication of micro–nano-roughened surface with superhydrophobic character on an aluminium alloy surface by a facile chemical etching process. *Bull. Mat. Sci.* 43 (1), 31. doi:10.1007/s12034-019-1998-7

Aussillous, P., and Quéré, D. (2001). Liquid marbles. *Nature* 411 (6840), 924–927. doi:10.1038/35082026

Autumn, K., Sitti, M., Liang, Y. A., Peattie, A. M., Hansen, W. R., Sponberg, S., et al. (2002). Evidence for van der Waals adhesion in gecko setae. *Proc. Natl. Acad. Sci. U. S. A.* 99 (19), 12252–12256. doi:10.1073/pnas.192252799

Bai, X., Yang, Q., Fang, Y., Yong, J., Bai, Y., Zhang, J., et al. (2020). Anisotropic, adhesion-switchable, and thermal-responsive superhydrophobicity on the femtosecond laser-structured shape-memory polymer for droplet manipulation. *Chem. Eng. J.* 400, 125930. doi:10.1016/j.cej.2020.125930

Ball, P. (1999). Engineering Shark skin and other solutions. *Nature* 400 (6744), 507–509. doi:10.1038/22883

Barthlott, W., and Neinhuis, C. (1997). Purity of the sacred lotus, or escape from contamination in biological surfaces. *Planta* 202 (1), 1–8. doi:10.1007/s004250050096

Basak, S. (2020). Walking through the biomimetic bandages inspired by Gecko's feet. *Biodes. Manuf.* 3 (2), 148–154. doi:10.1007/s42242-020-00069-5

Bechert, D. W., Bruse, M., Hage, W., and Meyer, R. (2000). Fluid mechanics of biological surfaces and their technological application. *Naturwissenschaften* 87 (4), 157–171. doi:10.1007/s001140050696

Bixler, G. D., and Bhushan, B. (2013). Fluid drag reduction with shark-skin riblet inspired microstructured surfaces. *Adv. Funct. Mat.* 23 (36), 4507–4528. doi:10.1002/adfm.201203683

Bohn, H. F., and Federle, W. (2004). Insect aquaplaning: *Nepenthes* pitcher plants capture prey with the peristome, a fully wettable water-lubricated anisotropic surface. *Proc. Natl. Acad. Sci. U. S. A.* 101 (39), 14138–14143. doi:10.1073/pnas.0405885101

Boinovich, L. B., Modin, E. B., Sayfutdinova, A. R., Emelyanenko, K. A., Vasiliev, A. L., and Emelyanenko, A. M. (2017). Combination of functional nanoengineering and nanosecond laser texturing for design of superhydrophobic aluminum alloy with exceptional mechanical and chemical properties. *ACS Nano* 11 (10), 10113–10123. doi:10.1021/acsnano.7b04634

Böke, F., Giner, I., Keller, A., Grundmeier, G., and Fischer, H. (2016). Plasma-Enhanced chemical vapor deposition (PE-CVD) yields better hydrolytical stability of biocompatible SiOx thin films on implant alumina ceramics compared to rapid thermal evaporation physical vapor deposition (PVD). *ACS Appl. Mat. Interfaces* 8 (28), 17805–17816. doi:10.1021/acsami.6b04421

Brown, P. S., and Bhushan, B. (2015). Mechanically durable, superoleophobic coatings prepared by layer-by-layer technique for anti-smudge and oil-water separation. *Sci. Rep.* 5 (1), 8701. doi:10.1038/srep08701

Cai, Y., Xu, Z., Wang, H., Lau, K. H. A., Ding, F., Sun, J., et al. (2019). A sequential process for manufacturing nature-inspired anisotropic superhydrophobic structures on AISI 316L stainless steel. *Nanomanuf. Metrol.* 2 (3), 148–159. doi:10.1007/s41871-019-00046-2

Cassie, A. B. D., and Baxter, S. (1944). Wettability of porous surfaces. *Trans. Faraday Soc.* 40, 546. doi:10.1039/tf9444000546

Chang, J., Zhang, L., and Wang, P. (2018). Intelligent environmental nanomaterials. *Environ. Sci. Nano* 5 (4), 811–836. doi:10.1039/c7en00760d

Chang, T., Panhwar, F., and Zhao, G. (2020). Flourishing self-healing surface materials: Recent progresses and challenges. *Adv. Mat. Interfaces* 7 (6), 1901959. doi:10.1002/admi.201901959

Chen, C., Pan, L., Li, H., Liu, Q., Li, F., Tu, J., et al. (2021). Conversion of superhydrophilicity to superhydrophobicity by changing the microstructure of carbon-high fly ash. *Mater. Lett.* 299, 130051. doi:10.1016/j.matlet.2021.130051

Chen, D. L., Mao, J. W., Chen, Z. D., Yu, K. X., Han, D. D., and Sun, H. B. (2018). Fabrication of bionic reed leaf superhydrophobic surface by laser processing. *Chin. Sci. Bull.* 64 (12), 1303–1308. doi:10.1360/n972018-00872

Chen, H., Zhang, P., Zhang, L., Liu, H., Jiang, Y., Zhang, D., et al. (2016). Continuous directional water transport on the peristome surface of Nepenthes alata. *Nature* 532 (7597), 85–89. doi:10.1038/nature17189

Chen, Z., Guo, Y., and Fang, S. (2010). A facial approach to fabricate superhydrophobic aluminum surface. *Surf. Interface Analysis Int. J. Devoted Dev. Appl. Tech. Analysis Surfaces, Interfaces Thin Films* 42 (1), 1–6. doi:10.1002/sia.3126

Cui, W., and Pakkanen, T. A. (2020). Fabrication of transparent icephobic surfaces with self-reparability: Effect of structuring and thickness of the lubricant-elastomer layer. *Appl. Surf. Sci.* 504, 144061. doi:10.1016/j.apsusc.2019.144061

Deo, D., Singh, S. P., Mohanty, S., Guhathakurata, S., Pal, D., and Mallik, S. (2022). Biomimicking of phyto-based super-hydrophobic surfaces towards prospective applications: A review. *J. Mater. Sci.* 57, 8569–8596. doi:10.1007/s10853-022-07172-1

Dimitrakellis, P., and Gogolides, E. (2018). Atmospheric plasma etching of polymers: A palette of applications in cleaning/ashing, pattern formation, nanotexturing and superhydrophobic surface fabrication. *Microelectron. Eng.* 194, 109–115. doi:10.1016/j.mee.2018.03.017

Dinh, T. H., Ngo, C. V., and Chun, D. M. (2018). Controlling the wetting properties of superhydrophobic titanium surface fabricated by UV nanosecond-pulsed laser and heat treatment. *Nanomater. (Basel).* 8 (10), 766. doi:10.3390/nano8100766

Dong, C., Gu, Y., Zhong, M., Li, L., Sezer, K., Ma, M., et al. (2011). Fabrication of superhydrophobic Cu surfaces with tunable regular micro and random nano-scale structures by hybrid laser texture and chemical etching. *J. Mater. Process. Technol.* 211 (7), 1234–1240. doi:10.1016/j.jmatprotec.2011.02.007

Dong, H., Cheng, M., Zhang, Y., Wei, H., and Shi, F. (2013). Extraordinary drag-reducing effect of a superhydrophobic coating on a macroscopic model ship at high speed. *J. Mat. Chem. A Mat.* 1 (19), 5886. doi:10.1039/c3ta10225d

Du, X., Gao, B., Li, Y., Song, Z., Zhu, X., and Chen, J. (2020). Fabrication of multiscale structured hydrophobic NiCrZrN coating with high abrasion resistance using multi-arc ion plating. *J. Alloys Compd.* 812, 152140. doi:10.1016/j.jallcom.2019.152140

Du, X., Xin, B., Xu, J., and Wang, C. (2021). Biomimetic superhydrophobic membrane with multi-scale porous microstructure for waterproof and breathable application. *Colloids Surfaces A Physicochem. Eng. Aspects* 612, 125924. doi:10.1016/j.colsurfa.2020.125924

Du, Y., Wu, T., Xie, H., and Qu, J. P. (2022). One-step laser etching of a bionic hierarchical structure on a silicone rubber surface with thermal and acid/alkali resistance and tunable wettability. *Soft Matter* 18 (17), 3412–3421. doi:10.1039/d2sm00242f

Du, Z., Ding, P., Tai, X., Pan, Z., and Yang, H. (2018). Facile preparation of Ag-coated superhydrophobic/superoleophilic mesh for efficient oil/water separation with excellent corrosion resistance. *Langmuir* 34 (23), 6922–6929. doi:10.1021/acs.langmuir.8b00640

Ehrhardt, M., Lorenz, P., Bauer, J., Heinke, R., Hossain, M. A., Han, B., et al. (2021). Dry etching of germanium with laser induced reactive micro plasma. *Lasers Manuf. Mat. Process.* 8 (3), 237–255. doi:10.1007/s40516-021-00147-1

Elhadj, S., Guss, G., Matthews, M. J., and Bass, L. (20122012). Laser-induced gas plasma etching of fused silica under ambient conditions[C]//Laser-Induced Damage in Optical Materials. *SPIE* 8530, 457–468. doi:10.1117/12.979814

Ellinas, K., Dimitrakellis, P., Sarkiris, P., and Gogolides, E. (2021). A review of fabrication methods, properties and applications of superhydrophobic metals. *Process. (Basel).* 9 (4), 666. doi:10.3390/pr9040666

Fadeeva, E., Truong, V. K., Stiesch, M., Chichkov, B. N., Crawford, R. J., Wang, J., et al. (2011). Bacterial retention on superhydrophobic titanium surfaces fabricated by femtosecond laser ablation. *Langmuir* 27 (6), 3012–3019. doi:10.1021/la104607g

Fan, Y., Li, S., Wei, D., Fang, Z., Han, Z., and Liu, Y. (2021). Bioinspired superhydrophobic cilia for droplets transportation and microchemical reaction. *Adv. Mat. Interfaces* 8 (24), 2101408. doi:10.1002/admi.202101408

Fang, Y., Sun, G., Cong, Q., Chen, G. h., and Ren, L. q. (2008). Effects of methanol on wettability of the non-smooth surface on butterfly wing. *J. Bionic Eng.* 5 (2), 127–133. doi:10.1016/s1672-6529(08)60016-5

Fang, Y., Yong, J., Chen, F., Huo, J., Yang, Q., Zhang, J., et al. (2018). Bioinspired fabrication of Bi/tridirectionally anisotropic sliding superhydrophobic PDMS surfaces by femtosecond laser. *Adv. Mat. Interfaces* 5 (6), 1701245. doi:10.1002/admi.201701245

Feng, L., Li, S., Li, Y., Li, H., Zhang, L., Zhai, J., et al. (2002). Super-hydrophobic surfaces: From natural to artificial. *Adv. Mat.* 14 (24), 1857–1860. doi:10.1002/adma.200290020

Feng, L., Zhang, Y., Xi, J., Zhu, Y., Wang, N., Xia, F., et al. (2008). Petal Effect: A superhydrophobic state with high adhesive force. *Langmuir* 24 (8), 4114–4119. doi:10.1021/la703821h

Feng, L., Zhang, Z., Mai, Z., Ma, Y., Liu, B., Jiang, L., et al. (2004). A super-hydrophobic and super-oleophilic coating mesh film for the separation of oil and water. *Angew. Chem. Int. Ed. Engl.* 116 (15), 2046–2048. doi:10.1002/ange.200353381

Feng, X., Sun, P., and Tian, G. (2022). Recent developments of superhydrophobic surfaces (SHS) for underwater drag reduction opportunities and challenges. *Adv. Mat. Interfaces* 9 (2), 2101616. doi:10.1002/admi.202101616

Feng, X., Zhang, X., and Tian, G. (2022). Recent advances in bioinspired superhydrophobic ice-proof surfaces: Challenges and prospects. *Nanoscale* 14 (16), 5960–5993. doi:10.1039/d2nr00964a

Fürstner, R., Barthlott, W., Neinhuis, C., and Walzel, P. (2005). Wetting and self-cleaning properties of artificial superhydrophobic surfaces. *Langmuir* 21 (3), 956–961. doi:10.1021/la0401011

Gao, D., Cao, J., and Guo, Z. (2019). Underwater manipulation of oil droplets and bubbles on superhydrophobic surfaces *via* switchable adhesion. *Chem. Commun.* 55 (23), 3394–3397. doi:10.1039/c9cc00271e

Gao, J., Wu, Y., Zhang, Z., Zhao, D., Zhu, H., Xu, K., et al. (2022). Achieving amorphous micro-nano superhydrophobic structures on quartz glass with a PTFE coating by laser back ablation. *Opt. Laser Technol.* 149, 107927. doi:10.1016/j.optlastec.2022.107927

Gao, X., Yan, X., Yao, X., Xu, L., Zhang, K., Zhang, J., et al. (2007). The dry-style antifogging properties of mosquito compound eyes and artificial analogues prepared by soft lithography. *Adv. Mat.* 19 (17), 2213–2217. doi:10.1002/adma.200601946

Gou, X., and Guo, Z. (2018). Superhydrophobic plant leaves with micro-line structures: An optimal biomimetic objective in bionic engineering. *J. Bionic Eng.* 15 (5), 851–858. doi:10.1007/s42235-018-0072-2

Gray-Munro, J., and Campbell, J. (2017). Mimicking the hierarchical surface topography and superhydrophobicity of the lotus leaf on magnesium alloy AZ31. *Mater. Lett.* 189, 271–274. doi:10.1016/j.matlet.2016.11.102

Gu, Y., Zhang, W., Mou, J., Zheng, S., Jiang, L., Sun, Z., et al. (2017). Research progress of biomimetic superhydrophobic surface characteristics, fabrication, and application. *Adv. Mech. Eng.* 9 (12), 168781401774685. doi:10.1177/1687814017746859

Guo, F., Duan, S., Wu, D., Matsuda, K., Wang, T., and Zou, Y. (2021). Facile etching fabrication of superhydrophobic 7055 aluminum alloy surface towards chloride environment anticorrosion. *Corros. Sci.* 182, 109262. doi:10.1016/j.corsci.2021.109262

Guo, X. J., Xue, C. H., Sathasivam, S., Page, K., He, G., Guo, J., et al. (2019). Fabrication of robust superhydrophobic surfaces *via* aerosol-assisted CVD and thermo-triggered healing of superhydrophobicity by recovery of roughness structures. *J. Mat. Chem. A Mat.* 7 (29), 17604–17612. doi:10.1039/c9ta03264a

Guo, Z., and Liu, W. (2007). Biomimic from the superhydrophobic plant leaves in nature: Binary structure and unitary structure. *Plant Sci.* 172 (6), 1103–1112. doi:10.1016/j.plantsci.2007.03.005

He, T., Wang, Z., Zhong, F., Fang, H., Wang, P., and Hu, W. (2019). Etching techniques in 2D materials. *Adv. Mat. Technol.* 4 (8), 1900064. doi:10.1002/admt.201900064

He, X., Li, G., Zhang, Y., Lai, X., Zhou, M., Xiao, L., et al. (2021). Bioinspired functional glass integrated with multiplex repellency ability from laser-patterned hexagonal texturing. *Chem. Eng. J.* 416, 129113. doi:10.1016/j.cej.2021.129113

Hoefnagels, H. F., Wu, D., De With, G., and Ming, W. (2007). Biomimetic superhydrophobic and highly oleophobic cotton textiles. *Langmuir* 23 (26), 13158–13163. doi:10.1021/la702174x

Huang, Y., Sarkar, D. K., and Chen, X. G. (2015). Superhydrophobic aluminum alloy surfaces prepared by chemical etching process and their corrosion resistance properties. *Appl. Surf. Sci.* 356, 1012–1024. doi:10.1016/j.apsusc.2015.08.166

Huang, Z., Geyer, N., Werner, P., de Boor, J., and Gosele, U. (2011). Metal-Assisted chemical etching of silicon: A review. *Adv. Mat.* 23 (2), 285–308. doi:10.1002/adma.201001784

Ijaola, A. O., Farayibi, P. K., and Asmatulu, E. (2020). Superhydrophobic coatings for steel pipeline protection in oil and gas industries: A comprehensive review. *J. Nat. Gas Sci. Eng.* 83, 103544. doi:10.1016/j.jngse.2020.103544

Jayarama, A., Kannarpady, G. K., Kale, S., Prabhu, S., and Pinto, . R (2021). Chemical etching of glasses in hydrofluoric acid: A brief review. *Mater. Today Proc.* 55, 46–51. doi:10.1016/j.matpr.2021.12.110

Jayaramulu, K., Datta, K. K. R., Rösler, C., Petr, M., Otyepka, M., Zboril, R., et al. (2016). Biomimetic superhydrophobic/superoleophilic highly fluorinated graphene oxide and ZIF-8 composites for oil-water separation. *Angew. Chem. Int. Ed.* 55 (3), 1178–1182. doi:10.1002/anie.201507692

Jiang, H. B., Zhang, Y. L., Liu, Y., Fu, X. Y., Li, Y. F., Liu, Y. Q., et al. (2016). Bioinspired few-layer graphene prepared by chemical vapor deposition on femtosecond laser-structured Cu foil. *Laser & Photonics Rev.* 10 (3), 441–450. doi:10.1002/lpor.201500256

Jiaqiang, E., Jin, Y., Deng, Y., Zuo, W., Zhao, X., Han, D., et al. (2018). Wetting models and working mechanisms of typical surfaces existing in nature and their application on superhydrophobic surfaces: A review. *Adv. Mater. Interfaces* 5, 1701052. doi:10.1002/admi.201701052

Jing, X., Xia, Y., Chen, F., Yang, C., Yang, Z., and Jaffery, S. H. I. (2022). Preparation of superhydrophobic glass surface with high adhesion. *Colloids Surfaces A Physicochem. Eng. Aspects* 633, 127861. doi:10.1016/j.colsurfa.2021.127861

Ke, P., Jiao, X. N., Ge, X. H., Xiao, W. M., and Yu, B. (2014). From macro to micro: Structural biomimetic materials by electrospinning. *RSC Adv.* 4 (75), 39704–39724. doi:10.1039/c4ra05098c

Khan, S. A., Boltaev, G. S., Iqbal, M., Kim, V., Ganeev, R. A., and Alnaser, A. S. (2021). Ultrafast fiber laser-induced fabrication of superhydrophobic and self-cleaning metal surfaces. *Appl. Surf. Sci.* 542, 148560. doi:10.1016/j.apsusc.2020.148560

Khandelwal, N., Barbole, R. S., Banerjee, S. S., Chate, G. P., Biradar, A. V., Khandare, J. J., et al. (2016). Budding trends in integrated pest management using advanced micro- and nano-materials: Challenges and perspectives. *J. Environ. Manag.* 184, 157–169. doi:10.1016/j.jenvman.2016.09.071

Kim, J. H., Mirzaei, A., Kim, H. W., and Kim, S. S. (2018). Facile fabrication of superhydrophobic surfaces from austenitic stainless steel (AISI 304) by chemical etching. *Appl. Surf. Sci.* 439, 598–604. doi:10.1016/j.apsusc.2017.12.211

Koch, K., Bhushan, B., and Barthlott, W. (2008). Diversity of structure, morphology and wetting of plant surfaces. *Soft Matter* 4 (10), 1943. doi:10.1039/b804854a

Kong, L. H. (2021). An environmentally friendly method for fabrication of superhydrophobic "pipe" with loss-free liquid transportation properties. *Surf. Coatings Technol.* 407, 126777. doi:10.1016/j.surfcoat.2020.126777

Kostal, E., Stroj, S., Kasemann, S., Matylitsky, V., and Domke, M. (2018). Fabrication of biomimetic fog-collecting superhydrophilic–superhydrophobic surface micropatterns using femtosecond lasers. *Langmuir* 34 (9), 2933–2941. doi:10.1021/acs.langmuir.7b03699

Krishnan, A., Krishnan, A. V., Ajith, A., and Shibli, S. (2021). Influence of materials and fabrication strategies in tailoring the anticorrosive property of superhydrophobic coatings. *Surfaces Interfaces* 25, 101238. doi:10.1016/j.surfin.2021.101238

Kumar, A., and Gogoi, B. (2018). Development of durable self-cleaning superhydrophobic coatings for aluminium surfaces via chemical etching method. *Tribol. Int.* 122, 114–118. doi:10.1016/j.triboint.2018.02.032

Kumari, S., Tyagi, M., and Jagadevan, S. (2019). Mechanistic removal of environmental contaminants using biogenic nano-materials. *Int. J. Environ. Sci. Technol. (Tehran).* 16 (11), 7591–7606. doi:10.1007/s13762-019-02468-3

Lasagni, A. F., Alamri, S., Aguilar-Morales, A. I., RoBler, F., Voisiat, B., and Kunze, T. (2018). Biomimetic surface structuring using laser based interferometric methods. *Appl. Sci.* 8 (8), 1260. doi:10.3390/app8081260

Lee, D. H., Park, J. S., Hwang, J. H., Kang, D., Yim, S. Y., and Kim, J. H. (2018). Fabrication of hollow nanoporous gold nanoshells with high structural tunability based on the plasma etching of polymer colloid templates. *J. Mat. Chem. C Mat.* 6 (23), 6194–6199. doi:10.1039/c8tc01658e

Lee, R. E. (1979). Microfabrication by ion-beam etching. *J. Vac. Sci. Technol.* 16 (2), 164–170. doi:10.1116/1.569897

Lee, S. G., Lim, H. S., Lee, D. Y., Kwak, D., and Cho, K. (2013). Tunable anisotropic wettability of rice leaf-like wavy surfaces. *Adv. Funct. Mat.* 23 (5), 547–553. doi:10.1002/adfm.201201541

Lee, Y., Ju, K. Y., and Lee, J. K. (2010). Stable biomimetic superhydrophobic surfaces fabricated by polymer replication method from hierarchically structured surfaces of Al templates. *Langmuir* 26 (17), 14103–14110. doi:10.1021/la102057p

Li, D., Wang, H., Luo, D., Liu, Y., Han, Z., and Ren, L. (2018). Corrosion resistance controllable of biomimetic superhydrophobic microstructured magnesium alloy by controlled adhesion. *Surf. Coatings Technol.* 347, 173–180. doi:10.1016/j.surfcoat.2018.04.078

Li, J., Liu, J., Huo, W., Yu, J., Liu, X., Haslinger, M., et al. (2022). Micro and nano materials and processing techniques for printed biodegradable electronics. *Mater. Today Nano* 18, 100201. doi:10.1016/j.mtnano.2022.100201

Li, K. K., Lei, J., Xie, Y. X., Lu, L., Zhang, S., Zhou, P., et al. (2021). An easy-to-implement method for fabricating superhydrophobic surfaces inspired by taro leaf. *Sci. China Technol. Sci.* 64 (12), 2676–2687. doi:10.1007/s11431-021-1855-2

Li, M. T., Liu, M., Yu, Y. H., Li, A. W., and Sun, H. B. (2019). Laser-structured graphene/reduced graphene oxide films towards bio-inspired superhydrophobic surfaces. *Bull. Chem. Soc. Jpn.* 92 (2), 283–289. doi:10.1246/bcsj.20180255

Li, P., Chen, X., Yang, G., Yu, L., and Zhang, P. (2014). Fabrication of a superhydrophobic etched copper–silver/stearic acid composite coating and evaluation of its friction-reducing and anticorrosion abilities. *Mat. Express* 4 (4), 309–316. doi:10.1166/mex.2014.1172

Li, X., Hetjens, L., Wolter, N., Li, H., Shi, X., and Pich, A. (2022b). Charge-reversible and biodegradable chitosan-based microgels for lysozyme-triggered release of vancomycin. *J. Adv. Res.* In Press. doi:10.1016/j.jare.2022.02.014

Li, X., Kong, L. D., Hu, W., Zhang, C., Pich, A., Shi, X., et al. (2022). Safe and efficient 2D molybdenum disulfide platform for cooperative imaging-guided photothermal-selective chemotherapy: A preclinical study. *J. Adv. Res.* 37, 255–266. doi:10.1016/j.jare.2021.08.004

Li, X., Li, H., Zhang, C., Pich, A., Xing, L., and Shi, X. (2021). Intelligent nanogels with self-adaptive responsiveness for improved tumor drug delivery and augmented chemotherapy. *Bioact. Mater.* 6 (10), 3473–3484. doi:10.1016/j.bioactmat.2021.03.021

Li, X., Lu, S., Xiong, Z., Hu, Y., Ma, D., Lou, W., et al. (2019). Light-addressable nanoclusters of ultrasmall iron oxide nanoparticles for enhanced and dynamic magnetic resonance imaging of arthritis. *Adv. Sci. (Weinh).* 6 (19), 1901800. doi:10.1002/advs.201901800

Li, X., Ouyang, Z., Li, H., Hu, C., Saha, P., Xing, L., et al. (2021). Dendrimer-decorated nanogels: Efficient nanocarriers for biodistribution *in vivo* and chemotherapy of ovarian carcinoma. *Bioact. Mater.* 6 (10), 3244–3253. doi:10.1016/j.bioactmat.2021.02.031

Li, X., Shi, T., Li, B., Chen, X., Zhang, C., Guo, Z., et al. (2019). Subtractive manufacturing of stable hierarchical micro-nano structures on AA5052 sheet with enhanced water repellence and durable corrosion resistance. *Mater. Des.* 183, 108152. doi:10.1016/j.matdes.2019.108152

Li, X., Sun, H., Li, H., Hu, C., Luo, Y., Shi, X., et al. (2021). Multi-responsive biodegradable cationic nanogels for highly efficient treatment of tumors. *Adv. Funct. Mat.* 31 (26), 2100227. doi:10.1002/adfm.202100227

Li, X., Xing, L., Hu, Y., Xiong, Z., Wang, R., Xu, X., et al. (2017). An RGD-modified hollow silica@Au core/shell nanoplatform for tumor combination therapy. *Acta Biomater.* 62, 273–283. doi:10.1016/j.actbio.2017.08.024

Li, X., Xing, L., Zheng, K., Wei, P., Du, L., Shen, M., et al. (2017). Formation of gold nanostar-coated hollow mesoporous silica for tumor multimodality imaging and photothermal therapy. *ACS Appl. Mat. Interfaces* 9 (7), 5817–5827. doi:10.1021/acsami.6b15185

Li, X., Xiong, Z., Xu, X., Luo, Y., Peng, C., Shen, M., et al. (2016). ^{99m}Tc-Labeled multifunctional low-generation dendrimer-entrapped gold nanoparticles for targeted SPECT/CT dual-mode imaging of tumors. *ACS Appl. Mat. Interfaces* 8 (31), 19883–19891. doi:10.1021/acsami.6b04827

Li, Y., Hu, J., Yang, K., Cao, B., Li, Z., Yang, L., et al. (2019). Synthetic control of Prussian blue derived nano-materials for energy storage and conversion application. *Mater. Today Energy* 14, 100332. doi:10.1016/j.mtener.2019.07.003

Li, Y., Liu, F., and Sun, J. (2009). A facile layer-by-layer deposition process for the fabrication of highly transparent superhydrophobic coatings. *Chem. Commun.* (19), 2730–2732. doi:10.1039/b900804g

Liao, R., Zuo, Z., Guo, C., Yuan, Y., and Zhuang, A. (2014). Fabrication of superhydrophobic surface on aluminum by continuous chemical etching and its anti-icing property. *Appl. Surf. Sci.* 317, 701–709. doi:10.1016/j.apsusc.2014.08.187

Liu, M., Wang, S., and Jiang, L. (2017). Nature-inspired superwettability systems. *Nat. Rev. Mat.* 2 (7), 17036. doi:10.1038/natrevmats.2017.36

Liu, R., Chi, Z., Cao, L., Weng, Z., Wang, L., Li, L., et al. (2020). Fabrication of biomimetic superhydrophobic and anti-icing Ti6Al4V alloy surfaces by direct laser interference lithography and hydrothermal treatment. *Appl. Surf. Sci.* 534, 147576. doi:10.1016/j.apsusc.2020.147576

Liu, S., Latthe, S. S., Yang, H., Liu, B., and Xing, R. (2015). Raspberry-like superhydrophobic silica coatings with self-cleaning properties. *Ceram. Int.* 41 (9), 11719–11725. doi:10.1016/j.ceramint.2015.05.137

Liu, S., Liu, X., Latthe, S. S., Gao, L., An, S., Yoon, S. S., et al. (2015). Self-cleaning transparent superhydrophobic coatings through simple sol–gel processing of fluoroalkylsilane. *Appl. Surf. Sci.* 351, 897–903. doi:10.1016/j.apsusc.2015.06.016

Liu, Y., Li, X., Jin, J., Liu, J., Yan, Y., Han, Z., et al. (2017). Anti-icing property of bio-inspired micro-structure superhydrophobic surfaces and heat transfer model. *Appl. Surf. Sci.* 400, 498–505. doi:10.1016/j.apsusc.2016.12.219

Liu, Y., Liu, J., Li, S., Han, Z., and Ren, L. (2013). Biomimetic superhydrophobic surface of high adhesion fabricated with micronano binary structure on aluminum alloy. *ACS Appl. Mat. Interfaces* 5 (18), 8907–8914. doi:10.1021/am4014715

Liu, Y., Yin, X., Zhang, J., Yu, S., Han, Z., and Ren, L. (2014). A electro-deposition process for fabrication of biomimetic super-hydrophobic surface and its corrosion resistance on magnesium alloy. *Electrochimica Acta* 125, 395–403. doi:10.1016/j.electacta.2014.01.135

Liu, Z., Yang, X., Pang, G., Zhang, F., Han, Y., Wang, X., et al. (2019). Temperature-based adhesion tuning and superwettability switching on superhydrophobic aluminum surface for droplet manipulations. *Surf. Coatings Technol.* 375, 527–533. doi:10.1016/j.surfcoat.2019.07.041

Lomga, J., Varshney, P., Nanda, D., Satapathy, M., Mohapatra, S., and Kumar, A. (2017). Fabrication of durable and regenerable superhydrophobic coatings with excellent self-cleaning and anti-fogging properties for aluminium surfaces. *J. Alloys Compd.* 702, 161–170. doi:10.1016/j.jallcom.2017.01.243

Lu, L., Zou, S., and Fang, B. (2021). The critical impacts of ligands on heterogeneous nanocatalysis: A review. *ACS Catal.* 11 (10), 6020–6058. doi:10.1021/acscatal.1c00903

Lu, Y., Yu, L., Zhang, Z., Wu, S., Li, G., Wu, P., et al. (2017). Biomimetic surfaces with anisotropic sliding wetting by energy-modulation femtosecond laser irradiation for enhanced water collection. *RSC Adv.* 7 (18), 11170–11179. doi:10.1039/c6ra28174e

Lv, Y., Song, C., Hou, Y., Shi, M., Li, Q., and Zhang, T. (2020). Bioinspired like lotus leaf hierarchical micropapillae structure for efficient oil-water separation and antibacterial performance. *J. Dispersion Sci. Technol.* 41 (11), 1690–1702. doi:10.1080/01932691.2019.1634588

Ma, L., Wang, L., Li, C., Guo, J., Shrotriya, P., Deng, C., et al. (2019). Hybrid nanosecond laser processing and heat treatment for rapid preparation of super-hydrophobic copper surface. *Metals* 9 (6), 668. doi:10.3390/met9060668

Manoharan, K., Anwar, M., and Bhattacharya, S. (2021). Development of hydrophobic paper substrates using silane and sol–gel based processes and deriving the best coating technique using machine learning strategies. *Sci. Rep.* 11 (1), 11352. doi:10.1038/s41598-021-90855-7

Michael, N., and Bhushan, B. (2007). Hierarchical roughness makes superhydrophobic states stable. *Microelectron. Eng.* 84 (3), 382–386. doi:10.1016/j.mee.2006.10.054

Milošev, I., Bakarič, T., Zanna, S., Seyeux, A., Rodic, P., Poberznik, M., et al. (2019). Electrochemical, surface-analytical, and computational DFT study of alkaline etched aluminum modified by carboxylic acids for corrosion protection and hydrophobicity. *J. Electrochem. Soc.* 166 (11), C3131–C3146. doi:10.1149/2.0181911jes

Ming, W., Wu, D., van Benthem, R., and de With, G. (2005). Superhydrophobic films from raspberry-like particles. *Nano Lett.* 5 (11), 2298–2301. doi:10.1021/nl0517363

Moghaddasi, Z., and Mohammadizadeh, M. R. (2022). Synthesis and effectiveness of Cu-infused TiO_2-SiO_2 based self-cleaning and antibacterial thin-films coating on ceramic tiles. *J. Sol-Gel Sci. Technol.* 1–9. doi:10.1007/s10971-022-05853-6

Mor, G. K., Carvalho, M. A., Varghese, O. K., Pishko, M. V., and Grimes, C. A. (2004). A room-temperature TiO_2-nanotube hydrogen sensor able to self-clean photoactively from environmental contamination. *J. Mat. Res.* 19 (2), 628–634. doi:10.1557/jmr.2004.19.2.628

Nageswaran, G., Jothi, L., and Jagannathan, S. (2019). *Plasma assisted polymer modifications Non-thermal plasma technology for polymeric materials*. Amsterdam, Netherlands: Elsevier, 95–127.

Nanda, D., Sahoo, A., Kumar, A., and Bhushan, B. (2019). Facile approach to develop durable and reusable superhydrophobic/superoleophilic coatings for steel mesh surfaces. *J. Colloid Interface Sci.* 535, 50–57. doi:10.1016/j.jcis.2018.09.088

Nguyen, V. H., Nguyen, B. D., Pham, H. T., Lam, S. S., Vo, D. V. N., Shokouhimehr, M., et al. (2021). Anti-icing performance on aluminum surfaces and proposed model for freezing time calculation. *Sci. Rep.* 11 (1), 3641. doi:10.1038/s41598-020-80886-x

Nguyen-Tri, P., Altiparmak, F., Nguyen, N., Tuduri, L., Ouellet-Plamondon, C. M., and Prud'homme, R. E. (2019). Robust superhydrophobic cotton fibers prepared by simple dip-coating approach using chemical and plasma-etching pretreatments. *Acs Omega* 4 (4), 7829–7837. doi:10.1021/acsomega.9b00688

Nguyen-Tri, P., Tran, H. N., Plamondon, C. O., Tuduri, L., Vo, D. V. N., Nanda, S., et al. (2019). Recent progress in the preparation, properties and applications of superhydrophobic nano-based coatings and surfaces: A review. *Prog. Org. Coatings* 132, 235–256. doi:10.1016/j.porgcoat.2019.03.042

Nosonovsky, M., and Bhushan, B. (2008). Energy transitions in superhydrophobicity: Low adhesion, easy flow and bouncing. *J. Phys. Condens. Matter* 20 (39), 395005. doi:10.1088/0953-8984/20/39/395005

Ou, J., Zhu, W., Xie, C., and Xue, M. (2019). Mechanically robust and repairable superhydrophobic zinc coating via a fast and facile method for corrosion resisting. *Materials* 12 (11), 1779. doi:10.3390/ma12111779

Pan, Q., Cao, Y., Xue, W., Zhu, D., and Liu, W. (2019). Picosecond laser-textured stainless steel superhydrophobic surface with an antibacterial adhesion property. *Langmuir* 35 (35), 11414–11421. doi:10.1021/acs.langmuir.9b01333

Panda, B. (2021). Corrosion resistant superhydrophobic aluminum alloy: A review. *IOP Conf. Ser. Mat. Sci. Eng.* 1017 (1), 012008. doi:10.1088/1757-899x/1017/1/012008

Parin, R., Martucci, A., Sturaro, M., Bortolin, S., Bersani, M., Carraro, F., et al. (2018). Nano-structured aluminum surfaces for dropwise condensation. *Surf. Coatings Technol.* 348, 1–12. doi:10.1016/j.surfcoat.2018.05.018

Parkin, I. P., and Palgrave, R. G. (2005). Self-cleaning coatings. *J. Mat. Chem.* 15 (17), 1689. doi:10.1039/b412803f

Peng, F., Zhang, D., Liu, X., and Zhang, Y. (2021). Recent progress in superhydrophobic coating on Mg alloys: A general review. *J. Magnesium Alloys* 9 (5), 1471–1486. doi:10.1016/j.jma.2020.08.024

Peng, H., Luo, Z., Li, L., Xia, Z., Du, J., and Zheng, B. (2019). Facile fabrication of superhydrophobic aluminum surfaces by chemical etching and its anti-icing/self-cleaning performances. *Mat. Res. Express* 6 (9), 096586. doi:10.1088/2053-1591/ab3173

Peng, S., and Deng, W. (2015). A simple method to prepare superamphiphobic aluminum surface with excellent stability. *Colloids Surfaces A Physicochem. Eng. Aspects* 481, 143–150. doi:10.1016/j.colsurfa.2015.04.037

Qian, C., Guang-hua, C., Yan, F., and Lu-quan, R. (1900). Super-hydrophobic characteristics of butterfly wing surface. *J. Bionic Eng.* 1 (4), 249–255.

Qu, J., Yu, C., Cui, R., Qin, J., Wang, H., and Cao, Z. (2018). Preparation of super-hydrophobic and corrosion resistant colored films on chemically etched 304 stainless steel substrate. *Surf. Coatings Technol.* 354, 236–245. doi:10.1016/j.surfcoat.2018.09.022

Qu, M., Zhang, B., Song, S., Chen, L., Zhang, J., and Cao, X. (2007). Fabrication of superhydrophobic surfaces on engineering materials by a solution-immersion process. *Adv. Funct. Mat.* 17 (4), 593–596. doi:10.1002/adfm.200600472

Qu, R., Zhang, W., Li, X., Liu, Y., Wei, Y., Feng, L., et al. (2020). Peanut leaf-inspired hybrid metal–organic framework with humidity-responsive wettability: Toward controllable separation of diverse emulsions. *ACS Appl. Mat. Interfaces* 12 (5), 6309–6318. doi:10.1021/acsami.9b21118

Ran, M., Zheng, W., and Wang, H. (2019). Fabrication of superhydrophobic surfaces for corrosion protection: A review. *Mater. Sci. Technol.* 35 (3), 313–326. doi:10.1080/02670836.2018.1560985

Rasouli, S., Rezaei, N., Hamedi, H., Zendehboudi, S., and Duan, X. (2021). Superhydrophobic and superoleophilic membranes for oil-water separation application: A comprehensive review. *Mater. Des.* 204, 109599. doi:10.1016/j.matdes.2021.109599

Richard, D., Clanet, C., and Quéré, D. (2002). Contact time of a bouncing drop. *Nature* 417 (6891), 811. doi:10.1038/417811a

Rius-Ayra, O., Castellote-Alvarez, R., Escobar, A. M., and Llorca-Isern, N. (2018). Superhydrophobic coating bioinspired on rice leaf: A first attempt to enhance erosion resistance properties at environmental conditions with ceramic particles [C]//Materials science forum. *Trans. Tech. Publ. Ltd.* 941, 1874–1879. doi:10.4028/www.scientific.net/MSF.941.1874

Rodič, P., Kapun, B., and Milošev, I. (2022). Superhydrophobic aluminium surface to enhance corrosion resistance and obtain self-cleaning and anti-icing ability. *Molecules* 27 (3), 1099. doi:10.3390/molecules27031099

Rodič, P., Kapun, B., Panjan, M., and Milosev, I. (2020). Easy and fast fabrication of self-cleaning and anti-icing perfluoroalkyl silane film on aluminium. *Coatings (Basel).* 10 (3), 234. doi:10.3390/coatings10030234

Rodič, P., and Milošev, I. (2019). One-step ultrasound fabrication of corrosion resistant, self-cleaning and anti-icing coatings on aluminium. *Surf. Coatings Technol.* 369, 175–185. doi:10.1016/j.surfcoat.2019.03.082

Román-Kustas, J., Hoffman, J. B., Reed, J. H., Gonsalves, A. E., Oh, J., Li, L., et al. (2020). Molecular and topographical organization: Influence on cicada wing wettability and bactericidal properties. *Adv. Mat. Interfaces* 7 (10), 2000112. doi:10.1002/admi.202000112

Rong, W., Zhang, H., Mao, Z., Chen, L., and Liu, X. (2021). Stable drag reduction of anisotropic superhydrophobic/hydrophilic surfaces containing bioinspired micro/nanostructured arrays by laser ablation. *Colloids Surfaces A Physicochem. Eng. Aspects* 622, 126712. doi:10.1016/j.colsurfa.2021.126712

Rus, A. Z. M., Mohid, S. R., Nurulsaidatulsyida, S., and Marsi, N. (2013). Biopolymer doped with titanium dioxide superhydrophobic photocatalysis as self-clean coating for lightweight composite. *Adv. Mater. Sci. Eng.*, 2013, 486253. doi:10.1155/2013/486253

Sajjadi, M., Ahmadpoor, F., Nasrollahzadeh, M., and Ghafuri, H. (2021). Lignin-derived (nano)materials for environmental pollution remediation: Current challenges and future perspectives. *Int. J. Biol. Macromol.* 178, 394–423. doi:10.1016/j.ijbiomac.2021.02.165

Saleema, N., Sarkar, D. K., Paynter, R. W., and Chen, X. G. (2010). Superhydrophobic aluminum alloy surfaces by a novel one-step process. *ACS Appl. Mat. Interfaces* 2 (9), 2500–2502. doi:10.1021/am100563u

Saleh, T. A., Baig, N., Alghunaimi, F. I., and Aljuryyed, N. W. (2020). A flexible biomimetic superhydrophobic and superoleophilic 3D macroporous polymer-based robust network for the efficient separation of oil-contaminated water. *RSC Adv.* 10 (9), 5088–5097. doi:10.1039/c9ra06579b

Saleh, T. A., and Baig, N. (2019). Efficient chemical etching procedure for the generation of superhydrophobic surfaces for separation of oil from water. *Prog. Org. Coatings* 133, 27–32. doi:10.1016/j.porgcoat.2019.03.049

Sam, E. K., Sam, D. K., Lv, X., Padmanabhan, D., Wesley, R. J., Obadiah, A., et al. (2019). Recent development in the fabrication of self-healing superhydrophobic surfaces. *Chem. Eng. J.* 373, 531–546. doi:10.1016/j.cej.2019.05.077

Scalisi, F. (2017). Nano-materials for architecture. *J. Civ. Eng. Archit.* 11, 1061. doi:10.17265/1934-7359/2017.12.001

Sethi, S. K., Kadian, S., Chauhan, R. P., Goel, R, and Manik, G. (2020). Fabrication and analysis of ZnO quantum dots based easy clean coating: A combined theoretical and experimental investigation. *ChemistrySelect* 5 (29), 8942–8950. doi:10.1002/slct.202001092

Sethi, S. K., Kadian, S., and Manik, G. (2022). A review of recent progress in molecular dynamics and coarse-grain simulations assisted understanding of wettability. *Archives Comput. Methods Eng.* 29, 3059–3085. doi:10.1007/s11831-021-09689-1

Sethi, S. K., and Manik, G. (2018). Recent progress in super hydrophobic/hydrophilic self-cleaning surfaces for various industrial applications: A review. *Polymer-Plastics Technol. Eng.* 57 (18), 1932–1952. doi:10.1080/03602559.2018.1447128

Sethi, S. K., Shankar, U., and Manik, G. (2019). Fabrication and characterization of non-fluoro based transparent easy-clean coating formulations optimized from molecular dynamics simulation. *Prog. Org. Coatings* 136, 105306. doi:10.1016/j.porgcoat.2019.105306

Sethi, S. K., Soni, L., Shankar, U., Chauhan, R. P., and Manik, G. (2020). A molecular dynamics simulation study to investigate poly(vinyl acetate)-poly(dimethyl siloxane) based easy-clean coating: An insight into the surface behavior and substrate interaction. *J. Mol. Struct.* 1202, 127342. doi:10.1016/j.molstruc.2019.127342

Shaikh, M. O., Yang, J. Y., and Chuang, C. H. (2021). Thermally stable and durable superhydrophobic surfaces on stainless steel sheets with microholes via acid pretreatment and modification with self-assembled monolayers. *Microfluid. Nanofluidics* 25 (11), 1–9. doi:10.1007/s10404-021-02499-8

Shao, C., Chi, J., Chen, Z., Cai, L., and Zhao, Y. (2019). Superwettable colloidal crystal micropatterns on butterfly wing surface for ultrasensitive detection. *J. colloid interface Sci.* 546, 122–129. doi:10.1016/j.jcis.2019.03.064

Sharma, K., Hooda, A., Goyat, M. S., Rai, R., and Mittal, A. (2021). A review on challenges, recent progress and applications of silica nanoparticles based superhydrophobic coatings. *Ceram. Int.* 48, 5922–5938. doi:10.1016/j.ceramint.2021.11.239

Siddiqui, M. T. H., Nizamuddin, S., Baloch, H. A., Mubarak, N., Al-Ali, M., Mazari, S. A., et al. (2019). Fabrication of advance magnetic carbon nano-materials and their potential applications: A review. *J. Environ. Chem. Eng.* 7 (1), 102812. doi:10.1016/j.jece.2018.102812

Song, J., Xu, W., Liu, X., Lu, Y., Wei, Z., and Wu, L. (2012). Ultrafast fabrication of rough structures required by superhydrophobic surfaces on Al substrates using an immersion method. *Chem. Eng. J.* 211, 143–152. doi:10.1016/j.cej.2012.09.094

Song, R., Zhang, N., Dong, H., Wang, P., Ding, H., Wang, J., et al. (2022). Three-dimensional biomimetic superhydrophobic nickel sponge without chemical modifications for efficient oil/water separation. *Sep. Purif. Technol.* 289, 120723. doi:10.1016/j.seppur.2022.120723

Stoddart, P. R., Cadusch, P. J., Boyce, T. M., Erasmus, R. M., and Comins, J. D. (2006). Optical properties of chitin: Surface-enhanced Raman scattering substrates based on antireflection structures on cicada wings. *Nanotechnology* 17 (3), 680–686. doi:10.1088/0957-4484/17/3/011

Stratakis, E., Bonse, J., Heitz, J., Siegel, J., Tsibidis, G., Skoulas, E., et al. (2020). Laser engineering of biomimetic surfaces. *Mater. Sci. Eng. R Rep.* 141, 100562. doi:10.1016/j.mser.2020.100562

Stratakis, E., Ranella, A., and Fotakis, C. (2011). Biomimetic micro/nanostructured functional surfaces for microfluidic and tissue engineering applications. *Biomicrofluidics* 5 (1), 013411. doi:10.1063/1.3553235

Sun, W., Wang, L., Yang, Z., Li, S., Wu, T., and Liu, G. (2017). Fabrication of polydimethylsiloxane-derived superhydrophobic surface on aluminium via chemical vapour deposition technique for corrosion protection. *Corros. Sci.* 128, 176–185. doi:10.1016/j.corsci.2017.09.005

Sun, Y., and Guo, Z. (2019). Recent advances of bioinspired functional materials with specific wettability: From nature and beyond nature. *Nanoscale Horiz.* 4 (1), 52–76. doi:10.1039/c8nh00223a

Sun, Y., Sui, X., Wang, Y., Liang, W., and Wang, F. (2020). Passive anti-icing and active electrothermal deicing system based on an ultraflexible carbon nanowire (CNW)/PDMS biomimetic nanocomposite with a superhydrophobic microcolumn surface. *Langmuir* 36 (48), 14483–14494. doi:10.1021/acs.langmuir.0c01745

Suresh Kumar, N., Padma Suvarna, R., Chandra Babu Naidu, K., Ratnamala, A., and Manjunatha, H. (2020). A review on biological and biomimetic materials and their applications. *Appl. Phys. A* 126 (6), 1–18. doi:10.1007/s00339-020-03633-z

Tadanaga, K., Morinaga, J., Matsuda, A., and Minami, T. (2000). Superhydrophobic–Superhydrophilic micropatterning on flowerlike alumina coating film by the Sol–Gel method. *Chem. Mat.* 12 (3), 590–592. doi:10.1021/cm990643h

Tavana, H., Amirfazli, A., and Neumann, A. W. (2006). Fabrication of superhydrophobic surfaces of *n*-hexatriacontane. *Langmuir* 22 (13), 5556–5559. doi:10.1021/la0607757

Tian, G., Xing, Z., Xie, Y., Deng, C., Wu, X., and Sun, X. (2017). "Aluminum and stainless steel base bionic super-hydrophobic surface preparation technology using in space instruments," in 2017 Chinese Automation Congress (CAC), Jinan, China, 20-22 October 2017 (IEEE), 5690–5694.

Tudu, B. K., Kumar, A., and Bhushan, B. (2019). Facile approach to develop anti-corrosive superhydrophobic aluminium with high mechanical, chemical and thermal durability. *Phil. Trans. R. Soc. A* 377 (2138), 20180272. doi:10.1098/rsta.2018.0272

Tuo, Y., Zhang, H., Rong, W., Jiang, S., Chen, W., and Liu, X. (2019). Drag reduction of anisotropic superhydrophobic surfaces prepared by laser etching. *Langmuir* 35 (34), 11016–11022. doi:10.1021/acs.langmuir.9b01040

Varshney, P., Mohapatra, S. S., and Kumar, A. (2016). Superhydrophobic coatings for aluminium surfaces synthesized by chemical etching process. *Int. J. Smart Nano Mater.* 7 (4), 248–264. doi:10.1080/19475411.2016.1272502

Waked, A. M. (2011). Nano materials applications for conservation of cultural heritage. *WIT Trans. Built Environ.* 118, 577–588. doi:10.2495/STR110481

Wan, Y., Chen, M., Liu, W., Shen, X., Min, Y., and Xu, Q. (2018). The research on preparation of superhydrophobic surfaces of pure copper by hydrothermal method and its corrosion resistance. *Electrochimica Acta* 270, 310–318. doi:10.1016/j.electacta.2018.03.060

Wan, Y., Wang, X., Zhang, M., Xu, J., and Yu, H. (2022). Biomimetic bamboo leaf double-sided microstructure composite surface and its delayed icing performance. *Surf. Topogr. Metrology Prop.* doi:10.1088/2051-672X/ac6c3e

Wan, Y., Zhang, C., Zhang, M., and Xu, J. (2021). Anti-condensation behavior of bamboo leaf surface (backside) and its bionic preparation. *Mat. Res. Express* 8 (5), 055002. doi:10.1088/2053-1591/abfc01

Wang, B., Liang, W., Guo, Z., and Liu, W. (2015). Biomimetic super-lyophobic and super-lyophilic materials applied for oil/water separation: A new strategy beyond nature. *Chem. Soc. Rev.* 44 (1), 336–361. doi:10.1039/c4cs00220b

Wang, D., Zhao, A., Jiang, R., Li, D., Zhang, M., Gan, Z., et al. (2012). Surface properties of bionic micro-pillar arrays with various shapes of tips. *Appl. Surf. Sci.* 259, 93–98. doi:10.1016/j.apsusc.2012.06.106

Wang, G., Zeng, Z., Wang, H., Zhang, L., Sun, X., He, Y., et al. (2015). Low drag porous ship with superhydrophobic and superoleophilic surface for oil spills cleanup. *ACS Appl. Mat. Interfaces* 7 (47), 26184–26194. doi:10.1021/acsami.5b08185

Wang, H., Wei, Y., Liang, M., Hou, L., Li, Y., and Guo, C. (2016). Fabrication of stable and corrosion-resisted super-hydrophobic film on Mg alloy. *Colloids Surfaces A Physicochem. Eng. Aspects* 509, 351–358. doi:10.1016/j.colsurfa.2016.09.027

Wang, S., and Jiang, L. (2007). Definition of superhydrophobic states. *Adv. Mat.* 19 (21), 3423–3424. doi:10.1002/adma.200700934

Wang, S., Yang, Z., Gong, G., Wang, J., Wu, J., Yang, S., et al. (2016). Icephobicity of penguins *Spheniscus humboldti* and an artificial replica of penguin feather with air-infused hierarchical rough structures. *J. Phys. Chem. C* 120 (29), 15923–15929. doi:10.1021/acs.jpcc.5b12298

Wang, X., Ding, H., Sun, S., Zhang, H., Zhou, R., Li, Y., et al. (2021). Preparation of a temperature-sensitive superhydrophobic self-cleaning SiO_2-TiO_2@ PDMS coating with photocatalytic activity. *Surf. Coatings Technol.* 408, 126853. doi:10.1016/j.surfcoat.2021.126853

Wang, X., Yu, H., Li, P., Zhang, Y., Wen, Y., Qiu, Y., et al. (2021). Femtosecond laser-based processing methods and their applications in optical device manufacturing: A review. *Opt. Laser Technol.* 135, 106687. doi:10.1016/j.optlastec.2020.106687

Watson, G. S., Green, D. W., Schwarzkopf, L., Li, X., Cribb, B. W., Myhra, S., et al. (2015). A gecko skin micro/nano structure – a low adhesion, superhydrophobic, anti-wetting, self-cleaning, biocompatible, antibacterial surface. *Acta biomater.* 21, 109–122. doi:10.1016/j.actbio.2015.03.007

Watson, G. S., and Watson, J. A. (2004). Natural nano-structures on insects—Possible functions of ordered arrays characterized by atomic force microscopy. *Appl. Surf. Sci.* 235 (1-2), 139–144. doi:10.1016/j.apsusc.2004.05.129

Wei, D., Wang, J., Li, S., Liu, Y., and Wang, H. (2021). Novel corrosion-resistant behavior and mechanism of a biomimetic surface with switchable wettability on Mg alloy. *Chem. Eng. J.* 425, 130450. doi:10.1016/j.cej.2021.130450

Wei, D., Wang, J., Liu, Y., Li, S., and Wang, H. (2021). Controllable superhydrophobic surfaces with tunable adhesion on Mg alloys by a simple etching method and its corrosion inhibition performance. *Chem. Eng. J.* 404, 126444. doi:10.1016/j.cej.2020.126444

Wenzel, R. N. (1936). Resistance of solid surfaces to wetting by water. *Ind. Eng. Chem.* 28 (8), 988–994. doi:10.1021/ie50320a024

Wong, T. S., Kang, S. H., Tang, S. K. Y., Smythe, E. J., Hatton, B. D., Grinthal, A., et al. (2011). Bioinspired self-repairing slippery surfaces with pressure-stable omniphobicity. *Nature* 477 (7365), 443–447. doi:10.1038/nature10447

Wu, D., Wang, J. N., Wu, S. Z., Chen, Q. D., Zhao, S., Zhang, H., et al. (2011). Three-level biomimetic rice-leaf surfaces with controllable anisotropic sliding. *Adv. Funct. Mat.* 21 (15), 2927–2932. doi:10.1002/adfm.201002733

Wu, R., Liang, S., Pan, A., Yuan, Z., Tang, Y., Tan, X., et al. (2012). Fabrication of nano-structured super-hydrophobic film on aluminum by controllable immersing method. *Appl. Surf. Sci.* 258 (16), 5933–5937. doi:10.1016/j.apsusc.2011.10.029

Wu, Y., Du, J., Liu, G., Chen, W.-Q., Chen, S., and Du, T. (2021). A review of self-cleaning technology to reduce dust and ice accumulation in photovoltaic power generation using superhydrophobic coating. *Renew. Energy* 185, 1034–1061. doi:10.1016/j.renene.2021.12.123

Xia, A., He, L., Qie, S., Zhang, J., Li, H., He, N., et al. (2022). Fabrication of an anti-icing aluminum alloy surface by combining wet etching and laser machining. *Appl. Sci.* 12 (4), 2119. doi:10.3390/app12042119

Xie, H., Huang, H. X., and Peng, Y. J. (2017). Rapid fabrication of bio-inspired nanostructure with hydrophobicity and antireflectivity on polystyrene surface replicating from cicada wings. *Nanoscale* 9 (33), 11951–11958. doi:10.1039/c7nr04176d

Xing, L., Zhou, Q., Chen, G., Sun, G., and Xing, T. (2022). Recent developments in preparation, properties, and applications of superhydrophobic textiles. *Text. Res. J.* doi:10.0040/5175221097716

Xu, M., Feng, Y., Li, Z., Wang, X., Li, C., Jiang, H., et al. (2019). A novel, efficient and cost-effective synthesis technique for the development of superhydrophobic glass surface. *J. Alloys Compd.* 781, 1175–1181. doi:10.1016/j.jallcom.2018.12.084

Xu, Q. F., Mondal, B., and Lyons, A. M. (2011). Fabricating superhydrophobic polymer surfaces with excellent abrasion resistance by a simple lamination templating method. *ACS Appl. Mat. Interfaces* 3 (9), 3508–3514. doi:10.1021/am200741f

Yang, H., Dou, X., Fang, Y., and Jiang, P. (2013). Self-assembled biomimetic superhydrophobic hierarchical arrays. *J. Colloid Interface Sci.* 405, 51–57. doi:10.1016/j.jcis.2013.05.040

Yang, H., Gao, Y., Qin, W., Sun, J., Huang, Z., Li, Y., et al. (2022). A robust superhydrophobic surface on AA3003 aluminum alloy with intermetallic phases *in-situ* pinning effect for corrosion protection. *J. Alloys Compd.* 898, 163038. doi:10.1016/j.jallcom.2021.163038

Yang, L., Shen, X., Yang, Q., Liu, J., Wu, W., Li, D., et al. (2021). Fabrication of biomimetic anisotropic super-hydrophobic surface with rice leaf-like structures by femtosecond laser. *Opt. Mater.* 112, 110740. doi:10.1016/j.optmat.2020.110740

Yang, S., Ju, J., Qiu, Y., He, Y., Wang, X., Dou, S., et al. (2014). Superhydrophobic materials: Peanut leaf inspired multifunctional surfaces (small 2/2014). *Small* 10 (2), 214. doi:10.1002/smll.201470010

Yang, Y., Li, X., Zheng, X., Chen, Z., Zhou, Q., and Chen, Y. (2018). 3D-Printed biomimetic super-hydrophobic structure for microdroplet manipulation and oil/water separation. *Adv. Mat.* 30 (9), 1704912. doi:10.1002/adma.201704912

Yang, Z., Liu, X., and Tian, Y. (2019). Hybrid laser ablation and chemical modification for fast fabrication of bio-inspired super-hydrophobic surface with excellent self-cleaning, stability and corrosion resistance. *J. Bionic Eng.* 16 (1), 13–26. doi:10.1007/s42235-019-0002-y

Yao, M., Zhang, P., Nie, J., and He, Y. (2021). The superhydrophobic fluorine-containing material prepared through biomimetic UV lithography for oil–water separation and anti-bioadhesion. *Macromol. Chem. Phys.* 222 (17), 2100149. doi:10.1002/macp.202100149

Yeganeh, M., and Mohammadi, N. (2018). Superhydrophobic surface of Mg alloys: A review. *J. Magnesium Alloys* 6 (1), 59–70. doi:10.1016/j.jma.2018.02.001

Yilgor, I., Bilgin, S., Isik, M., and Yilgor, E. (2012). Facile preparation of superhydrophobic polymer surfaces. *Polymer* 53 (6), 1180–1188. doi:10.1016/j.polymer.2012.01.053

Yong, J., Yang, Q., Chen, F., Zhang, D., Farooq, U., Du, G., et al. (2014). A simple way to achieve superhydrophobicity, controllable water adhesion, anisotropic sliding, and anisotropic wetting based on femtosecond-laser-induced line-patterned surfaces. *J. Mat. Chem. A* 2 (15), 5499–5507. doi:10.1039/c3ta14711h

Young, T., III (1805). An essay on the cohesion of fluids. *Philosophical Trans. R. Soc. Lond.* 95, 65–87. doi:10.1098/rstl.1805.0005

Yuan, Z., Bin, J., Wang, X., Peng, C., Wang, M., Xing, S., et al. (2014). Fabrication of superhydrophobic surface with hierarchical multi-scale structure on copper foil. *Surf. Coatings Technol.* 254, 151–156. doi:10.1016/j.surfcoat.2014.06.004

Zhan, Y., Yu, S., Amirfazli, A., Rahim Siddiqui, A., and Li, W. (2022). Recent advances in antibacterial superhydrophobic coatings. *Adv. Eng. Mat.* 24 (4), 2101053. doi:10.1002/adem.202101053

Zhang, B., Xu, W., Zhu, Q., Guan, F., and Zhang, Y. (2022). Nepenthes pitcher-inspired lubricant-infused slippery surface with superior anti-corrosion durability, hot water repellency and scratch resistance. *J. Industrial Eng. Chem.* 107, 259–267. doi:10.1016/j.jiec.2021.11.052

Zhang, G., Zhang, J., Xie, G., Liu, Z., and Shao, H. (2006). Cicada wings: A stamp from nature for nanoimprint lithography. *Small* 2 (12), 1440–1443. doi:10.1002/smll.200600255

Zhang, H., Yang, J., Chen, B., Liu, C., Zhang, M., and Li, C. (2015). Fabrication of superhydrophobic textured steel surface for anti-corrosion and tribological properties. *Appl. Surf. Sci.* 359, 905–910. doi:10.1016/j.apsusc.2015.10.191

Zhang, X., Zhao, J., Mo, J., Sun, R., Li, Z., and Guo, Z. (2019). Fabrication of superhydrophobic aluminum surface by droplet etching and chemical modification. *Colloids Surfaces A Physicochem. Eng. Aspects* 567, 205–212. doi:10.1016/j.colsurfa.2019.01.046

Zhang, Y., Liu, Z., Chen, A., Wang, Q., Zhang, J., Zhao, C., et al. (2020). Fabrication of micro-/submicro-/nanostructured polypropylene/graphene superhydrophobic surfaces with extreme dynamic pressure resistance assisted by single hierarchically porous anodic aluminum oxide template. *J. Phys. Chem. C* 124 (11), 6197–6205. doi:10.1021/acs.jpcc.9b12038

Zhang, Z., Zhao, J., Lei, Y., Wang, Y., Zhou, G., Xu, C., et al. (2020). Preparation of intricate nanostructures on 304 stainless steel surface by SiO_2-assisted HF etching for high superhydrophobicity. *Colloids Surfaces A Physicochem. Eng. Aspects* 586, 124287. doi:10.1016/j.colsurfa.2019.124287

Zhao, H., Sun, Q., Deng, X., and Cui, J. (2018). Earthworm-Inspired rough polymer coatings with self-replenishing lubrication for adaptive friction-reduction and antifouling surfaces. *Adv. Mat.* 30 (29), 1802141. doi:10.1002/adma.201802141

Zheng, H., Chang, S., Ma, G., and Wang, S. (2020). Anti-icing performance of superhydrophobic surface fabricated by femtosecond laser composited dual-layers coating. *Energy Build.* 223, 110175. doi:10.1016/j.enbuild.2020.110175

Zheng, S., Li, C., Zhang, Y., Xiang, T., Cao, Y., Li, Q., et al. (2021). A general strategy towards superhydrophobic self-cleaning and anti-corrosion metallic surfaces: An example with aluminum alloy. *Coatings (Basel).* 11 (7), 788. doi:10.3390/coatings11070788

Zheng, Y., Bai, H., Huang, Z., Tian, X., Nie, F. Q., Zhao, Y., et al. (2010). Directional water collection on wetted spider silk. *Nature* 463 (7281), 640–643. doi:10.1038/nature08729

Zheng, Y., Gao, X., and Jiang, L. (2007). Directional adhesion of superhydrophobic butterfly wings. *Soft Matter* 3 (2), 178–182. doi:10.1039/b612667g

Zheng, Y., Zhang, C., Wang, J., Liu, Y., Shen, C., and Yang, J. (2019). Robust adhesion of droplets via heterogeneous dynamic petal effects. *J. colloid interface Sci.* 557, 737–745. doi:10.1016/j.jcis.2019.09.070

Zhu, Z., Zhang, Y., and Sun, D. W. (2021). Biomimetic modification of freezing facility surfaces to prevent icing and frosting during freezing for the food industry. *Trends Food Sci. Technol.* 111, 581–594. doi:10.1016/j.tifs.2021.02.034

Milosev, I, Bakaric, T, Rodic, P, Zanna, S, Seyeux, A, Poberznik, M, et al. Superhydrophobic Coatings on Aluminium Based on Carboxylic Acids, *ECS Meeting Abstracts. IOP Publishing*, 2017 (12): 787.

frontiers | Frontiers in Bioengineering and Biotechnology

TYPE Original Research
PUBLISHED 09 August 2022
DOI 10.3389/fbioe.2022.923365

Construction of ultrasound-responsive urokinase precise controlled-release nanoliposome applied for thrombolysis

Yongliang Fan[1,2], Li Liu[3], Fang Li[3], Hang Zhou[3], Yizhou Ye[2], Chunping Yuan[4], Hongli Shan[4], Wangfu Zang[1]*, Yu Luo[4]* and Sijing Yan[5]*

[1]Department of Cardio-Thoracic Surgery, Shanghai 10th People's Hospital, School of Clinical Medicine of Nanjing Medical University, Shanghai, China, [2]Department of Cardiovascular Surgery, Shanghai General Hospital, Shanghai Jiao Tong University School of Medicine, Shanghai, China, [3]Department of Ultrasound Medicine, Chongqing University Cancer Hospital, Chongqing, China, [4]Shanghai Engineering Technology Research Center for Pharmaceutical Intelligent Equipment, Shanghai Frontiers Science Center for Druggability of Cardiovascular Non-coding RNA, Institute for Frontier Medical Technology, Shanghai University of Engineering Science, Shanghai, China, [5]Department of Ultrasound, Chongqing Hospital of Traditional Chinese Medicine, Chongqing, China

Urokinase is widely used in the dissolution of an acute pulmonary embolism due to its high biocatalytic effect. However, how to precisely regulate its dose, avoid the side effects of hemolysis or ineffective thrombolysis caused by too high or too low a dose, and seize the golden time of acute pulmonary embolism are the key factors for its clinical promotion. Therefore, based on the precise design of a molecular structure, an ultrasonic-responsive nanoliposome capsule was prepared in this paper. Singlet oxygen is continuously generated under the interaction of the ultrasonic cavitation effect and the sonosensitizer protoporphyrin, and the generated singlet oxygen will break the thiol acetone bond between the hydrophilic head and the hydrophobic tail of the liposome, and the lipid The body structure disintegrates rapidly, and the urokinase encapsulated inside is rapidly released, down-regulating the expression of fibrinogen in the body, and exerting a thrombolytic function. The *in vitro* and *in vivo* results show that the smart urokinase nanoliposomes prepared by us have sensitive and responsive cytocompatibility to ultrasound and good *in vivo* thrombolytic properties for acute pulmonary embolism, which provides a new strategy for clinical acute pulmonary embolism thrombolysis.

KEYWORDS

pulmonary embolism, urokinase, sonodynamic, protoporphyrin (PPIX), singlet oxygen

Check for updates

OPEN ACCESS

EDITED BY
Jinmyoung Joo,
Ulsan National Institute of Science and Technology, South Korea

REVIEWED BY
Qiang Shi,
Changchun Institute of Applied Chemistry, China
Nemany A.N. Hanafy,
Nano Science and Technology Institute, Kafrelsheikh University, Egypt
Rui Li,
Dalian University of Technology, China

*CORRESPONDENCE
Sijing Yan,
wennieyanyan@163.com
Wangfu Zang,
zangwf@hotmail.com
Yu Luo,
yuluo@sues.edu.cn

SPECIALTY SECTION
This article was submitted to Nanobiotechnology, a section of the journal Frontiers in Bioengineering and Biotechnology

RECEIVED 19 April 2022
ACCEPTED 04 July 2022
PUBLISHED 09 August 2022

CITATION
Fan Y, Liu L, Li F, Zhou H, Ye Y, Yuan C, Shan H, Zang W, Luo Y and Yan S (2022), Construction of ultrasound-responsive urokinase precise controlled-release nanoliposome applied for thrombolysis. *Front. Bioeng. Biotechnol.* 10:923365. doi: 10.3389/fbioe.2022.923365

COPYRIGHT
© 2022 Fan, Liu, Li, Zhou, Ye, Yuan, Shan, Zang, Luo and Yan. This is an open-access article distributed under the terms of the Creative Commons Attribution License (CC BY). The use, distribution or reproduction in other forums is permitted, provided the original author(s) and the copyright owner(s) are credited and that the original publication in this journal is cited, in accordance with accepted academic practice. No use, distribution or reproduction is permitted which does not comply with these terms.

1 Introduction

Pulmonary embolism (PE) refers to diseases or clinical syndromes caused by various emboli blocking the pulmonary artery or its branches, including pulmonary thromboembolism (PTE), fat embolism, amniotic fluid embolism, tumor embolism, etc (Konstantinides et al., 2019; van der Pol et al., 2019; Barco et al., 2020). Pulmonary thromboembolism is the most common type, commonly referred to as acute pulmonary embolism (APE) (Shonyela et al., 2015; Opris et al., 2017). Pulmonary embolism is often secondary to deep venous thrombosis (DVT), which is essentially a clinical manifestation of the same disease at different stages, collectively referred to as venous thromboembolism (VTE) (Stein et al., 2010; Kaditis and Alexopoulos, 2021).

The fatality rate of APE is also high, ranking third in Western countries after myocardial infarction and malignant tumors. It is estimated that about 10% of APE die within 1 h after onset, and the fatality rate of APE without diagnosis and treatment can reach 30% (Kostrubiec et al., 2012). With early intervention and treatment, the fatality rate can be reduced to 2–8%. Therefore, APE is a disease with a high morbidity rate, high misdiagnosis rate, and high mortality rate, which needs to be paid attention to by clinicians.

The morbidity and mortality of PE patients under the age of 40 are much lower than those of the elderly, and insufficient attention has been paid to it (Abe et al., 2019). However, some studies have shown that APE has been proved to be an important cause of death in young people. A study by Sakuma *et al.* in 2007 examined Autopsy records and found that APE contributed more to deaths in patients aged 20–39 than in other age groups, accounting for 2.3% of deaths (Taniguchi et al., 2012). In 2008, an autopsy study of 1,000 patients with pulmonary embolism in India by Nandita *et al.* found that pulmonary embolism tends to be younger (Nandita and Vasistha, 2008). In 2010, Yamada *et al.* found that compared with Westerners, Japanese people with pulmonary embolism tend to be younger and more feminine (Yamada et al., 2010). Renda *et al.* calculated that the detection rate of APE in the U.S. adult population during CTPA-assisted examination increased from 0.621‰ to 1.123‰, the incidence rate increased by about 80%, and the mortality rate during the first 3 months after diagnosis was estimated up to 15% (Hayiroglu et al., 2015).

Although surgery can effectively remove thrombus in blood vessels, the operation is difficult and risky, and requires high medical equipment in the hospital and the medical skills of doctors; complex preoperative preparation is required; there are many postoperative complications; the cost is also high (Ronsivalle et al., 2013; Steglich-Arnholm et al., 2015; Izura Gómez et al., 2018). In addition to surgery, drug thrombolysis can also be used (Vedantham et al., 2017; Mazzolai et al., 2018; Naylor et al., 2018; Bolcal et al., 2019). So far, the clinically used thrombolytic drugs are mainly urokinase (UrokinaSe, United Kingdom). Goldhaber *et al.* have done a series of studies on thrombolysis in acute pulmonary embolism, confirmed the efficacy of United Kingdom and rt-PA, and compared the dose, time, route, and specific implementation methods of the drugs so that the treatment tends to be standardized (Goldhaber and Bounameaux, 2012; Huang et al., 2014). A large-scale study organized by Professor Wang Chen in China believes that 50 mg can not only receive a good curative effect but also reduce the risk of bleeding. Thrombolysis must consider the risk of bleeding, so patients with bleeding risk are contraindications to thrombolysis (Muñiz, 2012). Therefore, there is an urgent need to explore a new therapy with reliable efficacy, simple operation, low side effects, and complications for acute thromboembolism.

Sonodynamic therapy (SDT) developed in recent years is a new treatment modality based on ultrasonic excitation of sonosensitizers to trigger sonochemical reactions and generate highly toxic reactive oxygen species (ROS). Compared with photothermal/photodynamic therapy (Li et al., 2022), ultrasound has a deeper soft tissue penetration depth (≥10 cm) than light and has better potential for clinical application and translation (Chen et al., 2021; Hu et al., 2021; Xu et al., 2021; Xu and Pu, 2021). The application effect of SDT has been widely studied, such as the generation of reactive oxygen species by applying ultrasound to activate the sonosensitizer molecules hematoporphyrin, titanium dioxide (TiO_2), *etc* (Gong et al., 2020). Clinical studies suggest that ultrasound can also accelerate thrombolysis, and is expected to be used for thrombus localization and blood flow monitoring.

Thereinto, this study intends to develop an advanced, safe and efficient thrombolysis technology by combining the advantages of deep tissue penetration of mechanical ultrasound and efficient thrombolysis of drug urokinase. Firstly, the nanocapsules are structurally modified. The ROS-sensitive (singlet oxygen) Linker is used to connect the hydrophilic and hydrophobic ends of the liposomes to obtain ultrasonic-responsive smart “nanocapsules”. The thrombolytic drug urokinase is enclosed inside the capsule. The prepared nanocapsules are injected into the body by intravenous injection, the embolism position is delineated by contrast CT imaging, and the ultrasound probe is aimed at the lesion site. The sonosensitizer in the main component of the nanocapsule liposome produces singlet oxygen and oxygen destruction under the action of ultrasound. The connection between the hydrophilic and hydrophobic liposomes and the collapse of the bilayer membrane structure. On the one hand, the precisely controlled release of the urokinase embolization site is achieved, the local drug concentration at the embolization site is increased, the embolization site is targeted, and the thrombolysis is rapid; on the other hand, it is loaded with The thrombolytic drug urokinase nanocapsules are not stimulated by exogenous ultrasound in other organs or tissues, the capsule structure remains intact, and urokinase is still “captured” in the capsule to avoid the risk of bleeding caused by systemic administration.

2 Experimental section

2.1 Materials and methods

Urokinase (United Kingdom) was obtained from Sigma-Aldrich Co. (Shanghai, China). DPPC, protoporphyrin (PpIX), DSPE. NH_2, PEG_{2k}-NH_2, and $^1O_2$-cleavable linker modified DSPE-S$(CH_3)_2$-S-COOH were purchased from Shanghai Aicheng Biological Technology Co., Ltd. (Shanghai, China). Fetal bovine serum (FBS), Dulbecco's Modified Eagle's Medium (DMEM), RPMI 1640, penicillin, streptomycin, and 0.25% trypsin-EDTA were purchased from Gibco (New York, United States). Cell counting kit-8 (CCK-8) was purchased from Shanghai Aicheng Biological Technology Co., Ltd. (Shanghai, China).

2.2 Synthesis of $^1O_2$-cleavable liposome fragment

Synthesis of DSPE-PpIX: Briefly, PpIX (0.3 M) was dispersed in 10 ml of methanol and EDC (0.9 M, 1 ml methanol) was rapidly infused into the PpIX solution. Then, the mixed solution was stirred for 30 min. Secondly, NHS (0.9 M) dispersed in 1 ml methanol was rapidly added to the mentioned mixed solution, and mixed using magnetic stirring for 3 h. The active PpIX was added dropwise into DSPE-NH_2 (0.1 M) dispersed in 10 ml of methanol at 300 rpm for 72 h. Finally, the product was then dialyzed against water using a dialysis bag (molecular weight cutoff of 5000 Da). The purified DSPE-PpIX was freeze-dried and stored at 4°C before use.

Synthesis of DSPE-S-C$(CH_3)_2$-S-PEG_{2k}: The synthesis of DSPE-S-C$(CH_3)_2$-S-PEG_{2k} is similar to that of DSPE-PpIX, which is briefly described as follows: Briefly, DSPE-S-C$(CH_3)_2$-S-COOH (0.1 M) was dispersed in 20 ml of DMSO and EDC (0.3 M, 1 ml DMSO) was rapidly infused into the DSPE solution. Then, the mixed solution was stirred for 30 min. Secondly, NHS (0.3 M) dispersed in 1 ml DMSO was rapidly added to the mentioned mixed solution and mixed using magnetic stirring for 3 h. The active DSPE-S-C$(CH_3)_2$-S-COOH was added dropwise into PEG_{2K}-NH_2 (0.1 M) dispersed in 20 ml of DMSO at 300 rpm for 72 h. Finally, the product was then dialyzed against water using a dialysis bag (molecular weight cutoff of 8–14 KDa). The purified DSPE-S-C$(CH_3)_2$-S-PEG_{2k} was freeze-dried and stored at 4°C before use.

2.3 Synthesis and characterization of ultrasound-activated ULU nanoliposomes

DSPE–PpIX, DSPE-S-C$(CH_3)_2$-S-$PEG_{2k,}$ and DPPC with a mass ratio of 5:25:1 were co-dissolved in 10 ml chloroform. The mixture solution was then evaporated to form a thin film using a rotary evaporator. Next, 20 ml of ultrapure water containing United Kingdom (2 mg) was added to the thin film and stirred at 55°C for 1 h. After the hydration process, the solution was sonicated in ice bath conditions for 60 min. The obtained solutions were then filtered using a 0.22-μm PVDF syringe-driven filter (Millipore, Bedford, United States) and then purified using ultrafiltration (cutoff molecular weight of 50,000 Da) at 5000 rpm three times to remove unloaded drugs. The obtained ULU nanoliposome (urokinase@lipsome, named as ULU) was stored at 4°C before use.

The ULU nanoliposome morphologies were imaged using JEM 2100F transmission electron microscope. The DLS and zeta potential of the obtained ULU nanoliposome were analyzed using the Zetasizer Nano series. UV-vis spectrophotometry was performed to investigate the Encapsulation Efficiency (EE, %) and Loading Efficiency (LE, %) of the United Kingdom (absorbance peak = 282 nm). The secondary structure changes before and after urokinase encapsulation were characterized by circular dichroism (CD). The colloidal stability of the ULU nanoliposome was evaluated using the Zetasizer Nano series. ULU nanoliposome dissolved in 1 × PBS was continuously observed for 7 days, and the corresponding DLS and PDI of the nanoparticles were recorded within 7 days.

2.4 Ultrasound activated release of United Kingdom

Singlet oxygen ($^1O_2$) was tested by ESR spectroscopy, see our previous work for details (Liang et al., 2020; Yang et al., 2021). ULU nanoliposome (25 mg) in 25 ml PBS buffer was irradiated for 0–5 min (1 W cm^{-2}) and placed into a 50 ml flat-bottom centrifuge tube. After reaching the set ultrasonic time point, the solution was transferred to a high-speed centrifuge tube, centrifuged at 13,000 rpm for 10 min, the supernatant was taken to test the UV-Vis spectrum, and the cumulative release was calculated based on the UV-Vis absorption standard curve of urokinase. All assays were conducted three times.

2.5 Hemolysis and cytotoxicity evaluation of the ULU nanoliposomes

Hemolysis experiments were performed according to the previous work (Luo et al., 2013). Pig Pulmonary microvascular endothelial cells (PC-001) were used in the present study. PC-001 cells were cultured in complete DMEM, containing 10% FBS, 100 U mL^{-1} penicillin, and 0.1 mg ml^{-1} streptomycin. PC-001 cells were cultured at 37°C under humidified conditions with a 5% CO_2 supply. PC-001 cells were plated in 96-well plates (5000 cells per well) and cultured overnight

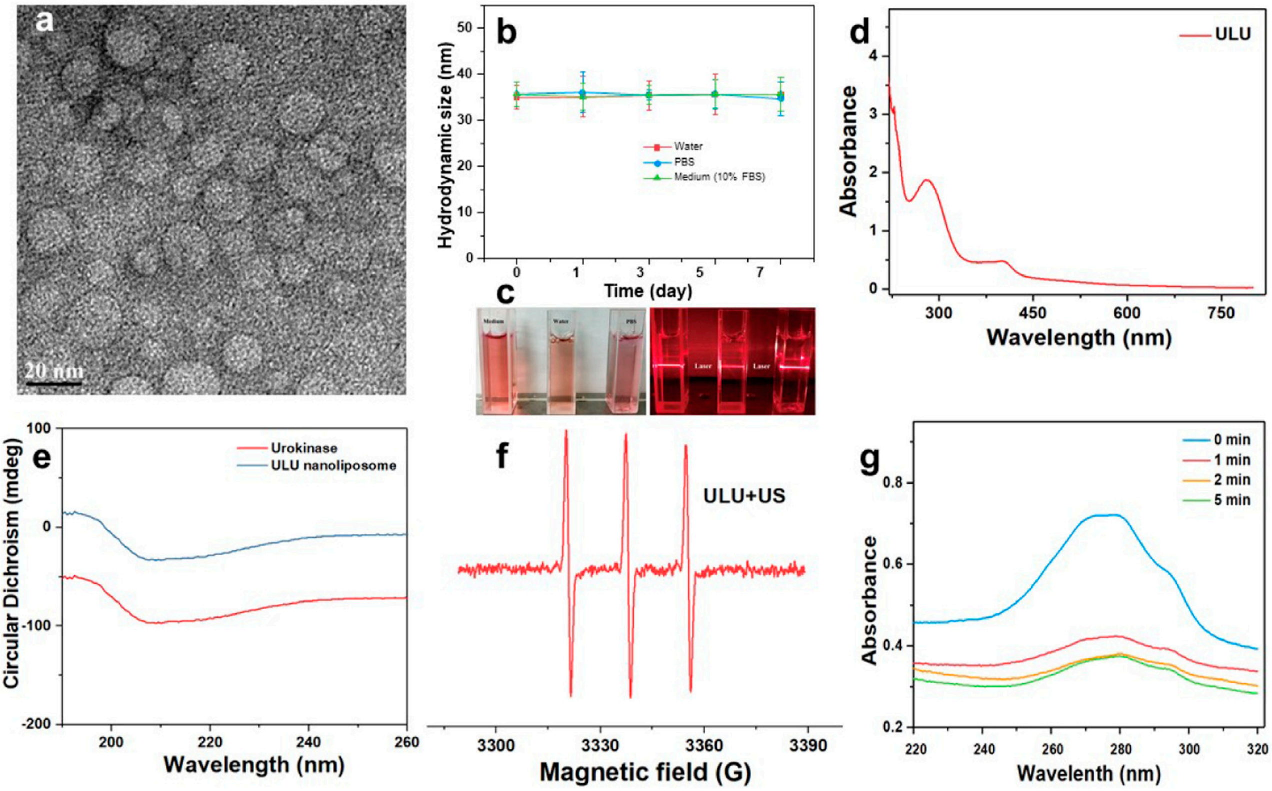

FIGURE 1
Transmission electron microscopy of ULU nanoliposome **(A)**, the hydrated particle size change **(B)**, and digital photographs **(C)** of colloidal stability of ULU nanoliposome dispersed in water, PBS, and cell culture medium (added 10% FBS) within 7 days; the UV-Vis absorption spectra of ULU nanoliposome **(D)**; Circular dichroism chromatogram of urokinase and the prepared ULU nanoliposome **(E)**; ESR spectra of ULU nanoliposome with the ultrasonic irradiation (1.0 W/cm^2, 5 min, **(F)**; UV-Vis absorption spectra of urokinase-containing nanoliposome (ULU) at different time points after ultrasonic stimulation at 1.0 W/cm^2, 5 min **(G)**.

and then co-cultured with ULU at various concentrations (0, 10, 50, 100, 200, and 500 μg ml^{-1}) for 24 h (0, 10, 50, 100, 200, and 500 μg ml^{-1} for 48 h). The cells were then washed three times with PBS and the CCK-8 agents were added to each well (10%). After 2 h coculture, the viabilities of PC-001 cells were measured at 450 nm using a microplate reader.

2.6 *In vivo* ultrasound performance of ULU nanoliposome

All animal experimental procedures were approved by the Ethical Committee of Shanghai 10th People's Hospital. Rabbits with pulmonary embolism were randomly divided into five groups ($n = 3$). Pulmonary imaging was performed using Digital subtraction angiography (DSA) techniques and through a tail vein with indoxyl. The ULU nanoliposomes (urokinase dose of 2,000 units) were *in situ* injected into the pulmonary vein utilizing a jugular vein catheter. Then, the ultrasound was performed on the rabbits in the ultrasound-induced thrombolysis group (1 W/cm^2, 5 min). After treatment, DSA imaging was used again to evaluate the efficiency of thrombolysis after pulmonary embolism.

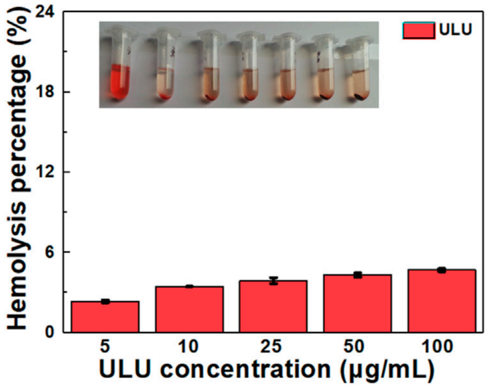

FIGURE 2
Hemolysis rate after 24 h co-culture of ULU nanoliposomes with erythrocytes.

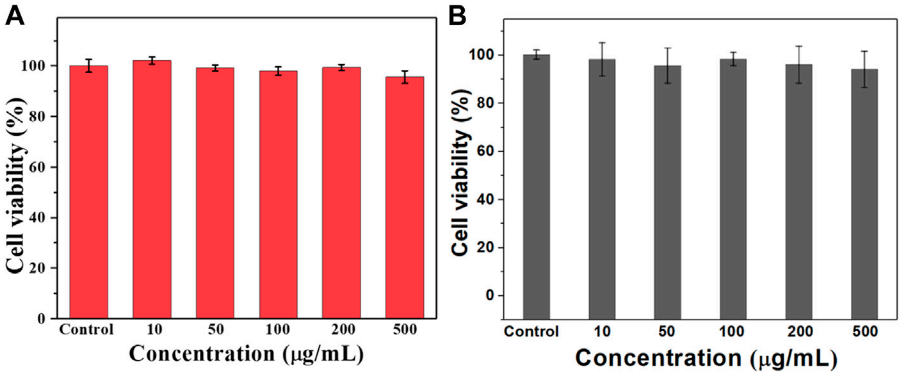

FIGURE 3
CCK8 was used to determine the survival rate of the nanoliposomes after co-culture with vascular endothelial cells for 24 h **(A)** and 48 h **(B)** to evaluate the cytotoxicity of the nanoliposomes.

Blood samples were collected from the auricular vein to test the biochemical and blood routine indexes of rabbits to evaluate the changes in fibrin content before and after treatment.

2.7 *In vivo* biocompatibility assessment of ULU nanoliposome

All animal experimental procedures were approved by the Ethical Committee of Shanghai 10th People's Hospital. The Kunming mice in each group were randomly divided into four groups. Major organs including heart, liver, spleen, lung, and kidney were collected and examined by H&E staining. The long-term biocompatibility of ULU nanoliposome was also assessed in healthy female Kunming mice. The mice in the treated groups were intravenously injected with 20 mg/kg of ULU nanoliposome. On day 0 and various post-injection time points (days 0, 30, 60, and 90), blood samples were examined for routine blood and biochemical analysis ($n = 3$). The corresponding major organs (heart, liver, spleen, lung, and kidney) were also examined by H&E staining at 0 and 90 days.

2.8 Statistical analysis

Data are shown as mean ± standard deviation. One-way analysis of variance (ANOVA) with Tukey's multiple comparisons test was performed to analyze the statistical significance among different groups. Statistical significance was divided as three categories: $^{*}p < 0.05$ $^{**}p < 0.01$, and $^{***}p < 0.001$.

3 Results and discussion

3.1 Synthesis and characterization of ULU

The chemical structures of important fragments DSPE-S-C$(CH_3)_2$-S-PEG$_{2k}$ and DSPE–PpIX of the synthetic ultrasound-responsive nanoliposomes were confirmed by ^{1}H NMR spectroscopy. As shown in Supplementary Figure S1, the characteristic peaks attributed to singlet oxygen cleavage bond and polyethylene glycol -CH_2CH_2- exist in the prepared product of DSPE-S-C$(CH_3)_2$-S-PEG$_{2k}$, indicating that the important fragments of ultrasonic-responsive nanoliposome were successfully synthesized. Sonodynamic-activated ULU was prepared using a film hydration method. In brief, a thin film composed of DSPE–PpIX, DSPE-S-C$(CH_3)_2$-S-PEG$_{2k}$, and DPPC with a feeding mass ratio of 5:25:1 was synthesized and then hydrated with ultrapure water including the United Kingdom. The hydrophilic United Kingdom and hydrophilic were encapsulated into ROS-responsive liposomes through hydrophilic interactions. As shown in the transmission electron microscopy (TEM) images (Figure 1A), ULU was spherical vesicles and showed a uniform size distribution (diameter ≈30 nm). Dynamic light scattering (DLS) revealed that the hydrodynamic size of ULU was approximately 31.3 ± 1.4 nm (SI, Supplementary Table S1). Moreover, the polydispersity indexes (PDI) of ULU were 0.23, suggesting good mono-dispersity of the ULU nanoliposomes (Supplementary Table S1). The zeta potential of ULU was measured at -28.9 mV and showed an elevated surface charge, indicating successful United Kingdom loading. Furthermore, the prepared ULU nanoparticles showed excellent colloidal stability

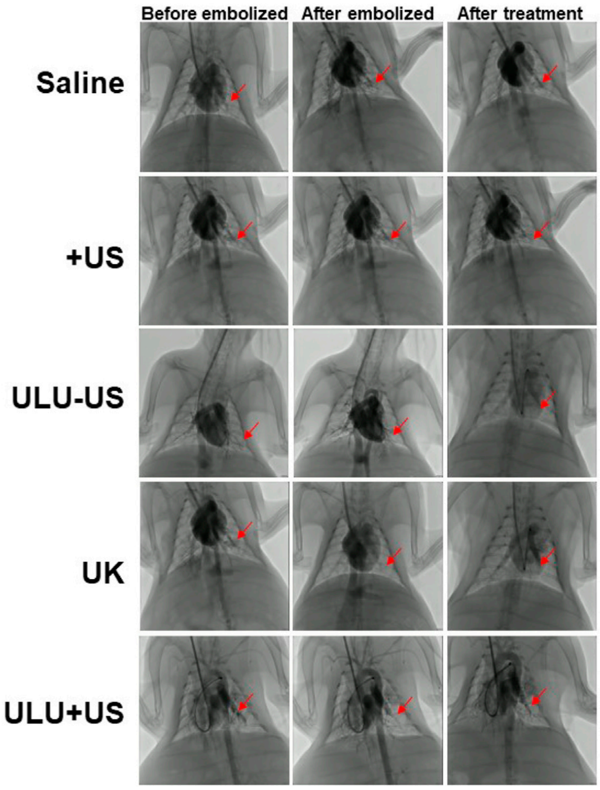

FIGURE 4
Digital subtraction imaging was used to evaluate the effect of pulmonary thrombolysis in rabbits receiving different treatment methods (Saline, US, ULU-US, United Kingdom, ULU + US, among the three groups (ULU-US, United Kingdom, ULU + US) had the same urokinase dose of 2,000 units, red arrows indicate recovery before and after pulmonary embolization and after treatment, *n* = 3).

due to their stable hydrodynamic size and PDI over 7 days (Figures 1B,C). Given the protein properties of urokinase (United Kingdom), we used UV-vis spectrophotometry to qualitatively and quantitatively evaluate whether the nanoliposomes successfully encapsulated urokinase and the amount of encapsulation. As shown in Figure 1D, the characteristic UV absorption peak around 280 nm was attributed to the United Kingdom, indicating that urokinase was successfully encapsulated in nanoliposomes by the thin-film method and ultrasonic self-assembly. Combined with the standard curve of the United Kingdom, the Encapsulation Efficiency (EE) and Loading Efficiency of urokinase in ULU nanoliposome were calculated to be 91.8% and 5.9%, respectively (SI, Supplementary Table S2). The spectra of liposome nanocapsules before and after encapsulation of urokinase were analyzed by infrared spectroscopy (SI, Supplementary Figure S2). The results found that when the nanocapsule ULU is obtained by self-assembly of urokinase and liposome fragments by phacoemulsification method, the infrared spectrum is not only In addition to the characteristic absorption peaks of free urokinase, there are also absorption peaks of liposome fragments, indicating that we successfully encapsulated urokinase in liposome nanocapsules by phacoemulsification.

3.2 Ultrasound-induced drug release performance

Urokinase is essentially a protein, and changes in its secondary structure determine the biological activity of the enzyme. Therefore, we determined whether the biological activity of the enzyme was affected by the changes in the secondary results of urokinase before and after encapsulation by circular dichroism. The results showed that the secondary structure of urokinase did not change significantly before and after encapsulation, suggesting that its biological activity was maintained (Figure 1E).

The ultrasound-activated properties and ultrasound-induced release of United Kingdom from ULU were further investigated. Under conditions of ultrasound (1.0 W/cm^2, 5 min), ULU nanoliposomes generate a large amount of singlet oxygen (Figure 1F), which further cuts the hydrophilic and hydrophobic ends of the improved nanoliposomes through singlet oxygen-sensitive linker. The nanoliposome capsule structure disintegrates and the urokinase encapsulated inside is released. UV-Vis absorption was performed on the supernatant before and after ultrasonic stimulation, combined with the UV absorption standard curve of urokinase, the cumulative release of the United Kingdom from ULU was 67.9% within 5 min (Figure 1G). The underlying mechanism can be explained as follows: Under ultrasonic excitation, protoporphyrins produce reactive oxygen species, which break the sensitive bonds in the liposome, and urokinase is released from the liposome nanospheres, resulting in the on-demand release of United Kingdom.

3.3 Hemolysis and cytotoxicity evaluation

Hemolysis is one of the important indicators to evaluate whether a drug can be administered intravenously. Therefore, we investigated the hemolysis by co-incubating the prepared ULU nanoliposomes with red blood cells. As shown in Figure 2, in the concentration range of 0–100 μg/ml, the hemolysis rate was lower than 5%. The results showed that ULU nanoliposomes have good blood compatibility, combined with *in vitro* ultrasonic stimulation to release urokinase. The results showed that, in the absence of external ultrasound, urokinase would not be released and would not cause hemolysis. Meanwhile, we co-cultured the prepared ULU nanoliposomes with vascular endothelial cells for 24 h and 48 h and tested the cell viability by the CCK8 method (Figures 3A,B). Within the concentration range (0–500 μg/ml),

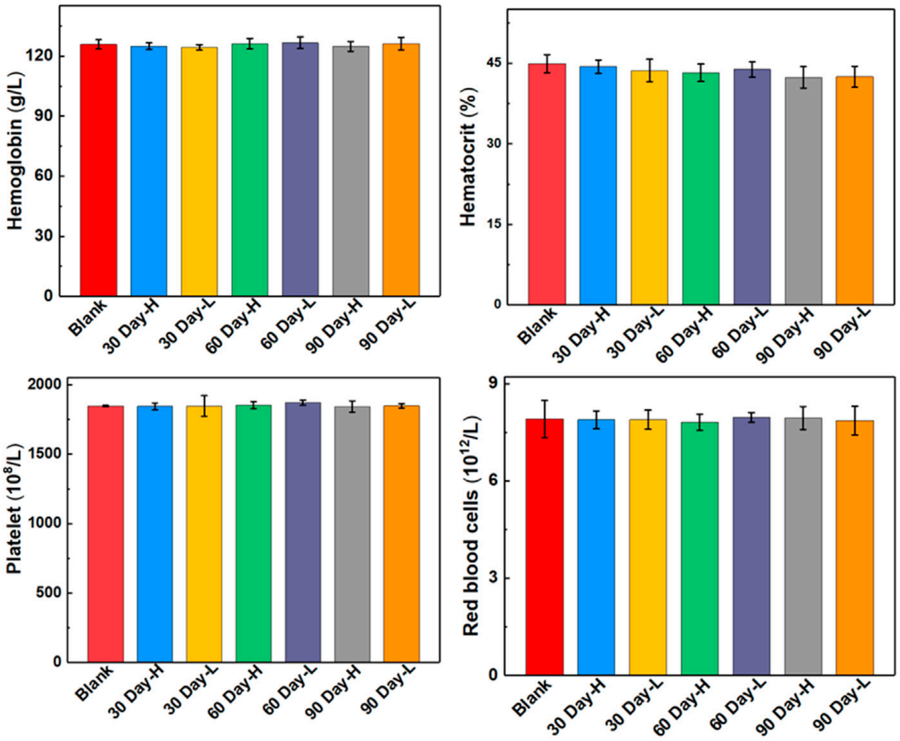

FIGURE 5
Blood routine indexes at different time points after ULU nanoliposome (20 mg/kg, *n* = 3) were injected into the tail vein of healthy mice.

the cell viability remained above 90% even at up to 500 μg/ml, indicating that the nanoliposomes have good cytocompatibility.

3.4 Ultrasound mediated thrombolysis of pulmonary embolism *in vivo*

Rabbits successfully constructed by jugular catheter were treated according to the established treatment regimen. It is can be seen that after a pulmonary embolism, the rabbits were given normal saline and blank liposome capsules without urokinase encapsulation (Figure 4 and Supplementary Figure S3–S7). After the treatment, the digital subtraction image of the lungs showed that the pulmonary embolism still existed, the blood vessels did not recover the blood flow, and the vital signs of the rabbits were gradually weakened and eventually died. However, when urokinase, a clinically used thrombolytic drug, was injected into rabbits with the same dose as urokinase nanoliposomes through the tail vein, and under the stimulation of ultrasound, there was no sign of blood flow recovery in pulmonary embolism within 30 min, and a little blood flow recovery in the lungs after 60 min, with no obvious therapeutic effect. It is worth noting that when the embolized rabbits received the ultrasound-responsive nanoliposome capsules, the blood flow of most of the blood vessels after artificial embolization was restored in the lungs 15 min later, and the blood flow of the originally blocked blood vessels was completely restored 30 min later, and the vital signs of the rabbits returned to the normal level. It is worth noting that we took blood from rabbits receiving different treatments and tested the concentration of fibrinogen in the blood (SI, Supplementary Figure S8). The results showed that when the embolized rabbits received a normal saline placebo, pure ultrasound and pure material treatment, the fibrinogen concentration in the blood was almost unchanged. While there was a slight decrease in blood fibrinogen concentrations when treated with pure urokinase, in contrast, when rabbits received ULU nanoliposomes and ultrasound treatment, blood fibrinogen concentrations decreased significantly. The results showed that it was upon stimulation by ultrasound that urokinase was released from the liposome capsules, which activated thrombolysis, resulting in a dramatic drop in fibrinogen concentrations. The observation of long-term survival showed that the rabbits had no abnormalities within 60 days after treatment, and the blood routine and biochemical structure showed that the rabbits had completely recovered.

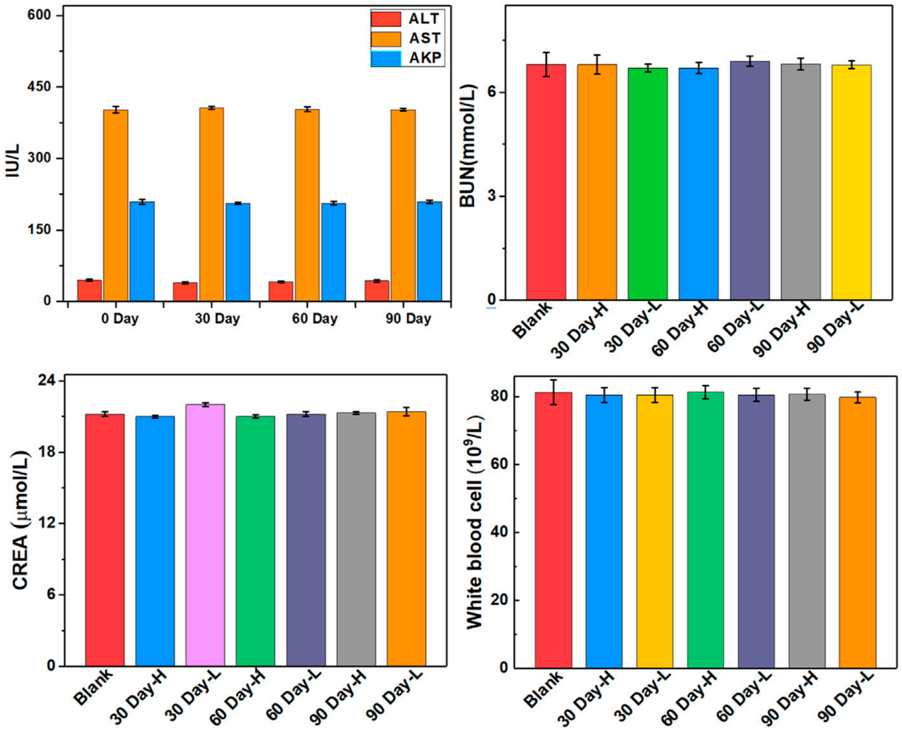

FIGURE 6
Important indicators of liver and kidney function at different time points after ULU nanoliposome (20 mg/kg, *n* = 3) were injected into the tail vein of healthy mice.

3.5 Biocompatibility of ULU nanoparticles *in vivo*

The biocompatibility and biotoxicity of the ULU nanoliposome were evaluated *in vivo*. No obvious behavioral abnormalities or weight loss were observed during the treatment of mice on 0 days and 90 days. Moreover, after treatment, H&E staining images showed that regions with necrosis or apoptosis were rarely detected in the murine major organs, including the heart, liver, spleen, and kidney in the different treatment groups (SI, Supplementary Figure S9). Additionally, analysis of long-term biotoxicity in mice revealed no significant differences in diversely vital blood parameters (Figure 5), and liver and kidney function indexes (Figure 6) among the 0 days, 30 days, 60 days, and 90 days. These results indicated the perfect biocompatibility of ULU nanoparticles for pulmonary embolism thrombolysis *in vivo*.

4 Conclusion

In conclusion, based on the fine chemical synthesis of molecular structure, nanoliposomes with the ultrasound-controlled release of urokinase were engineered and applied to the study of acute pulmonary embolism thrombolysis. The prepared ULU nanoliposomes have good colloid stability, blood compatibility, and cytocompatibility. More importantly, compared with the same dose of free urokinase, it has higher thrombolytic efficiency and safety, providing a good idea for the precise treatment of pulmonary embolism.

Data availability statement

The original contributions presented in the study are included in the article/Supplementary Material, further inquiries can be directed to the corresponding authors.

Ethics statement

The animal study was reviewed and approved by Shanghai General Hospital.

Author contributions

YF and LL contributed equally to this work; experiment design: WZ, SY, and YL; experiments: YF, LL, FL, and HZ; Data analysis: CY, HS, YF, LL, SY, and YL; manuscript writing: CY, HS, YF, WZ, SY, and YL. The final version has been approved by all of the authors.

Funding

This work was funded by the Chongqing Science and Health Collaborated Medical Research Project (2021MSXM157), and the Science and Technology Commission of Shanghai (20DZ2255900).

Conflict of interest

The authors declare that the research was conducted in the absence of any commercial or financial relationships that could be construed as a potential conflict of interest.

Publisher's note

All claims expressed in this article are solely those of the authors and do not necessarily represent those of their affiliated organizations, or those of the publisher, the editors and the reviewers. Any product that may be evaluated in this article, or claim that may be made by its manufacturer, is not guaranteed or endorsed by the publisher.

Supplementary material

The Supplementary Material for this article can be found online at: https://www.frontiersin.org/articles/10.3389/fbioe.2022.923365/full#supplementary-material

References

Abe, K., Kuklina, E. V., Hooper, W. C., and Callaghan, W. M. (2019). Venous thromboembolism as a cause of severe maternal morbidity and mortality in the United States. *Seminars Perinatology* 43, 200–204. doi:10.1053/j.semperi.2019.03.004

Barco, S., Mahmoudpour, S. H., Valerio, L., Klok, F. A., Münzel, T., Middeldorp, S., et al. (2020). Trends in mortality related to pulmonary embolism in the European region, 2000-15: Analysis of vital registration data from the WHO mortality database. *Lancet Respir. Med.* 8, 277–287. doi:10.1016/s2213-2600(19)30354-6

Bolcal, C., Kadan, M., Kubat, E., Erol, G., and Doğancı, S. (2019). Surgical treatment of a left ventricular apical thrombus via robotic surgery. *J. Card. Surg.* 34, 216–218. doi:10.1111/jocs.14000

Chen, H., Liu, L., Ma, A., Yin, T., Chen, Z., Liang, R., et al. (2021). Noninvasively immunogenic sonodynamic therapy with manganese protoporphyrin liposomes against triple-negative breast cancer. *Biomaterials* 269, 120639. doi:10.1016/j.biomaterials.2020.120639

Goldhaber, S. Z., and Bounameaux, H. (2012). Pulmonary embolism and deep vein thrombosis. *Lancet* 379, 1835–1846. doi:10.1016/s0140-6736(11)61904-1

Gong, X., Li, R., Wang, J., Wei, J., Ma, K., Liu, X., et al. (2020). A smart theranostic nanocapsule for spatiotemporally programmable photo-gene therapy. *Angew. Chem. Int. Ed.* 59, 21648–21655. doi:10.1002/anie.202008413

Hayiroglu, M. I., Bozbeyoglu, E., Akyuz, S., Yildirimturk, O., Bozbay, M., Bakhshaliyev, N., et al. (2015). Acute myocardial infarction with concomitant pulmonary embolism as a result of patent foramen ovale. *Am. J. Emerg. Med.* 33, 984. doi:10.1016/j.ajem.2014.12.025

Hu, H., Feng, W., Qian, X., Yu, L., Chen, Y., and Li, Y. (2021). Emerging nanomedicine-enabled/enhanced nanodynamic therapies beyond traditional photodynamics. *Adv. Mat.* 33, 2005062. doi:10.1002/adma.202005062

Huang, W., Goldberg, R. J., Anderson, F. A., Kiefe, C. I., and Spencer, F. A. (2014). Secular trends in occurrence of acute venous thromboembolism: The worcester VTE study (1985-2009). *Am. J. Med.* 127, 829–839. doi:10.1016/j.amjmed.2014.03.041

Izura Gómez, M., Misis Del Campo, M., Puyalto de Pablo, P., and Castaño Duque, C. (2018). Mechanical thrombectomy: An alternative for treating cerebral venous sinus thrombosis. *Emergencias* 30, 123–125.

Kaditis, A. G., and Alexopoulos, E. I. (2021). Pediatric pulmonary embolism: Not as rare as we think. *Pediatr. Pulmonol.* 56, 3089–3092. doi:10.1002/ppul.25609

Konstantinides, S. V., Meyer, G., Becattini, C., Bueno, H., Geersing, G. J., Harjola, V. P., et al. (2019). 2019 ESC Guidelines for the diagnosis and management of acute pulmonary embolism developed in collaboration with the European Respiratory Society (ERS). *Eur. Heart J.* 41, 543–603. doi:10.1093/eurheartj/ehz405

Kostrubiec, M., Łabyk, A., Pedowska-Włoszek, J., Pacho, S., Dzikowska-Diduch, O., Dul, P., et al. (2012). Rapid improvement of renal function in patients with acute pulmonary embolism indicates favorable short term prognosis. *Thromb. Res.* 130, E37–E42. doi:10.1016/j.thromres.2012.05.032

Li, X., Kong, L., Hu, W., Zhang, C., Pich, A., Shi, X., et al. (2022). Safe and efficient 2D molybdenum disulfide platform for cooperative imaging-guided photothermal-selective chemotherapy: A preclinical study. *J. Adv. Res.* 37, 255–266. doi:10.1016/j.jare.2021.08.004

Liang, K., Li, Z., Luo, Y., Zhang, Q., Yin, F., Xu, L., et al. (2020). Intelligent nanocomposites with intrinsic blood-brain-barrier crossing ability designed for highly specific MR imaging and sonodynamic therapy of glioblastoma. *Small* 16, 1906985. doi:10.1002/smll.201906985

Luo, Y., Wang, S., Shen, M., Qi, R., Fang, Y., Guo, R., et al. (2013). Carbon nanotube-incorporated multilayered cellulose acetate nanofibers for tissue engineering applications. *Carbohydr. Polym.* 91, 419–427. doi:10.1016/j.carbpol.2012.08.069

Mazzolai, L., Aboyans, V., Ageno, W., Agnelli, G., Alatri, A., Bauersachs, R., et al. (2018). Diagnosis and management of acute deep vein thrombosis: A joint consensus document from the European society of cardiology working groups of aorta and peripheral vascular diseases and pulmonary circulation and right ventricular function. *Eur. Heart J.* 39, 4208–4218. doi:10.1093/eurheartj/ehx003

Muñiz, A. E. (2012). Thrombolytic therapy for acute stroke in a teenager. *Pediatr. Emerg. Care* 28, 170–173. doi:10.1097/pec.0b013e318244788f

Nandita, K., and Vasistha, R. K. (2008). Pulmonary embolism in medical patients: An autopsy-based study. *Clin. Appl. Thrombosis/Hemostasis* 14, 159–167. doi:10.1177/1076029607308389

Naylor, A. R., Ricco, J. B., de Borst, G. J., Debus, S., de Haro, J., Halliday, A., et al. (2018). *Editor's Choice - Management of Atherosclerotic Carotid and Vertebral Artery Disease: 2017 Clinical Practice Guidelines of the European Society for Vascular Surgery*, 55, 3–81. doi:10.1016/j.ejvs.2017.06.021Editor's choice - management of atherosclerotic carotid and vertebral artery disease: 2017 clinical practice guidelines of the European society for vascular surgery (ESVS)*Eur. J. Vasc. Endovascular Surg.*

Opris, M., Nistor, D., and Sirbu, V. (2017). The choice between a simplified or an elaboratemortality risk prediction tool for patients with acute pulmonary embolism. *Int. J. Cardiol.* 229, 33. doi:10.1016/j.ijcard.2016.11.300

Ronsivalle, S., Faresin, F., Franz, F., Pedon, L., Rettore, C., Zonta, L., et al. (2013). A new management for limb graft occlusion after endovascular aneurysm repair adding a vollmar ring stripper: The unclogging technique. *Ann. Vasc. Surg.* 27, 1216–1222. doi:10.1016/j.avsg.2013.02.018

Shonyela, F. S., Yang, S., Liu, B., and Jiao, J. (2015). Postoperative acute pulmonary embolism following pulmonary resections. *Atcs* 21, 409–417. doi:10.5761/atcs.ra.15-00157

Steglich-Arnholm, H., Holtmannspötter, M., Kondziella, D., Wagner, A., Stavngaard, T., Cronqvist, M. E., et al. (2015). Thrombectomy assisted by carotid stenting in acute ischemic stroke management: Benefits and harms. *J. Neurol.* 262, 2668–2675. doi:10.1007/s00415-015-7895-0

Stein, P. D., Matta, F., Musani, M. H., and Diaczok, B. (2010). Silent pulmonary embolism in patients with deep venous thrombosis: A systematic review. *Am. J. Med.* 123, 426–431. doi:10.1016/j.amjmed.2009.09.037

Taniguchi, S., Fukuda, W., Fukuda, I., Watanabe, K., Saito, Y., Nakamura, M., et al. (2012). Outcome of pulmonary embolectomy for acute pulmonary thromboembolism: Analysis of 32 patients from a multicentre registry in Japan. *Interact. Cardiovasc. Thorac. Surg.* 14, 64–67. doi:10.1093/icvts/ivr018

van der Pol, L. M., Tromeur, C., Bistervels, I. M., Ni Ainle, F., van Bemmel, T., Bertoletti, L., et al. (2019). Pregnancy-adapted years algorithm for diagnosis of suspected pulmonary embolism. *N. Engl. J. Med.* 380, 1139–1149. doi:10.1056/nejmoa1813865

Vedantham, S., Goldhaber, S. Z., Julian, J. A., Kahn, S. R., Jaff, M. R., Cohen, D. J., et al. (2017). Pharmacomechanical catheter-directed thrombolysis for deep-vein thrombosis. *N. Engl. J. Med.* 377, 2240–2252. doi:10.1056/nejmoa1615066

Xu, C., and Pu, K. (2021). Second near-infrared photothermal materials for combinational nanotheranostics. *Chem. Soc. Rev.* 50, 1111–1137. doi:10.1039/d0cs00664e

Xu, M., Zhou, L., Zheng, L., Zhou, Q., Liu, K., Mao, Y., et al. (2021). Sonodynamic therapy-derived multimodal synergistic cancer therapy. *Cancer Lett.* 497, 229–242. doi:10.1016/j.canlet.2020.10.037

Yamada, N., Ota, S., Ying Liu, Y., Crane, M. M., Chang, C. M., Thaker, S., et al. (2010). Risk factors for nonfatal pulmonary embolism in a Japanese population: A hospital-based case-control study. *Angiology* 61, 269–274. doi:10.1177/0003319709335907

Yang, Z., Luo, Y., Hu, Y., Liang, K., He, G., Chen, Q., et al. (2021). Photothermo-promoted nanocatalysis combined with H 2 S-mediated respiration inhibition for efficient cancer therapy. *Adv. Funct. Mat.* 31, 2007991. doi:10.1002/adfm.202007991

frontiers | Frontiers in Bioengineering and Biotechnology

TYPE Mini Review
PUBLISHED 19 August 2022
DOI 10.3389/fbioe.2022.989537

Osteoimmunomodulation role of exosomes derived from immune cells on osseointegration

Yunchao Xiao[1,2†], Yanshu Ding[3†], Jingwen Zhuang[3], Ruoyue Sun[3], Hui Sun[4*] and Long Bai[5*]

[1]College of Materials and Textile Engineering, Jiaxing University, Jiaxing, China, [2]Nanotechnology Research Institute, Jiaxing University, Jiaxing, China, [3]Engineering Research Center for Biomedical Materials of Ministry of Education, College of Materials Science and Engineering, East China University of Science and Technology, Shanghai, China, [4]Department of Orthopaedic Surgery, Shanghai Jiao Tong University Affiliated Sixth People's Hospital, Shanghai, China, [5]Institute of Translational Medicine, Shanghai University, Shanghai, China

Check for updates

OPEN ACCESS

EDITED BY
Xin Li,
DWI—Leibniz-Institut für Interaktive Materialien, Germany

REVIEWED BY
Ying Yang,
University of Michigan, United States
Shige Wang,
University of Shanghai for Science and Technology, China
Juan Wang,
School of Medicine, Shanghai Jiao Tong University, China

*CORRESPONDENCE
Hui Sun,
sunshine20002000@126.com
Long Bai,
bailong2012@163.com

†These authors have contributed equally to this work

SPECIALTY SECTION
This article was submitted to Nanobiotechnology, a section of the journal Frontiers in Bioengineering and Biotechnology

RECEIVED 08 July 2022
ACCEPTED 25 July 2022
PUBLISHED 19 August 2022

CITATION
Xiao Y, Ding Y, Zhuang J, Sun R, Sun H and Bai L (2022), Osteoimmunomodulation role of exosomes derived from immune cells on osseointegration.
Front. Bioeng. Biotechnol. 10:989537.
doi: 10.3389/fbioe.2022.989537

COPYRIGHT
© 2022 Xiao, Ding, Zhuang, Sun, Sun and Bai. This is an open-access article distributed under the terms of the Creative Commons Attribution License (CC BY). The use, distribution or reproduction in other forums is permitted, provided the original author(s) and the copyright owner(s) are credited and that the original publication in this journal is cited, in accordance with accepted academic practice. No use, distribution or reproduction is permitted which does not comply with these terms.

Despite the high success rate of biomedical implants adopted clinically, implant failures caused by aseptic loosening still raise the risk of secondary surgery and a substantial economic burden to patients. Improving the stable combination between the implant and the host bone tissue, achieving fast and high-quality osseointegration can effectively reduce the probability of aseptic loosening. Accumulating studies have shown that the osteoimmunomodulation mediated by immune cells mainly dominated by macrophages plays a pivotal role in osseointegration by releasing active factors to improve the inflammatory microenvironment. However, the mechanism by which osteoimmunomodulation mediates osseointegration remains unclear. Recent studies have revealed that exosomes released by macrophages play a central role in mediating osteoimmunomodulation. The exosomes can be internalized by various cells participating in *de novo* bone formation, such as endothelial cells and osteoblasts, to intervene in the osseointegration robustly. Therefore, macrophage-derived exosomes with multifunctionality are expected to significantly improve the osseointegration microenvironment, which is promising in reducing the occurrence of aseptic loosening. Based on this, this review summarizes recent studies on the effects of exosomes derived from the immune cells on osseointegration, aiming to provide a theoretical foundation for improving the clinical success rate of biomedical implants and achieving high-quality and high-efficiency osseointegration.

KEYWORDS

osseointegration, osteoimmunomodulation, immune cells, exosomes, macrophages

1 Introduction

Biomedical implants for dentistry and orthopedics have been widely used, with more than 1.5 million patients receiving implant replacements annually (Alghamdi et al., 2014). With the development of social productivity and the improvement of medical and health conditions, the average lifespan expectancy has increased significantly, and the global aging trend has become much more apparent. Accordingly, the medical demand for implant replacement will show an accelerated upward trend. However, an 8-years investigation showed a 2–3% failure rate for dental implants (Pjetursson and Heimisdottir, 2018). Implant failure leads to the implementation of a second operation, which prolongs the patient's recovery period and brings patients huge mental pain and inconvenience. Despite the infection around the implant, over half of implant failures are due to aseptic loosening (Barnsley and Barnsley, 2019). Therefore, the ideal implant should avoid aseptic loosening, which can effectively promote osseointegration at the interface after implantation and prolong the service life of the implant.

Osseointegration was initially defined as "the direct structural and functional connection between the bone tissue and the implant surface" (Guglielmotti et al., 2019). In 2012, Zarb et al. redefined osseointegration as "a time-varying healing process that progressively achieves rigid binding of material to bone tissue and stable retention in bone during functional loading at the interface". This definition explains in more detail that osseointegration is a complex process that changes dynamically over time, mainly through four overlapping and synergistic stages: early clot formation, immune response, angiogenesis, and osteogenesis (Bai et al., 2021a). The immune cell-mediated inflammatory response begins immediately, usually within 12 h, and completes within 7 days after implantation. Immune cells include neutrophils, mast cells, and macrophages. Among them, macrophages play a crucial role in the immune response and are the primary effector cells of the inflammatory response (Bai et al., 2021b). Advances in osseointegration research have pinpointed the pivotal role of immune cells, especially macrophages, in manipulating angiogenesis and osteogenesis to achieve a fulfilled bone formation upon the implant surfaces (Bai et al., 2018). However, the underlying mechanism of the cross-talk between immune cells and bone formation-related cells is still unclear.

Exosomes are multivesicular bodies formed by intracellular lysosomal particles secreted by various cells such as bone marrow stem cells and macrophages (Jeppesen et al., 2019). Accumulated studies have depicted that exosomes play pivotal roles in tissue regeneration and multiple disease treatments (De Toro et al., 2015). Recent studies showed that exosomes secreted by immune cells could dominate bone formation through osteoimmunomodulation (Wei et al., 2019). Exosomes exist as a cell-free therapy and have superior advantages that other strategies do not possess, such as smaller size (40–160 nm), long circulatory half-life, low immunogenicity, accessible to cross the blood-brain barrier, easy production and storage, and no tumorigenicity, conferring it as an auspicious choice for regenerative medicine and biomedical treatment (Butler, 2002). However, at the same time, due to the heterogeneity of vesicles and the lack of specific targeting mechanisms, exosomes are often trapped in non-specific tissues, resulting in the lack of targeting ability in the process of regulating osseointegration of exosomes (Lai et al., 2014, Zhang et al., 2021). This review aims to summarize the role of exosomes secreted by multiple immune cells, especially the macrophages, in manipulating *de novo* bone formation and osseointegration; Meanwhile, we overview the effect of surface modification of biomaterials on the functionality of exosomes derived from immune cells.

2 Exosome

2.1 Source and description of exosomes

Exosomes are lipid-bound vesicles secreted by cells into the extracellular fluid. They are also called intraluminal vesicles (ILVS). They are mainly derived from vesicles formed by intracellular lysosomal granules. All cells can secrete exosomes regardless of normal or pathological conditions. They naturally exist in body fluids, including plasma, urine, and semen, which usually have a diameter between 30–150 nm. Specifically, the early cell plasma membrane germinates inward, causing endoderm proteins and other components to be phagocytosed, and in the process, it grows into a polycystic body (MVB). MVB is involved in the endocytosis and transportation of cellular material. Finally, part of the MVB is sent back to the lysosome, and part of the plasma membrane is fused and released into the extracellular fluid, of which exosomes are a part (Doyle and Wang, 2019). Ultracentrifugation is a traditional, efficient and reproducible method for purifying and extracting exosomes, which is suitable for purifying exosomes from cell culture media (Caradec et al., 2014). In their study, Webber et al. found that the use of ultracentrifugation on a sucrose pad was the best method to obtain high-purity exosome fractions suitable for purification of exosomes from cell culture media from urine and serum. The extracted exosomes are of low purity. While some commercial kits are used to isolate and study exosomes for various purposes, the kits are less time-consuming, less technically sensitive and more compatible with a limited number of biological samples compared to UC, and do not Special equipment is required (Helwa et al., 2017). One of the ways to label exosomes is by identifying the presence of proteins secreted by the exosomes, the most common and easiest of which is by immunoblotting, by biomarker exosome fractions compared to total cell lysates However, due to the huge differences in plasma protein concentrations and extremely low levels of other proteins such as cytokines, biomarkers are only used as prognostic indicators. Mass spectrometry is an important tool for assessing the quality of exosomes because of its repeatable and accurate quantification, strong ability to identify signals, and low signal-to-noise ratio (Rifai et al., 2006; Xu et al.,

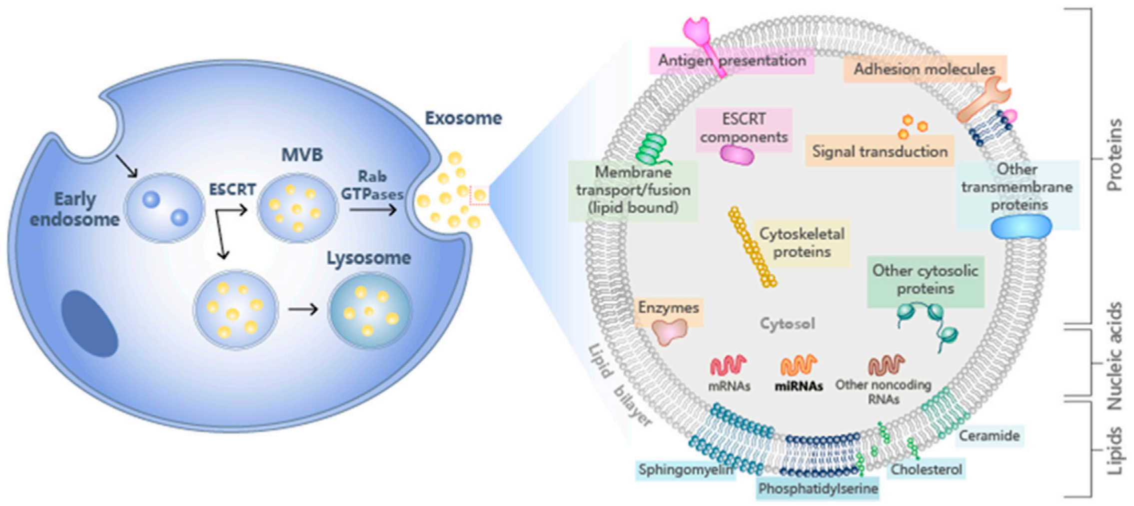

FIGURE 1
Schematic diagram of the composition of exosomes.

2020). The optimal storage temperature for long-term storage of exosomes used in clinical and research is -70°C. For short-term storage, exosome proteins will be degraded above 37°C (Lee et al., 2016).

2.2 Composition and function of exosomes

The contents of exosomes include receptors, transcription factors, enzymes, extracellular matrix proteins, lipids, nucleic acids, and various protein complexes on the surface. The analysis of exosome protein composition indicated that some proteins are common in all exosomes, and some belong to non-specific protein types. Furthermore, the lipid content of exosomes is cell-specific or conservative (Mashouri et al., 2019). The specific behavior of lipids in MVB is mainly determined by the nature of the hydrophobic tail (Stoorvogel et al., 2002). A common feature of different types of exosomes is the expression of their adhesion molecules. Adhesion molecules and adhesion receptor systems participate in various critical cellular processes such as cell growth and differentiation. Types of adhesion receptors on the cell surface are divided into the integrin family, immunoglobulin super protein family, cadherin family, and selectin family (Frenette and Wagner, 1996). Exosomes also contain a unique protein composition, including proteins such as Tsg101 (Guo et al., 2015). Tsg101 is a component of the endosome sorting complex (ESCRT) necessary for the transport mechanism, which plays a direct role in releasing nucleocapsids from the polycystic endosome into the cytoplasm (Luyet et al., 2008). Exosomes are also rich in lipids related to lipid rafts, such as sphingolipids and cholesterol (Wubbolts et al., 2003). Exosomes also contain functional biological enzymes.

The function of exosomes is to eliminate unfavorable biological molecules and play a role in immune surveillance. Exosomes containing microbial components can promote antigen presentation and macrophage activation (Schorey and Bhatnagar, 2008). Recent research has focused on the functionality of exosomes in antigen presentation. Exosomes promote T cell immunity during bacterial infection and are an essential source of extracellular antigens (Smith et al., 2017). Exosomes also play an important role in immune and metabolic regulation (Figure 1).

3 Osseointegration

3.1 The importance of osseointegration

With the continuous development of biomaterials, the emergence of biomedical implants provides an alternative solution for patients with bone injury. The implantation of the implants is divided into two stages. The first stage is the placement of artificial implants into the injured site within the bone tissue. After 3–6 months of bone regeneration, the implant and the alveolar bone complete tight osseointegration. This process requires sufficient bone mass to maintain strong support mechanically. Despite the favorable clinical success rate, the main reasons for implant failure are postoperative infection and aseptic loosening caused by poor osseointegration. Osseointegration is a sophisticated process that involves blood clots formation, the immune response of

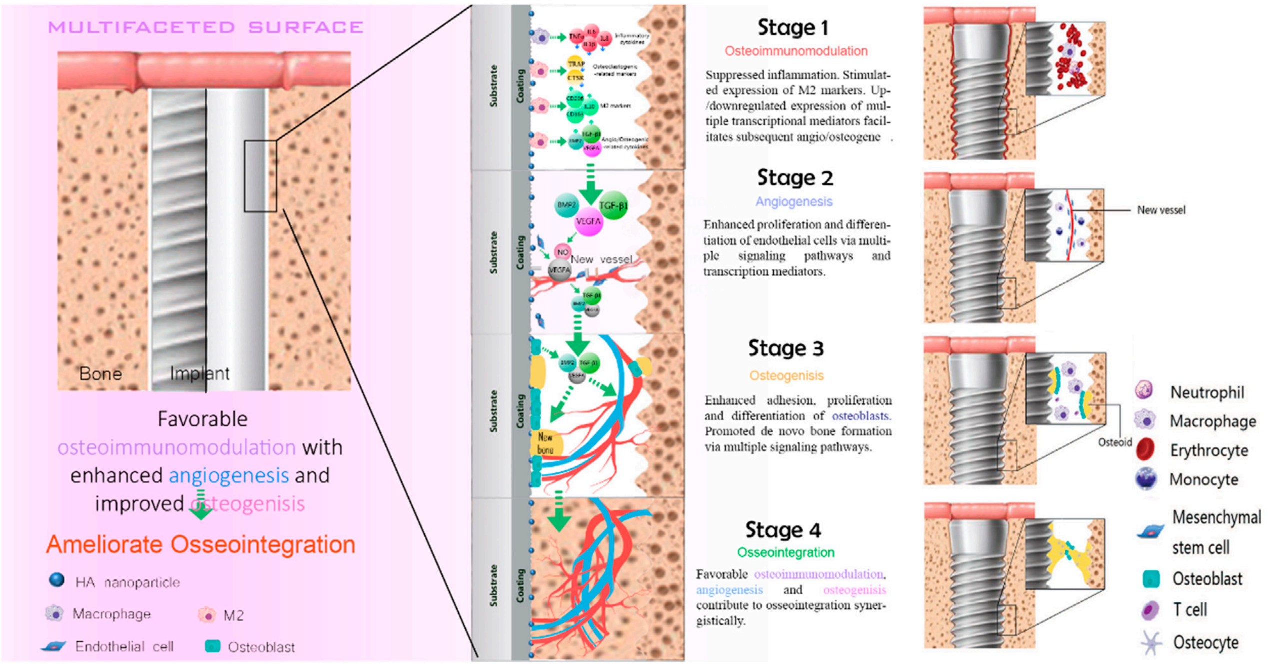

FIGURE 2
Schematic diagram of osseointegration.

immune cells, angiogenesis of endothelial cells, and new bone formation of the bone-related cells (Figure 2).

3.2 Early blood clot formation

The implantation of the implant will cause a certain degree of surgical damage to the blood vessels around the implant. This process usually lasts from a few minutes to a few hours. Blood will directly contact the implant, and then plasma proteins will be adsorbed on the implant's surface. Platelets promote hemostasis through activation, adhesion, and aggregation (Periayah et al., 2014). Platelets are activated at the interface, transforming the main platelet integrin αvβ3 from resting to the active conformation. The activated integrin continues interacting with the platelets (Terheyden et al., 2012). Phase interaction can lead to further activation of platelets. Activated platelets can mediate the expression of GPIIb/IIIa (or integrin αIIbβ3), glycoprotein-1 (TSP-1), and P-selectin (Agarwal and García, 2015). αIIbβ3 mediates platelet aggregation, forming thrombus, blocking blood vessel leakage, and at the same time binding to fibrin to generate more outward signals, leading to further platelet activation (Terheyden et al., 2012; Agarwal and García, 2015). TSP-1, thrombospondin-1, contributes to the activation of TGF-β1, a transforming growth factor. TGF-β1 plays an essential role in angiogenesis and tissue fibrosis (Ahamed et al., 2009). TSP-1 can induce platelet aggregation (Losic et al., 2015). The interaction between p-selectin and the ligand stabilizes the initial interaction of GP IIb/IIIa-fibrinogen, thereby forming numerous stable platelet aggregates (Berger et al., 1998). The expression of the above three signal molecules will cause local thrombin to increase (Guihard et al., 2015). Thrombin can convert fibrinogen into insoluble fibrin clots (Colnot et al., 2007).

3.3 Immune response

After the blood clot forms, the immune response starts immediately. The immunization process begins about 12 h after surgery and lasts 7 days. This process is mediated by immune cells residing in the bone marrow, including dendritic cells, T cells, B cells, macrophages, neutrophils, and mast cells. In the early stage, the inflammatory response is mediated by neutrophils. Neutrophils kill bacteria through reactive free radicals (oxygen-free radicals and hydroxyl radicals, chlorine-free radicals, and hypochlorite), and because this method is non-specific, It may also lead to the loss of surrounding healthy tissue. At the same time, it also secretes digestive enzymes, further aggravating the damage to adjacent tissues. Early period inflammation plays a decisive role in the future development of the immune defenses (Marchi et al., 2013). Neutrophils are in the terminal differentiation stage and have a short life span and will eventually be replaced by macrophages and lymphocytes. There is a special kind of macrophages in bone tissue called bone macrophages. Cytokines secreted by macrophages, such as BMP-2, TNF-α, and OSM, can regulate bone formation (Ferrarelli, 2013). At the same time, macrophages have multiple types, among which macrophages that are not activated are called the M0 type. After activation and differentiation, M1 and M2 are two phenotypes (Guastaldi et al., 2013). IL-6, IL-1β, and TNF-α expressed by M1 macrophages can promote inflammation, while IL-10 and CD206 expressed by M2 macrophages can inhibit inflammation (Chernousova and Epple, 2013). In addition, M2 macrophages can also manipulate a favorable immune microenvironment through cell growth factors such as BMP-2 and TNF-α (Marchi et al., 2013).

3.4 Angiogenesis

Angiogenesis at the bone-implant interface is considered a prerequisite for osseointegration. The process is also initiated within 24 h, accompanied by the immune response, which refers to the production process of new capillaries, including two forms of blood vessel formation and angiogenesis. Angiogenesis is the migration and aggregation of angioblasts (including progenitor cells of endothelial cells and blood cells) to a specific site to form the first batch of primitive blood vessels. Then new blood vessels are generated through a series of processes such as EC sprouting, migration, multiplication, vascular anastomosis, and pruning (Sivaraj and Adams, 2016). Angiogenesis is a key process that supports new bone formation in osseointegration. It also plays a crucial role in fracture repair and healing. Changes in local blood vessels are also closely related to many bone diseases such as osteoporosis (Brammer et al., 2012). Studies have shown that hypoxia and some growth factors are the main signals that drive angiogenesis in bone. These signals not only affect the angiogenesis process but also affect the subsequent osteogenesis process. The primary regulator of VEGFA in angiogenesis is produced and secreted by hypertrophic chondrocytes (Brammer et al., 2012). VEGFA can induce endothelial cell migration and proliferation by inducing its receptor VEGFR2. In addition, VEGFA isoforms can activate the β-catenin signaling pathway to promote angiogenesis and bone formation in bone tissue.

3.5 New bone formation

The formation of new bone is accompanied by angiogenesis. Osteoblasts and osteoclasts are the primary effector cells in the process of osteogenesis. There will be bone morphogenetic protein (BMP) in the wound at first. After the implant has initial stability, it will rub against the primary bone and be fixed in the damaged site. The amount of contact and the strength are closely related to the bone density of the host bone tissue. One week after implantation, the new bone is connected with the primary bone to form a secondary bone contact, and the first piece of braided bone is produced (Terheyden et al., 2012). The osteogenic process is closely related to the communication and cooperation between osteoblasts and osteoclasts. Osteoclastic bone resorption allows TGF-β and BMP to be released from the cell matrix, activating more osteoblasts to secrete the growth factors (Matsuo and Irie, 2008). Osteoblasts secrete the collagen matrix, which then rapidly mineralizes. Subsequently, the osteoclasts remove the braided bone and replace it with the layered bone. Consequently, the implant's surface is covered by mature layers of bone, and the osseointegration is completed immediately (Hoppe et al., 2011).

3.6 The importance of immune response in osseointegration

Since the implant is a foreign body, implantation will inevitably bring about an inflammation-driven process on the implant's surface and its vicinity. This process is manipulated by immune cells, and the early immune microenvironment determines the result of osseointegration (Bai et al., 2018). The immune response can affect bone formation by modulating the functionality of osteoblasts. That is, the immune system and the skeletal system are inextricably linked. The immune system can regulate bone tissue repair and regeneration through osteoimmunomodulation.

4 The role of immune cells derived exosomes in osseointegration

Wei et al. discovered that titanium nanotube implants loaded macrophage-derived exosomes greatly improved the production of ALP and BMP-2 protein of earl osteoblast. The combination of exosomes released from macrophages can enhance bone formation. Exogenous miR-5106 from M2 macrophages can stimulate bone marrow stem cells to differentiate into osteoblasts. Exosomes enhanced the proliferation of MC3T3-E1 cells compared to the control group in a study evaluating the influence of exosomes on the osteogenic differentiation of MC3T3-E1 cells. Exosomes also induce the expression of cellular type I collagen (present in bones, accounting for more than 90% of bone organic matter) and Runx2, which further facilitate bone formation (Komori, 2010). Moreover, exosomes can increase the adhesion and proliferation of bone marrow mesenchymal stem cells, and immobilized exosomes can increase the expression of the cell-derived factor (SDF-1) gene (Wang et al., 2020). Briefly, exosomes play a vital function in the body's immune system (Zhang et al., 2021).

4.1 Neutrophils and mast cell

Neutrophils are the most abundant white blood cells in the blood circulation and are also one of the first immune cells recruited around the implant. Neutrophils are derived from pluripotent stem cells in the bone marrow. After differentiation and development in the bone marrow, neutrophils' immunity is immediately innate. If the implant's surface is infected, IL-8 cytokines related to inflammation will respond and play an essential role in the activation of neutrophils. After being recruited around the implant, the first role played by neutrophils is phagocytosis, which can swallow part of bone debris and microorganisms. Subsequently, phagocytosis triggers the production of effective biocides such as reactive oxygen species such as hydrogen peroxide and superoxide free radicals. Neutrophils are the first and most important line for defending against microbial invasion. Mast cells are also derived from pluripotent bone marrow-derived stem cells. Mast cells can express various surface receptors, prompting them to cooperate with other immune cells to complete the immune process. At the same time, mast cells can produce numerous pro-inflammatory cytokines to affect cell recruitment and promote immunity (Mekori, 2004).

Neutrophil-derived exosomes are composed of a variety of proteins and RNAs. Under the stimulation of neutrophil exosomes, the acellular glycoprotein TSP-1 protein, which is related to blood clot formation and angiogenesis, is strongly expressed. The TSP-1 protein mainly exists in the platelet alpha granules, and the effect of TSP-1 on platelets is still unclear. However, studies have shown that TSP-1 plays a role in the platelet-endothelial interaction. The cAMP regulatory pathway has been learned to regulate platelet function at the injury site. Studies have shown that TSP-1 does not directly affect the blood clot formation process by activating platelets directly, but indirectly affects coagulation by reducing platelet inhibitors. TSP-1 triggers CD36-dependent signals to reduce the sensitivity of platelets to PGE-1 stimulated by endothelial-derived mediators, thereby weakening their ability to inhibit platelets (Roberts et al., 2010).

The contribution of mast cell exosomes is manifested in the transfer of molecules between cells, which promotes the communication between molecules. The exosomes secreted by mast cells not only affect the process of osseointegration through the components of the exosomes themselves but also have close connections with a variety of cell types. Mast cell-derived exosomes can activate B and T lymphocytes (Skokos et al., 2001). Mast cells are located close to blood vessels and assemble into piles, contributing to the secretion of clotting factors during inflammation, thus playing an immunological role. After activation, mast cells-derived exosomes induce PA1-1 expression in endothelial cells by the prothrombinase complex (Al-Nedawi et al., 2005).

TABLE 1 Composition and function of macrophage exosomes.

Type	Name	Function
mRNA	miR-222	Osteogenesis,anti-angiogenesis
mRNA	miR-223	Immune process
mRNA	miR-155	Endothelial cell function
mRNA	mmu-circ-000359	M1-M2

4.2 Macrophage

Macrophages are immune cells differentiated from hematopoietic stem cells. The cells that reside in blood vessels are called monocytes. Macrophages immigrate outside blood vessels and participate in innate immunity in vertebrates through phagocytosis to eliminate pathogens. Compared with Neutrophils, which live only a few months, the lifespan of macrophages can range from several months to several years. Macrophages not only have a phagocytic effect but are also responsible for the clearance of neutrophils after apoptosis. Macrophages that exist in bone tissue are called bone macrophages.

The exosomes derived from macrophages contain many tiny mRNA and micro RNA. mRNA is a type of endogenous, small molecule, and non-coding RNA that can bind to target genes, control the expression of target genes in reverse, regulate the production of cytokines, and affect cell functions. At the same time, mRNA itself also has specific functions as listed (Table 1)

mRNA is critical in the differentiation of macrophages into the M2 type. LPS may trigger the production of M1 macrophage markers, but when mmu-circ-0001359 exosomes were added, the expression of M1 macrophages was considerably decreased, whereas M2 macrophages were significantly elevated. As a result, when activated by LPS, mmu-circ-0001359 can enhance the transition of M1 macrophages to M2 macrophages. Through luciferase labeling and analysis to explore the mechanism of microRNA affecting the phenotype of macrophages, it is found that both FoxO1 and miR-183–5P are the targets of mmu-circ-0001359 (Shang et al., 2020). FoxO1 can be used as a regulator to affect the phenotype of macrophages. miR-5p controls the NF-κB signaling pathway in M1 macrophages via the targeted gene PPP2CA and stimulates the production of pro-inflammatory cytokines IL-1, IL-6, and TNF-α (Guo et al., 2020).

Exosomes derived from macrophages can promote macrophages' activation and regulate cytokine production *in vitro*. Due to the increased demand for cell metabolism during the inflammatory reaction and the reduction of cell metabolic substrates, it is easy to cause tissue cell hypoxia (Eltzschig and Carmeliet, 2011). Under hypoxia/serum deprivation h/SD conditions, BMSC activity decreases, and apoptosis of BMSCs increases. Meanwhile, under h/SD conditions, exosomes derived from M1 macrophages can be

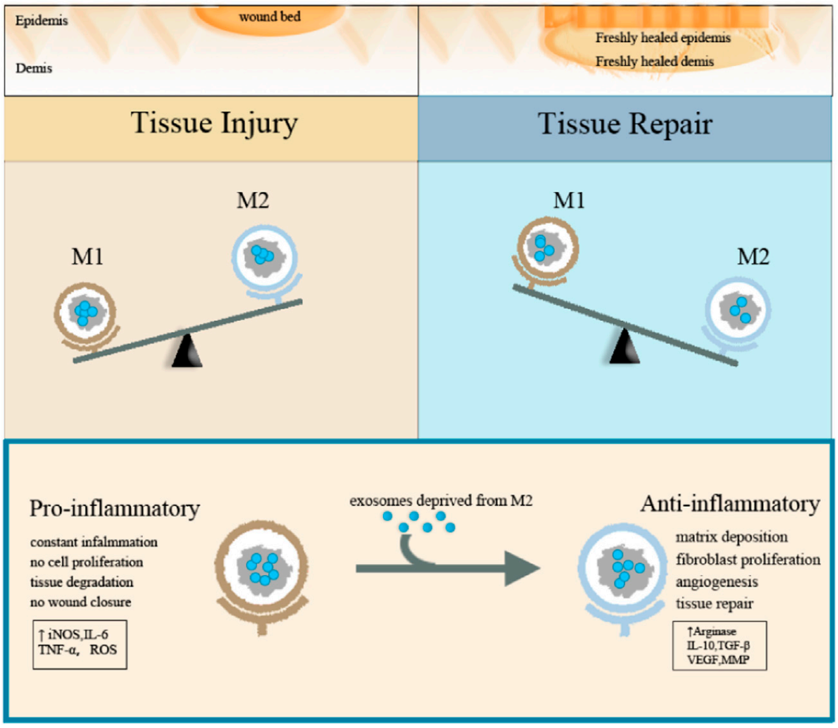

FIGURE 3
Schematic diagram of the function of macrophage exosomes.

released to bone marrow mesenchymal stem cells. miR-222 in the exosomes induces bone marrow mesenchymal stem cell apoptosis, thereby regulating bone formation (Qi et al., 2021). miR-222 also plays an important role in angiogenesis and is the most expressed gene in endothelial cells (Suárez et al., 2007). miR-222 is highly expressed in EC and VSMC. miR-222 inhibits endothelial cell migration, proliferation, and angiogenesis *in vitro* by targeting the stem cell factor receptor c-Kit and indirectly controlling the production of nitric oxide synthase. Two enzymes, Dicer and Drosha, mediate two processing routes that generate mRNA. miR-222 can act on c-Kit and e-NOS, two important pro-angiogenic regulators. Overexpression of miR-222 can indirectly reduce the expression of nitric oxide synthase. This affects endothelial cell functions, including inhibition of angiogenesis and wound healing. However, miR-222 can also promote blood vessel growth by reducing the expression of c-Kit in hematopoietic progenitor cells (Kuehbacher et al., 2008).

miR-223 is also enriched in exosomes produced by macrophages under hypoxic conditions (Krzywinska and Stockmann, 2018). The hypoxia response is regulated by the hypoxia-inducible factor HIF and the HIF signaling pathway, which plays an important role in the recruitment of immune cells (Zhu et al., 2019). miR-223 induces the production of more exosomes and locally activates the immune systems. In the inflammatory phase, the production and release of exosomes are abundant. As an innate immune regulatory factor, miR-223 can promote the differentiation of granulocytes and inhibit the differentiation of macrophages. The expression of miR-223 is highest in the bone marrow cavity, and it plays an important role in the differentiation of granulocytes and macrophages in the differentiation of bone marrow. miR-223 is a negative regulator of neutrophil activation and plays an important role in the regulation of neutrophil function. Overexpression of miR-223 will reduce the activity of the pyrin domain of the NLR family by directly targeting NLRP3, thereby inhibiting NLRP3-dependent production of IL-1β. Neutrophils are the key mediator of MTD-induced ALI, and miR-223 can inhibit the inflammatory activity of NLRP3 by inhibiting the number of Ly6G$^+$ neutrophils. Increased levels of miR-223 inhibit the expression of APAP-induced liver injury target gene IKK-α and inhibit the TLR-NF-κB inflammatory pathway. In addition, miR-223 can promote the polarization of macrophages to the anti-inflammatory M2 type by directly targeting Pknox1. LPS can reduce the expression of miR-223 through TLR4 and TLR3 activation. Meanwhile, an increase in the protein level of the STAT3 gene in the target gene of miR 223 leads to a selective increase in the IL-6 gene and the IL-1β gene, further increasing the inflammatory reaction. The IL-6 canonical signal pathway regulates the decline of miR-223, which leads to the increase of Ras homologous gene family and

Rho-B expression, induces the activation of NF-κB and MAPK signal pathways, and promotes TNF-α, IL-6, and IL-1β stimulated by LPS. In addition, miR-223 can also cause changes in the expression level of NLRP3 and inhibit the response of IL-1β to LPS stimulation (Yuan et al., 2018).

Macrophage exosomes can guide macrophage activation and transformation by driving the reprogramming of macrophages. Exosomes deprived of M2 macrophages can guide M1 macrophages to reprogram into M2 macrophages. INEOS is a typical M1 marker, while Arg-1 is a typical M2 marker. After treatment with exosomes derived from M2 macrophage, the expression of NOS (nitric oxide synthase) and arginine were significantly reduced and increased, respectively, while the results were opposite after treatment with exosomes derived from M1 macrophage. The western blot method also proved the change in the expression pattern of exosomes deprived of macrophage-specific markers. The experiment also proved that after treatment with exosomes derived from M2 macrophage, the local switching of exosomes deprived of M1 macrophage successfully promoted the re-epithelialization of exosomes deprived of M2 macrophage (Kim et al., 2019). Both forms of exosomes reduced the expression of the inflammatory cytokines such as IL-1β and TNF-α when compared to natural bone marrow macrophages treated with control PBS.

Exosomes derived from macrophages can create a favorable immune microenvironment. The major histocompatibility complex molecule and the costimulatory molecule CD86 are present on the surface of exosomes, which may enhance the immune response. Exosomes deprived of macrophages also contain a transmembrane protein lysosomal-associated membrane protein 2 (LAMP 2) and a cytosolic protein B actin, which is often detected in exosomes (Bouchareychas et al., 2020). Previous studies have shown that exosomes infected with inflammation may induce antigen-specific T cell responses. Exosomes from infected cells induce the expression of IFN-γ in $CD8^+$ and $CD4^+$ T cells, and CD69 expression is enhanced, reflecting the ability of exosomes to act as antigens to stimulate these two T cells populations.

Since macrophages can promote the angiogenesis process of endothelial cells, the entire macrophage population is defined as the pro-angiogenic cell population (Novoselova et al., 2015). After the inflammatory period begins, the immune microenvironment changes, which stimulates the polarization of macrophages (Zhang et al., 2017). Due to ischemia sexual and hypoxic stress, a large number of chemokines and pro-inflammatory cytokines are produced (including interferon IFN-γ, bacterial lipopolysaccharide (LPS), interleukin (IL)-1β, and tumor necrosis factor-α (TNF-α)), induces polarization of M1 macrophages. miR-155 is a regulator of M1 macrophage differentiation and one of the miRNAs with high content of M1 macrophages (Ortega et al., 2015). M1 type macrophage exosomes can transfer miR-155 into endothelial cells, and miR-155 can promote plasma soluble intercellular adhesion molecule-1 (SICAM -1) and soluble vascular cells by inhibiting the Akt-Enos pathway signaling pathway. miR-155 also targets the RAC1-PAK2 signaling pathway. Both RAC1 and PAK2 are proteins involved in angiogenesis. They control cell migration and cell-cell connection in endothelial cells, thereby regulating vascular permeability.

Macrophages and endothelial cells can establish contact through the cross-talk of exosomes. The communication process between macrophages and endothelial cells is crucial to the immune process and angiogenesis. Macrophage exosomes control the migration process of endothelial cells and then control the transport of integrins. The transport process of integrins includes internalization, circulation, and lysosomal degradation and mainly acts on connecting cells and neighboring cells or cells and their extracellular matrix. Macrophage exosomes induce integrin β1 lysosomal degradation and internalization and meanwhile promote integrin β1 ubiquitination and inhibiting the activation of the MEK/ERK pathway. The signaling pathway responds to extracellular stimuli and converts the signal into a cellular process by extracellular binding ligands to specific transmembrane receptors. The MEK/ERK signaling pathway is mainly responsible for regulating the phosphorylation sites of activity. Integrin β1 accumulates in the perinuclear area and no longer returns to the plasma membrane (Raman and Cobb, 2003; Shaul and Seger, 2007; Lee et al., 2014; Li et al., 2022). At the same time, integrin β3 is not affected by the action of the exosome.

M1 type macrophage exosomes can transmit pro-inflammatory signals and establish a local immune microenvironment. M1-type macrophages can enter the lymph nodes and are taken up by macrophages and dendritic cells. Exosomes deprived of M1 macrophages will induce macrophages to produce high levels of pro-inflammatory cytokines such as IL-6, IL-12, IFN-γ, TNF-α, and proteases, while exosomes deprived of M2 macrophages will induce macrophages to produce M2 phenotypes with low IL-6, low TNF-α, low IL-12, and high IL-4 and IL-10 (Figure 3).

Exosomes derived from macrophages significantly impact the proliferation and differentiation of mesenchymal stem cells. The exosomes produced by M1 macrophages promote the proliferation, osteogenic and adipogenic differentiation of bone marrow mesenchymal stem cells, and the exosomes produced by M2 macrophages can significantly boost the osteogenic differentiation of mesenchymal stem cells. miR-5106 is abundantly expressed in M2 macrophage exosomes. miR-5106 induced more obvious alkaline phosphatase activity. Moreover, exosomes derived from M2 macrophages have increased bone formation-related genes (ALP, osteopontin, RunX2, BMP-2, and BMP-7) (Chen et al., 2020). The three types of macrophage exosomes, M0, M1, and M2, all have inhibitory effects on cartilage differentiation (Bouchareychas et al., 2020; Xia et al., 2020).

4.3 T cell and B cell

Lymphocytes are divided into T lymphocytes, B lymphocytes, and natural killer cells (NK cells). They are the main cell group that constitutes the body's immune system and participate in body immunity and humoral immunity. T lymphocytes are made in the bone marrow and mature in the thymus, whereas B lymphocytes are synthesized in the bone marrow and mature in the thymus. T cells and B lymphocytes proliferate in the thymus and are then distributed to the immunological organs and tissues throughout the body via lymphatic and blood circulation to perform an immune function. (Skapenko et al., 2005; Smith-Garvin et al., 2009). Exosomes derived from T cells can regulate the internalization of T cells and endothelial cells in a CD47-dependent manner (Kaur et al., 2014).

4.4 NK-DC cell

Both NK cells and dendritic cells (DC) are two important components of innate immunity. NK cells are derived from bone marrow and have strong killing and immunity. Dendritic cells are formed as a result of the division of hematopoietic stem cells. NK cells mainly produce immune function through cytotoxicity and the secretion of cytokines. The cytotoxic activity is enhanced, and they express killer immunoglobulin-like receptors (CD16 and KIRS) and perforin. Factors are secreted in large quantities, expressing low levels of perforin and CD16 (Ferlazzo and Morandi, 2014). Dendritic cells are produced in large quantities, and dendritic cells are antigen-presenting cells that activate adaptive immune lymphocytes by identifying pathogens and sending pathogen information to the acquired immune system (Cooper et al., 2004). NK-DC interaction will lead to the maturation, activation, and cytokine production of both (Thomas and Yang, 2016).

Unlike other immune cells, exosomes produced by NK cells are in both resting and active states. These exosomes can express typical NK markers (CD56) when NK cells are activated and immune killer proteins (Fas-L and perforin) when NK cells are at rest status (Jiang et al., 2021). It is reported that NK cell exosomes have typical exosome proteins, such as Rab5b and MHC-I, but lack CD4 and CD8. NK cell-derived exosomes are effective for activated immune cells, which have considerable cytolytic activity and have no effect on resting immune cells (Lugini et al., 2012). Exosomes derived from NK cells under hypoxia contain higher levels of toxic proteins Fas-L, perforin, and granzyme B, and its cytotoxicity is significantly higher than that under normoxia. Meanwhile, hypoxia increases the production of exosomes (Jiang et al., 2021). DC cells exosome contain many proteins and antigens necessary to produce a robust immune response, such as MHC class Ⅰ, class Ⅱ, CD1, heat shock protein 70–90, CD9, CD63, CD81, CD11b, and CD54. Exosomes produced by DC cells activate immature CD4^{+} T cells through an indirect pathway (Giri and Schorey, 2008). CD4^{+} T plays an important role in assisting B cells to produce antibodies in immune protection, inducing macrophages to produce higher microbicidal activity, recruiting immune cells to inflammation sites and producing cytokines and chemokines, and coordinating the entire immune response (Zhu and Paul, 2008).

5 Outlook

As newly discovered in the past 30 years, exosomes have yet to be widely developed in terms of their functions and how they can be applied to clinical diagnosis, while the actual application process is still in its infancy. Since the average size of exosomes is less than 100 nm, the specific morphological structure cannot be displayed. It is unclear what happens when individual exosomes bind to the surface of recipient cells. However, as the practical resolving power of a microscope, lenses continue to develop and flow cytometry techniques develop, such analyses will be gradually practiced in the future. The rich composition of exosomes, special structural and morphological features, and distinct mechanisms of action are prerequisites for their role in immune responses and the promotion of intercellular communication. The role of immune cell exosomes in the four stages of osseointegration, especially the immune stage, has been confirmed by numerous studies, but whether the surface properties of different materials applied to implants affect the composition and function of immune cells exosomes has not yet been established clear, which will provide valuable guidance for improving the osseointegration.

6 Conclusion

Poor osseointegration at the implant interface due to the aspetic loosening will eventually result in implant failure, and a second surgery is required. Osseointegration is an integrative field in which the skeletal and immune systems interact intimately, with immune cells and their secreted exosomes functioning at all stages. The exosomes secreted by immune cells have unique immune regulation capabilities. After the hemostasis process, the immune response starts immediately, and immune cells are recruited to the area of inflammation. Inflammation will promote immune cell exosomes to release the inflammatory cytokine IL-8. In addition, related to inflammation, it can regulate the phenotype of macrophages by regulating mRNAs and proteins, thereby affecting the stage of immune inflammation, mediating intercellular communication, stimulating target cells, promoting antigen presentation, transmitting pathogens, and regulating immune responses. Additionally, the exosomes derived from immune cells, especially the macrophages, play a pivotal role in angiogenesis and osteogenesis. Moreover, macrophages can promote angiogenesis and osteogenesis by shaping the immune microenvironment with anti-inflammatory exosomes derived from M2 macrophages. Since immune cell exosomes are involved in the four stages of osseointegration, functionalized implants can be designed to target immune cell exosomes to regulate the process of osseointegration, which might be an effective way to avoid the aseptic loosening and improve the success of implantation.

Author contributions

YX and YD drafted the manuscript. H-JH did the experiments and performed the analysis. JZ, RS, and HS assisted in preparing the manuscript. HS and LB designed the framework of the review and critically revised the manuscript. All authors contributed to the article and approved the submitted version.

Funding

This work was jointly supported by the Natural Science Foundation of Zhejiang Province (No. LQ22C100002), the National Natural Science Foundation of China (81901898), and the China Postdoctoral Science Foundation (2019M661404, 2020T130192).

Conflict of interest

The authors declare that the research was conducted in the absence of any commercial or financial relationships that could be construed as a potential conflict of interest.

Publisher's note

All claims expressed in this article are solely those of the authors and do not necessarily represent those of their affiliated organizations, or those of the publisher, the editors and the reviewers. Any product that may be evaluated in this article, or claim that may be made by its manufacturer, is not guaranteed or endorsed by the publisher.

References

Agarwal, R., and García, A. J. (2015). Biomaterial strategies for engineering implants for enhanced osseointegration and bone repair. *Adv. Drug Deliv. Rev.* 94, 53–62. doi:10.1016/j.addr.2015.03.013

Ahamed, J., Janczak, C. A., Wittkowski, K. M., and Coller, B. S. (2009). *In vitro* and *in vivo* evidence that thrombospondin-1 (TSP-1) contributes to stirring- and shear-dependent activation of platelet-derived TGF-β1. *PLoS One* 4, e6608. doi:10.1371/journal.pone.0006608

Al-Nedawi, K., Szemraj, J., and Cierniewski, C. S. (2005). Mast cell-derived exosomes activate endothelial cells to secrete plasminogen activator inhibitor type 1. *Arterioscler. Thromb. Vasc. Biol.* 25, 1744–1749. doi:10.1161/01.ATV.0000172007.86541.76

Alghamdi, S. H., Beucken, V. D., Jeroen, P., and Jansen, A. J. (2014). Osteoporosis-fracture healing and osseointegration. *Drug Discov. Today* 13, 3–9. doi:10.1016/j.ddmod.2014.10.001

Bai, L., Chen, P., Zhao, Y., Hang, R., Yao, X., Tang, B., et al. (2021a). A micro/nano-biomimetic coating on titanium orchestrates osteo/angio-genesis and osteoimmunomodulation for advanced osseointegration. *Biomaterials* 278, 121162. doi:10.1016/j.biomaterials.2021.121162

Bai, L., Du, Z., Du, J., Yao, W., Zhang, J., Weng, Z., et al. (2018). A multifaceted coating on titanium dictates osteoimmunomodulation and osteo/angio-genesis towards ameliorative osseointegration. *Biomaterials* 162, 154–169. doi:10.1016/j.biomaterials.2018.02.010

Bai, L., Zhao, Y., Chen, P., Zhang, X., Huang, X., Du, Z., et al. (2021b). Targeting early healing phase with titania nanotube arrays on tunable diameters to accelerate bone regeneration and osseointegration. *Small* 17, 2006287. doi:10.1002/smll.202006287

Barnsley, L., and Barnsley, L. (2019). Detection of aseptic loosening in total knee replacements: a systematic review and meta-analysis. *Skelet. Radiol.* 48, 1565–1572. doi:10.1007/s00256-019-03215-y

Berger, Gt, Hartwell, D. W., and Wagner, D. D. (1998). P-Selectin and platelet clearance. *Blood* 92, 4446–4452. doi:10.1182/blood.V92.11.4446

Bouchareychas, L., Duong, P., Covarrubias, S., Alsop, E., Phu, T. A., Chung, A., et al. (2020). Macrophage exosomes resolve atherosclerosis by regulating hematopoiesis and inflammation via MicroRNA cargo. *Cell Rep.* 32, 107881. doi:10.1016/j.celrep.2020.107881

Brammer, K. S., Frandsen, C. J., and Jin, S. (2012). TiO_2 nanotubes for bone regeneration. *Trends Biotechnol.* 30, 315–322. doi:10.1016/j.tibtech.2012.02.005

Butler, J. S. (2002). The yin and yang of the exosome. *Trends Cell Biol.* 12, 90–96. doi:10.1016/S0962-8924(01)02225-5

Caradec, J., Kharmate, G., Hosseini-Beheshti, E., Adomat, H., Gleave, M., and Guns, E. (2014). Reproducibility and efficiency of serum-derived exosome extraction methods. *Clin. Biochem.* 47, 1286–1292. doi:10.1016/j.clinbiochem.2014.06.011

Chen, K., Jiao, Y., Liu, L., Huang, M., He, C., He, W., et al. (2020). Communications between bone marrow macrophages and bone cells in bone remodeling. *Front. Cell Dev. Biol.* 8, 598263. doi:10.3389/fcell.2020.598263

Chernousova, S., and Epple, M. (2013). Silver as antibacterial agent: ion, nanoparticle, and metal. *Angew. Chem. Int. Ed.* 52, 1636–1653. doi:10.1002/anie.201205923

Colnot, C., Romero, D. M., Huang, S., Rahman, J., Currey, J. A., Nanci, A., et al. (2007). Molecular analysis of healing at a bone-implant interface. *J. Dent. Res.* 86, 862–867. doi:10.1177/154405910708600911

Cooper, M. A., Fehniger, T. A., Fuchs, A., Colonna, M., and Caligiuri, M. A. (2004). NK cell and DC interactions. *Trends Immunol.* 25, 47–52. doi:10.1016/j.it.2003.10.012

De Toro, J., Herschlik, L., Waldner, C., and Mongini, C. (2015). Emerging roles of exosomes in normal and pathological conditions: new insights for diagnosis and therapeutic applications. *Front. Immunol.* 6, 203. doi:10.3389/fimmu.2015.00203

Doyle, L. M., and Wang, M. Z. (2019). Overview of extracellular vesicles, their origin, composition, purpose, and methods for exosome isolation and analysis. *Cells* 8 (7), 727. doi:10.3390/cells8070727

Eltzschig, H. K., and Carmeliet, P. (2011). Hypoxia and inflammation. *N. Engl. J. Med. Overseas. Ed.* 364, 656–665. doi:10.1056/NEJMra0910283

Ferlazzo, G., and Morandi, B. (2014). Cross-talks between natural killer cells and distinct subsets of dendritic cells. *Front. Immunol.* 5, 159. doi:10.3389/fimmu.2014.00159

Ferrarelli, L. K. (2013). An angiogenic switch. *Sci. Signal.* 6, ec167. doi:10.1126/scisignal.2004538

Frenette, P. S., and Wagner, D. D. (1996). Adhesion molecules. *N. Engl. J. Med. Overseas. Ed.* 334, 1526–1529. doi:10.1056/NEJM199606063342308

Giri, P. K., and Schorey, J. S. (2008). Exosomes derived from M. Bovis BCG infected macrophages activate antigen-specific CD4$^+$ and CD8$^+$ T cells *in vitro* and *in vivo*. *PLoS One* 3, e2461. doi:10.1371/journal.pone.0002461

Guastaldi, F. P. S., Yoo, D., Marin, C., Jimbo, R., Tovar, N., Zanetta-Barbosa, D., et al. (2013). Plasma treatment maintains surface energy of the implant surface and enhances osseointegration. *Int. J. Biomater.* 2013, 354125. doi:10.1155/2013/354125

Guglielmotti, M. B., Olmedo, D. G., and Cabrini, R. L. (2019). Research on implants and osseointegration. *Periodontol. 2000* 79, 178–189. doi:10.1111/prd.12254

Guihard, P., Boutet, M. A., Brounais-Le Royer, B., Gamblin, A. L., Amiaud, J., Renaud, A., et al. (2015). Oncostatin m, an inflammatory cytokine produced by macrophages, supports intramembranous bone healing in a mouse model of tibia injury. *Am. J. Pathol.* 185, 765–775. doi:10.1016/j.ajpath.2014.11.008

Guo, B. B., Bellingham, S. A., and Hill, A. F. (2015). The neutral sphingomyelinase pathway regulates packaging of the prion protein into exosomes. *J. Biol. Chem.* 290, 3455–3467. doi:10.1074/jbc.m114.605253

Guo, J., Duan, Z., Zhang, C., Wang, W., He, H., Liu, Y., et al. (2020). Mouse 4T1 breast cancer Cell-Derived exosomes induce proinflammatory cytokine production in macrophages via miR-183. *J. Immunol.* 205, 2916–2925. doi:10.4049/jimmunol.1901104

Helwa, I., Cai, J., Drewry, M. D., Zimmerman, A., Dinkins, M. B., Khaled, M. L., et al. (2017). A comparative study of serum exosome isolation using differential ultracentrifugation and three commercial reagents. *PLoS One* 12, e0170628. doi:10.1371/journal.pone.0170628

Hoppe, A., Güldal, N. S., and Boccaccini, A. R. (2011). A review of the biological response to ionic dissolution products from bioactive glasses and glass-ceramics. *Biomaterials* 32, 2757–2774. doi:10.1016/j.biomaterials.2011.01.004

Jeppesen, D. K., Fenix, A. M., Franklin, J. L., Higginbotham, J. N., Zhang, Q., Zimmerman, L. J., et al. (2019). Reassessment of exosome composition. *Cell* 177, 428–445. e18. doi:10.1016/j.cell.2019.02.029

Jiang, Y., Jiang, H., Wang, K., Liu, C., Man, X., and Fu, Q. (2021). Hypoxia enhances the production and antitumor effect of exosomes derived from natural killer cells. *Ann. Transl. Med.* 9, 473. doi:10.21037/atm-21-347

Kaur, S., Singh, S. P., Elkahloun, A. G., Wu, W., Abu-Asab, M. S., and Roberts, D. D. (2014). CD47-dependent immunomodulatory and angiogenic activities of extracellular vesicles produced by T cells. *Matrix Biol.* 37, 49–59. doi:10.1016/j.matbio.2014.05.007

Kim, H., Wang, S. Y., Kwak, G., Yang, Y., Kwon, I. C., and Kim, S. H. (2019). Exosome-guided phenotypic switch of M1 to M2 macrophages for cutaneous wound healing. *Adv. Sci.* 6, 1900513. doi:10.1002/advs.201900513

Komori, T. (2010). Regulation of osteoblast differentiation by Runx2. *Adv. Exp. Med. Biol.* 658, 43–49. doi:10.1007/978-1-4419-1050-9_5

Krzywinska, E., and Stockmann, C. (2018). Hypoxia, metabolism and immune cell function. *Biomedicines* 6, 56. doi:10.3390/biomedicines6020056

Kuehbacher, A., Urbich, C., and Dimmeler, S. (2008). Targeting microRNA expression to regulate angiogenesis. *Trends Pharmacol. Sci.* 29, 12–15. doi:10.1016/j.tips.2007.10.014

Lai, C. P., Mardini, O., Ericsson, M., Prabhakar, S., Maguire, C. A., Chen, J. W., et al. (2014). Dynamic biodistribution of extracellular vesicles *in vivo* using a multimodal imaging reporter. *ACS Nano* 8, 483–494. doi:10.1021/nn404945r

Lee, H. D., Kim, Y. H., and Kim, D-S. (2014). Exosomes derived from human macrophages suppress endothelial cell migration by controlling integrin trafficking. *Eur. J. Immunol.* 44, 1156–1169. doi:10.1002/eji.201343660

Lee, M., Ban, J-J., Im, W., Kim, M., and Engineering, B. (2016). Influence of storage condition on exosome recovery. *Biotechnol. Bioprocess Eng.* 21, 299–304. doi:10.1007/s12257-015-0781-x

Li, X., Hetjens, L., Wolter, N., Li, H., Shi, X., and Pich, A. (2022). Charge-reversible and biodegradable chitosan-based microgels for lysozyme-triggered release of vancomycin. *J. Adv. Res.* doi:10.1016/j.jare.2022.02.014

Losic, D., Aw, M. S., Santos, A., Gulati, K., and Bariana, M. (2015). Titania nanotube arrays for local drug delivery: recent advances and perspectives. *Expert Opin. Drug Deliv.* 12, 103–127. doi:10.1517/17425247.2014.945418

Lugini, L., Cecchetti, S., Huber, V., Luciani, F., Macchia, G., Spadaro, F., et al. (2012). Immune surveillance properties of human NK cell-derived exosomes. *J. Immunol.* 189, 2833–2842. doi:10.4049/jimmunol.1101988

Luyet, P-P., Falguières, T., Pons, V., Pattnaik, A. K., and Gruenberg, J. (2008). The ESCRT-I subunit TSG101 controls endosome-to-cytosol release of viral RNA. *Traffic* 9, 2279–2290. doi:10.1111/j.1600-0854.2008.00820.x

Marchi, J., Amorim, E. M., Lazar, D. R. R., Ussui, V., Bressiani, A. H. A., and Cesar, P. F. (2013). Physico-chemical characterization of zirconia–titania composites coated with an apatite layer for dental implants. *Dent. Mat.* 29, 954–962. doi:10.1016/j.dental.2013.07.002

Mashouri, L., Yousefi, H., Aref, A. R., Ahadi, A. M., Molaei, F., and Alahari, S. K. (2019). Exosomes: composition, biogenesis, and mechanisms in cancer metastasis and drug resistance. *Mol. Cancer* 18, 75. doi:10.1186/s12943-019-0991-5

Matsuo, K., and Irie, N. (2008). Osteoclast–osteoblast communication. *Arch. Biochem. Biophys.* 473, 201–209. doi:10.1016/j.abb.2008.03.027

Mekori, Y. A. (2004). The mastocyte: the "other" inflammatory cell in immunopathogenesis. *J. Allergy Clin. Immunol.* 114, 52–57. doi:10.1016/j.jaci.2004.04.015

Novoselova, E. G., Lunin, S. M., Khrenov, M. O., Parfenyuk, S. B., Novoselova, T. V., Shenkman, B. S., et al. (2015). Changes in immune cell signalling, apoptosis and stress response functions in mice returned from the BION-M1 mission in space. *Immunobiology* 220, 500–509. doi:10.1016/j.imbio.2014.10.021

Ortega, F. J., Moreno, M., Mercader, J. M., Moreno-Navarrete, J. M., Fuentes-Batllevell, N., Sabater, M., et al. (2015). Inflammation triggers specific microRNA profiles in human adipocytes and macrophages and in their supernatants. *Clin. Epigenetics* 7, 49. doi:10.1186/s13148-015-0083-3

Periayah, M. H., Halim, A. S., Yaacob, N. S., Mat Saad, A. Z., Hussein, A. R., Abdul Rashid, A. H., et al. (2014). Glycoprotein IIb/IIIa and P2Y12 induction by oligochitosan accelerates platelet aggregation. *Biomed. Res. Int.* 2014, 653149. doi:10.1155/2014/653149

Pjetursson, B. E., and Heimisdottir, K. (2018). Dental implants–are they better than natural teeth? *Eur. J. Oral Sci.* 126, 81–87. doi:10.1111/eos.12543

Qi, Y., Zhu, T., Zhang, T., Wang, X., Li, W., Chen, D., et al. (2021). M1 macrophage-derived exosomes transfer miR-222 to induce bone marrow mesenchymal stem cell apoptosis. *Lab. Invest.* 101, 1318–1326. doi:10.1038/s41374-021-00622-5

Raman, M., and Cobb, M. H. (2003). MAP kinase modules: many roads home. *Curr. Biol.* 13, R886–R888. doi:10.1016/j.cub.2003.10.053

Rifai, N., Gillette, M. A., and Carr, S. A. (2006). Protein biomarker discovery and validation: the long and uncertain path to clinical utility. *Nat. Biotechnol.* 24, 971–983. doi:10.1038/nbt1235

Roberts, W., Magwenzi, S., Aburima, A., and Naseem, K. M. (2010). Thrombospondin-1 induces platelet activation through CD36-dependent inhibition of the cAMP/protein kinase A signaling cascade. *Blood* 116, 4297–4306. doi:10.1182/blood-2010-01-265561

Schorey, J. S., and Bhatnagar, S. (2008). Exosome function: from tumor immunology to pathogen biology. *Traffic* 9, 871–881. doi:10.1111/j.1600-0854.2008.00734.x

Shang, Y., Sun, Y., Xu, J., Ge, X., Hu, Z., Xiao, J., et al. (2020). Exosomes from mmu_circ_0001359-Modified ADSCs attenuate airway remodeling by enancing FoxO1 Signaling-Mediated M2-like macrophage activation. *Mol. Ther. Nucl. Acids.* 19, 951–960. doi:10.1016/j.omtn.2019.10.049

Shaul, Y. D., and Seger, R. (2007). The MEK/ERK cascade: From signaling specificity to diverse functions. *Biochimica Biophysica Acta - Mol. Cell Res.* 1773, 1213–1226. doi:10.1016/j.bbamcr.2006.10.005

Sivaraj, K. K., and Adams, R. H. (2016). Blood vessel formation and function in bone. *Development* 143, 2706–2715. doi:10.1242/dev.136861

Skapenko, A., Leipe, J., Lipsky, P. E., and Schulze-Koops, H. (2005). The role of the T cell in autoimmune inflammation. *Arthritis Res.* 7, S4. doi:10.1186/ar1703

Skokos, D., Le Panse, S., Villa, I., Rousselle, J-C., Peronet, R., David, B., et al. (2001). Mast Cell-Dependent B and T lymphocyte activation is mediated by the secretion of immunologically active exosomes. *J. Immunol.* 166, 868–876. doi:10.4049/jimmunol.166.2.868

Smith, V. L., Cheng, Y., Bryant, B. R., and Schorey, J. S. (2017). Exosomes function in antigen presentation during an *in vivo Mycobacterium tuberculosis* infection. *Sci. Rep.* 7, 43578. doi:10.1038/srep43578

Smith-Garvin, J. E., Koretzky, G. A., and Jordan, M. S. (2009). T cell activation. *Annu. Rev. Immunol.* 27, 591–619. doi:10.1146/annurev.immunol.021908.132706

Stoorvogel, W., Kleijmeer, M. J., Geuze, H. J., and Raposo, G. (2002). The biogenesis and functions of exosomes. *Traffic* 3, 321–330. doi:10.1034/j.1600-0854.2002.30502.x

Suárez, Y., Fernández-Hernando, C., Pober, J. S., and Sessa, W. C. (2007). Dicer dependent MicroRNAs regulate gene expression and functions in human endothelial cells. *Circ. Res.* 100, 1164–1173. doi:10.1161/01.RES.0000265065.26744.17

Terheyden, H., Lang, N. P., Bierbaum, S., and Stadlinger, B. (2012). Osseointegration-communication of cells. *Clin. Oral Implants Res.* 23, 1127–1135. doi:10.1111/j.1600-0501.2011.02327.x

Thomas, R., and Yang, X. (2016). NK-DC crosstalk in immunity to microbial infection. *J. Immunol. Res.* 2016, 6374379. doi:10.1155/2016/6374379

Wang, X., Shah, F. A., Vazirisani, F., Johansson, A., Palmquist, A., Omar, O., et al. (2020). Exosomes influence the behavior of human mesenchymal stem cells on titanium surfaces. *Biomaterials* 230, 119571. doi:10.1016/j.biomaterials.2019.119571

Wei, F., Li, M., Crawford, R., Zhou, Y., and Xiao, Y. (2019). Exosome-integrated titanium oxide nanotubes for targeted bone regeneration. *Acta Biomater.* 86, 480–492. doi:10.1016/j.actbio.2019.01.006

Wubbolts, R., Leckie, R. S., Veenhuizen, P. T. M., Schwarzmann, G., Möbius, W., Hoernschemeyer, J., et al. (2003). Proteomic and biochemical analyses of human B cell-derived exosomes: potential implications for their function and multivesicular body formation. *J. Biol. Chem.* 278, 10963–10972. doi:10.1074/jbc.M207550200

Xia, Y., He, X-T., Xu, X-Y., Tian, B-M., An, Y., and Chen, F-M. (2020). Exosomes derived from M0, M1 and M2 macrophages exert distinct influences on the proliferation and differentiation of mesenchymal stem cells. *PeerJ* 8, e8970. doi:10.7717/peerj.8970

Xu, L., Gimple, R. C., Lau, W. B., Lau, B., Fei, F., Shen, Q., et al. (2020). The present and future of the mass spectrometry-based investigation of the exosome landscape. *Mass Spectrom. Rev.* 39, 745–762. doi:10.1002/mas.21635

Yuan, X., Berg, N., Lee, J. W., Le, T-T., Neudecker, V., Jing, N., et al. (2018). MicroRNA miR-223 as regulator of innate immunity. *J. Leukoc. Biol.* 104, 515–524. doi:10.1002/JLB.3MR0218-079R

Zhang, T., Jiang, M., Yin, X., Yao, P., and Sun, H. (2021). Mechanism of exosomes involved in osteoimmunity promoting osseointegration around titanium implants with small-scale topography. *Front. Bioeng. Biotechnol.* 9, 682384. doi:10.3389/fbioe.2021.682384

Zhang, X., Zhang, H., Gu, J., Zhang, J., Shi, H., Qian, H., et al. (2021). Engineered extracellular vesicles for cancer therapy. *Adv. Mat.* 33, 2005709. doi:10.1002/adma.202005709

Zhang, Y-H., He, M., Wang, Y., and Liao, A-H. (2017). Modulators of the balance between M1 and M2 macrophages during pregnancy. *Front. Immunol.* 8, 120. doi:10.3389/fimmu.2017.00120

Zhu, J., and Paul, W. E. (2008). CD4 T cells: fates, functions, and faults. *Blood* 112, 1557–1569. doi:10.1182/blood-2008-05-078154

Zhu, X., Shen, H., Yin, X., Yang, M., Wei, H., Chen, Q., et al. (2019). Macrophages derived exosomes deliver miR-223 to epithelial ovarian cancer cells to elicit a chemoresistant phenotype. *J. Exp. Clin. Cancer Res.* 38, 81. doi:10.1186/s13046-019-1095-1

frontiers | Frontiers in Bioengineering and Biotechnology

TYPE Original Research
PUBLISHED 13 September 2022
DOI 10.3389/fbioe.2022.1001994

PPy@Fe_3O_4 nanoparticles inhibit the proliferation and metastasis of CRC *via* suppressing the NF-κB signaling pathway and promoting ferroptosis

Zhilong Yu[1†], Shanshi Tong[2†], Chenyi Wang[1], Zizhen Wu[1], Yingjiang Ye[1], Shan Wang[1] and Kewei Jiang[1*]

[1]Department of Gastroenterological Surgery, Laboratory of Surgical Oncology, Beijing Key Laboratory of Colorectal Cancer Diagnosis and Treatment Research, Peking University People's Hospital, Beijing, China, [2]State Key Laboratory of Oncogenes and Related Genes, Shanghai Cancer Institute, Renji Hospital, School of Medicine, Shanghai Jiao Tong University, Shanghai, China

Check for updates

OPEN ACCESS

EDITED BY
Yu Luo,
Shanghai University of Engineering Sciences, China

REVIEWED BY
Nuo Yu,
Donghua University, China
Xijian Liu,
Shanghai University of Engineering Sciences, China

*CORRESPONDENCE
Kewei Jiang,
dr_jiangkewei@163.com

†These authors have contributed equally to this work

SPECIALTY SECTION
This article was submitted to Nanobiotechnology, a section of the journal Frontiers in Bioengineering and Biotechnology

RECEIVED 24 July 2022
ACCEPTED 18 August 2022
PUBLISHED 13 September 2022

CITATION
Yu Z, Tong S, Wang C, Wu Z, Ye Y, Wang S and Jiang K (2022), PPy@Fe_3O_4 nanoparticles inhibit the proliferation and metastasis of CRC via suppressing the NF-κB signaling pathway and promoting ferroptosis.
Front. Bioeng. Biotechnol. 10:1001994.
doi: 10.3389/fbioe.2022.1001994

COPYRIGHT
© 2022 Yu, Tong, Wang, Wu, Ye, Wang and Jiang. This is an open-access article distributed under the terms of the Creative Commons Attribution License (CC BY). The use, distribution or reproduction in other forums is permitted, provided the original author(s) and the copyright owner(s) are credited and that the original publication in this journal is cited, in accordance with accepted academic practice. No use, distribution or reproduction is permitted which does not comply with these terms.

Colorectal cancer (CRC) is one of the most common cancers of the digestive tract, and patients with advanced-stage cancer have poor survival despite the use of multidrug conventional chemotherapy regimens. Intra-tumor heterogeneity of cancerous cells is the main obstacle in the way to effective cancer treatments. Therefore, we are looking for novel approaches to eliminate just cancer cells including nanoparticles (NPs). PPy@Fe_3O_4 NPs were successfully synthesized through a portable method. The characterization of transmission electron microscopy (TEM), Fourier-Transformed infrared spectrometer, and X-ray powder diffraction have further proved successful preparation of PPy@Fe_3O_4 NPs. NIR irradiation was used to test the photothermal properties of NPs and an infrared camera was used to record their temperature. The direct effects of PPy@Fe_3O_4 NPs on colorectal cancer cell DLD1 were assessed using CCK8, plate clone, transwell, flow cytometry, and western blotting in CRC cell. The effect of PPy@Fe_3O_4 NPs on neoplasm growth in nude mice was evaluated *in vivo*. This study demonstrated that PPy@Fe_3O_4 NPs significantly inhibit the growth, migration, and invasion and promote ferroptosis to the untreated controls in colorectal cancer cells. Mechanical exploration revealed that PPy@Fe_3O_4 NPs inhibit the multiplication, migration, and invasion of CRC cells *in vitro* by modulating the NF-κB signaling pathway. Importantly, Ferroptosis inhibitors Fer-1 can reverse the changes in metastasis-associated proteins caused by NPs treatment. Collectively, our observations revealed that PPy@Fe_3O_4 NPs were blockers of tumor progression and metastasis in CRC. This study brought new insights into bioactive NPs, with application potential in curing CRC or other human disorders.

KEYWORDS

colorectal cancer, nanoparticles, metastasis, NF-κB, ferroptosis

Introduction

Colorectal cancer (CRC) ranks among the most common and devastating diseases of the digestive system globally (Bray et al., 2018; Siegel et al., 2021). There is no effective regime against this aggressive malignancy besides early surgical resection (Brenner et al., 2014). When patients are diagnosed with colorectal cancer, 15%–25% have liver metastases, and another 15%–25% develop them after radical resection of the primary tumor (Engstrand et al., 2018). However, radical resection of liver metastases is not possible in 80%–90% of cases (Modest et al., 2019). Among the reasons for this grim prognosis are the lack of obvious symptoms and reliable biomarkers for early diagnosis, as well as aggressive metastatic spread that leads to a poor response to treatment. Metastatic disease occurs in approximately 50% of diagnosed patients (Xu et al., 2019; Rebersek, 2020). Patients with advanced and metastatic cancer are generally treated with chemotherapy (Fan et al., 2021). The combination of radiation with chemotherapy is another option for treating unresectable, metastatic cancers (Koppe et al., 2005). Even so, both approaches are mainly aimed at improving survival rates and reducing symptoms of cancer (Aggarwal et al., 2013; Biller and Schrag, 2021).

With the rapid development of nanotechnology, nanoparticles (NPs) have provided a new approach for studying tumor therapies in recent years (Guan et al., 2022a; Zheng et al., 2021; Guan et al., 2022b). Nanomaterials refer to materials with at least one dimension ranging from 1 to 100 nm (Zheng et al., 2022). Due to their special dimensions, they have different optical, electromagnetic, biological, and thermal properties than general materials, making them more plastic (Sun et al., 2014; Enriquez-Navas et al., 2015; Duan et al., 2019; Li et al., 2021). The field has broad application prospects. Currently, nanomaterials treatment for cancer is mainly aimed at direct destruction of tumors, but in clinical treatment, high mortality rates of cancer are caused by the proliferation and metastasis of tumors, not the primary tumor site (Jiang et al., 2015; El-Toni et al., 2016). At present, the killing of tumors by nanoparticles mainly revolves around the photothermal properties and chemodynamic therapy of nanomaterials (Baek et al., 2016; Zhu et al., 2016; Tang et al., 2019), and nanoparticles' direct effect on tumor cells has been little studied. Revealing the specific mechanism of nanoparticles' effects on tumor cells is beneficial to promote the further application of nanoparticles in the human body.

Polypyrrole (PPy) is a kind of organic photothermal agent and photosensitizer, which can not only ablate cancer cells under infrared irradiation, and improve the effect of chemotherapy, but also has good biocompatibility, which can regulate cell adhesion, migration, protein secretion, and DNA synthesis as well as other processes under electric stimulation (Zhou et al., 2017; Liang et al., 2021; Miar et al., 2021). Human bodies require iron (Fe) as an essential trace element. Early studies found that the concentration of Fe in the body is negatively correlated with colorectal cancer. Therefore, people have high hopes for Fe treatment of tumors (Torti et al., 2018; Torti and Torti, 2020). There are also numerous studies that prove Fe supplementation can inhibit colorectal cancer development (Aksan et al., 2021; Phipps et al., 2021; Ploug et al., 2021). Whereas, some scholars believe that excess iron contributes to oxidative stress-induced colon damage and amplifies oncogenic signals. Therefore, the clinical application of Fe-containing drugs is limited (Padmanabhan et al., 2015; Wilson et al., 2018). It is possible to deliver nanoparticles to tumors through enhanced permeability and retention effect (EPR), and decompose iron ions directly in the tumor-specific microenvironment, which can avoid harming the normal colon.

Our study design and manufacture a novel composite nanomaterial PPy@Fe_3O_4 and demonstrate that it can directly kill tumors through photothermal therapy (PPT) and chemodynamic therapy (CDT). As well as evaluating the basic properties and biosafety of PPy@ Fe_3O_4 NPs, we observed their effects on colorectal cancer cell proliferation, migration and invasion *in vivo* and *in vitro* (Figure 1).

Materials and methods

Synthesis of PPy@Fe_3O_4 NPs

Dissolve 0.75 g of polyvinyl alcohol (PVA) in 10 ml of deionized water. Heated to 95°C, after dissolving PVA, 0.373g ferric chloride powder ($FeCl_3$ 2.30 mmol) was added to the above solution and stirred magnetically for an hour. Then the mixed solution was kept at 4°C and 69.2 μl pyrrole monomer (0.9970 mmol) was added slowly. After 4 h of stirring, the mixture was poured into a bowl. A dark green solution was produced, which indicated the successful synthesis of polypyrrole NPs. Then, 2.5 ml of the reaction solution was directly removed from the above steps, and then 15 ml of deionized water and 2 ml of ethanol were evenly mixed. Under the condition of full agitation, the temperature was rapidly heated to 70°C, and 1 ml of 1.0wt% ammonia solution was immediately dropped. After 30 min, inject another 1 ml 1.0wt% ammonia solution and keep the mixture at the same temperature for another 30 min. Centrifugation by separation (11,000 RPM; 50 min) PPy@Fe_3O_4 nanoparticles were collected and centrifuged (11,000 RPM; 50 min), washed three times with deionized water to remove impurities, and collected and dispersed in deionized water.

Characterization of PPy@ Fe_3O_4 NPs and photothermal effect evaluation

The morphologies of NPs were evaluated via transmission electron microscopy (TEM). In order to determine the

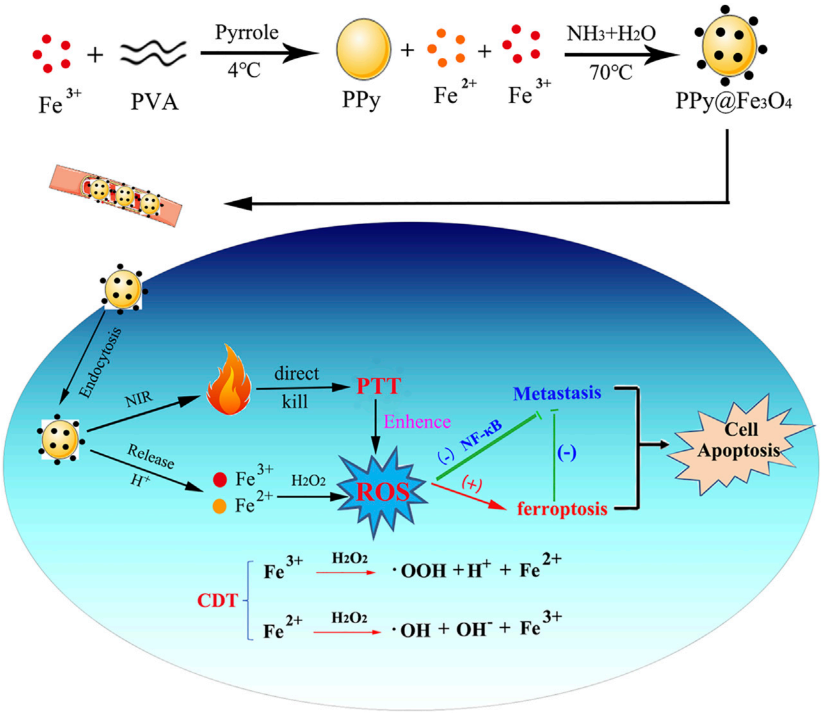

FIGURE 1
Scheme of the synthesis process and therapeutic mechanism of PPy@Fe_3O_4 NPs.

characteristics of NPs and their crystal structures, Fourier-Transformed Infrared (FTIR) spectrometers and X-ray powder diffraction methods were used. We then irradiated PPy@Fe3O4 NPs with NIR lasers at different wavelengths (100, 200, and 400 μg/ml) at different concentrations. A thermal imaging camera was used to monitor and record the temperature changes of the solution during the heating and cooling process to calculate the photothermal conversion efficiency (η).

Culture of the cancer cell lines

DLD1-1, SW480, and FHC colorectal cancer cell lines were purchased from ATCC. DLD1 and SW480 were colorectal cancer cells, and FHC was a normal colorectal epithelial cell. All cell lines were cultured in Dulbecco's Modified Eagle's Medium (DMEM) (Gibco, United States). All media were supplemented with 10% fetal bovine serum (FBS) and cells were grown in an incubator at 37°C and supplied with 5% CO_2.

Biosafety and flow cytometry analysis

In advance, DLD1, SW480, and FHC cells were plated in 96-well plates at $1*10^4$ cells per well and cultured for 24 h at 37°C under 5% CO_2. At various concentrations, PPy@Fe_3O_4 was added to the culture media for 24 h, followed by 18 h of incubation. In accordance with the manufacturer's instructions, relative cell viability was assessed using the Cell Counting Kit-8 (CCK-8, Yeasen, China).

Transwell migration assay

Transwell migration assays were conducted in Corning-Costar migration chambers with a pore size of 8 mm for studying CRC cell migration in transfected suspensions. As soon as possible, transfected cells were seeded into an FBS-free medium and conditioned DMEM containing 10% FBS was poured into the lower chamber. In the following 48 h, we removed the cells on the upper membrane surface and fixed and stained the cells on the bottom membrane surface with methanol and crystal violet. We photographed cells from five random fields (×40 magnifications) under the light microscope.

Western blotting

Equal amounts of samples were separated by 10% SDS-PAGE and transferred to PVDF membranes. Blocking membranes with 5% non-fat milk in TBST for 1 h, primary antibodies were incubated overnight at 4°C, followed by secondary antibodies at room temperature for 90 min. The immunoreactive bands were visualized using a ChemiLucent ECL kit (Millipore) and the ImageJ program (National Institutes of Health).

Determination of intracellular ROS

In accordance with the manufacturer's instructions, chloro-dihydrofluorescein diacetate (DCFH-DA) was used to determine intracellular ROS. Briefly, DLD1 cells were incubated with NPs (200 μg/ml^{-1}) at pH 6.5 for 3.5 h, followed by 30 min of incubation with H_2O_2 (100 mM, 200 μl). The cells were placed on an ice box at 4°C. Then the medium was replaced by 1 ml DCFH-DA (10 μM).

Animal experiments

All experiments on animals were conducted in accordance with "China National Standards for the Care and Use of Laboratory Animals" and were approved by the Ethics Committee of Renji Hospital Affiliated with Shanghai Jiaotong University School of Medicine. In order to establish colorectal cancer xenograft model, 20 male BALB/c athymic nude mice (4 weeks old) were randomly divided into four groups ($n = 5$) and injected subcutaneously with $1.0*10^7$ stable colorectal cells DLD1. A variety of intravenous preparations were administered: Control (groups 1), NIR(groups 2), NPs (200 μg/ml^{-1}) (groups 3), NIR + NPs (groups 4). We used an 808 nm laser (1.0 W cm^{-2}) to irradiate Groups 2 and 4 for 10 min respectively after 8 h and monitored temperature change by a thermal imaging camera. Prior to the mice being killed, tumor growth was monitored and measured with micrometer calipers every other day. After 28 days of treatment, immediately after harvest, organs and tumors were preserved in paraformaldehyde for further IHC testing and hematoxylin and eosin staining (H&E-stained).

Statistics

All data are presented as mean ± SD. Statistical analyses were performed with the $\chi 2$ test or the Student's t-test (two-tailed unpaired). All the data were analyzed using Origin and Graphpad. Moreover, $p < 0.05$ is considered statistically significant.

Results

Construction and physical characterization of PPy@Fe_3O_4

The PPy nanoparticles were firstly prepared, followed by ammonia addition at 70°C to convert Fe ions into Fe_3O_4 crystals. The Fe_3O_4 crystals were dispersed on the surface of PPy nanoparticles, forming PPy@Fe_3O_4 NPs with a size of ~70 nm, as shown in Figures 2A,B. Each PPy nanoparticle incorporated many Fe_3O_4 crystals. The FTIR spectrum confirmed the successful formation of PPy by showing the characteristic absorption peaks (Figure 2C). Fe_3O_4 crystal structures were confirmed by X-ray diffractograms (XRD) of NPs (Figure 2D). These results illustrated that the PPy@Fe_3O_4 NPs have been successfully synthesized.

Since PPy was introduced to Fe_3O_4 NPs, they demonstrated a strong and broad absorption spectrum from the visible to near-infrared (Figure 2E). As the NPs concentration increase, the temperature also increases gradually under NIR irradiation (Figure 2F). Based on the temperature changes of the solution during heating/cooling process, we determined the photothermal conversion efficiency (ŋ value) of NPs (Figures 2G,H). The ŋ value was significantly higher than that of traditional PPT agents at 52%. The above results showed that the PPy@Fe_3O_4 NPs have excellent photothermal effects, which endowed good performance for PTT.

PPy@Fe_3O_4 NPs inhibited growth and produced ROS *in vitro*

Biological applications of nanoparticles depend on their good biocompatibility. To evaluate its cytotoxicity, we used standard CCK-8 methods in DLD1, SW480, and FHC cells. As shown in Figure 3A, NPs exhibited excellent biocompatibility, except for NPs (400 ug/ml^{-1}), with mildly stronger cytotoxicity due to their chemodynamic reactions. To simulate the tumor microenvironment *in vitro*, we added the appropriate amount of hydrogen peroxide during cell treatment. Therefore, colorectal cancer cells were divided into 4 groups: 1) Control, (b)H_2O_2, (C) NPs, (d)NPs + H_2O_2. DLD1 cells proliferation was significantly decreased by treatments with NPs and H_2O_2 in plating colony and CCK8 assays demonstrating that PPy@Fe_3O_4 functions biologically in colorectal cancer (Figures 3B,C). For cell apoptosis assay, NPs and H_2O_2 treated group promoted apoptosis in DLD1 cells (Figure 3D). To verify the ROS production of NPs in DLD1, we observe dichloro-dihydrofluorescein diacetate staining (DCFH-DA) under confocal microscopic conditions, ROS levels were significantly augmented in cells treated with NPs and H_2O_2, indicating a promoting effect on ROS generation (Figure 3E).

PPy@Fe_3O_4 NPs suppressed metastasis and promoted ferroptosis in CRC cells

Transwell migration and invasion assays indicated that NPs and H_2O_2 treated group decreased the ability of migration and invasion (Figure 4A). Since epithelial-mesenchymal transition

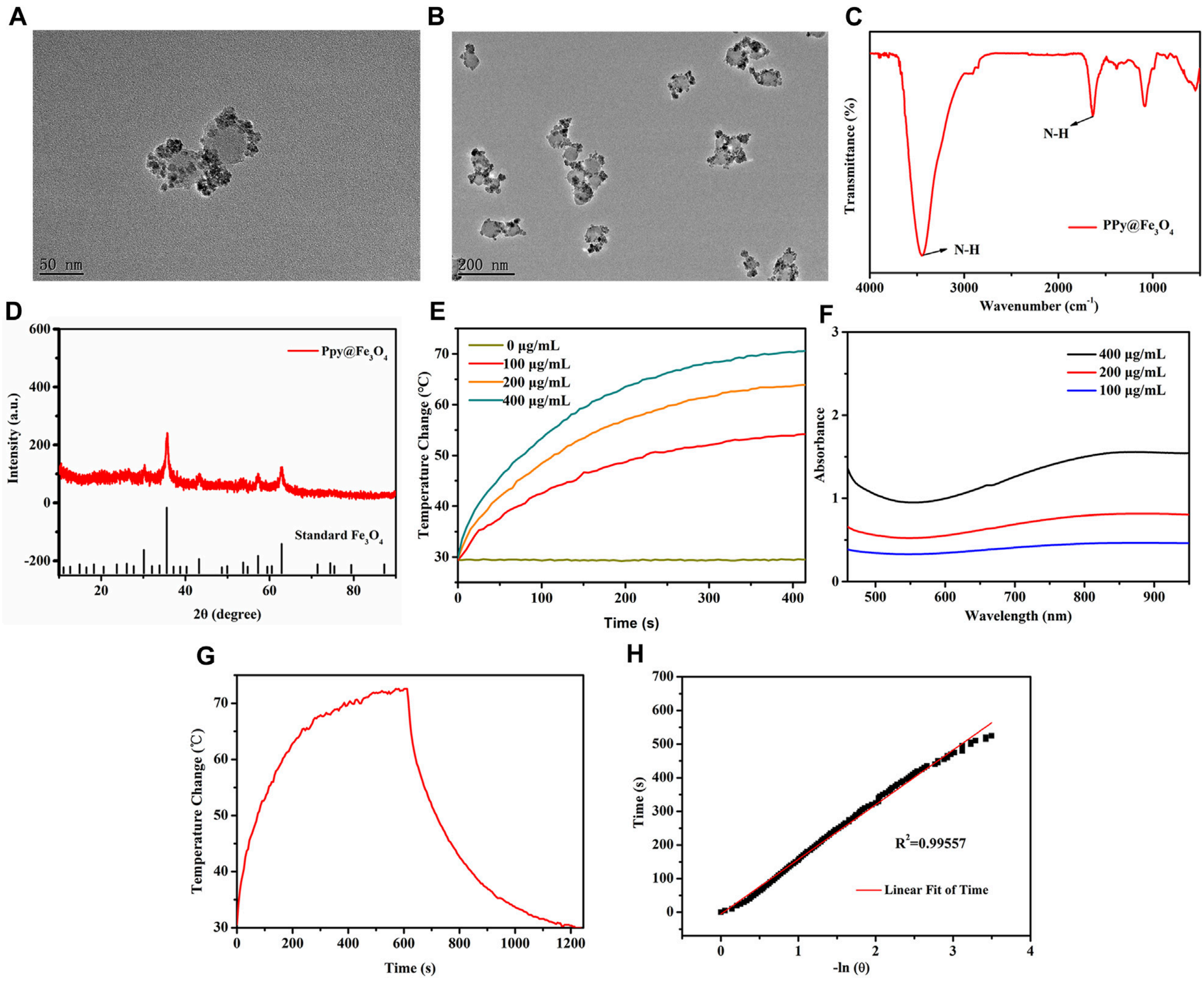

FIGURE 2
The characterization and photothermal properties of the PPy@Fe$_3$O$_4$ NPs. **(A,B)** High and Low TEM images of PPy@Fe$_3$O$_4$ NPs; **(C)** FTIR spectra of PPy@Fe$_3$O$_4$ NPs; **(D)** XRD spectra of PPy@Fe$_3$O$_4$ NPs; **(E)** UV-Vis-NIR absorption spectra of PPy@Fe$_3$O$_4$ NPs at different concentrations; **(F)** Temperature change curve with various concentrations of NPs; **(G)** Temperature curve of rising with irradiation and naturally cooling; **(H)** Linear regression curve of cooling process (red).

(EMT) plays a vital role in tumorigenesis, the relationship between NPs and EMT in CRC cells warranted further investigation. EMT biomarkers were used to identify whether NPs treated in CRC were related to EMT. The WB results showed that NPs inhibited the expression of the mesenchymal markers N-cadherin, Vimentin, Snail, MMP2, and MMP9, but induced the expressions of the epithelial marker E-cadherin (Figure 4B). Therefore, we inferred that PPy@Fe$_3$O$_4$ NPs inhibited tumor metastasis through inhibiting the EMT process.

In addition, studies also shown that the role of ROS in tumor cells is closely related to ferroptosis (Su et al., 2019; Chen et al., 2021a), and PPy@ Fe$_3$O$_4$ nanomaterials not only generate ROS in tumors, but also the constant conversion of Fe^{2+} and Fe^{3+} through the Fenton reaction, which also affects the iron ions metabolism. We speculated that NPs are associated with ferroptosis in tumor cells. Our data showed that PPy@Fe$_3$O$_4$ induced the expression of Xbp1, Homx1, and Keap1, but inhibited the expressions of GPX4 and NRF2 (Figure 4C). In addition, hydrogen peroxide has been reported to induce ferroptosis, which is consistent with our findings. Therefore, we inferred that PPy@Fe$_3$O$_4$ NPs can promote ferroptosis in CRC cells.

PPy@Fe$_3$O$_4$ NPs inhibited EMT via the NF-κB signaling pathway

NF-κB is involved in many cancer-related processes, including cell proliferation, apoptosis, angiogenesis, and

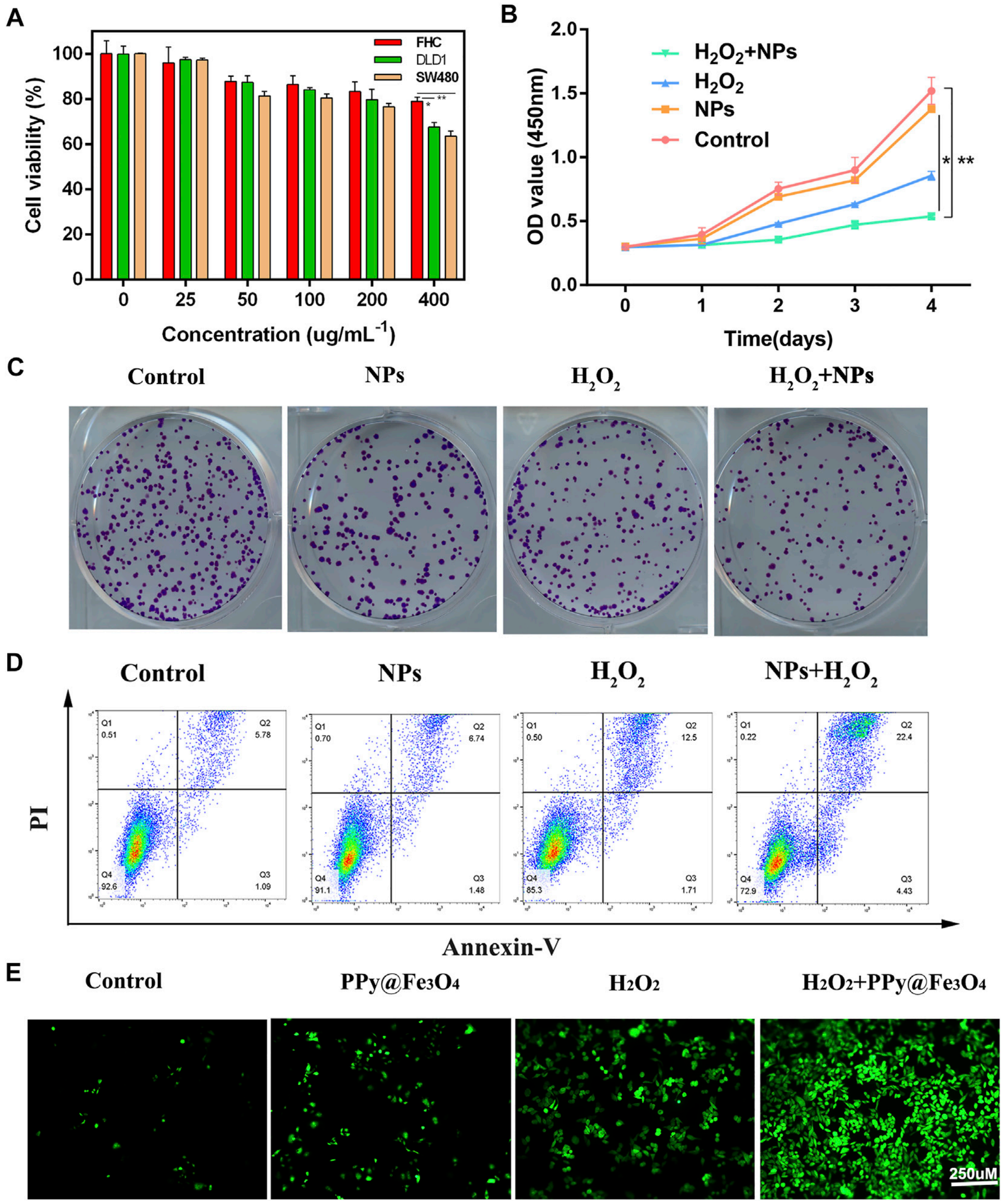

FIGURE 3
Effects of PPy@Fe_3O_4 NPs on regulating colorectal cancer cell growth, clone formation apoptosis and ROS generation. **(A)** Cell viability of the DLD1, SW480 and FHC cells after co-culture with NPs at different concentrations. **(B)** Cell viability CCK-8 assay in different groups. **(C)** Colony formation assay. Duplicated cells were subjected to the tumour cell colony formation assay in different groups. **(D)** Flow cytometric apoptosis assay. Colorectal cancer cell lines DLD1 were treated with H_2O_2, NPs, NPs + H_2O_2 or control, respectively, and then subjected to flow cytometric analysis. **(E)** Fluorescence images of DLD1 cells with various groups (Control, H_2O_2, NPs and NPs + H_2O_2). Scale bar: 250 μm **$p < 0.01$.

metastasis in colorectal cancer (Vaiopoulos et al., 2013; Patel et al., 2018). A previous study reported excessive ROS can reduce NF-κB activation by inhibiting IκB protein degradation (Morgan and Liu, 2011). So we hypothesized whether PPy@Fe_3O_4 inhibits tumor cell metastasis by inhibiting NF-κB signaling. As part of this study, we measured the expression and activity of NF-κB in CRC cells treated with NPs. There was a decrease in the levels of p-IKKα and p-IKKβ in DLD1, as well as an increase in the amounts of p-IκBα after treatment with NPs and H_2O_2. P65 levels did not change significantly, but phospho-p65 expression decreased. We discovered that the expression of phosphorylated (p)p65, p-IKKα, p-IKKβ, and IκBα, which are essential for

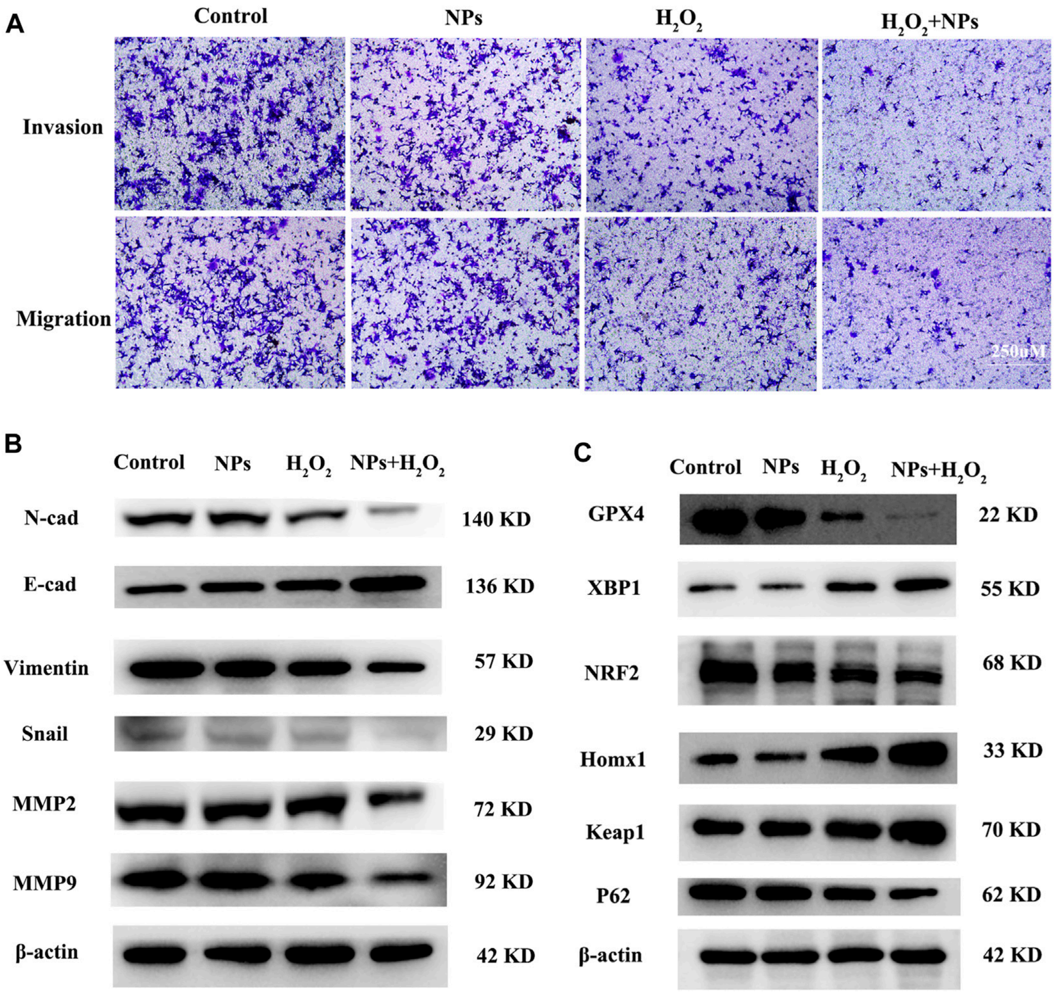

FIGURE 4
PPy@Fe_3O_4 NPs suppress cell migration and invasion, and promote cell ferroptosis *in vitro*. **(A)** Transwell migration and invasion assays of DLD1 cell with different treatment groups. **(B)** WB assays showed that metastasis-related proteins (E-Cadherin, N-Cadherin,Snail, MMP2, MMP9 and Vimentin) expression changed in different groups. **(C)** Ferroptosis-related proteins (GPX4, XBP1, NRF2, HOMX1 and Keap1) expression changed in the control group and other treated groups.

activating the NF-κB signaling pathway, were downregulated by NPs with H_2O_2 in DLD1 cells (Figure 5A).

Some studies have reported that there is an interaction between EMT and ferroptosis (Chen et al., 2020; Guan D. et al., 2022). GPX4, which is a negative regulator of ferroptosis, knockdown can enhance tumor cell oncogenic and metastatic activity (Huang et al., 2022). We suppose ferroptosis was increased after PPy@Fe_3O_4 treatment, and the metastatic ability of colorectal cancer cells was inhibited by increased GPX4 expression. After inhibition of tumor cell ferroptosis with ferroptosis inhibitors Ferrostatin-1 (Fer-1), western-blot analysis and transwell assays revealed increased metastatic potential of colorectal cancer cells, and the expression of EMT-related proteins was distinctly altered, with N-cadherin, Vimentin, Snail, MMP2 and MMP9 upregulated and E-cadherin downregulated (Figures 5B,C). These results demonstrated that PPy@Fe_3O_4 NPs inhibit CRC cells' metastasis by promoting cell ferroptosis and inhibiting the NF-κB signaling pathway.

In vitro cell experiment

In order to investigate the roles of PPy@Fe_3O_4 NPs *in vivo*, a nude mouse xenograft model of colorectal cancer was constructed. Tumor volume was monitored every other day throughout the experiment. As a result of NPs treatment, tumor growth was significantly inhibited (Figures 6A–C). There was no difference in tumor growth between the NIR and control groups, demonstrating that NIR alone cannot inhibit tumor growth. However, due to the synergistic effects of PTT and CDT, the tumor growth in the NPs +

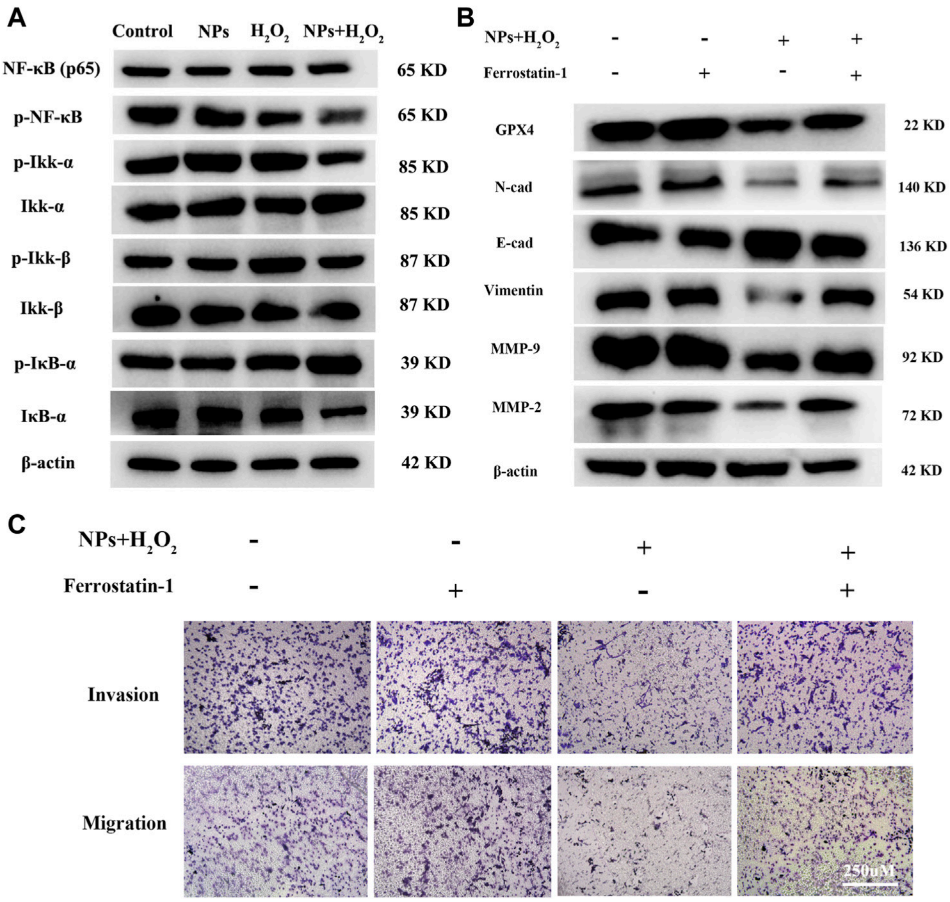

FIGURE 5
PPy@Fe_3O_4 NPs suppress CRC cells metastasis by promoting cell ferroptosis and inhibiting NF-κB signaling pathway. **(A)** Western blot. Colorectal cancer cell line DLD1 was treated with various groups (Control, H_2O_2, NPs and NPs + H_2O_2), and then subjected to Western blot analysis of the key proteins of the NF-KB signaling pathway (Ikk-β, p-Ikk-β, ikk-α, p-Ikk-α, NF-κβ, p-NF-κβ, IκB-α and p-IκB-α). **(B)** Effects of the ferroptosis inhibitor Ferrostatin-1 on PPy@Fe_3O_4 NPs-induced metastasis-related proteins expression. **(C)** Transwell showed that PPy@Fe_3O_4 NPs-induced cell migration and invasion were abolished after addition of the ferroptosis inhibitor Ferrostatin-1 in CRC cell.

NIR group was significantly inhibited. NIR group mice were irradiated with an 808 nm laser while their infrared thermal image and temperature were recorded simultaneously. Laser irradiation rapidly increased the temperature of the tumor in the NPs group to 55°C. It has been reported that apoptosis and necrosis of cancer cells can be induced when the temperature around the tumor is above 42°C (Sun et al., 2019). In contrast, the control group only experienced a very weak rise, less than 35°C (Figures 6D,E). In the colorectal tumor model, Ki-67, a marker of cell proliferation, was significantly downregulated in NPs + NIR groups after IHC analysis (Figure 6F). These results explicitly demonstrated that NPs with NIR could effectively prevent tumor growth *in vivo*. H&E staining of various treatment groups was carried out for the purpose of assessing the biosafety of NPs. According to the data, neither the control group nor other treatment groups showed obvious organ damage (Figure 6G), which further validated the PPy@Fe_3O_4 NPs were safe.

Discussion

PPy@Fe_3O_4 NPs were successfully synthesized by an facile method. They exhibited an excellent photothermal effect and could produce abundant ROS for CDT in the tumor microenvironment. Furthermore, NPs are adequate to modulate cellular response on their own (Setyawati and Leong, 2017; Cen et al., 2021). First, we used CCK8 to detect the viability of normal cells and tumor cells exposed to different concentrations of NPs to judge the biosafety of NPs. We then demonstrated *in vitro* that NPs can restrain the accretion and metastasis of CRC cells and promote ferroptosis. Finally, we found that NPs inhibit CRC cells growth by inducing ferroptosis and inhibiting NF-κB pathway. *In vivo* experiment results further confirmed the inhibition of NPs on tumor growth.

Our team has long been committed to the practical application of photothermal technology. PTT and CDT of nanoparticles have

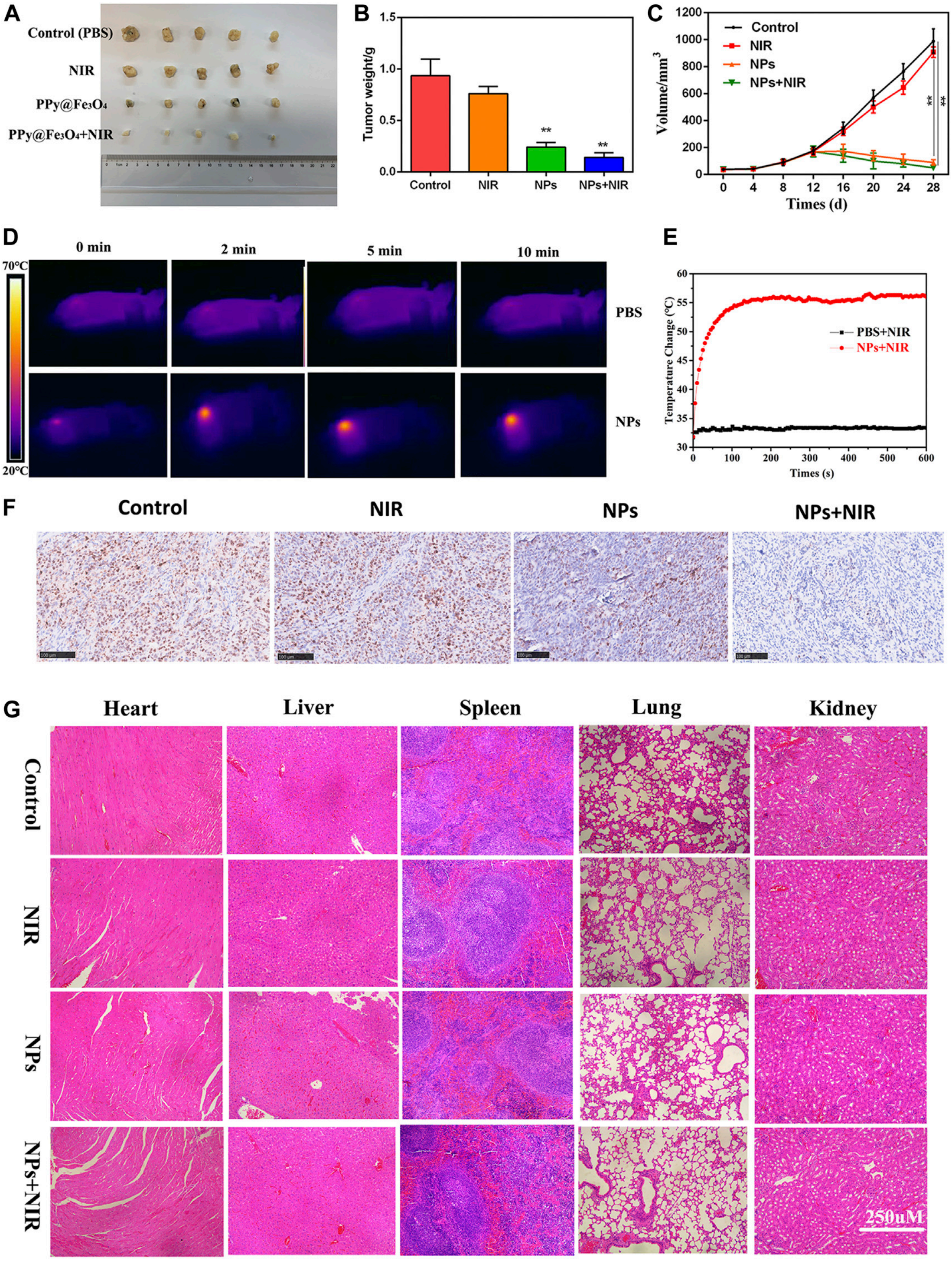

FIGURE 6
Anti-tumour activity of PPy@ Fe_3O_4 NPs in nude mouse tumour cell xenografts. **(A)** Images of subcutaneous xenograft tumors of DLD1 cells. **(B)** The final tumor weight of DLD1 cells was shown. **(C)** The tumor volume and change of different groups. **(D)** The temperature change and **(E)** infrared thermal imaging of the mice injected with PBS, NPs under laser irradiation. **(F)** Ki67 staining of the tumors in the control group and other treated groups. (scale bar: 100 μm). **(G)** H&E staining of the main organs from the control and treatment groups. (scale bar: 250 μm). $^{**}p < 0.01$.

enormous potential in cancer treatment (Huang et al., 2019; Zheng et al., 2021). CDT/PTT has demonstrated to be highly effective and relatively safe, and it can directly ablate cancer cells as well. Additionally, photothermal effects during PTT can speed up the Fenton-based process' reaction rate and enhance CDT (Yu et al., 2021; Zhang et al., 2022). With the development of nanotechnology, various targeted and multifunctional nanoparticles have been reported, which can deliver drugs and directly or indirectly activate the immune system to kill cancer cells (Hooftman and O'Neill, 2022; Luo et al., 2021; Sun et al., 2021). Although some nanomaterials have been used clinically in recent years, most of them have not achieved ideal clinical effects. In monotherapy, the continuing effects and biosafety of NPs on tumor cells require further study.

There is a new type of cell death called ferroptosis that differs from apoptosis, necrosis, and autophagy, which are all iron-dependent cell deaths (Chen et al., 2021b; Tang et al., 2021). As a metabolic disorder resulting from iron, ROS, and polyunsaturated fats, ferroptosis is characterized by deranged iron metabolism. Iron, lipid, and energy metabolism play a significant role in the sensitivity of tumor cells to ferroptosis (Lee et al., 2020; Li and Li, 2020; Jiang et al., 2021). Nanomedicine has become a new direction in the application of ferroptosis. Ultra-small PEG@ SiO_2 NPs induce ferroptosis and limit tumor growth in starving cancer cells by mediating iron overuptake (Ma et al., 2017). In addition, p53 plasmid-coated metal-organic network NPs lead to ferroptosis and tumor growth inhibition by blocking GSH synthesis (Zheng et al., 2017). In our study, we found that PPy@Fe_3O_4 NPs restrained CRC cells' growth and metastasis by promoting cell ferroptosis, and the exact mechanism needs to be further studied.

In normal physiology processes, NF-κB pathway coordinates the inflammatory process and participates in the regulation of various steps of the cell cycle and survival (DiDonato et al., 2012; Zhang et al., 2017). Binding to an inhibitory protein in the cytoplasm keeps it inactive. In response to the signal, its inhibitor is phosphorylated and proteolytically degraded, and NF-κB is translocated vigorously to the nucleus, where it promotes transcription of target genes (Vaiopoulos et al., 2013). Numerous pieces of evidence indicate that NF-κB has a key role in the initiation and propagation of CRC. Furthermore, the NF-κB signaling activation has been identified as a recognized event in the EMT process (Min et al., 2008). Liu et al. found that DCLK1 facilitates EMT via the NF-κB signaling pathway in CRC cells (Liu et al., 2018). Moreover, previous studies have shown that NF-κB regulates Vimentin and Snail expression directly by binding their promoters (Wu et al., 2004), which is consistent with our WB results. Herein, our study demonstrated that PPy@ Fe_3O_4 NPs inhibit CRC cell proliferation and metastasis by blocking the NF-κB signaling pathway.

Overall, we exhibited the suppressive role of NPs in the progression of CRC *in vitro* and *in vivo*. Furthermore, our results revealed that PPy@Fe_3O_4 has an excellent photothermal effect and photostability under NIR irradiation. PPy@Fe_3O_4 NPs can not only be used for PPT and CDT but also can inhibit the growth and metastasis of tumor cells by regulating the NF-κB signaling pathway. Therefore, a therapeutic strategy based on PPy@Fe_3O_4 NPs to attenuate tumor development may be a potential approach for CRC treatment.

Conclusion

PPy is a common non-toxic conductive polymer that is slightly soluble in water, other nanomaterials loaded with PPy can significantly improve their photothermal effect. In this study, we developed an NPs (PPy@Fe_3O_4) based on PPy to enhance the effect of PTT/CDT in CRC. The NPs displayed a high photothermal conversion efficiency of 52% because of PPy, which was much higher than that of traditional PPT agents. Besides, NPs were responsively decomposed in the tumor microenvironment to release the Fe ions of different valences, which promoted the generation of toxic OH from H_2O_2 for CDT. More importantly, we discovered a direct effect of NPs on colorectal cancer cells. PPy@Fe_3O_4 NPs can inhibit the growth and metastasis of colorectal cancer cells through the NF-κB signaling pathway, and promote cell ferroptosis.

Data availability statement

The original contributions presented in the study are included in the article/Supplementary Material, further inquiries can be directed to the corresponding authors.

Ethics statement

The animal study was reviewed and approved by Ethics Committee of Renji Hospital Affiliated with Shanghai Jiaotong University School of Medicine.

Author contributions

ZY and ST: Wrote the manuscript, *In vivo* and *in vitro* models. CW and ZW: Data curation, methodology; YY and SW: supervision, project administration; KJ: funding acquisition. All authors have read and agreed to the published version of the manuscript.

Funding

This study was supported by the National Scientific Center Project (No. 62088101) and the Industry-University-Research

Innovation Fund in Ministry of Education of the People's Republic of China (No. 2018A01013).

Conflict of interest

The authors declare that the research was conducted in the absence of any commercial or financial relationships that could be construed as a potential conflict of interest.

Publisher's note

All claims expressed in this article are solely those of the authors and do not necessarily represent those of their affiliated organizations, or those of the publisher, the editors and the reviewers. Any product that may be evaluated in this article, or claim that may be made by its manufacturer, is not guaranteed or endorsed by the publisher.

References

Aggarwal, C., Meropol, N. J., Punt, C. J., Iannotti, N., Saidman, B. H., Sabbath, K. D., et al. (2013). Relationship among circulating tumor cells, CEA and overall survival in patients with metastatic colorectal cancer. *Ann. Oncol.* 24 (2), 420–428. doi:10.1093/annonc/mds336

Aksan, A., Farrag, K., Aksan, S., Schroeder, O., and Stein, J. (2021). Flipside of the coin: Iron deficiency and colorectal cancer. *Front. Immunol.* 12, 635899. doi:10.3389/fimmu.2021.635899

Baek, S., Singh, R. K., Khanal, D., Patel, K. D., Lee, E. J., Leong, K. W., et al. (2016). Smart multifunctional drug delivery towards anticancer therapy harmonized in mesoporous nanoparticles. *Nanoscale* 7 (34), 14191–14216. doi:10.1039/c5nr02730f

Biller, L. H., and Schrag, D. (2021). Diagnosis and treatment of metastatic colorectal cancer: A review. *JAMA* 325 (7), 669–685. doi:10.1001/jama.2021.0106

Bray, F., Ferlay, J., Soerjomataram, I., Siegel, R. L., Torre, L. A., and Jemal, A. (2018). Global cancer statistics 2018: GLOBOCAN estimates of incidence and mortality worldwide for 36 cancers in 185 countries. *CA A Cancer J. Clin.* 68 (6), 394–424. doi:10.3322/caac.21492

Brenner, H., Kloor, M., and Pox, C. P. (2014). Colorectal cancer. *Lancet* 383 (9927), 1490–1502. doi:10.1016/S0140-6736(13)61649-9

Cen, D., Ge, Q., Xie, C., Zheng, Q., Guo, J., Zhang, Y., et al. (2021). ZnS@BSA nanoclusters potentiate efficacy of cancer immunotherapy. *Adv. Mat.* 33 (49), e2104037. doi:10.1002/adma.202104037

Chen, P., Li, X., Zhang, R., Liu, S., Xiang, Y., Zhang, M., et al. (2020). Combinative treatment of β-elemene and cetuximab is sensitive to KRAS mutant colorectal cancer cells by inducing ferroptosis and inhibiting epithelial-mesenchymal transformation. *Theranostics* 10 (11), 5107–5119. doi:10.7150/thno.44705

Chen, X., Kang, R., Kroemer, G., and Tang, D. (2021b). Broadening horizons: The role of ferroptosis in cancer. *Nat. Rev. Clin. Oncol.* 18 (5), 280–296. doi:10.1038/s41571-020-00462-0

Chen, X., Li, J., Kang, R., Klionsky, D. J., and Tang, D. (2021a). Ferroptosis: Machinery and regulation. *Autophagy* 17 (9), 2054–2081. doi:10.1080/15548627.2020.1810918

DiDonato, J. A., Mercurio, F., and Karin, M. (2012). NF-κB and the link between inflammation and cancer. *Immunol. Rev.* 246 (1), 379–400. doi:10.1111/j.1600-065X.2012.01099.x

Duan, X., Chan, C., and Lin, W. (2019). Nanoparticle-Mediated immunogenic cell death enables and potentiates cancer immunotherapy. *Angew. Chem. Int. Ed.* 58 (3), 670–680. doi:10.1002/anie.201804882

El-Toni, A. M., Habila, M. A., Labis, J. P., ALOthman, Z. A., Alhoshan, M., Elzatahry, A. A., et al. (2016). Design, synthesis and applications of core-shell, hollow core, and nanorattle multifunctional nanostructures. *Nanoscale* 8 (5), 2510–2531. doi:10.1039/c5nr07004j

Engstrand, J., Nilsson, H., Strömberg, C., Jonas, E., and Freedman, J. (2018). Colorectal cancer liver metastases - a population-based study on incidence, management and survival. *BMC Cancer* 18 (1), 78. doi:10.1186/s12885-017-3925-x

Enriquez-Navas, P. M., Wojtkowiak, J. W., and Gatenby, R. A. (2015). Application of evolutionary principles to cancer therapy. *Cancer Res.* 75 (22), 4675–4680. doi:10.1158/0008-5472.can-15-1337

Fan, A., Wang, B., Wang, X., Nie, Y., Fan, D., Zhao, X., et al. (2021). Immunotherapy in colorectal cancer: Current achievements and future perspective. *Int. J. Biol. Sci.* 17 (14), 3837–3849. doi:10.7150/ijbs.64077

Guan, D., Zhou, W., Wei, H., Wang, T., Zheng, K., Yang, C., et al. (2022c). Ferritinophagy-Mediated ferroptosis and activation of keap1/nrf2/HO-1 pathway were conducive to EMT inhibition of gastric cancer cells in action of 2,2'-Di-pyridineketone hydrazone dithiocarbamate butyric acid ester. *Oxid. Med. Cell. Longev.* 2022, 3920664. doi:10.1155/2022/3920664

Guan, S., Liu, X., Fu, Y., Li, C., Wang, J., Mei, Q., et al. (2022a). A biodegradable "Nano-donut" for magnetic resonance imaging and enhanced chemo/photothermal/chemodynamic therapy through responsive catalysis in tumor microenvironment. *J. Colloid Interface Sci.* 608 (1), 344–354. doi:10.1016/j.jcis.2021.09.186

Guan, S., Liu, X., Li, C., Wang, X., Cao, D., Wang, J., et al. (2022b). Intracellular mutual amplification of oxidative stress and inhibition multidrug resistance for enhanced sonodynamic/chemodynamic/chemo therapy. *Small* 18 (13), e2107160. doi:10.1002/smll.202107160

Hooftman, A., and O'Neill, L. A. J. (2022). Nanoparticle asymmetry shapes an immune response. *Nature* 601 (7893), 323–325. doi:10.1038/d41586-021-03806-7

Huang, G., Ma, L., Shen, L., Lei, Y., Guo, L., Deng, Y., et al. (2022). MIF/SCL3A2 depletion inhibits the proliferation and metastasis of colorectal cancer cells via the AKT/GSK-3β pathway and cell iron death. *J. Cell. Mol. Med.* 26 (12), 3410–3422. doi:10.1111/jcmm.17352

Huang, X., Deng, G., Han, Y., Yang, G., Zou, R., Zhang, Z., et al. (2019). Right $Cu_{2-x}S$@MnS core–shell nanoparticles as a photo/H_2O_2-responsive platform for effective cancer theranostics. *Adv. Sci. (Weinh).* 6 (20), 1901461. doi:10.1002/advs.201901461

Jiang, W. G., Sanders, A. J., Katoh, M., Ungefroren, H., Gieseler, F., Prince, M., et al. (2015). Tissue invasion and metastasis: Molecular, biological and clinical perspectives. *Semin. Cancer Biol.* 35, S244–S275. doi:10.1016/j.semcancer.2015.03.008

Jiang, X., Stockwell, B. R., and Conrad, M. (2021). Ferroptosis: Mechanisms, biology and role in disease. *Nat. Rev. Mol. Cell Biol.* 22 (4), 266–282. doi:10.1038/s41580-020-00324-8

Koppe, M. J., Bleichrodt, R. P., Oyen, W. J., and Boerman, O. C. (2005). Radioimmunotherapy and colorectal cancer. *Br. J. Surg.* 92 (3), 264–276. doi:10.1002/bjs.4936

Lee, H., Zandkarimi, F., Zhang, Y., Meena, J. K., Kim, J., Zhuang, L., et al. (2020). Energy-stress-mediated AMPK activation inhibits ferroptosis. *Nat. Cell Biol.* 22 (2), 225–234. doi:10.1038/s41556-020-0461-8

Li, D., and Li, Y. (2020). The interaction between ferroptosis and lipid metabolism in cancer. *Signal Transduct. Target. Ther.* 5 (1), 108. doi:10.1038/s41392-020-00216-5

Li, X., Li, W., Wang, M., and Liao, Z. (2021). Magnetic nanoparticles for cancer theranostics: Advances and prospects. *J. Control. Release* 335, 437–448. doi:10.1016/j.jconrel.2021.05.042

Liang, Y., Mitriashkin, A., Lim, T. T., and Goh, J. C. (2021). Conductive polypyrrole-encapsulated silk fibroin fibers for cardiac tissue engineering. *Biomaterials* 276, 121008. doi:10.1016/j.biomaterials.2021.121008

Liu, W., Wang, S., Sun, Q., Yang, Z., Liu, M., and Tang, H. (2018). *Retracted:* DCLK1 promotes epithelial-mesenchymal transition via the PI3K/akt/NF-κB pathway in colorectal cancer. *Int. J. Cancer* 142 (10), 2068–2079. doi:10.1002/ijc.31232

Luo, L., Li, X., Zhang, J., Zhu, C., Jiang, M., Luo, Z., et al. (2021). Enhanced immune memory through a constant photothermal-metabolism regulation for cancer prevention and treatment. *Biomaterials* 270, 120678. doi:10.1016/j.biomaterials.2021.120678

Ma, P., Xiao, H., Yu, C., Liu, J., Cheng, Z., Song, H., et al. (2017). Enhanced cisplatin chemotherapy by iron oxide nanocarrier-mediated generation of highly toxic reactive oxygen species. *Nano Lett.* 17 (2), 928–937. doi:10.1021/acs.nanolett.6b04269

Miar, S., Ong, J. L., Bizios, R., and Guda, T. (2021). Electrically stimulated tunable drug delivery from polypyrrole-coated polyvinylidene fluoride. *Front. Chem.* 9, 599631. doi:10.3389/fchem.2021.599631

Min, C., Eddy, S. F., Sherr, D. H., and Sonenshein, G. E. (2008). NF-κB and epithelial to mesenchymal transition of cancer. *J. Cell. Biochem.* 104, 733–744. doi:10.1002/jcb.21695

Modest, D. P., Pant, S., and Sartore-Bianchi, A. (2019). Treatment sequencing in metastatic colorectal cancer. *Eur. J. Cancer* 109, 70–83. doi:10.1016/j.ejca.2018.12.019

Morgan, M. J., and Liu, Z. G. (2011). Crosstalk of reactive oxygen species and NF-κB signaling. *Cell Res.* 21 (1), 103–115. doi:10.1038/cr.2010.178

Padmanabhan, H., Brookes, M. J., and Iqbal, T. (2015). Iron and colorectal cancer: Evidence from *in vitro* and animal studies. *Nutr. Rev.* 73 (5), 308–317. doi:10.1093/nutrit/nuu015

Patel, M., Horgan, P. G., McMillan, D. C., and Edwards, J. (2018). NF-κB pathways in the development and progression of colorectal cancer. *Transl. Res.* 197, 43–56. doi:10.1016/j.trsl.2018.02.002

Phipps, O., Brookes, M. J., and Al-Hassi, H. O. (2021). Iron deficiency, immunology, and colorectal cancer. *Nutr. Rev.* 79 (1), 88–97. doi:10.1093/nutrit/nuaa040

Ploug, M., Kroijer, R., Qvist, N., Lindahl, C. H., and Knudsen, T. (2021). Iron deficiency in colorectal cancer patients: A cohort study on prevalence and associations. *Colorectal Dis.* 23 (4), 853–859. doi:10.1111/codi.15467

Rebersek, M. (2020). Consensus molecular subtypes (CMS) in metastatic colorectal cancer -personalized medicine decision. *Radiol. Oncol.* 54 (3), 272–277. doi:10.2478/raon-2020-0031

Setyawati, M. I., and Leong, D. T. (2017). Mesoporous silica nanoparticles as an antitumoral-angiogenesis strategy. *ACS Appl. Mat. Interfaces* 9 (8), 6690–6703. doi:10.1021/acsami.6b12524

Siegel, R. L., Miller, K. D., Fuchs, H. E., and Jemal, A. (2021). Cancer statistics, 2021. *Ca. A Cancer J. Clin.* 71 (1), 7–33. doi:10.3322/caac.21654

Su, L. J., Zhang, J. H., Gomez, H., Murugan, R., Hong, X., Xu, D., et al. (2019). Reactive oxygen species-induced lipid peroxidation in apoptosis, autophagy, and ferroptosis. *Oxid. Med. Cell. Longev.* 2019, 1–13. doi:10.1155/2019/5080843

Sun, T., Zhang, Y. S., Pang, B., Hyun, D. C., Yang, M., and Xia, Y. (2014). Engineered nanoparticles for drug delivery in cancer therapy. *Angew. Chem. Int. Ed. Engl.* 53 (46), 12320–12364. doi:10.1002/anie.201403036

Sun, W., Ge, K., Jin, Y., Han, Y., Zhang, H., Zhou, G., et al. (2019). Bone-targeted nanoplatform combining zoledronate and photothermal therapy to treat breast cancer bone metastasis. *ACS Nano* 13 (7), 7556–7567. doi:10.1021/acsnano.9b00097

Sun, X., Zhang, Y., Li, J., Park, K. S., Han, K., Zhou, X., et al. (2021). Amplifying STING activation by cyclic dinucleotide-manganese particles for local and systemic cancer metalloimmunotherapy. *Nat. Nanotechnol.* 16 (11), 1260–1270. doi:10.1038/s41565-021-00962-9

Tang, D., Chen, X., Kang, R., and Kroemer, G. (2021). Ferroptosis: Molecular mechanisms and health implications. *Cell Res.* 31 (2), 107–125. doi:10.1038/s41422-020-00441-1

Tang, Z., Liu, Y., He, M., and Bu, W. (2019). Chemodynamic therapy: Tumour microenvironment-mediated Fenton and fenton-like reactions. *Angew. Chem. Int. Ed.* 58 (4), 946–956. doi:10.1002/anie.201805664

Torti, S. V., Manz, D. H., Paul, B. T., Blanchette-Farra, N., and Torti, F. M. (2018). Iron and cancer. *Annu. Rev. Nutr.* 38, 97–125. doi:10.1146/annurev-nutr-082117-051732

Torti, S. V., and Torti, F. M. (2020). Iron and cancer: 2020 vision. *Cancer Res.* 80 (24), 5435–5448. doi:10.1158/0008-5472.CAN-20-2017

Vaiopoulos, A. G., Athanasoula, K. C., and Papavassiliou, A. G. (2013). NF-κB in colorectal cancer. *J. Mol. Med.* 91 (9), 1029–1037. doi:10.1007/s00109-013-1045-x

Wilson, M. J., Harlaar, J. J., Jeekel, J., Schipperus, M., and Zwaginga, J. J. (2018). Iron therapy as treatment of anemia: A potentially detrimental and hazardous strategy in colorectal cancer patients. *Med. Hypotheses* 110, 110–113. doi:10.1016/j.mehy.2017.12.011

Wu, Y., Diab, I., Zhang, X., Izmailova, E. S., and Zehner, Z. E. (2004). Stat3 enhances vimentin gene expression by binding to the antisilencer element and interacting with the repressor protein, ZBP-89. *Oncogene* 23, 168–178. doi:10.1038/sj.onc.1207003

Xu, J., Fan, J., Qin, X., Cai, J., Gu, J., Wang, S., et al. (2019). Chinese guidelines for the diagnosis and comprehensive treatment of colorectal liver metastases (version 2018). *J. Cancer Res. Clin. Oncol.* 145 (3), 725–736. doi:10.1007/s00432-018-2795-1

Yu, N., Qiu, P., Ren, Q., Wen, M., Geng, P., Macharia, D. K., et al. (2021). Transforming a sword into a knife: Persistent phototoxicity inhibition and alternative therapeutical activation of highly-photosensitive phytochlorin. *ACS Nano* 15 (12), 19793–19805. doi:10.1021/acsnano.1c07241

Zhang, L., Forgham, H., Shen, A., Qiao, R., and Guo, B. (2022). Recent advances in single Fe-based nanoagents for photothermal-chemodynamic cancer therapy. *Biosens. (Basel)* 12 (2), 86. doi:10.3390/bios12020086

Zhang, Q., Lenardo, M. J., and Baltimore, D. (2017). 30 Years of NF-κB: A blossoming of relevance to human pathobiology. *Cell* 168 (1-2), 37–57. doi:10.1016/j.cell.2016.12.012

Zheng, D. W., Lei, Q., Zhu, J. Y., Fan, J. X., Li, C. X., Li, C., et al. (2017). Switching apoptosis to ferroptosis: Metal-organic network for high-efficiency anticancer therapy. *Nano Lett.* 17 (1), 284–291. doi:10.1021/acs.nanolett.6b04060

Zheng, N., Wang, Q., Li, C., Wang, X., Liu, X., Wang, X., et al. (2021). Responsive degradable theranostic agents enable controlled selenium delivery to enhance photothermal radiotherapy and reduce side effects. *Adv. Healthc. Mat.* 10 (10), e2002024. doi:10.1002/adhm.202002024

Zheng, N. N., Kong, W. Y., Huang, Z., Liu, X. J., Liang, S. H., Deng, G. Y., et al. (2022). Novel theranostic nanoagent based on CuMo2S3-PEG-Gd for MRI-guided photothermal/photodynamic/chemodynamic therapy. *Rare Met.* 41 (1), 45–55. doi:10.1007/s12598-021-01793-2

Zhou, X., Yang, A., Huang, Z., Yin, G., Pu, X., and Jin, J. (2017). Enhancement of neurite adhesion, alignment and elongation on conductive polypyrrole-poly (lactide acid) fibers with cell-derived extracellular matrix. *Colloids Surf. B Biointerfaces* 149, 217–225. doi:10.1016/j.colsurfb.2016.10.014

Zhu, X., Feng, W., Chang, J., Tan, Y. W., Li, J., Chen, M., et al. (2016). Temperature-feedback upconversion nanocomposite for accurate photothermal therapy at facile temperature. *Nat. Commun.* 7, 10437. doi:10.1038/ncomms10437

TYPE Correction
PUBLISHED 27 September 2023
DOI 10.3389/fbioe.2023.1148674

Check for updates

OPEN ACCESS

EDITED AND REVIEWED BY
Yu Luo,
Shanghai University of Engineering Sciences, China

*CORRESPONDENCE
Kewei Jiang,
dr_jiangkewei@163.com

†These authors have contributed equally to this work

RECEIVED 20 January 2023
ACCEPTED 18 September 2023
PUBLISHED 27 September 2023

CITATION
Yu Z, Tong S, Wang C, Wu Z, Ye Y, Wang S and Jiang K (2023), Corrigendum: PPy@Fe_3O_4 nanoparticles inhibit the proliferation and metastasis of CRC via suppressing the NF-κB signaling pathway and promoting ferroptosis.
Front. Bioeng. Biotechnol. 11:1148674.
doi: 10.3389/fbioe.2023.1148674

COPYRIGHT
© 2023 Yu, Tong, Wang, Wu, Ye, Wang and Jiang. This is an open-access article distributed under the terms of the Creative Commons Attribution License (CC BY). The use, distribution or reproduction in other forums is permitted, provided the original author(s) and the copyright owner(s) are credited and that the original publication in this journal is cited, in accordance with accepted academic practice. No use, distribution or reproduction is permitted which does not comply with these terms.

Corrigendum: PPy@Fe_3O_4 nanoparticles inhibit the proliferation and metastasis of CRC via suppressing the NF-κB signaling pathway and promoting ferroptosis

Zhilong Yu[1†], Shanshi Tong[2†], Chenyi Wang[1], Zizhen Wu[1], Yingjiang Ye[1], Shan Wang[1] and Kewei Jiang[1*]

[1]Department of Gastroenterological Surgery, Laboratory of Surgical Oncology, Beijing Key Laboratory of Colorectal Cancer Diagnosis and Treatment Research, Peking University People's Hospital, Beijing, China, [2]State Key Laboratory of Oncogenes and Related Genes, Shanghai Cancer Institute, Renji Hospital, School of Medicine, Shanghai Jiao Tong University, Shanghai, China

KEYWORDS
colorectal cancer, nanoparticles, metastasis, NF-κB, ferroptosis

A Corrigendum on
PPy@Fe_3O_4 nanoparticles inhibit the proliferation and metastasis of CRC via suppressing the NF-κB signaling pathway and promoting ferroptosis

by Yu Z, Tong S, Wang C, Wu Z, Ye Y, Wang S and Jiang K (2022). Front. Bioeng. Biotechnol. 10: 1001994. doi: 10.3389/fbioe.2022.1001994

In the published article, there was an error in Figures 2E, 5 as published. Modifications to UV absorption spectra in Figure 2E and NF-κB related protein typographical errors in the WB experiment in Figure 5 were made after a recheck of the figures, but not included in the final article. The corrected Figures 2, 5 and their captions appear below.

Additionally, the statistical method in the "Statistics" section and "PPy@Fe3O4 NPs inhibited EMT via the NF-κB signaling pathway" section were incorrect due to translation error and clerical error.

A correction has been made to **Materials and methods** section, subsection *Statistics*. A correction has also been made to the **Results** section, subsection *PPy@Fe3O4 NPs inhibited EMT via the NF-κB signaling pathway*, Paragraph 1. These sentences previously stated, respectively:

"Based on experiments performed in triplicate for cell proliferation, migration, and invasion, all data are presented as mean ± SEM. In the animal study of nude mice, the data are presented as mean ± SEM of 5 mice. Statistical analyses were performed with the χ2 test or the Student's t-test (two-tailed unpaired). All the data were analyzed using SPSS 22.0 software and $p < 0.05$ was considered significant."

"There was an increase in the levels of IKKα and IKKβ in DLD1, as well as a decrease in the amounts of IκBα after treatment with H_2O_2. P65 levels did not change significantly, but phospho-p65 expression increased. We discovered that the expression of phosphorylated (p) p65, IKKα, IKKβ, and IκBα, which are essential for activating the NF-κB signaling pathway, were downregulated by NPs with H_2O in DLD1 cells."

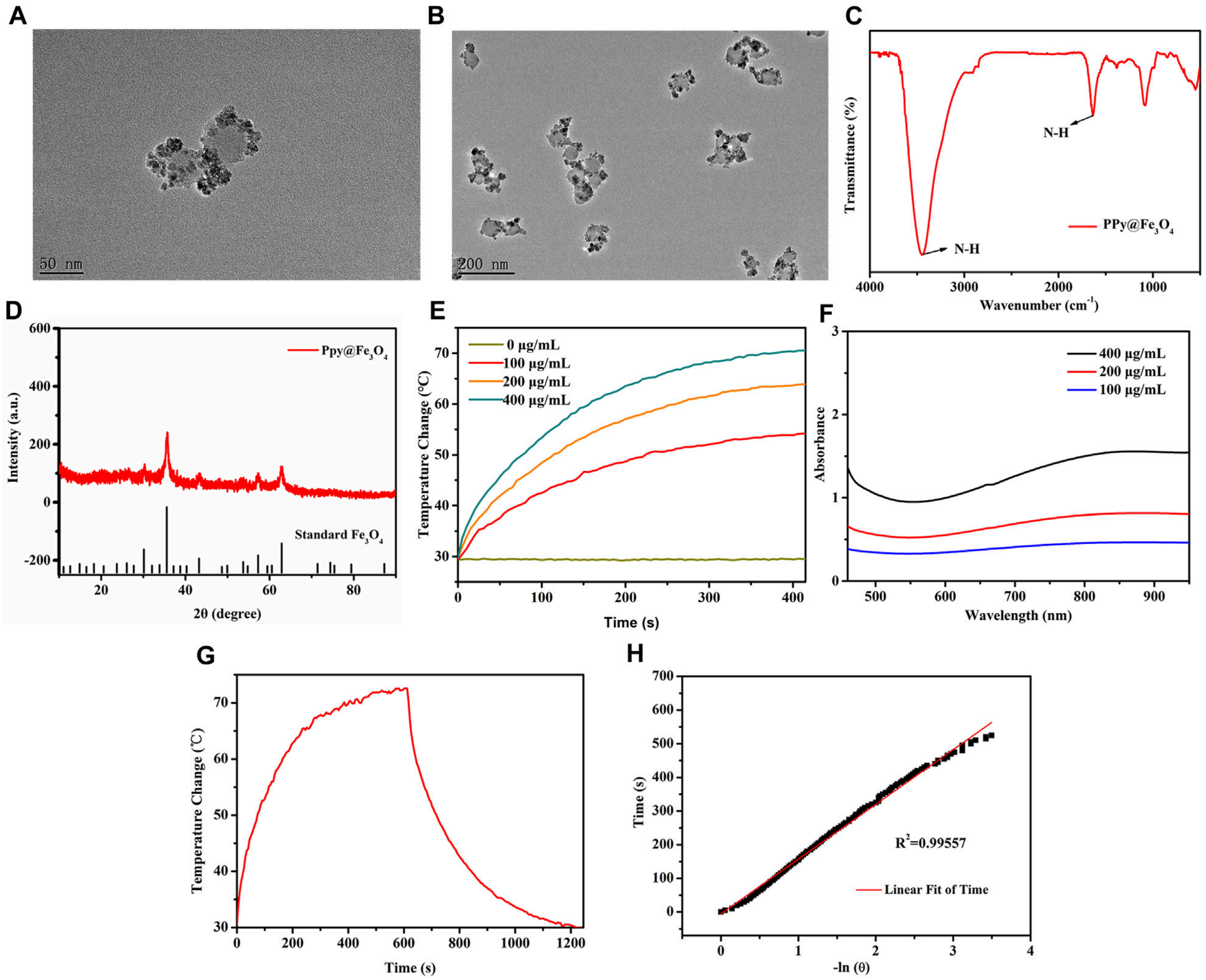

FIGURE 2
The characterization and photothermal properties of the PPy@Fe$_3$O$_4$ NPs. **(A,B)** High and Low TEM images of PPy@Fe$_3$O$_4$ NPs; **(C)** FTIR spectra of PPy@Fe$_3$O$_4$ NPs; **(D)** XRD spectra of PPy@Fe$_3$O$_4$ NPs; **(E)** UV-Vis-NIR absorption spectra of PPy@Fe$_3$O$_4$ NPs at different concentrations; **(F)** Temperature change curve with various concentrations of NPs; **(G)** Temperature curve of rising with irradiation and naturally cooling; **(H)** Linear regression curve of cooling process (red).

The corrected sentences appear below:

"All data are presented as mean ± SD. Statistical analyses were performed with the χ2 test or the Student's t-test (two-tailed unpaired). All the data were analyzed using Origin and Graphpad. Moreover, $p < 0.05$ is considered statistically significant."

"There was a decrease in the levels of p-IKKα and p-IKKβ in DLD1, as well as an increase in the amounts of p-IκBα after treatment with NPs and H_2O_2. P65 levels did not change significantly, but phospho-p65 expression decreased. We discovered that the expression of phosphorylated (p)p65, p-IKKα, p-IKKβ, and IκBα, which are essential for activating the NF-κB signaling pathway, were downregulated by NPs with H_2O_2 in DLD1 cells."

There was also an error in the **Funding** statement. National Nature Science Foundation of China (No. 81871962) has expired and ceased. The correct **Funding** statement appears below.

"This study was supported by the National Scientific Center Project (No. 62088101) and the Industry-University-Research Innovation Fund in Ministry of Education of the People's Republic of China (No. 2018A01013)."

The authors apologize for these errors and state that this does not change the scientific conclusions of the article in any way. The original article has been updated.

Publisher's note

All claims expressed in this article are solely those of the authors and do not necessarily represent those of their affiliated organizations, or those of the publisher, the editors and the reviewers. Any product that may be evaluated in this article, or claim that may be made by its manufacturer, is not guaranteed or endorsed by the publisher.

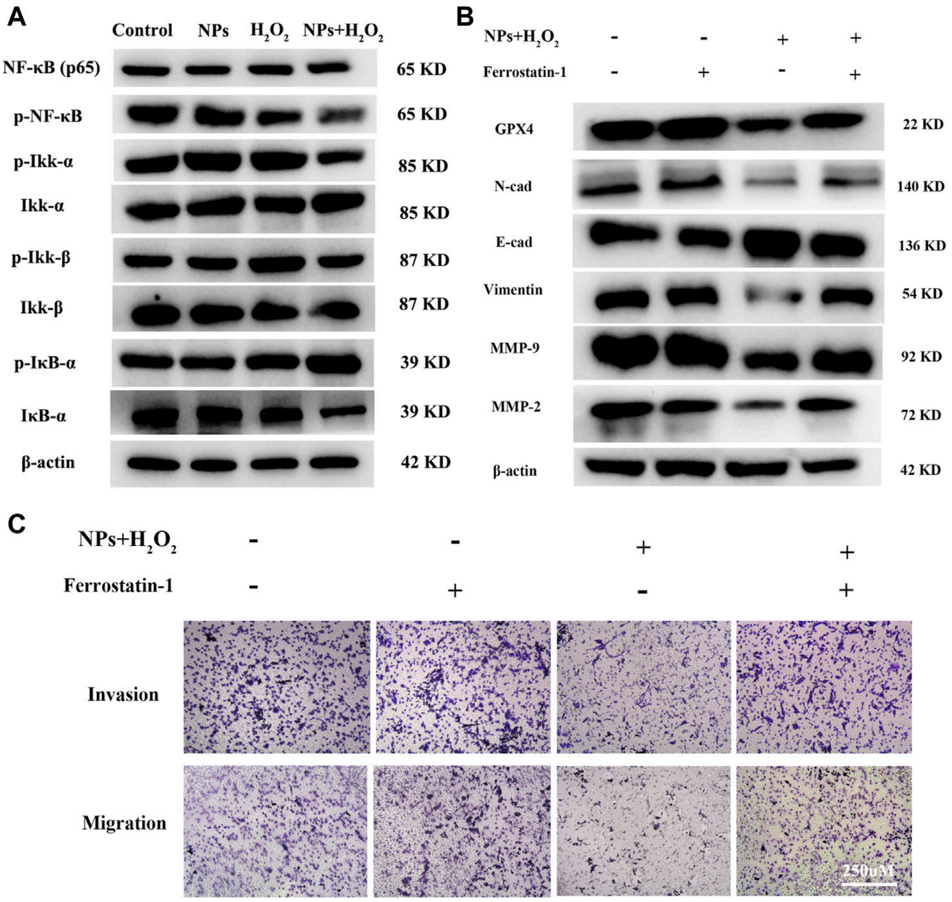

FIGURE 5
PPy@Fe_3O_4 NPs suppress CRC cells metastasis by promoting cell ferroptosis and inhibiting NF-κB signaling pathway. **(A)** Western blot. Colorectal cancer cell line DLD1 was treated with various groups (Control, H_2O_2, NPs and NPs + H_2O_2), and then subjected to Western blot analysis of the key proteins of the NF-KB signaling pathway (Ikk-β, p-Ikk-β, ikk-α, p-Ikk-α, NF-κβ, p-NF-κβ, IκB-α and p-IκB-α). **(B)** Effects of the ferroptosis inhibitor Ferrostatin-1 on PPy@Fe_3O_4 NPs-induced metastasis-related proteins expression. **(C)** Transwell showed that PPy@Fe_3O_4 NPs-induced cell migration and invasion were abolished after addition of the ferroptosis inhibitor Ferrostatin-1 in CRC cell.

frontiers | Frontiers in Bioengineering and Biotechnology

TYPE Original Research
PUBLISHED 16 September 2022
DOI 10.3389/fbioe.2022.986033

Check for updates

OPEN ACCESS

EDITED BY
Xin Li,
DWI—Leibniz-Institut für Interaktive Materialien, Germany

REVIEWED BY
Ahsan Hafiz Muhammad,
Bahauddin Zakariya University Multan Pakistan, Pakistan
Yi Lu,
RWTH Aachen University, Germany

*CORRESPONDENCE
Ming Cai,
caiming@zjut.edu.cn
Kai Yang,
yangkai@zjut.edu.cn

SPECIALTY SECTION
This article was submitted to Nanobiotechnology, a section of the journal Frontiers in Bioengineering and Biotechnology

RECEIVED 04 July 2022
ACCEPTED 01 August 2022
PUBLISHED 16 September 2022

CITATION
Wang J, Yu Y-D, Zhang Z-G, Wu W-C, Sun P-L, Cai M and Yang K (2022), Formation of sweet potato starch nanoparticles by ultrasonic—assisted nanoprecipitation: Effect of cold plasma treatment.
Front. Bioeng. Biotechnol. 10:986033.
doi: 10.3389/fbioe.2022.986033

COPYRIGHT
© 2022 Wang, Yu, Zhang, Wu, Sun, Cai and Yang. This is an open-access article distributed under the terms of the Creative Commons Attribution License (CC BY). The use, distribution or reproduction in other forums is permitted, provided the original author(s) and the copyright owner(s) are credited and that the original publication in this journal is cited, in accordance with accepted academic practice. No use, distribution or reproduction is permitted which does not comply with these terms.

Formation of sweet potato starch nanoparticles by ultrasonic —assisted nanoprecipitation: Effect of cold plasma treatment

Jian Wang[1], Yu-Die Yu[1], Zhi-Guo Zhang[2], Wei-Cheng Wu[2], Pei-Long Sun[1], Ming Cai[1]* and Kai Yang[1]*

[1]College of Food Science and Technology, Zhejiang University of Technology, Hangzhou, Zhejiang, China, [2]Food Science Institute, Zhejiang Academy of Agricultural Sciences, Hangzhou, Zhejiang, China

Starch nanoparticles (SNPs) were produced from sweet potato starches by ultrasonic treatment combined with rapid nanoprecipitation. The starch concentration, ultrasonic time, and the ratio of starch solution to ethanol were optimized through dynamic light scattering (DLS) technique to obtain SNPs with a Z-average size of 64.51 ± 0.15 nm, poly dispersity index (PDI) of 0.23 ± 0.01. However, after freeze drying, the SNPs showed varying degrees of aggregation depending on the particle size of SNPs before freeze-drying. The smaller the particle size, the more serious the aggregation. Therefore, we tried to treat SNPs with dielectric barrier discharge cold plasma before freeze drying. Properties including morphological features, crystalline structure and apparent viscosity of various starches were measured by field emission scanning electron microscopy (FE-SEM), X-ray diffraction (XRD), and rheometer, respectively. The results showed that, after cold plasma (CP) treatment, the aggregation of SNPs during freeze drying was significantly inhibited. Compared to the native sweet potato starch, SNPs showed a higher relative crystallinity and a lower apparent viscosity. After CP treatment, the relative crystallinity of CP SNPs was further higher, and the apparent viscosity was lower. This work provides new ideas for the preparation of SNPs and could promote the development of sweet potato SNPs in the field of active ingredient delivery.

KEYWORDS
sweet potato, starch nanoparticles, cold plasma, nanoprecipitation, ultra sonification

1 Introduction

Sweet potato starch is one of the richest sourced edible starches (Lyu et al., 2021). For broaden the field of application of sweet potato starch, physical, chemical, enzymatic or combined methods have been used to treat the starch in order to improve its structural and functional properties. Among these, preparation of starch nanoparticles (SNPs) is currently an important direction of analysis in the deep processing of starch. SNPs have been prepared through chemical, physical or biological methods to reduce the particle size of the original starch from the micron scale to the nanoscale. Nanoparticles have multiple beneficial attributes such as small size, more surface area, quantum size, and macroscopic quantum tunneling effect which are absent in conventional starches. Therefore, it is desired to prepare the nano-scale starch particles to improve their physical and chemical properties (Wang and Zhang, 2021). The performance of nano-materials like SNPs is strongly dependent on their characteristics, such as particle size, morphology, dispersion, microstructure, and rheology as well as how these characteristics change under different processing conditions (Perez Herrera et al., 2017; Dong et al., 2021; Li et al., 2021a; Li et al., 2021b).

There are two approaches for the preparation of SNPs, "top-down" and "bottom-up" approaches. The "top-down" approach uses physical or chemical means (hydrolysis, mechanical grinding, etc.) to prepare SNPs by decreasing the size of the starch particles. For example, SNPs were isolated from native starch granules by ball milling combined with acid hydrolysis (Ye et al., 2017). The "bottom-up" approach is to prepare SNPs by assembling starch molecules as basic units (e.g., nanoprecipitation and reverse-phase microemulsion). Among these methods, nanoprecipitation, also known as anti-solvent precipitation, has increasingly gained interest due to its simplicity and scalable potential (Martinez Rivas et al., 2017). In this method, a polymer is first dissolved in a solvent (good solvent) to form a homogeneous polymer phase, and then this polymer solution is transferred to another solvent (non-solvent) or the non-solvent is added to the good solvent in which the polymer is dissolved to cause the polymer to precipitate and form nanoparticles. Recently, ultrasonic assisted nanoprecipitation has been proved as an effective approach for producing SNPs with specific desired properties (Dong et al., 2022). However, after drying, the aggregation of SNPs would always happen, triggered by reducing surface energy to reach a steady state (Wang and Zhang, 2021).

In recent years, cold plasma (CP) treatment has been proved as an effective surface modification technique (cheap, eco-friendly, and non-thermal food processing technique) (Kopuk et al., 2022). CP consists of ultraviolet (UV) photons, ions, free electrons, and reactive species such as reactive nitrogen species (RNS) and reactive oxygen species (ROS), which is created by supplying different forms of energy like radio, electric fields, magnetic fields, and microwave frequencies (Wang et al., 2021; Laroque et al., 2022). Apart from general microbial and enzyme inactivation purposes, CP can effectively modify the food macromolecules through their interactions with reactive plasma species (Kopuk et al., 2022). For starch, CP treatment results in various surface modifications of starches by oxidation, etching, crosslinking, and depolymerization (Wongsagonsup et al., 2014; Gao et al., 2019; Sudheesh et al., 2019). However, there are few reports available on the modification of SNPs surface function by CP, the structural and functional changes of SNPs treated by CP were confirmed (Shen et al., 2022).

In the current study, we prepared sweet potato SNPs by ultrasonic-assisted dissolution of starch and subsequent rapid nanoprecipitation. SNPs were further treated with CP before freeze drying. We supposed that, SNPs will be electric charged by CP treatment, and the free radicals created by CP can cause skeletal breakage of SNPs, producing smaller fragments. The effect of CP on the preparation of SNPs was evaluated by the characterization of CP treated SNPs like multiscale structure, physicochemical, and rheological properties. This work could offer a novel idea for optimizing the preparation process of SNPs to inhibit the aggregation of SNPs during the drying process.

2 Materials and methods

2.1 Materials

Sweet potato starch was isolated from sweet potatoes obtained from Zhejiang Academy of Agricultural Sciences according to the method of Gani (Gani et al., 2012). The moisture content of obtained sweet potato starch was determined as 9.89% referring to GB5009.3-2016. Phosphate buffered saline (PBS) buffer (pH 7.4) used was from Adamas-beta (Adamas, Shanghai, China). Ethanol, sodium hydroxide (NaOH), and other chemical reagents (Shanghai Lingfeng Chemical Reagent Co., Ltd., Shanghai, China) were of analytical grade. All aqueous solutions were prepared in distilled water.

2.2 Preparation of starch nanoparticles

Sweet potato SNPs were prepared by ultrasonic-assisted dissolution of starch and subsequent rapid nanoprecipitation according to the method developed by (Ahmad et al., 2020; Dong et al., 2022) with some modifications. Briefly, the native sweet potato starch was dispersed in distilled water (2%, 5%, 8%, w/v) and gelatinized at 85°C for 30 min with stirring on a vortex mixer. The gelatinized starch paste was then sonicated for 5–25 min using a 20 kHz probe sonicator (JY98-IIIDN, Ningbo Scientz Biotechnology Co., Ltd., Ningbo, China) equipped with an ultrasonic horn and a tapered tip of 6 mm. The power output of 600 W and 3/5 s on/off pulses were applied to minimize heat generation. Nanoprecipitation was carried out by pouring sonicated starch paste solution rapidly into the ethanol (95%, v/v) under constant stirring. The volume ratio of starch solution to ethanol was 1:1, 1:2 and 1:5. After thorough mixing, an aliquot of the colloidal suspension obtained was diluted with distilled water for the analysis of the particle size and polydispersity index (PDI) by dynamic light scattering (DLS, see Section 2.5).

2.3 Cold plasma treatment

The cold plasma (CP) treatment was applied according to (Shen et al., 2022) with some modifications. Briefly, CP was generated by the dielectric barrier discharge (DBD) plasma apparatus (CTP-2000K, Nanjing Suman Electronics Co., Ltd., Nanjing, China), which was composed of a reaction cell (DBD-50), a voltage regulator, and a high frequency AC power (50 kV, 10 kHz). The SNPs were centrifugally separated and re-dispersed in PBS buffer to prepare SNP suspensions with a concentration of 5%. The prepared SNP suspensions were uniformly placed on the under-quartz medium (thickness: 3 mm) and put in a DBD reactor at room temperature. The plasma treatment conditions were as follows: the gas source was air, the distance of the two parallel electrodes was 1.3 cm, the input voltage was 90 ± 1 V, and the discharge was 1 A. The SNPs were treated for 90 s and named as CP SNPs.

2.4 Freeze-drying

The SNPs and CP SNPs were centrifugally separated and re-dispersed in PBS buffer to prepare SNP suspensions for freezing at −20°C overnight in a freezer. The frozen samples were then freeze-dried (Scientz-12N, Ningbo Scientz Biotechnology Co., Ltd., Ningbo, China) at −56°C for 2 days.

2.5 Particle size distribution

Particle size distributions of SNPs and CP SNPs were assessed by a dynamic light scattering instrument (Zetasizer NanoZS90, Malvern Instruments, Worcestershire, United Kingdom). The SNPs solution (0.01%, w/v) was prepared with distilled water and dispersed for 30 min with an ultrasonic cleaner (SB-300DTY, Ningbo Scientz Biotechnology Co. Ltd., Ningbo, China) for complete dispersion of particles. The pH of the suspension was adjusted to pH 7. The refractive index of water and starch were 1.33 and 1.53, respectively. The Z-average diameter and PDI were calculated by the Zetasizer software from three separate samples with five readings per sample.

2.6 Micromorphological features

The micromorphology of native starch, SNPs, and CP SNPs were observed using a field emission scanning electron microscopy (FE-SEM) (FESEM SU8220, Hitachi Ltd., Japan) at the accelerating voltage of 15.0 kV. Samples were sticked on a double-sided adhesive tape with the other side on a circular aluminum platform and coated with a thin layer of gold-palladium alloy.

2.7 X-ray diffraction

The crystalline characteristics of native starch, SNPs, and CP SNPs were determined using an X-ray diffractometer (Empyrean, PANalytical, Inc., Netherlands) at 45 kV and 40 mA Cu-Kα (λ = 0.1541 nm) radiations. The XRD measurements were scanned from 4° to 30° (2θ) with a scanning speed of 2°/min. The XRD diffractograms were collected using the MDI-Jade 6.0 software and the relative crystallinity (%) were calculated by the ratio between the areas of crystallin region and total area of the diffractogram.

2.8 Measurements of static rheological properties

SNPs, CP SNPs suspensions of 8% (w/v) and native starch paste solution of 2% (w/v) were prepared to satisfy the lowest viscosity that can be detected by the rheometer and then equilibrated at 25°C for 30 min before each test. The rheological tests were measured using a stress-controlled rheometer (Physica MCR300, Anton Paar GmbH, Stuttgard, Germany) with a cone and plate geometry (cone angle, 2°; diameter, 40 mm; truncation gap, 53 μm). The continuous shear tests were performed at 25°C to measure the apparent viscosity. The shear rate range was from 0.1 to 100 s^{-1} in an upward sweep followed immediately by a downward sweep from 100 to 0.1 s^{-1}. Three sweep cycles were conducted consecutively in order to understand the relationship between the apparent viscosity and the shear rate of the SNP suspensions as well as their thixotropic behaviors.

2.9 Re-dispersion stability

Dried native starch, SNPs and CP SNPs were redispersed in distilled water and stirred for 1 h, then the dispersions were diluted to 5% (w/v) with distilled water in tubes, and the photographs of the tubes were taken in 0 and 30 min.

2.10 Statistical analysis

All measurements were measured at least in duplicate. Means and standard deviations were calculated and differences between means were determined with Fishers Least Significant Difference (LSD) test at $p < 0.05$ significance level (Statgraphics Centurion XV).

3 Results and discussions

3.1 Effects of preparation parameters on the particle size of starch nanoparticles

3.1.1 Effect of starch concentration

Figure 1A shows the particle size and PDI of SNPs fabricated from different starch concentrations. With decrease in starch concentration from 8% to 2%, the particle size of SNPs decreased from 124.00 ± 11.74 nm to 64.51 ± 0.51 nm, and the PDI decreased from 0.32 ± 0.02 to 0.23 ± 0.01, indicating that the produced SNPs were smaller and more uniform. The ultrasound exerts an obvious impact on the structure of starch granules by the collapse of cavitation bubbles, disrupting starch granules, and the water diffusion breaks of the crystal structure (Zhu et al., 2012). Under the same sonication

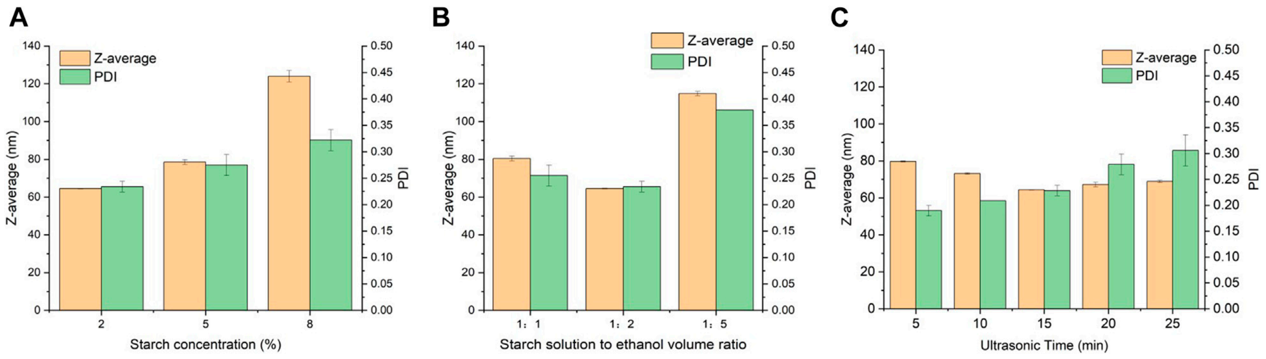

FIGURE 1
Effects of preparation parameters on the particle size of SNPs. **(A)** Starch concentration. **(B)** Starch solution to ethanol volume ratio. **(C)** Ultrasonic time.

condition, the low concentration starch solution will be subjected to more forces and decomposed more completely, and it is easier to self-assemble into nanoparticles with smaller particle size. On the other hand, in the process of nanoprecipitation after ultrasonication, the higher concentration of starch solution corresponds to more short-chain starch molecules per unit volume, and the more starch molecular chains diffuse into ethanol during alcohol deposition, which are more likely to polymerize and entangle into nanoparticles with larger particle size. In addition, an increase in the concentration of the starch solution leads to a decrease in water holding capacity and an increase in viscosity and gelling, which further hinder the precipitation of the starch solution by ethanol. Similar result was found in other work (Hebeish et al., 2013), as the initial starch concentration increased from 2.5% to 10%, the particle size of the SNPs increased from 132 to 396 nm, and PDI increased from 0.401 to 1.000. It was further found by TEM images that the SNPs prepared with starch concentrations of 2.5% and 5.0% had a clear spherical shape and did not aggregate, while the groups with starch concentrations of 7.5% and 10.0% had a strong tendency to aggregate, and these highly aggregated particles caused an increase in PDI and elevated the instability of the solution. Lower starch concentrations (2.5, 5%) were able to increase the penetration of ethanol in the starch and improve the dispersion of the nano-starch by forming a dextrinized starch with relatively low viscosity.

3.1.2. Effect of starch solution to ethanol volume ratio

As shown in Figure 1B, among the three starch solution to ethanol volume ratios, the SNPs with optimal particle size of 64.51 ± 0.15 nm, PDI of 0.23 ± 0.01 can be obtained at a starch solution to ethanol volume ratio of 1:2. Ethanol has a poor solubility for starch, so when starch solution is added dropwise to ethanol, a supersaturated solution of starch is formed, and the short-chain starch in the solution has a strong tendency to nucleate, and it is very easy to aggregate to form a double helix structure and then form starch granules. When the starch solution to ethanol volume ratio is low, little ethanol cannot create an environment of poor solvent, resulting in few nucleation sites and a slower growth trend of larger nanoparticles. Increasing the apportion of ethanol increases the diffusion distance during starch nucleation growth and limits the increase in nanoparticle size. Similar results were reported in other researches. (Wu et al., 2016) found that the average particle size of SNPs decreased from 213.1 ± 7.3 to 208.1 ± 1.0 nm, when the good solvent to poor solvent volume ratio changed from 1:5 to 1:30. (Kakran et al., 2012) found that as the good solvent to poor solvent ratio changed from 1:10 to 1:20, the length and diameter of nanoparticles decreased sharply from 1860 to 490 nm to 930 and 340 nm, respectively. When the ethanol ratio is too high, it may again make the repulsion in the solution too strong, the starch particles collision frequency increases, and excessive aggregation of starch particles leads to an increase in particle size. (Qiu et al., 2016) found that the particle size of SNPs was increased from 60 ± 1 nm to 92 ± 4 nm when the ratio of solvent to poor solvent was increased from 1:4 to 1:5.

3.1.3 Effect of ultrasonic treatment duration

As shown in Figure 1C, the particle size of SNPs decreased from 79.73 ± 0.23 nm to 64.35 ± 0.15 nm during the variation of the ultrasonic time from 5 to 15 min, showing a stable decreasing trend, which can be explained by the fact that with the increase of the ultrasonic time, a stronger force is generated, which in turn breaks down the starch paste into smaller short-chain starches, which in turn self-assemble to form smaller SNPs. (Boufi et al., 2018) also found that the ultrasound treatment gradually reduced the particle size of standard starch from 1,200 nm and stabilized it at about 40 nm. (Chang et al., 2017) found that the size distribution pattern of SNPs prepared from un-sonicated starch solution had three peaks, located at 70 nm, 400 nm and 3–6 μm, respectively, with the peaks in the range of 3–6 μm indicating the presence of large particles or aggregates. The average size of SNPs decreased from 221.6 to 95.0 nm after 30 min of sonication, indicating that the increase of

TABLE 1 Mean particle size and PDI of SNPs obtained by different preparation parameters before and after freeze-drying.

Operation parameters			**Before drying**		**After drying**	
Ultrasonic time/min	**Starch concentration /%**	**Starch solution to ethanol volume ratio**	**Mean size /nm**	**PDI**	**Mean size /nm**	**PDI**
5			79.73 ± 0.23^{cd}	0.19 ± 0.01^{a}	254.6 ± 3.4^{c}	0.51 ± 0.02^{b}
10			73.16 ± 0.42^{bc}	0.21 ± 0.00^{ab}	290.2 ± 5.7^{d}	0.34 ± 0.01^{a}
15	2		64.35 ± 0.15^{a}	0.23 ± 0.01^{ab}	353.2 ± 8.6^{e}	0.30 ± 0.08^{a}
20			67.21 ± 1.27^{ab}	0.28 ± 0.02^{cd}	268.0 ± 8.8^{c}	0.50 ± 0.03^{b}
25		1:2	68.87 ± 0.62^{ab}	0.31 ± 0.03^{d}	261.3 ± 2.9^{c}	0.54 ± 0.02^{b}
15	5		78.54 ± 1.25^{cd}	0.28 ± 0.02^{bc}	194.4 ± 2.3^{a}	0.67 ± 0.06^{b}
	8		124.0 ± 3.05^{e}	0.32 ± 0.02^{e}	308.0 ± 13.8^{d}	0.92 ± 0.04^{e}
	2	1:1	80.41 ± 1.30^{d}	0.26 ± 0.07^{bc}	266.3 ± 6.6^{c}	0.46 ± 0.04^{b}
		1:5	114.8 ± 1.15^{f}	0.38 ± 0.00^{e}	233.5 ± 2.5^{b}	0.33 ± 0.11^{a}

Values presented as mean ± SD, indicate the replicates of three experiments.
Values with different letters (a, b, c, d, e and f) are significantly different ($p < 0.05$).

ultrasonic time could result in smaller and more uniform SNPs. However, when the ultrasonic treatment exceeded 15 min, the tiny starch fragments regrouped into new particles or adhered to the surface of the starch particles, which in turn formed larger starch particles, and these large particles led to a non-uniform particle size distribution of SNPs and increased the PDI. This result is in relative agreement with the results of (Wang et al., 2020a) for the ultrasonic treatment of sweet potato starch, which both showed the same trend of increasing and then decreasing.

3.2 Freeze drying of sweet potato starch nanoparticles

As shown in Table 1, the particle size and PDI of freeze-dried SNPs were generally increased with significant differences ($p < 0.05$) compared to the SNPs before freeze-drying. It indicates that freeze-drying intensifies the aggregation, recrystallization and widens the inhomogeneity of distribution of SNPs. The common theories currently used to explain this aggregation phenomenon include capillary pressure theory, chemical bond theory, and crystal bridge theory (Wang et al., 2005), the most accepted of which is the hydrogen bonding theory, which states that the presence of a large number of hydroxyl groups on the surface of starch nanoparticles makes them prone to self-aggregate in solution to form microaggregates under hydrogen bonding and van der Waals forces (Kim et al., 2015). Similar result was reported in other research (Dong et al., 2022), after freeze-drying, the SNPs of regular corn origin and fava bean origin increased from 166.9 to 232.5 nm, 107.6–152.5 nm, and the PDI increased from 0.28 to 0.29, 0.26 to 0.42, respectively.

Observing from the variable of ultrasonic time (Table 1; Figure 2), it can be found that the increase in particle size and PDI after drying is related to the particle size of SNPs before drying, the smaller the particle size before freeze-drying, the larger the particle size and the smaller the PDI of the samples after freeze-drying. The smallest particle size of SNPs was 64.35 nm prepared by 15 min of ultrasonic time, and the particle size aggregated into the largest 353.20 nm after freeze-drying, while PDI was 0.30, it was the smallest among the PDI of all the freeze-dried SNPs, indicating that the smaller SNPs were more uniformly aggregated. The particle size of SNPs prepared by sonication for 5 min was the largest at 79.73 nm and aggregated into the smallest at 254.60 nm after freeze-drying. The same phenomenon was observed in other research (Sadeghi et al., 2017), when preparing SNPs using ethanol as a poor solvent. For investigating the effect of starch concentration, the ultrasonic time was kept same as 15 min, it was found that the PDI value of freeze-dried SNPs increased with increasing starch concentration from 2 to 8%, the span of particle distribution increased, and more insoluble large particles of starch appeared to collect at the bottom.

The starch solution to ethanol volume ratio also influenced the aggregation of SNPs (Table 1; Figure 3). The smaller size of SNPs also showed a stronger tendency to aggregate, with the freshly prepared SNPs having a particle size of 114.8 nm and PDI of 0.379 at a 1:5 ratio, and a particle size of 233.47 nm and PDI of 0.33 after freeze-drying and redispersion. (Dong et al., 2022) suggested that, the increase in the amount of ethanol caused the overgrowth of nanoparticles, because the supersaturation of starch molecules was too high for SNP formation, which in turn affects the redispersal of SNPs. When the starch solution to ethanol volume ratio is 1:1, freeze-dried SNPs show larger particle size and higher PDI, when the starch solution to ethanol volume ratio is higher (1:3, 1:5), the SNPs will show larger particle size and PDI. This phenomenon is contrary to our experiment, probably due to the fact that (Dong et al., 2022) prepared smaller SNPs when the starch

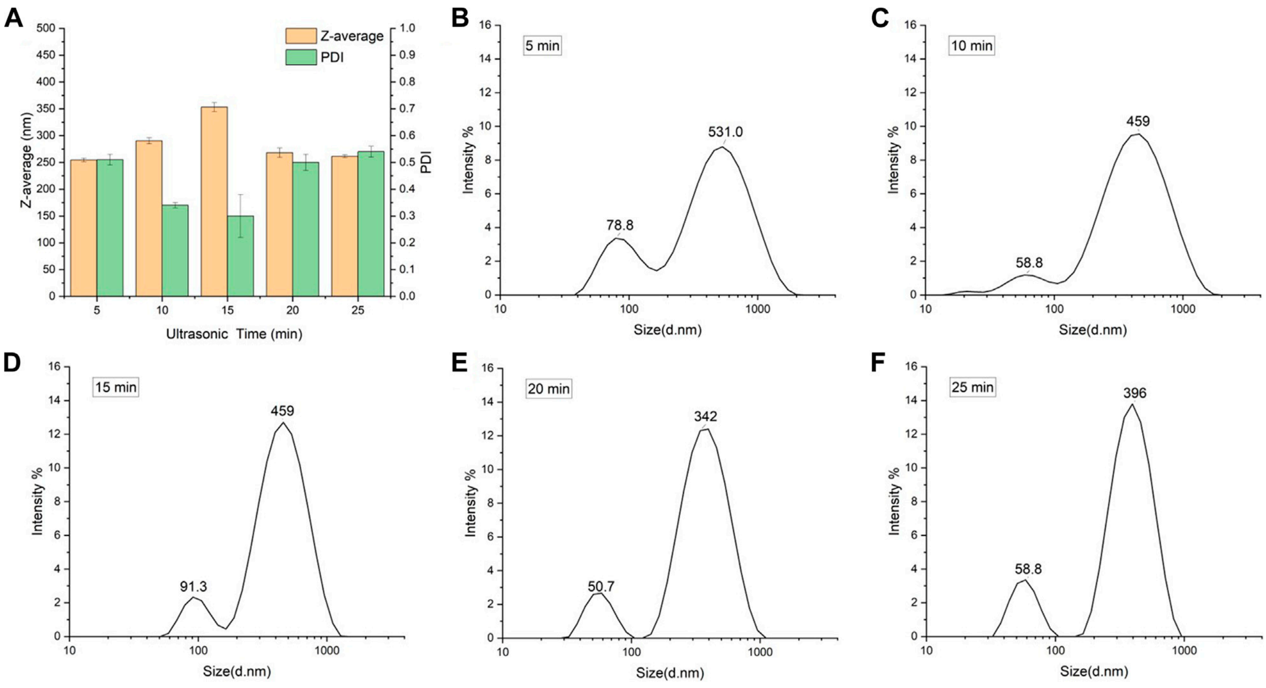

FIGURE 2
Particle size of freeze-dried SNPs prepared by different ultrasonic time. **(A)** Z-average and PDI. Size distribution of SNPs prepared by ultrasonification for 5 min **(B)**, 10 min **(C)**, 15 min **(D)**, 20 min **(E)**, and 25 min **(F)**.

solution to ethanol volume ratio was low, thus aggregating to produce larger particle size and narrower particle size distribution. In contrast, the particle size of the starch nanoparticles prepared in our experiment did not vary singularly with the starch solution to ethanol volume ratio; both too high and too low increased the particle size of the starch nanoparticles, so the similar trend was not observed.

3.3 Cold plasma treatment

Figure 4. shows the comparison of the particle size and PDI of SNPs before and after CP treatment. The particle size of the non-plasma treated group (control) increased from 79.19 to 169.80 nm and the PDI increased from 0.36 to 0.79, while the particle size of CP treated SNPs only changed from 82.41 to 97.30 nm and the PDI changed from 0.42 to 0.45, and no significant aggregation occurred. It indicated that there was no obvious aggregation phenomenon during freeze-drying. The SNPs before and after freeze-drying did not change much, and the CP treatment well inhibited the aggregation of SNPs during the freeze-drying process. (Chang et al., 2020) similarly found that the CP treatment changed the dispersion of SNPs and did not affect the particle size.

The depolymerization of starch by CP treatment has been widely reported (Gao et al., 2019; Shen et al., 2021), however, there are fewer studies on the effect of CP treatment on SNPs. The mechanism of plasma on starch is similar to the X-ray and gamma irradiation on it. Plasma treatment generates a series of highly active radicals, including superoxide radical (O^{2-}), hydroxyl radical (OH·), peroxy radical (ROO·), alkoxy radical (RO·), free radical (NO·), hydrogen peroxide (H_2O_2), organic peroxide (ROOR'), ozone (O^3), hypochlorite (HClO), singlet oxygen ($^1O_2$), aldehyde (HCOR) and peroxy nitrite (ONOOH). These free radicals cause skeletal breakage of polysaccharides, producing smaller fragments (Duan and Kasper, 2011).

3.4 Characterization of native starch, starch nanoparticles and cold plasma starch nanoparticles

3.4.1 Field emission scanning electron microscopy of native starch, starch nanoparticles and cold plasma starch nanoparticles

The FE-SEM images of native starch, SNPs, and CP SNPs are shown in Figure 5. The surface and edges of the native starch

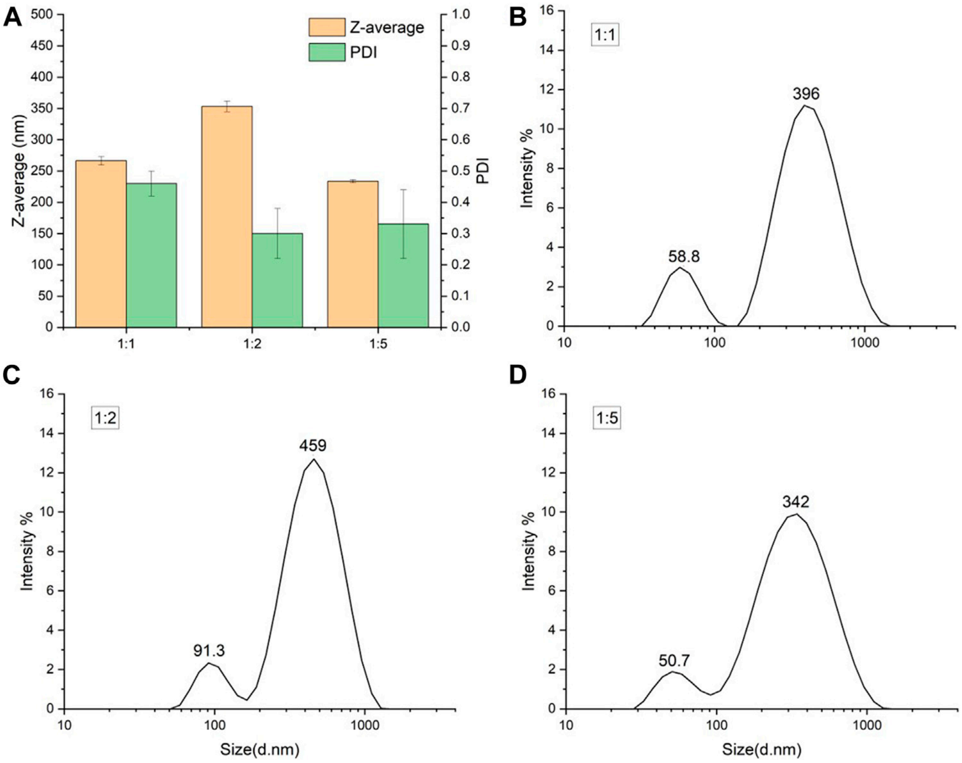

FIGURE 3
Particle size of freeze-dried SNPs prepared by different starch solution to ethanol volume ratios. **(A)** Z-average and PDI for three ratios. Size distribution of SNPs prepared at starch solution to ethanol volume ratio 1:1 **(B)**, 1:2 **(C)** and 1:5 **(D)**.

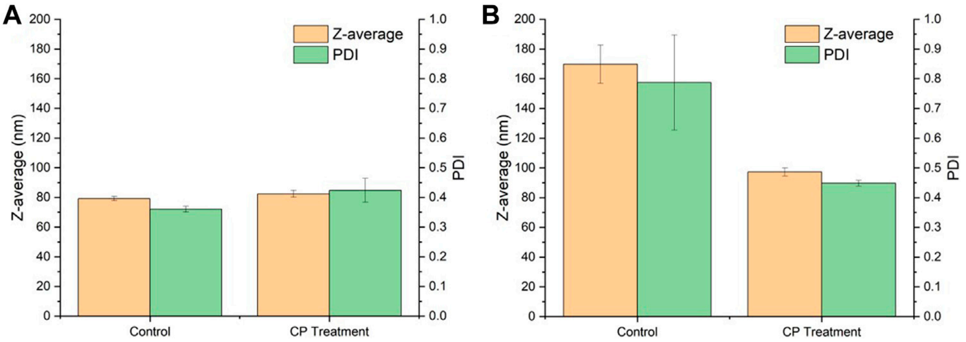

FIGURE 4
Effect of cold plasma treatment on the particle size of SNPs. **(A)** Before drying. **(B)** After drying.

particles are smooth, and the particles mainly exhibit round, oval, and polygonal shapes with particle sizes of 5–20 μm, which is consistent with other research (Kim et al., 2013; Wang et al., 2020b). Compared with the native starch, the adhesion between SNPs was more severe, and the adhered SNPs mainly showed a lamellar and spongy shape, which is similar to the shape of the SEM image obtained by (Dong et al., 2022). The adhesion phenomenon between SNPs may be due to the mutual

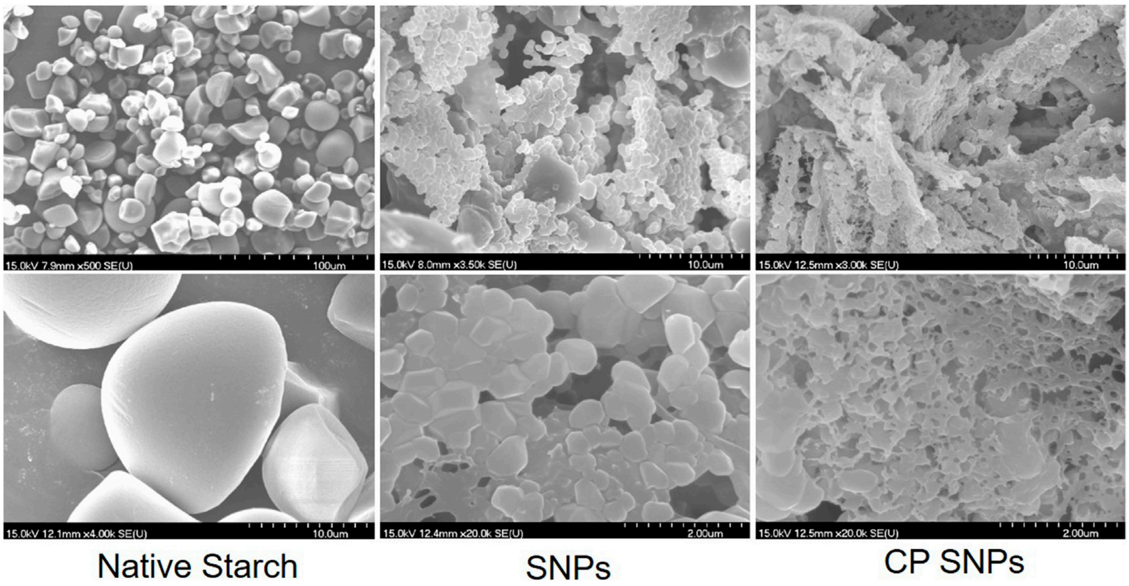

FIGURE 5
Field emission scanning electron micrographs (FE-SEM) of native starch, SNPs and CP SNPs.

attraction of hydrogen bonds between the particles, leading to tighter particle connections. The SEM images of SNPs showed that SNPs are mostly round and square in shape, the size of SNPs is in the range of 200–400 nm, which is basically in accordance with the particle size obtained by DLS. The freeze-drying process of SNPs is influenced by intermolecular and capillary forces, which force SNPs close to each other and bond by hydrogen bonding to reconstitute large granular crystals (Wang et al., 2005). Under the action of hydrogen bonds, these large particles will be automatically arranged, showing dense lamellar and spongy powders.

After CP treatment, the particle shape of CP SNPs completely disappears, interconnects more tightly and forms a tighter, more coiled fibrous network. (Charoenrein and Preechathammawong, 2012) also observed a spongy starch gel fibrous network in rice starch, and suggested that the formation of ice crystals during freezing and the aging of the starch were the main causes. Plasma treatment disrupts the functional groups on the surface of the SNPs and create new functional group. These new functional groups further affect the aggregation of the SNPs and promote the formation of gel webs.

3.4.2 Crystalline structure

The native starch, SNPs and CP SNPs were analyzed by X-ray diffraction analyser and the obtained diffraction patterns are shown in Figure 6A. The relative crystallinity of native starch, SNPs, and CP SNPs is 35.12%, 50.35% and 70.95%, respectively. It indicated that the crystalline region was destroyed during the preparation of SNPs and the crystallinity increased significantly ($p < 0.05$), while the plasma treatment further increased the crystallinity of starch ($p < 0.05$). In terms of characteristic peaks, strong diffraction peaks were observed at 5.6°, 17°, 18° and 23° for the naive starch (C-type starch), which is consistent with the reports about sweet potato starch (Kim et al., 2013; Wang et al., 2020b). After the formation of SNPs, all the diffraction peaks disappeared except the intensity of the diffraction peak at 23°, and new crystalline peaks were also observed on 22°, 27° and 28°, indicating that the crystalline shape of the starch changed significantly after formation of SNPs and new crystalline regions were generated. (Jhan et al., 2020; Jhan et al., 2021) similarly found disappearance of diffraction peaks and reduction in intensity when observing cereal SNPs. They attributed to the disruption of the ordered structure of branched starch during the ball milling preparation, resulting in the formation of more amorphous features in the starch granules. However, when ball milling of millet starch was performed to prepare SNPs, no crystallographic alteration was observed, and the diffraction spectra of SNPs were very similar to the native starch. The V-shaped starch crystal structure was mainly generated by the complex of straight-chain starch and ethanol, indicating that the cassava starch was ultrasonically alcohol deposited. (Ahmad et al., 2020) found that after preparation into SNPs, the peaks of the whole diffraction pattern all disappeared and became amorphous humps and the granules lost their crystallinity.

The crystallographic profiles of SNPs were almost unchanged after plasma treatment, and only the diffraction peaks at 22°, 23°,

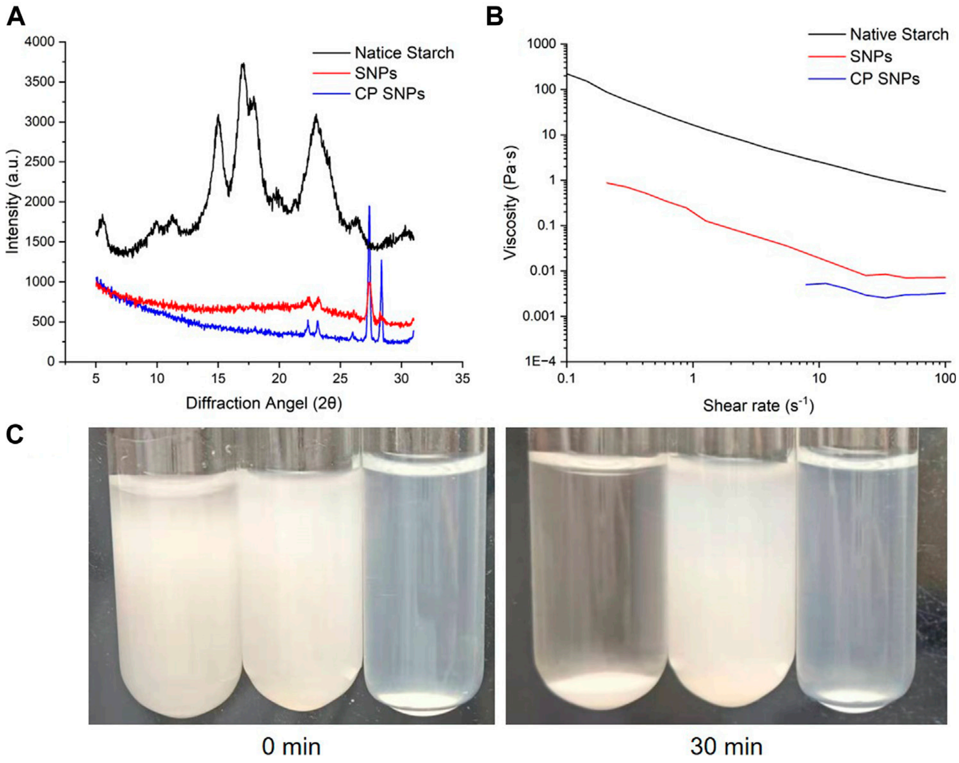

FIGURE 6
Properties of native starch, SNPs and CP SNPs. **(A)** X-ray diffraction patterns. **(B)** Apparent viscosity. **(C)** Photographs of re-dispersions of native starch (left), SNPs (middle) and CP SNPs (right) in water for 0 and 30 min.

27° and 28° became sharper, indicating that the plasma treatment further changed the crystal structure of SNPs. Except for sweet potato SNPs, no crystallographic changes were observed in rice starch (Thirumdas et al., 2017), corn starch (Sifuentes-Nieves et al., 2020), buckwheat, sorghum, wheat, and quinoa (Gao et al., 2019), when plasma was applied.

3.4.3 Rheological and flow properties

Figure 6B represents the variation of viscosity with shear rate for native starch, SNPs and CP SNPs. The results showed that the viscosity decreased with shear rate increasing and all samples exhibited shear thinning behaviour. Starch solutions and SNPs solutions are mostly non Newtonian fluid and often exhibit shear thinning (Che et al., 2008), indicating the presence of an associated network structure between starch molecules. However, SNPs solutions at low concentrations may also exhibit shear thickening. (Kumari et al., 2022) attributed the shear thickening behaviour of SNPs solutions to the surface charge and repulsive double layer of the particles. When the shear rate was 30 s^{-1}, the viscosity values containing native starch, SNPs and CP SNPs were 1.07, 0.008 and 0.003 Pa s, respectively. The viscosity of SNPs and CP SNPs was significantly lower than native starch. The same result was observed by (Kumari et al., 2022) in the preparation of SNPs, where the viscosity of the SNPs was consistently lower than that of the native starch throughout the flow curve, with a viscosity coefficient of 50.27 Pa·sn for 10% barley starch solution and only 0.0042 Pa·sn for 12% barley SNPs solution at a shear rate of 10 s^{-1}, indicating the viscosity of the SNPs solution was significantly lower.

Plasma treatment can further reduce the viscosity of SNPs. (Shen et al., 2021) attributed this phenomenon to the degradation of starch chains during plasma treatment, which reduces the interaction of gel components. It was found that plasma treatment reduced the peak viscosity and final viscosity, and the longer the treatment time, the greater the decrease in viscosity. (Bie et al., 2016) found that the consistency factor of 8% starch solution decreased from 23.69 Pa·sn to 3.37 Pa·sn after 5 min of plasma treatment, while the shear thinning behaviour of plasma starch also showed less pronounced, and it was speculated that the plasma treatment may have caused oxidation and breakage of the starch particles, reducing the water holding capacity and increasing the solubility, which in turn changed the rheological behaviour. This low viscosity nature of SNPs and CP SNPs will expand the application of starch in industry, since low viscosity starch solutions do not affect the viscosity of the product much even when blended into liquid food products and are very suitable for the preparation of juices and beverages.

3.4.4 Re-dispersion stability

Figure 6C shows the photos of native starch, SNPs, CP SNPs solutions with concentration of 5% at 0 min, 30 min, and found that the stability ranking was CP SNPs > SNPs > native starch. All of the native starch settled down after 30 min and the supernatant became completely clear water, indicating that the native starch was completely insoluble in water. The solubility of SNPs to water is better than the native starch, and it can be seen that it is basically still solution after 30 min, but there is also a mild sedimentation phenomenon. The bottom layer appears large particles of aggregates, the top layer solution becomes dilute and the solution colour becomes lighter. It is possible that by reducing the particle size of starch to the nanoscale, the bonds within and between hydrogen molecules are weakened and more hydroxyl groups are exposed, leading to more interactions with water molecules and thus increased solubility. (Jhan et al., 2021) found that at 90°C, the solubility of foxtail starch in water was 8.04% and sorghum starch was 9.08%, while the solubility of foxtail SNPs in water was 11.29% and 13.50% for sorghum nano starch, the water solubility of nanoparticles was generally greater. (Gonçalves et al., 2014) found that the solubility of araucaria angustifolia seeds starch in water increased from 3.27% to 16.90% after turning into starch granules. The water solubility of CP SNPs was the best, being a stable solution without delamination and precipitation. It may be due to the fact that CP treatment causes the SNPs to produce hydrophilic group carboxyl groups (Bie et al., 2016), which further enhances the stability of the solution. (Chang et al., 2020) found that CP treatment increased the absolute value of ζ-potential of the SNPs solution, and the SNPs solution exhibited slight precipitation when left for the same time at the same concentration, but the CP treated SNPs solution then remained stable.

4 Conclusion

In this research, sweet potato SNPs were prepared by ultrasonic-assisted dissolution of starch and subsequent rapid nanoprecipitation. After the optimization of preparation parameters, SNPs with mean particle size of 64.35 nm and PDI of 0.23 were obtained. However, the prepared SNPs would aggregate after drying. The results indicated that, SNPs with smaller size before drying would aggregate more seriously to become larger size after drying. For this, CP treatment was applied to SNPs before and after freeze drying. As a result, CP treatment would not change the particle size of SNPs before drying, but slowed down the aggregation and recrystallization of SNPs during the freeze drying. Among native starch, SNPs and CP SNPs, CP SNPs showed the lowest viscosity, the highest relative crystallinity and re-dispersion stability. Such a treatment strategy could offer an idea to inhibit the aggregation of SNPs, and the obtained CP SNPs could be used as nutraceutical or pharmaceutical carriers.

Data availability statement

The original contributions presented in the study are included in the article/Supplementary Material, further inquiries can be directed to the corresponding authors.

Author contributions

JW and Y-DY have contributed equally to this work. Experimental design: JW and Y-DY; experiments: JW, Y-DY, W-CW, and ZZ; data analysis: P-LS, KY, and MC; manuscript writing: Y-DY, JW, MC, and KY; W-CW, MC, and KY supervised the experiments and provided funding. The final version has been approved by all of the authors.

Funding

This study was supported by the Zhejiang Provincial Science and Technology Plan Project—Key R&D (Grant 2022C02041).

Conflict of interest

The authors declare that the research was conducted in the absence of any commercial or financial relationships that could be construed as a potential conflict of interest.

Publisher's note

All claims expressed in this article are solely those of the authors and do not necessarily represent those of their affiliated organizations, or those of the publisher, the editors and the reviewers. Any product that may be evaluated in this article, or claim that may be made by its manufacturer, is not guaranteed or endorsed by the publisher.

References

Ahmad, M., Gani, A., Hassan, I., Huang, Q., and Shabbir, H. (2020). Production and characterization of starch nanoparticles by mild alkali hydrolysis and ultra-sonication process. *Sci. Rep.* 10, 3533. doi:10.1038/s41598-020-60380-0

Bie, P., Pu, H., Zhang, B., Su, J., Chen, L., and Li, X. (2016). Structural characteristics and rheological properties of plasma-treated starch. *Innovative Food Sci. Emerg. Technol.* 34, 196–204. doi:10.1016/j.ifset.2015.11.019

Boufi, S., Bel Haaj, S., Magnin, A., Pignon, F., Imperor-Clerc, M., and Mortha, G. (2018). Ultrasonic assisted production of starch nanoparticles: structural characterization and mechanism of disintegration. *Ultrason. Sonochem.* 41, 327–336. doi:10.1016/j.ultsonch.2017.09.033

Chang, R., Lu, H., Tian, Y., Li, H., Wang, J., and Jin, Z. (2020). Structural modification and functional improvement of starch nanoparticles using vacuum cold plasma. *Int. J. Biol. Macromol.* 145, 197–206. doi:10.1016/j.ijbiomac.2019.12.167

Chang, Y., Yan, X., Wang, Q., Ren, L., Tong, J., and Zhou, J. (2017). High efficiency and low cost preparation of size controlled starch nanoparticles through ultrasonic treatment and precipitation. *Food Chem.* 227, 369–375. doi:10.1016/j.foodchem.2017.01.111

Charoenrein, S., and Preechathammawong, N. (2012). Effect of waxy rice flour and cassava starch on freeze-thaw stability of rice starch gels. *Carbohydr. Polym.* 90, 1032–1037. doi:10.1016/j.carbpol.2012.06.038

Che, L.-M., Li, D., Wang, L.-J., Özkan, N., Chen, X. D., and Mao, Z.-H. (2008). Rheological properties of dilute aqueous solutions of cassava starch. *Carbohydr. Polym.* 74, 385–389. doi:10.1016/j.carbpol.2008.03.007

Dong, H., Chen, L., Zhang, Q., Gao, J., and Vasanthan, T. (2021). Optimization of processing parameters to produce nanoparticles prepared by rapid nanoprecipitation of pea starch. *Food Hydrocoll.* 121, 106929. doi:10.1016/j.foodhyd.2021.106929

Dong, H., Zhang, Q., Gao, J., Chen, L., and Vasanthan, T. (2022). Preparation and characterization of nanoparticles from cereal and pulse starches by ultrasonic-assisted dissolution and rapid nanoprecipitation. *Food Hydrocoll.* 122, 107081. doi:10.1016/j.foodhyd.2021.107081

Duan, J., and Kasper, D. L. (2011). Oxidative depolymerization of polysaccharides by reactive oxygen/nitrogen species. *Glycobiology* 21, 401–409. doi:10.1093/glycob/cwq171

Gani, A., Bashir, M., Wani, S. M., and Masoodi, F. A. (2012). Modification of bean starch by γ-irradiation: effect on functional and morphological properties. *LWT* 49, 162–169. doi:10.1016/j.lwt.2012.04.028

Gao, S., Liu, H., Sun, L., Liu, N., Wang, J., Huang, Y., et al. (2019). The effects of dielectric barrier discharge plasma on physicochemical and digestion properties of starch. *Int. J. Biol. Macromol.* 138, 819–830. doi:10.1016/j.ijbiomac.2019.07.147

Gonçalves, P. M., Noreña, C. P. Z., Da Silveira, N. P., and Brandelli, A. (2014). Characterization of starch nanoparticles obtained from Araucaria angustifolia seeds by acid hydrolysis and ultrasound. *LWT - Food Sci. Technol.* 58, 21–27. doi:10.1016/j.lwt.2014.03.015

Hebeish, A., El-Rafie, M. H., El-Sheikh, M. A., and El-Naggar, M. E. (2013). Ultra-fine characteristics of starch nanoparticles prepared using native starch with and without surfactant. *J. Inorg. Organomet. Polym. Mat.* 24, 515–524. doi:10.1007/s10904-013-0004-x

Jhan, F., Gani, A., Noor, N., Ashraf, Z. U., Gani, A., and Shah, A. (2021). Characterisation and utilisation of nano-reduced starch from underutilised cereals for delivery of folic acid through human GI tract. *Sci. Rep.* 11, 4873. doi:10.1038/s41598-021-81623-8

Jhan, F., Shah, A., Gani, A., Ahmad, M., and Noor, N. (2020). Nano-reduction of starch from underutilised millets: Effect on structural, thermal, morphological and nutraceutical properties. *Int. J. Biol. Macromol.* 159, 1113–1121. doi:10.1016/j.ijbiomac.2020.05.020

Kakran, M., Sahoo, N. G., Tan, I. L., and Li, L. (2012). Preparation of nanoparticles of poorly water-soluble antioxidant curcumin by antisolvent precipitation methods. *J. Nanopart. Res.* 14, 757. doi:10.1007/s11051-012-0757-0

Kim, H.-Y., Park, S. S., and Lim, S.-T. (2015). Preparation, characterization and utilization of starch nanoparticles. *Colloids Surfaces B Biointerfaces* 126, 607–620. doi:10.1016/j.colsurfb.2014.11.011

Kim, J., Ren, C., and Shin, M. (2013). Physicochemical properties of starch isolated from eight different varieties of Korean sweet potatoes. *Starch - Stärke* 65, 923–930. doi:10.1002/star.201200217

Kopuk, B., Gunes, R., and Palabiyik, I. (2022). Cold plasma modification of food macromolecules and effects on related products. *Food Chem.* 382, 132356. doi:10.1016/j.foodchem.2022.132356

Kumari, S., Yadav, B. S., and Yadav, R. B. (2022). Effect of nano-conversion on morphological, rheological and thermal properties of barley starch. *J. Food Sci. Technol.* 59, 467–477. doi:10.1007/s13197-021-05029-0

Laroque, D. A., Seó, S. T., Valencia, G. A., Laurindo, J. B., and Carciofi, B. A. M. (2022). Cold plasma in food processing: design, mechanisms, and application. *J. Food Eng.* 312, 110748. doi:10.1016/j.jfoodeng.2021.110748

Li, X., Ouyang, Z., Li, H., Hu, C., Saha, P., Xing, L., et al. (2021a). Dendrimer-decorated nanogels: efficient nanocarriers for biodistribution *in vivo* and chemotherapy of ovarian carcinoma. *Bioact. Mat.* 6, 3244–3253. doi:10.1016/j.bioactmat.2021.02.031

Li, X., Sun, H., Li, H., Hu, C., Luo, Y., Shi, X., et al. (2021b). Multi-responsive biodegradable cationic nanogels for highly efficient treatment of tumors. *Adv. Funct. Mat.* 31, 2100227. doi:10.1002/adfm.202100227

Lyu, R., Ahmed, S., Fan, W., Yang, J., Wu, X., Zhou, W., et al. (2021). Engineering properties of sweet potato starch for industrial applications by biotechnological techniques including genome editing. *Int. J. Mol. Sci.* 22, 9533. doi:10.3390/ijms22179533

Martinez Rivas, C. J., Tarhini, M., Badri, W., Miladi, K., Greige-Gerges, H., Nazari, Q. A., et al. (2017). Nanoprecipitation process: from encapsulation to drug delivery. *Int. J. Pharm.* 532, 66–81. doi:10.1016/j.ijpharm.2017.08.064

Perez Herrera, M., Vasanthan, T., and Chen, L. (2017). Rheology of starch nanoparticles as influenced by particle size, concentration and temperature. *Food Hydrocoll.* 66, 237–245. doi:10.1016/j.foodhyd.2016.11.026

Qiu, C., Yang, J., Ge, S., Chang, R., Xiong, L., and Sun, Q. (2016). Preparation and characterization of size-controlled starch nanoparticles based on short linear chains from debranched waxy corn starch. *Lwt* 74, 303–310. doi:10.1016/j.lwt.2016.07.062

Sadeghi, R., Daniella, Z., Uzun, S., and Kokini, J. (2017). Effects of starch composition and type of non-solvent on the formation of starch nanoparticles and improvement of curcumin stability in aqueous media. *J. Cereal Sci.* 76, 122–130. doi:10.1016/j.jcs.2017.05.020

Shen, H., Ge, X., Zhang, B., Su, C., Zhang, Q., Jiang, H., et al. (2022). Preparing potato starch nanocrystals assisted by dielectric barrier discharge plasma and its multiscale structure, physicochemical and rheological properties. *Food Chem.* 372, 131240. doi:10.1016/j.foodchem.2021.131240

Shen, H., Guo, Y., Zhao, J., Zhao, J., Ge, X., Zhang, Q., et al. (2021). The multi-scale structure and physicochemical properties of mung bean starch modified by ultrasound combined with plasma treatment. *Int. J. Biol. Macromol.* 191, 821–831. doi:10.1016/j.ijbiomac.2021.09.157

Sifuentes-Nieves, I., Velazquez, G., Flores-Silva, P. C., Hernandez-Hernandez, E., Neira-Velazquez, G., Gallardo-Vega, C., et al. (2020). HMDSO plasma treatment as alternative to modify structural properties of granular starch. *Int. J. Biol. Macromol.* 144, 682–689. doi:10.1016/j.ijbiomac.2019.12.111

Sudheesh, C., Sunooj, K. V., Sinha, S. K., George, J., Kumar, S., Murugesan, P., et al. (2019). Impact of energetic neutral nitrogen atoms created by glow discharge air plasma on the physico-chemical and rheological properties of kithul starch. *Food Chem.* 294, 194–202. doi:10.1016/j.foodchem.2019.05.067

Thirumdas, R., Trimukhe, A., Deshmukh, R. R., and Annapure, U. S. (2017). Functional and rheological properties of cold plasma treated rice starch. *Carbohydr. Polym.* 157, 1723–1731. doi:10.1016/j.carbpol.2016.11.050

Wang, B., Zhang, W., Zhang, W., Mujumdar, A. S., and Huang, L. (2005). Progress in drying technology for nanomaterials. *Dry. Technol.* 23, 7–32. doi:10.1081/drt-200047900

Wang, H., Xu, K., Ma, Y., Liang, Y., Zhang, H., and Chen, L. (2020a). Impact of ultrasonication on the aggregation structure and physicochemical characteristics of sweet potato starch. *Ultrason. Sonochem.* 63, 104868. doi:10.1016/j.ultsonch.2019.104868

Wang, H., Yang, Q., Ferdinand, U., Gong, X., Qu, Y., Gao, W., et al. (2020b). Isolation and characterization of starch from light yellow, orange, and purple sweet potatoes. *Int. J. Biol. Macromol.* 160, 660–668. doi:10.1016/j.ijbiomac.2020.05.259

Wang, Y., Ye, Z., Li, J., Zhang, Y., Guo, Y., and Cheng, J.-H. (2021). Effects of dielectric barrier discharge cold plasma on the activity, structure and conformation of horseradish peroxidase (HRP) and on the activity of litchi peroxidase (POD). *LWT* 141, 111078. doi:10.1016/j.lwt.2021.111078

Wang, Y., and Zhang, G. (2021). The preparation of modified nano-starch and its application in food industry. *Food Res. Int.* 140, 110009. doi:10.1016/j.foodres.2020.110009

Wongsagonsup, R., Deeyai, P., Chaiwat, W., Horrungsiwat, S., Leejariensuk, K., Suphantharika, M., et al. (2014). Modification of tapioca starch by non-chemical route using jet atmospheric argon plasma. *Carbohydr. Polym.* 102, 790–798. doi:10.1016/j.carbpol.2013.10.089

Wu, X., Chang, Y., Fu, Y., Ren, L., Tong, J., and Zhou, J. (2016). Effects of non-solvent and starch solution on formation of starch nanoparticles by nanoprecipitation. *Starch - Stärke* 68, 258–263. doi:10.1002/star.201500269

Ye, F., Miao, M., Lu, K., Jiang, B., Li, X., and Cui, S. W. (2017). Structure and physicochemical properties for modified starch-based nanoparticle from different maize varieties. *Food Hydrocoll.* 67, 37–44. doi:10.1016/j.foodhyd.2016.12.041

Zhu, J., Li, L., Chen, L., and Li, X. (2012). Study on supramolecular structural changes of ultrasonic treated potato starch granules. *Food Hydrocoll.* 29, 116–122. doi:10.1016/j.foodhyd.2012.02.004

frontiers | Frontiers in Bioengineering and Biotechnology

TYPE Review
PUBLISHED 04 October 2022
DOI 10.3389/fbioe.2022.1039495

OPEN ACCESS

EDITED BY
Yu Luo,
Shanghai University of Engineering Sciences, China

REVIEWED BY
Mingxing Wang,
Changchun University of Chinese Medicine, China
Xiao Duan,
Changzhi Medical College, China

*CORRESPONDENCE
Bo Song,
ynkmsongbo6@126.com
Junzi Wu,
xnfz@ynutcm.edu.cn

[†]These authors have contributed equally to this work

SPECIALTY SECTION
This article was submitted to Nanobiotechnology,
a section of the journal
Frontiers in Bioengineering and Biotechnology

RECEIVED 08 September 2022
ACCEPTED 20 September 2022
PUBLISHED 04 October 2022

CITATION
Tong S, Li Q, Liu Q, Song B and Wu J (2022), Recent advances of the nanocomposite hydrogel as a local drug delivery for diabetic ulcers.
Front. Bioeng. Biotechnol. 10:1039495.
doi: 10.3389/fbioe.2022.1039495

COPYRIGHT
© 2022 Tong, Li, Liu, Song and Wu. This is an open-access article distributed under the terms of the Creative Commons Attribution License (CC BY). The use, distribution or reproduction in other forums is permitted, provided the original author(s) and the copyright owner(s) are credited and that the original publication in this journal is cited, in accordance with accepted academic practice. No use, distribution or reproduction is permitted which does not comply with these terms.

Recent advances of the nanocomposite hydrogel as a local drug delivery for diabetic ulcers

Sen Tong[1†], Qingyu Li[2†], Qiaoyan Liu[1], Bo Song[1*] and Junzi Wu[1*]

[1]School of Basic Medical, Yunnan University of Chinese Medicine, Kunming, Yunnan, China, [2]School of Medicine, Jianghan University, Wuhan, China

Diabetic ulcer is a serious complication of diabetes. Compared with that of healthy people, the skin of patients with a diabetic ulcer is more easily damaged and difficult to heal. Without early intervention, the disease will become increasingly serious, often leading to amputation or even death. Most current treatment methods cannot achieve a good wound healing effect. Numerous studies have shown that a nanocomposite hydrogel serves as an ideal drug delivery method to promote the healing of a diabetic ulcer because of its better drug loading capacity and stability. Nanocomposite hydrogels can be loaded with one or more drugs for application to chronic ulcer wounds to promote rapid wound healing. Therefore, this paper reviews the latest progress of delivery systems based on nanocomposite hydrogels in promoting diabetic ulcer healing. Through a review of the recent literature, we put forward the shortcomings and improvement strategies of nanocomposite hydrogels in the treatment of diabetic ulcers.

KEYWORDS

diabetic ulcer, nanocomposite hydrogel, nano delivery system, hydrogel, wet dressing

Introduction

Diabetes mellitus is a chronic disease caused by the disorder of glucose metabolism. Long-term hyperglycaemia will increase the blood viscosity of patients, weaken the elasticity of blood vessels and weaken the local skin barrier function of patients, resulting in diabetic ulcers such as diabetic foot ulcers, leg ulcers, and buttock pressure ulcers (Fiordaliso et al., 2016; Yeom et al., 2016; Sun et al., 2022). For normal people, when the skin is damaged, the skin lesions can quickly and naturally heal after the four stages of haemostasis, inflammation, proliferation and maturation (Gurtner et al., 2008). For patients with diabetes, due to the imbalance of an inflammatory reaction around the ulcer wound, increased oxidative stress, bacterial infection, insufficient angiogenesis, hypoxia of wound tissue and other reasons, the wound cannot follow the normal and orderly repair process, such that delayed healing or no healing occurs, requiring long-term bed rest (Demiot et al., 2006; Leal et al., 2015; Hassan et al., 2019; Fadol et al., 2021; Singh et al., 2022).

At present, there are a variety of clinical methods to treat diabetic ulcers, mainly based on blood glucose control, timely dressing, debridement and prevention and control of infection (Zubair and Ahmad, 2019; Boyko et al., 2022). However, the effect of treatment is not ideal. Even with these standardised treatments, only a small proportion of diabetic ulcers heal after 12–20 weeks, and most patients require more advanced interventions (Frykberg et al., 2020). According to past clinical experience, the traditional dry dressing can keep the wound dry and absorb part of the wound exudate (Jeffcoate et al., 2009). However, they cannot maintain the temperature and humidity of the wound and cannot protect the wound from bacterial invasion. Moreover, the traditional dressing readily adheres to the new granulation tissue of the wound, causing secondary injury when the dressing is changed (Hilton et al., 2004). These reasons contribute to the limitations of dry dressings in clinical practice.

With the continuous development of biomedical materials and in-depth studies of wound healing theory, investigators found that a clean and humid environment is more conducive to wound healing. Therefore, wet wound dressings, particularly hydrogels have attracted attention (Sirousazar et al., 2011; Zhang X. et al., 2019). A hydrogel is a water-insoluble gelatinous material. Compared with traditional dry dressings, hydrogels can create a healing environment faithfully reflecting the physiological state, provide extra moisture for dry and scabby wounds, moisten exposed tissues, and nerve endings and reduce pain when the dressing is changed (Li Y. et al., 2017; Zhou et al., 2018). Hydrogels can retain the active substances in the exudate of patients, promote cell division and migration and promote rapid wound healing. However, hydrogels have limitations such as low mechanical strength, sudden drug release, susceptibility to degradation and high storage requirements (Zhu et al., 2018; Ma et al., 2020; Luo Y. et al., 2022). Once dehydrated, the appearance and properties of hydrogels will be greatly affected, which limits their wide application in the biomedical field.

To overcome these limitations, researchers worldwide compete to conduct studies aimed to improve the mechanical properties of hydrogels. With the continuous development of nanotechnology, researchers have found that nanocomposite hydrogels can be prepared by introducing nanostructured particles into the hydrogel network through chemical bonding or physical adsorption. These methods can improve the mechanical strength of hydrogels and impart some new properties to hydrogels (Li et al., 2018; Chen et al., 2019; Shin et al., 2019; Abdollahi et al., 2021). Specifically, a nanocomposite hydrogel is a three-dimensional network formed by physical or chemical crosslinking of natural, synthetic hydrophilic polymers or both (Wei et al., 2019). It has abundant pores and good hydrophilicity, which is conducive to gas exchange and can maintain the fluid balance at the wound site (Xavier et al., 2015; Zhai et al., 2018). Its porous structure can simulate the structure and function of the extracellular matrix and promote cell migration, proliferation and maturation (Liu et al., 2021). Briefly, a nanocomposite hydrogel has the advantages of a hydrogel mentioned above and the excellent characteristics of nanoparticles. Furthermore, nanocomposite hydrogels are a well-characterised treatment method that promotes the healing of diabetic ulcers and provides a new strategy for the treatment of diabetic ulcers.

In particular, nanocomposite hydrogels are advantageous, because they can be loaded with small-molecule drugs, biomacromolecules, inorganic nanoparticles and other active substances that enhance the biological activity of nanocomposite hydrogels and further expand their application to wound management (Alvarez et al., 2014; Wu et al., 2019; Yang et al., 2021; Massironi et al., 2022; Rao et al., 2022). When a nanocomposite hydrogel is used as drug delivery system carrier, it can reach the lesion through active or passive transport, which is suitable for drug delivery to the skin, oral mucosa, eye and some gastrointestinal mucosa (Sapino et al., 2019; Wróblewska et al., 2020; Cheng et al., 2021; Li et al., 2022a). Compared with other types of nano carriers, nanocomposite hydrogels are similar to natural extracellular matrices, with good water dispersion and are easier to penetrate human skin, achieve the locally sustained and on demand release of drugs and form a physical barrier to create a clean and moist healing environment for the repair of diabetic ulcer (Lou et al., 2021; Girija et al., 2022). Compared with ordinary hydrogels, nanocomposite hydrogels have better mechanical properties, a longer swelling process and higher drug loading capacity (Qiu et al., 2021).

Nanohydrogels have attracted increasing attention because of their great potential for use as effective drug delivery systems. This review focuses on the promotion of ulcer healing in animal models of diabetes or patients with diabetes through loading small-molecule drugs, protein drugs, silver nanoparticles and other substances. Furthermore, we evaluated the challenges to translating these nanocomposite hydrogels to the clinic.

Application of a nanocomposite hydrogel delivery system to diabetic ulcers

Treatment of diabetic ulcers with nanocomposite hydrogel loaded with small-molecule drugs

There are many advantages in using nanocomposite hydrogel as a carrier of small-molecule drugs: 1) It can protect drugs and improve their stability (Qi et al., 2020). 2) It can increase the solubility of the drug (Bang et al., 2019). 3) The effective treatment time was increased by sustained

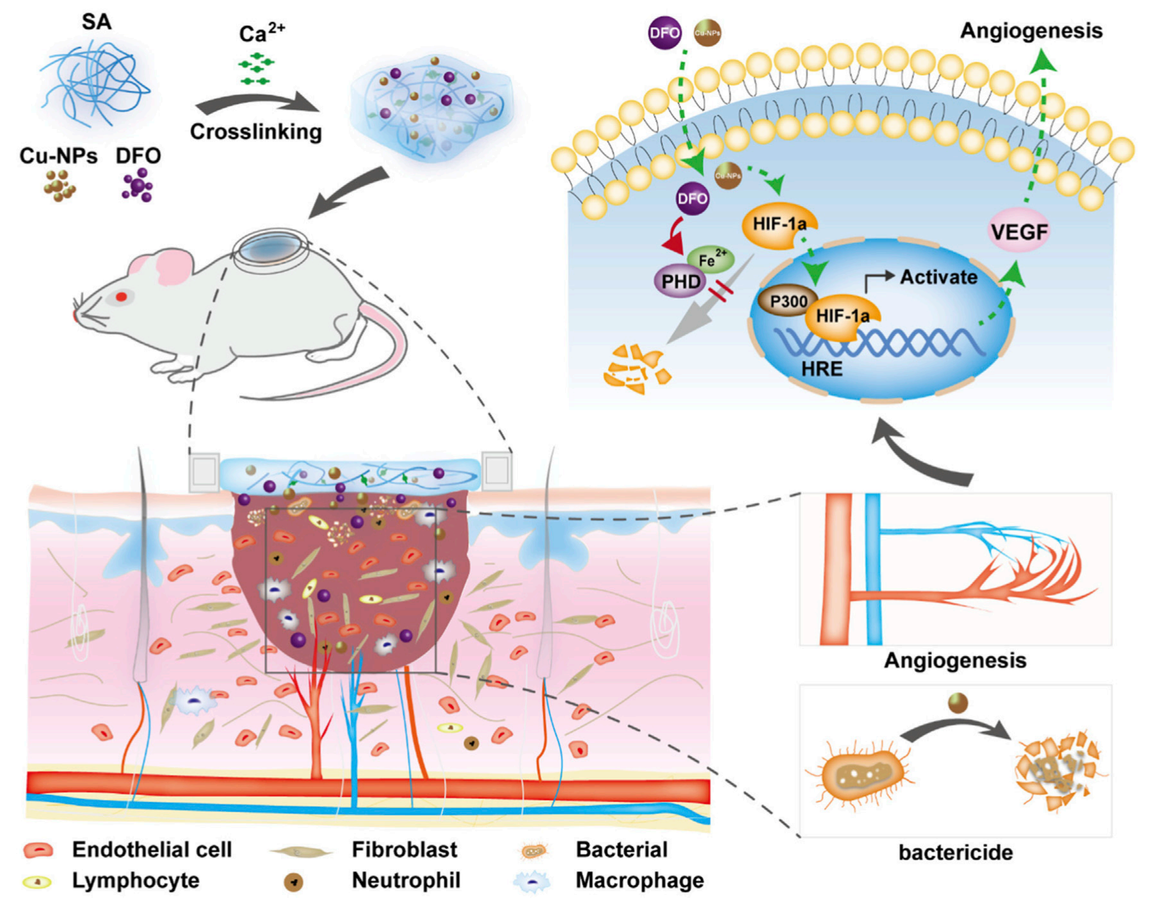

FIGURE 1
Schematic diagram of the strategy for the treatment of diabetic wound healing using bioactive hydrogel composites containing deferoxamine and copper nanoparticles. Reproduced from (Li et al., 2022b), with permission from Elsevier.

release of drugs (Luo F. Q. et al., 2022). 4) It can reduce the side effects of drugs (Yang X. et al., 2022). 5) The drug is delivered to the wound surface of a diabetic ulcer in a non-invasive or minimally invasive way to minimise tissue damage (Lei and Fan, 2022). At present, most patients with diabetic ulcers can be treated with small-molecule drugs during the early stage of disease. Combined with a patients' status, the development of a personalised treatment programme can achieve better treatment efficacy.

Deferoxamine (DFO), a small-molecule drug approved by the Food and Drug Administration (FDA) of the United States, has been used to induce angiogenesis in bone and skin regeneration (Lintel et al., 2022). DFO can induce angiogenesis and is used in the treatment of diabetic foot ulcers (Ram et al., 2015). It has been found that DFO-laden silk nanofiber hydraulics provided a sustained release of DFO for more than 40 days and is used to treat diabetic wounds, which can effectively regulate inflammation, regulate the migration and gene expression of endothelial cells, improve the deposition of the extracellular matrix and accelerate the healing of diabetic ulcers (Ding et al., 2021). Another study found that a sodium alginate composite hydrogel containing DFO and copper nanoparticles (Cu NPs) was prepared using a calcium ion crosslinking method, which conferred beneficial effects on diabetic ulcers (Li et al., 2022b). The hydrogel has synergistic effects on the proliferation, migration and angiogenesis of human umbilical vein endothelial cells *in vitro*. Further, the hydrogel upregulates vascular endothelial growth factor (VEGF) and hypoxia-inducible factor-1α, which can accelerate the healing of a diabetic ulcer (Figure 1).

4-Hydroxy-3-methoxycinnamic acid (ferulic acid) is a natural antioxidant with antibacterial activity. It can reduce blood glucose levels, scavenge free radicals, promote angiogenesis and so on (Karamać et al., 2017). It was found that ferulic acid was encapsulated into nanoparticles using the nano precipitation method, and then Carbopol 980 was added to form a ferulic acid nanohydrogel (Bairagi et al., 2018). The results of subsequent animal experiments show that a ferulic acid nanohydrogel significantly increases the content of

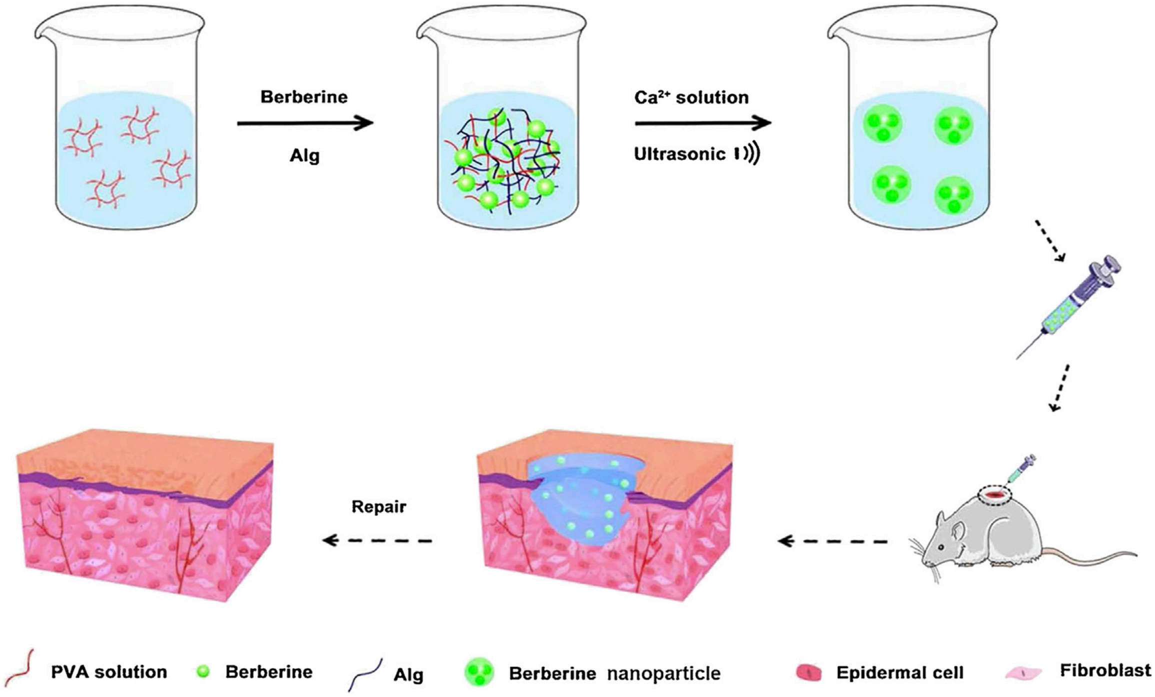

FIGURE 2
Preparation of a berberine nanohydrogel and its application to skin wound healing of diabetic rats. Reproduced from (Zhang et al., 2020), with permission from Elsevier.

hydroxyproline, promotes collagen deposition and promotes tissue repair and wound healing in diabetic rats.

3-Methyl-1-phenyl-2-pyrazolin-5-one (edaravone) strongly scavenges free radicals and promotes wound healing, although its poor stability and solubility hinders its local application (Fujisawa and Yamamoto, 2016; Parikh et al., 2016; Tamer et al., 2018). It was found that the sustained release of edaravone could be effectively achieved by loading edaravone nanoparticles into a sodium alginate hydrogel (Fan et al., 2019). Edaravone encapsulated in a nanocomposite hydrogel accelerates wound healing faster than free edaravone. This study further found that edaravone has different scavenging effects on reactive oxygen species. A low dose of edaravone benefits wound repair, while a high dose hinders wound healing.

Berberine has anti-inflammatory, antibacterial and hypoglycaemic effects, promoting the healing of diabetic ulcers (Dou et al., 2021; Maity et al., 2022; Zhang et al., 2022). However, owing to the low water solubility and lipid solubility of berberine, its oral bioavailability is low, which seriously limits the development and application of berberine as a pharmaceutical (Sahibzada et al., 2018). It has been found that a nanohydrogel can be used as a carrier for sustained release of berberine (Zhang et al., 2020). Berberine encapsulated in a nanohydrogel has stronger water holding capacity than ordinary berberine hydrogel and can promote the migration and proliferation of epidermal cells required for wound repair. Furthermore, berberine nanohydrogel could inhibit the expression of nuclear factor kappa-B, tumor necrosis factor-α, and interleukin 6 by activating silent information regulator 1 and increase the expression of VEGF and platelet endothelial cell adhesion molecule-1, which finally promoted the healing of diabetic ulcers (Figure 2).

7-Glucuronic acid 5,6-dihydroxyflavone (baicalin) can promote the expression of epidermal growth factor and VEGF and then enhance the regenerative ability of epidermal cells, endothelial cells, and fibrotic tissue, to induce wound healing (Zhang et al., 2011; Mao et al., 2021). It has been found that a baicalin-loaded nanohydrogel has suitable viscosity, good skin retention and good biocompatibility, which can antagonise the cytotoxic effects of hydrogen peroxide, regulate the inflammatory process and promote the healing of chronic wounds (Manconi et al., 2018).

Curcumin has been shown to promote wound healing (Jose et al., 2022). However, its water solubility and skin permeability are poor, which limits its local application (Naz and Ahmad, 2015). A recent study found that curcumin-loaded nanocomposite hydrogels can prolong the local treatment time of curcumin compared with ordinary curcumin hydrogels (Kamar et al., 2019). Slow release of curcumin can promote the healing of diabetic ulcers by improving

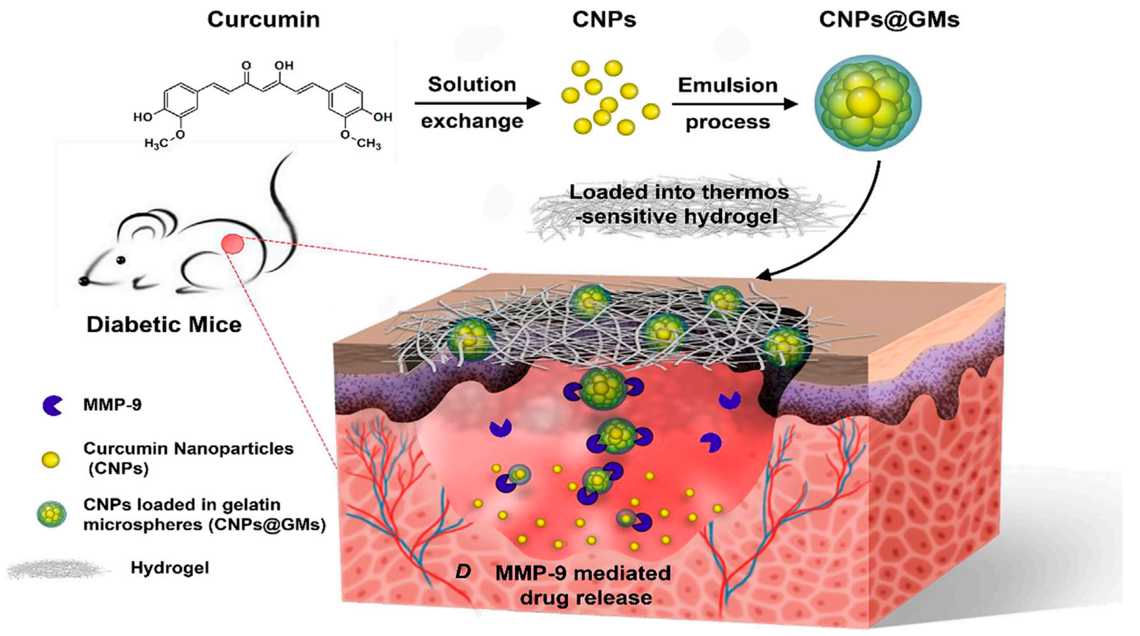

FIGURE 3
The preparation of curcumin nanoparticles/gelatin-microsphere hydrogel and the drug release process in the wound beds of diabetic mice. Reproduced from (Liu et al., 2018), with permission from American Chemical Society.

the wound closure rate, accelerating the formation of granulation tissue and the deposition of collagen deposition, thus enhancing the expression of VEGF and Aquaporin 3. Other studies have found that gelatin microspheres containing curcumin nanoparticles can ensure the stable release of curcumin in the wound surface, significantly improve the antioxidant effect and migration-inducing ability of curcumin and promote skin wound healing of diabetic mice (Liu et al., 2018) (Figure 3).

Previous studies have confirmed that quercetin or oleic acid alone can promote wound healing (Rodrigues et al., 2016; Jangde et al., 2018). A recent study found that the nanohydrogel prepared using quercetin and oleic acid can reduce the pain of patients with diabetic ulcers, improve the viscoelasticity of tissue and significantly shorten wound healing time (Gallelli et al., 2020).

Treatment of diabetic ulcers with nanocomposite hydrogel loaded with protein

At present, most studies focus on the use of protein hormones and growth factors to promote the healing of diabetic ulcers (Laiva et al., 2021; Oliveira et al., 2021; Mohammadi Tofigh and Tajik, 2022). Compared with small-molecule drugs, protein drugs have become a hot field of new drug development because of their high activity, high specificity, low physiological toxicity and good biocompatibility. However, the unique molecular structure and biochemical characteristics rapidly inactivate protein drugs in complex biological environments, which limits their application to biomedicine (Yu Y. et al., 2021). It has been shown that nanocomposite hydrogels can encapsulate protein drugs in their internal network structure, thus protecting them from the external environment (Li M. et al., 2017; Wang Z. et al., 2019; Zhou et al., 2022).

Proteins are important nutrients for the proliferation and remodelling of wound healing (Cheng et al., 2020; Smith et al., 2022). Proteins can promote the formation of capillaries, the proliferation of fibroblasts and the synthesis of collagen and improve the function of the immune system. Therefore, exogenous protein supplementation can promote wound healing and tissue repair (Kim et al., 2019; Lapi et al., 2021; Yang P. et al., 2022).

Insulin is a physiological hypoglycaemic agent, which is commonly used in the treatment of diabetes. Recent studies have found that local use of insulin can treat diabetic ulcer (Zhang and Lv, 2016; Vatankhah et al., 2017; Bhettani et al., 2020). Both free insulin and nano insulin encapsulated in a hydrogel can improve wound healing, although insulin in a nanocomposite hydrogel has a better therapeutic effect (Abdelkader et al., 2018). Furthermore, insulin can reduce inflammation, increase angiogenesis, induce the formation of granulation tissue, reconstruct the epidermis and completely deposit collagen.

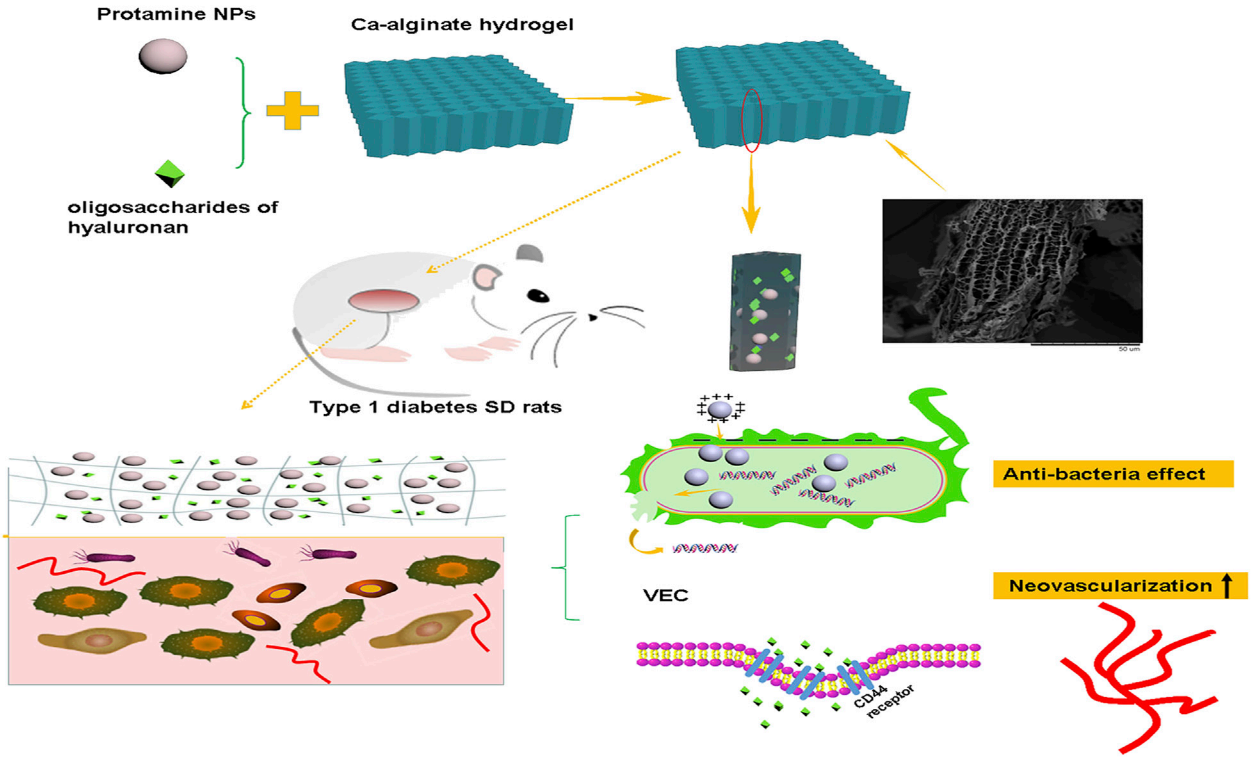

FIGURE 4
Application of a calcium alginate gel loaded with protamine nanoparticles and hyaluronan oligosaccharides in skin wound healing of type 1 diabetic rats. Reproduced from (Wang T. et al., 2019), with permission from Springer Nature.

Based on the hypothesis that regulating antibacterial and neovascularisation activities promotes diabetic wound healing, a pH-responsive calcium alginate hydrogel was reported, which loaded protamine nanoparticles and hyaluronic acid oligosaccharides, showing good homogeneity and biocompatibility (Wang T. et al., 2019; Guo et al., 2022; Liu et al., 2022). Protamine nanoparticles act as a cationic antibacterial peptide against various bacteria by disrupting their cell membranes. The addition of hyaluronic acid oligosaccharides promoted the migration of human umbilical vein endothelial cells *in vitro* and the secretion of VEGF. Protamine nanoparticles and hyaluronic acid oligosaccharides synergise to promote wound healing (Figure 4).

Silk fibroin is mainly composed of non-polar amino acids. It has good biocompatibility and no toxicity. It can promote cell proliferation and differentiation *in vivo* and *in vitro*, which is conducive to wound healing (Park Y. R. et al., 2018; Zhang Y. et al., 2019). However, it is difficult to prepare single-network silk fibroin hydrogels for the treatment of diabetic ulcers because of the secondary structural transformation of silk fibroin, which often produces a large β-sheet domain that greatly increases the brittleness of hydrogels (Xu et al., 2021). It has been found that natural biomaterials such as silk fibroin, carboxymethyl cellulose and manganese dioxide nanoflakes can be used to prepare injectable nanocomposite hydrogels, which can provide a moist wound healing environment, relieve inflammation, promote angiogenesis and matrix remodelling and adapt to the irregular wound shape of patients with diabetic ulcer (Pu et al., 2022). Numerous studies have shown that under the condition of high oxidative stress in patients with diabetes, the overexpression of matrix metalloproteinases impairs the formation of granulation tissue and the regeneration of the extracellular matrix (Wu et al., 2016). The above hydrogel can effectively neutralise excessive matrix metalloproteinases, reduce the level of inflammation and promote the integration of extracellular matrix and angiogenesis. The uniform dispersion of MnO_2 nanosheets endows hydrogels with outstanding reactive oxygen species scavenging ability that alleviates oxidative stress and produces sustained O_2 to promote angiogenesis.

In a study, an inflammatory memory peptide was extracted from absent in melanoma 2 to prepare a nanopeptide hydrogel (Cheng et al., 2018). Subsequently, *Akkermansia muciniphila*, a member of the intestinal microbiota with hypoglycaemic effect, was inoculated into the hydrogel. After subcutaneous injection, the hydrogel was delivered to the diabetic ischaemic ulcer tissue. It was found that the hydrogel could promote angiogenesis, regulate the immune response and reduce local glucose levels to obviously promote the healing of diabetic ulcers. Components of protein hydrolysates such as glutamic acid, aspartic acid and glycine can promote wound healing (Corsetti et al., 2017; Hung et al., 2019). A paper reports a multifunctional nanocomposite hydrogel with excellent tensile and compressive properties, rapid recovery ability, antibacterial activity and coagulation ability (Tavakoli et al., 2020). The presence of L-glutamic acid accelerates the migration of wound cells and the formation of a scar in rats with diabetic ulcer and promotes the synthesis of collagen on the wound surface.

Many studies have confirmed that wound healing is a complex process involving a variety of cells and cytokines (Park K. H. et al., 2018; Chen et al., 2018; Certelli et al., 2021; Schirmer et al., 2021). Patients with diabetes experience long-term wound healing because of the absence of local growth factors with diminished activity (such as the glycosylation of growth factor). Therefore, exogenous growth factors may promote wound healing.

Among growth factors, Epidermal Growth Factor (EGF) is a low-molecular-weight peptide composed of 53 amino acids (Guo et al., 2020). Previous studies have shown that EGF can greatly promote the proliferation and movement of keratinocytes and fibroblasts, granulation tissue formation, and extracellular matrix synthesis. Exogenous recombinant human EGF (rhEGF) is one of the most widely used growth factors in the treatment of diabetic ulcer (Tsang et al., 2003; Jeong et al., 2020; de Oliveira et al., 2022). A study reported that a chitosan-based composite hydrogel can be produced by compounding EGF-coated nanoparticles with silver ions using nanocapsule technology (Lee et al., 2021). The hydrogel can continuously release EGF and Ag^+, has obvious bactericidal effect and has good hydration effect, which makes it very suitable for wound exudation environment. Compared with other methods of treating diabetic ulcers, the hydrogel resulted in rapid collagen deposition, reduced inflammation, and faster wound healing in rats with diabetic ulcers. Another study reported that a chitosan-based nanocomposite hydrogel could be developed through nanotechnology, which encapsulates EGF nanoparticles, perfluorocarbon and polyhexamethylene biguanide (Lee and Lin, 2022). The hydrogel continuously released EGF and polyhexamethylene biguanide, which had antibacterial, anti-inflammatory, oxygen transport and enhanced cell growth activities. These functions allow the skin tissue integrity and function of diabetic rats to rapidly recover. In addition, a study reported that a polymer coupled to recombinant human epidermal growth factor incorporated into chitosan-based hydrogels, which retains the biological activity of EGF and confers better resistance to proteolysis (Hajimiri et al., 2016). It can promote the proliferation of fibroblasts *in vitro* and promote wound healing in diabetic rats.

Platelet-derived growth factor (PDGF), known as “trauma factor”, is mainly stored in platelet alpha granules (Walsh and Poole, 2017). When the body is injured, epithelial cells, endothelial cells, macrophages and immune cells secrete PDGF (Yang et al., 2020). They are directly or indirectly involved in inflammatory reaction, tissue and cell differentiation and proliferation of wound repair (Das et al., 2016; Jian et al., 2022). In 1997, the FDA approved *Becaplermin* containing a human recombinant platelet-derived growth factor BB (PDGF-BB) gel for the treatment of diabetic foot ulcers. A recent study reported that PDGF-BB encapsulated with a self-assembled peptide (RADA 16-I) can create a kind of nanohydrogel with good biocompatibility and biodegradability, which allows continuous delivery of PDGF-BB and destroys the bacterial biofilm (Santhini et al., 2022). Compared with the control group and untreated animals, the levels of hydroxyproline and ascorbic acid in *Rattus norvegicus* treated with the PDGF-BB nanohydrogel were significantly increased, which confirms the role of PDGF-BB nanohydrogel in promoting angiogenesis and wound healing.

Stromal cell-derived factor-1α (SDF-1α) is a key chemokine involved in the regulation of tissue and organ injury and repair with strong chemotaxis on diverse inflammatory and mesenchymal stem cells (Li et al., 2016). SDF-1α can promote angiogenesis and wound healing by inducing the migration of endothelial progenitor cells. After the expression of SDF-1α is inhibited, wound neovascularisation is significantly reduced, the inflammatory reaction is intensified and the wound healing rate is significantly reduced. To protect SDF-1α, Yu et al. (2020) prepared a kind of nanogel-loaded liposome that stimulates the recruitment of bone marrow mesenchymal stem cells, secretes cytokines, regulates the phenotypes of other effector cells and effectively promotes wound closure and tissue regeneration. Other studies have found that these nanocomposite hydrogels containing SDF-1α could influence macrophage phenotype and promote skin tissue regeneration in diabetic mice (Yu J. R. et al., 2021).

Moreover, combining small-molecule drugs with growth factors may be a promising method to promote wound healing. The curcumin and EGF modified by nanotechnology were encapsulated in hydrogels, which could release curcumin and EGF on demand and synchronise with wound healing. Specifically, curcumin is rapidly and continuously released during the early stage of wound healing to alleviate inflammation and oxidative stress, while EGF is relatively slow-acting and sustains late proliferation and extracellular matrix remodelling (Li Y. et al., 2021; Hu et al., 2021). A similar combination has been verified using nano lipid carriers (Lee et al., 2020).

Treatment of diabetic ulcers with nanocomposite hydrogel loaded with silver nanoparticles

Bacterial infection is an important factor that hinders wound healing of diabetic ulcers (Kishibe et al., 2018; Zhang R. et al., 2021; Roy et al., 2022). The decomposition products of diabetic ulcer skin tissue and the persistent high-glucose environment provide an excellent culture medium for the growth and reproduction of bacteria. A large number of bacteria enter the human body through the wound and go deep into the tissue,

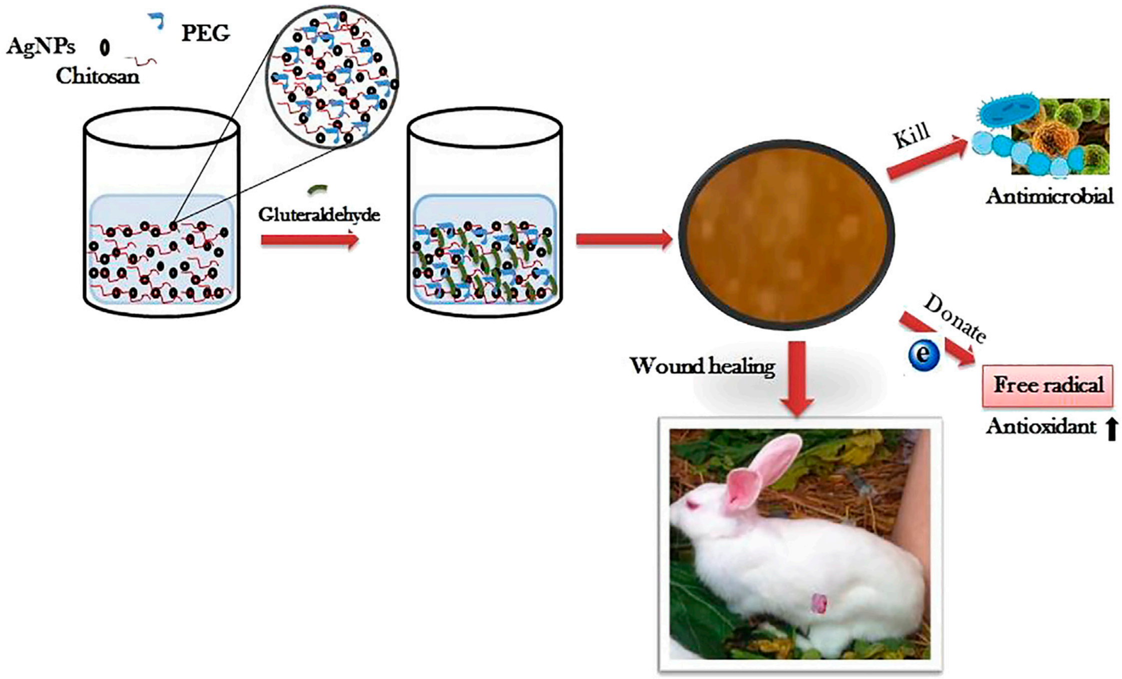

FIGURE 5
The preparation process of Silver nanoparticle impregnated chitosan-PEG hydrogel and its therapeutic effect on diabetic rabbit wounds. Reproduced from (Masood et al., 2019), with permission from Elsevier.

leading to sepsis and even death (Shaheen et al., 2021; Xie et al., 2022). Early, active and effective control can prevent chronic infection and accelerate wound healing (Han and Kang, 2013).

Most metal nanoparticles possess antibacterial effects, among which that of silver nanoparticles is the strongest. Silver nanoparticles have excellent antibacterial properties through controlling the slow release of silver ions from their surface (Devi et al., 2017; Shankar and Rhim, 2017; Li M. et al., 2021; Haghniaz et al., 2021). In addition to antibacterial activity, silver nanoparticles have been observed to be anti-inflammatory, induce apoptosis of neutrophils, reduce the activity of matrix metalloproteinases, accelerate wound healing and reduce the formation of a scar (Wong et al., 2009; Sivakumar et al., 2017; Shehabeldine et al., 2022).

Recent studies have shown that bamboo cellulose nanocrystals can be impregnated with silver nanoparticles to obtain inexpensive nanocomposite hydrogels (Singla et al., 2017). The levels of pro-inflammatory cytokines IL-6 and TNF-α were significantly decreased, and the expression of collagen and growth factors (FGF, PDGF, VEGF) were significantly increased in mice with diabetic ulcers treated with topical application of this hydrogel. In addition, re-epithelialisation, angiogenesis and collagen deposition were improved, and wound healing was accelerated. Similarly, a type of chitosan polyethylene glycol hydrogel impregnated with silver nanoparticles was recently reported (Masood et al., 2019). Compared with the blank chitosan polyethylene glycol hydrogel, the silver nanoparticle-impregnated hydrogel has higher porosity, higher expansion and stronger antibacterial and antioxidant properties *in vitro*. The chitosan polyethylene glycol hydrogel impregnated with silver nanoparticles can slowly and continuously releases silver nanoparticles within 7 days, can accelerate the re-epithelisation and collagen deposition of diabetic wounds of rabbits and have better wound healing ability (Figure 5).

Recently, it has been reported that a novel antifouling and anti-infective hydrogel can be prepared by mixing silver nanoparticles with chitosan and dextran. After treatment with this hydrogel, the wounds of diabetic SD rats contracted rapidly, and the expression levels of $CD68^+$ and $CD3^+$ were upregulated (Shi et al., 2019). It is suggested that the hydrogel can promote the activation of immune cells and accelerate wound healing by promoting fibroblast migration, granulation tissue formation and angiogenesis. For example, Huang et al. (2017) synthesised nanocomposite hydrogels containing silver nanoparticles, showing high water content and antifouling and antibacterial properties. They achieve good absorption of exudates and are easily removed from wounds. The embedded silver nanoparticles continuously release Ag^+ and eliminate adsorbed bacteria by interacting

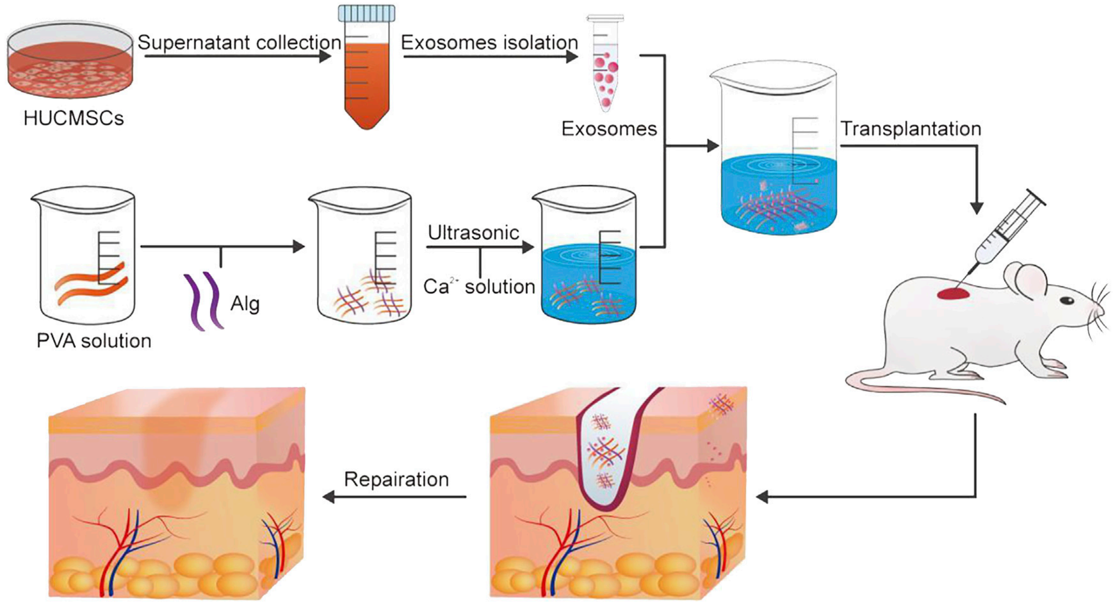

FIGURE 6
The preparation method of exosomes and the application of exosomes in wound healing. Reproduced from (Zhang Y. et al., 2021), with permission from Elsevier.

with sulfur-containing proteins on bacterial membrane. Furthermore, Ragothaman et al. (2021) have fabricated a nanohydrogel system coated with silver nanoparticles and melatonin, in which silver nanoparticles act as antibacterials and melatonin as an antioxidant and anti-inflammatory agent. The synergistic effect of the two drugs results in rapid tissue regeneration, collagen deposition and angiogenesis in the wound site of Wistar albino rats.

However, the latest research shows that silver nanoparticles readily agglomerate, and high concentration of Ag^+ will have adverse side effects on human cells and tissues (Rana and Kalaichelvan, 2013). Based on this, a nanohydrogel loaded with functional Ag_2S quantum dots was reported (Du et al., 2022). It can improve the bacterial clearance rate, increase the collagen coverage area and upregulate the expression of VEGF. It shows high biocompatibility and serves a new way for the treatment of infectious diabetic ulcers.

Other considerations

Exosomes are lipid bilayer extracellular vesicles secreted by various cells, which contain a series of bioactive substances such as proteins, lipids, RNA and DNA. They can promote angiogenesis, stimulate collagen deposition, inhibit inflammation and accelerate wound healing (Chen et al., 2021; Zhao et al., 2021; Wang et al., 2022). Previous studies have shown that the lack of exosomes may lead to delayed wound healing in patients with diabetic ulcers. It was found that the bioactive scaffold was prepared by wrapping exosomes from human umbilical cord mesenchymal stem cells in polyvinyl alcohol/alginate nanohydrogels (Zhang Y. et al., 2021). It has good biocompatibility and can effectively load exosomes to make them active. The hydrogel can promote the expression of smooth muscle actin, scavenger receptor class B type 1, platelet endothelial cell adhesion molecule-1 and VEGF by activating the ERK1/2 pathway and accelerate the wound healing of diabetic ulcers of rats. Furthermore, exosomes encapsulated in the nanohydrogel could promote the wound healing, proliferation, migration and angiogenesis of human umbilical cord mesenchymal stem cells in rats with diabetic ulcers more quickly than normally injected exosomes (Figure 6).

Recent studies have shown that platelet-rich plasma comprising numerous cell growth factors can accelerate wound healing by regulating cell proliferation (Menchisheva et al., 2019; Devereaux et al., 2020; Qian et al., 2020). However, most of the platelet-rich plasma used in the clinic is liquid, which cannot be fixed in the local area, and the growth factors in platelet-rich plasma is released too fast to maintain the long-term effective concentration. Recently, it has been reported that the plasma-rich gel is an effective carrier to protect platelet growth (Li et al., 2022a). *In vivo* studies showed that the hydrogel significantly promotes the healing of full-thickness skin wounds by enhancing granulation tissue formation, promoting collagen deposition and accelerating re-epithelialisation and neovascularisation.

Oxygen is the most important nutrient for cell survival. Insufficient oxygen delivery prevents cell migration and angiogenesis and reduces cell growth and differentiation, thereby delaying wound healing (Shiekh et al., 2020; Tu et al., 2022). Recently, a new technology is reported, which can transform the traditional gel dressing by adding freeze-dried nano-oxygen-containing powder to obtain a nano-sized oxygen-containing gel, which can deliver dissolved oxygen to the local wound surface (Yang Z. et al., 2022). The hydrogel promotes cell migration, angiogenesis and cell viability by antagonising the hypoxic environment of epithelial cells, endothelial cells and fibroblasts. Animal experiments showed that a nano-oxygen-containing gel has substantial effects on wound healing and flap survival in diabetic mice.

Increasing evidence shows that mesenchymal stem cells can promote wound healing of diabetic ulcers by promoting cell proliferation and differentiation and extracellular matrix synthesis, releasing growth factors and promoting angiogenesis (Han et al., 2019; Lv et al., 2020; Wang et al., 2022). Recently, it has been reported that nanopeptide hydrogels can improve the survival and proliferation efficiency of mesenchymal stem cells and enhance their differentiation potential and secretory activity (Xue et al., 2022). The hydrogel can regulate inflammatory reactions by downregulating inflammatory factors and upregulating VEGF to promote angiogenesis, thus accelerating the healing of diabetic ulcers.

Recently, researchers have found that proteins in egg white play an important role in wound healing (Ge et al., 2021). Based on this, montmorillonite/polyvinyl alcohol nanocomposite hydrogels containing egg white were prepared using a cyclic freeze-thaw method (Jahani-Javanmardi et al., 2016). Such hydrogels are transparent, and the equilibrium water content and gas exchange rate are very close to those of human skin. Moreover, it is suitable for dry diabetic ulcer wounds.

Discussion

Diabetic skin ulcers are a serious complication caused by the internal environmental changes and the local pathological changes of skin caused by diabetes. Many studies have shown that a nanocomposite hydrogel is an ideal local drug delivery method to promote the healing of diabetic ulcers and has achieved satisfactory therapeutic effects. Nanocomposite hydrogels have the advantages of small particle size, high water content, long drug released property and good biocompatibility and biodegradability. They can also be used for the delivery of small-molecule drugs, protein drugs and silver nanoparticles to promote the healing of diabetic ulcers. In conclusion, nanocomposite hydrogels are expected to serve as a new dressing for large-scale clinical treatment of diabetic ulcer patients.

However, there are still problems to be solved. For example, most nanocomposite hydrogels are in the early stage of experimental or clinical development, and there is a lack of large-scale clinical studies to establish efficacy and safety. The preparation of some hydrogels is complex, which makes it difficult to widely apply them to the clinic. To reduce the adverse reactions in clinical treatment, it is necessary to accurately control a series of properties of nanocomposite hydrogels, such as crosslinking degree, porosity, swelling, mechanical properties, cell adhesion and permeability and to simulate the extracellular matrix microenvironment as much as possible to maintain the characteristics and activity of each component. Furthermore, it is important to determine the optimal moisture removal rate of the composite hydrogel and to determine the optimal moisture content of the composite hydrogel for patients with diabetes. It can be predicted that our research on nanocomposite hydrogel materials will be more detailed, and the preparation methods will be more advanced. More new nanocomposite hydrogel carriers will be developed and applied to clinical drug delivery, which will benefit more patients with chronic ulcers.

Author contributions

JW was the corresponding author and participated in the conception and design of the study. BS organized the work and reviewed the article. ST prepared the manuscript and wrote the main part of the manuscript. QL (2nd author) helped to edit the manuscript through constructive discussions. QL (3rd author) helped to revise the manuscript and obtain the rights to the images. All authors agreed on the final version of the manuscript.

Funding

This investigation was supported by the Yunnan Province Natural Science Foundation Project (202001AU070117) and Young Scientists Fund of the National Natural Science Foundation of China (82104403).

Acknowledgments

The authors are thankful to the editor and reviewers of this manuscript for providing excellent suggestions for the improvement of manuscript.

Conflict of interest

The authors declare that the research was conducted in the absence of any commercial or financial relationships that could be construed as a potential conflict of interest.

Publisher's note

All claims expressed in this article are solely those of the authors and do not necessarily represent those of their affiliated organizations, or those of the publisher, the editors and the reviewers. Any product that may be evaluated in this article, or claim that may be made by its manufacturer, is not guaranteed or endorsed by the publisher.

References

Abdelkader, D. H., Tambuwala, M. M., Mitchell, C. A., Osman, M. A., El-Gizawy, S. A., Faheem, A. M., et al. (2018). Enhanced cutaneous wound healing in rats following topical delivery of insulin-loaded nanoparticles embedded in poly(vinyl alcohol)-borate hydrogels. *Drug Deliv. Transl. Res.* 8 (5), 1053–1065. doi:10.1007/s13346-018-0554-0

Abdollahi, Z., Zare, E. N., Salimi, F., Goudarzi, I., Tay, F. R., and Makvandi, P. (2021). Bioactive carboxymethyl starch-based hydrogels decorated with CuO nanoparticles: Antioxidant and antimicrobial properties and accelerated wound healing *in vivo*. *Int. J. Mol. Sci.* 22 (5), 2531. doi:10.3390/ijms22052531

Alvarez, G. S., Hélary, C., Mebert, A. M., Wang, X., Coradin, T., and Desimone, M. F. (2014). Antibiotic-loaded silica nanoparticle-collagen composite hydrogels with prolonged antimicrobial activity for wound infection prevention. *J. Mat. Chem. B* 2 (29), 4660–4670. doi:10.1039/c4tb00327f

Bairagi, U., Mittal, P., Singh, J., and Mishra, B. (2018). Preparation, characterization, and *in vivo* evaluation of nano formulations of ferulic acid in diabetic wound healing. *Drug Dev. Ind. Pharm.* 44 (11), 1783–1796. doi:10.1080/03639045.2018.1496448

Bang, T. H., Van, T. T. T., Hung, L. X., Ly, B. M., Nhut, N. D., Thuy, T. T. T., et al. (2019). Nanogels of acetylated ulvan enhance the solubility of hydrophobic drug curcumin. *Bull. Mat. Sci.* 42 (1), 1. doi:10.1007/s12034-018-1682-3

Bhettani, M. K., Rehman, M., Altaf, H. N., and Altaf, O. S. (2020). Effectiveness of topical insulin dressings in management of diabetic foot ulcers. *World J. Surg.* 44 (6), 2028–2033. doi:10.1007/s00268-019-05321-3

Boyko, E. J., Zelnick, L. R., Braffett, B. H., Pop-Busui, R., Cowie, C. C., Lorenzi, G. M., et al. (2022). Risk of foot ulcer and lower-extremity amputation among participants in the diabetes control and complications trial/epidemiology of diabetes interventions and complications study. *Diabetes Care* 45 (2), 357–364. doi:10.2337/dc21-1816

Certelli, A., Valente, P., Uccelli, A., Grosso, A., Di Maggio, N., D'Amico, R., et al. (2021). Robust angiogenesis and arteriogenesis in the skin of diabetic mice by transient delivery of engineered VEGF and PDGF-BB proteins in fibrin hydrogels. *Front. Bioeng. Biotechnol.* 9, 688467. doi:10.3389/fbioe.2021.688467

Chen, L., Qin, L., Chen, C., Hu, Q., Wang, J., and Shen, J. (2021). Serum exosomes accelerate diabetic wound healing by promoting angiogenesis and ECM formation. *Cell Biol. Int.* 45 (9), 1976–1985. doi:10.1002/cbin.11627

Chen, Y., Zheng, K., Niu, L., Zhang, Y., Liu, Y., Wang, C., et al. (2019). Highly mechanical properties nanocomposite hydrogels with biorenewable lignin nanoparticles. *Int. J. Biol. Macromol.* 128, 414–420. doi:10.1016/j.ijbiomac.2019.01.099

Chen, Z., Fu, S., Wu, Z., Chen, J., Huang, Y., Wang, Y., et al. (2018). Relationship between plasma angiogenic growth factors and diabetic foot ulcers. *Clin. Chim. Acta* 482, 95–100. doi:10.1016/j.cca.2018.03.035

Cheng, L., Cai, Z., Ye, T., Yu, X., Chen, Z., Yan, Y., et al. (2020). Injectable polypeptide-protein hydrogels for promoting infected wound healing. *Adv. Funct. Mat.* 30 (25), 2001196. doi:10.1002/adfm.202001196

Cheng, P., Yao, L., Chen, X., Su, X., Su, X., Huang, Q., et al. (2018). An inflammatory memory and angiogenic self-assembling nanofiber hydrogel scaffold seeded with Akkermansia muciniphila to accelerate the healing of diabetic ischemic ulcers. *RSC Adv.* 8 (31), 17357–17364. doi:10.1039/c8ra01662c

Cheng, Z., Qing, R., Hao, S., Ding, Y., Yin, H., Zha, G., et al. (2021). Fabrication of ulcer-adhesive oral keratin hydrogel for gastric ulcer healing in a rat. *Regen. Biomater.* 8 (2), rbab008. doi:10.1093/rb/rbab008

Corsetti, G., Romano, C., Pasini, E., Marzetti, E., Calvani, R., Picca, A., et al. (2017). Diet enrichment with a specific essential free amino acid mixture improves healing of undressed wounds in aged rats. *Exp. Gerontol.* 96, 138–145. doi:10.1016/j.exger.2017.06.020

Das, S., Majid, M., and Baker, A. B. (2016). Syndecan-4 enhances PDGF-BB activity in diabetic wound healing. *Acta Biomater.* 42, 56–65. doi:10.1016/j.actbio.2016.07.001

de Oliveira, B., Oliveira, B. C., Deutsch, G., Pessanha, F. S., Thiré, R., and de Castilho, S. R. (2022). rhEGF-loaded hydrogel in the treatment of chronic wounds in patients with diabetes: Clinical cases. *Gels* 8 (8), 523. doi:10.3390/gels8080523

Demiot, C., Fromy, B., Saumet, J. L., and Sigaudo-Roussel, D. (2006). Preservation of pressure-induced cutaneous vasodilation by limiting oxidative stress in short-term diabetic mice. *Cardiovasc. Res.* 69 (1), 245–252. doi:10.1016/j.cardiores.2005.09.005

Devereaux, J., Dargahi, N., Fraser, S., Nurgali, K., Kiatos, D., and Apostolopoulos, V. (2020). Leucocyte-rich platelet-rich plasma enhances fibroblast and extracellular matrix activity: Implications in wound healing. *Int. J. Mol. Sci.* 21 (18), 6519. doi:10.3390/ijms21186519

Devi, G. K., Kumar, K. S., Parthiban, R., and Kalishwaralal, K. (2017). An insight study on HPTLC fingerprinting of Mukia maderaspatna: Mechanism of bioactive constituents in metal nanoparticle synthesis and its activity against human pathogens. *Microb. Pathog.* 102, 120–132. doi:10.1016/j.micpath.2016.11.026

Ding, Z., Zhang, Y., Guo, P., Duan, T., Cheng, W., Guo, Y., et al. (2021). Injectable desferrioxamine-laden silk nanofiber hydrogels for accelerating diabetic wound healing. *ACS Biomater. Sci. Eng.* 7 (3), 1147–1158. doi:10.1021/acsbiomaterials.0c01502

Dou, Y., Huang, R., Li, Q., Liu, Y., Li, Y., Chen, H., et al. (2021). Oxyberberine, an absorbed metabolite of berberine, possess superior hypoglycemic effect via regulating the PI3K/Akt and Nrf2 signaling pathways. *Biomed. Pharmacother.* 137, 111312. doi:10.1016/j.biopha.2021.111312

Du, T., Xiao, Z., Cao, J., Wei, L., Li, C., Jiao, J., et al. (2022). NIR-activated multi-hit therapeutic Ag(2)S quantum dot-based hydrogel for healing of bacteria-infected wounds. *Acta Biomater.* 145, 88–105. doi:10.1016/j.actbio.2022.04.013

Fadol, E. M., Suliman, H. M., Osman, B., Abdalla, S. A., Osman, W. J. A., Mohamed, E. M., et al. (2021). Therapeutic outcomes evaluation of adjuvant hyperbaric oxygen therapy for non-healing diabetic foot ulcers among sudanese patients. *Diabetes & Metabolic Syndrome Clin. Res. Rev.* 15 (4), 102173. doi:10.1016/j.dsx.2021.06.010

Fan, Y., Wu, W., Lei, Y., Gaucher, C., Pei, S., Zhang, J., et al. (2019). Edaravone-loaded alginate-based nanocomposite hydrogel accelerated chronic wound healing in diabetic mice. *Mar. Drugs* 17 (5), 285. doi:10.3390/md17050285

Fiordaliso, F., Clerici, G., Maggioni, S., Caminiti, M., Bisighini, C., Novelli, D., et al. (2016). Prospective study on microangiopathy in type 2 diabetic foot ulcer. *Diabetologia* 59 (7), 1542–1548. doi:10.1007/s00125-016-3961-0

Frykberg, R. G., Franks, P. J., Edmonds, M., Brantley, J. N., Téot, L., Wild, T., et al. (2020). A multinational, multicenter, randomized, double-blinded, placebo-controlled trial to evaluate the efficacy of cyclical topical wound oxygen (TWO2) therapy in the treatment of chronic diabetic foot ulcers: The TWO2 study. *Diabetes Care* 43 (3), 616–624. doi:10.2337/dc19-0476

Fujisawa, A., and Yamamoto, Y. (2016). Edaravone, a potent free radical scavenger, reacts with peroxynitrite to produce predominantly 4-NO-edaravone. *Redox Rep.* 21 (3), 98–103. doi:10.1179/1351000215y.0000000025

Gallelli, G., Cione, E., Serra, R., Leo, A., Citraro, R., Matricardi, P., et al. (2020). Nano-hydrogel embedded with quercetin and oleic acid as a new formulation in the treatment of diabetic foot ulcer: A pilot study. *Int. Wound J.* 17 (2), 485–490. doi:10.1111/iwj.13299

Ge, H., Jiang, Y., Ning, Z., Hu, Z., Ma, S., Shao, Y., et al. (2021). Supplementation of egg white peptides on attenuating skin mechanical damage symptoms: A promising way to accelerate wound healing process. *Food Funct.* 12 (17), 7688–7698. doi:10.1039/d1fo01525g

Girija, A. R., Balasubramanian, S., and Cowin, A. J. (2022). Nanomaterials-based drug delivery approaches for wound healing. *Curr. Pharm. Des.* 28 (9), 711–726. doi:10.2174/1381612828666220328121211

Guo, C., Wu, Y., Li, W., Wang, Y., and Kong, Q. (2022). Development of a microenvironment-responsive hydrogel promoting chronically infected diabetic wound healing through sequential hemostatic, antibacterial, and angiogenic activities. *ACS Appl. Mat. Interfaces* 14 (27), 30480–30492. doi:10.1021/acsami.2c02725

Guo, H. F., Abd Hamid, R., Mohd Ali, R., Chang, S. K., Rahman, M. H., Zainal, Z., et al. (2020). Healing properties of epidermal growth factor and tocotrienol-rich fraction in deep partial-thickness experimental burn wounds. *Antioxidants (Basel)* 9 (2), 130. doi:10.3390/antiox9020130

Gurtner, G. C., Werner, S., Barrandon, Y., and Longaker, M. T. (2008). Wound repair and regeneration. *Nature* 453 (7193), 314–321. doi:10.1038/nature07039

Haghniaz, R., Rabbani, A., Vajhadin, F., Khan, T., Kousar, R., Khan, A. R., et al. (2021). Anti-bacterial and wound healing-promoting effects of zinc ferrite nanoparticles. *J. Nanobiotechnology* 19 (1), 38. doi:10.1186/s12951-021-00776-w

Hajimiri, M., Shahverdi, S., Esfandiari, M. A., Larijani, B., Atyabi, F., Rajabiani, A., et al. (2016). Preparation of hydrogel embedded polymer-growth factor conjugated nanoparticles as a diabetic wound dressing. *Drug Dev. Ind. Pharm.* 42 (5), 707–719. doi:10.3109/03639045.2015.1075030

Han, C., Jeong, D., Kim, B., Jo, W., Kang, H., Cho, S., et al. (2019). Mesenchymal stem cell engineered nanovesicles for accelerated skin wound closure. *ACS Biomater. Sci. Eng.* 5 (3), 1534–1543. doi:10.1021/acsbiomaterials.8b01646

Han, H. S., and Kang, S. B. (2013). Relations between long-term glycemic control and postoperative wound and infectious complications after total knee arthroplasty in type 2 diabetics. *Clin. Orthop. Surg.* 5 (2), 118–123. doi:10.4055/cios.2013.5.2.118

Hassan, M. A., Tamer, T. M., Rageh, A. A., Abou-Zeid, A. M., Abd El-Zaher, E. H. F., and Kenawy, E. R. (2019). Insight into multidrug-resistant microorganisms from microbial infected diabetic foot ulcers. *Diabetes & Metabolic Syndrome Clin. Res. Rev.* 13 (2), 1261–1270. doi:10.1016/j.dsx.2019.01.044

Hilton, J. R., Williams, D. T., Beuker, B., Miller, D. R., and Harding, K. G. (2004). Wound dressings in diabetic foot disease. *Clin. Infect. Dis.* 39 (2), S100–S103. doi:10.1086/383270

Hu, B., Gao, M., Boakye-Yiadom, K. O., Ho, W., Yu, W., Xu, X., et al. (2021). An intrinsically bioactive hydrogel with on-demand drug release behaviors for diabetic wound healing. *Bioact. Mat.* 6 (12), 4592–4606. doi:10.1016/j.bioactmat.2021.04.040

Huang, K. T., Fang, Y. L., Hsieh, P. S., Li, C. C., Dai, N. T., and Huang, C. J. (2017). Non-sticky and antimicrobial zwitterionic nanocomposite dressings for infected chronic wounds. *Biomater. Sci.* 5 (6), 1072–1081. doi:10.1039/c7bm00039a

Hung, S. Y., Tsai, J. S., Yeh, J. T., Chen, K. H., Lin, C. N., Yang, H. M., et al. (2019). Amino acids and wound healing in people with limb-threatening diabetic foot ulcers. *J. Diabetes Complicat.* 33 (10), 107403. doi:10.1016/j.jdiacomp.2019.06.008

Jahani-Javanmardi, A., Sirousazar, M., Shaabani, Y., and Kheiri, F. (2016). Egg white/poly (vinyl alcohol)/MMT nanocomposite hydrogels for wound dressing. *J. Biomaterials Sci. Polym. Ed.* 27 (12), 1262–1276. doi:10.1080/09205063.2016.1191825

Jangde, R., Srivastava, S., Singh, M. R., and Singh, D. (2018). *In vitro* and *in vivo* characterization of quercetin loaded multiphase hydrogel for wound healing application. *Int. J. Biol. Macromol.* 115, 1211–1217. doi:10.1016/j.ijbiomac.2018.05.010

Jeffcoate, W. J., Price, P. E., Phillips, C. J., Game, F. L., Mudge, E., Davies, S., et al. (2009). Randomised controlled trial of the use of three dressing preparations in the management of chronic ulceration of the foot in diabetes. *Health Technol. Assess.* 13 (54), 1–86. doi:10.3310/hta13540

Jeong, S., Kim, B., Park, M., Ban, E., Lee, S. H., and Kim, A. (2020). Improved diabetic wound healing by EGF encapsulation in gelatin-alginate coacervates. *Pharmaceutics* 12 (4), 334. doi:10.3390/pharmaceutics12040334

Jian, K., Yang, C., Li, T., Wu, X., Shen, J., Wei, J., et al. (2022). PDGF-BB-derived supramolecular hydrogel for promoting skin wound healing. *J. Nanobiotechnology* 20 (1), 201. doi:10.1186/s12951-022-01390-0

Jose, J., Pai, A. R., Gopakumar, D. A., Dalvi, Y., Ruby, V., Bhat, S. G., et al. (2022). Novel 3D porous aerogels engineered at nano scale from cellulose nano fibers and curcumin: An effective treatment for chronic wounds. *Carbohydr. Polym.* 287, 119338. doi:10.1016/j.carbpol.2022.119338

Kamar, S. S., Abdel-Kader, D. H., and Rashed, L. A. (2019). Beneficial effect of Curcumin Nanoparticles-Hydrogel on excisional skin wound healing in type-I diabetic rat: Histological and immunohistochemical studies. *Ann. Anat. - Anatomischer Anzeiger* 222, 94–102. doi:10.1016/j.aanat.2018.11.005

Karamać, M., Koleva, L., Kancheva, V. D., and Amarowicz, R. (2017). The structure-antioxidant activity relationship of ferulates. *Molecules* 22 (4), 527. doi:10.3390/molecules22040527

Kim, M., Lee, Y. S., Yoo, Y. M., Choi, J. J., Kim, H. N., Kang, C., et al. (2019). Exogenous CLASP2 protein treatment enhances wound healing *in vitro* and *in vivo*. *Wound Repair Regen.* 27 (4), 345–359. doi:10.1111/wrr.12713

Kishibe, M., Griffin, T. M., Goslawski, M., Sinacore, J., Kristian, S. A., and Radek, K. A. (2018). Topical nicotinic receptor activation improves wound bacterial infection outcomes and TLR2-mediated inflammation in diabetic mouse wounds. *Wound Repair Regen.* 26 (6), 403–412. doi:10.1111/wrr.12674

Laiva, A. L., O'Brien, F. J., and Keogh, M. B. (2021). SDF-1α gene-activated collagen scaffold restores pro-angiogenic wound healing features in human diabetic adipose-derived stem cells. *Biomedicines* 9 (2), 160. doi:10.3390/biomedicines9020160

Lapi, I., Kolliniati, O., Aspevik, T., Deiktakis, E. E., Axarlis, K., Daskalaki, M. G., et al. (2021). Collagen-containing fish sidestream-derived protein hydrolysates support skin repair via chemokine induction. *Mar. Drugs* 19 (7), 396. doi:10.3390/md19070396

Leal, E. C., Carvalho, E., Tellechea, A., Kafanas, A., Tecilazich, F., Kearney, C., et al. (2015). Substance P promotes wound healing in diabetes by modulating inflammation and macrophage phenotype. *Am. J. Pathol.* 185 (6), 1638–1648. doi:10.1016/j.ajpath.2015.02.011

Lee, H. J., Jeong, M., Na, Y. G., Kim, S. J., Lee, H. K., and Cho, C. W. (2020). An EGF- and curcumin-Co-encapsulated nanostructured lipid carrier accelerates chronic-wound healing in diabetic rats. *Molecules* 25 (20), 4610. doi:10.3390/molecules25204610

Lee, Y. H., Hong, Y. L., and Wu, T. L. (2021). Novel silver and nanoparticle-encapsulated growth factor co-loaded chitosan composite hydrogel with sustained antimicrobility and promoted biological properties for diabetic wound healing. *Mater. Sci. Eng. C* 118, 111385. doi:10.1016/j.msec.2020.111385

Lee, Y. H., and Lin, S. J. (2022). Chitosan/PVA hetero-composite hydrogel containing antimicrobials, perfluorocarbon nanoemulsions, and growth factor-loaded nanoparticles as a multifunctional dressing for diabetic wound healing: Synthesis, characterization, and *in vitro*/*in vivo* evaluation. *Pharmaceutics* 14 (3), 537. doi:10.3390/pharmaceutics14030537

Lei, H., and Fan, D. (2022). A combination therapy using electrical stimulation and adaptive, conductive hydrogels loaded with self-assembled nanogels incorporating short interfering RNA promotes the repair of diabetic chronic wounds. *Adv. Sci.* 2022, e2201425. doi:10.1002/advs.202201425

Li, B., Zhang, Y., Wu, C., Guo, B., and Luo, Z. (2018). Fabrication of mechanically tough and self-recoverable nanocomposite hydrogels from polyacrylamide grafted cellulose nanocrystal and poly(acrylic acid). *Carbohydr. Polym.* 198, 1–8. doi:10.1016/j.carbpol.2018.06.047

Li, M., Hu, M., Zeng, H., Yang, B., Zhang, Y., Li, Z., et al. (2021a). Multifunctional zinc oxide/silver bimetallic nanomaterial-loaded nanofibers for enhanced tissue regeneration and wound healing. *J. Biomed. Nanotechnol.* 17 (9), 1840–1849. doi:10.1166/jbn.2021.3152

Li, M., Li, H., Li, X., Zhu, H., Xu, Z., Liu, L., et al. (2017a). A bioinspired alginate-gum Arabic hydrogel with micro-/nanoscale structures for controlled drug release in chronic wound healing. *ACS Appl. Mat. Interfaces* 9 (27), 22160–22175. doi:10.1021/acsami.7b04428

Li, Q., Guo, Y., Chen, F., Liu, J., and Jin, P. (2016). Stromal cell-derived factor-1 promotes human adipose tissue-derived stem cell survival and chronic wound healing. *Exp. Ther. Med.* 12 (1), 45–50. doi:10.3892/etm.2016.3309

Li, S., Dong, Q., Peng, X., Chen, Y., Yang, H., Xu, W., et al. (2022a). Self-healing hyaluronic acid nanocomposite hydrogels with platelet-rich plasma impregnated for skin regeneration. *ACS Nano* 16, 11346–11359. doi:10.1021/acsnano.2c05069

Li, S., Wang, X., Chen, J., Guo, J., Yuan, M., Wan, G., et al. (2022b). Calcium ion cross-linked sodium alginate hydrogels containing deferoxamine and copper nanoparticles for diabetic wound healing. *Int. J. Biol. Macromol.* 202, 657–670. doi:10.1016/j.ijbiomac.2022.01.080

Li, Y., Han, Y., Wang, X., Peng, J., Xu, Y., and Chang, J. (2017b). Multifunctional hydrogels prepared by dual ion cross-linking for chronic wound healing. *ACS Appl. Mat. Interfaces* 9 (19), 16054–16062. doi:10.1021/acsami.7b04801

Li, Y., Leng, Q., Pang, X., Shi, H., Liu, Y., Xiao, S., et al. (2021b). Therapeutic effects of EGF-modified curcumin/chitosan nano-spray on wound healing. *Regen. Biomater.* 8 (2), rbab009. doi:10.1093/rb/rbab009

Lintel, H., Abbas, D. B., Lavin, C. V., Griffin, M., Guo, J. L., Guardino, N., et al. (2022). Transdermal deferoxamine administration improves excisional wound healing in chronically irradiated murine skin. *J. Transl. Med.* 20 (1), 274. doi:10.1186/s12967-022-03479-4

Liu, J., Chen, Z., Wang, J., Li, R., Li, T., Chang, M., et al. (2018). Encapsulation of curcumin nanoparticles with MMP9-responsive and thermos-sensitive hydrogel improves diabetic wound healing. *ACS Appl. Mat. Interfaces* 10 (19), 16315–16326. doi:10.1021/acsami.8b03868

Liu, K., Dai, L., and Li, C. (2021). A lignocellulose-based nanocomposite hydrogel with pH-sensitive and potent antibacterial activity for wound healing. *Int. J. Biol. Macromol.* 191, 1249–1254. doi:10.1016/j.ijbiomac.2021.10.006

Liu, X., Zhou, S., Cai, B., Wang, Y., Deng, D., and Wang, X. (2022). An injectable and self-healing hydrogel with antibacterial and angiogenic properties for diabetic wound healing. *Biomater. Sci.* 10 (13), 3480–3492. doi:10.1039/d2bm00224h

Lou, P., Liu, S., Wang, Y., Pan, C., Xu, X., Zhao, M., et al. (2021). Injectable self-assembling peptide nanofiber hydrogel as a bioactive 3D platform to promote chronic wound tissue regeneration. *Acta Biomater.* 135, 100–112. doi:10.1016/j.actbio.2021.08.008

Luo, F. Q., Xu, W., Zhang, J. Y., Liu, R., Huang, Y. C., Xiao, C., et al. (2022a). An injectable nanocomposite hydrogel improves tumor penetration and cancer treatment efficacy. *Acta Biomater.* 147, 235–244. doi:10.1016/j.actbio.2022.05.042

Luo, Y., Cui, L., Zou, L., Zhao, Y., Chen, L., Guan, Y., et al. (2022b). Mechanically strong and on-demand dissoluble chitosan hydrogels for wound dressing applications. *Carbohydr. Polym.* 294, 119774. doi:10.1016/j.carbpol.2022.119774

Lv, Q., Deng, J., Chen, Y., Wang, Y., Liu, B., and Liu, J. (2020). Engineered human adipose stem-cell-derived exosomes loaded with miR-21-5p to promote diabetic cutaneous wound healing. *Mol. Pharm.* 17 (5), 1723–1733. doi:10.1021/acs.molpharmaceut.0c00177

Ma, Z., Song, W., He, Y., and Li, H. (2020). Multilayer injectable hydrogel system sequentially delivers bioactive substances for each wound healing stage. *ACS Appl. Mat. Interfaces* 12 (26), 29787–29806. doi:10.1021/acsami.0c06360

Maity, B., Alam, S., Samanta, S., Prakash, R. G., and Govindaraju, T. (2022). Antioxidant silk fibroin composite hydrogel for rapid healing of diabetic wound. *Macromol. Biosci.* 22, e2200097. doi:10.1002/mabi.202200097

Manconi, M., Manca, M. L., Caddeo, C., Cencetti, C., di Meo, C., Zoratto, N., et al. (2018). Preparation of gellan-cholesterol nanohydrogels embedding baicalin and evaluation of their wound healing activity. *Eur. J. Pharm. Biopharm.* 127, 244–249. doi:10.1016/j.ejpb.2018.02.015

Mao, X., Li, Z., Li, B., and Wang, H. (2021). Baicalin regulates mRNA expression of VEGF-c, Ang-1/Tie2, TGF-β and Smad2/3 to inhibit wound healing in streptozotocin-induced diabetic foot ulcer rats. *J. Biochem. Mol. Toxicol.* 35 (11), e22893. doi:10.1002/jbt.22893

Masood, N., Ahmed, R., Tariq, M., Ahmed, Z., Masoud, M. S., Ali, I., et al. (2019). Silver nanoparticle impregnated chitosan-PEG hydrogel enhances wound healing in diabetes induced rabbits. *Int. J. Pharm. X.* 559, 23–36. doi:10.1016/j.ijpharm.2019.01.019

Massironi, A., Franco, A. R., Babo, P. S., Puppi, D., Chiellini, F., Reis, R. L., et al. (2022). Development and characterization of highly stable silver NanoParticles as novel potential antimicrobial agents for wound healing hydrogels. *Int. J. Mol. Sci.* 23 (4), 2161. doi:10.3390/ijms23042161

Menchisheva, Y., Mirzakulova, U., and Yui, R. (2019). Use of platelet-rich plasma to facilitate wound healing. *Int. Wound J.* 16 (2), 343–353. doi:10.1111/iwj.13034

Mohammadi Tofigh, A., and Tajik, M. (2022). Comparing the standard surgical dressing with dehydrated amnion and platelet-derived growth factor dressings in the healing rate of diabetic foot ulcer: A randomized clinical trial. *Diabetes Res. Clin. Pract.* 185, 109775. doi:10.1016/j.diabres.2022.109775

Naz, Z., and Ahmad, F. J. (2015). Curcumin-loaded colloidal carrier system: Formulation optimization, mechanistic insight, *ex vivo* and *in vivo* evaluation. *Int. J. Nanomedicine* 10, 4293–4307. doi:10.2147/ijn.S82788

Oliveira, B. C., de Oliveira, B., Deutsch, G., Pessanha, F. S., and de Castilho, S. R. (2021). Effectiveness of a synthetic human recombinant epidermal growth factor in diabetic patients wound healing: Pilot, double-blind, randomized clinical controlled trial. *Wound Repair Regen.* 29 (6), 920–926. doi:10.1111/wrr.12969

Parikh, A., Kathawala, K., Tan, C. C., Garg, S., and Zhou, X. F. (2016). Development of a novel oral delivery system of edaravone for enhancing bioavailability. *Int. J. Pharm. X.* 515 (1-2), 490–500. doi:10.1016/j.ijpharm.2016.10.052

Park, K. H., Han, S. H., Hong, J. P., Han, S. K., Lee, D. H., Kim, B. S., et al. (2018a). Topical epidermal growth factor spray for the treatment of chronic diabetic foot ulcers: A phase III multicenter, double-blind, randomized, placebo-controlled trial. *Diabetes Res. Clin. Pract.* 142, 335–344. doi:10.1016/j.diabres.2018.06.002

Park, Y. R., Sultan, M. T., Park, H. J., Lee, J. M., Ju, H. W., Lee, O. J., et al. (2018b). NF-κB signaling is key in the wound healing processes of silk fibroin. *Acta Biomater.* 67, 183–195. doi:10.1016/j.actbio.2017.12.006

Pu, Y., Wang, P., Yang, R., Tan, X., Shi, T., Ma, J., et al. (2022). Bio-fabricated nanocomposite hydrogel with ROS scavenging and local oxygenation accelerates diabetic wound healing. *J. Mat. Chem. B* 10 (21), 4083–4095. doi:10.1039/d2tb00343k

Qi, H., Yang, L., Shan, P., Zhu, S., Ding, H., Xue, S., et al. (2020). The stability maintenance of protein drugs in organic coatings based on nanogels. *Pharmaceutics* 12 (2), 115. doi:10.3390/pharmaceutics12020115

Qian, Z., Wang, H., Bai, Y., Wang, Y., Tao, L., Wei, Y., et al. (2020). Improving chronic diabetic wound healing through an injectable and self-healing hydrogel with platelet-rich plasma release. *ACS Appl. Mat. Interfaces* 12 (50), 55659–55674. doi:10.1021/acsami.0c17142

Qiu, W., Han, H., Li, M., Li, N., Wang, Q., Qin, X., et al. (2021). Nanofibers reinforced injectable hydrogel with self-healing, antibacterial, and hemostatic properties for chronic wound healing. *J. Colloid Interface Sci.* 596, 312–323. doi:10.1016/j.jcis.2021.02.107

Ragothaman, M., Kannan Villalan, A., Dhanasekaran, A., and Palanisamy, T. (2021). Bio-hybrid hydrogel comprising collagen-capped silver nanoparticles and melatonin for accelerated tissue regeneration in skin defects. *Mater. Sci. Eng. C* 128, 112328. doi:10.1016/j.msec.2021.112328

Ram, M., Singh, V., Kumawat, S., Kumar, D., Lingaraju, M. C., Uttam Singh, T., et al. (2015). Deferoxamine modulates cytokines and growth factors to accelerate cutaneous wound healing in diabetic rats. *Eur. J. Pharmacol.* 764, 9–21. doi:10.1016/j.ejphar.2015.06.029

Rana, S., and Kalaichelvan, P. T. (2013). Ecotoxicity of nanoparticles. *ISRN Toxicol.* 2013, 1–11. doi:10.1155/2013/574648

Rao, K. M., Suneetha, M., Zo, S., Won, S. Y., Kim, H. J., and Han, S. S. (2022). Injectable nanocomposite hydrogel as wound dressing agent with tunable multifunctional property. *Mater. Lett.* 307, 131062. doi:10.1016/j.matlet.2021.131062

Rodrigues, H. G., Vinolo, M. A., Sato, F. T., Magdalon, J., Kuhl, C. M., Yamagata, A. S., et al. (2016). Oral administration of linoleic acid induces new vessel formation and improves skin wound healing in diabetic rats. *PLoS One* 11 (10), e0165115. doi:10.1371/journal.pone.0165115

Roy, R., Zayas, J., Singh, S. K., Delgado, K., Wood, S. J., Mohamed, M. F., et al. (2022). Overriding impaired FPR chemotaxis signaling in diabetic neutrophil stimulates infection control in murine diabetic wound. *Elife* 11, e72071. doi:10.7554/eLife.72071

Sahibzada, M. U. K., Sadiq, A., Faidah, H. S., Khurram, M., Amin, M. U., Haseeb, A., et al. (2018). Berberine nanoparticles with enhanced *in vitro* bioavailability: Characterization and antimicrobial activity. *Drug Des. devel. Ther.* 12, 303–312. doi:10.2147/dddt.S156123

Santhini, E., Parthasarathy, R., Shalini, M., Dhivya, S., Mary, L. A., and Padma, V. V. (2022). Bio inspired growth factor loaded self assembling peptide nano hydrogel for chronic wound healing. *Int. J. Biol. Macromol.* 197, 77–87. doi:10.1016/j.ijbiomac.2021.12.026

Sapino, S., Peira, E., Chirio, D., Chindamo, G., Guglielmo, S., Oliaro-Bosso, S., et al. (2019). Thermosensitive nanocomposite hydrogels for intravitreal delivery of cefuroxime. *Nanomater. (Basel)* 9 (10), 1461. doi:10.3390/nano9101461

Schirmer, L., Atallah, P., Freudenberg, U., and Werner, C. (2021). Chemokine-capturing wound contact layer rescues dermal healing. *Adv. Sci. (Weinh).* 8 (18), e2100293. doi:10.1002/advs.202100293

Shaheen, M. M. A., Al Dahab, S., Abu Fada, M., and Idieis, R. (2021). Isolation and characterization of bacteria from diabetic foot ulcer: Amputation, antibiotic resistance and mortality rate. *Int. J. Diabetes Dev. Ctries.*, 2021 1–9. doi:10.1007/s13410-021-00997-7

Shankar, S., and Rhim, J. W. (2017). Facile approach for large-scale production of metal and metal oxide nanoparticles and preparation of antibacterial cotton pads. *Carbohydr. Polym.* 163, 137–145. doi:10.1016/j.carbpol.2017.01.059

Shehabeldine, A. M., Salem, S. S., Ali, O. M., Abd-Elsalam, K. A., Elkady, F. M., and Hashem, A. H. (2022). Multifunctional silver nanoparticles based on chitosan: Antibacterial, antibiofilm, antifungal, antioxidant, and wound-healing activities. *J. Fungi (Basel).* 8 (6), 612. doi:10.3390/jof8060612

Shi, G., Chen, W., Zhang, Y., Dai, X., Zhang, X., and Wu, Z. (2019). An antifouling hydrogel containing silver nanoparticles for modulating the therapeutic immune response in chronic wound healing. *Langmuir* 35 (5), 1837–1845. doi:10.1021/acs.langmuir.8b01834

Shiekh, P. A., Singh, A., and Kumar, A. (2020). Data supporting exosome laden oxygen releasing antioxidant and antibacterial cryogel wound dressing OxOBand alleviate diabetic and infectious wound healing. *Data Brief.* 31, 105671. doi:10.1016/j.dib.2020.105671

Shin, D. Y., Cheon, K. H., Song, E. H., Seong, Y. J., Park, J. U., Kim, H. E., et al. (2019). Fluorine-ion-releasing injectable alginate nanocomposite hydrogel for enhanced bioactivity and antibacterial property. *Int. J. Biol. Macromol.* 123, 866–877. doi:10.1016/j.ijbiomac.2018.11.108

Singh, K., Maity, P., Koroma, A. K., Basu, A., Pandey, R. K., Vander Beken, S., et al. (2022). Angiogenin released from ABCB5(+) stromal precursors improves healing of diabetic wounds by promoting angiogenesis. *J. Invest. Dermatol.* 142 (6), 1725–1736. doi:10.1016/j.jid.2021.10.026

Singla, R., Soni, S., Patial, V., Kulurkar, P. M., Kumari, A., S, M., et al. (2017). *In vivo* diabetic wound healing potential of nanobiocomposites containing bamboo cellulose nanocrystals impregnated with silver nanoparticles. *Int. J. Biol. Macromol.* 105 (1), 45–55. doi:10.1016/j.ijbiomac.2017.06.109

Sirousazar, M., Kokabi, M., and Hassan, Z. M. (2011). *In vivo* and cytotoxic assays of a poly(vinyl alcohol)/clay nanocomposite hydrogel wound dressing. *J. Biomaterials Sci. Polym. Ed.* 22 (8), 1023–1033. doi:10.1163/092050610x497881

Sivakumar, A. S., Krishnaraj, C., Sheet, S., Rampa, D. R., Kang, D. R., Belal, S. A., et al. (2017). Interaction of silver and gold nanoparticles in mammalian cancer: As real topical bullet for wound healing- A comparative study. *Vitro Cell. Dev. Biol. -Animal.* 53 (7), 632–645. doi:10.1007/s11626-017-0150-5

Smith, T. J., Wilson, M., Whitney, C., Fagnant, H., Neumeier, W. H., Smith, C., et al. (2022). Supplemental protein and a multinutrient beverage speed wound healing after acute sleep restriction in healthy adults. *J. Nutr.* 152 (6), 1560–1573. doi:10.1093/jn/nxac064

Sun, J., Han, K., Xu, M., Li, L., Qian, J., Li, L., et al. (2022). Blood viscosity in subjects with type 2 diabetes mellitus: Roles of hyperglycemia and elevated plasma fibrinogen. *Front. Physiol.* 13, 827428. doi:10.3389/fphys.2022.827428

Tamer, T. M., Valachová, K., Hassan, M. A., Omer, A. M., El-Shafeey, M., Mohy Eldin, M. S., et al. (2018). Chitosan/hyaluronan/edaravone membranes for anti-inflammatory wound dressing: *In vitro* and *in vivo* evaluation studies. *Mater. Sci. Eng. C* 90, 227–235. doi:10.1016/j.msec.2018.04.053

Tavakoli, S., Mokhtari, H., Kharaziha, M., Kermanpur, A., Talebi, A., and Moshtaghian, J. (2020). A multifunctional nanocomposite spray dressing of Kappa-carrageenan-polydopamine modified ZnO/L-glutamic acid for diabetic wounds. *Mater. Sci. Eng. C* 111, 110837. doi:10.1016/j.msec.2020.110837

Tsang, M. W., Wong, W. K., Hung, C. S., Lai, K. M., Tang, W., Cheung, E. Y., et al. (2003). Human epidermal growth factor enhances healing of diabetic foot ulcers. *Diabetes Care* 26 (6), 1856–1861. doi:10.2337/diacare.26.6.1856

Tu, C., Lu, H., Zhou, T., Zhang, W., Deng, L., Cao, W., et al. (2022). Promoting the healing of infected diabetic wound by an anti-bacterial and nano-enzyme-containing hydrogel with inflammation-suppressing, ROS-scavenging, oxygen and nitric oxide-generating properties. *Biomaterials* 286, 121597. doi:10.1016/j.biomaterials.2022.121597

Vatankhah, N., Jahangiri, Y., Landry, G. J., Moneta, G. L., and Azarbal, A. F. (2017). Effect of systemic insulin treatment on diabetic wound healing. *Wound Repair Regen.* 25 (2), 288–291. doi:10.1111/wrr.12514

Walsh, T. G., and Poole, A. W. (2017). Platelets protect cardiomyocytes from ischemic damage. *TH Open* 1 (1), e24–e32. doi:10.1055/s-0037-1603928

Wang, P., Theocharidis, G., Vlachos, I. S., Kounas, K., Lobao, A., Shu, B., et al. (2022). Exosomes derived from epidermal stem cells improve diabetic wound healing. *J. Invest. Dermatol.* 142 (9), 2508–2517. doi:10.1016/j.jid.2022.01.030

Wang, T., Zheng, Y., Shi, Y., and Zhao, L. (2019a). pH-responsive calcium alginate hydrogel laden with protamine nanoparticles and hyaluronan oligosaccharide promotes diabetic wound healing by enhancing angiogenesis and antibacterial activity. *Drug Deliv. Transl. Res.* 9 (1), 227–239. doi:10.1007/s13346-018-00609-8

Wang, Z., Zhang, R. X., Zhang, C., Dai, C., Ju, X., and He, R. (2019b). Fabrication of stable and self-assembling rapeseed protein nanogel for hydrophobic curcumin delivery. *J. Agric. Food Chem.* 67 (3), 887–894. doi:10.1021/acs.jafc.8b05572

Wei, D., Liu, Q., Liu, Z., Liu, J., Zheng, X., Pei, Y., et al. (2019). Modified nano microfibrillated cellulose/carboxymethyl chitosan composite hydrogel with giant network structure and quick gelation formability. *Int. J. Biol. Macromol.* 135, 561–568. doi:10.1016/j.ijbiomac.2019.05.091

Wong, K. K., Cheung, S. O., Huang, L., Niu, J., Tao, C., Ho, C. M., et al. (2009). Further evidence of the anti-inflammatory effects of silver nanoparticles. *ChemMedChem* 4 (7), 1129–1135. doi:10.1002/cmdc.200900049

Wróblewska, M., Szymańska, E., Szekalska, M., and Winnicka, K. (2020). Different types of gel carriers as metronidazole delivery systems to the oral mucosa. *Polym. (Basel)* 12 (3), 680. doi:10.3390/polym12030680

Wu, H., Li, F., Shao, W., Gao, J., and Ling, D. (2019). Promoting angiogenesis in oxidative diabetic wound microenvironment using a nanozyme-reinforced self-protecting hydrogel. *ACS Cent. Sci.* 5 (3), 477–485. doi:10.1021/acscentsci.8b00850

Wu, Z., Zheng, X., Gong, M., and Li, Y. (2016). Myricetin, a potent natural agent for treatment of diabetic skin damage by modulating TIMP/MMPs balance and oxidative stress. *Oncotarget* 7 (44), 71754–71760. doi:10.18632/oncotarget.12330

Xavier, J. R., Thakur, T., Desai, P., Jaiswal, M. K., Sears, N., Cosgriff-Hernandez, E., et al. (2015). Bioactive nanoengineered hydrogels for bone tissue engineering: A growth-factor-free approach. *ACS Nano* 9 (3), 3109–3118. doi:10.1021/nn507488s

Xie, S., Huang, K., Peng, J., Liu, Y., Cao, W., Zhang, D., et al. (2022). Self-propelling nanomotors integrated with biofilm microenvironment-activated NO release to accelerate healing of bacteria-infected diabetic wounds. *Adv. Healthc. Mat.* 2022, e2201323. doi:10.1002/adhm.202201323

Xu, Z., Qiu, W., Fan, X., Shi, Y., Gong, H., Huang, J., et al. (2021). Stretchable, stable, and degradable silk fibroin enabled by mesoscopic doping for finger motion triggered color/transmittance adjustment. *ACS Nano* 15, 12429–12437. doi:10.1021/acsnano.1c05257

Xue, J., Sun, N., and Liu, Y. (2022). Self-assembled nano-peptide hydrogels with human umbilical cord mesenchymal stem cell spheroids accelerate diabetic skin wound healing by inhibiting inflammation and promoting angiogenesis. *Int. J. Nanomedicine* 17, 2459–2474. doi:10.2147/ijn.S363777

Yang, L., Zhang, L., Hu, J., Wang, W., and Liu, X. (2021). Promote anti-inflammatory and angiogenesis using a hyaluronic acid-based hydrogel with miRNA-laden nanoparticles for chronic diabetic wound treatment. *Int. J. Biol. Macromol.* 166, 166–178. doi:10.1016/j.ijbiomac.2020.10.129

Yang, P., Li, S., Zhang, H., Ding, X., and Tan, Q. (2022a). LRG1 accelerates wound healing in diabetic rats by promoting angiogenesis via the wnt/β-catenin signaling pathway. *Int. J. Low. Extrem. Wounds* 2022, 15347346221081610. doi:10.1177/15347346221081610

Yang, X., Zhan, P., Wang, X., Zhang, Q., Zhang, Y., Fan, H., et al. (2020). Polydopamine-assisted PDGF-BB immobilization on PLGA fibrous substrate enhances wound healing via regulating anti-inflammatory and cytokine secretion. *PLoS One* 15 (9), e0239366. doi:10.1371/journal.pone.0239366

Yang, X., Zhang, C., Deng, D., Gu, Y., Wang, H., and Zhong, Q. (2022b). Multiple stimuli-responsive MXene-based hydrogel as intelligent drug delivery carriers for deep chronic wound healing. *Small* 18 (5), e2104368. doi:10.1002/smll.202104368

Yang, Z., Chen, H., Yang, P., Shen, X., Hu, Y., Cheng, Y., et al. (2022c). Nano-oxygenated hydrogels for locally and permeably hypoxia relieving to heal chronic wounds. *Biomaterials* 282, 121401. doi:10.1016/j.biomaterials.2022.121401

Yeom, E., Byeon, H., and Lee, S. J. (2016). Effect of diabetic duration on hemorheological properties and platelet aggregation in streptozotocin-induced diabetic rats. *Sci. Rep.* 6, 21913. doi:10.1038/srep21913

Yu, J. R., Janssen, M., Liang, B. J., Huang, H. C., and Fisher, J. P. (2020). A liposome/gelatin methacrylate nanocomposite hydrogel system for delivery of stromal cell-derived factor-1α and stimulation of cell migration. *Acta Biomater.* 108, 67–76. doi:10.1016/j.actbio.2020.03.015

Yu, J. R., Varrey, P., Liang, B. J., Huang, H. C., and Fisher, J. P. (2021a). Liposomal SDF-1 alpha delivery in nanocomposite hydrogels promotes macrophage phenotype changes and skin tissue regeneration. *ACS Biomater. Sci. Eng.* 7 (11), 5230–5241. doi:10.1021/acsbiomaterials.1c01140

Yu, Y., Shao, Y., Zhou, M., and Li, W. (2021b). Polyethylene glycol-derived polyelectrolyte-protein nanoclusters for protein drug delivery. *RSC Adv.* 11 (46), 28651–28658. doi:10.1039/d1ra05055a

Zhai, M., Xu, Y., Zhou, B., and Jing, W. (2018). Keratin-chitosan/n-ZnO nanocomposite hydrogel for antimicrobial treatment of burn wound healing: Characterization and biomedical application. *J. Photochem. Photobiol. B Biol.* 180, 253–258. doi:10.1016/j.jphotobiol.2018.02.018

Zhang, J. J., Zhou, R., Deng, L. J., Cao, G. Z., Zhang, Y., Xu, H., et al. (2022). Huangbai liniment and berberine promoted wound healing in high-fat diet/Streptozotocin-induced diabetic rats. *Biomed. Pharmacother.* 150, 112948. doi:10.1016/j.biopha.2022.112948

Zhang, K., Lu, J., Mori, T., Smith-Powell, L., Synold, T. W., Chen, S., et al. (2011). Baicalin increases VEGF expression and angiogenesis by activating the ERR/PGC-1 pathway. *Cardiovasc. Res.* 89 (2), 426–435. doi:10.1093/cvr/cvq296

Zhang, P., He, L., Zhang, J., Mei, X., Zhang, Y., Tian, H., et al. (2020). Preparation of novel berberine nano-colloids for improving wound healing of diabetic rats by acting Sirt1/NF-κB pathway. *Colloids Surfaces B Biointerfaces* 187, 110647. doi:10.1016/j.colsurfb.2019.110647

Zhang, R., Jiang, G., Gao, Q., Wang, X., Wang, Y., Xu, X., et al. (2021a). Sprayed copper peroxide nanodots for accelerating wound healing in a multidrug-resistant bacteria infected diabetic ulcer. *Nanoscale* 13 (37), 15937–15951. doi:10.1039/d1nr04687j

Zhang, X., Sun, D., and Jiang, G. C. (2019a). Comparative efficacy of nine different dressings in healing diabetic foot ulcer: A bayesian network analysis. *J. Diabetes* 11 (6), 418–426. doi:10.1111/1753-0407.12871

Zhang, Y., Lu, L., Chen, Y., Wang, J., Chen, Y., Mao, C., et al. (2019b). Polydopamine modification of silk fibroin membranes significantly promotes their wound healing effect. *Biomater. Sci.* 7 (12), 5232–5237. doi:10.1039/c9bm00974d

Zhang, Y., Zhang, P., Gao, X., Chang, L., Chen, Z., and Mei, X. (2021b). Preparation of exosomes encapsulated nanohydrogel for accelerating wound healing of diabetic rats by promoting angiogenesis. *Mater. Sci. Eng. C* 120, 111671. doi:10.1016/j.msec.2020.111671

Zhang, Z., and Lv, L. (2016). Effect of local insulin injection on wound vascularization in patients with diabetic foot ulcer. *Exp. Ther. Med.* 11 (2), 397–402. doi:10.3892/etm.2015.2917

Zhao, B., Zhang, X., Zhang, Y., Lu, Y., Zhang, W., Lu, S., et al. (2021). Human exosomes accelerate cutaneous wound healing by promoting collagen synthesis in a diabetic mouse model. *Stem Cells Dev.* 30 (18), 922–933. doi:10.1089/scd.2021.0100

Zhou, L., Gao, Y., Cai, Y., Zhou, J., Ding, P., Cohen Stuart, M. A., et al. (2022). Controlled synthesis of PEGylated polyelectrolyte nanogels as efficient protein carriers. *J. Colloid Interface Sci.* 620, 322–332. doi:10.1016/j.jcis.2022.04.030

Zhou, Y., Gao, L., Peng, J., Xing, M., Han, Y., Wang, X., et al. (2018). Bioglass activated albumin hydrogels for wound healing. *Adv. Healthc. Mat.* 7 (16), e1800144. doi:10.1002/adhm.201800144

Zhu, J., Han, H., Ye, T. T., Li, F. X., Wang, X. L., Yu, J. Y., et al. (2018). Biodegradable and pH sensitive peptide based hydrogel as controlled release system for antibacterial wound dressing application. *Molecules* 23 (12), 3383. doi:10.3390/molecules23123383

Zubair, M., and Ahmad, J. (2019). Potential risk factors and outcomes of infection with multidrug resistance among diabetic patients having ulcers: 7 years study. *Diabetes & Metabolic Syndrome Clin. Res. Rev.* 13 (1), 414–418. doi:10.1016/j.dsx.2018.10.014

frontiers | Frontiers in Bioengineering and Biotechnology

TYPE Original Research
PUBLISHED 10 October 2022
DOI 10.3389/fbioe.2022.1004414

Check for updates

OPEN ACCESS

EDITED BY
Yu Luo,
Shanghai University of Engineering Sciences, China

REVIEWED BY
Xilin Bai,
Northeast Normal University, China
Xijian Liu,
Shanghai University of Engineering Sciences, China
Yu Chong,
Soochow University, China

*CORRESPONDENCE
Jindong Xia,
sjzxyyxiajd_21@126.com

SPECIALTY SECTION
This article was submitted to Nanobiotechnology, a section of the journal Frontiers in Bioengineering and Biotechnology

RECEIVED 27 July 2022
ACCEPTED 30 August 2022
PUBLISHED 10 October 2022

CITATION
Liu K, Liu C and Xia J (2022), The r_1 relaxivity and T_1 imaging properties of dendrimer-based manganese and gadolinium chelators in magnetic resonance imaging.
Front. Bioeng. Biotechnol. 10:1004414.
doi: 10.3389/fbioe.2022.1004414

COPYRIGHT
© 2022 Liu, Liu and Xia. This is an open-access article distributed under the terms of the Creative Commons Attribution License (CC BY). The use, distribution or reproduction in other forums is permitted, provided the original author(s) and the copyright owner(s) are credited and that the original publication in this journal is cited, in accordance with accepted academic practice. No use, distribution or reproduction is permitted which does not comply with these terms.

The r_1 relaxivity and T_1 imaging properties of dendrimer-based manganese and gadolinium chelators in magnetic resonance imaging

Kai Liu[1], Changcun Liu[2] and Jindong Xia[1]*

[1]Department of Radiology, Shanghai Songjiang District Central Hospital, Shanghai, China, [2]Department of Nuclear Medicine, Shanghai General Hospital, Shanghai Jiao Tong University School of Medicine, Shanghai, China

We report the preparation and characterization of gadolinium (Gd)- or manganese (Mn)-loaded dendrimers and Gd-loaded dendrimer-entrapped gold nanoparticles (Gd-Au DENPs) to examine the relationship between the number of metal ion chelators and r_1 relaxivity. In this study, amine-terminated fifth-generation poly(amidoamine) dendrimers ($G5.NH_2$) modified with different numbers of DOTA-NHS chelators were used to chelate Gd and Mn ions. The remaining amine groups were then acetylated completely, followed by the use of materials with better r_1 relaxivities and T_1-weighted imaging performances as templates to synthesize Gd-Au DENPs. The Gd and Mn chelators as well as Gd-Au DENPs were characterized *via* different techniques. We show that the r_1 relaxivity and T_1 imaging performance increase with loading of greater numbers of Gd and Mn ions on the $G5.NH_2$ and that the acetylation process affects the relaxivity and imaging properties to a certain extent. After entrapment with Au NPs, the r_1 relaxivity and T_1-weighted imaging performance of Gd-Au DENPs decrease with greater loading of Au NPs. This systematic study of the relaxivities and T_1-weighted imaging performances of Gd, Mn, and Gd-Au DENP chelators are expected to be a theoretical basis for developing multifunctional dual-mode contrast agents.

KEYWORDS

dendrimer, manganese, gadolinium, r_1 relaxivity, T_1-weighted MR imaging

Introduction

Magnetic resonance (MR) imaging is one of the most powerful noninvasive medical imaging techniques with good spatial resolution and high sensitivity, offering superior 3D details and topographic information on soft-tissue contrast (Chan and Wong, 2007; Taboada et al., 2007; Xiao et al., 2023). To increase the signal-to-noise ratio of information acquired from normal tissues and tumors, it is necessary to use contrast agents (Aime et al., 2009). To date, various contrast agents have been used for clinical diagnosis, such as gadolinium (Gd)-based small molecular (DTPA, DOTA, NOTA) contrast agents in T_1-

TABLE 1 Linear fitting of the r_1 relaxivities of G5.NH_2-DOTA(Mn) and G5.NH_2-DOTA(Gd) before and after acetylation as functions of Mn and Gd concentrations, respectively.

Sample	Before acetylation ($mM^{-1}s^{-1}$)	After acetylation ($mM^{-1}s^{-1}$)
G5.NH_2-$DOTA_5$(Mn)	1.16	0.55
G5.NH_2-$DOTA_{10}$(Mn)	2.66	1.90
G5.NH_2-$DOTA_{20}$(Mn)	2.52	1.66
G5.NH_2-$DOTA_{30}$(Mn)	2.54	1.26
G5.NH_2-$DOTA_5$(Gd)	5.77	7.06
G5.NH_2-$DOTA_{10}$(Gd)	6.92	9.24
G5.NH_2-$DOTA_{20}$(Gd)	7.59	9.67
G5.NH_2-$DOTA_{30}$(Gd)	7.69	9.77

weighted MR imaging and iron oxide nanoparticles (NPs)-based contrast agents in T_2-weighted MR imaging (Miao et al., 2021; Meng et al., 2022). Unfortunately, these small-molecule-based contrast agents cannot be used for long-circulation imaging owing to their short circulation times in the blood and quick elimination from the body through urine (Prencipe et al., 2009). Although iron oxide NPs display excellent MR imaging properties and are widely used as negative MR contrast agents (Le et al., 2022; Luo et al., 2022), their clinical use has several disadvantages; in particular, negative contrast effects and magnetic susceptibility artifacts are observed, which could mislead the clinical diagnosis. Therefore, it is crucial to develop novel carriers for MR imaging contrast agents to overcome these drawbacks.

Among the macromolecular family, poly(amidoamine) (PAMAM) dendrimers are a class of highly branched, monodispersed, and synthetic macromolecules with well-defined three-dimensional architectures, composition, and abundant terminal functional groups (Shi et al., 2008). The unique structural properties of PAMAM allow their use as a platform for constructing various kinds of contrast agents, such as dendrimer-based Mn- or Gd-loaded agents for MR imaging, Gd-loaded dendrimer-entrapped gold nanoparticles (Gd-Au DENPs) for CT/MR applications (Chen et al., 2013), and ^{99m}Tc labeled Mn-loaded dendrimer-based contrast agents for SPECT/MR imaging applications (Liu et al., 2012; Fan et al., 2020). The PAMAM dendrimer has been widely researched for single- and multi-mode contrast agents, but there are still some questions that have not been well resolved. First, the relationship between the r_1 relaxivity of the chelate numbers modified onto the dendrimer and loading amount of the metal ions is not clearly understood. Second, given the same modified condition (same number of chelates and same mole amounts of metal ions), which among Mn- or Gd-based contrast agents have better r_1 relaxivity and T_1-weighted MR imaging performance? Third, after entrapping gold NPs, the effects of r_1 relaxivity and T_1-weighted MR imaging performance of Gd-loaded Au DENPs as CT/MR dual-mode contrast agents are not investigated in detail. Based on these questions, in the present study, the amine-terminated fifth-generation poly(amidoamine) (G5.NH_2) dendrimers were first modified with 2, 2′, 2′′-(10-(2-(2, 5-dioxopyrrolidin1-aryloxy)-2-oxoethyl)-1, 4, 7,1 0-tetraazacyclododecane-1, 4, 7-triyl) triacetin acid (DOTA-NHS) in mole ratios of 1:5, 1:10, 1:20, and 1:30; then, the modified G5.NH_2 dendrimers were used as templates to chelate Gd(III) and Mn(II). After acetylation of the remaining dendrimer terminal amines, G5.NHAc-DOTA-Gd or G5.NHAc-DOTA-Mn were formed. The formed Gd and Mn chelators were characterized thoroughly *via* different techniques, and the material with the highest r_1 relaxivity was chosen as the template to entrap Au NPs to prepare the Gd-Au DENPs.

Experimental methods

Materials

Ethylenediamine core G5.NH_2 PAMAM dendrimers (molecular weight = 26,010 g/mol) with polydispersity index values less than 1.08 were purchased from Dendritech (Midland, MI, USA). Polyethylene glycol (PEG) monomethyl ether with a carboxyl group at one end (*m*PEG-COOH) was obtained from Shanghai Yanyi Biotechnology Corporation (Shanghai, China). $Gd(NO_3)_3.6H_2O$, $MnSO_4.H_2O$, $HAuCl_4.4H_2O$, acetic anhydride, triethylamine, and all other chemicals as well as solvents were purchased from Sinopharm Chemical Reagent Co., Ltd. (Shanghai, China). Sodium borohydride was purchased from J&K Chemical Ltd. (Shanghai, China). DOTA-NHS was purchased from CheMatech (Dijon, France). The water used in all experiments was purified using a Milli-Q Plus185 water purification system (Millipore, Bedford, MA) with a resistivity greater than 18.2 MΩ cm.

Fabrication of G5.NH_2 with DOTA

About 13.00 mg of G5.NH_2 dissolved in DMSO (4 mL) was reacted with 5 molar equivalents of DOTA-NHS (1.87 mg, 2 mL in DMSO) under vigorous magnetic stirring, and purification was performed similar to that noted in our previous report (Wen et al., 2013). The reaction was stopped after 24 h to obtain the raw product G5.NH_2-$DOTA_5$. Then, G5.NH_2-$DOTA_{10}$, G5.NH_2-$DOTA_{20}$, and G5.NH_2-$DOTA_{30}$ were fabricated in a similar manner.

Synthesis of G5.NH_2-DOTA-Mn and G5.NH_2-DOTA-Gd

The formed G5.NH_2-$DOTA_5$, G5.NH_2-$DOTA_{10}$, G5.NH_2-$DOTA_{20}$, and G5.NH_2-$DOTA_{30}$ were used as templates to

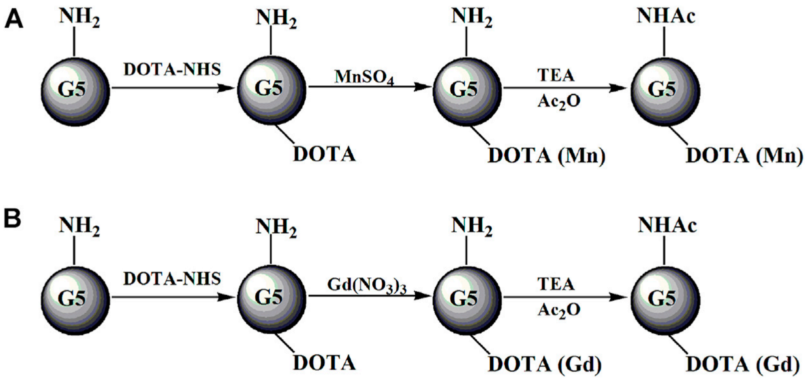

FIGURE 1
Schematic illustration of the preparation of G5.NHAc-DOTA$_n$(Gd) **(A)** or G5.NHAc-DOTA$_n$(Mn) **(B)**. TEA and Ac$_2$O represent triethylamine and acetic anhydride, respectively.

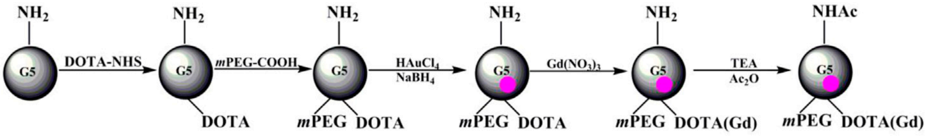

FIGURE 2
Schematic illustration of the preparation of (Au^0)$_n$-G5.NHAc-*m*PEG-DOTA$_{30}$(Gd). TEA and Ac$_2$O represent triethylamine and acetic anhydride, respectively.

chelate Mn(II) (Figure 1A) or Gd(III) (Figure 1B) ions. Aqueous $MnSO_4$ (1.27 mg/mL, 1 mL in water) and $Gd(NO_3)_3$ (3.39 mg/mL, 1 mL in water) solutions with $MnSO_4$/DOTA and $Gd(NO_3)_3$/DOTA in a molar ratio of 1.5: 1 were added to G5.NH$_2$-DOTA$_5$ under vigorous stirring to chelate Mn(II) or Gd(III) ions, respectively. The reaction was performed for 24 h to obtain G5.NH$_2$-DOTA$_5$(Mn) or G5.NH$_2$-DOTA$_5$(Gd) as the products. Then, half the volumes of G5.NH$_2$-DOTA$_5$(Mn) and G5.NH$_2$-DOTA$_5$(Gd) solutions were removed for dialysis for 3 days (three times per day, 2 L of water each time) to remove the excess Mn(II) or Gd(III) ions. Six molar equivalents of the dendrimer terminal amine triethylamine (53 μL) were added to the remaining G5.NH$_2$-DOTA$_5$(Mn)$_5$ and G5.NH$_2$-DOTA$_5$(Gd)$_5$ solutions. After 30 min, acetic anhydride (33 μL, equal to 5 molar equivalents of the dendrimer terminal amine) was added dropwise into the solutions under vigorous magnetic stirring, and the solutions were allowed to react at room temperature with stirring for 24 h. Then, the DMSO, excess reactants, and byproducts were removed from the mixture by extensive dialysis with water (9 times, 2 L) for 3 days, followed by lyophilization to obtain the G5.NHAc-DOTA$_5$(Mn) and G5.NHAc-DOTA$_5$(Gd). The G5.NH$_2$-DOTA$_{10}$(Mn), G5.NH$_2$-DOTA$_{20}$(Mn), G5.NH$_2$-DOTA$_{30}$(Mn), G5.NH$_2$-DOTA$_{10}$(Gd), G5.NH$_2$-DOTA$_{20}$(Gd), G5.NH$_2$-DOTA$_{30}$(Gd), and their acetylated materials were also formed similarly.

Synthesis of (Au^0)$_n$-G5.NHAc-*m*PEG$_{15}$-DOTA$_{30}$(Gd)

About 13.00 mg of G5.NH$_2$ dissolved in DMSO (4 mL) was reacted with 30 molar equivalents of DOTA-NHS (11.22 mg, 5 mL in DMSO) under vigorous magnetic stirring (Figure 2). The reaction was stopped after 24 h to obtain G5.NH$_2$-DOTA$_{30}$ as the raw product. Then, 15.00 mg of *m*PEG-COOH dissolved in 5 mL DMSO and 15 molar equivalents of G5.NH$_2$ was reacted with EDC (14.38 mg in 2 mL DMSO) for 15 min at room temperature. Next, NHS (8.63 mg, in 1 mL DMSO) was added to the above solution under vigorous magnetic stirring for 3 h. The EDC/NHS-activated *m*PEG-COOH was then added dropwise into the DMSO solution of the raw product of G5.NH$_2$-DOTA$_{30}$ under vigorous magnetic stirring. The reaction was continued for 3 days to obtain G5.NH$_2$-DOTA$_{30}$-*m*PEG$_{15}$ conjugates as the raw products. Then, $HAuCl_4$ solution

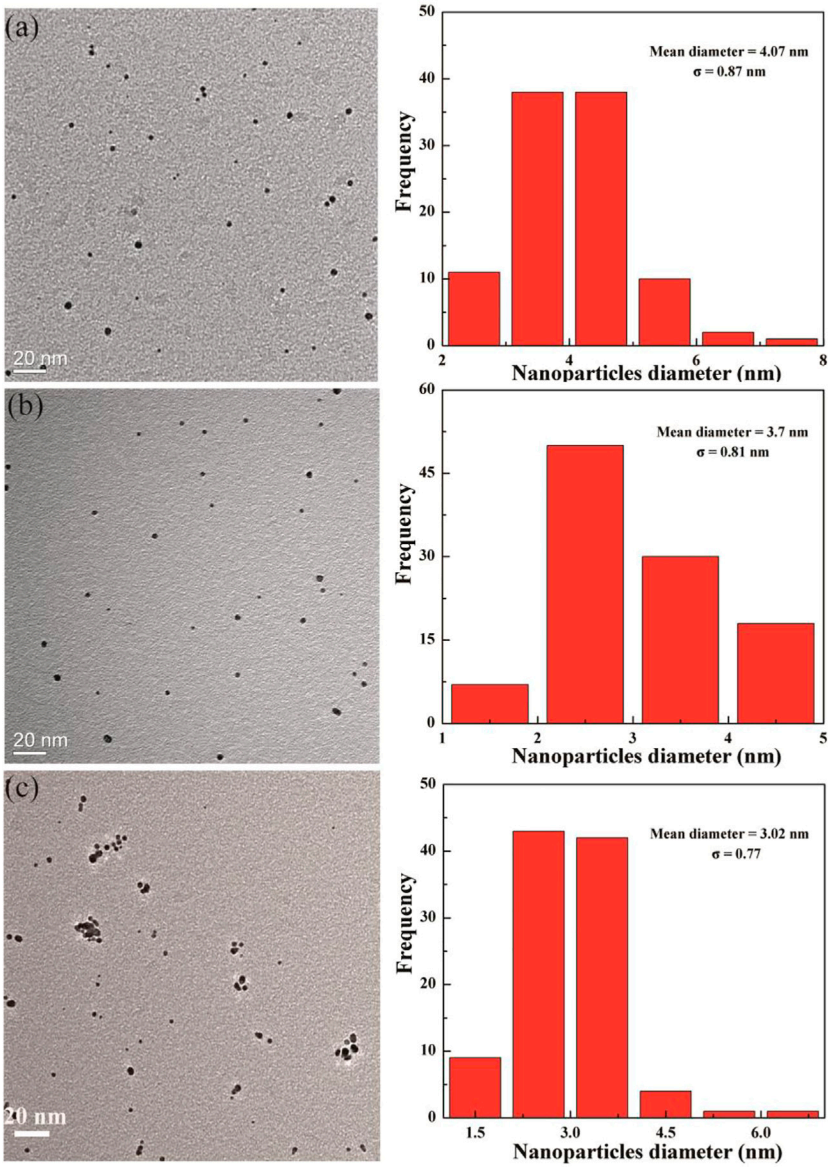

FIGURE 3
Transmission electron microscopy images of $(Au^0)_{50}$G5.NHAc-mPEG-$DOTA_{30}$(Gd) **(A)**, $(Au^0)_{75}$ G5.NHAc-*m*PEG-$DOTA_{30}$(Gd) **(B)**, and $(Au^0)_{100}$G5.NHAc-*m*PEG-$DOTA_{30}$(Gd) **(C)** DENPs.

(5 mg/mL, 2.06 mL in water) was added under vigorous stirring. After 1 h, an icy cold $NaBH_4$ solution (4.73 mg/mL, 1 mL in water/methanol, v/v = 2:1) with 5 molar equivalents of the gold salt was added to the gold salt/dendrimer mixture under vigorous stirring. The solution turned a deep-red color after the addition of $NaBH_4$, and the stirring was continued for 3 h to complete the reaction. Then, acetylation of the excess terminal amines was performed similar to the process in our previous work (Liu et al., 2012). The mixture was purified by dialysis as described previously to remove the excess DMSO and other reagents. The Au DENPs were then purified and dried by lyophilization.

Characterization techniques

^{1}H NMR spectra were recorded with a Bruker DRX 400 nuclear magnetic resonance spectrometer. Samples were dissolved in D_2O before the measurements. The size and morphology of the Gd-Au

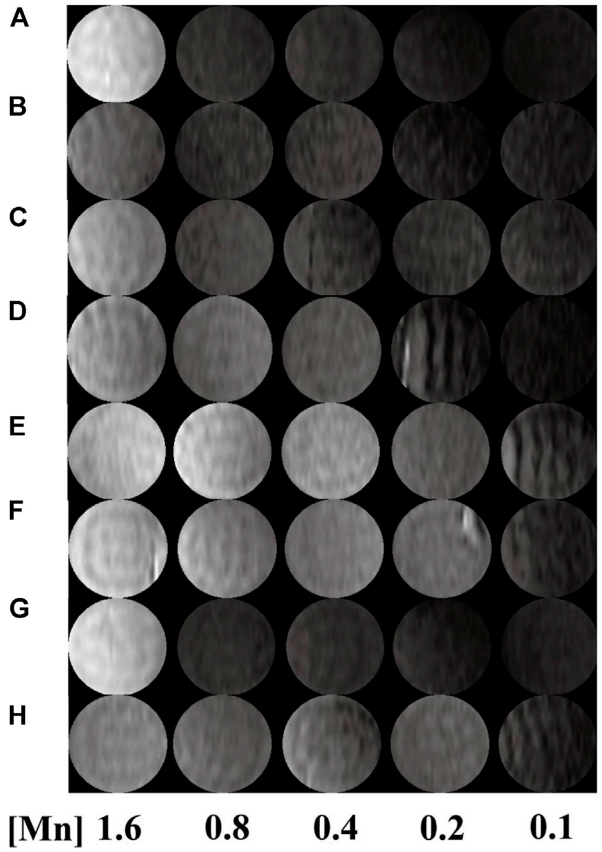

FIGURE 4
T_1-weighted images of G5.NH_2-$DOTA_5$(Mn), G5.NH_2-$DOTA_{10}$(Mn), G5.NH_2-$DOTA_{20}$(Mn), and G5.NH_2-$DOTA_{30}$(Mn) **(A, C, E, G)** before and **(B, D, F, H)** after acetylation as functions of Mn^{2+} concentrations.

DENPs were characterized by using a JEOL 2010F analytical electron microscope (JEOL, Japan) operating at 200 kV. Transmission electron microscopy (TEM) samples were prepared by the deposition of a dilute particle suspension (1 mg/mL, 5 μL) onto a carbon-coated copper grid and air dried before measurements. For each sample, at least 100 NPs from different TEM images were randomly selected and measured using ImageJ software (http://www.rsb.info.nih.gov/ij/download.html) to assess the average size and size distribution. The compositions of Mn, Gd, and Au of the formed materials were determined by inductively coupled plasma optical emission spectroscopy (ICP-OES, Leeman Prodigy, USA). The surface potentials of each material before and after acetylation were measured using a Zetasizer Nano ZS system (Worcestershire, UK) equipped with a standard 633 nm laser. The r_1 relaxivity and T_1-weighted images of the Gd and Mn chelates were obtained using a 0.5 T NMI20 equipment (Newman, China) with a wrist receiver coil.

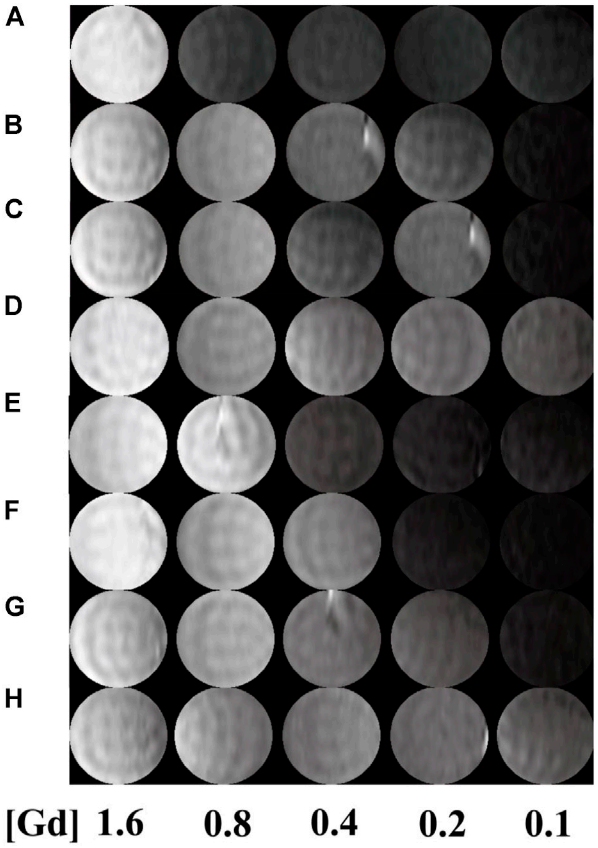

FIGURE 5
T_1-weighted images G5.NH_2-$DOTA_5$(Gd), G5.NH_2-$DOTA_{10}$(Gd), G5.NH_2-$DOTA_{20}$(Gd), and G5.NH_2-$DOTA_{30}$(Gd) **(A, C, E, G)** before and **(B, D, F, H)** after acetylation as functions of Gd^{3+} concentrations.

Results and discussion

Synthesis and characterization of G5.NH_2-DOTA

The ^1H NMR technique was used to investigate the actual number of DOTA units conjugated onto each G5.NH_2 molecule, as in our previous work (Supplementary Figure S1;Wen et al., 2013). After conjugation of different ratios of DOTA-NHS, the numbers of remaining dendrimer terminal amine groups in each of the G5.NH_2 molecules were estimated to be 105.8, 102.5, 99.6, and 90.1, and the numbers of DOTA units per G5.NH_2 molecule were calculated as 4.2, 7.5, 10.4, and 19.9 (Supplementary Table S1); these numbers are slightly lower than the theoretical values of 5, 10, 20, and 30 based on the initial molar feed ratios.

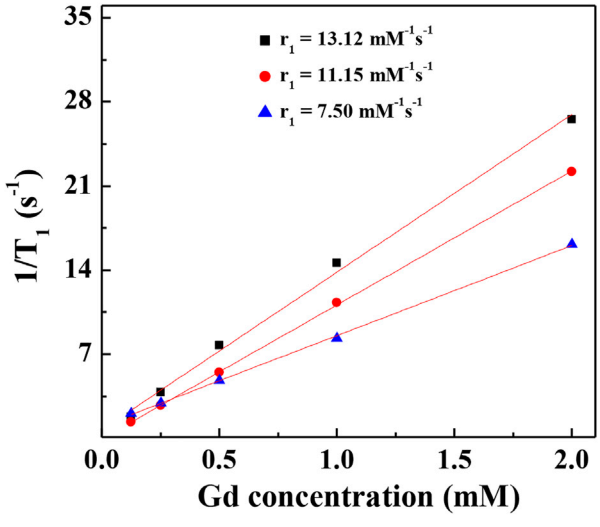

FIGURE 6
Linear fitting $1/T_1$ of $(Au^0)_{50}$G5.NHAc-*m*PEG-$DOTA_{30}$(Gd) (black square), $(Au^0)_{75}$ G5.NHAc-*m*PEG-$DOTA_{30}$(Gd) (red circle), and $(Au^0)_{100}$G5.NHAc-*m*PEG-$DOTA_{30}$(Gd) (blue triangle) DENPs at Gd concentrations of 2, 1, 0.5, 0.25 and 0.125 mM.

Fabrication and characterization of G5.NHAc–DOTA(Mn) and G5.NHAc-DOTA(Gd)

The numbers of Gd(III) and Mn(II) ions complexed with each dendrimer were measured as shown in Supplementary Table S2. It is clear that the number of ions per $G5.NH_2$ molecule of the Gd-based chelate is slightly higher than the DOTA number on the surface of the dendrimer, which is consistent with the observations in our previous work (Wen et al., 2013). The reason for this is likely the fact that besides the Gd(III) ions chelated within the DOTA ligands on the surfaces of the G5 dendrimers, small portions of the Gd(III) ions are complexed with the interior tertiary amine groups of the dendrimer. In contrast, the number of Mn(II) ions complexed with each $G5.NH_2$ molecule was estimated to be 23.3 when the initial molar feed ratio of the DOTA/dendrimer was 30:1; this is less than the theoretical value of 30 attached DOTA moieties on each dendrimer. Compared with the Mn-based chelates, the Gd-based chelates thus have better chelating abilities.

To utilize the $G5.NH_2$ modifications to Gd- and Mn-based chelates in biological applications, it is necessary to explore their cytotoxicities before and after acetylation. Our previous report shows that the $G5.NH_2$ displays significant cytotoxicity because of more than 100 amino groups on the surface of the $G5.NH_2$ dendrimer. To investigate the changes in the zeta potentials of each of the materials before and after acetylation, the zeta potential of each material was measured. As shown in Supplementary Table S3, the zeta potential of each material decreased sharply after acetylation. This may be attributed to the redundant amino groups of $G5.NH_2$ being changed into acetamide groups with acetic anhydride through acetylation.

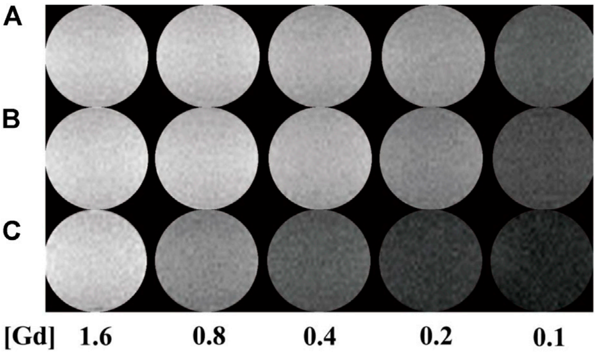

FIGURE 7
T_1-weighted images of **(A–C)** $(Au^0)_{50}$G5.NHAc-*m*PEG-$DOTA_{30}$(Gd), $(Au^0)_{75}$ G5.NHAc-*m*PEG-$DOTA_{30}$(Gd), and $(Au^0)_{100}$G5.NHAc-*m*PEG-$DOTA_{30}$(Gd) DENPs at Gd concentrations of 1.6, 0.8, 0.4, 0.2, and 0.1 mM.

Synthesis and characterization of {$(Au^0)_n$-G5.NHAc-*m*PEG_{15}-$DOTA_3$(Gd)} DENPs

The size and morphology of Au DENPs of different compositions were characterized by TEM (Figure 3). The diameters of the $(Au^0)_{50}$-G5.NHAc-*m*PEG_{15}-$DOTA_{30}$-Gd, $(Au^0)_{75}$-G5.NHAc-*m*PEG_{15}-$DOTA_{30}$-Gd, and $(Au^0)_{100}$-G5.NHAc-*m*PEG_{15}-$DOTA_{30}$-Gd DENPs were 4.1, 3.7, and 3.0 nm, respectively. The diameter of the Au DENPs increased slightly with the high dendrimer/Au salt molar ratio, which is very close to that noted in our previous study (Wen et al., 2013).

T_1-weighted imaging and r_1 relaxivity of Mn-based and Gd-based chelates

T_1-weighted imaging was conducted to verify the potential of the formed Mn-based (Figure 4) as well as Gd-based (Figure 5) materials as MR contrast agents. The proton longitudinal relaxation times (T_1) of these sixteen samples in water were measured with a 0.5 T NMI20 MRI system (Newman, China) with Mn^{2+} and Gd^{3+} concentrations of 0.1, 0.2, 0.4, 0.8, and 1.6 mM. As shown in Figure 3 and Figure 4, signal enhancements are observed in the T_1-weighted images in a number-dependent manner with increases in the numbers of DOTA-Mn and DOTA-Gd ions per $G5.NH_2$. For the Mn-chelates, the signal enhancements in the T_1-weighted images were inconspicuous even though the number of DOTA-Mn increased to 20. We found that the signals of the Mn chelates weakened after acetylation. On the contrary, the signals of the Gd chelates increased slightly after acetylation. As shown in Table 1, the r_1 relaxivity of the DOTA-Mn increased from 1.16 to 2.54 $mM^{-1}s^{-1}$ with increase in number from 5 to 30 per $G5.NH_2$. After acetylation, the r_1 relaxivity of the DOTA-Mn decreased obviously from 1.90 to 0.55 $mM^{-1}s^{-1}$. The r_1 relaxivity results follow the same trends as the T_1-weighted images. The r_1 relaxivity of the Gd-based chelates increased from 5.77 to 7.69 $mM^{-1}s^{-1}$ with increase in the numbers of DOTA-Gd from 5 to 30 per $G5.NH_2$. However, the r_1 relaxivities of the Gd-based chelates increased from 7.06 to 9.77 after acetylation, which is different from those of the Mn-based chelates. We speculate that the increased r_1 relaxivities of the Gd- and Mn-based chelates may be due to the additional DOTA conjugates on the $G5.NH_2$ to form nanoclusters as it has been noted in literature that the cluster structure could promote water exchange rate to increase the r_1 relaxivity (Matsumoto and Jasanoff, 2008).

T_1-weighted imaging and r_1 relaxivity of Gd-Au DENPs

It has been reported that Au NPs could be used as CT contrast agents because they have good biocompatibility. To investigate the relationship between the number of gold NPs and r_1 relaxivity of the Gd-based chelates, we fabricated different G5:Au mole ratios of 1:50, 1:75, and 1:100 NPs and measured the r_1 relaxivities (Figure 6) of Gd-Au DENPs as well as obtained their T_1-weighted images (Figure 7). Figure 4 shows that with the increase in the amount of gold atoms per $G5.NH_2$, the r_1 relaxivity decreased from 13.11 to 7.50 $mM^{-1}s^{-1}$. This is attributed to the fact that the gold NPs being entrapped in the interior of the $G5.NH_2$ primary cavity structure changed and that the $G5.NH_2$ molecule became tight, leading to reduced water exchange rate between its interior and exterior.

Conclusion

We systematically investigated the relationship between r_1 relaxivity and number of metal ions per dendrimer in this study. T_1 relaxometry measurements show that the formed G5.NHAc-DOTA(Gd) NPs have an r_1 relaxivity of 9.77 mM^{-1} s^{-1} when the number of DOTA is 30. Compared with dendrimer-based Gd chelators, the Mn-based materials show lower r_1 relaxivity and poor T_1 imaging properties for the same number of DOTA units. When the mole ratio of gold to G5 is as high as 100:1, the r_1 relaxivity of G5.NHAc-$DOTA_{30}$-Gd decreased to 7.50 $mM^{-1}s^{-1}$ and T_1 imaging property was weakened. With appropriate tuning of the number of ions per G5 and the Gd/Au composition, the formed Gd-based or Gd/Au NPs may be applied in dual-mode MR/CT imaging and diagnosis of particular diseases (e.g., cancer) with high accuracies.

Data availability statement

The original contributions presented in the study are included in the article/Supplementary Material, and further inquiries can be directed to the corresponding author.

Author contributions

KL and CL contributed equally to this work. Experiment design: JX; experiments: KL and CL; data analysis: KL, CL, and JX; manuscript writing: KL, CL, and JX. The final version has been approved by all authors.

Funding

This work was funded by the Songjiang District Science and Technology Commission (Mechanism of BmK CT-mediated radioiodine combined with temozolomide in the treatment of glioblastoma: No. 21SJKJGG155).

Conflict of interest

The authors declare that the research was conducted in the absence of any commercial or financial relationships that could be construed as a potential conflict of interest.

Publisher's note

All claims expressed in this article are solely those of the authors and do not necessarily represent those of their affiliated organizations, or those of the publisher, the editors, and the reviewers. Any product that may be evaluated in this article or claim that may be made by its manufacturer is not guaranteed or endorsed by the publisher.

Supplementary material

The Supplementary Material for this article can be found online at https://www.frontiersin.org/articles/10.3389/fbioe.2022.1004414/full#supplementary-material

References

Aime, S., Castelli, D. D., Crich, S. G., Gianolio, E., and Terreno, E. (2009). Pushing the sensitivity envelope of lanthanide-based magnetic resonance imaging (MRI) contrast agents for molecular imaging applications. *Acc. Chem. Res.* 42 (7), 822–831. doi:10.1021/ar800192p

Chan, K. W.-Y., and Wong, W.-T. (2007). Small molecular gadolinium (III) complexes as MRI contrast agents for diagnostic imaging. *Coord. Chem. Rev.* 251 (17), 2428–2451. doi:10.1016/j.ccr.2007.04.018

Chen, Q., Li, K., Wen, S., Liu, H., Peng, C., Cai, H., et al. (2013). Targeted CT/MR dual mode imaging of tumors using multifunctional dendrimer-entrapped gold nanoparticles. *Biomaterials* 34 (21), 5200–5209. doi:10.1016/j.biomaterials.2013.03.009

Fan, Y., Tu, W., Shen, M., Chen, X., Ning, Y., Li, J., et al. (2020). Dendrimer-based nanosensitizers: Targeted tumor hypoxia dual-mode CT/MR imaging and enhanced radiation therapy using dendrimer-based nanosensitizers (adv. Funct. Mater. 13/2020). *Adv. Funct. Mat.* 30 (13), 2070082. doi:10.1002/adfm.202070082

Le, T. T., Nguyen, T. N. L., Nguyen, H. D., Phan, T. H. T., Pham, H. N., Le, D. G., et al. (2022). Multimodal imaging contrast property of nano hybrid Fe3O4@Ag fabricated by seed-growth for medicinal diagnosis. *Chemistryselect* 7 (25). doi:10.1002/slct.202201374

Liu, H., Shen, M., Zhao, J., Guo, R., Cao, X., Zhang, G., et al. (2012). Tunable synthesis and acetylation of dendrimer-entrapped or dendrimer-stabilized gold–silver alloy nanoparticles. *Colloids Surfaces B Biointerfaces* 94, 58–67. doi:10.1016/j.colsurfb.2012.01.019

Luo, M., Yukawa, H., and Baba, Y. (2022). Fluorescent/magnetic nano-aggregation via electrostatic force between modified quantum dot and iron oxide nanoparticles for bimodal imaging of U87MG tumor cells. *Anal. Sci.* 38, 1141–1147. doi:10.1007/s44211-022-00153-z

Matsumoto, Y., and Jasanoff, A. (2008). T_2 relaxation induced by clusters of superparamagnetic nanoparticles: Monte Carlo simulations. *Magn. Reson. Imaging* 26 (7), 994–998. doi:10.1016/j.mri.2008.01.039

Meng, Q., Wu, M., Shang, Z., Zhang, Z., and Zhang, R. (2022). Responsive gadolinium(III) complex-based small molecule magnetic resonance imaging probes: Design, mechanism and application. *Coord. Chem. Rev.* 2022, 214398. doi:10.1016/j.ccr.2021.214398

Miao, Y., Chen, P., Yan, M., Xiao, J., Hong, B., Zhou, K., et al. (2021). Highly sensitive T-1-T-2 dual-mode MRI probe based on ultra-small gadolinium oxide-decorated iron oxide nanocrystals. *Biomed. Mat.* 16 (4), 044104. doi:10.1088/1748-605x/abef54

Prencipe, G., Tabakman, S. M., Welsher, K., Liu, Z., Goodwin, A. P., Zhang, L., et al. (2009). PEG branched polymer for functionalization of nanomaterials with ultralong blood circulation. *J. Am. Chem. Soc.* 131 (13), 4783–4787. doi:10.1021/ja809086q

Shi, X., Wang, S. H., Swanson, S. D., Ge, S., Cao, Z., Van Antwerp, M. E., et al. (2008). Dendrimer-functionalized shell-crosslinked iron oxide nanoparticles for *in-vivo* magnetic resonance imaging of tumors. *Adv. Mat.* 20 (9), 1671–1678. doi:10.1002/adma.200702770

Taboada, E., Rodríguez, E., Roig, A., Oró, J., Roch, A., and Muller, R. N. (2007). Relaxometric and magnetic characterization of ultrasmall iron oxide nanoparticles with high magnetization evaluation as potential T_1 magnetic resonance imaging contrast agents for molecular imaging. *Langmuir* 23 (8), 4583–4588. doi:10.1021/la063415s

Wen, S., Li, K., Cai, H., Chen, Q., Shen, M., Huang, Y., et al. (2013). Multifunctional dendrimer-entrapped gold nanoparticles for dual mode CT/MR imaging applications. *Biomaterials* 34 (5), 1570–1580. doi:10.1016/j.biomaterials.2012.11.010

Xiao, X., Cai, H., Huang, Q., Wang, B., Wang, X., Luo, Q., et al. (2023). Polymeric dual-modal imaging nanoprobe with two-photon aggregation-induced emission for fluorescence imaging and gadolinium-chelation for magnetic resonance imaging. *Bioact. Mat.* 19, 538–549. doi:10.1016/j.bioactmat.2022.04.026

frontiers | Frontiers in Bioengineering and Biotechnology

TYPE Original Research
PUBLISHED 28 November 2022
DOI 10.3389/fbioe.2022.1078137

Check for updates

OPEN ACCESS

EDITED BY
Yu Luo,
Shanghai University of Engineering Sciences, China

REVIEWED BY
Tuanwei Sun,
Shenzhen University, China
Chao Qi,
Chongqing University, China

*CORRESPONDENCE
Bin-Bin Li,
libb26@mail.sysu.edu.cn
Chang-Hua Zhang,
zhchangh@mail.sysu.edu.cn
Yu-Long He,
heyulong@mail.sysu.edu.cn

†These authors have contributed equally to this work

SPECIALTY SECTION
This article was submitted to Nanobiotechnology, a section of the journal Frontiers in Bioengineering and Biotechnology

RECEIVED 24 October 2022
ACCEPTED 14 November 2022
PUBLISHED 28 November 2022

CITATION
Liu P, Wang Q, Li K, Bi B, Wen Y-F, Qiu M-J, Zhao J, Li B-B, Zhang C-H and He Y-L (2022), A DFX-based iron nanochelator for cancer therapy. *Front. Bioeng. Biotechnol.* 10:1078137. doi: 10.3389/fbioe.2022.1078137

COPYRIGHT
© 2022 Liu, Wang, Li, Bi, Wen, Qiu, Zhao, Li, Zhang and He. This is an open-access article distributed under the terms of the Creative Commons Attribution License (CC BY). The use, distribution or reproduction in other forums is permitted, provided the original author(s) and the copyright owner(s) are credited and that the original publication in this journal is cited, in accordance with accepted academic practice. No use, distribution or reproduction is permitted which does not comply with these terms.

A DFX-based iron nanochelator for cancer therapy

Peng Liu[1,2†], Qiang Wang[1,2†], Kuan Li[1,2], Bo Bi[1,2], Ying-Fei Wen[3], Miao-Juan Qiu[3], Jing Zhao[3], Bin-Bin Li[1,2]*, Chang-Hua Zhang[1,2]* and Yu-Long He[1,2]*

[1]Digestive Diseases Center, The Seventh Affiliated Hospital of Sun Yat-Sen University, Sun Yat-Sen University, Shenzhen, Guangdong, China, [2]Guangdong Provincial Key Laboratory of Digestive Cancer Research, The Seventh Affiliated Hospital of Sun Yat-sen University, Sun Yat-Sen University, Shenzhen, Guangdong, China, [3]Scientific Research Center, The Seventh Affiliated Hospital of Sun Yat-Sen University, Sun Yat-Sen University, Shenzhen, Guangdong, China

Iron as an essential element, is involved in various cellular functions and maintaining cell viability, cancer cell is more dependent on iron than normal cell due to its chief characteristic of hyper-proliferation. Despite that some of the iron chelators exhibited potent and broad antitumor activity, severe systemic toxicities have limited their clinical application. Polyaminoacids, as both drug-delivery platform and therapeutic agents, have attracted great interests owing to their different medical applications and biocompatibility. Herein, we have developed a novel iron nanochelator PL-DFX, which composed of deferasirox and hyperbranched polylysine. PL-DFX has higher cytotoxicity than DFX and this effect can be partially reversed by Fe^{2+} supplementation. PL-DFX also inhibited migration and invasion of cancer cells, interfere with iron metabolism, induce phase G1/S arrest and depolarize mitochondria membrane potential. Additionally, the anti-tumor potency of PL-DFX was also supported by organoids derived from clinical specimens. In this study, DFX-based iron nanochelator has provided a promising and prospective strategy for cancer therapy *via* iron metabolism disruption.

KEYWORDS

polylysine, deferasirox, iron, nanochelator, cancer therapy

Introduction

Iron is fundamental for cell function involved biomolecule syntheses, respiration, metabolism and DNA replication. Cancer cell requires more iron to facilitate its proliferation and growth (Zhang, 2014; Torti et al., 2018), which has been investigated by numerous studies conducted in cell, animal model and epidemiology (Torti and Torti, 2013). A meta-analysis involved 33 studies showed that higher iron intake increased the risk of colorectal cancer (Nelson, 2001). Multiple pathway such as Wnt and JAK-STAT3 signaling has been activated in tumor development and metastasis induced by iron overload (Ebina et al., 1986; Hann et al., 1991; Brookes et al., 2008; Xue et al., 2016; Schwartz et al., 2021), while iron depletion led to suppression of tumor growth and metastasis (Torti et al., 2018).

Iron chelators, like deferoxamine (DFO) and deferasirox (DFX), which can decrease the iron level in tissue, are commonly used for the treatment of iron-overload diseases such as thalassemia (Sridharan and Sivaramakrishnan, 2018). Accumulating evidence has revealed that iron chelators have robust and broad antitumor activities (Yu et al., 2012), and also have clinical efficacy in non-neoplastic diseases (Xu et al., 2022). Deferasirox, also known as ICL670, is a kind of oral iron chelator and has been approved by FDA for clinical treatment of blood-transfusion-related iron overload (Diaz-Garcia et al., 2014). In contrast to DFO, DFX has similar or better efficacy and more favorable safety profile (Nick et al., 2002; Cappellini, 2008; Vichinsky et al., 2013). Deferasirox also demonstrated antitumor effect in oesophageal, cervical, pancreatic, lung and gastric cancer (Ford et al., 2013; Lui et al., 2013; Choi et al., 2016; Amano et al., 2020; Zhou et al., 2022). However, deferasirox, as a small molecular agent, has several severe adverse effects, the most common was nephrotoxicity and occurred in ten percent of patients who received iron chelation treatment (Gattermann et al., 2010; Diaz-Garcia et al., 2014; Kattamis, 2019). Thus, despite iron homeostasis is a promising target in different cancer models, there is a lack of efficient and safe delivery system to suppress the side effect of deferasirox and maintain its efficiency at the same time.

The rise of nanomedicine has provided new strategies for cancer therapy (He et al., 2021; Yang et al., 2022). Polyaminoacids has attracted great attention in the regards of both bioactive agents and drug carrier. Polyaminoacids was characterized by good biocompatibility, ease of modification and slow degradability (Boddu et al., 2021). Polylysine, which produced by *streptomyces albulus*, is a natural poly (amino acid) polymer composed of lysine with amino groups on the side chains (Tao et al., 2015; Boddu et al., 2021). Polylysine, as a drug carrier for cancer therapy, possesses the following advantages: (A) Polylysine can enhance the therapeutic efficacy of drugs loaded. For example, polylysine can enhance the therapeutic efficacy of drugs when polymerize it with methotrexate, (B) polylysine is rich in cations, thus can penetrate biofilms and especially interact with tumor cells commonly possessing negatively charged membranes (Vasir and Labhasetwar, 2008; Zhou et al., 2015; Narayanan et al., 2022), and (C) Polylysine is biodegradable which could prevent accumulative cytotoxicity and facilitate downstream processing. Herein, a DFX-based iron nanochelator, which was formed by deferasirox loaded hyperbranched polylysine, was designed and synthesized for cancer therapy *via* iron deficiency. PL-DFX induced dysregulation of the iron homeostasis and increased the potency of DFX in gastrointestinal tumor cells. PL-DFX also demonstrated remarkable antitumor effects in patient-derived gastric and colorectal tumor organoids. Overall, this novel iron nanochelator provides new insights for cancer therapy.

Materials and methods

Materials

Deferasirox was purchased from Aladdin Biotechnology (Shanghai, Chain). Cell culture medium, trypsin, penicillin-streptomycin and fetal bovine serum were purchased from Gibco (Guangzhou, China). Cell counting kit-8 (CCK8) was purchased from Yeasen (shanghai, China). Annexin V-FITC/PI apoptosis Kit, cell cycle kit, mitochondria membrane potential detection (JC-1) kit and calcein-AM were purchased from Beyotime (Shanghai, China).

Syntheses of hyperbranched polylysine

Firstly, the hyperbranched polylysine was synthesized by following method (Figure 1): Lysine·HCl (27.40 g, 150 mmol) and KOH (8.42 g, 150 mmol) was completely stirred by mortar until well mixed. The mixture was transferred into open 1 L round bottom flask and stirred under 240°C with 3 mol% H_3BO_3 as catalyst. The flask was opened to allow water formed in the reaction to escape. The reaction was stopped and cooled to room temperature after 5 h. The crud product was collected by dissolving in methanol. The KCl formed during the reaction was filtered off. The methanol was evaporated and the product was dissolved in water. The aqueous solution was then lyophilized to afford polylysine solid in 85% yield.

Syntheses of PL-DFX

The DFX loading reaction was carried out as follows (Figure 1): the hyperbranched polylysine (274.0 mg, 1.50 mmol) synthesized in the former step was dissolved in DMSO (30 ml), DIPEA (100 μl) was then added to the solution. DFX (280.0 mg, 0.75 mmol) in DMSO (20 ml) and EDC (152.2 mg, 0.080 mmol) was added. The two solution was then mixed in one flask and stirred at room temperature for 5 h. The solution was dialyzed (Spectra/pro MWCO = 1000) against acetonitrile (500 ml). The precipitate was collected and washed with acetonitrile for three times in a glass filter. The crude product was dissolved in minimum of DMSO and dialyzed against water (500 ml, three times). The product was lyophilized to appear as white to yellow solid (yield = 56%).

Characterization of PL-DFX

^{1}H NMR was recorded at room temperature on a Bruker Avance III 600 MHz nuclear magnetic resonance spectrometer; FTIR: IR spectra was recorded by using FT-IR Spectrometer Platform INVENIO; UV-Vis: UV-Vis spectra was measured by

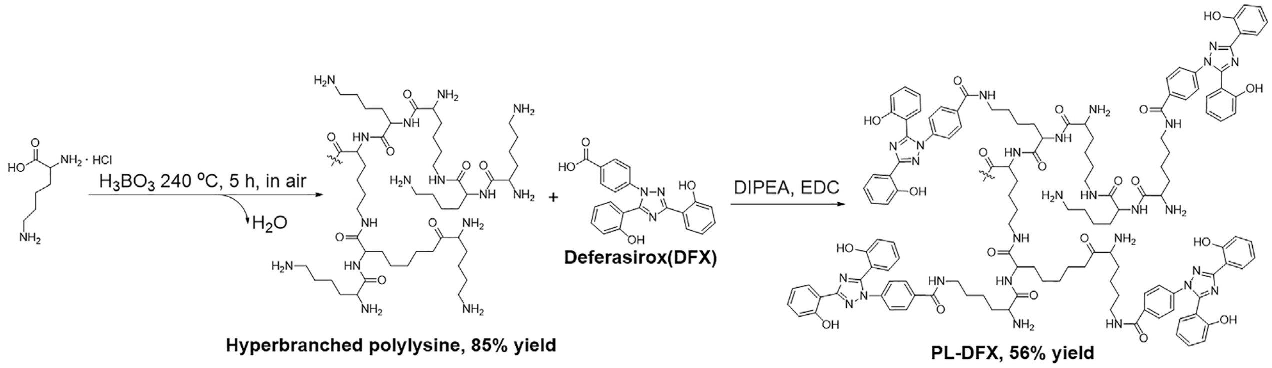

FIGURE 1
Schematic illustration of PL-DFX synthesis and fabrication.

Agilent Cary UV-Vis spectormeter; Lyophilized: Lypholization was carried on a Freeze Dryer Lyophilizer VriTis Benchtop 4KBTZL.

In order to evaluate drug loading efficiency of PL-DFX, calibration curve of DFX has been illustrated by the UV absorbance of 0, 2, 4, 6, 8, 10 μg/ml DFX dissolved in PBS. The absorbances of diluted solutions were measured at 245 nm using UV/Visible spectrophotometer. The plot of UV absorbance *versus* DFX concentration was subjected to linear regression analysis. The 1.00 mg of PL-DFX was weighed precisely, the amide bond linked polylysine and DFX was hydrolyzed by aqueous solution of HCl (2 M), the DFX was separated by chromatographic column and dissolved in 50 ml PBS to determine the drug concentration. The drug loading efficiency was calculated based on equation LE (%) = We/Wm × 100%.

Cell culture

The human gastric carcinoma cell (HGC-27) was cultured in RPMI 1640 (Gibco). The human colorectal carcinoma cells (DLD-1 and HCT-116) were cultured in RPMI 1640 (Gibco) and McCoy's 5A respectively. The human renal tubular epithelial cell (HK2) was cultured in DMEM (Gibco). All media were supplemented with 10% fetal bovine serum (FBS, Gibco) and 1% penicillin-streptomycin (Gibco). All cells were cultured and incubated in a humidified atmosphere at 37°C with 5% CO_2.

Cell viability

Cell viability was analyzed by cell-counting kit-8 (CCK8) assay. Briefly, cells were seeded into 96-well plates at a density of 5000–10000 cells per well and incubated overnight. Then drugs were added at different concentrations. 48 h after treatment, cell viability was measured according to the manufacturer's instructions.

Apoptosis assay

Evaluation of apoptosis assay was performed by using Apoptosis Kit. According to the manufacturer's instructions, cells were seeded into 6-well plates and incubated with PL-DFX (25 μM) at 37°C for 0 h, 24 h and 48 h. Then the cells were collected and stained with Annexin V-FITC and PI for 20 min. After staining, the cells were evaluated by flow cytometry.

Wound healing

HGC-27 cells were seeded into 6-well plates at the density of 5×10^5 per well and incubated for 24 h at 37°C. Then using a sterile pipette tip to scratch the cells. After washing 3 times with PBS, the medium containing DFX (12.5 μM) and PL-DFX (12.5 μM) was added to the wells. Finally, photos of wound healing were taken at 0 h and 24 h, respectively.

Transwell

Transwell chambers were placed into a 24-well plate and 60 μl of diluted Matrigel was added to each chamber. Once the Matrigel was solidified at 37°C, 200 μl of cell suspension (5×10^4 cells per chamber) which contained DFX (40 μM) and PL-DFX (40 μM) was added into the chamber, and 700 μl of medium containing 10% FBS in the lower chamber. Then cells were incubated at 37°C for 48 h. After washed two times with PBS, cells were fixed with 4% paraformaldehyde for 30 min and dyed with crystal violet for 30 min. Removed the excess dye, the chamber were dried at room temperature and photos were taken.

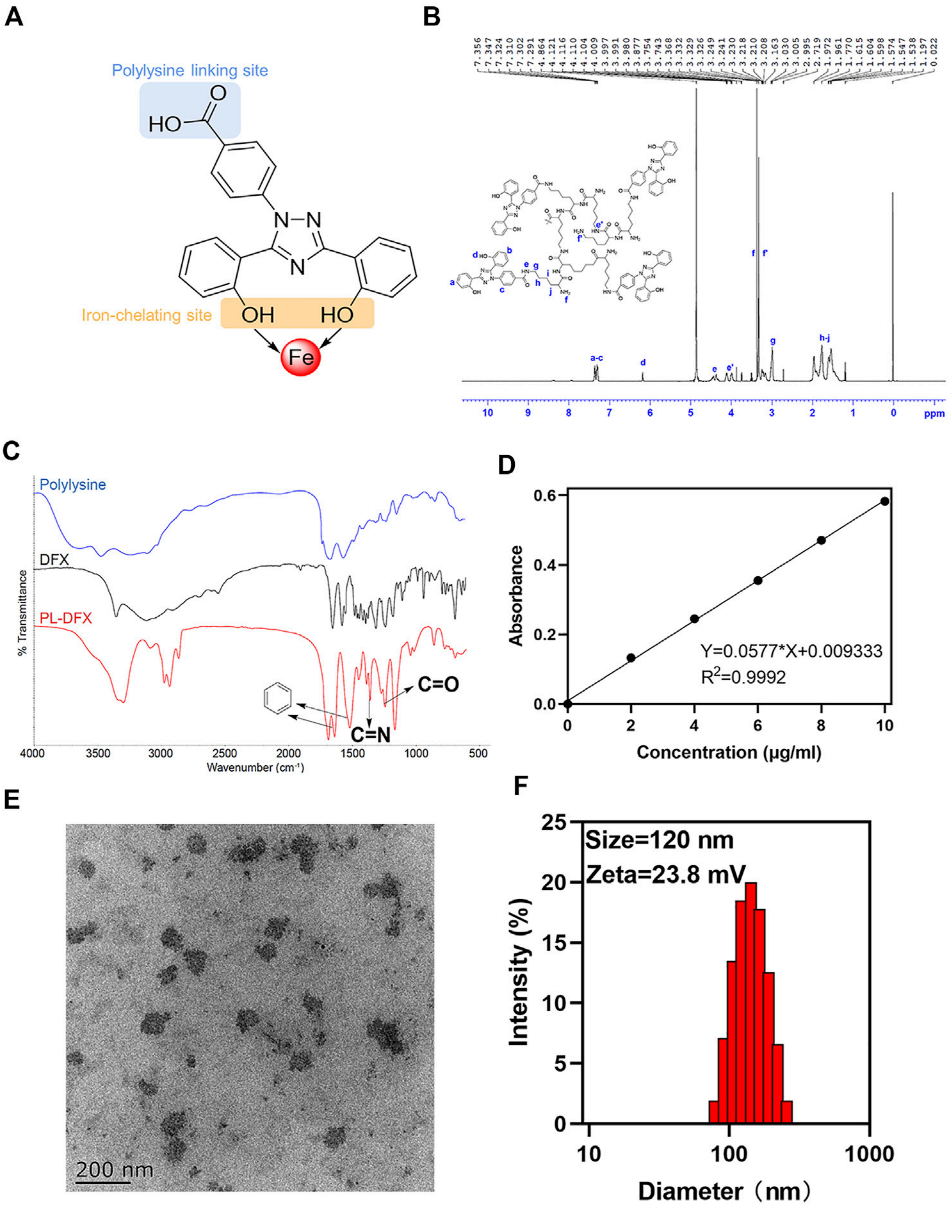

FIGURE 2
Characterization of PL-DFX nanochelator. **(A)** The polylysine linking site and iron-chelating site in the structure of DFX. **(B)** 1H-NMR spectra of PL-DFX. **(C)** FTIR spectra of PL-DFX. **(D)** UV absorbance *versus* DFX concentration plot. **(E)** TEM image of PL-DFX. **(F)** Size distribution of PL-DFX.

Labile iron pool

The cellular LIP was measured as described previously (Prus and Fibach, 2008; Komoto et al., 2021). Briefly, cells were seeded into 6-well plates and incubated with DFX (25 μM) and PL-DFX (12.5 μM) for 48 h. After washed with PBS, these cells were incubated with calcein-AM (0.5 μM) at 37°C for 15 min protected from light. The mean fluorescence intensity was measured by using flow cytometry.

Cell cycle

Cells were seeded into 6-well plates and cultured at 37°C overnight. Then cells were incubated with DFX (25 μM) and PL-

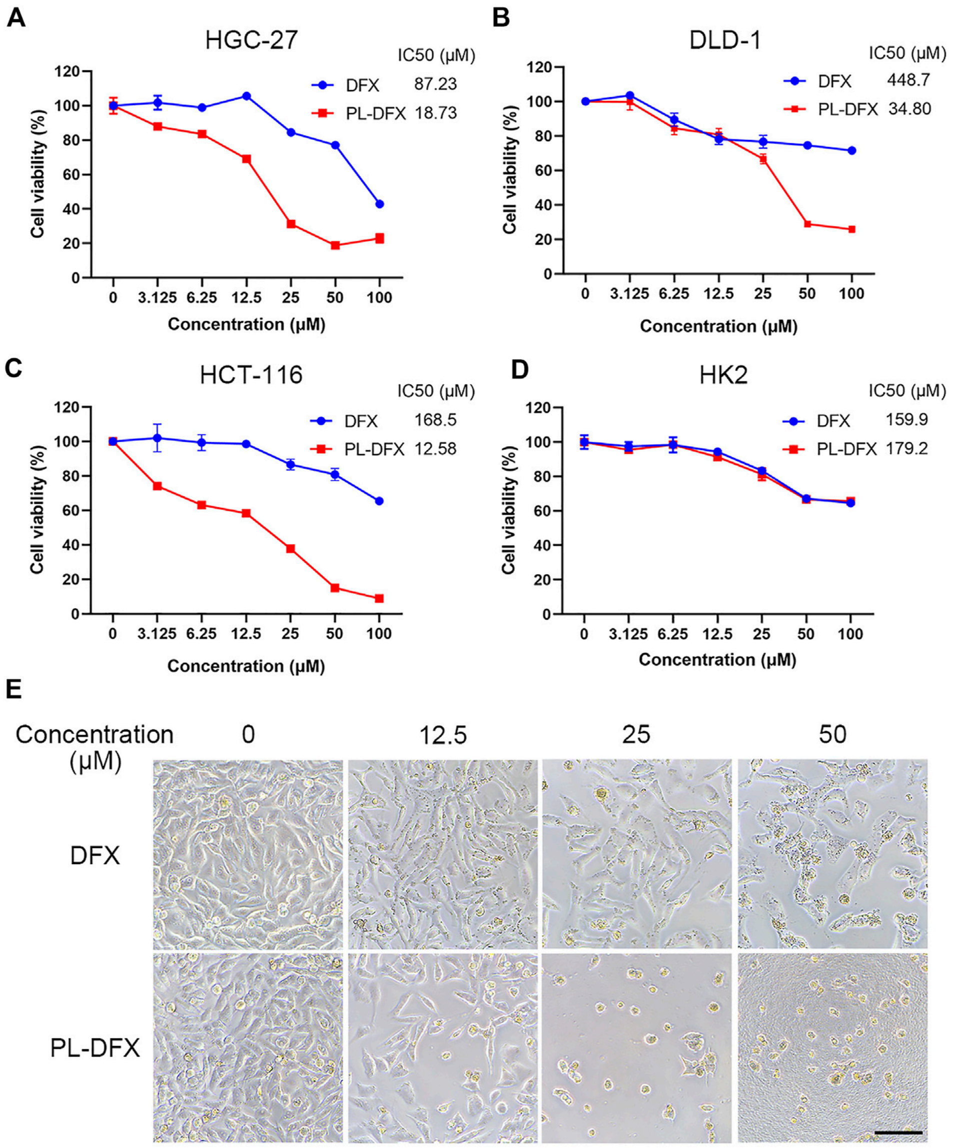

FIGURE 3
Cytotoxicity of PL-DFX *in vitro*. **(A–C)** Cell viabilities of HGC-27, DLD-1, and HCT-116 after incubated with DFX and PL-DFX for 48 h was measured by CCK8. **(D)** Cell viabilities of HK2 after incubated with DFX and PL-DFX for 24 h was measured by CCK8. **(E)** Microscopic images of HGC-27 after incubated with DFX and PL-DFX for 48 h. Scale bar = 100 μm.

DFX (12.5 μM) for 24 h. At the end of incubation, cells were collected and fixed in 75% ethanol for 24 h at 4°C. Then the cells were washed with PBS and stained with propidium iodide (PI) solution containing RNase A at 37°C for 30 min protected from the light. Finally, the cells were analyzed by flow cytometry.

Mitochondria membrane potential

Cells were seeded into 6-well plates and incubated overnight. Then cells were treated with DFX (50 μM) and PL-DFX (25 μM) for 24 h. After treatment, cells were stained with JC-1 dyeing working solution for 20 min and washed three times with JC-1 buffer according to the manufacturer's protocol. Finally, cells were collected and analyzed by flow cytometry.

Establishing and passaging of organoids

This study was approved by the ethical committee of the Seventh Affiliated Hospital of Sun Yat-Sen University and

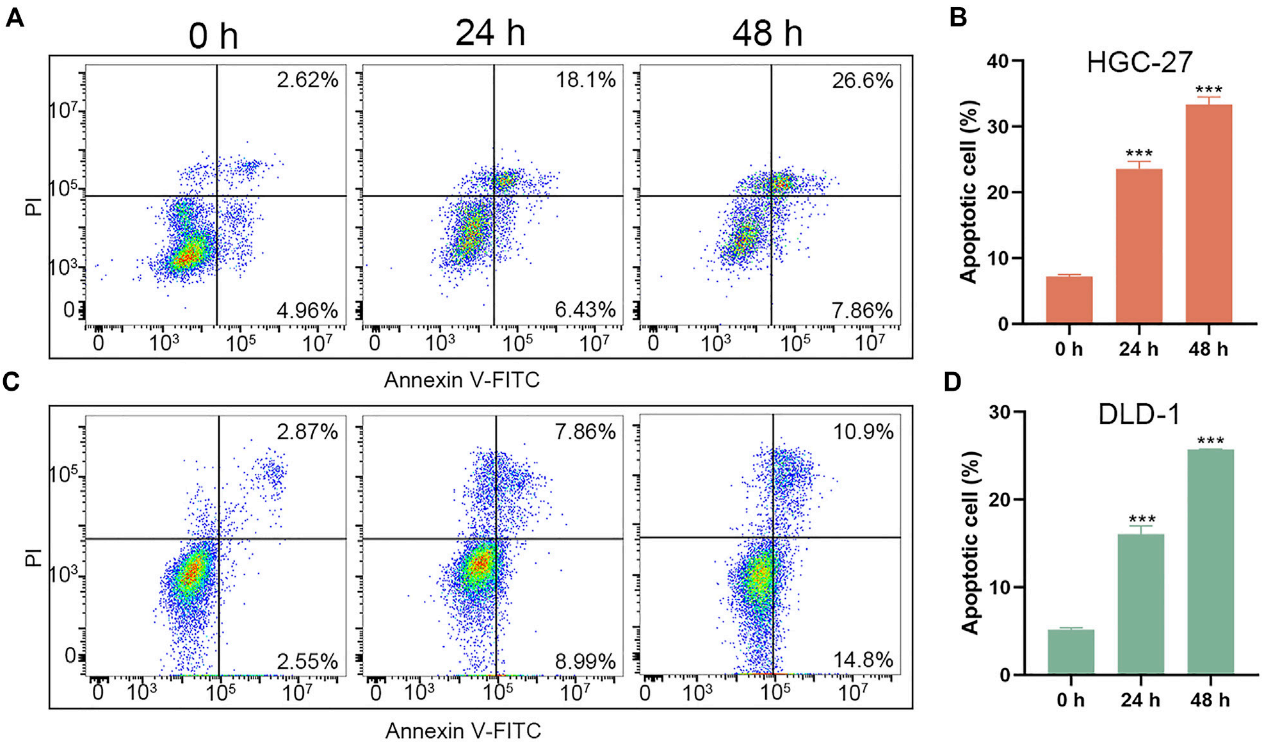

FIGURE 4
Pro-apoptotic effect of PL-DFX in HGC-27 and DLD-1 cells. **(A,B)** Apoptotic cells rate of HGC-27 incubated with PL-DFX (25 μM) for 0 h, 24 h and 48 h **(C,D)** Apoptotic cells rate of DLD-1 incubated with PL-DFX (25 μM) for 0 h, 24 h and 48 h.

performed in compliance with the Declaration of Helsinki. Written informed consents were obtained from all patients.

Establishing of organoids

The clinical specimens were rinsed in PBS containing penicillin-streptomycin 5 times and then sheared into 1–3 mm^3 small piece. The tissue fragments were digested for 2 h and supernatant was taken. After centrifugation, supernatant was removed and the remaining was resuspended with DMEM containing FBS. Centrifuged again, the cells were resuspended with DMEM and Matrigel at the ratio of 1:1 by volume. The mixed liquid was added into prewarmed 96-well plates with 10 μl per well then incubated at 37°C for 30 min. Once the Matrigel was solidified, 100 μl of medium was added to each well and cells were cultured at 37°C with 5% CO_2.

Passaging of organoids

Organoids were digested with TripLE (Gibco) at 37°C for 30 min and then centrifuged at 7000 rpm for 1min. The supernatant was discarded and cells were washed one time with DMEM. Then cells were resuspended in DMEM and mixed with Matrigel (Corning) at the ratio of 1:1 by volume. Subsequent steps were described above.

Cytotoxicity of PL-DFX in organoids

Organoids were digested, centrifuged and resuspended as previously described. The cell suspension was added into prewarmed 96-well plates with 5 μl per well and then incubated at 37°C for 30 min. Once the Matrigel was solidified, 75 μl of organoid-conditioned medium was added and cells were cultured at 37°C and 5% CO_2. Two days later, different concentrations of PL-DFX (75 μl) were added to the wells and organoids were cultured for an additional 120 h. Then, 10 μl of CCK8 reagent was added into each well and incubated for another 4–6 h, and the absorbance of each well was measured at 450 nm by microplate reader (BioTek, SynergyH1, United States).

Statistical analysis

Data was analyzed by GraphPad 8, and results were presented as mean ± SD. Comparisons between two

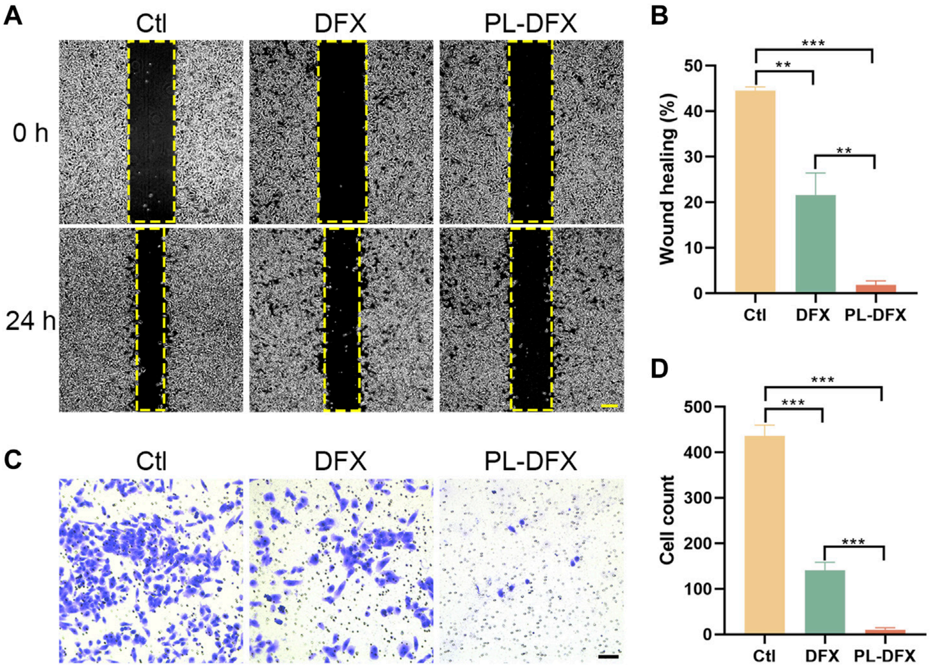

FIGURE 5
Inhibition of migration and invasion *in vitro*. **(A,B)** Microscopic image and statistical chart of wound healing assay in HGC-27 incubated with DFX (12.5 μM) and PL-DFX (12.5 μM) for 24 h. Scale bar: 200 μm. **(C,D)** Microscopic image and statistical chart of transwell invasion assay in HGC-27 incubated with DFX (40 μM) and PL-DFX (40 μM) for 48 h. Scale bar: 100 μm.

independent groups were performed by using Student's *t* test. *, ** and *** indicate that *p-value* < 0.05, 0.01 and 0.001, respectively.

Results and discussion

Design, preparation, and characterization of PL-DFX

The iron nanochelator PL-DFX composed of deferasirox and hyperbranched polylysine. In the choice of DFX and polylysine linkage site, we have carefully selected the carboxyl group on the opposite site to the"iron-catching"domain of DFX in order to avoid its iron decrease potency (Figure 2A). Firstly, the hyperbranched polylysine was synthesized, followed by DFX loading *via* amide bond formation based on the protocol in the method part. The purified product was characterized by ^{1}H NMR (Bruker 600 MHz. MeOD, 298K) and FTIR (Figures 2B,C). According to the FTIR spectrum of PL-DFX, peaks at 3296.88 cm^{-1} represented the O-H streching, and the peaks at 1643.38 and 1625.29 cm^{-1} represented the benzene streching in the DFX molecule. Additionally, the multi peaks at 7.291–7.356 ppm of ^{1}H NMR spectrum belong to the aromatic ring proton of DFX, which indicated the drug loading was successful.

Moreover, according to the UV absorbance of DFX (Figure 2D), the drug loading efficiency calculated was 34%. Size and zeta potential are key parameters of nanoparticle efficacy. Nanoparticle with around 100 nm diameter and positive charge can be more easily uptaken by tumor cells (Albanese et al., 2010). The transmission electron microscopy (TEM) demonstrated that PL-DFX was spherical in morphology and monodisperse nanoparticles (Figure 2E). The diameter and zeta potential of PL-DFX, as illustrated by Figure 2F, were 120 nm and 23.8 mV, respectively.

Cell viability and apoptosis

Accumulating evidence has confirmed the antitumor effects of DFX *in vitro* and *in vivo* (Ford et al., 2013; Amano et al., 2020; Zhou et al., 2022). Polylysine-based delivery platform can enhance the anti-tumor effects of drugs (Thambi et al., 2016; Toshiyama et al., 2019). Herein, CCK8 assay was used to evaluate the cytotoxicity of DFX and PL-DFX in HGC-27, DLD-1, and HCT-116 cells. IC50 value was also calculated from the dose-response curves shown. As illustrated in Figures 3A–C, cytotoxicity of DFX and PL-DFX against these tumor cells

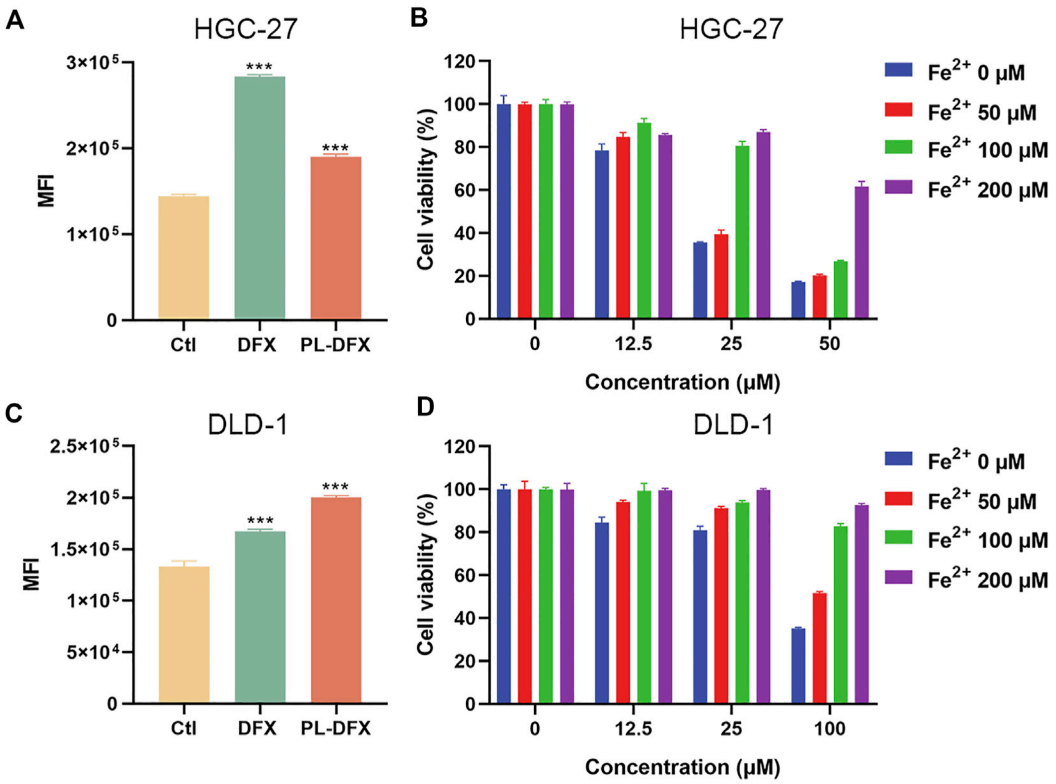

FIGURE 6
Disruption of cellular iron metabolism. **(A,C)** Flow cytometric analysis of intracellular iron of HGC-27 and DLD-1 using calcein-AM after treatment with DFX (25 μM) and PL-DFX (12.5 μM) for 48 h **(B,D)** Cell viabilities of HGC-27 and DLD-1 after treatment with PL-DFX in the presence or absence of Fe^{2+} for 48 h.

was in a concentration-dependent manner, and cell viability decreased with increasing concentrations of drugs. Compared to DFX, cells incubated with the same concentration of PL-DFX (at equivalent concentrations of DFX) showed lower viability. PL-DFX inhibited HGC-27, DLD-1 and HCT-116 with IC50 values of 18.73 μM, 34.80 μM and 12.58 μM, which were significantly lower than IC50 values of DFX (87.23 μM, 448.7 μM and 168.5 μM, respectively). The bright field images also showed that PL-DFX exhibited greater ability to inhibit cell proliferation than DFX (Figure 3E). The higher the PL-DFX concentration, the lesser number of cells, and the cells became small and round.

Polylysine, as a biodegradable drug delivery platform, not only enhances the cytotoxicity of free drugs in tumor cells, while showing no higher toxicity in non-tumor cells (Du et al., 2020; Zhu et al., 2021). Due to nephrotoxicity of DFX, the cytotoxicity of DFX and PL-DFX was also investigated in human renal tubular epithelial cells (HK2). PL-DFX did not display enhanced cytotoxicity in HK2 cells, which was similar with DFX (Figure 3D). These results confirmed that the antitumor effect and biosafety of PL-DFX were superior to DFX.

Besides, we further evaluated the pro-apoptotic effects of PL-DFX against HGC-27 and DLD-1 by using Annexin V-FITC/PI kit. As illustrated in Figures 4A–D, the percentage of overall apoptotic cells incubated with PL-DFX for 48 h was 34.46% in HGC-27 and 25.7% in DLD-1, which was significantly higher than that at 24 h (24.53% in HGC-27 and 16.85% in DLD-1) and 0 h (7.58% in HGC-27 and 5.42% in DLD-1). These results indicated the time-dependent cytotoxicity of PL-DFX. In summary, polylysine carrier could enhance the anti-tumor effects of deferasirox in the tumor cells.

Migration and invasion

Next, we also explored the impact of DFX and PL-DFX on cell migration and invasion *in vitro* by wound healing and transwell invasion assays. As shown in Figures 5A,B, after 24 h incubation, the wound healing rate of PL-DFX group was 2.53%, which was significantly lower than that of control and DFX groups (43.65% and 25.66%, respectively). The transwell assay also displayed that the cell count

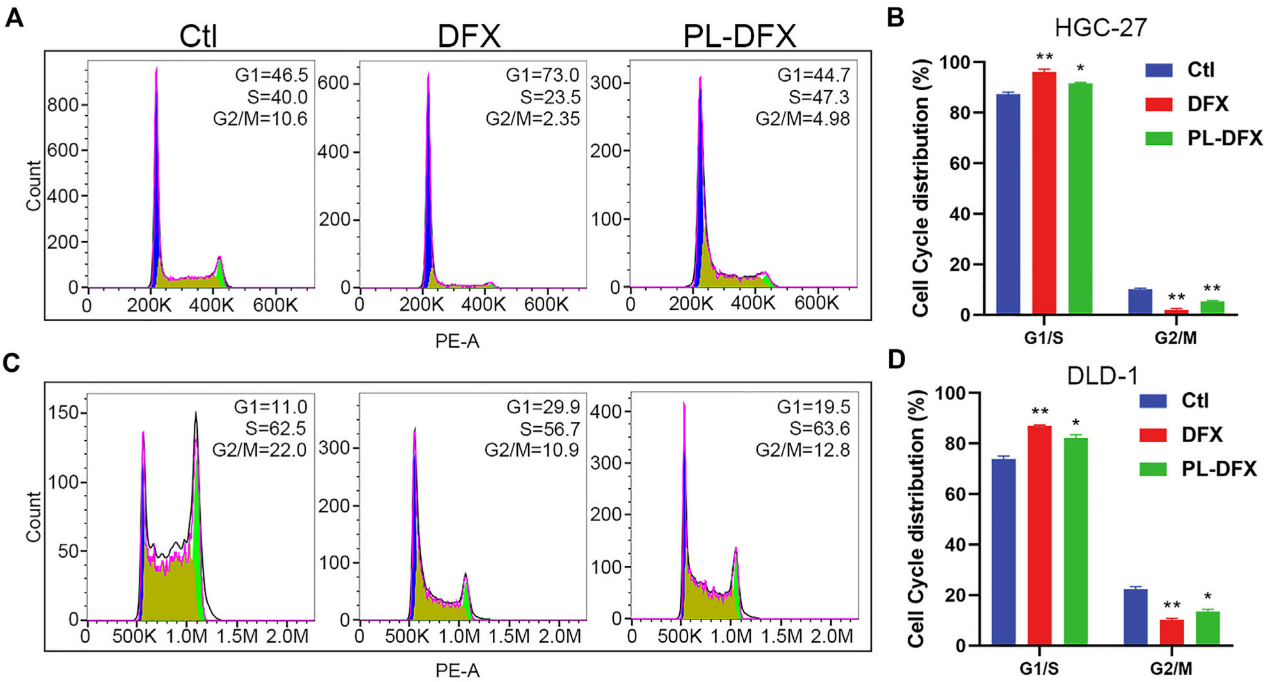

FIGURE 7
Impact of DFX and PL-DFX on cell cycle. **(A,B)** Cell cycle distribution of HGC-27 incubated with DFX (25 μM) and PL-DFX (12.5 μM) for 24 h **(C,D)** Cell cycle distribution of DLD-1 incubated with DFX (25 μM) and PL-DFX (12.5 μM) for 24 h.

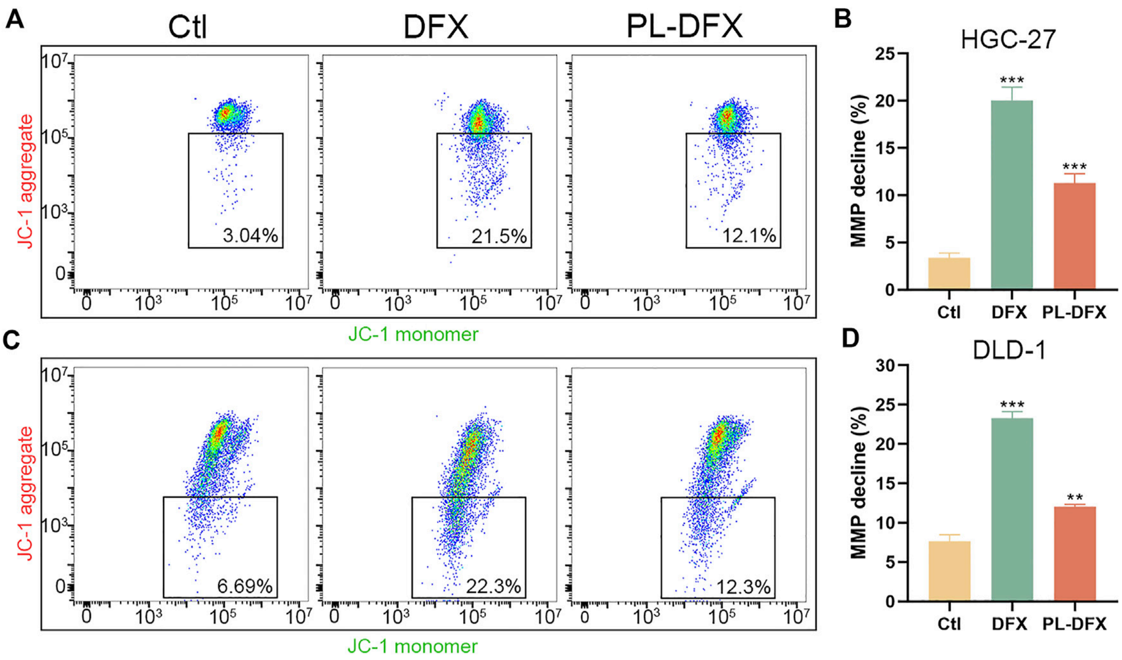

FIGURE 8
Impact of DFX and PL-DFX on mitochondria membrane potential. **(A,B)** Mitochondria membrane potential detected by JC-1 in HGC-27 cells incubated with DFX (50 μM) and PL-DFX (25 μM) for 24 h **(C,D)** Mitochondria membrane potential detected by JC-1 in DLD-1 cells incubated with DFX (50 μM) and PL-DFX (25 μM) for 24 h.

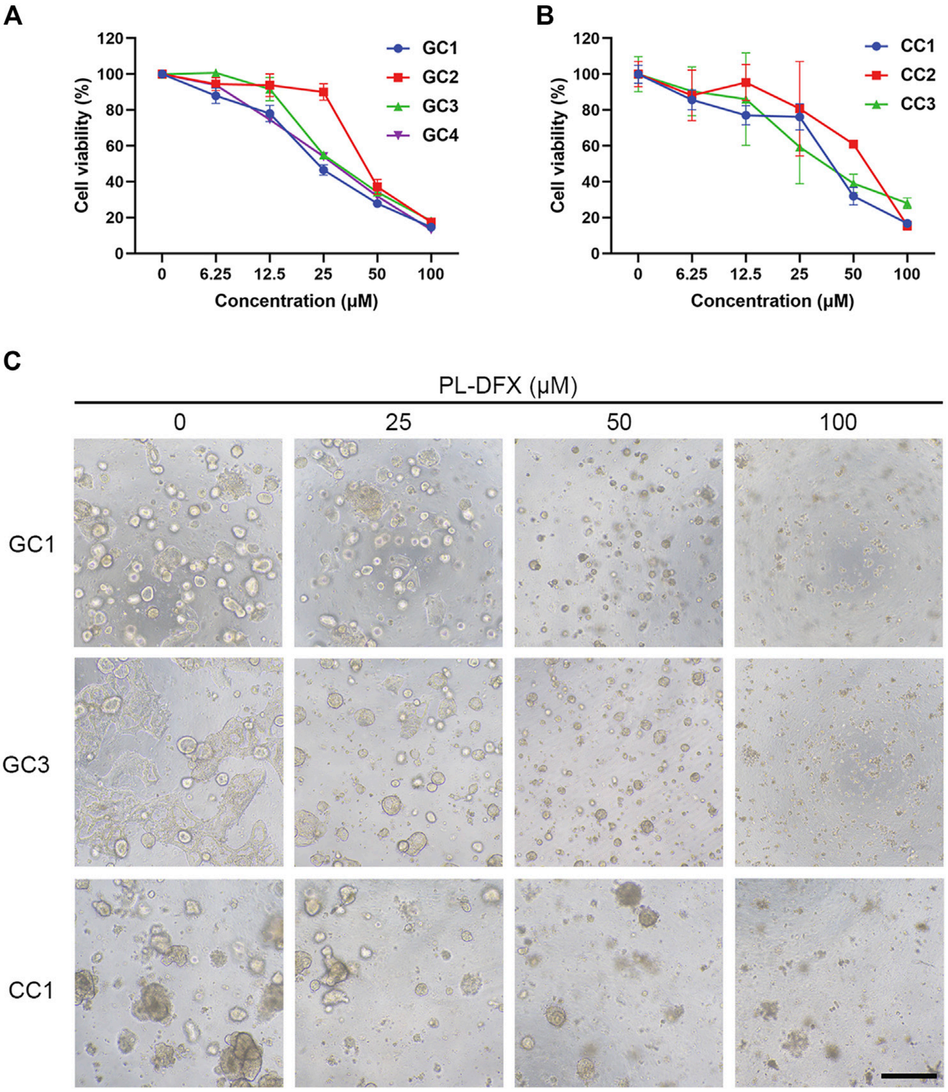

FIGURE 9
Cytotoxicity of PL-DFX in organoids. **(A)** Cell viability of gastric cancer organoids after treatment with various concentrations of PL-DFX for 120 h. **(B)** Cell viability of colorectal cancer organoids after treatment with various concentrations of PL-DFX for 120 h. **(C)** Microscopic images of gastric and colorectal cancer organoids after treatment with PL-DFX for 120 h. Scale bar: 300 μm. (GC: gastric cancer organoid; CC: colorectal cancer organoid).

of invasive HGC-27 cells incubated with PL-DFX for 24 h was significantly lower than that of control and DFX groups (Figures 5C,D). The above observation indicated that the ability of DFX loaded on polylysine to inhibit migration and invasion was greater than free deferasirox.

Disruption of iron metabolism

The cellular labile iron pool (LIP) was measured by using the calcein-AM (Prus and Fibach, 2008; Komoto et al., 2021). Although, calcein-AM has been frequently used to evaluate the cell viability and calcium, its fluorescence is quenched when binding with cellular iron. Iron chelators can inhibit the formation of complexation and increase the fluorescence intensity of calcein. Therefore, the changes in fluorescence intensity of calcein indicates the change in intracellular iron levels. As shown in Figures 6A,C, compared with the control, HGC-27 and DLD-1 cells incubated with DFX and PL-DFX had increased calcein fluorescence, indicating reduction of intracellular iron levels and similar iron-chelating ability of both. Moreover, after incubation with PL-DFX, supplement of

Fe^{2+} can partially reverse the cytotoxicity of PL-DFX in HGC-27 and DLD-1 cells (Figures 6B,D). Herein, in the structure of PL-DFX nanoparticles, the conjugation between polylysine and deferasirox do not affect iron chelating ability of deferasirox.

Cell cycle and mitochondrial membrane potential

We have demonstrated that PL-DFX has similar iron chelating ability with DFX. Next, the impact of PL-DFX on biological functions of HGC-27 and DLD-1 cells was performed. Iron is essential for the activity of ribonucleotide reductase, and iron depletion can inhibit the DNA synthesis and cause G1/S arrest (Chantrel-Groussard et al., 2006; Yu et al., 2007). Herein, as shown in Figure 7, similar to the previous study, compared to the control group, cells incubated with DFX displayed obviously phase G1/S arrest. As expected, PL-DFX also resulted in an increased proportion of cells in G1/S phase.

Iron plays a key role in mitochondria biological function and biosynthesis (Paul et al., 2017), and iron deficiency can compromise mitochondria function (Hoes et al., 2018). Decreased mitochondria membrane potential (MMP) is a hallmark of mitochondria dysfunction. Thus, the impact of DFX and PL-DFX on mitochondria membrane potential was investigated by using JC-1. As illustrated in Figure 8, iron deficiency induced by DFX resulted in decreased MMP. Similar to DFX, PL-DFX also depolarized the MMP in HGC-27 and DLD-1 cells.

Cytotoxicity of PL-DFX in organoids

Cell line is an important platform for drug development and screening. However, variations between cell lines and original tumors are responsible for the failure of the drug-based clinical trials (Kamb, 2005; Caponigro and Sellers, 2011; Barretina et al., 2012). Organoid, which established from patient-derived tumor tissue, resembles the original tumors in terms of biological characteristics and heterogeneity, and organoid-based drug screening methods have yield satisfactory results (Drost and Clevers, 2018). Therefore, we utilized the organoids which established from patient-derived gastric and colorectal cancer tissues to evaluate the clinical efficacy of PL-DFX. As shown in Figures 9A,B, the viability of organoids decreased with increasing the concentrations of PL-DFX. Besides, the PL-DFX treated organoids displayed smaller in size and fewer in number in compared to control organoids in both gastric cancer organoids (GC) and colorectal cancer organoids (CC) (Figure 9C).

Conclusion

In summary, a novel iron nanochelator (PL-DFX) was designed and successfully synthesized *via* conjugation chemically between polylysine and deferasirox. This iron nanochelator, which prepared with around 120-nm diameter and positive charge, displayed higher cytotoxicity and greater capacity to inhibit migration and invasion than free DFX. Similar to DFX, PL-DFX also could disrupt cellular iron metabolism and biological functions involved iron, such as cell cycle and mitochondria membrane potential. Besides, its efficacy was also validated in the gastric and colorectal tumor organoids. Taken together, this study provides a new insight for cancer therapy *via* iron chelation.

Data availability statement

The raw data supporting the conclusions of this article will be made available by the authors, without undue reservation.

Ethics statement

The studies involving human participants were reviewed and approved by Medical Ethics Committee of the Seventh Affiliated Hospital, Sun Yat-sen University. The patients/participants provided their written informed consent to participate in this study.

Author contributions

PL: experiment, data curation, formal analysis, software and writing original draft. QW: data curation, formal analysis, software and visualization. JZ: conceptualization, investigation, draft review and editing. KL, BB, Y-FW, and M-JQ: resource and software. B-BL, C-HZ, and Y-LH: resource, experiment, conceptualization, investigation, draft review and editing, funding acquisition and project administration. All authors read and approved the final manuscript.

Funding

This work was supported by National Natural Science Foundation of China (81902426, 82073148, U20A20379), Guangdong Provincial Key Laboratory of Digestive Cancer Research (2021B1212040006), Sanming Project of Medicine in Shenzhen (SZSM201911010), Shenzhen Key Medical Discipline Construction Fund (SZXK016).

Conflict of interest

The authors declare that the research was conducted in the absence of any commercial or financial relationships that could be construed as a potential conflict of interest.

Publisher's note

All claims expressed in this article are solely those of the authors and do not necessarily represent those of their affiliated organizations, or those of the publisher, the editors and the reviewers. Any product that may be evaluated in this article, or claim that may be made by its manufacturer, is not guaranteed or endorsed by the publisher.

References

Albanese, A., Sykes, E. A., and Chan, W. C. (2010). Rough around the edges: The inflammatory response of microglial cells to spiky nanoparticles. *ACS Nano* 4 (5), 2490–2493. doi:10.1021/nn100776z

Amano, S., Kaino, S., Shinoda, S., Harima, H., Matsumoto, T., Fujisawa, K., et al. (2020). Invasion inhibition in pancreatic cancer using the oral iron chelating agent deferasirox. *BMC Cancer* 20 (1), 681. doi:10.1186/s12885-020-07167-8

Barretina, J., Caponigro, G., Stransky, N., Venkatesan, K., Margolin, A. A., Kim, S., et al. (2012). The Cancer Cell Line Encyclopedia enables predictive modelling of anticancer drug sensitivity. *Nature* 483 (7391), 603–607. doi:10.1038/nature11003

Boddu, S. H. S., Bhagav, P., Karla, P. K., Jacob, S., Adatiya, M. D., Dhameliya, T. M., et al. (2021). Polyamide/Poly(Amino acid) polymers for drug delivery. *J. Funct. Biomater.* 12 (4), 58. doi:10.3390/jfb12040058

Brookes, M. J., Boult, J., Roberts, K., Cooper, B. T., Hotchin, N. A., Matthews, G., et al. (2008). A role for iron in Wnt signalling. *Oncogene* 27 (7), 966–975. doi:10.1038/sj.onc.1210711

Caponigro, G., and Sellers, W. R. (2011). Advances in the preclinical testing of cancer therapeutic hypotheses. *Nat. Rev. Drug Discov.* 10 (3), 179–187. doi:10.1038/nrd3385

Cappellini, M. D. (2008). Long-term efficacy and safety of deferasirox. *Blood Rev.* 22 (2), S35–S41. doi:10.1016/S0268-960X(08)70007-9

Chantrel-Groussard, K., Gaboriau, F., Pasdeloup, N., Havouis, R., Nick, H., Pierre, J. L., et al. (2006). The new orally active iron chelator ICL670A exhibits a higher antiproliferative effect in human hepatocyte cultures than O-trensox. *Eur. J. Pharmacol.* 541 (3), 129–137. doi:10.1016/j.ejphar.2006.05.001

Choi, J. H., Kim, J. S., Won, Y. W., Uhm, J., Park, B. B., and Lee, Y. Y. (2016). The potential of deferasirox as a novel therapeutic modality in gastric cancer. *World J. Surg. onc.* 14, 77. doi:10.1186/s12957-016-0829-1

Diaz-Garcia, J. D., Gallegos-Villalobos, A., Gonzalez-Espinoza, L., Sanchez-Nino, M. D., Villarrubia, J., and Ortiz, A. (2014). Deferasirox nephrotoxicity-the knowns and unknowns. *Nat. Rev. Nephrol.* 10 (10), 574–586. doi:10.1038/nrneph.2014.121

Drost, J., and Clevers, H. (2018). Organoids in cancer research. *Nat. Rev. Cancer* 18 (7), 407–418. doi:10.1038/s41568-018-0007-6

Du, X., Yin, S., Xu, L., Ma, J., Yu, H., Wang, G., et al. (2020). Polylysine and cysteine functionalized chitosan nanoparticle as an efficient platform for oral delivery of paclitaxel. *Carbohydr. Polym.* 229, 115484. doi:10.1016/j.carbpol.2019.115484

Ebina, Y., Okada, S., Hamazaki, S., Ogino, F., Li, J. L., and Midorikawa, O. (1986). Nephrotoxicity and renal cell carcinoma after use of iron- and aluminum-nitrilotriacetate complexes in rats. *J. Natl. Cancer Inst.* 76 (1), 107–113.

Ford, S. J., Obeidy, P., Lovejoy, D. B., Bedford, M., Nichols, L., Chadwick, C., et al. (2013). Deferasirox (ICL670A) effectively inhibits oesophageal cancer growth *in vitro* and *in vivo*. *Br. J. Pharmacol.* 168 (6), 1316–1328. doi:10.1111/bph.12045

Gattermann, N., Finelli, C., Porta, M. D., Fenaux, P., Ganser, A., Guerci-Bresler, A., et al. (2010). Deferasirox in iron-overloaded patients with transfusion-dependent myelodysplastic syndromes: Results from the large 1-year EPIC study. *Leukemia Res.* 34 (9), 1143–1150. doi:10.1016/j.leukres.2010.03.009

Hann, H. W., Stahlhut, M. W., and Menduke, H. (1991). Iron enhances tumor growth. Observation on spontaneous mammary tumors in mice. *Cancer* 68 (11), 2407–2410. doi:10.1002/1097-0142(19911201)68:11<2407::aid-cncr2820681113>3.0.co;2-n

He, T., Luo, Y., Zhang, Q., Men, Z., Su, T., Fan, L., et al. (2021). Hyalase-mediated cascade degradation of a matrix barrier and immune cell penetration by a photothermal microneedle for efficient anticancer therapy. *ACS Appl. Mat. Interfaces* 13 (23), 26790–26799. doi:10.1021/acsami.1c06725

Hoes, M. F., Grote Beverborg, N., Kijlstra, J. D., Kuipers, J., Swinkels, D. W., Giepmans, B. N. G., et al. (2018). Iron deficiency impairs contractility of human cardiomyocytes through decreased mitochondrial function. *Eur. J. Heart Fail.* 20 (5), 910–919. doi:10.1002/ejhf.1154

Kamb, A. (2005). What's wrong with our cancer models? *Nat. Rev. Drug Discov.* 4 (2), 161–165. doi:10.1038/nrd1635

Kattamis, A. (2019). Renal function abnormalities and deferasirox. *Lancet Child Adolesc. Health* 3 (1), 2–3. doi:10.1016/S2352-4642(18)30350-X

Komoto, K., Nomoto, T., El Muttaqien, S., Takemoto, H., Matsui, M., Miura, Y., et al. (2021). Iron chelation cancer therapy using hydrophilic block copolymers conjugated with deferoxamine. *Cancer Sci.* 112 (1), 410–421. doi:10.1111/cas.14607

Lui, G. Y., Obeidy, P., Ford, S. J., Tselepis, C., Sharp, D. M., Jansson, P. J., et al. (2013). The iron chelator, deferasirox, as a novel strategy for cancer treatment: Oral activity against human lung tumor xenografts and molecular mechanism of action. *Mol. Pharmacol.* 83 (1), 179–190. doi:10.1124/mol.112.081893

Narayanan, P., Anitha, A. K., Ajayakumar, N., and Kumar, K. S. (2022). Poly-lysine dendritic nanocarrier to target epidermal growth factor receptor overexpressed breast cancer for methotrexate delivery. *Mater. (Basel)* 15 (3), 800. doi:10.3390/ma15030800

Nelson, R. L. (2001). Iron and colorectal cancer risk: Human studies. *Nutr. Rev.* 59 (5), 140–148. doi:10.1111/j.1753-4887.2001.tb07002.x

Nick, H., Wong, A., Acklin, P., Faller, B., Jin, Y., Lattmann, R., et al. (2002). ICL670A: Preclinical profile. *Adv. Exp. Med. Biol.* 509, 185–203. doi:10.1007/978-1-4615-0593-8_10

Paul, B. T., Manz, D. H., Torti, F. M., and Torti, S. V. (2017). Mitochondria and iron: Current questions. *Expert Rev. Hematol.* 10 (1), 65–79. doi:10.1080/17474086.2016.1268047

Prus, E., and Fibach, E. (2008). Flow cytometry measurement of the labile iron pool in human hematopoietic cells. *Cytometry* 73 (1), 22–27. doi:10.1002/cyto.a.20491

Schwartz, A. J., Goyert, J. W., Solanki, S., Kerk, S. A., Chen, B., Castillo, C., et al. (2021). Hepcidin sequesters iron to sustain nucleotide metabolism and mitochondrial function in colorectal cancer epithelial cells. *Nat. Metab.* 3 (7), 969–982. doi:10.1038/s42255-021-00406-7

Sridharan, K., and Sivaramakrishnan, G. (2018). Efficacy and safety of iron chelators in thalassemia and sickle cell disease: A multiple treatment comparison network meta-analysis and trial sequential analysis. *Expert Rev. Clin. Pharmacol.* 11 (6), 641–650. doi:10.1080/17512433.2018.1473760

Tao, Y., Chen, X., Jia, F., Wang, S., Xiao, C., Cui, F., et al. (2015). New chemosynthetic route to linear epsilon-poly-lysine. *Chem. Sci.* 6 (11), 6385–6391. doi:10.1039/c5sc02479j

Thambi, T., Son, S., Lee, D. S., and Park, J. H. (2016). Poly(ethylene glycol)-b-poly(lysine) copolymer bearing nitroaromatics for hypoxia-sensitive drug delivery. *Acta Biomater.* 29, 261–270. doi:10.1016/j.actbio.2015.10.011

Torti, S. V., Manz, D. H., Paul, B. T., Blanchette-Farra, N., and Torti, F. M. (2018). Iron and cancer. *Annu. Rev. Nutr.* 38, 97–125. doi:10.1146/annurev-nutr-082117-051732

Torti, S. V., and Torti, F. M. (2013). Iron and cancer: More ore to be mined. *Nat. Rev. Cancer* 13 (5), 342–355. doi:10.1038/nrc3495

Toshiyama, R., Konno, M., Eguchi, H., Takemoto, H., Noda, T., Asai, A., et al. (2019). Poly(ethylene glycol)-poly(lysine) block copolymer-ubenimex conjugate targets aminopeptidase N and exerts an antitumor effect in hepatocellular carcinoma stem cells. *Oncogene* 38 (2), 244–260. doi:10.1038/s41388-018-0406-x

Vasir, J. K., and Labhasetwar, V. (2008). Quantification of the force of nanoparticle-cell membrane interactions and its influence on intracellular trafficking of nanoparticles. *Biomaterials* 29 (31), 4244–4252. doi:10.1016/j.biomaterials.2008.07.020

Vichinsky, E., Torres, M., Minniti, C. P., Barrette, S., Habr, D., Zhang, Y., et al. (2013). Efficacy and safety of deferasirox compared with deferoxamine in sickle cell disease: Two-year results including pharmacokinetics and concomitant hydroxyurea. *Am. J. Hematol.* 88 (12), 1068–1073. doi:10.1002/ajh.23569

Xu, L., Sun, Z., Xing, Z., Liu, Y., Zhao, H., Tang, Z., et al. (2022). Cur@SF NPs alleviate Friedreich's ataxia in a mouse model through synergistic iron chelation and antioxidation. *J. Nanobiotechnol.* 20 (1), 118. doi:10.1186/s12951-022-01333-9

Xue, X., Ramakrishnan, S. K., Weisz, K., Triner, D., Xie, L., Attili, D., et al. (2016). Iron uptake via DMT1 integrates cell cycle with JAK-STAT3 signaling to promote colorectal tumorigenesis. *Cell Metab.* 24 (3), 447–461. doi:10.1016/j.cmet.2016.07.015

Yang, Z., Luo, Y., Yu, H., Liang, K., Wang, M., Wang, Q., et al. (2022). Reshaping the tumor immune microenvironment based on a light-activated nanoplatform for efficient cancer therapy. *Adv. Mater.* 34 (11), e2108908. doi:10.1002/adma.202108908

Yu, Y., Gutierrez, E., Kovacevic, Z., Saletta, F., Obeidy, P., Suryo Rahmanto, Y., et al. (2012). Iron chelators for the treatment of cancer. *Curr. Med. Chem.* 19 (17), 2689–2702. doi:10.2174/092986712800609706

Yu, Y., Kovacevic, Z., and Richardson, D. R. (2007). Tuning cell cycle regulation with an iron key. *Cell Cycle* 6 (16), 1982–1994. doi:10.4161/cc.6.16.4603

Zhang, C. (2014). Essential functions of iron-requiring proteins in DNA replication, repair and cell cycle control. *Protein Cell* 5 (10), 750–760. doi:10.1007/s13238-014-0083-7

Zhou, N., Cui, Y., Zhu, R., Kuang, Y., Ma, W., Hou, J., et al. (2022). Deferasirox shows inhibition activity against cervical cancer *in vitro* and *in vivo*. *Gynecol. Oncol.* 166 (1), 126–137. doi:10.1016/j.ygyno.2022.05.006

Zhou, Z., Tang, J., Sun, Q., Murdoch, W. J., and Shen, Y. (2015). A multifunctional PEG-PLL drug conjugate forming redox-responsive nanoparticles for intracellular drug delivery. *J. Mat. Chem. B* 3 (38), 7594–7603. doi:10.1039/c5tb01027f

Zhu, D., Zhang, H., Huang, Y., Lian, B., Ma, C., Han, L., et al. (2021). A self-assembling amphiphilic peptide dendrimer-based drug delivery system for cancer therapy. *Pharmaceutics* 13 (7), 1092. doi:10.3390/pharmaceutics13071092

frontiers | Frontiers in Bioengineering and Biotechnology

TYPE Original Research
PUBLISHED 13 February 2023
DOI 10.3389/fbioe.2023.1123477

Check for updates

OPEN ACCESS

EDITED BY
Xin Li,
DWI-Leibniz-Institut für Interaktive
Materialien, Germany

REVIEWED BY
Yong Hu,
Tongji University, China
Yi Lu,
RWTH Aachen University, Germany

*CORRESPONDENCE
Derek J. Irvine,
✉ Derek.Irvine@nottingham.ac.uk
Ming Ni,
✉ gendianqing@163.com

SPECIALTY SECTION
This article was submitted to Nanobiotechnology, a section of the journal Frontiers in Bioengineering and Biotechnology

RECEIVED 14 December 2022
ACCEPTED 19 January 2023
PUBLISHED 13 February 2023

CITATION
Wang K, Ni M, Dundas AA, Dimitrakis G and Irvine DJ (2023), Ring opening polymerisation of ε-caprolactone with novel microwave magnetic heating and cyto-compatible catalyst. *Front. Bioeng. Biotechnol.* 11:1123477. doi: 10.3389/fbioe.2023.1123477

COPYRIGHT
© 2023 Wang, Ni, Dundas, Dimitrakis and Irvine. This is an open-access article distributed under the terms of the Creative Commons Attribution License (CC BY). The use, distribution or reproduction in other forums is permitted, provided the original author(s) and the copyright owner(s) are credited and that the original publication in this journal is cited, in accordance with accepted academic practice. No use, distribution or reproduction is permitted which does not comply with these terms.

Ring opening polymerisation of ε-caprolactone with novel microwave magnetic heating and cyto-compatible catalyst

Kaiyang Wang[1], Ming Ni[2]*, Adam A. Dundas[3], Georgios Dimitrakis[4] and Derek J. Irvine[3]*

[1]Shanghai Engineering Technology Research Center for Pharmaceutical Intelligent Equipment, Shanghai Frontiers Science Center for Druggability of Cardiovascular Non-Coding RNA, Institute for Frontier Medical Technology, Shanghai University of Engineering Science, Shanghai, China, [2]Department of Orthopaedics, Shanghai Key Laboratory for Prevention and Treatment of Bone and Joint Diseases, Shanghai Institute of Traumatology and Orthopaedics, Ruijin Hospital, Shanghai Jiao Tong University School of Medicine, Shanghai, China, [3]Centre for Additive Manufacturing, Faculty of Engineering, University of Nottingham, Nottingham, United Kingdom, [4]George Green Institute for Electromagnetics Research, Faculty of Engineering, University of Nottingham, Nottingham, United Kingdom

We report on the ring-opening polymerization of ε-caprolactone incorporated with a magnetic susceptible catalyst, $FeCl_3$, *via* the use of microwave magnetic heating (HH) which primarily heats the bulk with a magnetic field (H-field) from an electromagnetic field (EMF). Such a process was compared to more commonly used heating methods, such as conventional heating (CH), i.e., oil bath, and microwave electric heating (EH), which is also referred to as microwave heating that primarily heats the bulk with an electric field (E-field). We identified that the catalyst is susceptible to both the E-field and H-field heating, and promoted the heating of the bulk. Which, we noticed such promotion was a lot more significant in the HH heating experiment. Further investigating the impact of such observed effects in the ROP of ε-caprolactone, we found that the HH experiments showed a more significant improvement in both the product Mwt and yield as the input power increased. However, when the catalyst concentration was reduced from 400:1 to 1600:1 (Monomer:Catalyst molar ratio), the observed differentiation in the Mwt and yield between the EH and the HH heating methods diminished, which we hypothesized to be due to the limited species available that were susceptible to microwave magnetic heating. But comparable product results between the HH and EH heating methods suggest that the HH heating method along with a magnetic susceptible catalyst could be an alternative solution to overcome the penetration depth problem associated with the EH heating methods. The cytotoxicity of the produced polymer was investigated to identify its potential application as biomaterials.

KEYWORDS

microwave synthesis, magnetic susceptible catalyst, biomaterial fabrication, PCL synthesis, controlled polymerization

1 Introduction

In recent years, the development of polymers that are environmentally friendly and biodegradable has generated substantial effort toward the polymerization of cyclic esters (Bartnikowski et al., 2019; Tsang et al., 2019; Li et al., 2021; Lu et al., 2022a; Cao et al., 2023). Poly lactones possess good biodegradability and biocompatibility and have shown great potential due to their mechanical compatibility and ability to mix with other polymers (Fortelny et al., 2019; Tabasum et al., 2019; Yang et al., 2021; Backes et al., 2022). In particular, poly ε-caprolactone (PCL) has been utilized in different fields such as tissue engineering, drug delivery systems, microelectronics, and environmentally friendly packaging (Siddiqui et al., 2018; Zhang et al., 2019; Thakur et al., 2021; Backes et al., 2022; Lu et al., 2022b). It is one of the most important and widely studied poly-lactones thanks to its controllable polymerization characterization (Labet and Thielemans, 2009; Nuyken and Pask, 2013) and biodegradability (Bartnikowski et al., 2019; da Silva and de Torresi, 2019; Suzuki et al., 2021). This has led to numerous research including its catalytic systems, polymerization mechanisms, and processing techniques.

In most commercialized PCL synthesis, ring-opening polymerization (ROP) is the preferable route (Li et al., 2020; Rosa et al., 2021). This process is a one-step polymerization that can be catalysed by various metal complexes ranging from simple metal halides to complex organometallics (Kundys et al., 2018; De Hoe et al., 2022), and can be controlled in terms of the molecular weight (Mwt) and the polydispersity (Đ).

However, the difficulty of removing the catalyst residue and the cytotoxicity associated with such residues in the final product is the major problem that hinders PCL from biomedical applications (Gowda and Chakraborty, 2009; Hege and Schiller, 2014). To decrease the toxicity and improve the energy efficiency towards the principle of green chemistry, various catalyst systems, and processing techniques were studied. Among different catalysts that have been investigated, iron (III) halides were found to be an effective catalyst and can be used in fabricating biocompatible materials (Petrenko et al., 2011; Hege and Schiller, 2014). These studies have paved the way for intensifying the process. However, these reactions were found to be finished in hours even days, making the processing time-consuming and unflavoured for high product throughput (Engel et al., 2019; Dabbaghi et al., 2021).

Microwave heating (MWH) is a processing technique that delivers a fast polymerization rate and shortened reaction time from hours to minutes. Previous studies found that the reaction time could be reduced significantly when utilizing the MWH to the ROP of ε-caprolactone, compared to using the conventional heating (CH) method in identical conditions (Liao et al., 2002; Yu et al., 2003; Li et al., 2007; Nguyen et al., 2014; Fimberger and Wiesbrock, 2016). However, the majority of the studies focused on the dielectric materials and their interactions with the electric field (E-field), largely ignoring the presence of the magnetic field (H-field) in a microwave electromagnetic field (EMF) (Tanaka et al., 2008; Horikoshi et al., 2012). Some pioneer studies successfully applied the microwave H-field heating to superconducting materials, magnetic solids, ferrofluids, and aqueous electrolyte solutions (Ceylan et al., 2011; Horikoshi et al., 2012; Borsari et al., 2018; Loharkar et al., 2019; Siebert et al., 2019; Xiong et al., 2021; Chen et al., 2022). However, there is no research on using the microwave H-field heating method for polymerization chemistry.

The purpose of this work was to study the effect of potential parameters, such as input power and concentration of magnetic susceptible material, on the selective heating in the microwave magnetic heating method. Microwave electric heating is commonly used in chemical synthesis, however, as the most of the materials in a reaction can interact with the microwave and absorb the microwave electric energy, the energy cannot travel into the centre of the bulk before dissipated (Galan et al., 2017; Amini et al., 2021). This very small penetration depth of microwaves poses design challenges in the scale up of microwave processes (Zhang et al., 2017; Morte et al., 2019). On the other hand, in the microwave magnetic heating, most of the organic materials do not possess any magnetic susceptibility, and will not compete in absorbing the magnetic field energy. In fact, most of the magnetic field energy are potentially consumed by the magnetic susceptible catalyst, and because of their low concentration compared to the bulk material (normally less than 5% wt in a reaction), the magnetic field energy has greater potentials to penetrate deeper into the bulk compared to the microwave electric heating. Therefore, this allows the process to bypass the penetration depth obstacle while maintaining the bespoken microwave heating effect even in a scaled-up process.

This paper describes the first experimental studies of applying a magnetic susceptible catalyst and the microwave magnetic heating for the polymerization of the ε-caprolactone. The characteristics, kinetics, and mechanism of the polymerization initiated by $FeCl_3$ and Benzyl alcohol (BzOH) using microwave magnetic heating were reported and compared to identical reactions that were conducted with the conventional heating and the microwave electric heating methods. As PCL is commonly used for fabrication of biomaterials, the cytocompatibility of the produced polymer was investigated for future biological applications.

2 Experimental

2.1 Materials

$FeCl_3$ (97% purity) was bought from Sigma Aldrich. The sample was dried in an oven at 70°C for 1 day before moving it into a desiccator for storage at room temperature. The ε-caprolactone monomers (97% purity) and Benzyl alcohol (98% purity) were bought from Sigma Aldrich without further purification. Fetal bovine serum (FBS) was bought from Zhejiang Tianhang Biotechnology Co., Ltd. Phosphate buffered saline was bought from Cytiva. Anhydrous ethanol (≥99.7%) was purchased from Shanghai Titan Scientific Co., Ltd.

2.2 Reactor geometries

In conventional heating (CH) ROP reactions, a standard oil bath was used where oil temperature was controlled by a thermocouple in the oil bath. The temperature was also cross-referenced to an internal bulk temperature measurement using an OF probe. A single-mode Sairem MiniFlow 200SS operating at 2.45 GHz was used as the microwave generator for both microwave electric heating (EH) and microwave magnetic heating (HH) experiments. All EH ROP reactions were conducted using the MiniFlow with a TE cavity equipped with an optic fibre (OF) probe thermometer. The OF probe was inserted directly into the reaction mixture for accurate and immediate temperature feedback. In HH ROP reactions, a MiniFlow with a TM cavity was used. An OF probe was again used for temperature detection. The procedure and validation of the heating samples at electric and magnetic dominant locations are described in the Appendix.

2.3 Heating experiment procedures

In heating experiments, 18 mg of $FeCl_3$ was weighted and dissolved in 10 mL of the ε-caprolactone (CL) to make a solution of monomer to catalyst molar ratio ([M]:[C]) of 800:1. The solution was transferred into a reaction vessel for degasification. A quartz tube (diameter of 3 mm) with an open at the top was inserted into the rubber stopper on the sealed reaction vessel for the insertion of an OF thermometer, the sample was then sent for degasification. After degasification, the sample was sent to a TE cavity or a TM cavity for the EH or HH experiment.

2.4 ROP reaction procedure

In typical conventional heating (CH) ROP reaction, the monomer, catalyst, and initiator were weighted for specific [monomer]:[catalyst]; [initiator] ([M]:[C]:[I]) ratio (i.e., 36 mg of $FeCl_3$, 0.12 mL of BzOH, and 10 mL CL were weighted for [M]:[C]:[I] ratio of 400:1:5). These reactants were then transferred into separate reaction vessels, which was sealed with a rubber stopper, for degasification with argon. After 10 min of degasification, the monomer and initiator were transferred into a reaction vessel that contained the catalyst. The vessel was then immersed in an oil bath, which was preheated to the set temperature, to start the reaction.

During the kinetic study, 0.2 mL of the sample was sampled using a syringe. The obtained sample was transferred into a glass sample container and stored in the fridge at −20°C.

In the MWH reaction, identical preparation procedures as described in CH were conducted, but instead of sending to an oil bath, a TE cavity and a TM cavity were used for the EH and the HH, respectively. The internal bulk temperature was continuously monitored using an OF thermometer inserted directly into the reaction mixture *via* the quartz tube on the stopper. In these MWH experiments, the temperature measurements from OF probe were used to control the power input required to keep the bulk temperature constant at the target set point.

2.5 Analytical characterisation procedures

2.5.1 Gel permeation chromatography (GPC)

GPC characterization experiments were performed on a Polymer Labs GPC-120 instrument at 35°C equipped with a PLgel 5 μm Guard column and two PLgel 5 μ MIXED-E columns in series coupled with a refractive index detector using HPLC grade THF as the mobile phase at a flow of 1.0 cm^3 min^{-1}. The GPC was calibrated with polystyrene narrow polydispersity index (Đ) standards close to 1.00. All GPC equipment and standards were supplied by Polymer Laboratories (Varian). GPC data was analysed using the Cirrus GPC offline software package.

2.5.2 Nuclear magnetic resonance (NMR)

^{1}H NMR spectra were recorded at 25°C using a Bruker DPX-300 spectrometer (300 MHz). Chemical shifts were recorded in δ_H (ppm). Samples are prepared as solutions in $CDCl_3$. The monomer conversion was determined by comparing the integral of methylene proton resonance adjacent to the oxygen of the carbonyl group for the monomer (-CH2OCO-, δ = 4.24 ppm) and polymer (-CH2OCO-, δ = 4.07 ppm). An end-group analysis can also be done to identify the degree of polymerization (DP). It is done by comparing the integral of methylene proton resonance adjacent to the carbonyl group (H_x, δ = 4.1 ppm) to that of methylene proton of benzyl alcohol (H_x, δ = 5.1 ppm).

2.6 Cytotoxicity studies

The cytotoxicity of all the samples was determined by CCK-8 assay. The polymer sample produced with [M]:[C] ratio of 400:1 and 800:1 were first soaked with 75% ethanol solution for 2 h, then UV sterilized for 12 h 6 g of the sterilized sample was transferred into 6 mL of the culture media containing 15% fetal bovine serum (FBS) and soaked for 24 h to get leached out media. The soaked sample was centrifuged at 1000 rpm for 5 min and the supernatant was used for cell cytotoxicity studies.

A 5×10^3 cells/well was seeded for 24 h in a 96-well plate and incubated at 37°C with 5% CO_2. The media was then replaced with the prepared sample supernatant (100 μL). The plate was incubated at 37°C for 1 day, 3 days, and 5 days, accordingly in the CO_2 incubator.

The media were disposed of at the end of the incubation and washed with PBS solution 3 times before adding serum-free medium containing 10% of CCK-8 (100 μL). The samples were then incubated in the CO_2 incubator for 1 h. Absorbance was recorded using a Tecan Spark microplate reader at 450 nm.

3 Results and discussion

3.1 Heating experiments

In our previous study, we identified that the presence of the catalyst could have a significant effect on the heating of the bulk (Wang et al., 2017). Therefore, a series of heating experiments were conducted first to identify if the chosen catalyst is susceptible to microwave electromagnetic heating (EMH) and can be reflected by the increment of the solvent bulk temperature. Two EMH heating methods were used: a) microwave E-field heating (EH), where the E-field is at a dominant position, and b) microwave H-field heating (HH), where the H-field is at a dominant position. However, it should be noticed that although it is heated at an E-field or an H-field dominant position, there is still a presence of the other field heating the sample. For example, a weak E-field is still present when conducting an H-field heating experiment, and *vice versa*. No initiators were added to the system ensuring no polymerization occurs during the heating experiment. The temperature profile was monitored with time by the inserted optic fibre (OF) temperature sensor in the sample. The OF temperature sensor was reported to be able to achieve a direct measurement of the reaction medium bulk temperature by previous researchers (Robinson et al., 2010a; Robinson et al., 2010b; Adlington et al., 2014; Nguyen et al., 2014). The maximum input power was set to 150 W for all experiments unless mentioned otherwise. The temperature profiles and power profiles of the heating experiments were recorded by the MiniFlow and were shown in Figure 1 for both the EH and HH heating methods.

Figure 1 shows the temperature profiles and absorbed power variation with time during the EMH experiments for all samples. The power absorption was calculated as the difference between the

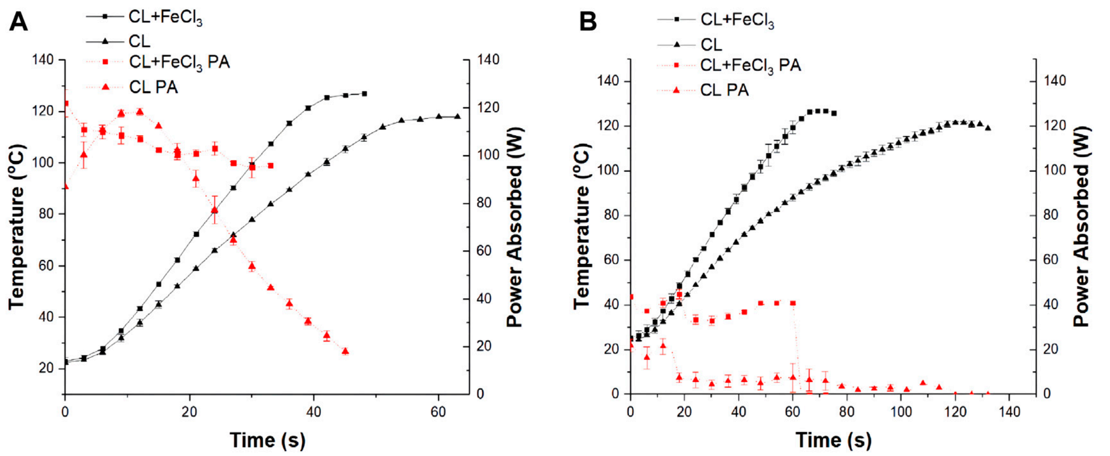

FIGURE 1
Example of typical temperature profile (black solid line) and power profile (red dot line) of CL and CL + FeCl$_3$ mixture (n = 5) using **(A)** EH and **(B)** HH heating methods at 150 W input power. PA, power absorbed.

incident and the reflected power during the experiment. It must be noted that impedance matching was only carried out during the onset of the heating trial and was not maintained continuously throughout the experiment. Therefore, the power absorption data may also be influenced by any differences in the reflected power due to impedance “mismatch” that potentially takes place during the duration of the experiment as the samples are heated up. As the result, a constant decreasing trend in the absorbed power profile was observed for all samples.

Figure 1A demonstrated the heating profile of the neat CL monomer on its own when no FeCl$_3$ or initiator was present, and the identical monomer with FeCl$_3$. The neat monomer was able to be heated efficiently with the E-field heating. However, when FeCl$_3$ was present in the monomer, the heating of the bulk was enhanced, i.e., a temperature difference of up to 20°C was obtained compared to the neat monomer at the same time mark. This temperature difference along with the additional 19 W absorbed by the FeCl$_3$ sample suggested that this additional power should be absorbed by FeCl$_3$ and distributed within the bulk to result in such temperature differences.

Meanwhile, reviewing the heating profile of the same samples in the H-field heating as shown in Figure 1B an even greater temperature difference (up to 33°C) was observed with a similar amount of additional power absorbed (around 20 W) by a the FeCl$_3$ sample in comparison to the EH heating experiment. This greater temperature difference was detected by the HH heating method, indicating a significantly stronger magnetic selective heating from the presence of the catalyst.

It should be reminded that the catalyst used in these heating experiments were in the molar ratio of 1:800 to the bulk media. With this little amount of the catalyst used, the catalyst must underwent excessive heating to contribute such observed temperature differences.

However, it should be noted that the MiniFlow can only detect the E-field energy that is being put into and reflected, ignoring the presence of the H-field energy. As the sample was located at the H-field dominant position where only a small amount of energy from the weak E-field was absorbed by the sample, and thus the reading of the power profiles was found to be lower compared to the EH heating experiment. But it should be reminded that this weak E-field heating together with the strong H-field heating contributes to the heating of the bulk in these HH experiments. To identify if the observed temperature difference purely originated from the weak E-field heating, another series of low-power EH experiments were conducted, and the temperature and power profiles were shown in Figure 2.

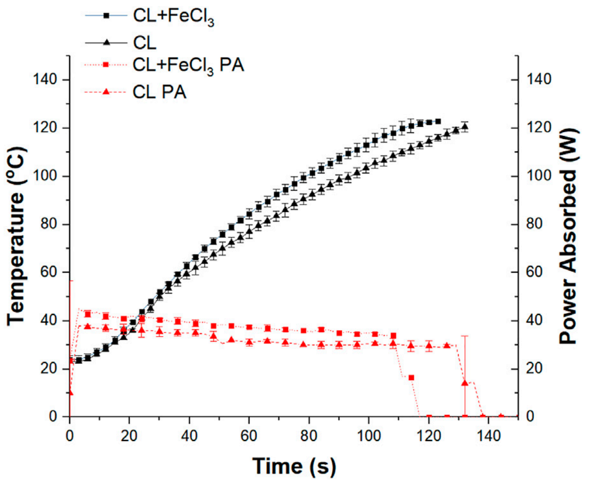

FIGURE 2
Temperature profile (black solid line) and power profile (red dot line) of CL and CL + FeCl$_3$ mixture (n = 5) using EH at 50 W input power.

In Figure 2, the CL sample took approximately 125 s to reach 120°C which was similar to the time required for CL in the H-field heating experiment shown in Figure 1B (120 s–120°C), this suggested that both samples should be experiencing a similar level of the E-field heating. Additionally, the power absorbed by the CL + FeCl$_3$ sample (≈40 W) is similar to that in the HH experiment at the beginning of the experiment. However, this time, the CL + FeCl$_3$ sample took around 120 s to reach 120°C rather than 60 s for the HH experiment. This obvious difference between the two heating profiles confirms that the

TABLE 1 Average results of ROP of CL with $FeCl_3$ and BzOH at various temperature at [M]:[C]:[I] ratio of 400:1:5.

Entry	Temperature (°C)	time (min)	Heating method	Mn^a (g mol^{-1})	Mp^a (g mol^{-1})	Đ^a	Conversion (%)
1	50	25	CH	3200	5000	1.42	59.2
2	50	25	EH	3500	5400	1.27	88.5
3	50	25	HH	4700	6600	1.37	91.5
4	75	25	CH	3900	6300	1.43	97.0
5	75	25	EH	4500	6200	1.33	99.9
6	75	25	HH	5000	8000	1.39	99.9
7	100	25	CH	3700	6700	1.31	84.3
8	100	25	EH	4200	8300	1.68	99.9
9	100	25	HH	4700	9700	1.55	96.3
10	125	25	CH	2500	5300	1.66	64.2
11	125	25	EH	3100	7100	1.97	76.6
12	125	25	HH	4300	9400	1.66	83.7
13	150	25	CH	1900	4900	1.81	62.1
14	150	25	EH	2700	6200	1.87	73.3
15	150	25	HH	3100	7900	1.83	81.7

[a] Determined by GPC, measured in THF, at 35°C.

[b] Determined by ^1H-NMR.

$FeCl_3$ should be experiencing significant H-field heating in the HH experiment and resulted in such heating enhancement of the bulk.

On the other hand, from this weak E-field heating experiment, it was also realized that the temperature differences observed in the EH experiment from Figure 1A were not reproduced in Figure 2. This suggested that such observed temperature difference in the EH experiment was only obvious at high input power levels.

From these heating experiments, it was noticed that the heating of the neat CL in the HH required an additional 60 s to reach the set temperature compared to the EH heating method, this was because the CL sample was only heated by the weak E-field present in the HH. Conversely, for the CL + $FeCl_3$ sample, it only required an additional 15 s to reach the set temperature compared to the EH heating method. Such a significant reduction in heating time (from 120 s to 60 s) in the heating of CL + $FeCl_3$ sample suggested that the magnetic susceptible $FeCl_3$ was significantly heated from the H-field so that it was able to achieve a similar heating performance compared to the EH. In the H-field heating, rather than a significant portion of the heating from the E-field, it should be that the catalyst was being selectively heated by the H-field and only a relatively minor part, in this case, was related to the weak E-field heating to the bulk.

From the heating experiments, we have demonstrated that the catalyst must experienced significant selective heating effects to contribute such different bulk heating performance, as the catalyst concentration used was only 0.125% molar ratio.

3.2 ROP reactions with various heating methods

A key aim of the present study was to define the effect that the presence of the selective heating effect on the catalyst has upon the performance of its catalytic activity in polymerization reactions. Thus, bulk ring-opening polymerization (ROP) of CL was conducted next using CH, EH, and HH heating methods. BzOH was chosen as the initiator because it is the most common alcohol used as the initiator in ROP reactions. Additionally, Hege and Schiller found that ROP using $FeCl_3$ performed best with BzOH as the initiator (Hege and Schiller, 2014). Therefore, BzOH was selected to be the initiator for all ROP reactions.

The influences of reaction conditions, including temperature, monomer to catalyst molar ratio ([M] [C] ratio), and input power was investigated. A wide range of temperatures from 50 to 150°C was selected, the latter of which is a typical operation temperature for ROP polymerization. In this study, three [M]:[C] ratios were used 400:1, 800:1, and 1600:1. and six different input power were studied, which were 25, 50, 75, 100, 125, and 150 W.

3.2.1 Effect of temperature

The effect of temperature on the bulk polymerization of CL initiated by $FeCl_3$ and BzOH was first investigated as shown in Table 1. At 50°C, a 60% conversion was achieved after 25 min by using the CH (Table 1 entry 1). The temperature was then increased to 75°C, and the polymerization reactions were able to achieve 97% conversion within 25 min (Table 1 entry 4). However, as the temperature was further increased to 100, 125, and 150°C, the polydispersity (Đ) started to get broaden, and the conversion dropped to 84%, 64%, and 62%, respectively at 25 min mark (Table 1 entry 7, 10, 13). This was due to the undesired transesterification side reactions taking place at elevated temperatures or at long reaction times leading to the formation of cyclic polymer or "back-biting" (Gong et al., 2021). As a result, the Đ value increased as the temperature increased as shown in Table 1 as well as from GPC trace shown in the support document Supplementary Figure S6).

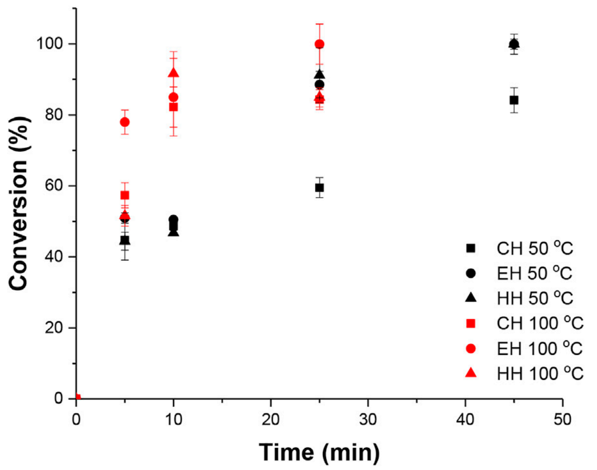

FIGURE 3
Comparison of conversion versus time plots for ROP of CL in CH (n = 3) using $FeCl_3$ between 50°C and 100°C.

These results from the CH experiment were then compared to those conducted with electromagnetic heating (EMH) including the EH and HH heating methods. It was observed that changing from the CH to the EMH, the conversion of the ROP at 50°C for 25 min was increased from 59% in the CH to 88% and 91% in the EH and HH heating methods, respectively (Table 1 Entry 1, 2 and 3). However, the EMH experiments followed the same trend as CH experiments that the product reached peak Mwt at 100°C, and started to show a reduction in the conversion and broadening in Đ at elevated temperatures.

Directly comparing Mwt results from the CH and the EMH, the EMH results showed improvements in the Mwt of produced polymer, in terms of M_n and M_p. e.g., at 150°C, the M_n value for the EH and the HH at 25 min were 2,700 and 3100 g mol^{-1} which was 35% and 55% higher than that in the CH. Improvement in Mwt was found to be more significant in HH than EH (typically ~15%–33% greater at each point compared to the EH results). This was hypothesized to be due to the difference in the heating mechanism as found in heating experiments, where both the monomer and the catalyst are susceptible to strong E-field heating, but only the catalyst is susceptible to strong H-field heating. Such differences in the heating could result in selective heating of the species that potentially affect the initiation and/or the propagation step of the polymerization. The heat concentrated around the monomer and/or the catalyst due to the selective heating could potentially promote the polymerization on the site and enhance the initiation and/or propagation.

To further elaborate on the effects of temperature on the polymerization, a series of kinetic studies were then conducted with three heating methods, detailed kinetic study plots are shown in the supporting documents Supplementary Figures S7–S9. Figure 3 demonstrates a comparison of kinetic studies between 50 and 100°C with the CH, the EH, and the HH. The blue markers are for reactions at 50°C and the red markers are for that at 100°C.

Inspecting Figure 3, when using 50°C as the reaction temperature, the initial reaction conversion was similar among the three heating methods up to 25 min mark. Whereas at 100°C, significant conversion differences were observed from 5 min mark (above 80% conversion for EMH heating methods and only around 55% for the CH heating method). This could potentially be a combination of higher reaction temperature and excessive exposure to microwave energy at the beginning of the heating step. A large amount of energy (up to 150 W) was being put into the system at the beginning of the reaction, and the time that the sample was exposed to such an amount of power before reaching the set temperature was significantly different for different reaction temperatures. The effects of microwave energy were investigated and will be discussed in later sections.

TABLE 2 Summary of the rate constant (Kapp) at different temperatures using CH, EH, and HH. Condition [CL]:[$FeCl_3$] = 400:1.

Temperature (°C)	CH	EH	HH
	kapp (min^{-1})	kapp (min^{-1})	kapp (min^{-1})
50	0.035	0.069	0.059
75	0.130	0.156	0.154
100	0.173	0.332	0.279

Based on the temperature study, we have identified that the raised reaction temperature can significantly accelerate the polymer propagation. In fact, in combination with magnetic selective heating effects, the catalyst reaction site would be at an elevated temperature to further accelerate the propagation rate, and thus a higher M_p results were obtained for HH experiments which are 17%–33% greater than the EH experiment at each reaction temperature.

3.2.2 Activation energy calculation

The previous empirical results suggested that the application of EMH heating methods promotes the reaction significantly, therefore, to identify if this purely originated from thermal effects, the activation energy required for the polymerization was studied next.

To do this, the rate of propagation (K_{app}) for each heating method at various temperature were calculated based on the kinetic plot of ln (M_0/M) *versus* reaction time conducted various temperatures. Kinetic plots for the CH, EH, and HH experiments can be found in the supporting document Supplementary Figures S10–S12, respectively. From the plots, the K_{app} value can be calculated by identifying the slope of the plot for first-order reactions. The summary of the K_{app} values is shown in Table 2.

Analysis of the kinetic plots, a straight-line relationship holds for ln (M_0)/M as a function of reaction time at 50–100°C. This linear relationship demonstrated that polymerization is a controlled first-order reaction. However, this relationship deviated from the trend line at 125 and 150°C. This was due to the competition in side reactions causing the reaction to losing its control. Therefore, only the controlled first-order reactions were selected to calculate the polymerization rate constant (K_{app}), based on the gradient of the kinetic plots from the ROP reactions and is summarised in Table 2.

Inspecting the data in Table 2 led to the conclusion that the K_{app} value of all the EH and the HH was at least 1.4 and 1.1 times higher than that from the CH experiment at the same bulk temperature. This again shows that the presence of selective heating in the EMH promotes the polymerization rate, as the EH heats both the

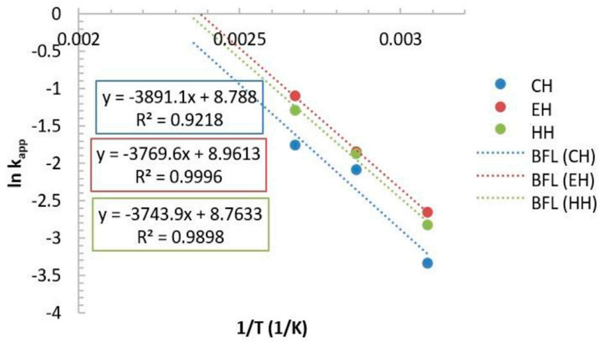

FIGURE 4
The relationship between lnKapp versus the reciprocal of absolute temperature. Condition [CL]: [$FeCl_3$] = 400:1.

monomer and the catalyst (reaction site) directly, while the HH primarily heats the catalyst. Both heating methods resulted in concentrated local heating above the measured bulk temperature which facilitated the reaction rate.

The activation energy of the polymerization was then established based on these temperatures by plotting ln (K_{app}) against 1/T for all heating methods. The Arrhenius plot is shown in Figure 4.

The Arrhenius plot was noted to have similar gradients among the three heating methods. From the plot, it was able to calculate the activation energy (E_a) using the Arrhenius equation. It was found that there were no significant differences in the E_a between all heating methods. Indeed, the E_a calculated for the CH, the EH, and the HH was 32.5, 31.3, and 31.1 kJ/mol, respectively. Such results suggested that the mechanism of the reaction was not altered by different heating methods. The observed differences in the K_{app} when the EMH was applied purely originated from thermal effects. The EMH heating methods potentially created heat concentration around/at the catalyst *via* selective heating, and accelerated the polymerisation of the monomer.

3.2.3 Effects of microwave electromagnetic energy

As previously mentioned, in a typical EMH experiment, the MiniFlow starts with putting maximum microwave EM energy (150 W) to the bulk to elevate the temperature to the desired point, once reaching and holding at the temperature, only minimized amount of energy was applied. In addition, a higher power would be required to hold at a higher temperature due to increased heat loss to the surrounding, an example of a typical temperature and power profile for EMH reaction can be found in the supporting document Supplementary Figure S13. Therefore, for reactions at 100°C, the bulk spent a long time (around 50 s) under high-intensity EM energy (150 W) compared to that at 50°C (around 20 s). In addition, the power required to maintain at 50°C and 100°C were different (around 10 W and 30 W for 50°C and 100°C, respectively). These empirical observations be the potential reason for the observed conversion differences at the beginning of the reaction at different temperatures.

To further understand this, the effects of different EM energy/power were then studied. Short reactions at different input powers with both the EH and the HH heating methods were studied. These reactions were conducted for 180 s at 100°C for all samples. The characteristics and yield data of polymer products for the set of reactions were contained in Tables 3, 4 for the EH and HH experiment, respectively.

Comparing the results from Table 3 to Table 4, at low input power (at 25 and 50 W), both EH and HH heating results were very similar in both yield and product polymer Mwt characteristics. However, by putting in more power, the differences in the conversion and Mwt became more significant between the two heating methods at identical conditions, i.e., up to 60% differences in M_n and 15% in conversion. Further inspecting the GPC trace from Figure 5, PCL produced from the HH at 150 W input power showed a signal trace from 10.9 min, whereas the GPC trace for the EH started from around 11.5 min. This difference in signal detection suggested that the Mwt of polymer produced from the HH was significantly higher than that obtained with the EH. These observations exhibited an identical trend as previous ROP studies showed in Table 1 where higher PCL Mwt were obtained with the HH than that with the EH, and a broadened GPC peak was found for the HH product than the EH product.

These scenarios showed that the differentiation between HH and EH in terms of Mwt and conversion was more significant at high input power. In the EH heating method, both the monomer and the catalyst compete in absorbing the E-field energy, therefore, the selective heating effect on the catalyst is not maximized. However, in the HH heating scenario, only the magnetic susceptible catalyst can absorb the H-field energy from the alternating EM field, this allows the catalyst to experience a stronger concentrated local heating compared to the EH heating method. This stronger magnetic selective heating effect provides a rapid increase in reaction temperature and achieves a higher local temperature than the bulk. As previously discussed, due to the selective heating of the catalyst in the HH experiment, the reaction site temperature could be significantly higher, and therefore caused the acceleration in the ROP and the side reactions which resulted in a higher product Mwt and a broadened peak distribution as we identified in the temperature study.

3.2.4 Effects of catalyst concentration

Previous studies have shown that if the species that is being selectively heated is presented in too small a quantity, the predominant heating effects from EMH would be diminished (Adlington et al., 2014). Therefore, ROP reactions with reduced catalyst load were also studied at 100°C, to investigate if the observed enhancement in the HH heating method would diminish at lower catalyst concentration. The obtained results are shown in Table 5, and the detailed results for the ROP at different catalyst loads at various temperatures were summarised in supporting documents Supplementary Tables S2, S3.

Inspecting Table 5, reducing the catalyst concentration significantly slow down the reaction because fewer reaction sites are available for the polymerisation, and the reaction time was extended from 25 to 120 min. In the meantime, more monomers were able to attach to a polymer chain, and thus, higher Mwt results were able to be achieved at identical conversion.

It was notice that Mwt results for the HH heating method were superior than the EH results at [M]:[C] ratios of 400:1 and 800:1, but such difference was diminished as the catalyst load was reduced to [M]:[C] ratio of 1600:1. For example, at [M]:[C] ratio of 400:1 and 800:1, the M_p results for the HH experiments were 17% and 12% higher than the EH experiments, respectively; but at [M]:[C] ratio of 1600:1,

TABLE 3 Average results of ROP of CL with $FeCl_3$ and BzOH using various input power at [M]:[C] ratio of 400:1 for 3 min with EH.

Input power (W)	Mn^a (g mol^{-1})	Mp^a (g mol^{-1})	Đ^a	Conversion (%)
25W	2100	2630	1.19	54.33
50W	2300	2900	1.21	65.63
75W	1620	2750	1.5	64.15
100W	2430	3040	1.232	71.67
125W	2460	3110	1.231	76.41
150W	2260	3080	1.31	79.67

[a]Determined by GPC, measured in THF, at 35°C.
[b]Determined by.^{1}H-NMR.

TABLE 4 Average results of ROP of CL with $FeCl_3$ and BzOH using various input power at [M]:[C] ratio of 400:1 for 3 min with HH.

Input power (W)	Mn^a (g mol^{-1})	Mp^a (g mol^{-1})	Đ^a	Conversion (%)
25W	2090	2070	1.41	50.73
50W	2210	3400	1.39	55.15
75W	2580	4360	1.38	67.32
100W	2700	4000	1.31	82.30
125W	2700	4060	1.53	82.72
150W	3020	3870	1.37	83.22

[a]Determined by GPC, measured in THF, at 35°C.
[b]Determined by.^{1}H-NMR.

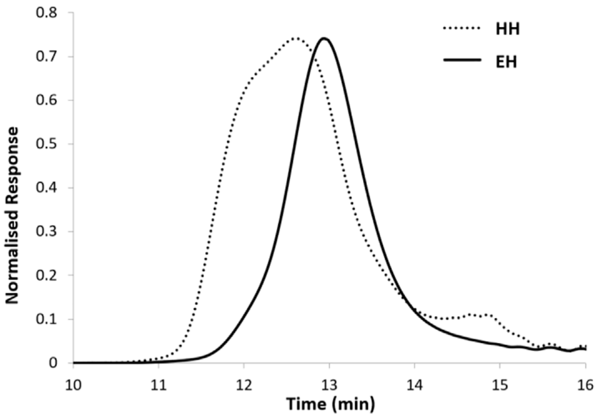

FIGURE 5
Comparison of the GPC trace of the product polymer synthesized with identical reaction time under E-field (solid line) and H-field (dot line) heating at a power of 150 W. Condition [CL]:[$FeCl_3$] = 400:1.

the M_p result for EH experiment is 4% greater than the HH experiment. This suggested that the reduction in the catalyst was more significant in the HH than the EH, as the $FeCl_3$ is the main species that is susceptible to the H-field heating.

If a specie that undergoes the magnetic selective heating is too small in quantity, the predominant heating method remains as EH due to the presence of the electric field. As a result, comparable product Mwt and conversion between the EH and the HH were obtained. This observation agrees with our previous study; (Wang et al., 2017); however, it should be noted that although no superior Mwt and conversion were obtained from the HH heating method, comparable results were still obtainable compared to the EH heating method. Considering that as both monomer and catalyst absorb the E-field energy, less energy can travel to the centre of the bulk and result in a small penetration depth in the EH heating method. On the other hand, only the catalyst which is in a small amount is absorbing the H-field energy, the H-field energy would be able to travel further into the bulk, therefore, providing more opportunities in scaling up the process and potentially overcome the design challenges in the EH heating methods related to the penetration depth.

3.3 Cytotoxicity studies

CCK-8 cell viability assay was performed to assess the polymer cytotoxicity and the results were summarised in Figure 6. As shown in the Figure, it is very obvious that a distinct cell toxicity between the polymer produced with [M]:[C] ratio of 400:1 and 800:1. For PCL produced with [M]:[C] ratio of 800:1, the cell viability maintains above 70% throughout the testing period, suggesting that the polymer remains non-toxic to cells. On the other hand, the polymer produced with [M]:[C] ratio of 400:1 has a detrimental effect to cell over the testing period. This was due to a higher concentration of the catalyst used in the synthesis.

TABLE 5 Average results of ROP of CL with $FeCl_3$ and BzOH at various [M]:[C] ratios at 100°C.

Entry	[M]:[C]	Time (min)	Heating method	M_n[a] ($gmol^{-1}$)	M_p[a] ($gmol^{-1}$)	Đ[a]	Conversion[b] (%)
1	400:1	25	CH	3700	6700	1.31	84.3
2	400:1	25	EH	4200	8300	1.68	99.9
3	400:1	25	HH	4700	9700	1.55	96.3
4	800:1	45	CH	5000	7900	1.56	63.6
5	800:1	45	EH	5700	9800	1.46	76.4
6	800:1	45	HH	6300	11000	1.44	79.1
7	1600:1	120	CH	6700	8900	1.23	51.7
8	1600:1	120	EH	7500	10100	1.20	71.1
9	1600:1	120	HH	7500	9700	1.24	67.9

[a]Determined by GPC, measured in THF, at 35 C.
[b]Determined by.^{1}H-NMR.

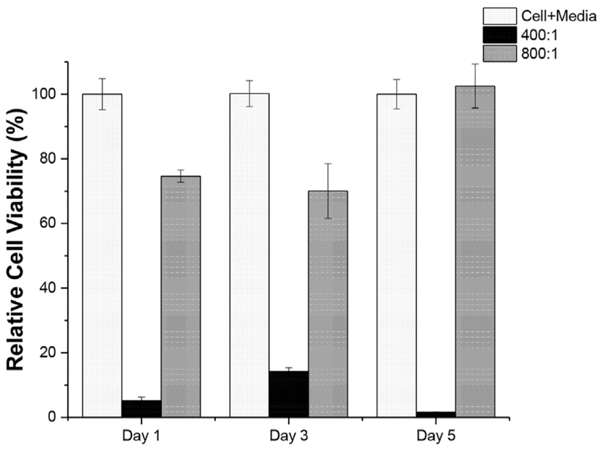

FIGURE 6
Percent cell viability of Panc02 cells at day 1, 3, and 5 (n = 5) for Cell + Media sample and PCL polymer produced with [M]:[C] ratio of 400:1 and 800:1. Values are expressed as relative % viability; mean ± SD.

Although $FeCl_3$ was can be used in fabrication of biocompatible materials (Petrenko et al., 2011; Hege and Schiller, 2014), the cytotoxicity of the produced material still needs to be assessed. The result shows that the amount of $FeCl_3$ needs to be controlled properly as a high $FeCl_3$ load ([M]:[C] ratio of 400:1) condition is harmful to cells, but if controlled at a proper level (i.e., at [M]:[C] ratio of 800:1) the produced PCL is non-toxic to the cell and can be potentially used as cyto-compatible materials.

4 Conclusion

For the first time, microwave magnetic heating (HH), where the magnetic field (H-field) from an electromagnetic field is dominant, is applied to the bulk ROPs of a lactone monomer with a magnetic susceptible and biocompatible catalyst. Superior Mwt were found in the HH at a high catalyst load compared to EH and CH methods, indicating the efficiency of the magnetic susceptible catalyst was enhanced by the HH. However, the activation energy for all heating methods was similar, suggesting the polymerization mechanism was not affected by the heating method and the observed differences in the EMH methods purely originated from thermal effects. Reducing the catalyst load diminishes the Mwt differences between the EH and HH methods. This could potentially be due to the species that are susceptible to the H-field heating being present in smaller quantities. In such case, the selective H-field heating could not provide a superior concentrated local heating than the EH, but comparable results were still achievable in the HH at low catalyst load, suggesting that the HH could still be a potential alternative heating method to the EH. Cytocompatibility studies showed the produced PCL is harmless when the catalyst load is controlled at the proper level.

Data availability statement

The original contributions presented in the study are included in the article/Supplementary Material, further inquiries can be directed to the corresponding authors.

Author contributions

Experiment design: KW, MN, AAD, GD, and DJI; Experiments: KW; Simulation: AAD; Data analysis: KW, MN, AAD, GD, and DJI; Manuscript writing: KW, MN, AAD, GD, and DJI.

Acknowledgments

The authors wish to thank the Institute for Frontier Medical Technology at the Shanghai University of Engineering Science and the University of Nottingham for the support of the present work.

Conflict of interest

The authors declare that the research was conducted in the absence of any commercial or financial relationships that could be construed as a potential conflict of interest.

Publisher's note

All claims expressed in this article are solely those of the authors and do not necessarily represent those of their affiliated organizations, or those of the publisher, the editors and the reviewers. Any product that may be evaluated in this article, or claim that may be made by its manufacturer, is not guaranteed or endorsed by the publisher.

Supplementary material

The Supplementary Material for this article can be found online at: https://www.frontiersin.org/articles/10.3389/fbioe.2023.1123477/full#supplementary-material

References

Adlington, K., McSweeney, R., Dimitrakis, G., Kingman, S. W., Robinson, J. P., and Irvine, D. J. (2014). Enhanced '*in situ*'catalysis via microwave selective heating: catalytic chain transfer polymerisation. *RSC Adv.* 4, 16172–16180. doi:10.1039/c4ra00907j

Amini, A., Latifi, M., and Chaouki, J. (2021). Electrification of materials processing via microwave irradiation: A review of mechanism and applications. *Appl. Therm. Eng.* 193, 117003. doi:10.1016/j.applthermaleng.2021.117003

Backes, E. H., Harb, S. V., Beatrice, C. A. G., Shimomura, K. M. B., Passador, F. R., Costa, L. C., et al. (2022). Polycaprolactone usage in additive manufacturing strategies for tissue engineering applications: A review. *J. Biomed. Mater. Res. Part B-Appl. Biomater.* 110, 1479–1503. doi:10.1002/jbm.b.34997

Bartnikowski, M., Dargaville, T. R., Ivanovski, S., and Hutmacher, D. W. (2019). Degradation mechanisms of polycaprolactone in the context of chemistry, geometry and environment. *Prog. Polym. Sci.* 96, 1–20. doi:10.1016/j.progpolymsci.2019.05.004

Borsari, E., Freire, B. G. G., Garcia, F. G., Silva, M. S., Silva, C. C., and Simoes, A. Z. (2018). Microwave-hydrothermal synthesis of Y3Fe3.35Al1.65O12 nanoparticles for magneto-hyperthermia application. *J. Mater. Sci.Mater. Electron.* 29, 18020–18029. doi:10.1007/s10854-018-9988-x

Cao, X., Luo, Q., Song, F., Liu, G., Chen, S., Li, Y., et al. (2023). Effects of oxidative torrefaction on the physicochemical properties and pyrolysis products of hemicellulose in bamboo processing residues. *Indust. Crops Prod.* 191, 115986. doi:10.1016/j.indcrop.2022.115986

Ceylan, S., Coutable, L., Wegner, J., and Kirschning, A. (2011). Inductive heating with magnetic materials inside flow reactors. *Chem.A Eur. J.* 17, 1884–1893. doi:10.1002/chem.201002291

Chen, Y. Q., Wang, Y. X., Zhang, F., Li, H. X., Dong, B. B., Min, Z. Y., et al. (2022). Preparation of special ceramics by microwave heating: a review. *J. Inorg. Mater.* 37, 841–852.

da Silva, A. C., and de Torresi, S. I. C. (2019). Advances in conducting, biodegradable and biocompatible copolymers for biomedical applications. *Front. Mater.* 6, 98. doi:10.3389/fmats.2019.00098

Dabbaghi, A., Ramazani, A., Farshchi, N., Rezaei, A., Bodaghi, A., and Rezayati, S. (2021). Synthesis, physical and mechanical properties of amphiphilic hydrogels based on polycaprolactone and polyethylene glycol for bioapplications: A review. *J. Indust. Eng. Chem.* 101, 307–323. doi:10.1016/j.jiec.2021.05.051

De Hoe, G. X., Sucu, T., and Shaver, M. P. (2022). Sustainability and polyesters: Beyond metals and monomers to function and fate. *Accounts Chem. Res.* 55, 1514–1523. doi:10.1021/acs.accounts.2c00134

Engel, J., Cordellier, A., Huang, L., and Kara, S. (2019). Enzymatic ring-opening polymerization of lactones: Traditional approaches and alternative strategies. *Chemcatchem* 11, 4983–4997. doi:10.1002/cctc.201900976

Fimberger, M., and Wiesbrock, F. (2016). "Microwave-assisted synthesis of polyesters and polyamides by ring-opening polymerization," in *Microwave-assisted polymer synthesis*, 149–182.

Fortelny, I., Ujcic, A., Fambri, L., and Slouf, M. (2019). Phase structure, compatibility, and toughness of PLA/PCL blends: A review. *Front. Mater.* 6, 206. doi:10.3389/fmats.2019.00206

Galan, A.-M., Calinescu, I., Trifan, A., Winkworth-Smith, C., Calvo-Carrascal, M., Dodds, C., et al. (2017). New insights into the role of selective and volumetric heating during microwave extraction: Investigation of the extraction of polyphenolic compounds from sea buckthorn leaves using microwave-assisted extraction and conventional solvent extraction. *Chem. Eng. Process. Process Intensif.* 116, 29–39. doi:10.1016/j.cep.2017.03.006

Gong, C. H., Li, J. X., Yi, C. W., and Qu, S. L. (2021). Catalytic regulation of oligomers in polycaprolactone. *Mol. Catal.* 508, 111594. doi:10.1016/j.mcat.2021.111594

Gowda, R. R., and Chakraborty, D. (2009). Environmentally benign process for bulk ring opening polymerization of lactones using iron and ruthenium chloride catalysts. *J. Mol. Catal. A Chem.* 301, 84–92. doi:10.1016/j.molcata.2008.11.010

Hege, C. S., and Schiller, S. M. (2014). Non-toxic catalysts for ring-opening polymerizations of biodegradable polymers at room temperature for biohybrid materials. *Green Chem.* 16, 1410–1416. doi:10.1039/c3gc42044b

Horikoshi, S., Sumi, T., and Serpone, N. (2012). Unusual effect of the magnetic field component of the microwave radiation on aqueous electrolyte solutions. *J. Microw. Power Electromagn. Energy* 46, 215–228. doi:10.1080/08327823.2012.11689838

Kundys, A., Bialecka-Florjanczyk, E., Fabiszewska, A., and Malajowicz, J. (2018). Candida antarctica lipase B as catalyst for cyclic esters synthesis, their polymerization and degradation of aliphatic polyesters. *J. Polym. Environ.* 26, 396–407. doi:10.1007/s10924-017-0945-1

Labet, M., and Thielemans, W. (2009). Synthesis of polycaprolactone: a review. *Chem. Soc. Rev.* 38, 3484–3504. doi:10.1039/b820162p

Li, H., Liao, L., and Liu, L. (2007). Kinetic investigation into the non-thermal microwave effect on the ring-opening polymerization of ε-caprolactone. *Macromol. rapid Commun.* 28, 411–416. doi:10.1002/marc.200600648

Li, F. H., Shi, Y., Li, P. Z., and Jiang, T. C. (2020). Research progress of ring-opening polymerization of epsilon-caprolactone initiated by degradable biopolymers. *Curr. Org. Chem.* 24, 1507–1516. doi:10.2174/1385272824999200709125407

Li, X., Sun, H., Li, H., Hu, C., Luo, Y., Shi, X., et al. (2021). Multi-responsive biodegradable cationic nanogels for highly efficient treatment of tumors. *Adv. Funct. Mater.* 31, 2100227. doi:10.1002/adfm.202100227

Liao, L., Liu, L., Zhang, C., He, F., Zhuo, R., and Wan, K. (2002). Microwave-assisted ring-opening polymerization of ϵ-caprolactone. *J. Polym. Sci. Part A Polym. Chem.* 40, 1749–1755. doi:10.1002/pola.10256

Loharkar, P. K., Ingle, A., and Jhavar, S. (2019). Parametric review of microwave-based materials processing and its applications. *J. Mater. Res. Technology-Jmr&T* 8, 3306–3326. doi:10.1016/j.jmrt.2019.04.004

Lu, Y., Gao, Y., Yang, H., Hu, Y., and Li, X. (2022a). Nanomedicine-boosting icaritin-based immunotherapy of advanced hepatocellular carcinoma. *Mil. Med. Res.* 9, 69. doi:10.1186/s40779-022-00433-9

Lu, Y., Luo, Q., Jia, X., Tam, J. P., Yang, H., Shen, Y., et al. (2022b). Multidisciplinary strategies to enhance therapeutic effects of flavonoids from Epimedii Folium: Integration of herbal medicine, enzyme engineering, and nanotechnology. *J. Pharm. Anal.* doi:10.1016/j.jpha.2022.12.001

Morte, M., Dean, J., Kitajima, H., and Hascakir, B. (2019). Increasing the penetration depth of microwave radiation using acoustic stress to trigger piezoelectricity. *Energy Fuels* 33, 6327–6334. doi:10.1021/acs.energyfuels.9b01150

Nguyen, N. T., Greenhalgh, E., Kamaruddin, M. J., Carmichael, K., Dimitrakis, G., Kingman, S. W., et al. (2014). Understanding the acceleration in the ring-opening of lactones delivered by microwave heating. *Tetrahedron* 70, 996–1003. doi:10.1016/j.tet.2013.11.031

Nuyken, O., and Pask, S. D. (2013). Ring-opening polymerization—an introductory review. *Polymers* 5, 361–403. doi:10.3390/polym5020361

Petrenko, Y. A., Gurin, I. V., Volkova, N. A., Mazur, S. P., and Sandomirskii, B. P. (2011). The use of catalytic carbon deposits as 3D carriers for human bone marrow stromal cells. *Bull. Exp. Biol. Med.* 151, 539–542. doi:10.1007/s10517-011-1376-y

Robinson, J., Kingman, S., Irvine, D., Licence, P., Smith, A., Dimitrakis, G., et al. (2010a). Understanding microwave heating effects in single mode type cavities—theory and experiment. *Phys. Chem. Chem. Phys.* 12, 4750–4758. doi:10.1039/b922797k

Robinson, J., Kingman, S., Irvine, D., Licence, P., Smith, A., Dimitrakis, G., et al. (2010b). Electromagnetic simulations of microwave heating experiments using reaction vessels made out of silicon carbide. *Phys. Chem. Chem. Phys.* 12, 10793–10800. doi:10.1039/c0cp00080a

Rosa, R. P., Ferreira, F. V., and Lona, L. M. F. (2021). Modeling of ring opening polymerization: A short review with insights on how to develop the method of moments. *Chem. Eng. Sci.* 246, 116934. doi:10.1016/j.ces.2021.116934

Siddiqui, N., Asawa, S., Birru, B., Baadhe, R., and Rao, S. (2018). PCL-based composite scaffold matrices for tissue engineering applications. *Mol. Biotechnol.* 60, 506–532. doi:10.1007/s12033-018-0084-5

Siebert, J. P., Hamm, C. M., and Birkel, C. S. (2019). Microwave heating and spark plasma sintering as non-conventional synthesis methods to access thermoelectric and magnetic materials. *Appl. Phys. Rev.* 6, 041314. doi:10.1063/1.5121442

Suzuki, M., Tachibana, Y., and Kasuya, K. (2021). Biodegradability of poly(3-hydroxyalkanoate) and poly(ε-caprolactone) via biological carbon cycles in marine environments. *Polym. J.* 53, 47–66. doi:10.1038/s41428-020-00396-5

Tabasum, S., Younas, M., Zaeem, M. A., Majeed, I., Majeed, M., Noreen, A., et al. (2019). A review on blending of corn starch with natural and synthetic polymers, and inorganic nanoparticles with mathematical modeling. *Int. J. Biol. Macromol.* 122, 969–996. doi:10.1016/j.ijbiomac.2018.10.092

Tanaka, M., Kono, H., and Maruyama, K., Selective heating mechanism of magnetic metal oxides by alternating magnetic field in microwave sintering process. arXiv preprint arXiv:0806.3055 (2008).

Thakur, M., Majid, I., Hussain, S., and Nanda, V. (2021). Poly(ε-caprolactone): A potential polymer for biodegradable food packaging applications. *Packag. Technol. Sci.* 34, 449. doi:10.1002/pts.2572

Tsang, Y. F., Kumar, V., Samadar, P., Yang, Y., Lee, J., Ok, Y. S., et al. (2019). Production of bioplastic through food waste valorization. *Environ. Int.* 127, 625–644. doi:10.1016/j.envint.2019.03.076

Wang, K. Y., Dimitrakis, G., and Irvine, D. J. (2017). Exemplification of catalyst design for microwave selective heating and its application to efficient *in situ* catalyst synthesis. *Chem. Eng. Process.-Process Intensif.* 122, 389–396. doi:10.1016/j.cep.2017.01.012

Xiong, G. W., Jia, J., Zhao, L. L., Liu, X. Y., Zhang, X. L., Liu, H., et al. (2021). Non-thermal radiation heating synthesis of nanomaterials. *Sci. Bull.* 66, 386–406. doi:10.1016/j.scib.2020.08.037

Yang, X. J., Wang, Y. T., Zhou, Y., Chen, J. Y., and Wan, Q. B. (2021). The application of polycaprolactone in three-dimensional printing scaffolds for bone tissue engineering. *Polymers* 13, 2754. doi:10.3390/polym13162754

Yu, Z., Liu, L., and Zhuo, R. (2003). Microwave-improved polymerization of ϵ-caprolactone initiated by carboxylic acids. *J. Polym. Sci. Part A Polym. Chem.* 41, 13–21. doi:10.1002/pola.10546

Zhang, Y. Z., Hwang, J. Y., Peng, Z. W., Andriese, M., Li, B. W., Huang, X. D., et al. (2017). "Penetration depth of microwave in tire rubber," in 8th International Symposium on High-Temperature Metallurgical Processing, San Diego, CA, 403–410.

Zhang, Y. B., Liu, X. C., Zeng, L. D., Zhang, J., Zuo, J. L., Zou, J., et al. (2019). Tissue engineering: Polymer fiber scaffolds for bone and cartilage tissue engineering (adv. Funct. Mater. 36/2019). *Adv. Funct. Mater.* 29, 1970246. doi:10.1002/adfm.201970246

frontiers | Frontiers in Bioengineering and Biotechnology

TYPE Original Research
PUBLISHED 16 March 2023
DOI 10.3389/fbioe.2023.1130523

Check for updates

OPEN ACCESS

EDITED BY
Yu Luo,
Shanghai University of Engineering Sciences, China

REVIEWED BY
Xiaojun Zhou,
Donghua University, China
Ricardo João Borges Pinto,
University of Aveiro, Portugal

*CORRESPONDENCE
Chunpu Wang,
✉ W13703146012@126.com

SPECIALTY SECTION
This article was submitted to Nanobiotechnology, a section of the journal Frontiers in Bioengineering and Biotechnology

RECEIVED 23 December 2022
ACCEPTED 09 March 2023
PUBLISHED 16 March 2023

CITATION
Ji Y and Wang C (2023), Magnetic iron oxide nanoparticle-loaded hydrogels for photothermal therapy of cancer cells. *Front. Bioeng. Biotechnol.* 11:1130523. doi: 10.3389/fbioe.2023.1130523

COPYRIGHT
© 2023 Ji and Wang. This is an open-access article distributed under the terms of the Creative Commons Attribution License (CC BY). The use, distribution or reproduction in other forums is permitted, provided the original author(s) and the copyright owner(s) are credited and that the original publication in this journal is cited, in accordance with accepted academic practice. No use, distribution or reproduction is permitted which does not comply with these terms.

Magnetic iron oxide nanoparticle-loaded hydrogels for photothermal therapy of cancer cells

Yunfei Ji[1] and Chunpu Wang[2]*

[1]Department of Critical Care Medicine, Chengde Central Hospital, Chengde, Hebei, China, [2]Department of Cardiothoracic Surgery, Chengde Central Hospital, Chengde, Hebei, China

Introduction: Non-invasive photothermal therapy (PTT) is a competitive treatment for solid tumors, while the efficacy is largely dependent on the effective retention of photothermal converters in tumor tissues.

Methods: Herein, the development of iron oxide (Fe_3O_4) nanoparticle-loaded alginate (ALG) hydrogel platform for PTT of colorectal cancer cells is reported. Fe_3O_4 nanoparticles synthesized *via* coprecipitation method after reaction of 30 min have a small size (61.3 nm) and more suitable surface potential, and can mediate PTT under near-infrared (NIR) laser irradiation. The premix of Fe_3O_4 nanoparticles and ALG hydrogel precursors can be gelatinized by Ca^{2+}-mediated cross-linking to form this therapeutic hydrogel platform.

Results: The formed Fe_3O_4 nanoparticles can be effectively taken up by CT26 cancer cells and induce the death of CT26 cells *in vitro* under NIR laser irradiation because of their excellent photothermal property. In addition, Fe_3O_4 nanoparticle-loaded ALG hydrogels show negligible cytotoxicity at the studied concentration range, but can significantly kill cancer cells after PTT effect.

Conclusion: This ALG-based hydrogel platform provides a valuable reference for subsequent in vivo studies and other related studies on Fe_3O_4 nanoparticle-loaded hydrogels.

KEYWORDS

iron oxide nanoparticles, hydrogels, cancer therapy, photothermal therapy, light

1 Introduction

Cancer has long been one of the most lethal diseases that threat human health (Navya et al., 2019; Ding et al., 2022; Jing et al., 2022). Although surgery, chemotherapy, and radiotherapy are the mainstays of cancer treatment in the past, their limitations such as low specificity and high risk of recurrence, have forced researchers to divert their attention beyond these traditional treatments to explore more effective therapy (Meng et al., 2020; Caballero et al., 2022). Photothermal therapy (PTT) is a very promising cancer treatment modality emerging in recent years (Zhang et al., 2020; Dong et al., 2021). Utilizing photothermal converters to capture and transform external light, the local heat generated during PTT can induce intracellular protein denaturation and apoptosis. Especially for tumor tissues with dense blood vessels and hindered heat dissipation, PTT is an extremely promising method for tumor ablation (Cristofolini et al., 2016). Gold nanoparticles, carbon-based nanomaterials, and some small-molecule dyes have been used as photothermal agents for cancer PTT (Liu et al., 2007; Bardhan et al., 2011; Espinosa et al., 2016). Unfortunately, the applications of most of these materials are limited due to their low retention and potential toxicity (Espinosa et al., 2016). Therefore, it is very important to explore safe and degradable photothermal agents. Biodegradable iron oxide (Fe_3O_4) nanoparticles have been approved by the Food and Drug Administration (FDA) as a magnetic resonance imaging (MRI) contrast agent. In addition, the strong absorption of Fe_3O_4 nanoparticles in the near-infrared (NIR) window can be utilized for PTT (Shubayev et al., 2009; Anselmo and Mitragotri, 2015).

In general, many nanoparticles after intravenous injection are readily taken up by macrophages in the blood circulation and cleared by the reticuloendothelial system, thus hindering the aggregation of nanoparticles in tumors (Li et al., 2014). Therefore, the reliability of the carriers is of great significance for the performance of the anti-tumor ability of the nano-formulations. Hydrogels are a burgeoning class of three-dimensional polymer networks (Griffin et al., 2015; Vegas et al., 2016; Puiggalí-Jou et al., 2021). As a drug delivery system, hydrogels can not only release drugs controllably to fully exert anticancer efficacy, but also obviously weaken systemic toxicity in the form of intravenous administration. In addition, such hydrogel-based therapeutic platforms can reduce the numbers of drug administrations while maintaining biosafety (Almawash et al., 2022). Currently, alginate (ALG)-based hydrogels have enabled great advances in biomedicine due to their non-immunogenicity, excellent biocompatibility, and mild gel-forming conditions. ALG is a natural linear anionic polymer that can crosslink with divalent cations to form hydrogels (Lee and Mooney, 2012; Liu et al., 2021). By mixing with ALG hydrogel precursors and forming hydrogels after injection, many hydrophilic drugs and nanoparticles can be easily loaded and aggregated in tumor tissues with a relatively longer residence time after administration to exert therapeutic effects (Kim and Martin, 2006; Goncalves et al., 2014). However, the use of ALG hydrogels for loading of Fe_3O_4 nanoparticles for effective cancer PTT has not been explored.

In this work, a Fe_3O_4 nanoparticle-loaded hydrogel (Fe_3O_4 hydrogel) was constructed for cancer PTT. Fe_3O_4 nanoparticles were synthesized by chemical synthesis and mixed with ALG hydrogel precursors to form a homogeneous injectable solution. The Fe_3O_4 hydrogel was then successfully prepared *in vitro* by mixing with Ca^{2+} solution at a concentration similar to that in biological tissues. After NIR irradiation, the cell viability of CT26 cells co-incubated with Fe_3O_4 hydrogels was significantly lower than that in the control group, and the photothermal killing ability of the Fe_3O_4 hydrogels was not shielded by the ALG hydrogel carrier. The Fe_3O_4 nanoparticle-loaded hydrogels reported in this study significantly inhibited the viability of colorectal cancer cells.

2 Materials and methods

2.1 Materials

Ferrous chloride tetrahydrate ($FeCl_2$ $4H_2O$), ferric chloride hexahydrate ($FeCl_3$ $6H_2O$), sodium hydroxide (NaOH) and ALG were purchased from Shanghai Sinopharm Chemical Reagent Co., RPMI 1640 cell culture medium, fetal bovine serum (FBS), and penicillin-streptomycin were obtained from Gibco (Grand Island, NY, United States). Cell counting kit-8 (CCK-8) was purchased from Dojindo Laboratories (Kumamoto, Japan). Ultrapure water used in the experiments was prepared using a water purification system (PALL Cascada, MI, United States).

2.2 Characterization techniques

The UV-visible spectra of Fe_3O_4 nanoparticles were characterized by Persee spectrophotometer (TU-1810, Beijing, China). The surface morphologies of Fe_3O_4 hydrogels were observed using a scanning electron microscope (SEM, HITACHI, Japan). The hydrodynamic diameters and zeta potentials of Fe_3O_4 nanoparticles were measured using a Zetasizer Nano-series (Nano-ZS90, Malvern, United Kingdom). The Fe concentrations were measured by using an inductively coupled plasma atomic emission spectroscopy (ICP-AES) system (Hudson, NH, United States).

2.3 Synthesis of Fe_3O_4 nanoparticles

Fe_3O_4 nanoparticles were synthesized according to a previous report (Hu et al., 2015). In brief, 178 mg $FeCl_2$ $4H_2O$ and 314 mg $FeCl_3$ $6H_2O$ were dissolved in deionized (DI) water. Then 10 mL of NaOH solution (200 mg/mL) was added to the above solution. After mixing well, the solution was placed in a water bath at 80°C for 30 min or 2 h, respectively. The obtained samples were used to evaluate the influence of the reaction times on the properties of the nanoparticles. Subsequently, the mixed solution was placed on a magnetic stirrer to precipitate the synthesized Fe_3O_4 nanoparticles, and the upper liquid was discarded. Then Fe_3O_4 nanoparticles were dispersed in 10 mL water under sonication. The above steps were repeated at least 5 times to purify the Fe_3O_4 nanoparticles.

2.4 Synthesis of Fe_3O_4 hydrogels

To prepare Fe_3O_4 hydrogels, Fe_3O_4 nanoparticles were mixed with ALG solution to obtain AF mixture solution and the solution was then injected into Ca^{2+} (1.8 mM) solution. AF solutions at different concentrations of ALG (0.5, 1, 2.5, 5, 10 μg/mL) were slowly injected into the Ca^{2+} solution (1.8 mM). Then photographs were taken at different times after injection of solutions.

2.5 Evaluation of *in vitro* photothermal effect

To evaluate the photothermal properties of Fe_3O_4 nanoparticles and Fe_3O_4 hydrogels, 200 μL of Fe_3O_4 solution or Fe_3O_4 hydrogels at the Fe concentration of 200 μg/mL were placed in a 96-well plate. Then, 808 nm laser at different power densities (0.5, 1.0, and 1.5 W/cm^2) was used to irradiate the solutions for 5 min. Thermal images of solutions were obtained using a thermal infrared camera and the temperatures of the solution were recorded under laser irradiation. To investigate the effect of Fe concentrations on the photothermal properties, Fe_3O_4 nanoparticles or Fe_3O_4 hydrogels at different Fe concentrations (100, 200, 350, 500 μg/mL) were irradiated by

808 nm laser (1 W/cm^2) for 5 min. DI water was used as the control group. These solutions were irradiated by a laser at the power density of 1 W/cm^2. The laser was turned on/off every 5 min for 50 min to evaluate the photothermal stability of Fe_3O_4 nanoparticles and Fe_3O_4 hydrogels.

2.6 Evaluation of *in vitro* cellular uptake

CT26 cancer cells were cultured in RPMI 1640 cell medium containing penicillin, streptomycin and 10% FBS at 37°C and 5% CO_2. The cells were incubated with Fe_3O_4 nanoparticles at the Fe concentration of 100 μg/mL for different time. The cellular uptake efficacy was evaluated using ICP-AES.

2.7 Evaluation of *in vitro* cytotoxicity

The cytotoxicity of CT26 cancer cells after incubation with Fe_3O_4 nanoparticles or Fe_3O_4 hydrogels was investigated using the CCK-8 assay. CT26 cancer cells were cultured with 100 μL of fresh cell culture medium in 96-well plates (10,000 cells per well) and incubated for 24 h. The cell culture medium was then discarded and Fe_3O_4 solutions or Fe_3O_4 hydrogels (1 μg/mL for ALG) at different Fe concentrations (25, 50, 100, 200 and 400 μg/mL) were added into the cell culture medium. Meanwhile, 1 μL of Ca^{2+} solution (180 mM) was added into the wells containing Fe_3O_4 nanoparticles and ALG to form Fe_3O_4 hydrogels. After the incubation of cells for 24 h, the cell culture medium was discarded and the cells were carefully washed with PBS to remove free Fe_3O_4 nanoparticles. Cell culture medium containing 10% CCK-8 agent was then added into each well. After incubation of the cells for 2 h, the absorbance value of each well at 450 nm was detected using a microplate reader. The cells treated with PBS were used as a control. The ratio of absorbance values was used to calculate cell viability.

2.8 Evaluation of *in vitro* therapeutic efficacy

To evaluate the therapeutic effect of Fe_3O_4 nanoparticles and Fe_3O_4 hydrogels, CT26 cancer cells were seeded in 96-well plates (10,000 cells per well) and incubated at 37°C and 5% CO_2 for 24 h. For Fe_3O_4 nanoparticle treatment group, the cell culture medium was discarded and 10 μL Fe_3O_4 nanoparticles at the Fe concentration of 200 μg/mL was added into each well containing 190 μL cell culture medium. For Fe_3O_4 hydrogel treatment group, the cell culture medium was discarded, and 10 μL solution of Fe_3O_4 nanoparticles (200 μg/mL) and ALG (the concentration of ALG was 1 μg/mL) was added into each well containing 189 μL cell culture medium, and then 1 μL of Ca^{2+} solution (180 mM) was added into the wells to form Fe_3O_4 hydrogels. The formed hydrogels could stick to cells for cell incubation. After incubation of cells for 12 h, the cells were irradiated by 808 nm laser (1 W/cm^2) for 5 min. After that, the cells were incubated for another 12 h and the hydrogels were removed, and then cell viability was detected by CCK-8 assay.

2.9 Statistical analysis

Significant difference between the experimental statistics is analyzed by One-way ANOVA and indicated as (*), $p < 0.01$ by (**) and $p < 0.001$ by (***).

3 Results and discussion

3.1 Synthesis and characterization of Fe_3O_4 nanoparticles

To investigate the effect of different reaction times on the properties of Fe_3O_4 nanoparticles, the hydrodynamic sizes and surface zeta potentials of the Fe_3O_4 nanoparticles formed after the reaction for 30 min or 2 h were measured. The hydrodynamic diameter of Fe_3O_4 nanoparticles with 30 min of reaction was 61.3 nm, which was much smaller than that of 2 h (1,624 nm) (Figures 1A, B). Meanwhile, the surface zeta potential of Fe_3O_4 nanoparticles formed *via* a 30 min reaction (−21.4 mV) was lower than that of 2 h (−6.8 mV) (Figure 1C). These results indicated that the Fe_3O_4 nanoparticles obtained by reacting for 30 min had a smaller diameter and a more suitable surface potential. The Fe_3O_4 nanoparticles formed *via* a 30 min of reaction had a smaller size, and thus they would show a higher stability. Stronger steric stabilization and less electrostatic stabilization may lead to their lower surface potential (Shah et al., 2014). Therefore, the reaction time was set at 30 min in the following study. In addition, the UV-Vis absorption spectra of Fe_3O_4 nanoparticles were evaluated (Figure 1D). The absorbance value at 850 nm increased with increasing Fe concentrations measured using ICP-AES, which could enable their PTT applications (Yang et al., 2017).

3.2 Evaluation of the photothermal conversion efficacy of Fe_3O_4 nanoparticles

To evaluate the photothermal conversion efficacy, the Fe_3O_4 nanoparticle solutions were irradiated by an 808 nm laser. The thermal images were captured and the temperatures of the solutions were recorded. At the same Fe concentration, the temperatures of the solutions gradually increased with increasing laser time, which reached a maximum after 5 min of laser irradiation (Figure 2A). In order to evaluate the relationship between different power densities and the temperature increases, lasers at different power densities (0.5, 1, 1.5 W/cm^2) were used. Higher power densities achieved a greater increase in solution temperatures. The solution temperature increased to 35.5, 42.3, and 43.5°C after 5 min of laser irradiation at the power densities of 0.5, 1, and 1.5 W/cm^2, respectively (Figure 2B). The solutions at different Fe concentrations showed different degrees of temperature increases after irradiation by 808 nm laser (1 W/cm^2) for the same time (Figure 2C). The temperature of solutions at Fe concentrations of 100, 200, 350, and 500 μg/mL increased to 37.0, 42.3, 47.3, 55.0°C, respectively (Figure 2D). In contrast, the temperature of PBS solution showed no significant change after laser irradiation. The photothermal stability of Fe_3O_4 nanoparticles was then evaluated.

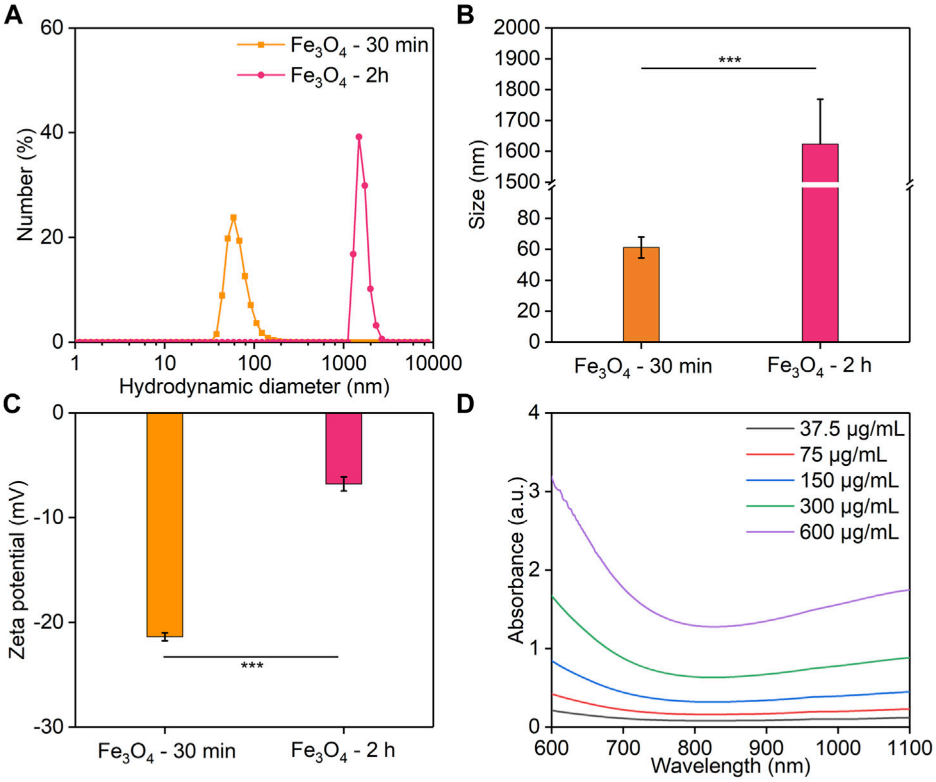

FIGURE 1
Characterization of Fe_3O_4 nanoparticles. **(A,B)** Hydrodynamic diameter. **(C)** The zeta potential of Fe_3O_4 nanoparticles obtained for a reaction time of 30 min or 2 h. **(D)** UV-visible spectra of Fe_3O_4 nanoparticles with different Fe concentrations.

After five cycles of heating and natural cooling, the temperature increases of the Fe_3O_4 nanoparticle solutions did not change significantly, indicating their good photothermal stability.

3.3 Preparation and characterization of Fe_3O_4 hydrogels

To prepare Fe_3O_4 hydrogels, Fe_3O_4 nanoparticles were added to ALG solutions at different concentrations (0.5, 1, 2.5, 5, 10 mg/mL) and the solutions were slowly injected into 10 mL Ca^{2+} solution (1.8 mM). The hydrogels could be formed *via* cross-linking of ALG by Ca^{2+}. The rate of hydrogel formation increased with the increasing of ALG concentrations (Figure 3A). When the solution with a ALG concentration of 0.5, 1 or 2.5 mg/mL was injected into the Ca^{2+} solution, hydrogels could be formed. However, the formed hydrogels disintegrated rapidly in solution due to the low cross-linkage of the formed hydrogels. When the concentration of ALG was 5 or 10 mg/mL, the formed hydrogels were able to maintain stability state for a long time without significant morphological changes due to the high cross-linking degree. Therefore, the concentration of ALG was set at 5 mg/mL in the following experiments. The SEM images showed that nanoparticles were attached to the surface of the hydrogels, which proved that Fe_3O_4 nanoparticles could be effectively encapsulated into the hydrogels (Figures 3B, C).

3.4 Evaluation of photothermal conversion efficacy of Fe_3O_4 hydrogels

The Fe_3O_4 hydrogels were irradiated using an 808 nm laser to study their photothermal conversion properties. The thermal images were captured and temperatures of the hydrogels were recorded. The temperatures of Fe_3O_4 hydrogel solutions gradually increased with the increasing of laser irradiation time, which reached the maximum after laser irradiation for 5 min (Figure 4A). Meanwhile, the temperatures of the hydrogel solutions irradiated by 808 nm laser at different power densities (0.5, 1, 1.5 W/cm^2) for 5 min were different. The solution temperature increased to 35.1, 41.3, and 43.9°C after 5 min of laser irradiation at power densities of 0.5, 1, and 1.5 W/cm^2, respectively (Figure 4B), indicating that higher power densities could achieve better photothermal effects. The temperature increases of the Fe_3O_4 hydrogel solutions were not significantly different for power density of 1 and 1.5 W/cm^2, so the power density used in the subsequent experiments was set at 1 W/cm^2. The photothermal performance of Fe_3O_4 hydrogels at different Fe concentrations was also evaluated. After 5 min of 808 nm (1 W/cm^2) laser irradiation, the temperature of the hydrogel solutions at Fe concentrations of 100, 200, 350, and 500 μg/mL increased to 34.6, 41.3, 46.4, and 55.2°C, respectively (Figures 4C, D). These concentrations were used for photothermal effect evaluation because the Fe_3O_4

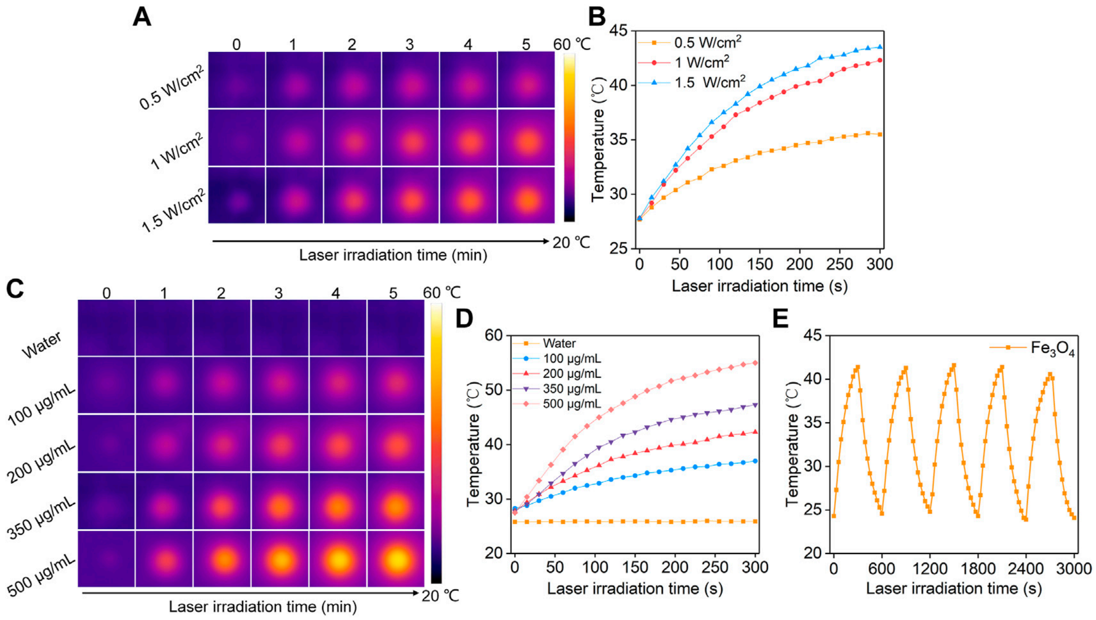

FIGURE 2
Evaluation of photothermal conversion efficiency. **(A)** Thermal imaging of Fe_3O_4 nanoparticle solution under 808 nm laser irradiation at power densities of 0.5, 1.0, and 1.5 W/cm^2. **(B)** Temperature profiles of Fe_3O_4 nanoparticle solution under different power densities of 808 nm laser irradiation. **(C)** Thermal imaging of Fe_3O_4 nanoparticle solutions at concentrations of 100, 200, 350, and 500 μg/mL under 808 nm laser irradiation at a power density of 1.0 W/cm^2. **(D)** Temperature profiles of Fe_3O_4 nanoparticle solutions at different concentrations under 808 nm laser (1.0 W/cm^2) irradiation. **(E)** The photothermal stability evaluation of the Fe_3O_4 nanoparticle solutions after 5 laser cycles.

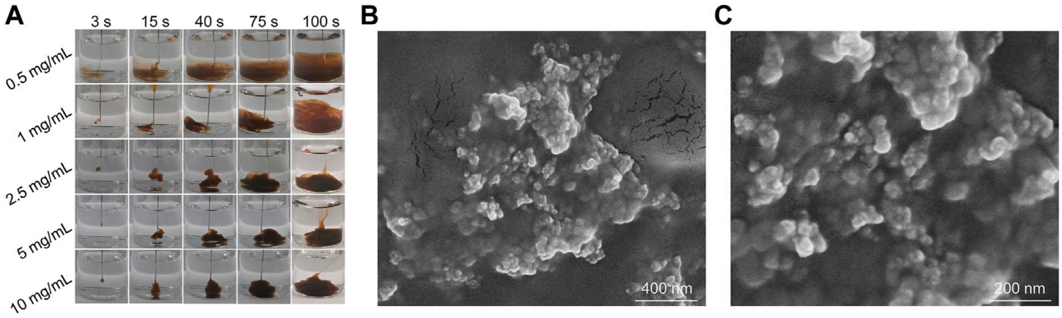

FIGURE 3
Characterization of Fe_3O_4 hydrogels. **(A)** Photographs of AF solutions at different ALG concentrations injected into Ca^{2+} solutions at different times. **(B,C)** SEM images of Fe_3O_4 hydrogels.

nanoparticles at these concentration ranges could obviously increase temperatures under laser irradiation (Chen et al., 2023). Meanwhile, the photothermal stability of the Fe_3O_4 hydrogels was evaluated (Figure 4E). The temperature increase did not change significantly after five cycles of heating/cooling, indicating that the Fe_3O_4 hydrogels had good photothermal stability. There was no significant difference between the photothermal performance of Fe_3O_4 hydrogels and Fe_3O_4 nanoparticles, indicating that the loading of Fe_3O_4 nanoparticles into hydrogels did not affect their photothermal performance.

3.5 Evaluation of *in vitro* treatment efficiency

The *in vitro* cellular uptake of Fe_3O_4 nanoparticles by cancer cells was evaluated using ICP-AES. The cellular uptake of Fe_3O_4 nanoparticles was pivotal to induce therapeutic effect for Fe_3O_4 nanoparticle-treated cells. After incubation the cells with Fe_3O_4 nanoparticles, the Fe uptake in cancer cells gradually increased in a time dependent manner (Figure 5A). After 24 h, the cellular Fe level increased by 6.6-fold. These results suggested the effective cellular uptake of Fe_3O_4 nanoparticles by cancer cells. To evaluate the cytotoxicity, CT26 cancer cells were co-incubated with Fe_3O_4

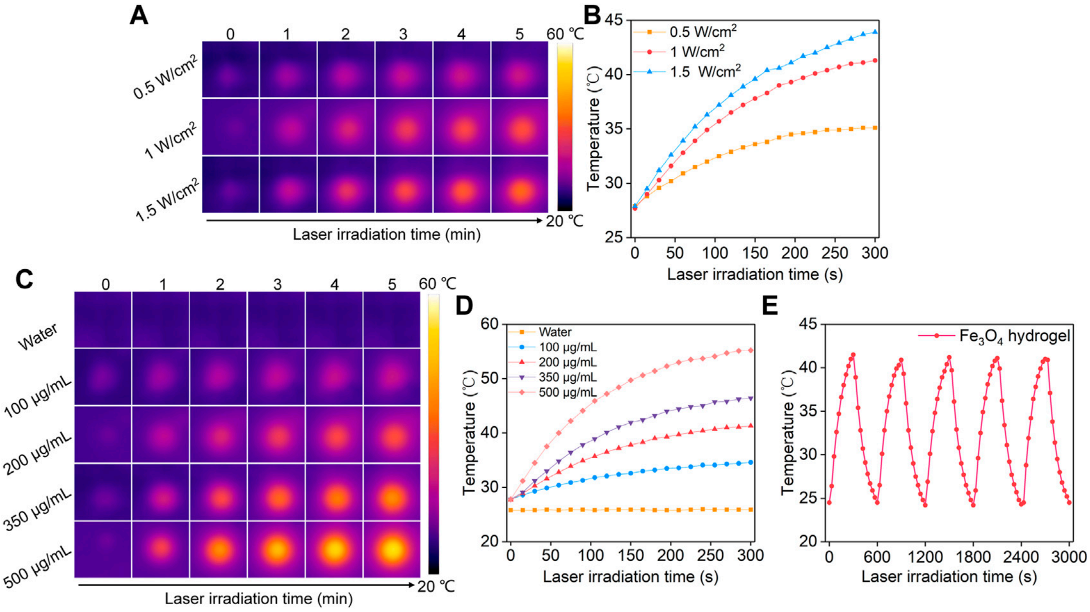

FIGURE 4
Evaluation of photothermal conversion efficiency of Fe_3O_4 hydrogels. **(A)** Thermal imaging of Fe_3O_4 hydrogels under 808 nm laser irradiation at power densities of 0.5, 1.0, and 1.5 W/cm^2. **(B)** Temperature profiles of Fe_3O_4 hydrogels under 808 nm laser irradiation at different power densities. **(C)** Thermal imaging of hydrogels at concentrations of 100, 200, 350, and 500 μg/mL under 808 nm laser irradiation at a power density of 1.0 W/cm^2. **(D)** Temperature profiles of Fe_3O_4 hydrogels at different concentrations under 808 nm laser (1.0 W/cm^2) irradiation. **(E)** The photothermal stability evaluation of Fe_3O_4 hydrogels after 5 laser cycles.

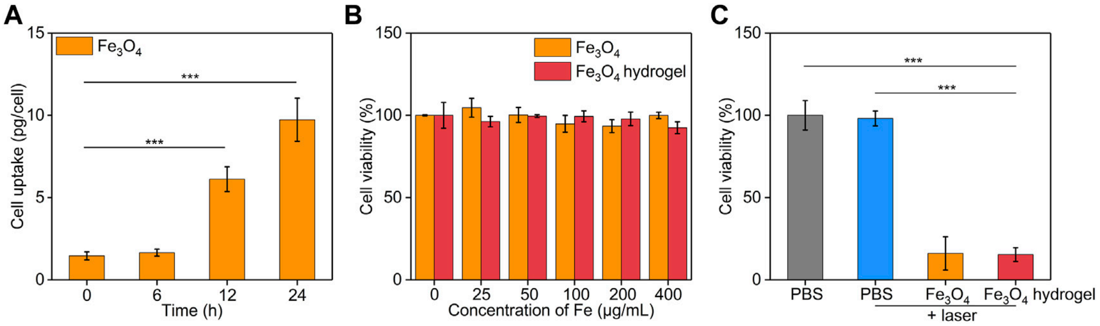

FIGURE 5
In vitro treatment efficacy evaluation. **(A)** Cellular uptake assay of Fe_3O_4 nanoparticles by CT26 cancer cells. **(B)** Cell viability of CT26 cancer cells after treatment with Fe_3O_4 nanoparticles or Fe_3O_4 hydrogels at different Fe concentrations for 24 h. **(C)** Cell viability of CT26 cancer cells after incubation with PBS, Fe_3O_4 nanoparticles, or Fe_3O_4 hydrogels with or without 808 nm laser irradiation (1.0 W/cm^2, 5 min).

nanoparticles or Fe_3O_4 hydrogels for 24 h. The cell viability of CT26 cells was higher than 92.5% after incubation with Fe_3O_4 nanoparticles or Fe_3O_4 hydrogels even when the Fe concentration was as high as 400 μg/mL (Figure 5B), indicating that both Fe_3O_4 nanoparticles and Fe_3O_4 hydrogels had good biosafety and cytocompatibility. The *in vitro* therapeutic effects of Fe_3O_4 nanoparticles and Fe_3O_4 hydrogels were then evaluated using CCK-8 assay. CT26 cancer cells were irradiated by 808 nm laser (1 W/cm^2) for 5 min, and the cell viability was not significantly reduced compared to that in the control group, indicating that cancer cells were not killed by laser irradiation alone (Figure 5C). When CT26 cells were treated with Fe_3O_4 nanoparticles or Fe_3O_4 hydrogels plus laser irradiation, the cell activity of cells decreased to 16.1% and 15.4%, respectively. The cell vitality of cells in Fe_3O_4 nanoparticles + laser and Fe_3O_4 hydrogels + laser was similar. These results verified the therapeutic effect of Fe_3O_4 hydrogels. Although the therapeutic efficacy of Fe_3O_4 hydrogels was similar to that of Fe_3O_4 nanoparticles, the Fe_3O_4 hydrogels could maintain a high concentration at injected sites and obviously reduce systemic toxicity in the form of intravenous administration, which would contribute to their future *in vivo* studies.

4 Conclusion

Herein, we report the development of Fe_3O_4 nanoparticle-loaded hydrogel platform (Fe_3O_4 hydrogels) for PTT of colon cancer cells. The synthesis of Fe_3O_4 nanoparticles could be achieved after 30 min of reaction, and the formed Fe_3O_4 nanoparticles showed a smaller diameter, a more suitable surface potential and a good photothermal conversion efficacy under 808 nm laser irradiation. The cross-linking of ALG solutions containing Fe_3O_4 nanoparticles by Ca^{2+} led to the formation of Fe_3O_4 hydrogels. The obtained Fe_3O_4 hydrogels also showed a high photothermal conversion efficiency under 808 nm laser irradiation. Both Fe_3O_4 nanoparticles and Fe_3O_4 hydrogels were found to have good cytocompatibility. *In vitro* therapeutic efficacy evaluation showed that the PTT effect mediated by Fe_3O_4 nanoparticle-loaded hydrogels could obviously kill CT26 cancer cells, which was similar to that of Fe_3O_4 nanoparticles. Although Fe_3O_4 nanoparticles have been used for cancer PTT, we for the first time report the uses of Fe_3O_4 nanoparticle-loaded hydrogels for effective PTT. In view of the different characteristics of Fe_3O_4 nanoparticles, such as imaging, magnetism, and Fenton reaction, this platform may also be used for combinational therapy of cancer.

Data availability statement

The original contributions presented in the study are included in the article/supplementary material, further inquiries can be directed to the corresponding author.

Author contributions

CW: Corresponding authors, conception, design of the study and revising the manuscript; YJ: acquisition, analysis, interpretation of the data, and drafting the article. All authors read and approved the final manuscript.

Funding

This study was supported by the Chengde Central Hospital.

Conflict of interest

The authors declare that the research was conducted in the absence of any commercial or financial relationships that could be construed as a potential conflict of interest.

Publisher's note

All claims expressed in this article are solely those of the authors and do not necessarily represent those of their affiliated organizations, or those of the publisher, the editors and the reviewers. Any product that may be evaluated in this article, or claim that may be made by its manufacturer, is not guaranteed or endorsed by the publisher.

References

Almawash, S., Osman, S. K., Mustafa, G., and El Hamd, M. A. (2022). Current and future prospective of injectable hydrogels-design challenges and limitations. *Pharmaceuticals* 15, 371. doi:10.3390/ph15030371

Anselmo, A. C., and Mitragotri, S. (2015). A review of clinical translation of inorganic nanoparticles. *AAPS J.* 17, 1041–1054. doi:10.1208/s12248-015-9780-2

Bardhan, R., Lal, S., Joshi, A., and Halas, N. J. (2011). Theranostic nanoshells: From probe design to imaging and treatment of cancer. *Acc. Chem. Res.* 44, 936–946. doi:10.1021/ar200023x

Caballero, D., Abreu, C. M., Lima, A. C., Neves, N. N., Reis, R. L., and Kundu, S. C. (2022). Precision biomaterials in cancer theranostics and modelling. *Biomaterials* 280, 121299. doi:10.1016/j.biomaterials.2021.121299

Chen, S., Lv, Y., Wang, Y., Kong, D., Xia, J., Li, J., et al. (2023). Tumor acidic microenvironment-responsive promodulator iron oxide nanoparticles for photothermal-enhanced chemodynamic immunotherapy of cancer. *ACS Biomater. Sci. Eng.* 9, 773–783. doi:10.1021/acsbiomaterials.2c01287

Cristofolini, L., Szczepanowicz, K., Orsi, D., Rimoldi, T., Albertini, F., and Warszynski, P. (2016). Hybrid polyelectrolyte/Fe_3O_4 nanocapsules for hyperthermia applications. *ACS Appl. Mat. Interfaces* 8, 25043–25050. doi:10.1021/acsami.6b05917

Ding, M. B., Zhang, Y. J., Li, J. C., and Pu, K. Y. (2022). Bioenzyme-based nanomedicines for enhanced cancer therapy. *Nano Converg.* 9, 7. doi:10.1186/s40580-022-00297-8

Dong, T. X., Jiang, J., Zhang, H., Liu, H. Y., Zou, X. M., Niu, J. M., et al. (2021). PFP@PLGA/Cu12Sb4S13-mediated PTT ablates hepatocellular carcinoma by inhibiting the RAS/MAPK/MT-CO1 signaling pathway. *Nano Converg.* 8, 29. doi:10.1186/s40580-021-00279-2

Espinosa, A., Di Corato, R., Kolosnjaj-Tabi, J., Flaud, P., Pellegrino, T., and Wilhelm, C. (2016). Duality of iron oxide nanoparticles in cancer therapy: Amplification of heating efficiency by magnetic hyperthermia and photothermal bimodal treatment. *ACS Nano* 10, 2436–2446. doi:10.1021/acsnano.5b07249

Goncalves, M., Figueira, P., Maciel, D., Rodrigues, J., Shi, X. Y., Tomas, H., et al. (2014). Antitumor efficacy of doxorubicin-loaded laponite/alginate hybrid hydrogels. *Macromol. Biosci.* 14, 110–120. doi:10.1002/mabi.201300241

Griffin, D. R., Weaver, W. M., Scumpia, P. O., Di Carlo, D., and Segura, T. (2015). Accelerated wound healing by injectable microporous gel scaffolds assembled from annealed building blocks. *Nat. Mat.* 14, 737–744. doi:10.1038/nmat4294

Hu, Y., Yang, J., Wei, P., Li, J., Ding, L., Zhang, G., et al. (2015). Facile synthesis of hyaluronic acid-modified Fe_3O_4/Au composite nanoparticles for targeted dual mode MR/CT imaging of tumors. *J. Mat. Chem. B* 3, 9098–9108. doi:10.1039/c5tb02040a

Jing, Z. W., Du, Q. Z., Zhang, X. J., and Zhang, Y. (2022). Nanomedicines and nanomaterials for cancer therapy: Progress, challenge and perspectives. *Chem. Eng. J.* 446, 137147. doi:10.1016/j.cej.2022.137147

Kim, D. H., and Martin, D. C. (2006). Sustained release of dexamethasone from hydrophilic matrices using PLGA nanoparticles for neural drug delivery. *Biomaterials* 27, 3031–3037. doi:10.1016/j.biomaterials.2005.12.021

Lee, K. Y., and Mooney, D. J. (2012). Alginate: Properties and biomedical applications. *Prog. Polym. Sci.* 37, 106–126. doi:10.1016/j.progpolymsci.2011.06.003

Li, C., Chen, T., Ocsoy, I., Zhu, G., Yasun, E., You, M., et al. (2014). Gold-coated Fe_3O_4 nanoroses with five unique functions for cancer cell targeting, imaging and therapy. *Adv. Funct. Mat.* 24, 1772–1780. doi:10.1002/adfm.201301659

Liu, J. S., Qing, X. Q., Zhang, Q., Yu, N. Y., Ding, M. B., Li, Z. H., et al. (2021). Oxygen-producing proenzyme hydrogels for photodynamic-mediated metastasis-inhibiting combinational therapy. *J. Mat. Chem. B* 9, 5255–5263. doi:10.1039/d1tb01009c

Liu, Z., Cai, W. B., He, L. N., Nakayama, N., Chen, K., Sun, X. M., et al. (2007). *In vivo* biodistribution and highly efficient tumour targeting of carbon nanotubes in mice. *Nat. Nanotechnol.* 2, 47–52. doi:10.1038/nnano.2006.170

Meng, X. Y., Zhang, X. Z., Liu, M., Cai, B., He, N. Y., and Wang, Z. F. (2020). Fenton reaction-based nanomedicine in cancer chemodynamic and synergistic therapy. *Appl. Mat. Today* 21, 100864. doi:10.1016/j.apmt.2020.100864

Navya, P. N., Kaphle, A., Srinivas, S. P., Bhargava, S. K., Rotello, V. M., and Daima, H. K. (2019). Current trends and challenges in cancer management and therapy using designer nanomaterials. *Nano Converg.* 6, 23. doi:10.1186/s40580-019-0193-2

Puiggalí-Jou, A., Babeli, I., Roa, J. J., Zoppe, J. O., Garcia-Amorós, J., Ginebra, M. P., et al. (2021). Remote spatiotemporal control of a magnetic and electroconductive hydrogel network via magnetic fields for soft electronic applications. *ACS Appl. Mat. Interfaces* 13, 42486–42501. doi:10.1021/acsami.1c12458

Shah, R., Eldridge, D., Palombo, E., and Harding, I. (2014). Optimisation and stability assessment of solid lipid nanoparticles using particle size and zeta potential. *J. Phys. Sci.* 25, 59–75.

Shubayev, V. I., Pisanic, T. R., and Jin, S. H. (2009). Magnetic nanoparticles for theragnostics. *Adv. Drug Deliv. Rev.* 61, 467–477. doi:10.1016/j.addr.2009.03.007

Vegas, A. J., Veiseh, O., Doloff, J. C., Ma, M., Tam, H. H., Bratlie, K., et al. (2016). Combinatorial hydrogel library enables identification of materials that mitigate the foreign body response in primates. *Nat. Biotechnol.* 34, 345–352. doi:10.1038/nbt.3462

Yang, J., Fan, L., Xu, Y., and Xia, J. (2017). Iron oxide nanoparticles with different polymer coatings for photothermal therapy. *J. Nanopart. Res.* 19, 333. doi:10.1007/s11051-017-4031-3

Zhang, H. J., Pei, Y. M., Zhang, X. G., Zhu, L., Hou, L., Chang, J. B., et al. (2020). Engineering of an intelligent cascade nanoreactor for sequential improvement of microenvironment and enhanced tumor phototherapy. *Appl. Mat. Today* 18, 100494. doi:10.1016/j.apmt.2019.100494

frontiers | Frontiers in Bioengineering and Biotechnology

TYPE Original Research
PUBLISHED 24 May 2023
DOI 10.3389/fbioe.2023.1196839

H_2O_2/O_2 self-supply and Ca^{2+} overloading MOF-based nanoplatform for cascade-amplified chemodynamic and photodynamic therapy

Yujia Liang, Zhengmin Cai, Yamei Tang, Chenglin Su, Liye Xie, Yan Li* and Xinqiang Liang*

Guangxi Medical University Cancer Hospital, Nanning, China

Introduction: Reactive oxygen species (ROS)-mediated therapies have typically been considered as noninvasive tumor treatments owing to their high selectivity and efficiency. However, the harsh tumor microenvironment severely impairs their efficiency.

Methods: Herein, the biodegradable Cu-doped zeolitic imidazolate framework-8 (ZIF-8) was synthesized for loading photosensitizer Chlorin e6 (Ce6) and CaO_2 nanoparticles, followed by surface decoration by hyaluronic acid (HA), obtaining HA/CaO_2-Ce6@Cu-ZIF nano platform.

Results and Discussion: Once HA/CaO_2-Ce6@Cu-ZIF targets tumor sites, the degradation of Ce6 and CaO_2 release from the HA/CaO_2-Ce6@Cu-ZIF in response to the acid environment, while the Cu^{2+} active sites on Cu-ZIF are exposed. The released CaO_2 decompose to generate hydrogen peroxide (H_2O_2) and oxygen (O_2), which alleviate the insufficiency of intracellular H_2O_2 and hypoxia in tumor microenvironment (TME), effectively enhancing the production of hydroxyl radical (•OH) and singlet oxygen ($^1O_2$) in Cu^{2+}-mediated chemodynamic therapy (CDT) and Ce6-induced photodynamic therapy (PDT), respectively. Importantly, Ca^{2+} originating from CaO_2 could further enhance oxidative stress and result in mitochondrial dysfunction induced by Ca^{2+} overloading.

Conclusion: Thus, the H_2O_2/O_2 self-supplying and Ca^{2+} overloading ZIF-based nanoplatform for cascade-amplified CDT/PDT synergistic strategy is promising for highly efficient anticancer therapy.

KEYWORDS

CaO_2, MOFs, H_2O_2/O_2 self-supply, chemodynamic therapy, photodynamic therapy

Check for updates

OPEN ACCESS

EDITED BY
Xin Li,
Leibniz Institute for Interactive Materials (DWI), Germany

REVIEWED BY
Muhammad Nafees,
University of Engineering and Technology, Pakistan
Se-Hyeong Jung,
ETH Zürich, Switzerland
Yi Lu,
RWTH Aachen University, Germany

*CORRESPONDENCE
Yan Li,
liyan26@gxmu.edu.cn
Xinqiang Liang,
xx03716@163.com

RECEIVED 30 March 2023
ACCEPTED 05 May 2023
PUBLISHED 24 May 2023

CITATION
Liang Y, Cai Z, Tang Y, Su C, Xie L, Li Y and Liang X (2023), H_2O_2/O_2 self-supply and Ca^{2+} overloading MOF-based nanoplatform for cascade-amplified chemodynamic and photodynamic therapy.
Front. Bioeng. Biotechnol. 11:1196839.
doi: 10.3389/fbioe.2023.1196839

COPYRIGHT
© 2023 Liang, Cai, Tang, Su, Xie, Li and Liang. This is an open-access article distributed under the terms of the Creative Commons Attribution License (CC BY). The use, distribution or reproduction in other forums is permitted, provided the original author(s) and the copyright owner(s) are credited and that the original publication in this journal is cited, in accordance with accepted academic practice. No use, distribution or reproduction is permitted which does not comply with these terms.

1 Introduction

Cancer is one of the most lethal diseases and causes millions of deaths annually with increasing mortality worldwide. Considering the high risk and death rate of cancer, scientists around the world have dedicated themselves to achieving effective and precise diagnoses as well as safe and hazard-free therapy to fight against it. With the rapid development in nanotechnology over the past 2 decades, nanomaterials have provided an advanced approach from anti-cancer experts and are expected to be used in cancer imaging and treatment therapy. (Wang et al., 2021a; Yang et al., 2021a; Zhang et al., 2021; Zhou et al., 2021; Shan et al., 2022; Zhang et al., 2022; Li et al., 2023; Lu et al., 2023). Metal-organic frameworks (MOFs) with potential biological performance, such as biocompatibility, cytotoxicity, and biodistribution, have been extensively studied in nanotherapeutics. (Wang et al., 2019a; Xie et al., 2019a; Yang et al., 2019a; Zhang et al., 2019a; Zhao et al., 2019; Pandey et al., 2020). MOFs are a series of crystallized porous materials coordinated by metal-containing cores (e.g., metal ions and clusters) and organic linkers (e.g., carboxylate ligands, phosphonates, sulfonates, and other negatively charged ligands). MOFs are not only good carriers of nanocargo (drugs and contrast agents) because of their porous and oriented structure but also contrast agents themselves due to their multifunctional building blocks. (Wang et al., 2019b; Cai et al., 2019; Ren et al., 2019; Rojas et al., 2019). Importantly, with good biodegradability and biocompatibility, MOF composites could be constructed as physiological environment-accommodative synergist therapy platforms. (Wang et al., 2021b; Liang et al., 2021; Bian et al., 2022). Because of this, incorporating functionalized compositions and comprehensive structures within MOFs to obtain nanoplatforms with collective properties and advanced performance has attracted much attention.

As a major molecule produced during oxidative stress, reactive oxygen species (ROS) contains singlet oxygen ($^1O_2$), superoxide anions (O_2^-), and hydroxyl radicals (•OH), which are considered to be essential factors in the occurrence, development, and recurrence of cancer. (Yang et al., 2019b; Li et al., 2021a; Tao et al., 2022; Truong Hoang et al., 2022; Yu et al., 2022; Cao et al., 2023). Furthermore, depending on their high selectivity and unrecognized drug resistance, ROS-mediated therapies such as chemodynamic therapy (CDT) (Zhao et al., 2021a; Yang et al., 2021b; Zhou et al., 2021) and photodynamic therapy (PDT) (Zhang et al., 2019b; Zhao et al., 2021b; Rui et al., 2021) have been considered as noninvasive anti-cancer treatments. CDT utilizes the Fenton/Fenton-like reaction between catalysts and hydrogen peroxide (H_2O_2) to generate cytotoxic •OH, (Chen et al., 2020; Wang et al., 2020; Cao et al., 2021), while PDT relies on nontoxic photosensitizers that are activated by visible or/and near-infrared (NIR) light to convert oxygen (O_2) to $^1O_2$. (Deng et al., 2017; Xie et al., 2019a; Yang et al., 2019c; Monro et al., 2019; Sivasubramanian et al., 2019). However, the harsh tumor microenvironment (TME) is an obstacle against achieving highly efficient therapeutic efficacy. Compared to normal cells, TME exhibits unique characteristics, such as mildly acidic conditions (pH = 5.5–6.5), internal hypoxic environment, high levels of intracellular glutathione (GSH, ~10×10^{-3} M), excessive H_2O_2, ($50–100 \times 10^{-6}$ M), and hypoxia conditions. (Wang et al., 2018; Peng et al., 2021; Chang et al., 2022). The low intracellular H_2O_2 concentration and inherent hypoxia at tumor sites result in the low ROS production efficiency of CDT and PDT, respectively. In addition, the strong antioxidant GSH in TME also would downregulate the ROS level, aggravating the attenuation of antitumor efficiency. Li et al. loaded the chemotherapy prodrug disulfiram (DSF) and coated glucose oxidase (GOD) on the surface of Cu/ZIF-8 nanospheres and finally encapsulated manganese dioxide (MnO_2) nanoshells to achieve efficient DSF-based cancer chemotherapy and dual-enhanced CDT. The MnO_2 layer could achieve GSH depletion and relieve tumor hypoxia in the TME, the released Mn^{2+} could initiate T_1-MRI for the tracking of the nanocatalyst *in vivo*, and the O_2 produced in the reaction could oxidize glucose to H_2O_2 and gluconic acid in the presence of GOD. (Li et al., 2021b). Thus, engineering H_2O_2/O_2 self-supplying therapeutic nanoplatforms to increase *in situ* the H_2O_2 and O_2 concentration at tumor sites and constructing a CDT/PDT strategy to achieve a more synergistic effect than that of single-mode might be possible solutions.

More attractively, most of the latest research has provided approaches to improve the propagation of H_2O_2 and relieve hypoxia at tumor sites. (Wang et al., 2019c; Liu et al., 2019). Among them, a highly biocompatible metal peroxide, calcium peroxide (CaO_2), has received widespread attention because of its excellent advantages, such as the simultaneous generation of O_2 and H_2O_2 immediately following a reaction with water, serving as a donor of H_2O_2, and eliminating GSH in response to TME. (Sun et al., 2021a; Sun et al., 2021b; Liu et al., 2022a; Liu et al., 2022b). Additionally, overloaded exogenous Ca^{2+} could induce mitochondrial damage and further disorder the oxidative stress, resulting in the imbalance of calcium transport channel and accelerating tumor calcification-mediated apoptosis. (Zhang et al., 2019c; He et al., 2021; Wan et al., 2021; Docampo and Vercesi, 2022; Zheng et al., 2022). Hence, CaO_2 could be appreciated as an advanced candidate for the rational design of multifunctional nanoplatforms for promoting CDT and PDT efficiency while achieving mitochondrial-localized Ca^{2+} overloading, ultimately allowing amplification of intracellular ROS-mediated therapeutic effect. (Hu et al., 2020; Shen et al., 2021; Chen et al., 2022).

Zeolitic imidazolate framework-8 (ZIF-8), composed of the coordination of Zn ions with 2-methylimidazole (2-MeIM), is a promising MOF for the construction of therapeutic nanoplatforms. (Xie et al., 2019b; Qin et al., 2019; Yang et al., 2020; Wang et al., 2021c; Jiang et al., 2022; Li et al., 2022). In this study, the biodegradable Cu-doped ZIF-8 was synthesized for loading photosensitizer Chlorin e6 (Ce6) and CaO_2 nanoparticles (NPs), followed by surface modification by hyaluronic acid (HA), finally obtaining HA/CaO_2-Ce6@Cu-ZIF nano platform. Once HA/CaO_2-Ce6@Cu-ZIF targets tumor sites through HA-mediated active endocytosis and degrading by hyaluronidase (HAase), the degradation of Ce6 and CaO_2 is released from the HA/CaO_2-Ce6@Cu-ZIF in response to the acid environment, while the Cu^{2+} active sites on Cu-ZIF are exposed. The released CaO_2 decompose to generate H_2O_2 and O_2, which alleviates the insufficiency of intracellular H_2O_2 and hypoxia in TME, effectively amplifying the production of •OH and $^1O_2$ in Cu^{2+}-mediated CDT and Ce6-induced PDT, respectively. Importantly, Ca^{2+} originating from CaO_2 could further amplify the oxidative stress and lead to mitochondrial dysfunction induced by Ca^{2+} overloading. Thus, the H_2O_2/O_2 self-supplying and Ca^{2+} overloading MOF-based nanoplatform for cascade-amplified CDT/PDT synergistic strategy is promising for highly efficient anticancer therapy.

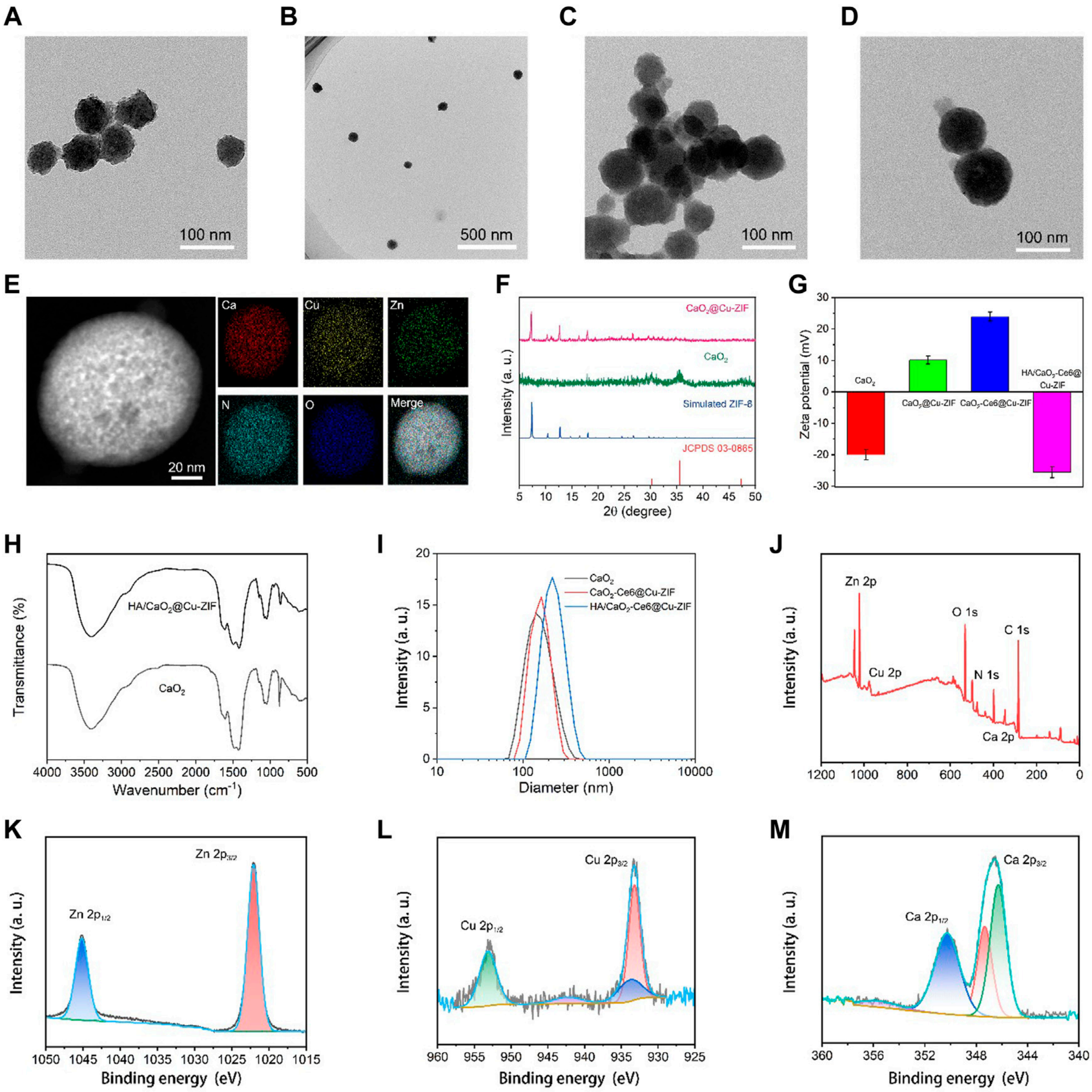

FIGURE 1
TEM images of **(A,B)** CaO_2 NPs and **(C,D)** CaO_2@Cu-ZIF. **(E)** Corresponding area-elemental mapping of CaO_2@Cu-ZIF. **(F)** XRD patterns of stimulated ZIF-8, CaO_2, and CaO_2@Cu-ZIF. **(G)** Zeta potentials of CaO_2, CaO_2@Cu-ZIF, CaO_2-Ce6@Cu-ZIF, and HA/CaO_2-Ce6@Cu-ZIF. **(H)** FT-IR spectrum of CaO_2 and HA/CaO_2-Ce6@Cu-ZIF. **(I)** DLS of CaO_2, CaO_2-Ce6@Cu-ZIF, and HA/CaO_2-Ce6@Cu-ZIF. **(J)** XPS spectrum of HA/CaO_2-Ce6@Cu-ZIF. **(K–M)** High-resolution XPS spectrum of Zn, Cu, and Ca, respectively.

2 Experimental section

2.1 Chemicals

$Zn(NO_3)_2•6H_2O$ (0.1 M), 2-MeIM ($C_4H_6N_2$, 99%), $Cu(NO_3)_2•3H_2O$ (AR), $CaCl_2$ (97%), and HA (10 k) were purchased from Shanghai Aladdin Technology Co., Ltd. Ce6, DAPI, MTT, calcein-AM, and PI were supplied by Sigma-Aldrich. The annexin V-FITC/PI apoptosis kit was obtained from MultiScience Biotech Co., Ltd. All liquid chemical reagents were used without further purification.

2.2 Synthesis of CaO_2 NPs

CaO_2 NPs were obtained by a hydrolysis–precipitation process. A specific amount of $CaCl_2$ (1 g) was sent into the HA (50 mL, 0.1 M) solution at room temperature under continuous stirring for 30 min. After that, $NH_3•H_2O$ (5 mL, 1 M) and H_2O_2 (1.5 mL, 30%) were sequentially injected and synthesized for 3 h. Afterward, NaOH (1.0 mL, 1 M) was added under ultrasound. Finally, the CaO_2 NPs were purified by centrifugation (13,000 rpm, 10 min) and sequentially washed with NaOH solution, pure water, and anhydrous ethanol three times.

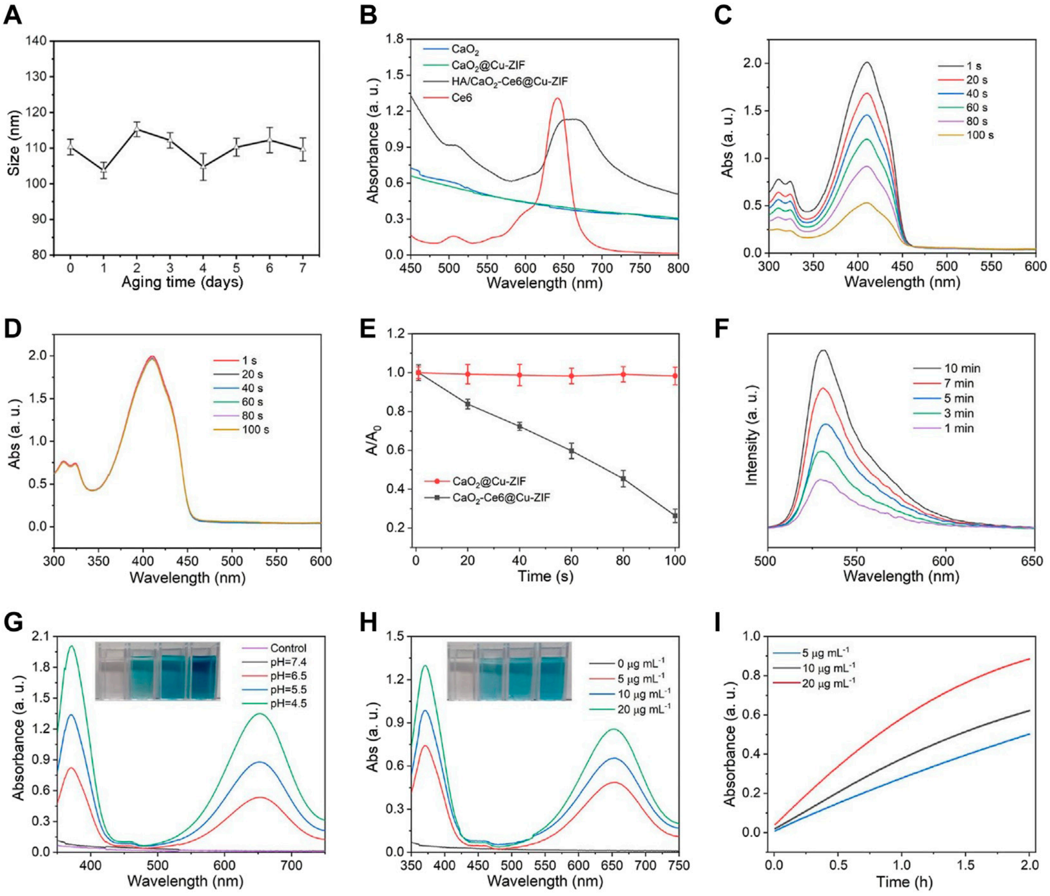

FIGURE 2
(A) Particle sizes of HA/CaO_2-Ce6@Cu-ZIF within 7 days in cell medium. **(B)** UV-vis absorption spectra of Ce6, CaO_2, CaO_2@Cu-ZIF, and HA/CaO_2-Ce6@Cu-ZIF. **(C)** UV-vis absorption of DPBF mixed with HA/CaO_2-Ce6@Cu-ZIF as a function of reaction time under 650 nm laser irradiation. **(D)** UV-vis absorption of DPBF mixed with PBS at same condition. **(E)** Relative intensity value of UV-vis absorption peak at 410 nm for DPBF mixed with HA/CaO_2-Ce6@Cu-ZIF and PBS, respectively. **(F)** Fluorescence spectra of DCFH-DA mixed with HA/CaO_2-Ce6@Cu-ZIF under 650 nm laser irradiation for different time. **(G)** UV-vis spectra of TMB + HA/CaO_2-Ce6@Cu-ZIF under pH at 4.5, 5.5, 6.5, and 7.4. **(H)** UV-vis spectra of TMB + HA/CaO_2-Ce6@Cu-ZIF at the concentration of HA/CaO_2-Ce6@Cu-ZIF as 0, 5, 15, and 20 μg/mL under pH 6.5. **(I)** UV-vis absorption peak at 650 nm for TMB + HA/CaO_2-Ce6@Cu-ZIF at the concentration of HA/CaO_2-Ce6@Cu-ZIF as 5, 15, and 20 μg/mL with different times. All laser pump powers are 0.5 W/cm^2.

2.3 Synthesis of HA/CaO_2-Ce6@Cu-ZIF

The HA/CaO_2-Ce6@Cu-ZIF was prepared via an unfussy one-step method. A specific $Zn(NO_3)_2$•$6H_2O$ (300 mg) and $Cu(NO_3)_2$•$3H_2O$ (50 mg) were dissolved in methanol (100 mL) and formed an uniform solution. Then, 2-MeIM (190 mg), HA-stabilized CaO_2 NPs (50 mg), and Ce6 (20 mg) dissolved in the methanol solution (100 mL) were added drip by drip and reacted for at least 30 min under N_2 atmosphere. Finally, the HA/CaO_2-Ce6@Cu-ZIF was collected by centrifugation (13,000 rpm, 10 min) and washed with methanol three times.

2.4 Characterizations

TME images and corresponding elemental mapping were collected from Tecnai T20 at an accelerating voltage of 200 kV. The size of nanoparticles was calculated using Image J for 100 counting number. XRD patterns were obtained from Bruker D8 ADVANCE (Cu Kα radiation (λ = 0.154 nm) at 40 kV and 40 mA. Zeta potential and DLS measurements were gained by Zetasizer Ultra with He-Ne laser (633 nm). UV-vis absorption spectra were acquired from Shimadzu UV-1601. XPS spectra were analyzed from Rigaku DMAX-2400. FT-IR spectrum was accumulated from Nicolet Avatar 360 with the KBr wafer technique. ICP-OES measurements were surveyed from iCAP 6000 series. CLSM images were captured from Leica SP8. Flow cytometry was measured using BD accuri C6.

2.5 ROS generation estimation

The generation of •OH was analyzed by TMB chromogenic reaction in pH, concentration, and time-dependent manners. The generation of $^1O_2$ was determined by the DPBF chemical probe.

2.6 *In vitro* experiments

Cellular uptake of as-synthesized materials was operated on Panc02 cells. Cells were seeded in 6-well plates with a density of 1 ×

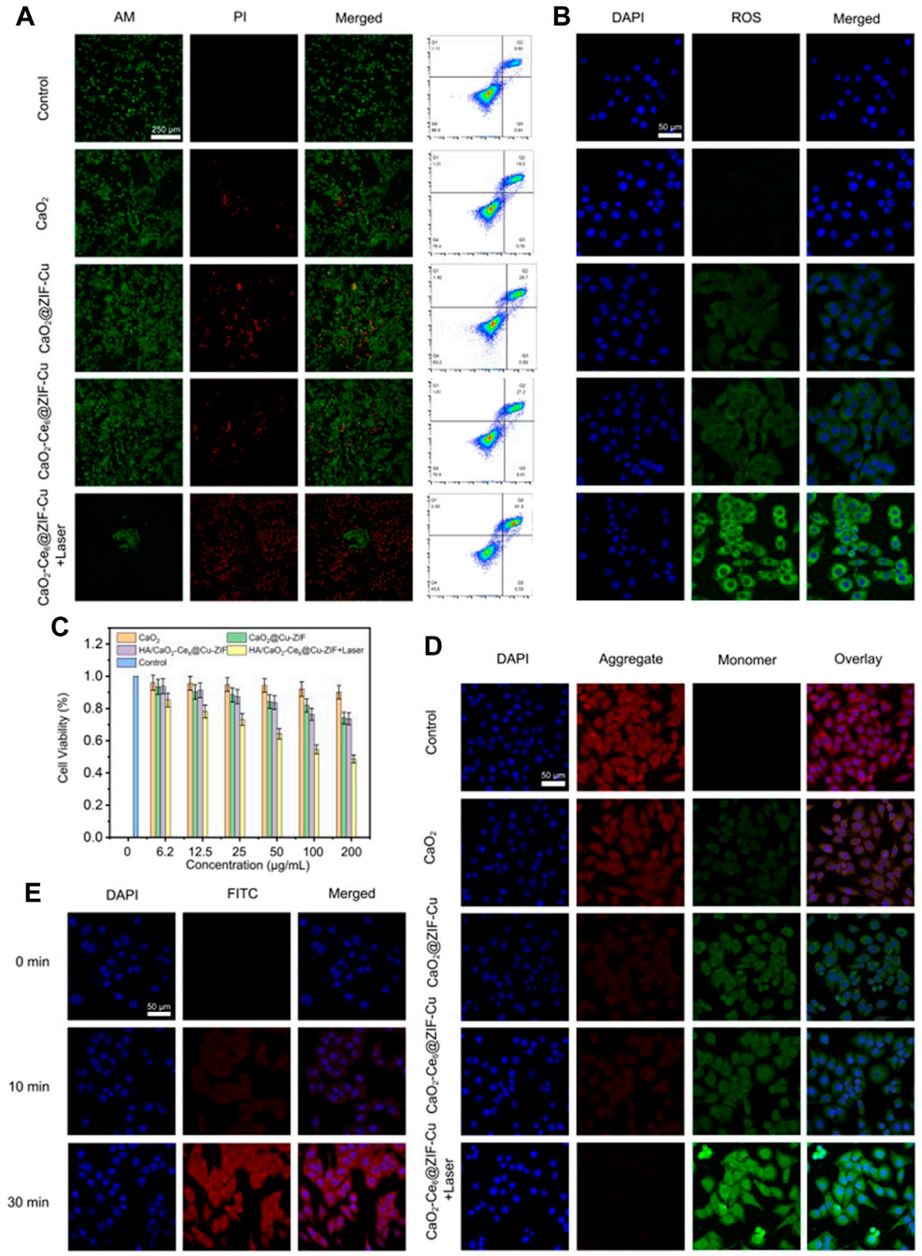

FIGURE 3
(A) Calcein-AM/PI double staining of Panc02 cells with different treatments and corresponding flow cytometry analysis by annexin V-FITC apoptosis detection kit. **(B)** Intracellular ROS level of Panc02 cells with different treatments. **(C)** Relative cell viabilities of Panc02 cells after treatment with different samples. **(D)** JC-1 staining of Panc02 cells after different treatments. **(E)** CLSM images of Panc02 cells incubated with HA/CaO_2-Ce6@Cu-ZIF for different times.

10^5 cells per well. The MTT cell assay was employed to evaluate the biocompatibility and toxicity of as-synthesized materials on L929 and Panc02 cells, respectively. Moreover, the live/dead cell assay was conducted to verify the cytotoxicity of the material on Panc02 cells. For intracellular ROS detection, a DCFH-DA chemical fluorescence probe was used. For the mitochondrial integrity assay, JC-1 staining kits were used to determine the J-monomer and J-aggregates separately. The intracellular fluorescence was observed by CLSM.

2.7 *In vivo* experiments

To investigate the biodistribution, the Panc02 tumor-bearing C57BL/6 mice were intravenously administered as-synthesized materials. For biodistribution investigation, the mice were sacrificed after 0, 2, 6, 12, 24, and 48 h. The heart, liver, lungs, spleen, kidneys, and tumors were collected for Cu contraction measurement. To estimate the anti-tumor efficacy of as-synthesized materials, the Panc02 tumor-bearing C57BL/6 mice were randomly placed into five groups (n = 5): control, CaO_2, CaO_2@Cu-ZIF, HA/CaO_2-Ce6@Cu-ZIF, and HA/CaO_2-Ce6@Cu-ZIF + Laser. During the treatment process, the tumor sizes and weights of mice were recorded once every 2 days: tumor volume = (tumor length) × (tumor width)^2/2 (mm^3).

2.8 Histology examination

After treatment process, the tumor and main organs (heart, liver, spleen, lung, and kidney) were collected for (H&E) staining according to the standard protocol for confirming caused injury.

2.9 Statistical analysis

All results were presented as mean ± S.D. Means were indicated using the student's t-test. Statistical significance was determined at a value of $^*p < 0.05$, $^{**}p < 0.01$, $^{***}p < 0.001$.

3 Results and discussion

3.1 Characterization of HA/CaO_2-Ce6@Cu-ZIF nanoplatform

The synthesis of HA/CaO_2-Ce6@Cu-ZIF was done through a two-step process. At first, CaO_2 NPs were synthesized through a hydrolysis-precipitation process. Then, the HA/CaO_2-Ce6@Cu-ZIF was synthesized through a simple one-step method. In detail, a specific $Zn(NO_3)_2{\bullet}6H_2O$ and $Cu(NO_3)_2{\bullet}3H_2O$ were dissolved in methanol and formed a uniform solution. Following this, 2-MeIM, HA-stabilized CaO_2 NPs, and Ce6 dissolved in the methanol solution were added drop by drop and reacted for 30 min to obtain HA/CaO_2-Ce6@Cu-ZIF. As revealed by transmission electron microscopy (TEM), the CaO_2 NPs are about 90 ± 2.3 nm, demonstrating the uniform size distribution. (Figures 1A, B). X-ray diffraction (XRD) pattern reveals that the synthesized CaO_2 NPs show obvious peaks at 30.1°, 35.6°, and 47.3° (Figure 1F), which is consistent with the JCPDS, No. 03-0865 according to previous literature for CaO_2. (Sun et al., 2021a). After this, Cu-ZIF was utilized to encapsulate the CaO_2 NPs and Ce6 via a self-assembly method to obtain the HA/CaO_2-Ce6@Cu-ZIF nanoplatform. The TEM image shows that the HA/CaO_2-Ce6@Cu-ZIF presents a regular octahedral shape with a particle size of around 110 ± 3.8 nm (Figures 1C, D). The homogeneous distributions of Zn, Cu, Ca, N, and O elements in HA/CaO_2-Ce6@Cu-ZIF are revealed by the elemental mapping, which demonstrates the successful loading of CaO_2 NPs (Figure 1E). Moreover, the XRD pattern of HA/CaO_2-Ce6@Cu-ZIF is consistent with that of ZIF-8, indicating that the as-synthesized materials are well held in the crystal structure of ZIF-8 (Figure 1F). (Li et al., 2021b) To endow the CaO_2-Ce6@Cu-ZIF with higher hydrophilicity for further biological application, HA with superior biocompatibility and targeted ability was employed for surface modification. As displayed in Figure 1G, the zeta potentials of CaO_2, CaO_2@Cu-ZIF, CaO_2-Ce6@Cu-ZIF, and HA/CaO_2-Ce6@Cu-ZIF are −20.03, +10.12, +23.9, and −25.6 mV, respectively, indicating that the CaO_2 NPs and Ce6 are successfully introduced into the Cu-ZIF and HA are effectively modified on the surface of as-synthesized materials. Meanwhile, the size distribution of CaO_2, CaO_2-Ce6@Cu-ZIF, and HA/CaO_2-Ce6@Cu-ZIF was obtained from the dynamic light scattering (DLS) measurements, the polydispersity index of which was 0.18, 0.19, and 0.17, respectively, demonstrating the good stable ability of HA modification. Figure 1I shows the hydrodynamic diameter is 142, 164, and 220 nm, respectively. The Fourier transform infrared (FT-IR) spectrum was recorded in the wavelength range of 500–4,000 cm^{-1} (Figure 1H), also suggesting the sequential addition of CaO_2, Ce6, and HA, finally forming HA/CaO_2-Ce6@Cu-ZIF. (Li et al., 2021a). As shown in X-ray photoelectron spectroscopy (XPS), HA/CaO_2-Ce6@Cu-ZIF was also performed to evaluate the valence electron distribution, and the spectra are presented in which the coexistence of Zn, Cu, Ca, N, and O signals appear (Figure 1J). The high-resolution XPS of Zn, Cu, and Ca are shown in Figures 1K–M. In the high-resolution XPS of Cu spectrum, 933.3 and 953.6 eV peaks are assigned to Cu 2P3/2 and Cu 2p1/2, respectively. In addition, the satellite peaks at around 943.1 eV demonstrate the presence of Cu^{2+}. (Li et al., 2021b). All the above materials' characterizations imply the rational design and synthesis of H_2O_2/O_2 self-supply and Ca^{2+} overloading MOF-based nanoplatform.

3.2 CDT/PDT synergistic effect of HA/CaO_2-Ce6@Cu-ZIF nano platform

The stability experiments of HA/CaO_2-Ce6@Cu-ZIF show that the as-synthesized materials maintain good dispersion within 7 days in cell medium (Figure 2A).The ultraviolet-visible (UV-vis) absorption spectra of Ce6, CaO_2, CaO_2@Cu-ZIF, and HA/CaO_2-Ce6@Cu-ZIF was shown in Figure 2B. Compared with the broad peak of CaO_2 and CaO_2@Cu-ZIF ranging from 450 to 800 nm, the absorption band of HA/CaO_2-Ce6@Cu-ZIF not only has the broad peak of CaO_2@Cu-ZIF but also exhibits the typical characteristic peak of Ce6 around 650 nm. Encouraged by the results from the photo-properties of HA/CaO_2-Ce6@Cu-ZIF, the $^1O_2$ generation of PDT effect was explored by the UV-vis spectrum, where the 1,3-diphenylisobenzofuran (DPBF) was used as a real-time probe. The HA/CaO_2-Ce6@Cu-ZIF and PBS solutions were irradiated by 650 nm laser (0.5 W/cm^2), respectively. At first, the HA/CaO_2-Ce6@Cu-ZIF could release Ce6 under acidic conditions. Then, DPBF could be oxidized by $^1O_2$ which was generated from the combination of the released Ce6, light, and self-supplying O_2, so that the absorption peak of the DPBF (the specific absorption wavelength was at 410 nm) gradually decreased along with time increase (Figure 2C). However, the absorption peak of the DPBF solution that was treated with PBS was almost unchanged (Figure 2D). The relative intensity value of the UV-vis absorption peak at 410 nm for DPBF mixed with HA/CaO_2-Ce6@Cu-ZIF and PBS, respectively, further demonstrates the apparent decrease of DPBF absorption intensity (Figure 2E). To further confirm the production of $^1O_2$, the 2′,7′-dichlorodihydrofluorescein diacetate (DCFH-DA) was also used (Figure 2F). And the results are consistent with the above. For •OH detection, a typical colorimetric analysis based on 3,3′,5,5′-tetramethyl-benzidine (TMB) was utilized to investigate the CDT

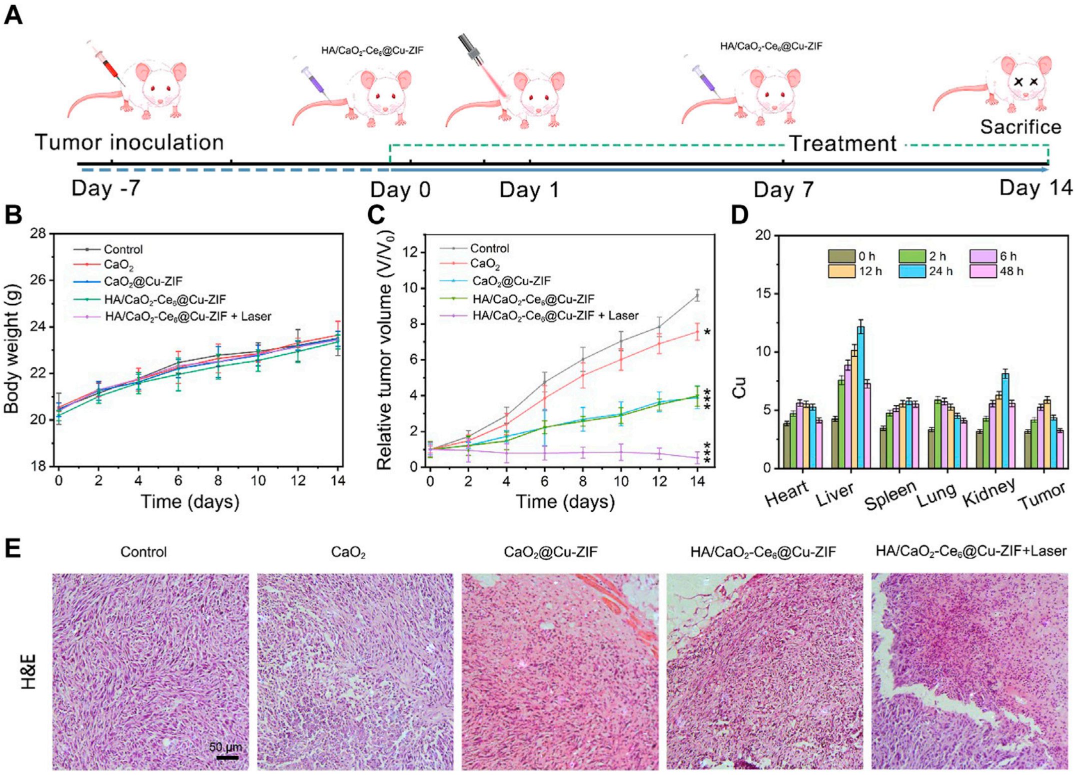

FIGURE 4
(A) Schematic illustration of Panc02 tumor-bearing mice model and treatment process. **(B)** Body weights and **(C)** relative tumor volume change curves of Panc02 tumor-bearing mice after various treatments. **(D)** Biodistribution of HA/CaO_2-Ce6@Cu-ZIF in main organs and tumors at different time points (n = 3). **(E)** H&E-stained photographs of tumor slices obtained from Panc02 tumor-bearing mice in different groups after treatment.

effect of HA/CaO_2-Ce6@Cu-ZIF. HA/CaO_2-Ce6@Cu-ZIF can catalyze the oxidation of TMB to yield blue-colored oxTMB with typical absorbances at 370 and 652 nm. Considering the biodegradable properties related to the pH value of HA/CaO_2-Ce6@Cu-ZIF, the influence of the pH on •OH generation was first analyzed (pH = 4.5, 5.5, 6.5, and 7.4). The result shows that the pH has a significant influence on the •OH generation (Figure 2G). There is no evident •OH generation at pH 7.4, while the ability of •OH generation remarkably increases with the downregulation of pH. Then the concentration effect of HA/CaO_2-Ce6@Cu-ZIF for •OH generation was also investigated (Figure 2H). It shows an advanced ability of •OH generation along with the increased concentration (5, 15, and 20 μg/mL under pH 6.5). The •OH generation ability of HA/CaO_2-Ce6@Cu-ZIF related to time was also investigated (Figure 2I).

3.3 *Invitro* experiments of HA/CaO_2-Ce6@Cu-ZIF nanoplatform

Given the successful construction of HA/CaO_2-Ce6@Cu-ZIF and advanced ROS generation capacity, the therapeutic effect of HA/CaO_2-Ce6@Cu-ZIF against Panc02 cells *in vitro* was further investigated. The therapeutic performance was first examined through the calcein-AM and propidium iodide (PI) double-staining assay (Figure 3A). The confocal laser scanning microscopy (CLSM) images show that the HA/CaO_2-Ce6@Cu-ZIF + Laser group exhibits the highest red-green ratio, where the red represents dead cells and green represents living cells, indicating the excellent anti-cancer effect of HA/CaO_2-Ce6@Cu-ZIF. Meanwhile, the flow cytometric apoptosis assay with Annexin V-FITC and PI staining was used to calculate the apoptotic cell death mediated by HA/CaO_2-Ce6@Cu-ZIF. The apoptotic ratio induced by HA/CaO_2-Ce6@Cu-ZIF under irradiation was 51.83% (the sum of Q2 and Q3), which was markedly higher than other groups under the same condition. This is mainly attributed to synergistic H_2O_2/O_2 self-supplying CDT/PDT synergistic effect. The intracellular ROS triggered by HA/CaO_2-Ce6@Cu-ZIF under laser irradiation was further investigated using a 2,7-dichlorofluorescein diacetate (DCFH-DA) probe, which can be hydrolyzed to DCFH. This can be rapidly oxidized by the generated ROS and form DCF with green-fluorescent (excited by 488 nm). The CLSM images exhibit that there is almost no green fluorescence in the control and CaO_2 groups. On the contrary, weak green fluorescence is exhibited in CaO_2@Cu-ZIF and HA/CaO_2-Ce6@Cu-ZIF groups. The strongest green fluorescence in the HA/CaO_2-Ce6@Cu-ZIF + Lase group indicates that HA/CaO_2-Ce6@Cu-ZIF under laser irradiation could generate more toxic ROS to induce tumor cell death (Figure 3B). The cytocompatibility of HA/CaO_2-Ce6@Cu-ZIF on L929 normal cells was evaluated by the 3-(4,5-dimethylthiazol-2-yl)-2,5-diphenyltetrazolium bromide (MTT) method (tetramethylazole salt microenzyme reaction colorimetric assay). As shown in Supplementary Figure S1, HA/CaO_2-Ce6@Cu-

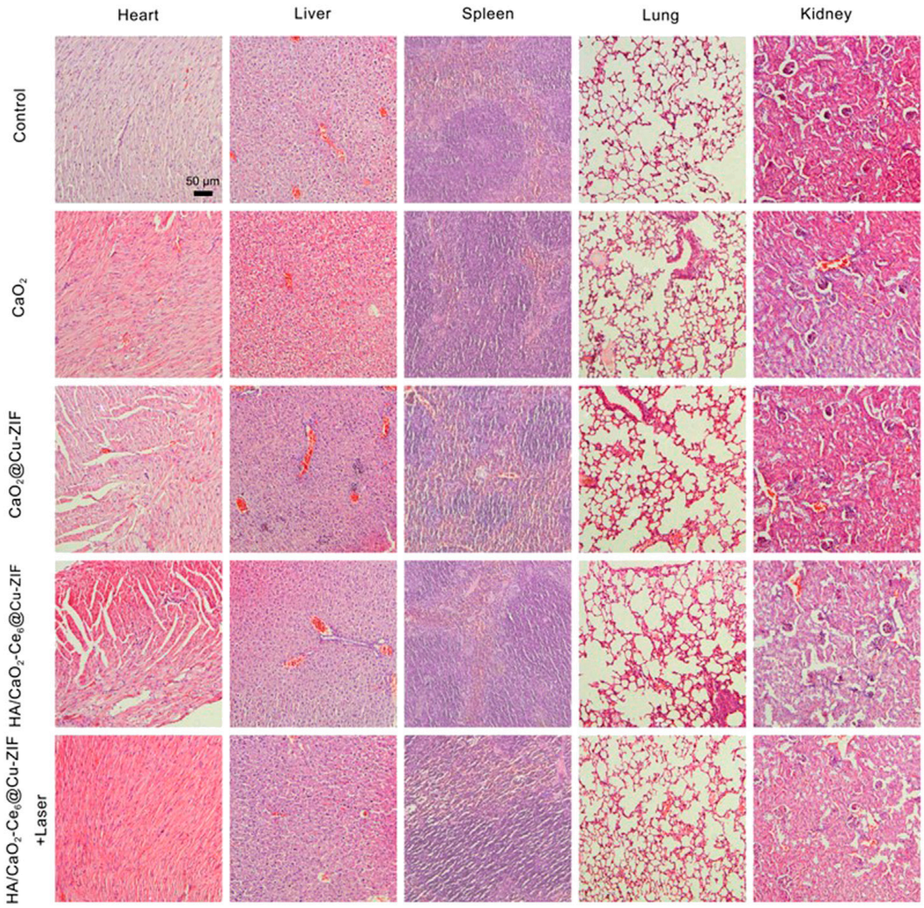

FIGURE 5
Representative H&E tissue sections from mice to monitor the histological change in heart, liver, spleen, lung, and kidney excised from different groups after treatment.

ZIF does not exhibit significant cytotoxicity to L929 cells, and the viability of cells treated with as-synthesized material for 24 h was 92.5% even at a concentration of 500 μg/mL, demonstrating the "silent" HA in the normal cellular microenvironment. Afterward, MTT assay was also used to estimate the cytotoxicity on Panc02 cells. Compared with others, the inhibition rate of HA/CaO_2-Ce6@Cu-ZIF under laser irradiation is as high as 53.5%, where the concentration of HA/CaO_2-Ce6@Cu-ZIF is 200 μg/mL (Figure 3C). Given that the Ca^{2+} overloading originating from CaO_2 could further enhance the oxidative stress and result in mitochondrial dysfunction, the mitochondrial integrities of different treatment groups were examined through JC-1 staining flow cytometry (Figure 3D). The qualitative comparison of J-monomer (green) and J-aggregates (red) following various treatments shows that the group treated with HA/CaO_2-Ce6@Cu-ZIF under laser irradiation exhibits abundant mitochondria damage. The endocytosis process of HA/CaO_2-Ce6@Cu-ZIF in Panc02 cells was evaluated using specific fluorescence properties of Ce6. As is known, when excited with 488 nm light, the loaded Ce6 can radiate green fluorescence. As shown in Figure 3E, the results suggest that HA/CaO_2-Ce6@Cu-ZIF could be effectively endocytosed by Panc02 cells and the internalization amount increased with prolonged time.

3.4 *In vivo experiments* of HA/CaO_2-Ce6@Cu-ZIF nanoplatform

Inspired by the promising *in vitro* CDT/PDT synergistic effect of HA/CaO_2-Ce6@Cu-ZIF nanoplatform, the *in vivo* therapeutic assay in Panc02 tumor-bearing C57BL/6 mice model was conducted. When the tumor sizes reached about 100 mm^3, twenty-five Panc02 tumor-bearing mice were randomly divided into five groups, followed by treatments: control, CaO2, CaO_2@Cu-ZIF, HA/CaO_2-Ce6@Cu-ZIF, and v) HA/CaO_2-Ce6@Cu-ZIF + Laser. As depicted in Figure 4A, Panc02 tumor-bearing mice were treated by intravenous administration on 1 and 7 days with injection doses of 15 mg/kg of mouse body weight. The body weight (Figure 4B) and tumor volume (Figure 4C) of mice were measured every 2 days during the treatment process. Moreover, the time-dependent Cu biodistribution of HA/CaO_2-Ce6@Cu-ZIF at the tumor and major organs were evaluated (Figure 4D). The results indicate an effective accumulation of HA/CaO_2-Ce6@Cu-ZIF at the tumor site, ensuring the following synergistic CDT/PDT therapeutics. In Figure 4B, during the treatment period, all the mice feature slight weight increases, demonstrating the negligible negative impacts of these treatments on the health of mice. As exhibited in Figure 4C, the relative tumor volume was notably suppressed in HA/

CaO_2-Ce6@Cu-ZIF + Laser group in comparison with the other groups. Specifically, the suppression rate of the HA/CaO_2-Ce6@Cu-ZIF + Laser group was determined to be 60.8%, calculated from the variation in the relative tumor volume. This high suppression is attributed to the HA/CaO_2-Ce6@Cu-ZIF induced cascade-amplified CDT/PDT therapy as follows: 1) CaO_2 decomposed to generate H_2O_2 and O_2, which alleviated the insufficiency of intracellular H_2O_2 and relieved hypoxia conditions in TME; 2) H_2O_2/O_2 self-supplying effectively enhanced the production of •OH and $^1O_2$ in Cu^{2+}-mediated CDT and Ce6-induced PDT, respectively and 3) Ca^{2+} originated from CaO_2 could further enhance the oxidative stress and result in mitochondrial dysfunction induced by Ca^{2+} overloading. Intensive therapeutic efficacy was also confirmed by hematoxylin and eosin (H&E) staining of tumor sections from each group (Figure 4E). The results were consistent with the above tumor growth data. Additionally, the histological observations of major organs (heart, liver, spleen, lung, and kidney) present negligible acute pathological toxicities and adverse effects during the treatment duration for the control or treated groups (Figure 5). These results demonstrate that HA/CaO_2-Ce6@Cu-ZIF is of high biocompatibility.

4 Conclusion

In summary, a biodegradable HA/CaO_2-Ce6@Cu-ZIF nanoplatform was rationally constructed for a H_2O_2/O_2 self-supplying and Ca^{2+} overloading CDT/PDT synergistic strategy. After arriving at tumor sites via the specific HA targeted effect, HA/CaO_2-Ce6@Cu-ZIF responded to acidic conditions in TME and released CaO_2 NPs and Ce6, as well as exposed Cu^{2+} active sites within Cu-ZIF. The released CaO_2 NPs further decomposed to efficiently generate H_2O_2 and O_2 simultaneously for enhancing •OH and $^1O_2$ production in Cu^{2+}-mediated CDT and Ce6-participated PDT, respectively. In addition, the accompanying Ca^{2+} overloading generated by the decomposition of CaO_2 NPs could induce mitochondrial dysfunction in tumor cells, further contributing to the combined CDT/PDT. Thus, this work provides an alternative strategy for smart reprogramming TME to improve the efficacy of synergistic CDT/PDT treatment.

Data availability statement

The original contributions presented in the study are included in the article/Supplementary Material, further inquiries can be directed to the corresponding authors.

Ethics statement

The animal study was reviewed and approved by Guangxi Medical University Cancer Hospital.

Author contributions

Experimental design: YuL; experiments: YaL, ZC, CS, and LX; data analysis: CS, YT, and LX; and manuscript writing: YuL and XL. All authors listed have made a substantial, direct, and intellectual contribution to the work and approved it for publication.

Funding

This study was partially supported by the National Natural Science Foundation (No. 81260083).

Conflict of interest

The authors declare that the research was conducted in the absence of any commercial or financial relationships that could be construed as a potential conflict of interest.

Publisher's note

All claims expressed in this article are solely those of the authors and do not necessarily represent those of their affiliated organizations, or those of the publisher, the editors and the reviewers. Any product that may be evaluated in this article, or claim that may be made by its manufacturer, is not guaranteed or endorsed by the publisher.

Supplementary material

The Supplementary Material for this article can be found online at: https://www.frontiersin.org/articles/10.3389/fbioe.2023.1196839/full#supplementary-material

SUPPLEMENTARY FIGURE S1
Biocompatibility of CaO2 @Cu-ZIF and HA/CaO2-Ce6@Cu-ZIF.

References

Bian, Y., Liu, B., Liang, S., Ding, B., Zhao, Y., Jiang, F., et al. (2022). Cu-based MOFs decorated dendritic mesoporous silica as tumor microenvironment responsive nanoreactor for enhanced tumor multimodal therapy. *Chem. Eng. J.* 435, 135046. doi:10.1016/j.cej.2022.135046

Cai, W., Wang, J., Chu, C., Chen, W., Wu, C., and Liu, G. (2019). Metal-organic framework-based stimuli-responsive systems for drug delivery. *Adv. Sci.* 6 (1), 1801526. doi:10.1002/advs.201801526

Cao, C., Wang, X., Yang, N., Song, X., and Dong, X. (2021). Recent advances of cancer chemodynamic therapy based on Fenton/Fenton-like chemistry. *Chem. Sci.* 13, 863–889. doi:10.1039/d1sc05482a

Cao, X., Luo, Q., Song, F., Liu, G., Chen, S., Li, Y., et al. (2023). Effects of oxidative torrefaction on the physicochemical properties and pyrolysis products of hemicellulose in bamboo processing residues. *Industrial Crops Prod.* 191, 115986. doi:10.1016/j.indcrop.2022.115986

Chang, M., Hou, Z., Wang, M., Li, C., Al Kheraif, A. A., and Lin, J. (2022). Tumor microenvironment responsive single-atom nanozymes for enhanced antitumor therapy. *Chemistry* 28 (15), e202104081. doi:10.1002/chem.202104081

Chen, Q., Yang, D., Yu, L., Jing, X., and Chen, Y. (2020). Catalytic chemistry of iron-free Fenton nanocatalysts for versatile radical nanotherapeutics. *Mater. Horizons* 7 (2), 317–337. doi:10.1039/c9mh01565e

Chen, Y. C., Liu, Y. J., Lee, C. L., Pham, K. Y., Manoharan, D., Thangudu, S., et al. (2022). Engineering H2 O2 and O2 self-supplying nanoreactor to conduct synergistic chemiexcited photodynamic and calcium-overloaded therapy in orthotopic hepatic tumors. *Adv. Healthc. Mater* 11, e2201613. doi:10.1002/adhm.202201613

Deng, K., Li, C., Huang, S., Xing, B., Jin, D., Zeng, Q., et al. (2017). Recent progress in near infrared light triggered photodynamic therapy. *Small* 13 (44), 1702299. doi:10.1002/smll.201702299

Docampo, R., and Vercesi, A. E. (2022). Mitochondrial Ca(2+) and reactive oxygen species in trypanosomatids. *Antioxid. Redox Signal* 36 (13-15), 969–983. doi:10.1089/ars.2021.0058

He, J., Fu, L. H., Qi, C., Lin, J., and Huang, P. (2021). Metal peroxides for cancer treatment. *Bioact. Mater* 6 (9), 2698–2710. doi:10.1016/j.bioactmat.2021.01.026

Hu, Y., Wang, X., Zhao, P., Wang, H., Gu, W., and Ye, L. (2020). Nanozyme-catalyzed oxygen release from calcium peroxide nanoparticles for accelerated hypoxia relief and image-guided super-efficient photodynamic therapy. *Biomater. Sci.* 8 (10), 2931–2938. doi:10.1039/d0bm00187b

Jiang, F., Zhao, Y., Yang, C., Cheng, Z., Liu, M., Xing, B., et al. (2022). A tumor microenvironment-responsive Co/ZIF-8/ICG/Pt nanoplatform for chemodynamic and enhanced photodynamic antitumor therapy. *Dalton Trans.* 51 (7), 2798–2804. doi:10.1039/d1dt04120g

Li, X., Sun, H., Li, H., Hu, C., Luo, Y., Shi, X., et al. (2021). Multi-Responsive biodegradable cationic nanogels for highly efficient treatment of tumors. *Adv. Funct. Mater.* 31 (26), 2100227. doi:10.1002/adfm.202100227

Li, W., Zhou, X., Liu, S., Zhou, J., Ding, H., Gai, S., et al. (2021). Biodegradable nanocatalyst with self-supplying fenton-like ions and H2O2 for catalytic cascade-amplified tumor therapy. *Acs Appl. Mater. Interfaces* 13 (43), 50760–50773. doi:10.1021/acsami.1c14598

Li, C., Ye, J., Yang, X., Liu, S., Zhang, Z., Wang, J., et al. (2022). Fe/Mn bimetal-doped ZIF-8-coated luminescent nanoparticles with up/downconversion dual-mode emission for tumor self-enhanced NIR-II imaging and catalytic therapy. *ACS Nano* 16, 18143–18156. doi:10.1021/acsnano.2c05152

Li, X., Hetjens, L., Wolter, N., Li, H., Shi, X., and Pich, A. (2023). Charge-reversible and biodegradable chitosan-based microgels for lysozyme-triggered release of vancomycin. *J. Adv. Res.* 43, 87–96. doi:10.1016/j.jare.2022.02.014

Liang, S., Xiao, X., Bai, L., Liu, B., Yuan, M., Ma, P., et al. (2021). Conferring Ti-based MOFs with defects for enhanced sonodynamic cancer therapy. *Adv. Mater* 33, e2100333. doi:10.1002/adma.202100333

Liu, J., Liu, T., Du, P., Zhang, L., and Lei, J. (2019). Metal-organic framework (MOF) hybrid as a tandem catalyst for enhanced therapy against hypoxic tumor cells. *Angew. Chem. Int. Ed.* 58 (23), 7890–7894. doi:10.1002/ange.201903475

Liu, B., Bian, Y., Yuan, M., Zhu, Y., Liu, S., Ding, H., et al. (2022). L-buthionine sulfoximine encapsulated hollow calcium peroxide as a chloroperoxidase nanocarrier for enhanced enzyme dynamic therapy. *Biomaterials* 289, 121746. doi:10.1016/j.biomaterials.2022.121746

Liu, B., Bian, Y., Liang, S., Yuan, M., Dong, S., He, F., et al. (2022). One-step integration of tumor microenvironment-responsive calcium and copper peroxides nanocomposite for enhanced chemodynamic/ion-interference therapy. *Acs Nano* 16 (1), 617–630. doi:10.1021/acsnano.1c07893

Lu, Y., Luo, Q., Jia, X., Tam, J. P., Yang, H., Shen, Y., et al. (2023). Multidisciplinary strategies to enhance therapeutic effects of flavonoids from Epimedii Folium: Integration of herbal medicine, enzyme engineering, and nanotechnology. *J. Pharm. Analysis* 13 (3), 239–254. doi:10.1016/j.jpha.2022.12.001

Monro, S., Colon, K. L., Yin, H., Roque, J., 3rd, Konda, P., Gujar, S., et al. (2019). Transition metal complexes and photodynamic therapy from a tumor-centered approach: Challenges, opportunities, and highlights from the development of TLD1433. *Chem. Rev.* 119 (2), 797–828. doi:10.1021/acs.chemrev.8b00211

Pandey, A., Dhas, N., Deshmukh, P., Caro, C., Patil, P., Luisa García-Martín, M., et al. (2020). Heterogeneous surface architectured metal-organic frameworks for cancer therapy, imaging, and biosensing: A state-of-the-art review. *Coord. Chem. Rev.* 409, 213212. doi:10.1016/j.ccr.2020.213212

Peng, S., Xiao, F., Chen, M., and Gao, H. (2021). Tumor-microenvironment-Responsive nanomedicine for enhanced cancer immunotherapy. *Adv. Sci. (Weinh)* 9, e2103836. doi:10.1002/advs.202103836

Qin, Y. T., Peng, H., He, X. W., Li, W. Y., and Zhang, Y. K. (2019). pH-Responsive polymer-stabilized ZIF-8 nanocomposites for fluorescence and magnetic resonance dual-modal imaging-guided chemo-/photodynamic combinational cancer therapy. *ACS Appl. Mater Interfaces* 11 (37), 34268–34281. doi:10.1021/acsami.9b12641

Ren, S.-Z., Zhu, D., Zhu, X.-H., Wang, B., Yang, Y.-S., Sun, W.-X., et al. (2019). Nanoscale metal–organic-frameworks coated by biodegradable organosilica for pH and redox dual responsive drug release and high-performance anticancer therapy. *ACS Appl. Mater. Interfaces* 11 (23), 20678–20688. doi:10.1021/acsami.9b04236

Rojas, S., Arenas-Vivo, A., and Horcajada, P. (2019). Metal-organic frameworks: A novel platform for combined advanced therapies. *Coord. Chem. Rev.* 388, 202–226. doi:10.1016/j.ccr.2019.02.032

Rui, W., Xingshu, L., and Juyoung, Y. (2021). Organelle-targeted photosensitizers for precision photodynamic therapy. *ACS Appl. Mater. Interfaces* 13, 19543. doi:10.1021/acsami.1c02019

Shan, X., Zhao, Z., Wang, C., Sun, J., He, Z., Luo, C., et al. (2022). Emerging prodrug-engineered nanomedicines for synergistic chemo-phototherapy. *Chem. Eng. J.* 442, 136383. doi:10.1016/j.cej.2022.136383

Shen, J., Yu, H., Shu, Y., Ma, M., and Chen, H. (2021). A robust ROS generation strategy for enhanced chemodynamic/photodynamic therapy via H2O2/O-2 self-supply and Ca2+ overloading. *Adv. Funct. Mater.* 31 (50), 2106106. doi:10.1002/adfm.202106106

Sivasubramanian, M., Chuang, Y. C., and Lo, L. W. (2019). Evolution of nanoparticle-mediated photodynamic therapy: From superficial to deep-seated cancers. *Molecules* 24 (3), 520. doi:10.3390/molecules24030520

Sun, Q., Liu, B., Zhao, R., Feng, L., Wang, Z., Dong, S., et al. (2021). Calcium peroxide-based nanosystem with cancer microenvironment-activated capabilities for imaging guided combination therapy via mitochondrial Ca2+ overload and chemotherapy. *Acs Appl. Mater. Interfaces* 13 (37), 44096–44107. doi:10.1021/acsami.1c13304

Sun, Q., Liu, B., Wang, Z., Feng, L., Zhao, R., Dong, S., et al. (2021). H2O2/O2 self-supplementing and GSH-depleting Ca2+ nanogenerator with hyperthermia-triggered, TME-responsive capacities for combination cancer therapy. *Chem. Eng. J.* 425, 131485. doi:10.1016/j.cej.2021.131485

Tao, W., Wang, N., Ruan, J., Cheng, X., Fan, L., Zhang, P., et al. (2022). Enhanced ROS-boosted phototherapy against pancreatic cancer via nrf2-mediated stress-defense pathway suppression and ferroptosis induction. *ACS Appl. Mater Interfaces* 14 (5), 6404–6416. doi:10.1021/acsami.1c22861

Truong Hoang, Q., Ravichandran, V., Nguyen Cao, T. G., Kang, J. H., Ko, Y. T., Lee, T. I., et al. (2022). Piezoelectric Au-decorated ZnO nanorods: Ultrasound-triggered generation of ROS for piezocatalytic cancer therapy. *Chem. Eng. J.* 435, 135039. doi:10.1016/j.cej.2022.135039

Wan, Y., Fu, L. H., Li, C., Lin, J., and Huang, P. (2021). Conquering the hypoxia limitation for photodynamic therapy. *Adv. Mater* 33 (48), e2103978. doi:10.1002/adma.202103978

Wang, L., Huo, M., Chen, Y., and Shi, J. (2018). Tumor microenvironment-enabled nanotherapy. *Adv. Healthc. Mater* 7 (8), e1701156. doi:10.1002/adhm.201701156

Wang, H., Yu, D., Fang, J., Cao, C., Liu, Z., Ren, J., et al. (2019). Renal-clearable porphyrinic metal–organic framework nanodots for enhanced photodynamic therapy. *ACS Nano* 13 (8), 9206–9217. doi:10.1021/acsnano.9b03531

Wang, C., Jia, X., Zhen, W., Zhang, M., and Jiang, X. (2019). Small-sized MOF-constructed multifunctional diagnosis and therapy platform for tumor. *ACS Biomaterials Sci. Eng.* 5 (9), 4435–4441. doi:10.1021/acsbiomaterials.9b00813

Wang, D., Wu, H., Lim, W. Q., Phua, S. Z. F., Xu, P., Chen, Q., et al. (2019). A mesoporous nanoenzyme derived from metal-organic frameworks with endogenous oxygen generation to alleviate tumor hypoxia for significantly enhanced photodynamic therapy. *Adv. Mater* 31 (27), e1901893. doi:10.1002/adma.201901893

Wang, W., Jin, Y., Xu, Z., Liu, X., Bajwa, S. Z., Khan, W. S., et al. (2020). Stimuli-activatable nanomedicines for chemodynamic therapy of cancer. *Wiley Interdiscip. Rev. Nanomed Nanobiotechnol* 12, e1614. doi:10.1002/wnan.1614

Wang, H., Gao, L., Fan, T., Zhang, C., Zhang, B., Al-Hartomy, O. A., et al. (2021). Strategic design of intelligent-responsive nanogel carriers for cancer therapy. *ACS Appl. Mater Interfaces* 13 (46), 54621–54647. doi:10.1021/acsami.1c13634

Wang, Z., Sun, Q., Liu, B., Kuang, Y., Gulzar, A., He, F., et al. (2021). Recent advances in porphyrin-based MOFs for cancer therapy and diagnosis therapy. *Coord. Chem. Rev.* 439, 213945. doi:10.1016/j.ccr.2021.213945

Wang, W., Pan, X., Yang, H., Wang, H., Wu, Q., Zheng, L., et al. (2021). Bioactive metal-organic frameworks with specific metal-nitrogen (M-N) active sites for efficient sonodynamic tumor therapy. *ACS Nano* 15, 20003–20012. doi:10.1021/acsnano.1c07547

Xie, Z., Cai, X., Sun, C., Liang, S., Shao, S., Huang, S., et al. (2019). O2-Loaded pH-responsive multifunctional nanodrug carrier for overcoming hypoxia and highly efficient chemo-photodynamic cancer therapy. *Chem. Mater.* 31 (2), 483–490. doi:10.1021/acs.chemmater.8b04321

Xie, Z., Liang, S., Cai, X., Ding, B., Huang, S., Hou, Z., et al. (2019). O2-Cu/ZIF-8@Ce6/ZIF-8@F127 composite as a tumor microenvironment-responsive nanoplatform with enhanced photo-/chemodynamic antitumor efficacy. *ACS Appl. Mater. Interfaces* 11, 31671. doi:10.1021/acsami.9b10685

Yang, P., Men, Y., Tian, Y., Cao, Y., Zhang, L., Yao, X., et al. (2019). Metal-organic framework nanoparticles with near-infrared dye for multimodal imaging and guided phototherapy. *ACS Appl Mater Interfaces* 11 (12), 11209–11219. doi:10.1021/acsami.9b01286

Yang, B., Chen, Y., and Shi, J. (2019). Reactive oxygen species (ROS)-Based nanomedicine. *Chem. Rev.* 119 (8), 4881–4985. doi:10.1021/acs.chemrev.8b00626

Yang, G., Phua, S. Z. F., Lim, W. Q., Zhang, R., Feng, L., Liu, G., et al. (2019). A hypoxia-responsive albumin-based nanosystem for deep tumor penetration and excellent therapeutic efficacy. *Adv. Mater* 31 (25), e1901513. doi:10.1002/adma.201901513

Yang, X. X., Feng, P., Cao, J., Liu, W., and Tang, Y. (2020). Composition-engineered metal-organic framework-based microneedles for glucose-mediated transdermal insulin delivery. *ACS Appl Mater Interfaces* 12 (12), 13613–13621. doi:10.1021/acsami.9b20774

Yang, Y., Wu, H., Liu, B., and Liu, Z. (2021). Tumor microenvironment-responsive dynamic inorganic nanoassemblies for cancer imaging and treatment. *Adv. Drug Deliv. Rev.* 179, 114004. doi:10.1016/j.addr.2021.114004

Yang, L., Shaojie, Z., Xingwu, J., Yanyan, L., Kun, W., Chaochao, W., et al. (2021). Intracellular mutual promotion of redox homeostasis regulation and iron metabolism disruption for enduring chemodynamic therapy. *Adv. Funct. Mater.* 31, 2010390. doi:10.1002/adfm.202010390

Yu, Y., Wu, S., Zhang, L., Xu, S., Dai, C., Gan, S., et al. (2022). Cationization to boost both type I and type II ROS generation for photodynamic therapy. *Biomaterials* 280, 121255. doi:10.1016/j.biomaterials.2021.121255

Zhang, Z., Sang, W., Xie, L., and Dai, Y. (2019). Metal-organic frameworks for multimodal bioimaging and synergistic cancer chemotherapy. *Coord. Chem. Rev.* 399, 213022. doi:10.1016/j.ccr.2019.213022

Zhang, Y., Bo, S., Feng, T., Qin, X., Wan, Y., Jiang, S., et al. (2019). A versatile theranostic nanoemulsion for architecture-dependent multimodal imaging and dually augmented photodynamic therapy. *Adv. Mater* 31 (21), e1806444. doi:10.1002/adma.201806444

Zhang, M., Song, R., Liu, Y., Yi, Z., Meng, X., Zhang, J., et al. (2019). Calcium-overload-mediated tumor therapy by calcium peroxide nanoparticles. *Chem* 5 (8), 2171–2182. doi:10.1016/j.chempr.2019.06.003

Zhang, Y., Zhang, X., Yang, H., Yu, L., Xu, Y., Sharma, A., et al. (2021). Advanced biotechnology-assisted precise sonodynamic therapy. *Chem. Soc. Rev.* 50, 11227. doi:10.1039/d1cs00403d

Zhang, S., Liu, Y., Cao, Y., Zhang, S., Sun, J., Wang, Y., et al. (2022). Targeting the microenvironment of vulnerable atherosclerotic plaques: An emerging diagnosis and therapy strategy for atherosclerosis. *Adv. Mater* 34 (29), e2110660. doi:10.1002/adma.202110660

Zhao, X., Zhang, Z., Cai, X., Ding, B., Sun, C., Liu, G., et al. (2019). Postsynthetic ligand exchange of metal–organic framework for photodynamic therapy. *ACS Appl. Mater. Interfaces* 11 (8), 7884–7892. doi:10.1021/acsami.9b00740

Zhao, P., Jiang, Y., Tang, Z., Li, Y., Sun, B., Wu, Y., et al. (2021). Constructing electron levers in perovskite nanocrystals to regulate the local electron density for intensive chemodynamic therapy. *Angew. Chem. Int. Ed. Engl.* 60 (16), 8905–8912. doi:10.1002/anie.202100864

Zhao, L. P., Chen, S. Y., Zheng, R. R., Kong, R. J., Rao, X. N., Chen, A. L., et al. (2021). Self-delivery nanomedicine for glutamine-starvation enhanced photodynamic tumor therapy. *Adv. Healthc. Mater* 11, e2102038. doi:10.1002/adhm.202102038

Zheng, P., Ding, B., Zhu, G., Li, C., and Lin, J. (2022). Biodegradable Ca2+ nanomodulators activate pyroptosis through mitochondrial Ca2+ overload for cancer immunotherapy. *Angew. Chem. Int. Ed. Engl.* 134. doi:10.1002/ange.202204904

Zhou, Y., Fan, S., Feng, L., Huang, X., and Chen, X. (2021). Manipulating intratumoral Fenton chemistry for enhanced chemodynamic and chemodynamic-synergized multimodal therapy. *Adv. Mater* 33 (48), e2104223. doi:10.1002/adma.202104223

Frontiers in
Bioengineering and Biotechnology

Accelerates the development of therapies, devices, and technologies to improve our lives

A multidisciplinary journal that accelerates the development of biological therapies, devices, processes and technologies to improve our lives by bridging the gap between discoveries and their application.

Discover the latest Research Topics

See more →

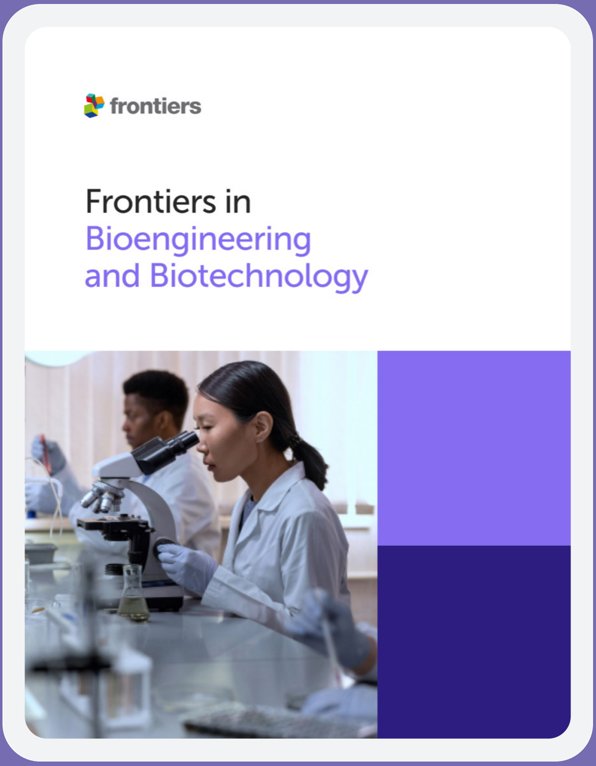

Frontiers
Avenue du Tribunal-Fédéral 34
1005 Lausanne, Switzerland
frontiersin.org

Contact us
+41 (0)21 510 17 00
frontiersin.org/about/contact